4-2020

Applications of Image Processing Techniques and Spatial Data Analytics for Pressure Mapping Analysis

Joan Yamil Martinez
Western Michigan University, Jnmart@gmail.com

APPLICATIONS OF IMAGE PROCESSING TECHNIQUES AND SPATIAL DATA ANALYTICS FOR PRESSURE MAPPING ANALYSIS

by

Joan Yamil Martinez

A dissertation submitted to the Graduate College
in partial fulfillment of the requirements
for the degree of Doctor of Philosophy
Industrial Engineering
Western Michigan University
April 2020

Doctoral Committee:

Steven Butt, Ph.D., Chair
Tycho Fredericks, Ph.D., CPE
Lee Wells, Ph.D.
Ikhlas Abdel-Qader, Ph.D.

APPLICATIONS OF IMAGE PROCESSING TECHNIQUES AND SPATIAL DATA ANALYTICS FOR PRESSURE MAPPING ANALYSIS

Joan Yamil Martinez, Ph.D.

Western Michigan University, 2020

The technological advancements in sensors, monitoring systems, and tracking devices are changing how we study our environment; big data sets are becoming more and more prevalent due to the increase of information gathered with ease. One system benefiting from these technological improvements is pressure mapping technology, an easy-to-use and cost-effective solution for assessing contact pressure distributions. Pressure mapping systems generally produce data sets of very large volume, especially when used for continuous tracking and monitoring, and are widely used for research in fields of ergonomics, sports, industries, and health disciplines.

Pressure mapping systems are particularly important in the study of human-chair seating interactions. Researchers have widely used pressure mapping systems to study these interactions and their relationship with comfort/discomfort across different conditions. The analysis of seating pressure maps usually consists in evaluating descriptive pressure measures and using visual feedback for assessing pressure distributions. Unfortunately, current analytical techniques do not provide clear insights about pressure distribution patterns nor spatial relationships within seating pressure maps; these are needed to further understand human-chair interactions. The need for additional pressure distribution measures, along with quantitative techniques for assessing and comparing pressure maps, have also been emphasized in literature.

This work studies the applications of machine learning, spatial data analytics, digital image processing, and optimal image registration as new techniques for pressure mapping analysis, with

the objective of implementing these techniques to pre-process, analyze, and compare seating pressure map images. The results of this study demonstrate the practicality and effectiveness of using these techniques for (1) removing extrinsic pressure artifacts (outliers) by using density-based spatial clustering, (2) measuring distribution patterns and spatial relationships by using spatial autocorrelation and statistical features of images, and (3) aligning and comparing pressure map by using image registration and similarity/dissimilarity coefficients.

The use of DBSCAN and DENCLUE clustering algorithms were found to be suitable for identifying and eliminating extrinsic pressure artifacts (outliers), with obtained overall accuracies over ninety-nine percent. Moran's I spatial autocorrelation measure, and image statistical features of Skewness, Correlation (GLSD), Gradient Contrast/Mean (GLD), Gradient Second Moment (GLD), and Homogeneity (GLSD) were found to be appropriate for measuring unique aspects of pressure distributions within pressure maps. Image registration based on the minimization of the Mean Square Error (MSE) was also suitable for aligning pressure map images, with similarity and dissimilarity coefficients of Pearson Correlation Coefficient, Minimum Ratio, L_1 Norm, and Intensity Ratio Variance being particularly unique when comparing aligned pressure maps.

These methodologies can help future seating research by providing additional analytical tools for a better understanding of user-chair interactions and their relationships with sitting comfort/discomfort, in both static and dynamic sitting environments. While findings in this study are in the context of task seating (i.e. mousing and typing), these techniques can also be tailored and employed in other seating research applications (e.g., automobile seating, aircraft pilot seats, and paraplegic seating), non-seating pressure map research (e.g., gait analysis, industrial applications, and sports fields), or research studies using spatially related three-dimensional datasets (e.g., surface topography, contour data, and heat maps).

ACKNOWLEDGMENTS

I would like to express my deepest appreciation to my Ph.D. advisor, Dr. Steven Butt, whom I will always be grateful for his relentless support, encouragement, and dedication throughout these years; thank you very much for making this dream a reality. I would also like to extend my sincere gratitude to Dr. Tycho Fredericks, for the profound belief in my work, valuable advice, and guidance during this journey. Many thanks to my committee members, Dr. Lee Wells and Dr. Ikhlas Abdel-Qader, for their extensive knowledge and useful contributions.

I very much appreciate the assistance of Dr. Megan Hammond, Dr. Teresa Bellingar, and Dr. Timothy Green, for their constructive advice, positive criticism, and insightful suggestions. Special thanks should also go to all staff of the WMU IE department, specially to Dr. Azim Houshyar, Dr. Bob White, and Jerri Pursley, thank you for always advocating for my success.

I am extremely grateful to my parents, Gloria and Pericles, for their love, prayers, and continuous support throughout my life. I also wish to thank my brothers, sister, extended family, and dear friends for the care and encouragement provided during this long process.

And finally, to my wife Lina, for being my beacon of light throughout difficult times, thank you very much for all your patience, and for always providing emotional support, care, and love.

Joan Yamil Martinez

TABLE OF CONTENTS

Table of Contents—Continued

Table of Contents—Continued

CHAPTER

Table of Contents—Continued

CHAPTER

APPENDICES

Table of Contents—Continued

APPENDICES

LIST OF TABLES

List of Tables—Continued

LIST OF FIGURES

LIST OF EQUATIONS

List of Equations—Continued

CHAPTER I

INTRODUCTION

The technological advancements in sensors, monitoring systems, tracking devices, and the growth of Internet of Things (IoT) are changing how we interact and study our environment. Big data sets are becoming more and more prevalent due to the increase of information gathered with ease. A demanding emphasis in the analysis of such data sets is currently in place to help and support the decision-making process. One of the technologies benefiting from these improvements is pressure mapping systems, a practical and convenient solution for assessing contact pressure distributions. Pressure mapping systems generally produce data sets of very large volume, especially when used for continuous tracking and monitoring, and are widely used for research in fields of ergonomics, sports, industries, and health disciplines (Fredericks et al., 2016; Makhsous et al., 2012; Misiewicz et al., 2015; Nagel et al., 2008).

Pressure mapping systems are particularly important in the study of human-chair sitting interactions. Researchers have widely used pressure mapping systems to study these interactions and their relationship with sitting comfort/discomfort (Zemp et al., 2016). With employees spending more time than ever in a seated position, studies of sitting comfort/discomfort have been prevalent (Cascioli et al., 2011; De Looze et al., 2003; Openshaw, 2011; Zemp et al., 2015). The advent of computers and visual display units (VDUs) lead to high demands in jobs where tasks are mostly sedentary, with prolonged computer use being now common and expected in current working environments (Afanuh & Johnson, 2017; Studebaker & Murphy, 2014). Office-based workers, in particular, have been reported to spend between four to six hours of their working hours performing sedentary sitting tasks, with a high proportion of their sitting times accrued in bouts of at least 20 or 30 minutes of prolonged sitting (Hadgraft et al., 2016; Thorp et al., 2012).

Prolonged sitting time has been associated with workers' discomfort, dissatisfaction, fatigue and reduced performance (Chester et al., 2002; M. H. Liao & Drury, 2000; Pitman & Ntuen, 1996; Waongenngarm et al., 2015). The decrease in performance, as a result of prolonged sitting and the environmental stressors associated with it, has been a subject of study. As fatigue and discomfort levels increase, workers may shift their attention from the task at hand to the mitigation of discomfort, especially when high levels of discomfort are reported (M. H. Liao & Drury, 2000; Pitman & Ntuen, 1996). Prolonged sitting time may also have a drastic effect in workers' health. Several health issues have been reported due to improper sitting postures and prolonged sitting time with low levels of seating comfort. Musculoskeletal disorders in the back, neck, shoulders, arms and legs have been reported with Low Back Pain (LBP) being particularly common (Zemp et al., 2015, 2016). Lis et al. (2007) remarked that sitting by itself does not increase the likelihood of having LBP but rather the combination of awkward postures and sitting for more than half a workday. A comfortable and ergonomic-oriented working environment should be provided and aimed at promoting employees' health and well-being. Additionally, when considering the task and users' characteristics, matching a proper task chair with an ergonomics training program can be beneficial to worker's comfort and productivity. Studies have documented improvements in productivity and overall efficiency of over nine percent when investing in appropriate and comfortable chairs (Miles, 2001; Peck, 1992).

Researchers and chair manufacturers have constantly studied human-chair interactions across different conditions (Cascioli et al., 2016; Fenety et al., 2000; Makhsous et al., 2012;

Stinson et al., 2002). Many of these studies have used objective measures, such as measurements of postures, body movements, electromyography, foot volume change, magnet resonance imaging and motion tracking systems (Zemp et al., 2015); however, the use of pressure measuring systems has been predominant in seating research for being an easy and cost-effective solution to assess the pressure measurements of seat pans and backrests (Zemp et al., 2016).

Pressure Mapping

Pressure mapping is an evaluation tool for assessing pressure distributions. A pressure mapping system consists of a pressure interface, a data acquisition unit, and a computer software. Different technologies are currently available for pressure measurement systems, with their differences lying in the type of sensor used: capacitive, resistive, piezoelectric, or piezoresistive (Ashruf, 2005; Bloss, 2011). Even if sensor technologies are manufactured under different principles, the underlying concept is the same: to output an electrical signal proportional to the measured pressure (Ashruf, 2005). The sensors in the pressure interface can be arranged as a grid-based mat, as single-point sensors, or designed for specific pressure solutions (see Fig. 1). The sensors' output signals are sent to the data acquisition electronics for sampling and processing, and then sent to a computer (via wired or wireless connection) for collection and analysis using the proprietary software solution provided by the pressure mapping manufacturer.

A pressure mapping system measures the uniaxial pressure loads applied to the sensors, and records them as the interface pressure between two surfaces. Pressure mapping systems do not measure shear or contour forces (Fenety et al., 2000; A. R. Kumar, 2007). The reliability and accuracy of pressure mapping systems have been questioned by researchers. A calibration procedure, where a uniform pressure is applied across the interface, has been recommended by researchers before a pressure mapping system is used. This procedure minimizes sensors' output variations and system errors, and it also mitigates problems of pressure drift, repeatability, linearity and hysteresis (Misiewicz et al., 2015). Researchers have also concluded that measures of pressure mapping systems are accurate, repeatable, and reliable (Misiewicz et al., 2015; Stinson et al., 2002, 2003).

Figure 1. Pressure mapping systems. Left: Mat (NexGen Ergonomics), Right: Glove (BodiTrak)

There is no defined protocol for using pressure mapping systems in seating research; however, many researchers agree that pressure measures should be collected after a set amount of sitting time to avoid pressure drift. Several studies have shown that pressure values from pressure mapping systems will increase over time for the first few minutes of sitting time (Crawford et al., 2005; Stinson et al., 2002; Zemp et al., 2016). This increase in pressure has been partially attributed to a phenomenon known as pressure creep, where pressure values increase over time while the load on sensors remain constant (Stinson et al., 2002). Researchers recommend recording pressure maps after the first 2 to 8 minutes of sitting time, where values of pressure measures tend to stabilize after that period (Crawford et al., 2005; Stinson et al., 2002). Grid-based interfaces, or pressure sensing mats, are generally used in seating research. Their main purpose is to assess the contact pressure between a chair and its user. Figure 2 shows an example of a subject's seating pressure map obtained using a pressure sensing mat. This figure shows values of pressure represented using a colormap, with the center of pressure displayed as a black cell.

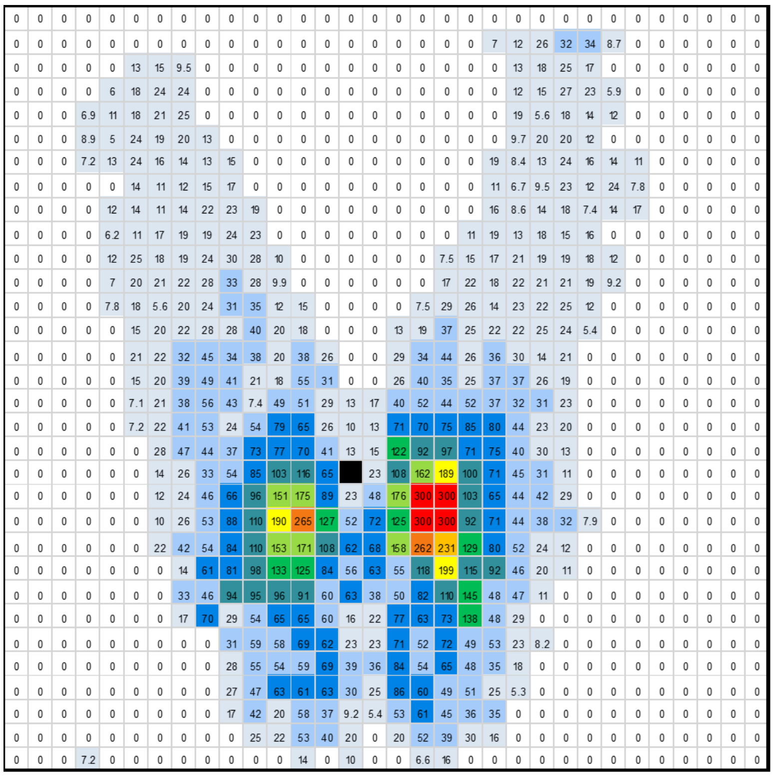

Figure 2. Example of a subject's pressure map (mmHg) during sitting

Pressure sensing mats are commercially available in many sizes and resolutions. Researchers have used pressure sensing mats with sensors configured in a 15 x 15 array, a 16 x 16 array, or a 32 x 32 array (Crawford et al., 2005; Fredericks et al., 2016; Stinson et al., 2002; Zemp et al., 2016). Measurements of pressure obtained from pressure sensing mats are generally given in units of millimeters of mercury (mmHg) and are generally outputted as stacked columns, with each column representing a pressure map frame. The maximum sampling frequencies are a function of the number of sensing elements, the sensors' technologies, and the data acquisition system's capabilities. Sampling frequencies are generally set between 1 Hz and 10 Hz (Makhsous et al., 2012; Zemp et al., 2016). While more detail is provided when using high-resolution pressure mats (e.g., 32 x 32) and high-frequency data acquisition units (e.g., 10Hz sampling), it is important to note that this combination can easily produce large amounts of data in a short period of time.

Grid-base pressure mapping interfaces such as pressure mats are also prone to interferences due to torque forces, shear forces, pinches, and/or creases; these can create false or unwanted pressure readings in non-contact regions of the pressure interface (see Fig. 3). The detection of these unwanted readings (i.e., extrinsic pressure artifacts) is essential before running any further analysis. Many of the pressure measures depicted in the next section are sensitive to these pressure artifacts, and the removal of these is of vital importance to obtain true and accurate results.

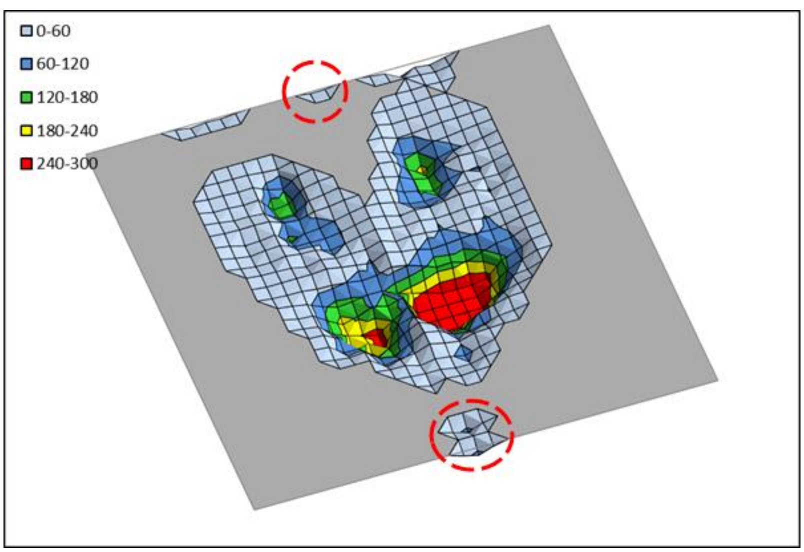

Figure 3. Example of a subject's pressure map frame with marked pressure artifacts

Seating Pressure Measures

Researchers have used various seating pressure measures when assessing user-chair interactions during sitting (Butt et al., 2005; Fenety et al., 2000; Titus & Polgar, 2009; Zemp et al., 2015, 2016). Table 1 shows a comprehensive list of pressure measures commonly used in seating research along with their definitions.

Table 1. Seating pressure measures commonly used in seating research studies

Seating pressure measure	Definition
Sum of pressure	Total amount of pressure of all sensors
Mean pressure	Average of all non-zero sensor values
Maximum pressure	Highest individual sensor value
Contact area	Number of sensors with non-zero values
Center of pressure	Point of application of the resultant forces of all non-zero sensor values
Coefficient of Variation	Ratio of the standard deviation of pressure to the average pressure
Pressure gradient	Change in pressure per unit distance for each individual non-zero sensor value
Maximum pressure gradient	Highest pressure gradient
Mean pressure gradient	Average of pressure gradients
IT* dispersion index	Ratio of sum of pressure under ischial tuberosities in relation to sum of pressure

*Ischial Tuberosities

Pressure measures described in Table 1 were shown to be useful in describing human-chair interactions (Zemp et al., 2015). Most of these measures rely on basic measures of pressure map readings (e.g., average, maximum, and standard deviation), while others require expert knowledge to locate specific regions of interest (e.g., IT dispersion index). Unfortunately, many of these seating pressure measures have some limitations when describing the spatial relationship or pressure distribution patterns within a pressure map. Figure 4 shows examples of pressure maps from two different subjects during sitting. This figure shows significant differences between respective pressure maps in terms of the shape, location, and pressure distribution patterns. However, when calculating commonly used pressure measures, such as sum of pressure, contact area, or coefficient of variations, there are no substantial differences between these measures (see Table 2). Due to information loss, one might incorrectly conclude that no significant differences are present between these pressure maps from the perspective of these objective measures. New pressure mapping measures are needed to detect these differences by recovering information loss.

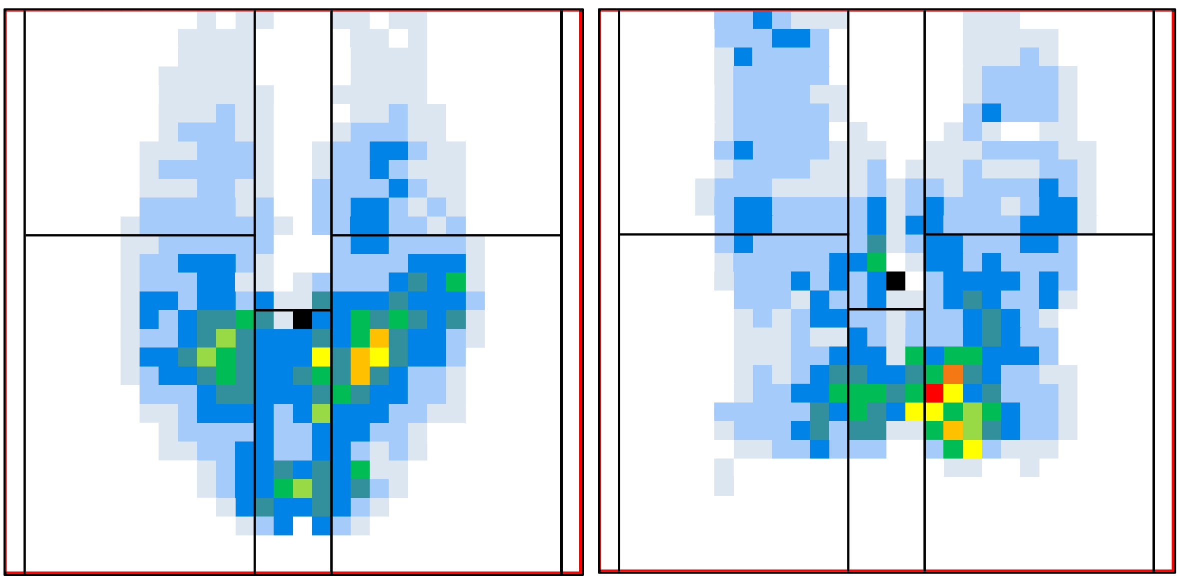

Figure 4. Example of subjects' pressure map differences during sitting

Table 2. Seating pressure measures for pressure maps shown in Figure 4

Pressure measure	**Sample 117-1-958 (Left)**	**Sample 109-1-1141 (Right)**	**Relative Δ (%)**
Sum of pressure (mmHg)	10,246.31	10,237.17	-0.09 %
Contact area	384	398	3.65 %
Coefficient of Variation	0.71	0.72	1.41 %

Researchers have used the visual feedback provided by the pressure mapping systems' software as a way to identify differences or similarities between pressure maps (Stinson et al., 2003; Titus & Polgar, 2009). However, visual feedback assessment is not a practical approach when comparing numerous subjects' pressure maps, or when assessment of continuous pressure maps is needed during dynamic sitting. The need for new seating pressure measures and comparative techniques for pressure maps have also been emphasized in current literature (Zemp et al., 2015, 2016). These new techniques should be cross-functional for applications in static (i.e., single map) and dynamic (i.e., sequential temporal maps) environments.

The focus of this research is to study the applications of unsupervised machine learning techniques, spatial data analytics, digital image processing, and optimal image registration methods as additional analytical tools for pressure mapping analysis. The objectives are to (1) introduce new techniques for pre-processing pressure maps (data cleansing), (2) introduce new pressure measures, and (3) introduce a toolset for aligning and comparing pressure maps. New analytical tools are discussed and presented in the context of seating research, but extensions to other potential applications in research using non-seating pressure maps are briefly discussed in the conclusions.

A literature review is presented in the next chapter where the use and practicality of current seating pressure measures are discussed. A review of current analytical techniques used in dynamic sitting research and methods for pressure map aggregation/comparison is also presented. Literature on the use of interdisciplinary tools and their application in the context of seating research is also examined.

CHAPTER II

LITERATURE REVIEW

Pressure Measures

Researchers, along with chair manufacturers, have conducted sitting research using pressure mapping systems across different conditions (Crawford et al., 2005; Fenety et al., 2000; Fredericks et al., 2016; Makhsous et al., 2012; Stinson et al., 2002; Zemp et al., 2016). Zemp et al. (2015) examined the relationship between subjective comfort/discomfort and pressure measurements while sitting in office chairs. In their literature review, the authors identified several pressure measures used by researchers in their studies: sum of pressure, average pressure, peak pressure, contact area, and center of pressure. While some of these measures were suggested as suitable measures for assessing comfort/discomfort when sitting in office chairs, the authors emphasized the importance of using different parameters of pressure distribution, with applications in both static and dynamic environments, to further evaluate human-chair interactions.

Zemp et al. (2016) also evaluated the relationships between specific pressure measures and their usefulness in differentiating pressure distributions between office chairs. The authors listed several pressure measures such as mean pressure, pressure standard deviation, contact area, mass/force, peak pressure and transverse pressure gradients as commonly used among researchers. Measures of peak and mean pressures were particularly highlighted as the only measures used for evaluating and identifying different among the different office chairs and seating positions. The authors also emphasized the need for suitable pressure measurements and/or methodologies in order to compare office chairs or seating positions.

In the study conducted by Zemp et al. (2016), another main objective was to understand the inter-relationships and correlation between pressure measures during sitting. To achieve this, the authors conducted a study using 20 subjects (15 males, 5 females), nine selected office chairs from six different manufacturers, and two pressure sensor mats placed on both the backrest and seat pan of each chair. The study task simulated the use of a visual display unit (VDU) in a workplace environment by requesting subjects to choose a sitting posture and place their fingers on a keyboard while fixing their eyes on the screen. After a one-minute sitting settling time, the authors obtained the average pressure readings collected during a 5-second time interval and proceeded to calculate various common measures of pressure distribution.

Early in the study, Zemp et al. (2016) emphasized the need of new pressure measures; however, the authors calculated seating pressure measures commonly used in the literature: peak pressure, mean pressure, standard deviation of pressure, total contact area, and force. The authors also included measures of pressure gradient, and defined the gradient as the geometrical addition of the pressure derivate of the two sensor mat directions (x, y) resulting in a $m - 1 \times n - 1$ matrix (Zemp et al., 2016, p. 4). With the gradient matrix, the authors calculated measures of maximum gradient, mean gradient and standard deviation of the gradient. Partial correlation analysis was used as a dimension reduction technique to isolate possible meaningful pressure measures for evaluating office chairs. The authors found that four measures (contact area, force, maximum gradient, and mean gradient) could describe pressure distributions on the seat pan, and three measures were needed for the backrest (standard deviation of pressure, force, and standard deviation of gradient).

As one of the key objectives in the study was to evaluate the effectiveness of the pressure measures in comparing pressure distributions between office chairs, the use of the reduced set of measures – found during partial correlation analyses – to measure their effectiveness in comparing pressure distribution among different office chairs would have been insightful. However, the authors decided to use the entire set of calculated pressure measures during their analysis. Results from the study indicated that office chair differences were meaningful when evaluating the seat pan measures of max gradient, mean gradient, and standard deviation of gradient. The study also found that all measures, with the exception of contact area, were meaningful in finding differences between the backrests of the office chairs during a reclined position – when subjects where in full contact with the backrest. Zemp et al. (2016) acknowledged that differences in seat pan and backrest pressure measures among office chairs can be caused by many unknown factors, and that studied pressure measures were also limited to static evaluations of pressure distributions within their research work.

Dynamic Sitting

Research has also shown that sitting is a dynamic activity (Fenety, 1995; Fleischer et al., 1987). Seated subjects move continuously and more often according to tasks demands (Fenety et al., 2000). Dynamic sitting is considered a natural behavior for prolonged sitting subjects. It is common for subjects to constantly move to: (1) avoid undesirable static work postures, (2) reduce the discomfort from static loadings, and/or (3) increase the blood flow in weight bearing regions of the buttocks (Butt et al., 2005; Winkel, 1986). The use of dynamic sitting pressure measures, for analysis in continuous sitting applications, could be useful in understanding subjects' sitting behavior and user-chair dynamic interactions.

Bhatnager et al. (1985) and Fenety et al. (2000) have studied, to some extent, the relationship between discomfort and movement; both suggesting that sitting discomfort and seated movements are time dependent, where movements increase over time possibly due to discomfort. Others researchers have successfully incorporated continuous pressure measures, such as center of pressure, during in-chair-movement in their studies (Cascioli et al., 2016; Fenety et al., 2000). Unfortunately, relying solely on tracking and monitoring of the movement of the center of pressure does not provide clear insights about pressure distribution patterns during dynamic sitting (e.g., positional shifts, dynamic pressure redistributions, and/or postural changes).

Fujimaki & Mitsuya (2002) proposed the use of neural networks as an evaluation method for dynamic body pressure distributions. The authors found that it was possible to evaluate dynamic pressure mapping data by measuring the changes in ignited neurons over time. These neurons were then used as input for a clustering algorithm to identify pressure patterns related to discomfort. A drawback of tracking changes in neurons is that neural networks are created in a subject-by-subject basis and cannot be used as a generalizable measure of dynamic pressure redistributions.

Pressure Maps Aggregation

Standardizing and aggregating pressure maps have also been discussed in the literature. Interfaces in pressure mapping systems are usually configured for high sensitivity, making them capable of recording minor variations of pressure during a testing period. Some pressure mapping systems include data acquisition units that are also capable of recording many readings over a short period of time when using high frequency sampling. Nevertheless, results from pressure mapping analyses are often based on few pressure map readings collected in a short period of time. Some researchers have used a single pressure map frame for their analyses, while others have used the average of pressure maps collected in less than a five seconds period – a technique commonly used for aggregating pressure maps (Butt et al., 2005; Zemp et al., 2016).

Since pressure mapping systems record raw pressure, direct comparison between subjects' pressure maps is often not appropriate due to differences in subjects' anthropometry. Butt et al. (2005) proposed a methodology for aggregating multiple pressure map readings into a standardized composite pressure map. The methodology described in the study use averages of multiple pressure maps frames, from an individual's recording session, to create an aggregate map. The aggregate maps were then normalized using the maximum pressure value recorded in the map. The resulting aggregate pressure maps are unitless and used to compare pressure maps between subjects. This aggregation method could also be useful when comparing within-subject pressure maps (e.g., different time intervals, different chairs used, or a pre- and post- clinical intervention). A composite pressure map method was also proposed by the authors where the unitless pressure maps were combined using unweighted averages.

Image Processing

Tan et al. (2001) speculated that pattern recognition algorithms developed for computer vision could be applied for interpreting sitting postures from the analysis of pressure distribution data. The authors introduced pattern recognition techniques using principal components analysis on grayscale images of pressure maps. Techniques such as these have been previously applied to the problem of computer face recognition (Pentland et al., 1994; Turk & Pentland, 1991). Tan et al. (2001) described that one of the disadvantages of using principal component analysis, in the context of seating pressure distributions, is the lack of physical interpretations associated with eigen-posture spaces (p. 267).

Techniques from computer vision and image registration fields have been extensively applied to medical imaging (Kurani et al., 2004; Oliveira & Tavares, 2014; Tang & Chen, 2012); these techniques are primarily used to find matching alignments of medical images (Fig. 5). Alignment of medical images is required when working with different imaging sources (e.g., tomography, magnetic resonance imaging, and positron emission tomography) or when working with spatiotemporal image sequences. Image processing techniques are also used to measure the similarity relationship between sets of images, extract global image descriptors, and/or apply image transformation functions (Goshtasby, 2012).

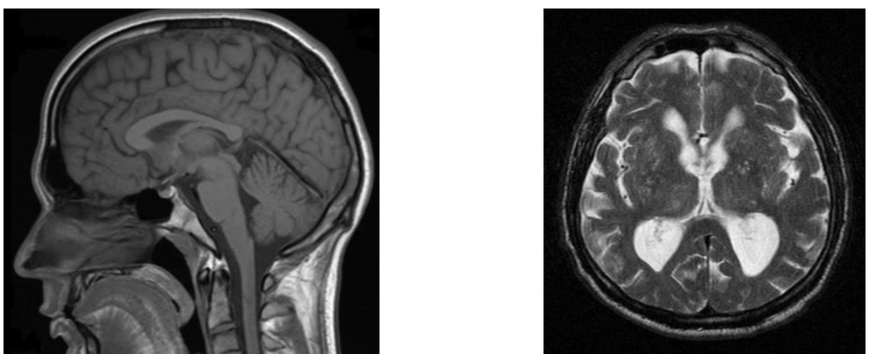

Figure 5. Magnetic resonance scan (left), Scanned brain tissue section (right)

Source: Left (Januschka, 2006) CC BY-SA 3.0, Right (Dilmen, 2005) CC BY-SA 3.0.

Bogie et al. (2008) introduced a multistage Longitudinal Analysis and Self-Registration (LASR) technique that emphasizes in real-time within-subject seating pressure image analysis. Unfortunately, the LASR algorithm requires certain conditions to be met for it to be implemented successfully. The algorithm assumes that the imaging scale is constant over time and that a symmetric pressure map is present. Pressure map symmetry is particularly important as the algorithm uses the midline of the pressure map image as a registration landmark. Other requirements include a replication of the seating position between evaluations, and collecting pressure maps with easily-identified pressure landmarks. Even with proper conditions in place, authors could see misalignments between pressure map images after applying the LASR algorithm.

While the benefits of introducing image processing techniques in the analysis of pressure mapping are evident, no other additional studies have been found to date where extensive use of image processing techniques are used for evaluating sitting pressure maps.

Spatial Data Analytics

The evolution of Geographic Information Systems (GIS) has been possible thanks to advancements and developments in the field of spatial data analytics (Goodchild & Haining, 2003). Spatial data analysis is dynamically integrated with GIS to allow the manipulation of raw geographical, topological, and geometric information to analyze possible spatial relationships (Anselin, 1992). Many geographically-based studies require use of spatial analytics to find such relationships, with many implementing spatial dependency or autocorrelation measures in their studies (Banerjee, 2016; Menafoglio & Secchi, 2017; Reibel, 2007).

Applications and techniques used in spatial data analytics can be extended for evaluating and analyzing the spatial relationships in pressure maps. Grid-base pressure interfaces (i.e., pressure mats) measure and record pressure readings in a two-dimensional space. The resulting pressure maps can then be rendered as three-dimensional (3D) topographic surfaces by using the measured values of pressure on the z-axis (see Fig. 6). To date, no studies have been found where spatial data analytics have been introduced for evaluating pressure maps.

Implementing spatial data analytics in pressure mapping analysis, while manipulating pressure maps as geographical and/or topographical surfaces, could help in identifying spatial relationships or space features descriptors. In particular, the use of spatial clustering can be a viable pre-processing technique for cleaning extrinsic pressure artifacts and outliers in raw pressure maps. To date, no studies were found where spatial outlier detection techniques are used in pressure mapping applications.

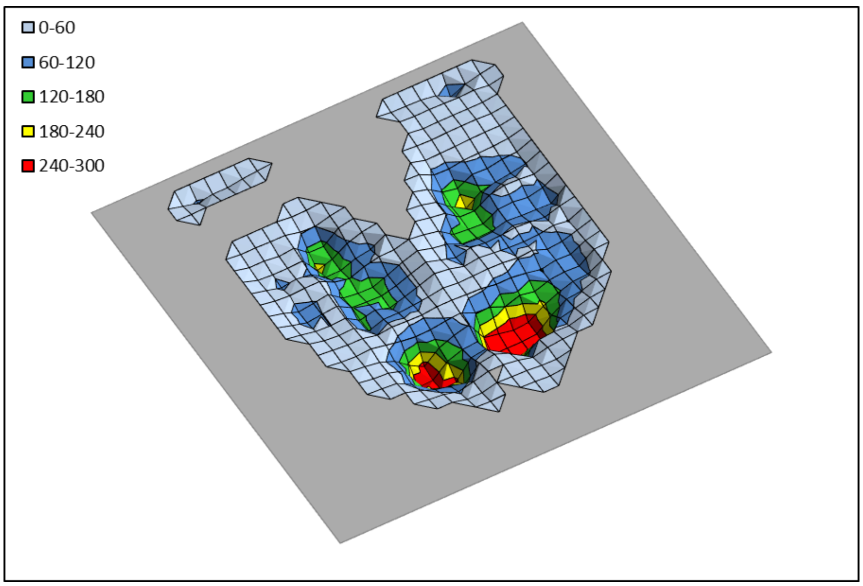

Figure 6. Example of a 3D surface representation of a subject's pressure map frame

CHAPTER III

RATIONALE AND OBJECTIVES

Problem Statement

Researchers have relied on pressure mapping systems to study human-chair-comfort interactions under various sitting conditions (Cascioli et al., 2016; Crawford et al., 2005; Fenety, 1995; Fenety et al., 2000; Fredericks et al., 2016; Higer & James, 2016; Stinson et al., 2003; Zemp et al., 2016). These systems collect pressure maps readings and analyze pressure measures such as sum of pressure, average pressure, peak pressure, contact area, coefficient of variation, and center of pressure. While some pressure measures have been considered suitable for assessing human-chair interactions and their relations to seating comfort/discomfort, researchers have emphasized the importance of using different measures of pressure distribution to further understand these interactions (Zemp et al., 2015).

Many of the analytical tools used in sitting research rely on simplified measures of pressure, such as calculating basic descriptive measures of pressure (see Table 1) or tracking of the center of pressure during dynamic sitting. These measures do not provide clear insights about spatial relationships (e.g., pressure correlation, location, and orientation) or pressure distribution patterns (e.g., pressure continuity, localized gradients, and homogeneity) in static or dynamic pressure maps. Furthermore, there are very few studies examining comparative techniques for seating research using pressure mapping technology; these techniques are important for the analysis and comparison of within-subject or between-subjects pressure maps.

Butt et al. (2005) proposed aggregation and normalization methods for comparing pressure maps, however, the described methods required pressure maps to be invariant to a maps' position and orientation. One important factor that needs to be considered when comparing or measuring similarities between pressure maps is scaling. Differences in subjects' anthropometry not only affect the magnitude of pressure readings, but the size and shape of the pressure maps is also affected by anthropometric differences. While scaling algorithms can be implemented for comparing pressure maps, it is not appropriate for research involving human subjects (e.g., seating research). Scaling algorithms will distort subject's anthropometry and cover dissimilarities due to true differences in size between subjects.

The need for new analytical tools for pressure mapping is clear. The following is a list summarizing some of the drawbacks of currently used pressure mapping measures and comparative techniques in the context of seating research.

(1) Common pressure measures, such as sum of pressure, contact area, and coefficient of variation, lack information in regard to spatial relationships, pressure distribution patterns, localized gradients, or homogeneity within pressure levels.

(2) Current dynamic measures, including center of pressure, do not provide clear insights about changes in pressure distribution patterns during positional shifts and/or postural changes.

(3) The use of visual feedback assessment is not a practical approach for comparing pressure maps. Current quantitative comparative techniques expect pressure maps to be in a similar location and orientation, while other require certain conditions such as pressure maps symmetry and identifiable pressure landmarks to be met (e.g., LARS). Additionally, these quantitative techniques mostly rely on calculating individual differences between pressure readings; there is a need for global comparative measures with undemanding assessment.

Research Objective

To address many of the drawbacks of current pressure mapping analysis, this study sought to evaluate new potential pressure measures and new methodologies for comparing pressure maps by using interdisciplinary tools from image processing and spatial data analytics. In a specific manner, the objectives of this study were to:

(1) introduce methods for detecting and removing extrinsic pressure artifacts (i.e., pressure reading outliers) by implementing unsupervised machine learning and spatial data clustering as a pre-preprocessing data cleansing technique;

(2) introduce new pressure measures, for both static and dynamic settings, by evaluating measures in spatial data analytics, digital image processing, and use of statistical features of images as new pressure measures; and

(3) introduce a toolset for aligning and comparing static and dynamic pressure maps by using optimal image registration methods and similarity/dissimilarity coefficients.

Proposed pressure measures and analytical tools are discussed and presented in this study in the context of seating research, but extensions to other potential applications in research using non-seating pressure maps are briefly discussed in the conclusions.

Study Significance

Findings from this study are aimed to providing researchers additional analytical tools for a better understanding of user-chair interactions, in both static and dynamic sitting environments, and to help further evaluate sitting comfort/discomfort. Concurrent validation of potential pressure measures is investigated by studying their relationship to commonly used pressure measures, with possible use and interpretations in the context of human-chair interactions.

CHAPTER IV

METHODS AND PROCEDURES

To evaluate potential techniques for pre-processing, measuring, and comparing pressure maps, a previously collected dataset containing a number of seating pressure maps is used in this study. Information about the participants, apparatus, and data collection procedures used for creating this dataset is discussed early in this chapter.

This chapter also introduces the spatial data analytics and image processing techniques that were evaluated as new methodologies for pressure mapping analysis. Presented techniques will be grouped according to their discipline and purpose as per the following categories: (1) spatial clustering, (2) spatial autocorrelation, (3) image statistical features, and (4) image registration and similarity/dissimilarity coefficients. In alignment with these categories, this study is divided in the following four research steps:

(1) Evaluate the use of density-based spatial clustering techniques as pre-processing techniques for detecting and removing extrinsic pressure artifacts (i.e., outliers) within seating pressure maps.

(2) Evaluate the use of spatial autocorrelation measures as new pressure measures for static and dynamic seating pressure map applications.

(3) Evaluate the use of first-order and second-order image statistical features as new pressure measures for static and dynamic seating pressure map applications.

(4) Evaluate the application of image registration techniques as a pre-processing technique for aligning and matching pressure maps, and the subsequent use of similarity and dissimilarity coefficients as global comparative measures between registered pressure map images.

Thorough descriptions of the techniques and methodologies used in this study are presented in this chapter Details about data sampling strategies, testing procedures, and research outcomes are also presented for each research step. A case study is also used to demonstrate the use and application of selected techniques and methodologies under a dynamic sitting environment.

Dataset

As explained earlier in this chapter, the dataset used in this study was collected previously, and it was used in studies where results from an applied-research perspective were reported (Hammond et al., 2018; Martinez et al., 2018). This dataset was originally collected to evaluate human-chair interactions under user-defined seat pan contours. These studies were approved by Human Subjects Institutional Review Board at Western Michigan University (see Appendix A).

This research uses the information of the pressure maps included in the dataset as a testing and validation platform for the various techniques presented in this chapter. A brief description of the participants, testing apparatus, and collection protocol used to create the dataset is described in the following subsections.

Participants

Continuous pressure maps collected from 82 volunteers (35 males/47 females) are included in the dataset. Participants were recruited through word-of-mouth and classroom announcements among the WMU community. All participants indicated no pre-existing musculoskeletal disorders. Descriptive statistics of selected anthropometric measurements are presented in Table 3.

Table 3. Selected anthropometric measurements for 82 participants

Variable	Mean	SD	Min	Max
Age (years)	23.33	6.03	18.00	58.00
Height (mm)	1689.03	77.00	1552.00	1874.00
Mass (kg)	67.05	12.50	44.00	105.69
BMI (kg/m^2)	23.46	3.88	17.08	35.24
Hip Breadth (mm)	365.38	66.80	210.00	495.00
Buttock-Popliteal Length (Right) (mm)	486.60	32.42	410.00	600.00

Apparatus

Participants used a custom test chair able to accommodate 95th percentile users with no armrests, a mesh backrest, and an adjustable seat pan. The adjustable seat pan used 49 electric linear actuators placed beneath a 1” PORON® padding foam in a 7 x 7 grid configuration. Each actuator provided a vertical stroke of 6 inches, with a swiveling plate attachment of 2.5 inches in diameter set at the clevis end for contouring purposes. By using these adjustable actuators, subjects created various contours and shapes in the seat pan. The pressure maps included in the dataset were recorded under the various user-defined seat pan contours given the adjustability of the actuators. This is particularly valuable to this study as new methodologies and potential pressure measures must be valid and reliable under various sitting contours (i.e., different chairs).

Interface contact pressure was measured using a pressure mapping interface attached on top of the chair’s padding foam (FSA Industrial Seat and Back Systems, Verg Inc., USA). The pressure interface mat consisted of 1024 (32 × 32) rectangular pressure elements (sensors), each 15 mm x 15 mm in size, with a maximum pressure response of 300 mmHg. The distance between each sensor was approximately 19.37 mm in the horizontal (lateral) direction and 16.56 mm in the vertical (anterior-posterior) direction. The sampling frequency was set at an approximate rate of 5 Hz.

Data Collection Procedure

This dataset contains continuous pressure mapping data for each participant recorded in three different sessions. A session, lasting up to 2 hours, consisted of activities where subjects performed simulated office-related tasks (typing and mousing) using a desktop computer. At the start of each session, participants were randomly exposed to a pre-defined starting pattern and were allowed to change the height of the actuators after each interval (5 minutes). Participants made the necessary changes to the seat pan according to their levels of comfort/discomfort.

Spatial Clustering

The first application of spatial data analytics is integrating unsupervised spatial clustering algorithms for the analysis and evaluation of pressure maps. Numerous unsupervised clustering algorithms have been developed over time (Amini et al., 2014; N. Kumar & Sivasathya, 2014; Xu et al., 1997). The goal of clustering techniques is to group data streams into meaningful classes or groups. Unsupervised clustering algorithms can discover and cluster data without prior knowledge (training) of the number of clusters or types of groups. Among unsupervised clustering algorithms, density-based clustering algorithms have favorable characteristics due to their ability to identify arbitrary shapes and detection of outliers (Amini et al., 2014).

Application of density-based clustering algorithms can result in potential pre-processing techniques for the detection and removal of unwanted pressure readings that are caused by extrinsic pressure artifacts such as torque forces, shear forces, pinches, and/or creases in the pressure mapping interface. These pressure artifacts are considered "outliers" for the purpose of this study. Five potential pressure mapping outlier detection techniques are evaluated in this study based on the following unsupervised density-based clustering algorithms:

- DBSCAN (Ester et al., 1996):
    - Clustering according to density-based connectivity analysis
- OPTICS (Ankerst et al., 1999):
    - Extension of DBSCAN with a wider range of parameter settings
- DBCLASD (Xiaowei Xu et al., 1998):
    - Clustering based on probability distribution of neighbor's distances
- DENCLUE (Hinneburg & Keim, 1998):
    - Clustering based on sets of density distribution functions
- HDBSCAN (Campello et al., 2015):
    - Clustering according to variations of local densities

Table 4 shows the list of parameters used for each density-based clustering algorithms being studied. As choosing correct combinations of parameters settings is crucial for the performance of any clustering method, appropriate ranges and/or combinations of parameter settings are also studied for each clustering method. The purpose of this step is to choose a density-based clustering algorithm where the correct identification of extrinsic pressure artifacts and true contact pressure readings is maximized; in other words, increase the outlier and non-outlier detection accuracies.

Table 4. Parameters of Spatial Clustering Methods

Method	**Parameters**			
DBSCAN	Epsilon	Minimum samples		
OPTICS	Xi	Minimum samples	Minimum Size	Epsilon
HDBSCAN	Minimum Size	Minimum samples	Leaf Size	
DENCLUE	Epsilon	Minimum density		
DBCLASD	Nearest Neighbors			

The following list shows a brief description of each parameter shown in Table 4:

- Epsilon: The maximum convergence threshold parameter (e.g. distance) between two samples for one to be considered as in the neighborhood of the other.
- Minimum samples: The number of samples in a neighborhood for a point to be considered as a core point.
- Xi: Determines the minimum steepness on the reachability plot that constitutes a cluster boundary.
- Minimum size: Minimum number of samples in a cluster.
- Leaf size: The number of points in a leaf node of the tree.
- Minimum density: The minimum kernel density required for a cluster attractor to be considered a cluster and not noise.
- Nearest neighbors: Number of K-neighbors to find from a given point.

Clustering methods are primarily evaluated in their ability to correctly identify outlying and non-outlying pressure readings from a selection of pressure maps included in the dataset with known outlier readings. The computational demands of these algorithms are also examined when evaluating a single pressure map (i.e., static clustering) and continuous pressure maps (i.e., dynamic clustering).

Data Sampling

To evaluate the outlier-detection accuracies of these clustering methods, a subset of the dataset consisting of twenty-eight samples (28) of pressure maps with known pre-identified outliers and twenty-eight samples (28) of pressure maps without outliers is used (named <u>cluster data subset</u>). Selected samples of pressure maps with and without outliers are shown in Appendix F and Appendix G respectively. The selection criteria for these pressure map samples were based on the different levels of contact area (i.e., number of contact cells). Additionally, pressure map samples were obtained from different subjects to measure accuracies of clustering methods when considering pressure maps of different sizes and shapes.

Two variations of the cluster data subset are used as input for the clustering methods: (1) a subset with only the information of the locations of pressure readings (referred to as “location input data”), and (2) a subset with information about the locations and standardized pressure data of the pressure readings (referred to as “location-pressure input data”). All clustering algorithms are instructed to only consider non-zero pressure cells during computation.

A case study is also conducted where selected clustering methodologies are evaluated in a dynamic environment by using a 5-minute sitting interval sample that includes a number of sequential spatio-temporal pressure images from one of the subjects in the dataset (named dynamic data subset).

Testing Procedures

Using the cluster data subset with location input data, different combinations of parameter settings are tested for each clustering method with the goal of achieving the best outliers/non-outliers detection performance (parameter settings are shown in Table 9, Chapter 5). Each clustering method is evaluated based on their accuracies score (percent [%] of correctly classified outliers and percent [%] of correctly classified non-outliers). In a similar fashion, different combinations of parameter settings are tested for each clustering method when using the location-pressure input data (see Table 9, Chapter 5). The objective is the identify cluster methods that can select naturally occurring pressure clusters from subjects’ pressure maps. Validation of the performance of these clustering methods was also made via visual feedback.

The first section in the case study includes an evaluation of the applications of selected clustering methods to pre-process continuous seating pressure maps (i.e., detection and removal of outliers) while examining overall accuracies and computational demands. This pre-processed dynamic data subset is used for subsequent case study analyses.

Algorithms for clustering methods were coded and implemented using the Python programming language. A condensed form of the Python script used for running clustering algorithms and data visualization routines can be seen in Appendix C.

Outcomes

The following outcomes were pursued for this step: (1) Recommendations of clustering methods and suggested parameters settings, given cluster performance accuracies, for identifying outliers and non-outliers pressure readings in the context of sitting pressure maps, and (2) to examine the computational demands of using recommended algorithms for detecting outliers/non-outliers pressure readings.

Spatial Autocorrelation

The second application of spatial data analytics is integrating spatial autocorrelation measures for the analysis and evaluation of pressure maps. While many statistical approaches often assume that measured outcomes are independent of each other, measures of a spatial nature often exhibit some degree of spatial autocorrelation (UCLA: Statistical Consulting Group, 2020). Spatial autocorrelation measures the relationship of variable outcomes as related to their distance; more specifically, it measures the correlation between variable values that is strictly due to their proximity in a geographical space (Kalogirou, 2019).

In seating pressure maps, measures of pressure at different locations are generally not independent. The pressure readings in a seating pressure map are generally spatially related as the pressure measures at neighboring locations are usually similar to one another. For example, measurements in proximity to a prominent bony region, such as an ischial tuberosity, are closer in their pressure values than measurements made at other distant locations in the pressure map. The degree of the similarity among proximate pressure readings can be measured using spatial autocorrelation measures.

One important aspect when calculating spatial autocorrelation is defining the relationship between locations, which is generally based on the proximities and distances between them. A weight matrix w_{ij} is generally constructed to define the distance relationship between locations. This weight matrix, often row-standardized (i.e., sum of row weights is one), can be specified in many ways, but values in the weight matrix are generally up to the researcher's decision. Gunaratna et al. (2005) presented examples of the approaches used by researchers to calculating and specifying the spatial weight matrix; these are presented as follows:

- The weight for any two different locations is constant
- A constant weight for observations within a specified distance
- K nearest neighbors have a fixed weight, all others are zero
- Weight is proportional to the inverse distance (absolute, squared, or truncated)

Based on these examples, this study used three variations of contiguity-based weight matrices to evaluate the sensitivities of spatial autocorrelation measures to extreme values and/or variances in small neighborhoods. The weight matrices used in this study are described below with a graphical representation of the weight values shown in Figure 7.

1. Constant weight for the eight nearest observations (Queen)
2. Constant weight for observations within a $2\sqrt{2}$ cell distance (Constant Distance)
3. Weight is inversely proportional within a $2\sqrt{2}$ cell distance (Inverse Distance)

0	0	0	0	0
0	1	1	1	0
0	1		1	0
0	1	1	1	0
0	0	0	0	0

(a) Queen

1	1	1	1	1
1	1	1	1	1
1	1		1	1
1	1	1	1	1
1	1	1	1	1

(b) Constant Distance

0.35	0.45	0.50	0.45	0.35
0.45	0.71	1	0.71	0.45
0.50	1		1	0.50
0.45	0.71	1	0.71	0.45
0.35	0.45	0.50	0.45	0.35

(c) Inverse Distance

Figure 7. Contiguity-based weight matrices for spatial autocorrelation measures

This study evaluated the selected weighting approaches using two different measures of spatial autocorrelation: $Moran's\ I$ (Moran, 1950) and $Geary's\ C$ (Geary, 1954). Given a weight matrix w_{ij} and a two-dimensional matrix X with n elements, the mathematical definitions of the spatial autocorrelation measures used in this study are as follow:

Eq. 1 - Moran's I

$$I = \frac{n}{S_0} \frac{\sum_i \sum_j w_{ij}(x_i - \bar{x})(x_j - \bar{x})}{\sum_i (x_i - \bar{x})^2} \quad ; \ where \quad S_o = \sum\nolimits_i \sum\nolimits_j w_{ij}$$

Eq. 2 - Geary's C

$$C = \frac{n-1}{2S_0} \frac{\sum_i \sum_j w_{ij}(x_i - x_j)^2}{\sum_i (x_i - \bar{x})^2} \quad ; \ where \quad S_o = \sum\nolimits_i \sum\nolimits_j w_{ij}$$

The main objective in this step is to evaluate measures of spatial autocorrelation – such as Moran's I and Geary's C – to be used as global pressure map descriptors in a static (single pressure maps) and dynamic (continuous pressure maps) environments. In the context of seating pressure mapping, measures of spatial correlation could help measure the presence of localized high/low pressure clusters (i.e., hot spots), measure pressure readings interconnectedness, and/or surface map smoothness and continuity.

Data Sampling

To evaluate the application of spatial autocorrelation measures as global pressure map descriptors, a subset of the dataset consisting of twenty samples (20) of pressure maps from different subjects was used (named static data subset). To gain a better insight about the uniqueness and usefulness of spatial autocorrelation measures, selecting pressure maps exhibiting different levels of pressure variability was desired. Out the currently used pressure measures, the coefficient of variation is a good indicator of pressure variances within a pressure map; for this reason, the selection criteria used for obtaining the pressure map samples was based on various levels of coefficient of variation. Selected samples are shown in Appendix H.

Testing Procedures

For each pressure map sample included in the static data subset, measures of Moran's I and Geary's C were calculated using all three different weight matrices. To evaluate their statistical association, correlation analyses – using the Pearson product-moment correlation – were completed for all six variations of spatial autocorrelation measures, and also between some of the known pressure measures (Table 1). When strong correlations ($R^2 \geq 0.8$) appeared during the correlation analysis, regression models were conducted with emphasis in finding unusual observations (i.e., points with large leverage values or extreme standardized residuals). If a pressure map was marked as an unusual observation, a comparative visual feedback was used between the pressure map and a chosen reference pressure map with a similar predictor value. The objective was to identify possible differences – as global pressure map descriptors – between the highly correlated measures. Differences in terms of each measures' ability to detect presence of localized high/low pressure clusters, surface map smoothness, and pressure level contiguity were considered.

A section of the case study also includes an evaluation of spatial autocorrelation measures under a dynamic environment (i.e., dynamic sitting). The (pre-processed) dynamic data subset (after removing outliers with spatial clustering techniques) will be used to assess the practicality of using spatial autocorrelation as dynamic pressure measures. Using time series plots, emphasis is given in evaluating sequential indexes where considerable changes in measures of spatial autocorrelation occur. Comparative visual feedback of selected sequences of pressure maps is used to confirm detected in-chair-movements.

Algorithms for calculating spatial autocorrelation measures were coded and implemented using the Python programming language. A condensed form of the Python script used for calculating commonly known pressure measures, spatial autocorrelation measures, and data visualization routines can be seen in Appendix D. The python script also contains correlation algorithms used to generate correlograms based on the Pearson product-moment correlation. The correlograms are created applying hierarchical clustering techniques and were used to visually identify clusters of correlated and non-correlated measures.

Outcomes

The following outcomes were pursued for this step: (1) Recommendations for selecting a weight matrix for calculating spatial autocorrelation measures in the context of seating pressure maps, (2) use and interpretation of spatial autocorrelation measures in the context of human-seating interaction, and (3) to examine the computational demands of using various combinations of weight matrices and spatial autocorrelation measures.

Image Statistical Features

Pressure mapping systems measure and collect information about contact pressure between a subject (or object) and a pressure interface, either using a single grid-based flexible mat or individual sensor pads. Collected data from such systems are recorded in common manometric units such as pound per square inch (PSI) or millimeters of mercury (mmHg). Using re-scaling techniques, contact pressure measures can be transformed into picture elements (pixels) with intensities ranging from 0 (black) to 255 (white) (Tan et al., 2001). Unfortunately, a consequence of this re-scaling technique is information loss. For pressure maps included in the dataset, range of possible pressure values will be reduced from 0 - 300 mmHg to 0 - 255 pixel intensities. To avoid information loss, this study modified image processing algorithms to accommodate discrete value ranges from 0 - 300 pixel intensities (see Appendix D).

After transforming pressure readings into pixels, the location of the sensors in the pressure interface are used to project these pixels into a scaled two-dimensional space. This results in a grayscale-image representation of the pressure map in raster graphics. This transformation ensures that the resolution of the resulting images matches the resolution of the pressure interface (i.e., 32 x 32). Obtaining these low-resolution images was favorable to this study given their low computational demand requirements. Image processing techniques, such as image statistical features, are now able to be applied to resulting grayscale images of the dataset' pressure maps.

Statistical features of images were evaluated as potential global descriptors of pressure maps, with the objective of supplementing pressure measures commonly used in seating research (Table 1). The first- and second-order statistics of image intensities (i.e., pressure readings) characterize the statistical properties of an image. First-order statistics are based on the probabilities that pixels will have particular intensities in an image, while second-order statistics consider the probabilities that pixel pairs – in predefined positions with respect to each other – will have particular intensities in an image (Goshtasby, 2012).

First-Order Statistical Features. The probability distribution of intensities in an image needs to be defined first to be able to calculate first-order statistical features. Letting $H(i)$ denote the number of pixels with discrete intensity i, and S the total number of pixels in an image, then

Eq. 3 - Intensities probability distribution

$$p(i) = \frac{H(i)}{S} \quad ; \qquad i = 0, \dots, 300 \text{ (max } cell\ pressure\text{)}$$

First-order statistical features, such as peak pressure, average pressure (μ), and pressure variation (σ), are already being used in seating research (see Table 1), but other unique features used to characterize images can also be calculated from the probability distributions shown in Equation 3. The skewness (see Eq. 4) is a statistical feature that measures the asymmetry of pixel intensities, while the kurtosis (see Eq. 5) is a statistical feature that measures the degree of similarity of the pixel intensity distribution to a normal distribution.

Eq. 4 - Skewness

$$\gamma = \frac{1}{\sigma^3} \sum_{i=0}^{255} (i - \mu)^3 \, p(i)$$

Eq. 5 - Kurtosis

$$\kappa = \frac{1}{\sigma^4} \sum_{i=0}^{255} (i - \mu)^4 \, p(i) - 3$$

Other first-order statistical features that could be helpful in describing properties of pressure map images are the ones based on Gray-Level Differences (GLD) of adjacent pixels. Intensity variations from adjacent pixels can be obtained from calculating gray-level differences in different directions (Goshtasby, 2012). If $H(g|\theta)$ denotes the number of adjacent pixels in direction θ that have an absolute intensity $g = |i_1 - i_2|$, and $h(g|\theta) = H(g|\theta)/\sum_g H(g|\theta)$ is the probability that adjacent pixels have absolute intensity difference g when scanned in direction θ $(0°, 45°, 90°\ or\ 135°)$, the following statistical features can be calculated:

Eq. 6 - Gradient contrast

$$GLD_1(\theta) = \sum_g g^2 h(g|\theta)$$

Eq. 7 - Gradient second moment

$$GLD_2(\theta) = \sum_g [h(g|\theta)]^2$$

Eq. 8 - Gradient entropy

$$GLD_3(\theta) = -\sum_g h(g|\theta) \log h(g|\theta)$$

Eq. 9 - Gradient mean

$$GLD_4(\theta) = \sum_g h(g|\theta) g$$

Eq. 10 - Inverse-difference moment

$$GLD_5(\theta) = \sum_g \frac{h(g|\theta)}{(g^2 + 1)}$$

Second-Order Statistical Features. To determine second-order statistical features, a Gray-Level Spatial-Dependence (GLSD) or co-occurrence matrix (GLCM) $\left(h(i_1, i_2|\theta)\right)$ is created with entries $(i_1,\ i_2)$ showing the number of adjacent pixels at direction θ with intensity i_1 and i_2 in the first and second pixel respectively. Since $h(i_1, i_2|\theta+\pi) = h(i_2, i_1|\theta)$, and the co-occurrence matrix for θ and $\theta+\pi$ contain the same information, a co-occurrence matrix for direction θ $(0°, 45°, 90°\ or\ 135°)$ can be calculated as the sum of $h(i_1, i_2|\theta)$ and its transpose $h(i_2, i_1|\theta)$ (Goshtasby, 2012). Letting M be the number of columns in an image and N be the number of rows in an image, the Joint Conditional Probability Density (JCPD) can be obtained as follow:

Eq. 11 - GLSD joint conditional probability density

$$p(i_1, i_2|\theta) = \frac{h(i_1, i_2|\theta) + h(i_2, i_1|\theta)}{(M-1)N}$$

The following features can be calculated using the JCPD of the co-occurrence matrix:

Eq. 12 - Energy

$$GLSD_1(\theta) = \sum_{i_1}\sum_{i_2}[p(i_1, i_2|\theta)]^2$$

Eq. 13 - Contrast

$$GLSD_2(\theta) = \sum_{i_1}\sum_{i_2}(i_1 - i_2)^2 p(i_1, i_2|\theta)$$

Eq. 14 - Correlation

$$GLSD_3(\theta) = \sum_{i_1}\sum_{i_2}\frac{\left(i_1 - \mu_{i_1}\right)\left(i_2 - \mu_{i_2}\right)}{\sigma_{i_1}\sigma_{i_2}} p(i_1, i_2|\theta),$$

$$where\ \mu_{i_n} and\ \sigma_{i_n} denote\ the\ mean\ and\ std.dev\ of\ \sum\nolimits_{i_{3-n}} h(i_1, i_2|\theta)$$

Eq. 15 - Entropy

$$GLSD_4(\theta) = -\sum_{i_1}\sum_{i_2} p(i_1, i_2|\theta)\log p(i_1, i_2|\theta)$$

Eq. 16 - Homogeneity

$$GLSD_5(\theta) = \sum_{i_1}\sum_{i_2} \frac{p(i_1, i_2|\theta)}{1 + (i_1 - i_2)^2}$$

In a similar manner to the spatial autocorrelation research step, the main objective in this step is to evaluate first- and second-order statistical features as global descriptors of pressure maps images, with specific properties and applications in both static (single pressure maps) and dynamic (continuous pressure maps) environments. This step focuses in determining what each statistical feature is measuring, from a seating pressure mapping perspective, that commonly used sitting pressure measures (Table 1) are not able to and, more importantly, how to interpret these statistical features in the context of human-chair interactions.

The common pressure measures shown in Table 5 were calculated to find their association with the first-order and second-order statistical features presented in this section. Measures of spatial autocorrelation are additionally considered during correlation analyses to also find their relationship with measures of statistical features.

Table 5. First-order statistical features

Contact Cells*	Sum of Pressure*	Standard Deviation*
Coefficient of Variation*	Skewness	Kurtosis

* Common Pressure Measures

A scanning direction θ $(e.g., 0°, 45°, 90°\ or\ 135°)$ needs to be defined for calculating the first-order statistical features based on Gray-Level Differences (GLD). Table 6 shows the two directions that are considered in this study, where $\theta = 0°$ measures differences in the horizontal or lateral direction (X) of the pressure map image, and $\theta = 90°$ measures differences in the vertical or anterior-posterior direction (Y) of the pressure map image. These same directions were also used for calculating the second-order statistical features based on Gray-Level Spatial-Dependence (GLSD) (see Table 7).

Table 6. Gray-Level Differences (GLD) statistical features

Direction: $\theta = 0°$	Direction: $\theta = 90°$
Gradient Contrast X	Gradient Contrast Y
Gradient Second Moment X	Gradient Second Moment Y
Gradient Entropy X	Gradient Entropy Y
Gradient Mean X	Gradient Mean Y
Inverse-Difference Moment X	Inverse-Difference Moment Y

Table 7. Gray-Level Spatial-Dependence (GLSD) statistical features

Direction: $\theta = 0°$	Direction: $\theta = 90°$
Energy X	Energy Y
Contrast X	Contrast Y
Correlation X	Correlation Y
Entropy X	Entropy Y
Homogeneity X	Homogeneity Y

Data Sampling

The static data subset obtained in the spatial autocorrelation step is again used for this research step. The static data subset is used to evaluate these statistical features as global pressure map descriptors. An extra subset was also created consisting of ten (10) paired samples of static pressure maps from different subjects where no significant differences $(|\Delta| < 5\%)$ are seen between common pressure measures (named paired data subset). Figure 4 and Table 2 (Chapter 1) shows an example of a paired sample from two different subjects where no significant differences are seen between common pressure measures. The selection criteria for these paired-pressure maps samples were based on different levels of contact area (i.e., number of contact cells), sum of pressure, and coefficient of variation. Selected sample pairs are shown in Appendix J.

Testing Procedures

All first-order and second-order statistical features were calculated for each pressure map sample in the static data subset. While calculating these statistical features, only non-zero pressure cells were considered. As with the previous step (i.e., spatial autocorrelation), correlation analyses using the Pearson product-moment correlation were performed within all statistical feature measures and known pressure measures (Table 5) to evaluate their statistical association. All six variations of spatial autocorrelation measures were also included during correlation analyses.

It was expected that some of these features and measures were highly correlated in the context of seating pressure maps; dimension reduction techniques focused on feature selections (e.g., high correlation filters) were used to select features that can explain different user-chair interaction phenomenon. Hierarchical clustering was used in the resulting correlation matrix to find clusters of measures that have strong correlations ($R^2 \geq 0.8$). Regression models within these correlated clusters were conducted with emphasis in finding unusual observations (i.e., points with large leverage values or extreme standardized residuals) between clustered measures.

For pressure maps marked as unusual observations, comparative visual feedback was used between the pressure maps and selected reference pressure maps (with a similar predictor values). The objective was again to identify possible differences – as global pressure map descriptors – between these highly correlated measures. Differences in terms of each measures' ability to detect presence of localized high/low pressure clusters, acute pressure points, surface map smoothness and texture, and pressure level contiguity were considered. In addition, research evaluated these unusual observations by expanding their respective regression models with other clustered and non-clustered measures to find possible supplemental explanatory variables.

After dimension reduction techniques, selected spatial autocorrelation measures and selected first-order and second-order statistical features were evaluated to find any significant differences ($|\Delta| > 5\%$) between corresponding paired samples of pressure maps included in the paired data subset. The main focus while doing this analysis is to determine – if significant differences are found – what each statistical feature is measuring, from a pressure mapping perspective, that common seating pressure measures are not able to by means of visual feedback.

For studying the dynamic application of measures of statistical features of images, first-order and second-order statistical features were calculated for each continuous sitting interval sample included in the (pre-processed) dynamic data subset during the case study. Using time series plots, emphasis is given in evaluating sequential indexes where considerable changes in measures of statistical features occur. Comparative visual feedback of selected sequences of pressure maps was also used to confirm detected in-chair-movements.

Algorithms for calculating first-order and second-order statistical features were also coded and implemented using the Python programming language. A condensed form of the Python script used for calculating statistical features of pressure map images is also included in Appendix D. The same python code used to generate the correlation correlograms based on hierarchical clustering techniques also include these image statistical features.

Outcomes

The following outcomes were pursued for this step: (1) Selection of unique and meaningful measures of statistical features in the context of seating pressure map, (2) validation of pressure map statistical features as complementary measures to common pressure measures, and (3) use and interpretation of selected statistical features of pressure map images in the context of human-seating interaction.

Image Registration and Similarity/Dissimilarity Coefficients

A similarity (dissimilarity) measure between two sequences of measurements $X = \{x_i,\ i = 1,..,n\}$ and $Y = \{y_i,\ i = 1,..,n\}$ quantifies the dependency (independency) between the sequences. If X and Y represent pixel intensities from resulting rasterized images of pressure mapping data, measures of the similarity (dissimilarity) between pressure maps can be obtained. In seating pressure maps, similarity measures can be useful when evaluating and comparing pressure maps between subjects (comparison of pressure readings and spatial distributions) or for within-subject assessments (evaluation of dynamic sitting or clinical intervention effects). Implementing similarity and dissimilarity measures, as global comparative measure for pressure mapping analysis, could potentially eliminate current requirements of using comparative visual feedback with a set of objective measures for undemanding assessment.

Similarity/dissimilarity measures have been studied and formulated for many years. Some measures use raw intensities from images, while other apply transformations to image intensities (e.g., normalization, ranking, or joint probability functions). Goshtasby (2012) evaluated the accuracies and speeds of 16 similarity measures and 11 dissimilarity measures using both synthetic and real images. Goshtasby also evaluated the sensitivity of the measures using combinations of intensity variations and noise. Goshtasby concluded that absolute superiority of one measure against others cannot be reached; however, better performances – using percent of correct matches between images – were found when using the following similarities and dissimilarities measures:

Similarity Measures

Eq. 17 - Pearson correlation coefficient

$$r = \frac{\sum_{i=1}^{n}(x_i - \bar{x})(y_i - \bar{y})}{\{\sum_{i=1}^{n}(x_i - \bar{x})^2\}^{\frac{1}{2}}\{\sum_{i=1}^{n}(y_i - \bar{y})^2\}^{\frac{1}{2}}}$$

Eq. 18 - Tanimoto measure

$$S_T = \frac{X^T Y}{\|X - Y\|^2 + X^T Y}$$

Eq. 19 - Minimum ratio

$$m_r = \frac{1}{n}\sum_{i=1}^{n} r_i, \qquad where\ r_i = \min\left\{\frac{x_i + \varepsilon}{y_i + \varepsilon}\ ,\ \frac{y_i + \varepsilon}{x_i + \varepsilon}\right\}, and$$

$$\varepsilon = small\ number\ (e.g., 1).$$

Dissimilarity Measures

Eq. 20 - L_1 norm

$$L_1 = \sum_{i=1}^{n}|x_i - y_i|$$

Eq. 21 - Square L_2 norm

$$L_2^2 = \sum_{i=1}^{n}(x_i - y_i)^2$$

Eq. 22 - Intensity-ratio variance

$$R_V = \frac{1}{n}\sum_{i=1}^{n}(r_i - \bar{r})^2\ ;\ where\ r_i = \frac{x_i + \varepsilon}{y_i + \varepsilon},\ \ \bar{r} = \frac{1}{n}\sum_{i=1}^{n} r_i\ , and$$

$$\varepsilon = small\ number\ (e.g., 1).$$

Image Registration

One major drawback of the similarity/dissimilarity measures is that, to accurately measure the relationship between images, images should be invariant to location and orientation. If the images to be compared are not generally located in the same x-y regions of space or the orientation and angular position of the images are significantly different, using similarity/dissimilarity coefficients without applying transformation functions to the images might not be appropriate.

Sitting is a dynamic activity. Subjects constantly shift the location and orientation of their pressure contact area with the purpose of relieving discomfort. Preferences in terms of sitting postures and sitting placement in the seat pan are common issues when comparing seating pressure maps. There is a need for implementing repositioning algorithms in pressure mapping analysis.

Various parametric and non-parametric spatial transformation techniques have been developed for image registration. Modersitzki (2004) evaluated several of these transformation techniques with mixed results. Landmark-based techniques require placements of “soft markers” in images (see Fig. 8). The registration process in landmark-based techniques is governed by the placement and correspondence of these user-defined landmarks. These markers generally require expert knowledge for manual marking and/or sophisticated image analysis tools for automatic detection (Modersitzki, 2004, p. 27); one major drawback when using landmark-based techniques.

As the evaluation of continuous dynamic pressure maps or comparison of multiple-subject pressure maps is desired, the automatic detection of image features is a desired approach for repositioning and reorienting pressure maps. Registration techniques such as Principal Axes Transformations (PAT) and optimal parametric registrations work under this principle.

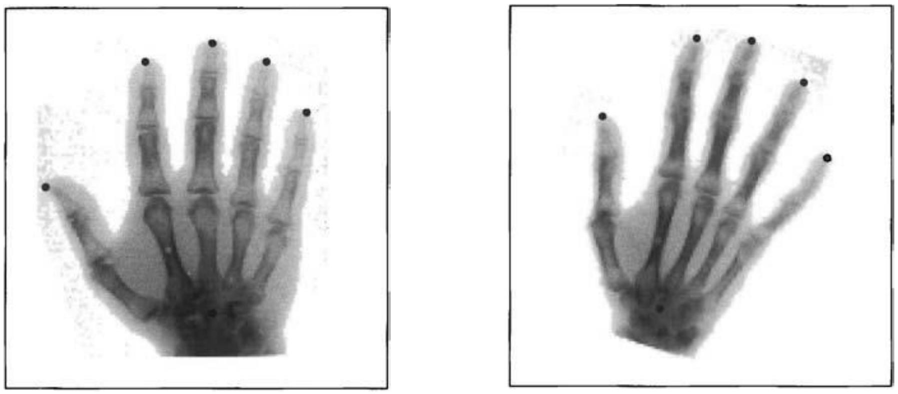

Figure 8. Examples of “soft markers” required for landmark-based techniques. (Modersitzki, 2004, p. 31). Reproduced with permission of the Licensor through PLSclear.

PAT can have different approaches according to the distribution assumption; a standard approach – more sensitive to data perturbation – generally uses a Gaussian distribution, while a more robust approach is achieved by using a Cauchy distribution (Modersitzki, 2004). PAT works by initially calculating the center of mass and the eigen decomposition of the covariance matrix. These calculated measures are used as matching features between images.

PAT registration is accomplished by translating the center of mass and then rotating and scaling the resulting orthogonal axis to match the reference image (Alpert et al., 1990). An example of the application of this technique can be seen in Figure 9. The problem of using the center of mass of the images (i.e., center of pressure) for aligning pressure images is that it often results in misalignments and/or mismatches of the pressure distribution shapes between pressure maps. Figure 10 shows an example where a PAT transformation would be not appropriate, as the translation and alignment of the center of pressures would results in an incorrect image registration.

Another issue of using PAT registration is that it applies scaling transformations for matching the orthogonal axis of the images. While scaling algorithms can be implemented for comparing pressure maps, it is not appropriate for research involving human subjects (e.g., seating research). Scaling algorithms will distort subject's anthropometry and cover the dissimilarities of true differences between subjects due to their size.

Figure 9. PAT example. Reference (left). Template (center). PAT Transformation (right). (Modersitzki, 2004, p. 53). Reproduced with permission of the Licensor through PLSclear.

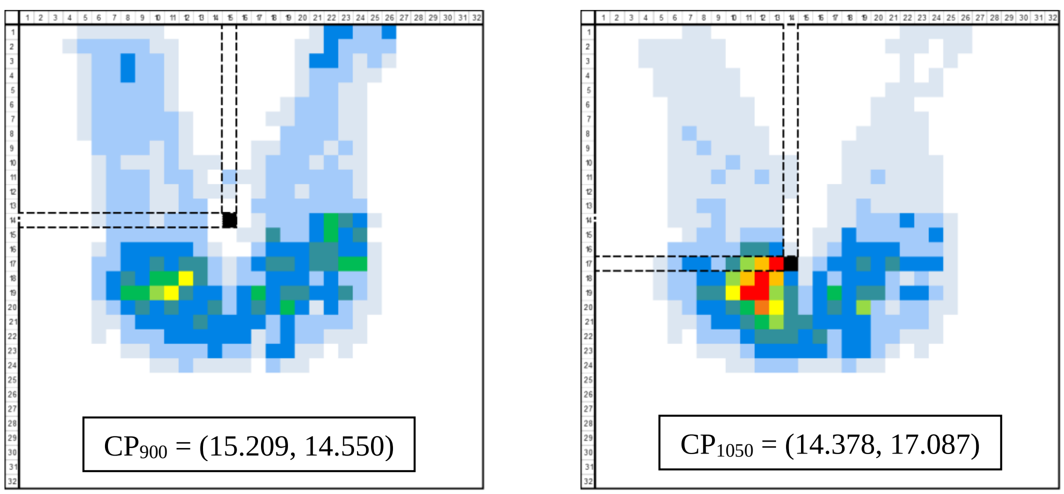

Figure 10. CP locations for pressure maps samples 120-1-900 (left) vs 120-1-1050 (right).

In a different manner, optimal registration techniques use parameterized finite-dimensional optimization routines (e.g., Steepest descent, Gauss-Newton, or Levenberg-Marquardt) to minimize differentiability between images (Modersitzki, 2004). Selection of the minimalization/maximization objective function defines the optimization approach used for image registration. A straightforward approach is the minimization of Sums of Squared Differences (SSD) or Mean Squared Error (MSE) of pixel intensities; while another approach, Mutual Information (MI), maximizes the entropy of the images' joint density. Using the same reference and template images shown in Figure 9, results of applying MI and MSE affine transformation to the template image can be seen in Figure 11.

Figure 11. Reference (left). Affine Linear MI (center). Affine Linear MSE (right) (Modersitzki, 2004, p. 71). Reproduced with permission of the Licensor through PLSclear.

This study evaluated the performances of optimal parametric registrations techniques based on MSE and MI registrations in the context of seating pressure mapping images. Rigid transformations with rotational and translational capabilities were considered during registration. Affine linear transformation, like the ones used in Figure 11, are not considered in this study as shear and scaling transformations are not desired for contact pressure maps with human subjects. As explained earlier, scaling and shear transformations are not appropriate for research involving human subjects (e.g., seating research) as they distort the subject's anthropometry and cover dissimilarities due to true differences in size between pressure maps.

The following are the mathematical definitions of the MSE and MI image registration techniques given a reference image (X) and a template image (Y) with pixel intensities I_{Xk} and I_{Yk} respectively, a transformation function a, image density ρ, and image entropy $\mathbb{E}$ (Modersitzki, 2004; Pataky et al., 2009):

Eq. 23 - Optimal Linear Registration (MSE)

$$Min\ (MSE)\ ;\ MSE = \frac{1}{n}\sum_{k}\left(I_{Xk} - I_{Y_a k}\right)^2$$

Eq. 24 - Optimal Linear Registration (MI)

$$Max\ (MI)\ ;\ \ MI = -\mathbb{E}_{\rho_{X,Y_a}}\left[\log\frac{\rho_{X,Y_a}}{\rho_X \rho_{Y_a}}\right]$$

By applying random transformations to randomly selected seating pressure maps, the accuracies of the translational and rotational capabilities of each image registration method can be measured by using the similarity and dissimilarity measures described in the previous section. At optimality, the similarity (dissimilarity) measures should be relatively close to 100% (0) if a good registration or image match is made by the registration method.

The main objectives in this research step are to (1) introduce image registration as an alignment technique, and (2) use similarity and dissimilarity measures as way of comparing registered pressure maps. Image registration techniques of optimal linear registration based on minimization of the Mean Squared Errors (MSE) and optimal linear registration based on maximization of the Mutual Information (MI) were evaluated in this study.

Data Sampling

To evaluate the translational and rotational capabilities of the image registration techniques, a subset of the dataset consisting of ten (10) samples of pressure maps was used. The selection criteria for these pressure map samples were based on different levels of contact area (i.e., number of contact cells). Two random transformations, each with a random translational and rotational shift, were then applied to each pressure map to create the synthetic transformed data subset. Selected samples with applied random transformations are shown in Appendix L.

Conditional sampling was also used for extracting sets of images exhibiting significant pressure map shifts. These samples are used for evaluating the feasibility of using image registration techniques and similarity/dissimilarity measures for analyzing and comparing pressure maps during dynamic sitting movements. As the distance needed for the center of pressure to travel one pressure map cell is approximately one inch $\left(\sqrt{19.37^2 + 16.56^2} = 25.5mm\right)$, a significant location shift was considered as a distance greater than one inch between the pressure maps' centers of pressures $(\Delta\, CP > 1\ in)$. Twenty (20) paired-samples were selected where potentially significant sitting movements were detected (named registration data subset), with each paired sample being selected from indexes within a continuous sitting interval (same subject). Distances between the center of pressure of selected paired-samples can be seen in Appendix N, while the pressure maps for the selected paired-samples can be seen in Appendix O.

Testing Procedures

Using the transformed data subset, the accuracies of the translational and rotational capabilities of image registration techniques are evaluated using proposed similarity/dissimilarity coefficients ($\varepsilon = 1$ is used when required). Because the transformed pressure maps included in this subset are in fact the same pressure maps as the reference maps (with very small differences due to the random transformation being applied), the resulting values of the similarity and dissimilarity coefficients can be used to benchmark registrations optimality. Visual feedback is also used to identify differences at optimality between image registration techniques.

When calculating similarities and dissimilarities coefficients between pressure maps, two scenarios were considered: (1) Only pairwise non-zero pressure cells between pressure maps are considered (referred to as masked), and (2) unbalanced pairwise pressure cells (i.e., a non-zero pressure cell and a zero pressure cell data pair) are accepted (referred to as non-masked).

The registration data subset was used to evaluate the performances of image registration techniques under dynamic sitting. Visual feedback was used to assess the image correspondence at optimality by using pressure map overlays and visual differences in pressure map images. Because pressure maps in this subset are inherently different, similarity and dissimilarity coefficients are only used as comparative measures post-registration. Improved values in measures of similarity/dissimilarity do not necessarily indicate a better registration, but if pressure maps images indeed share a number of commonalities and features, an increase (decrease) in similarity (dissimilarity) measures is usually obtained. Difference in applications of masked and non-masked variations of measures of similarity and dissimilarity coefficients were also evaluated.

To study the dynamic application of proposed comparative techniques, the case study includes a section where continuous and sequential pressure maps are registered and compared (using similarities and dissimilarities coefficients) to the initial pressure map frame. The objective is to evaluate the feasibility of using continuous similarities and dissimilarities coefficients as comparative dynamic pressure measures after image registration techniques are applied.

Due to the temporal nature of the (pre-processed) dynamic data subset, it is expected that the overall location and orientation of sequential pressure maps to not be significantly different over time, especially if significant in-chair movements do not occur. But if otherwise, any significant pressure redistribution, postural change, and/or positional shift made by the subject could potentially be captured by the continuous similarities and dissimilarities coefficients. Time series plots were used to assess the changes in continuous values of similarities and dissimilarities coefficients during the 5-minute dynamic sitting interval sample.

For the dynamic case study, an additional dynamic pressure measure was also examined by comparing the distance traveled by the center of pressure (CP) of the template image (i.e. the one being transformed) at registration optimality. Comparing the distance of the locations of the centers of pressure between images is often not appropriate (see Fig. 10), but tracking the distance traveled by the center of pressure of the template image after registration could be a good indicator of in-chair movement, particularly for positional shifts in the seat pan. Assessments of $CP_{original}$ vs $CP_{transformed}$ distances were done using time series plots. The objective was to evaluate significant registration translations of the CP during the dynamic sitting interval sample.

Visual feedback was also used during the case study to validate the image correspondence when significant changes in similarities coefficients, dissimilarities coefficients, or $CP_{transformed}$ translations were seen in their respective time series plots. Visual feedback assessment was made using pressure maps overlays to highlight differences in pressure between pressure map images at registration optimality.

Algorithms for applying random transformations to pressure map images, implementing MI and MSE image registration, calculating similarities and dissimilarities coefficients (masked and non-masked), and data visualization routines were coded and executed using the Python programming language. A condensed form of the Python script can be seen in Appendix E.

Outcomes

The following outcomes were pursued for this last step: (1) Recommendations of registration techniques for transforming and aligning pressure maps in the context of seating pressure maps, (2) use and interpretation of similarity and dissimilarity coefficients as global comparative measures in the context of seating pressure maps, and (3) examining the computational demands of using proposed comparative techniques for transforming and comparing pressure maps in both static (paired-samples) and dynamic (continuous pressure maps) environments.

Summary of Methods and Procedures

Various subsets of the main dataset were used for the research steps in this study. The cluster data subset was used to evaluate density-based spatial clustering techniques as pre-processing methods for detecting and removing extrinsic pressure artifacts (i.e., outliers) in seating pressure maps. The static data subset and paired data subset were used to evaluate the uniqueness, feasibilities, and interpretations of seating pressure measures based on spatial autocorrelation, first-order image statistical features, and second-order image statistical features. The transformed data subset and registration data subset were used to evaluate the application of image registration techniques for aligning and matching pressure maps, and also to evaluate the use of similarity and dissimilarity coefficients as global comparative measures between registered pressure map images.

The dynamic data subset was used as a case study for evaluating the dynamic applications of selected methods and measures. The subset was initially pre-processed using spatial clustering to remove extrinsic pressure artifacts (i.e. outliers). Measures of spatial autocorrelation and image statistical features were then calculated, and their dynamic behavior was assessed using time series plots. At the end, image registrations were performed between each pressure map frame and the initial frame, with assessments of similarity and dissimilarity coefficients using time series plots.

A summary table of the research objectives, along with the methodologies, research procedures, and outcome goals for each research step is shown in Table 8.

Table 8. Summary of research steps

Research Objectives	• **Objective 1:** Introduce methods for detecting and removing extrinsic pressure artifacts (i.e., outliers) by implementing unsupervised machine learning and spatial data clustering. • **Objective 2:** Introduce new pressure measures, with static and dynamic sitting applications, by evaluating measures of spatial autocorrelation and statistical features of images. • **Objective 3:** Introduce a toolset for aligning and comparing static and dynamic pressure maps by using optimal image registration methods and similarity/dissimilarity coefficients.			
Steps	Step 1 **Spatial Clustering**	Step 2 **Spatial Autocorrelation**	Step 3 **Image Statistical Features**	Step 4 **Image Registration and Similarity/Dissimilarity**
Methods and Data Sampling	Implementation of DBSCAN, OPTICS, HDBSCAN, DENCLUE, and DBCLASD clustering algorithms using Python	Moran's I and Geary's C spatial autocorrelation measures implementation using Python	Implementation of Gray-Level Differences (GLD) and Gray-Level Spatial-Dependence (GLSD) features using Python	Implementation of Mean Squared Errors (MSE) and Mutual Information (MI) linear registrations using Python.
	Selection of parameter settings (location-only input data and location-pressure input data)	Implementation of weight matrices (queen, constant distance, and inverse distance)	Selection of directions of interest ($\theta = 0°$ and $\theta = 90°$)	Similarities and dissimilarities coefficients with calculation variations (masked and non-masked)
	Accuracy score metrics: Overall accuracy (%), Outliers accuracy (%), and Non-Outliers accuracy (%)	Pearson correlation analysis using correlation matrix and correlogram with hierarchical correlation clustering.		Selection of parameters and settings for optimization routines
	Data Samples: *Cluster data subset:* 28/28 pressure maps with/without extrinsic pressure artifacts based on contact cells levels	Data Samples: *Static data subset:* 20 pressure maps based on CV levels. *Paired data subset:* 10 paired-samples with relative contact cells, sum of pressure and CV differences $\lvert\Delta\rvert < 5\%$, in various levels of these measures.		Data Samples: *Transformed data subset:* 10 samples, each with 2 random transformations. *Registration data subset:* 20 within-subject paired-samples with $\Delta\ CP > 1''$.
	Case Study Data Sample: Dynamic data subset: A single 5-minute interval of continuous pressure maps exhibiting dynamic sitting phenomena			
Testing Procedures	Evaluate combinations of parameter settings for best accuracy score metrics (*cluster data subset*)	Calculate common pressure measures, spatial autocorrelations, GLD, and GLSD statistical features (*static and paired data subsets*)		Evaluate translational and rotational capabilities of image registration techniques using similarity and dissimilarity coefficients (*Transformed data subset*)
	Examine computation demands of selected methods	Evaluate highly correlated measures ($R^2 \geq 0.8$) using regression models and comparative visual feedback		

Table 8—Continued

Steps	Step 1 **Spatial Clustering**	Step 2 **Spatial Autocorrelation**	Step 3 **Image Statistical Features**	Step 4 **Image Registration and Similarity/Dissimilarity**
Testing Procedures and Pursued Outcomes	Evaluate and recommend spatial clustering methods using results of accuracy scores and visual feedback assessments	Evaluate weight matrix effect and computation demands. Weight matrix recommendations.		Evaluate image registration accuracies under dynamic sitting. Visual feedback of registration via pressure maps overlays and highlights of pressure differences. (*Registration data subset*)
		Select unique measures of spatial autocorrelation, GLD, and GLSD statistical features from correlation and regression models analyses		Study differences among similarity and dissimilarity coefficients. Examine computation demands.
	Case Study: Evaluate selected clustering methods for pre-processing continuous pressure maps (i.e., detection/removal of outliers). Examine accuracy scores and computational demands. Pre-process dynamic data subset using spatial clustering method with highest overall accuracy (*Dynamic data subset*)	Validation and interpretation of spatial autocorrelation and statistical features of images in the context of human-seating interaction.		Recommend registration techniques for aligning pressure maps. Interpretation and use of similarity and dissimilarity coefficients as comparative measures.
		Case Study: Calculate and evaluate selected spatial autocorrelation and image statistical features as dynamic pressure measures. Assess changes in measures using time series plots. Comparative visual feedback of selected sequences of pressure maps to confirm detected in-chair-movements. (*Pre-processed dynamic data subset*)		Case Study: Evaluate sequential registration using the first frame as reference. Examine computation demands. Using time series plots, assess similarities and dissimilarities coefficients as dynamic measures. Examine CP translations after registrations. Visual feedback of registration via pressure maps overlays (*Pre-processed dynamic data subset*)
Step Goal	Introduce density-based spatial clustering methods for detecting and removing extrinsic pressure map artifacts **(Objective 1)**	Introduce new pressure measures based on spatial data analytics and image processing techniques for static and dynamic pressure map applications **(Objective 2)**		Introduce new methodologies for comparing pressure maps using image registration techniques and similarity/dissimilarity coefficients **(Objective 3)**

The following chapters [Chapter 5 (Results) and Chapter 6 (Case Study)] show the results obtained from completing the research steps in this study (Table 8). The results of the applications of spatial clustering methods, measures of spatial autocorrelation, image statistical features, and image registration and similarity and dissimilarity coefficients are presented in Chapter 5. The feasibilities, uniqueness, and practicalities of the proposed methods are discussed within the following chapter subsection: (1) Spatial Clustering, (2) Spatial Autocorrelation and Image Statistical Features, and (3) Image Registration and Similarity/Dissimilarity Coefficients. Summaries of the findings obtained from applying proposed methodologies to each data subset are also included in their respective chapter subsection, along with research notes and recommendations.

Results of using selected methodologies in a 5-minute interval of sequential pressure map images (dynamic data subset) are presented in Chapter 6 as a case study. This case study initially evaluates the feasibility and practicality of using selected density-based spatial clustering techniques for detecting and removing extrinsic pressure artifacts (outliers) under a continuous setting (dynamic pressure map samples). Using the pre-processed dynamic data subset, the results of selected measures of spatial autocorrelation and image statistical features are also shown in this chapter, with discussions of their evaluations as potential dynamic pressure measures. The pre-processed dynamic data subset is also used to evaluate the applications of image registration and similarity/dissimilarity coefficients as comparative pressure mapping techniques under a dynamic sitting environment. Results and evaluations of the feasibility and practicality of using continuous dynamic registration and the use of similarity/dissimilarity coefficients as potential dynamic pressure measures are also presented and discussed in the chapter.

CHAPTER V

RESULTS

Python, a high-level, general-purpose, scripting programming language, was used to obtain the results presented in this chapter . The scripts shown in Appendix C, Appendix D , and Appendix E were executed with Python 3.7 under the Spyder 3.3.4 Integrated Development Environment (IDE), using a desktop computer with a quadcore Intel i7-4770K CPU clocked at 3.90 Ghz, 16 GB of DD3 RAM at 1600 Mhz, and running the Windows 10 operating system. These same algorithms were also used to obtain the results presented in the following chapter (Chapter 6).

In this study, the numerical naming convention used for the pressure maps samples are in the format “Subject-Trial-Index”. The dataset used in this study contains continuous seating pressure readings collected from eighty-two different subjects. Three different trials, each up to 2 hours of collection time, are included for each subject, with a number of sequential indexes constituting a trial. As indexes are recorded sequentially, these have a direct relation to time. In this dataset, the pressure map readings were captured at approximately one-second intervals, each being recorded as an Index. As a naming convention example, the sample “109-2-1” represents the first pressure map captured (Index 1) during the second recording session (Trial 2) for Subject 109. The eighty-two subjects are labeled sequentially from Subject 109 to Subject 190 as originally named in the dataset.

The results in this chapter are presented in three sections, each following the main objectives of this study: (1) Spatial Clustering, where methods for detecting and removing extrinsic pressure artifacts are evaluated, (2) Spatial Autocorrelation and Image Statistical Features, where new potential pressure measures are studied, and (3) Image Registration and Similarity and Dissimilarity Coefficients, where methods for aligning and comparing pressure maps are examined.

Spatial Clustering

To evaluate the outlier-detection accuracies of the studied clustering methods, a subset of the dataset (cluster data subset) was created using stratified sampling of subjects' pressure maps based on the distribution of contact areas (i.e., contact cells) (see Fig. 12). The cluster data subset consists of twenty-eight samples (28) of pressure maps with unwanted pressure artifacts and twenty-eight samples without pressure artifacts (see Appendix F and Appendix G). Expert knowledge was used for selecting and marking the extrinsic pressure artifacts (i.e. outliers), if any, in each seating pressure map sampled.

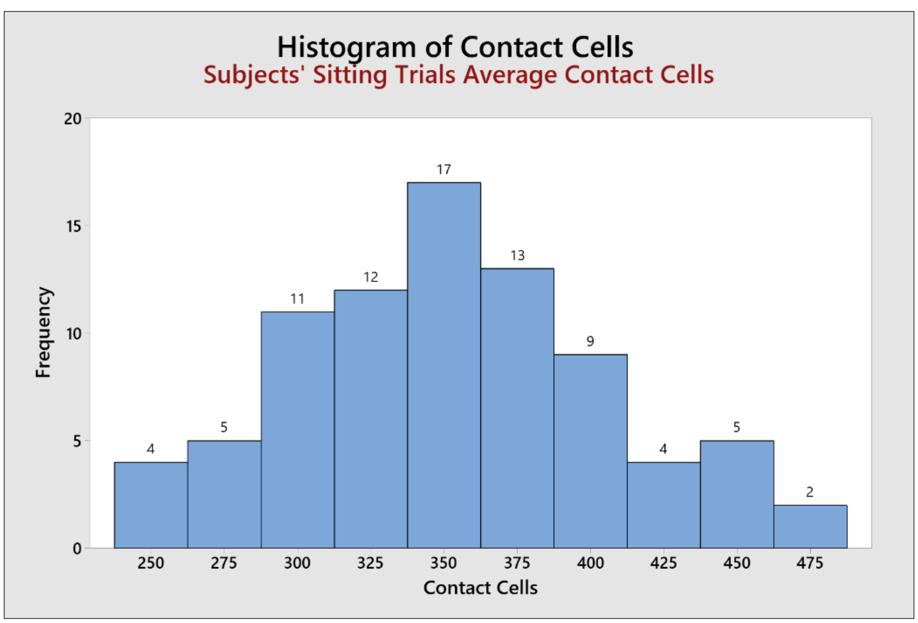

Figure 12. Histogram of subjects' average contact cells.

Two variations of the OPTICS clustering algorithm were considered: (1) OPTICS_DBSCAN where clusters are extracted using a DBSCAN-like method with an epsilon parameter (eps), and (2) OPTICS_XI where clusters are extracted using automatic technique, as specified by Ankerst et al. (1999), with a Xi parameter.

A sensitivity analysis for the parameters of each clustering algorithm (Table 4) was carried out to find possible ranges of values (minimum to maximum) where clustering algorithms where able to detect outliers while retaining the non-outliers as true pressure readings. Ten random samples with outliers where chosen from the cluster data subset to carry out the sensitivity analysis. Eight different combinations or sets of parameter settings were chosen to be evaluated for the DBSCAN, OPTICS_DBSCAN, OPTICS_XI, and HDBSCAN clustering methods, using possible values of Epsilon (*eps*), Minimum samples (*min_samples*), Xi (*xi*), Minimum size (*min_size*), and Leaf size (*leaf_size*) from the ranges of values found during the sensitivity analysis (see Table 9).

In a similar manner, five different combinations or sets of parameter settings were evaluated for DENCLUE and DBCLASD clustering methods, using possible values of Epsilon (*eps*), Minimum density (*min_density*), and Nearest Neighbors (as a % of pressure map *Area*) from the ranges of values found during the sensitivity analysis (see Table 10).

Note that combinations or sets of parameter settings are chosen according to the input data used for the clustering method. Findings during the sensitivity analysis typically resulted in different ranges of values (minimum to maximum) for each clustering method's parameters when using either the location input data or location-pressure input data.

Table 9. Clustering methods parameters sets 1-8, location and location-pressure input data

Set	DBSCAN	DBSCAN (NP)	OPTICS_XI	OPTICS_XI (NP)	OPTICS_ DBSCAN	OPTICS_ DBSCAN (NP)	HDBSCAN	HDBSCAN (NP)
1	eps:2.00 min_samples:1	eps:1.80 min_samples:5	xi:0.065 min_samples:3 min_size:0.10	xi:0.010 min_samples:3 min_size:0.10	eps:1.80 min_samples:5	eps:1.80 min_samples:5	min_size:9.00 min_samples:1 leaf_size:5.00	min_size:9.00 min_samples:1 leaf_size:5.00
2	eps:2.20 min_samples:3	eps:1.60 min_samples:8	xi:0.080 min_samples:3 min_size:0.20	xi:0.050 min_samples:5 min_size:0.15	eps:2.00 min_samples:6	eps:1.60 min_samples:8	min_size:6.00 min_samples:3 leaf_size:5.00	min_size:6.00 min_samples:3 leaf_size:5.00
3	eps:1.80 min_samples:3	eps:2.00 min_samples:8	xi:0.070 min_samples:2 min_size:0.15	xi:0.020 min_samples:5 min_size:0.15	eps:2.20 min_samples:3	eps:2.00 min_samples:5	min_size:8.00 min_samples:2 leaf_size:5.00	min_size:8.00 min_samples:2 leaf_size:5.00
4	eps:1.80 min_samples:5	eps:1.80 min_samples:8	xi:0.100 min_samples:3 min_size:0.15	xi:0.060 min_samples:3 min_size:0.15	eps:1.60 min_samples:5	eps:1.80 min_samples:8	min_size:10.00 min_samples:1 leaf_size:8.00	min_size:10.00 min_samples:3 leaf_size:8.00
5	eps:2.00 min_samples:5	eps:2.00 min_samples:10	xi:0.070 min_samples:5 min_size:0.20	xi:0.030 min_samples:5 min_size:0.20	eps:2.00 min_samples:10	eps:2.00 min_samples:8	min_size:10.00 min_samples:2 leaf_size:4.00	min_size:10.00 min_samples:2 leaf_size:4.00
6	eps:1.80 min_samples:6	eps:1.80 min_samples:10	xi:0.070 min_samples:5 min_size:0.10	xi:0.020 min_samples:5 min_size:0.10	eps:1.50 min_samples:4	eps:1.60 min_samples:10	min_size:3.00 min_samples:1 leaf_size:8.00	min_size:3.00 min_samples:1 leaf_size:8.00
7	eps:2.00 min_samples:6	eps:2.50 min_samples:10	xi:0.050 min_samples:3 min_size:0.05	xi:0.010 min_samples:3 min_size:0.05	eps:1.80 min_samples:8	eps:1.60 min_samples:4	min_size:6.00 min_samples:2 leaf_size:3.00	min_size:6.00 min_samples:2 leaf_size:3.00
8	eps:2.50 min_samples:8	eps:2.20 min_samples:10	xi:0.100 min_samples:3 min_size:0.40	xi:0.030 min_samples:3 min_size:0.40	eps:2.20 min_samples:8	eps:2.00 min_samples:10	min_size:12.00 min_samples:3 leaf_size:5.00	min_size:12.00 min_samples:3 leaf_size:5.00

Note: (NP) = No Pressure → Location input data

Table 10. Clustering methods parameters sets 9-13, location and location-pressure input data

Set	DENCLUE	DENCLUE (NP)	DBCLASD	DBCLASD (NP)
9	eps:1.0e-06 min_density:5.0e-04	eps:1.0e-01 min_density:1.0e-03	Area:28.5%	Area:50%
10	eps:1.0e-03 min_density:5.0e-04	eps:1.0e-01 min_density:2.0e-03	Area:33%	Area:67%
11	eps:2.0 min_density:4.0e-04	eps:2.0 min_density:1.5e-03	Area:40%	Area:80%
12	eps:2.0 min_density:3.0e-04	eps:2.0 min_density:1.8e-03	Area:20%	Area:33%
13	eps:1.0 min_density:2.0e-04	eps:1.0 min_density:1.3e-03	Area:12%	Area:20%

Note: NP = No Pressure → Location input data

The following subsections show the results for each clustering method when using these defined sets of parameters. The best combinations of input data plus parameter settings are chosen for each method in terms of outlier and non-outlier accuracies, that is, their abilities to detect extrinsic pressure artifacts (outliers) and true contact pressure readings (non-outliers). Measure of "Outliers accuracy" calculate the proportion of pre-identified outliers being detected as outliers, while measure of "Non-Outliers accuracy" calculate the proportion of true contact pressure readings being detected as non-outliers. "Overall accuracy" is the calculated weighted average of both Outliers and Non-Outliers accuracies. A set of clustering method's parameters are considered for further evaluation if both average Outliers and Non-Outliers accuracies results are above 0.90.

DBSCAN

DBSCAN algorithms were implemented from the Python module Scikit-learn (v0.20.3) (Pedregosa et al., 2011). A graphical summary of the average accuracies obtained when using DBSCAN, with both location and location-pressure data input, is presented in Figure 13. The top-left panel show overall average accuracies for each set of parameters and input data. The bottom-left panel shows average non-outlier accuracies when using seating pressure map samples without outliers. Right panels show average outliers (top-right) and non-outliers (bottom-right) accuracies when using seating pressure map samples with pre-identified outliers. Results indicate that DBSCAN algorithms generally show higher average accuracies for detecting outliers when the pressure reading locations are used as input data as compared to using the location-pressure information as input data.

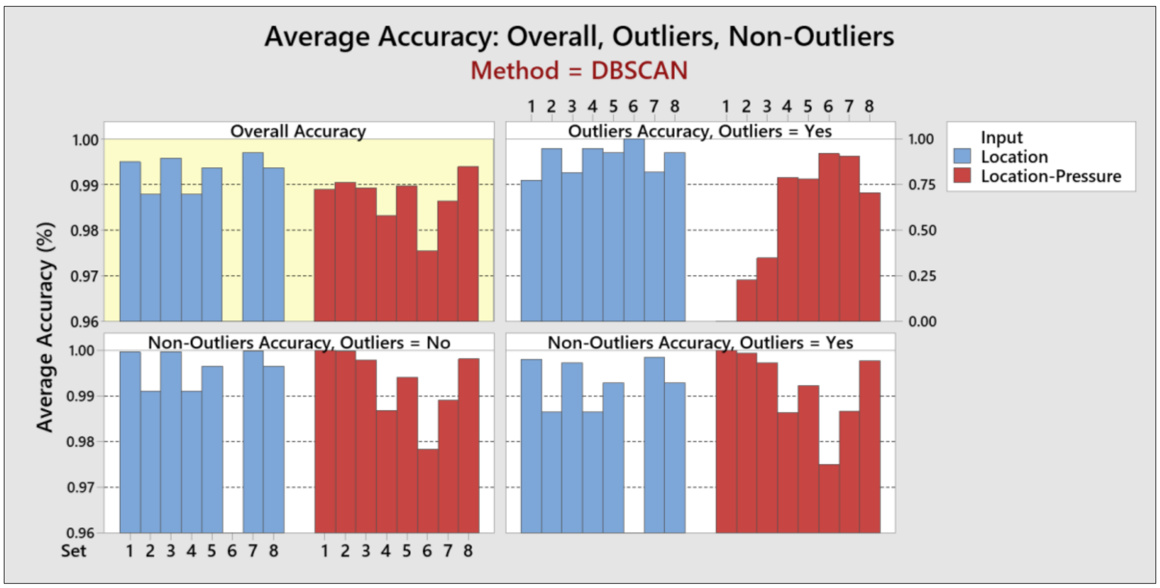

Figure 13. DBSCAN – Overall, Outliers, Non-Outliers average accuracy by set

Table 11 and Table 12 show descriptive statistics of accuracies results for all sets of parameters used in DBSCAN algorithms when using both location and location-pressure input data respectively, with sets of parameter chosen for further evaluation in bold. DBSCAN parameters sets 2 and 4, using location input data, yielded the same accuracy results in each sample; similarly, sets 5 and 8 also yielded the same accuracy results for each sample (see Table 11). A good combination of high outlier and non-outlier average accuracies were also obtained by these sets (2, 4, 5 and 8). Other sets either marked many pressure readings as outliers (e.g., Set 6) or are somewhat conservative in marking outliers (e.g., Sets 1, 3, and 7).

Table 11. DBSCAN – Accuracies results by set (location input data)

Variable	Set	Mean	StDev	Minimum	Maximum
Overall Accuracy	7	0.997	0.008	0.953	1.000
	3	0.996	0.010	0.953	1.000
	1	0.995	0.011	0.941	1.000
	5/8	**0.994**	**0.009**	**0.964**	**1.000**
	2/4	**0.988**	**0.010**	**0.961**	**1.000**
	~~6~~	~~0.011~~	~~0.014~~	~~0.000~~	~~0.059~~
Outliers Accuracy	~~6~~	~~1.000~~	~~0.000~~	~~1.000~~	~~1.000~~
	2/4	**0.949**	**0.194**	**0.111**	**1.000**
	5/8	**0.925**	**0.179**	**0.333**	**1.000**
	7	0.817	0.262	0.000	1.000
	3	0.815	0.284	0.000	1.000
	1	0.772	0.334	0.000	1.000
Non-Outliers Accuracy	1	0.999	0.003	0.985	1.000
	3	0.999	0.004	0.975	1.000
	7	0.999	0.004	0.975	1.000
	5/8	**0.995**	**0.008**	**0.964**	**1.000**
	2/4	**0.989**	**0.010**	**0.959**	**1.000**
	~~6~~	~~0.000~~	~~0.000~~	~~0.000~~	~~0.000~~

***Note**: Sets in **bold** are chosen for further evaluation (accuracies > 0.90)*

Table 12 shows that, when using the location-pressure information as input data, higher average outlier accuracies were obtained by sets of parameters 6 and 7. Unfortunately, these high average outlier accuracies were obtained at the expense of lower average non-outlier accuracies when compared to results using location input data (Table 11). By comparing the average outliers and non-outlier accuracy results obtained when using parameters set 5 (or 8) with location input data (0.925 and 0.995 respectively) to the average accuracy results obtained when using parameters set 6 with location-pressure data (0.920 and 0.977 respectively), we see that higher outlier and non-outlier accuracies were obtained when using the location of pressure reading as input data with suitable DBSCAN parameters (e.g., Sets 5 or 8).

Table 12. DBSCAN – Accuracy results by set (location-pressure input data)

Variable	Set	Mean	StDev	Minimum	Maximum
Overall Accuracy	8	0.994	0.010	0.941	1.000
	2	0.991	0.013	0.941	1.000
	5	0.990	0.012	0.941	1.000
	1	0.989	0.014	0.941	1.000
	3	0.989	0.013	0.941	1.000
	7	**0.986**	**0.012**	**0.950**	**1.000**
	4	0.983	0.016	0.924	1.000
	6	**0.976**	**0.018**	**0.918**	**1.000**
Outliers Accuracy	**6**	**0.920**	**0.227**	**0.000**	**1.000**
	7	**0.907**	**0.233**	**0.000**	**1.000**
	4	0.787	0.315	0.000	1.000
	5	0.782	0.318	0.000	1.000
	8	0.706	0.335	0.000	1.000
	3	0.349	0.329	0.000	1.000
	2	0.230	0.276	0.000	1.000
	~~1~~	~~0.000~~	~~0.000~~	~~0.000~~	~~0.000~~
Non-Outliers Accuracy	~~1~~	~~1.000~~	~~0.000~~	~~1.000~~	~~1.000~~
	2	1.000	0.001	0.994	1.000
	3	0.998	0.003	0.986	1.000
	8	0.998	0.003	0.985	1.000
	5	0.993	0.006	0.976	1.000
	7	**0.988**	**0.009**	**0.970**	**1.000**
	4	0.987	0.011	0.942	1.000
	6	**0.977**	**0.016**	**0.928**	**1.000**

***Note**: Sets in **bold** are chosen for further evaluation (accuracies > 0.90)*

Out of all the combinations of parameter settings and input data, DBSCAN parameters used in sets 2/4 and 5/8 with location input data resulted in high average outlier accuracies (0.949 and 0.925 respectively) and high average non-outlier accuracies (0.989 and 0.995 respectively). Figure 14 shows boxplots for DBSCAN outlier accuracies for all parameter sets when using location input data. Results from sets 2 and 5 are highlighted to show points of individual pressure maps where Outliers accuracies were not 1 (100%). Figure 15 shows examples of the outlier reference maps where Outliers accuracies below 0.80 were found in any of these sets (2/4 and 5/8). The figure also shows cross-referenced clustering results between sets 2/4 and 5/8 for these outlier reference maps. DBSCAN failed to detect a significant number of outliers in pressure map samples 172-2-1047 and 144-1-779 when using parameter sets 2/4; but it was otherwise successful in detecting outliers in all other maps at the expense of marking some non-outlier readings as outliers. In contrast, DBSCAN successfully detected the group of outliers in sample 172-2-1047 when using parameter sets 5/8, but it was more conservative in marking outliers in all other maps presented in the figure. All DBSCAN sets (location or pressure-location) failed to mark the group of outliers referenced in sample 144-1-779 (see Fig. 15, 2nd row).

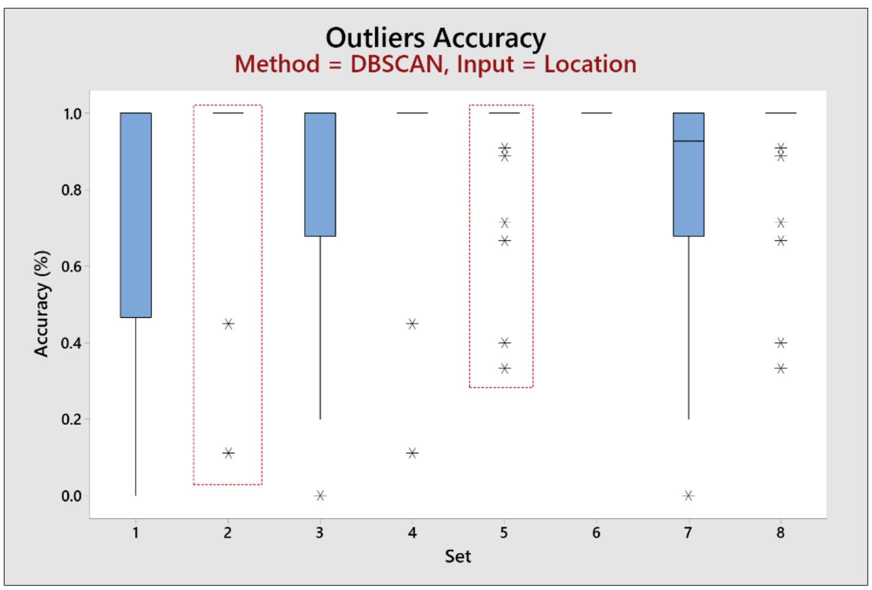

Figure 14. DBSCAN – Outliers accuracy boxplots by set (location input data)

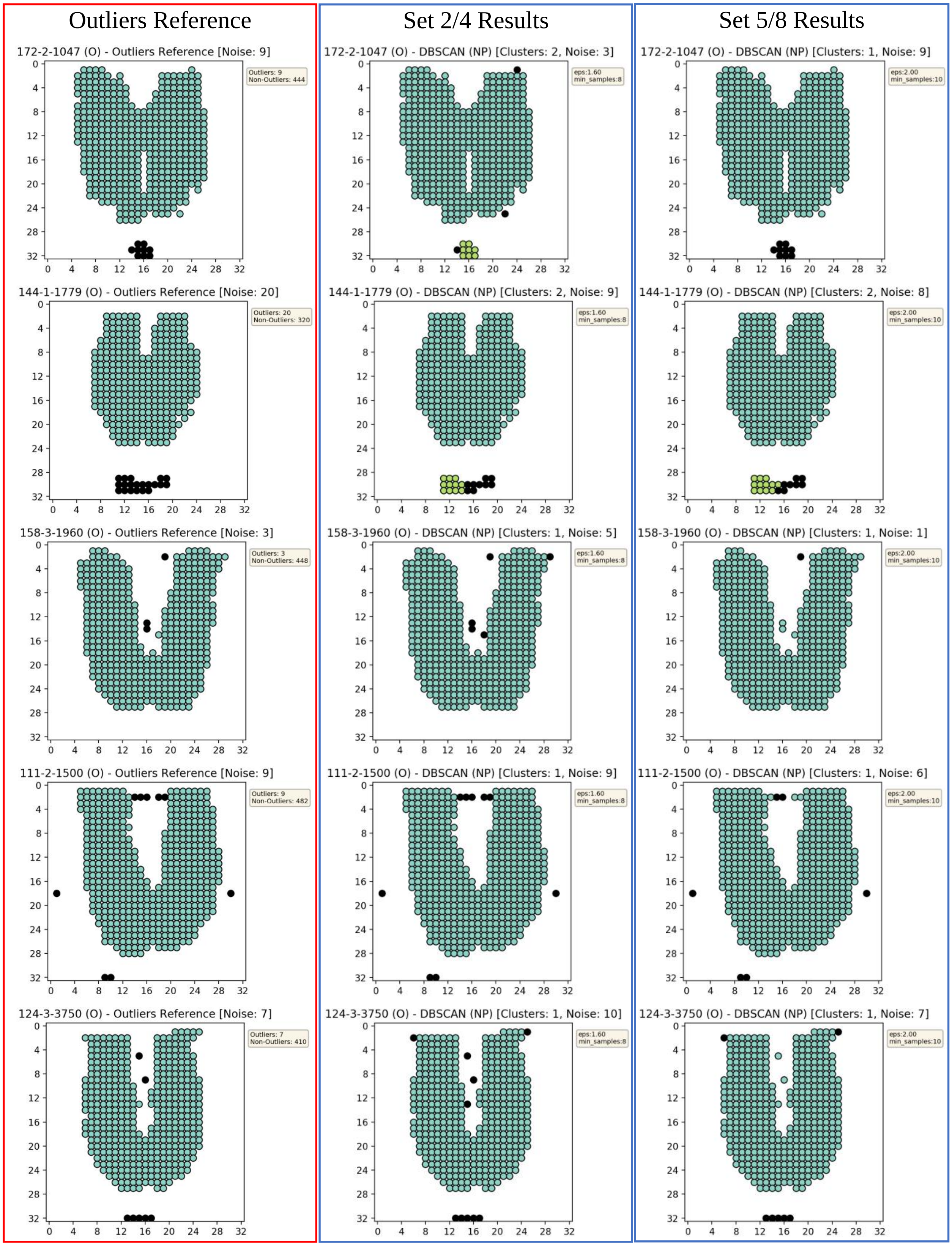

Figure 15. DBSCAN – Low outlier accuracy samples in sets 2/4 and 5/8 (location input data)

Figure 16 shows boxplots for DBSCAN Non-Outlier accuracies for all parameter sets when using location input data. Results from sets 2 and 5 are highlighted to show points of individual pressure maps where Non-Outliers accuracies were not 1 (100%). Non-Outliers accuracies results when using parameters sets 5/8 where generally higher compared to results when using parameters sets 2/4. It is important to note that the Non-Outliers accuracies results obtained from these sets (2, 4, 5, or 8) were above 0.95 for all samples. Figure 17 show examples where Non-Outliers accuracies between 0.95 and 0.98 were found in any of these sets (2/4 and 5/8). Here we see that DBSCAN algorithms, when using parameters settings from either of these sets, mostly marked pressure readings as outliers when a significant departure from the main contiguous pressure cluster is found (e.g., samples 175-3-1142 and 175-2-1208).

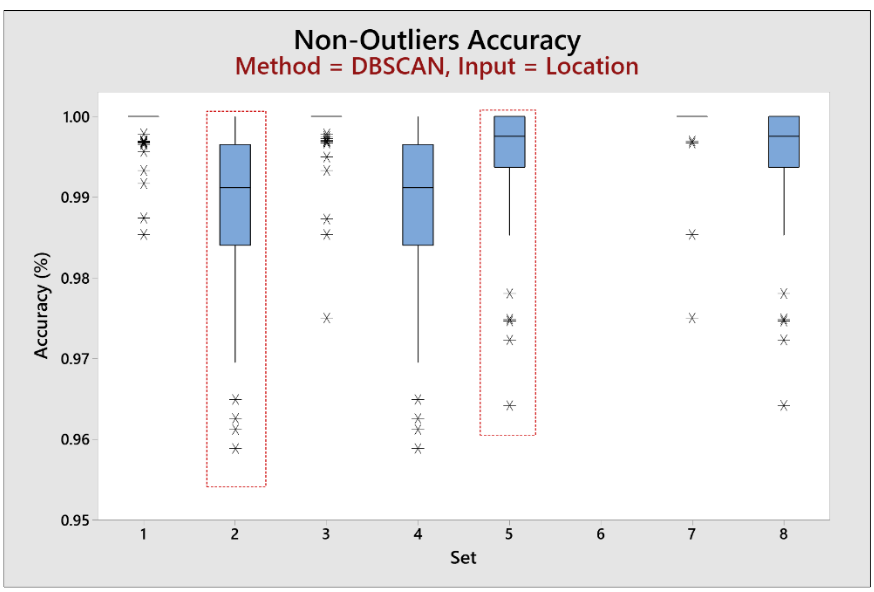

Figure 16. DBSCAN – Non-outliers accuracy boxplots by set (location input data)

In summary, using the location information as input data, parameters of epsilon between 1.60 - 1.8 with minimum samples at 8 (sets 2/4), or epsilon parameters between 2.00 - 2.20 with minimum samples at 10 (sets 5/8) were found as adequate when using DBSCAN algorithms for detecting outlier/non-outliers seating pressure readings in a 32x32 pressure map. If preservation of all true pressure readings is of utmost importance, using DBSCAN with the epsilon parameter at 2.5 with minimum samples at 10 (set 7) resulted in an acceptable average Outliers accuracy (0.817), while maintaining a very high average Non-Outliers accuracy (0.999); only four out of the fifty-six pressure map samples did not show a perfect Non-Outliers accuracy score, all were at least 0.9751 when using location input data and DBSCAN parameters from set 7 (see Fig. 16).

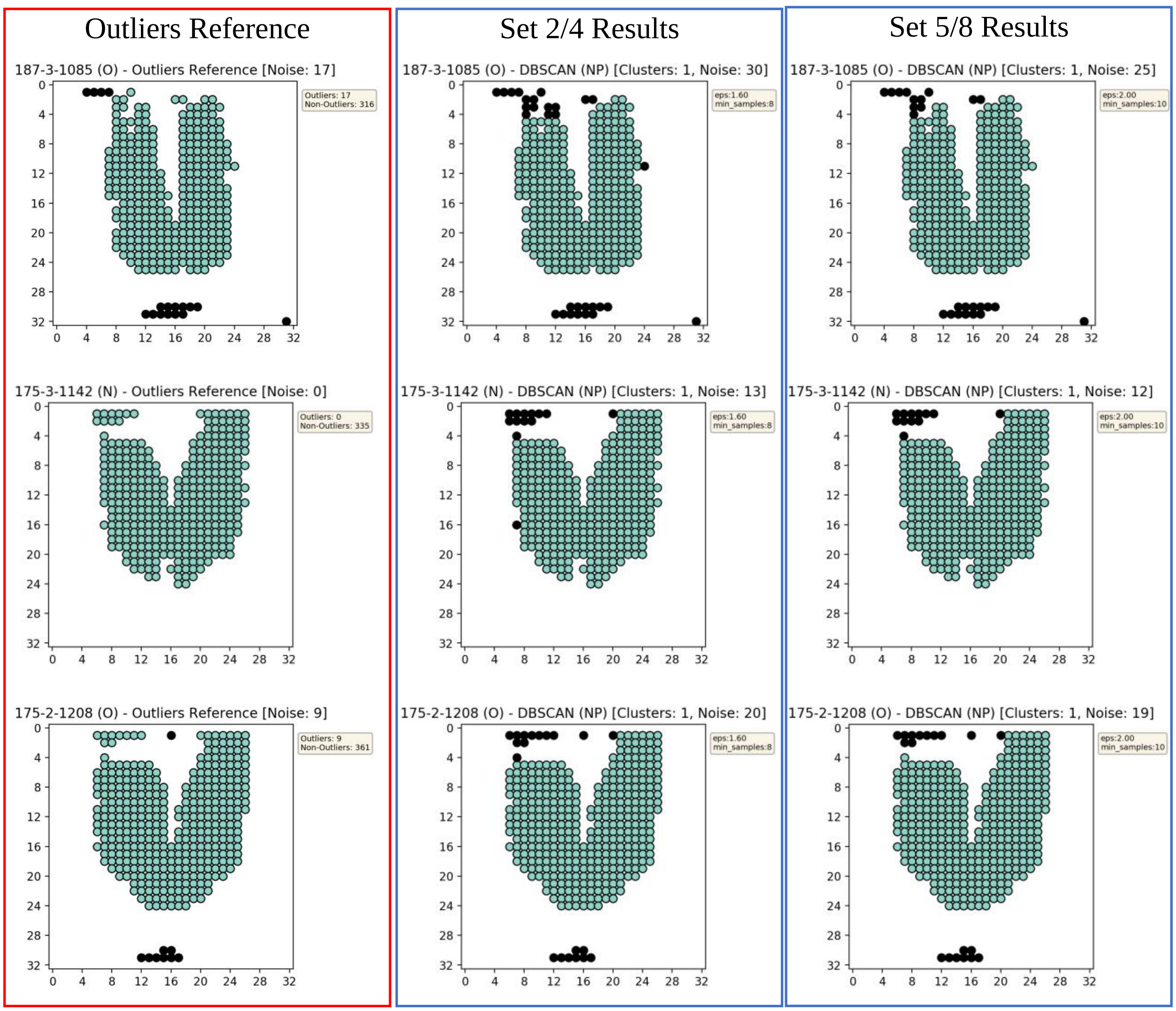

Figure 17. DBSCAN – Sets 2/4 and 5/8 samples, non-outlier accuracy <0.98 (location input data)

OPTICS_XI

OPTICS_XI algorithms were also implemented from the Python module Scikit-learn (v0.20.3) (Pedregosa et al., 2011). A graphical summary of OPTICS_XI average accuracies, with both location and location-pressure data input, is presented in Figure 18. As with similar figures, the top-left panel show average overall accuracies for each set of parameters and input data. Right panels show average outliers (top-right) and non-outliers (bottom-right) accuracies for each set of parameters when using seating pressure map samples with pre-identified outliers. The bottom-left panel shows average non-outlier when using seating pressure map samples without outliers. Results indicate that OPTICS_XI algorithms generally show higher average accuracies for detecting outliers when using both pressure readings and location information as input data. When using only pressure readings location as input data, lower average outlier accuracies (<0.9) but higher average non-outlier accuracies (>0.9) were obtained, indicating a more conservative approach when marking outliers.

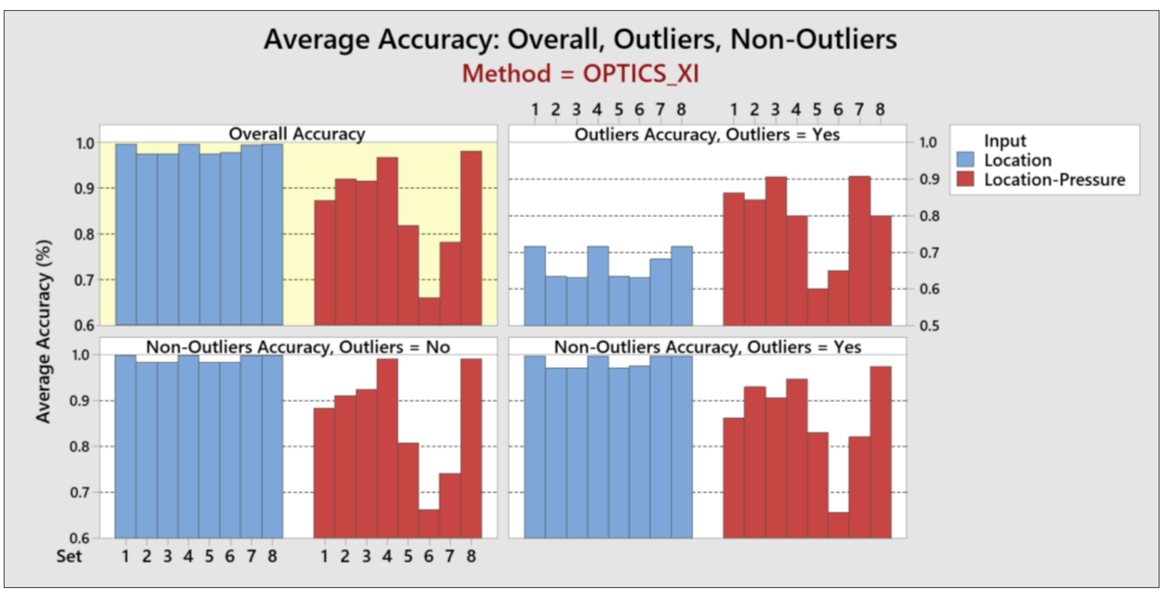

Figure 18. OPTICS_XI – Overall, Outliers, Non-Outliers average accuracy by set

Table 13 show descriptive statistics of accuracies results for all sets of parameters used in OPTICS_XI algorithms when using both pressure readings and location information as input data. Results from using parameters settings in set 3 resulted in high average Outliers accuracy (0.905) and high average Non-Outlier accuracy (0.915).

Table 13. OPTICS_XI – Accuracy results by set (location-pressure input data)

Variable	**Set**	**Mean**	**StDev**	**Minimum**	**Maximum**
Overall Accuracy	8	0.981	0.074	0.446	1.000
	4	0.968	0.124	0.241	1.000
	2	0.920	0.193	0.241	1.000
	3	**0.916**	**0.197**	**0.241**	**1.000**
	1	0.873	0.239	0.241	1.000
	5	0.818	0.308	0.207	1.000
	7	0.782	0.299	0.051	1.000
	6	0.661	0.380	0.101	1.000
Outliers Accuracy	7	0.907	0.260	0.000	1.000
	3	**0.905**	**0.233**	**0.000**	**1.000**
	1	0.863	0.320	0.000	1.000
	2	0.844	0.319	0.000	1.000
	4	0.799	0.353	0.000	1.000
	8	0.799	0.353	0.000	1.000
	6	0.650	0.462	0.000	1.000
	5	0.602	0.465	0.000	1.000
Non-Outliers Accuracy	8	0.983	0.076	0.435	1.000
	4	0.969	0.126	0.227	1.000
	2	0.920	0.195	0.227	1.000
	3	**0.915**	**0.199**	**0.227**	**1.000**
	1	0.873	0.242	0.227	1.000
	5	0.819	0.313	0.207	1.000
	7	0.781	0.302	0.051	1.000
	6	0.660	0.387	0.101	1.000

***Note**: Sets in **bold** are chosen for further evaluation (accuracies > 0.90)*

Figures 19 and 20 show boxplots for OPTICS_XI Outliers and Non-Outliers accuracies, respectively, for all parameter sets when using the location-pressure input data. Set 3 is highlighted to show points of individual pressure maps where Outliers and Non-Outliers accuracies were not 1 (100%). Note that non-outlier accuracies were very low on many samples

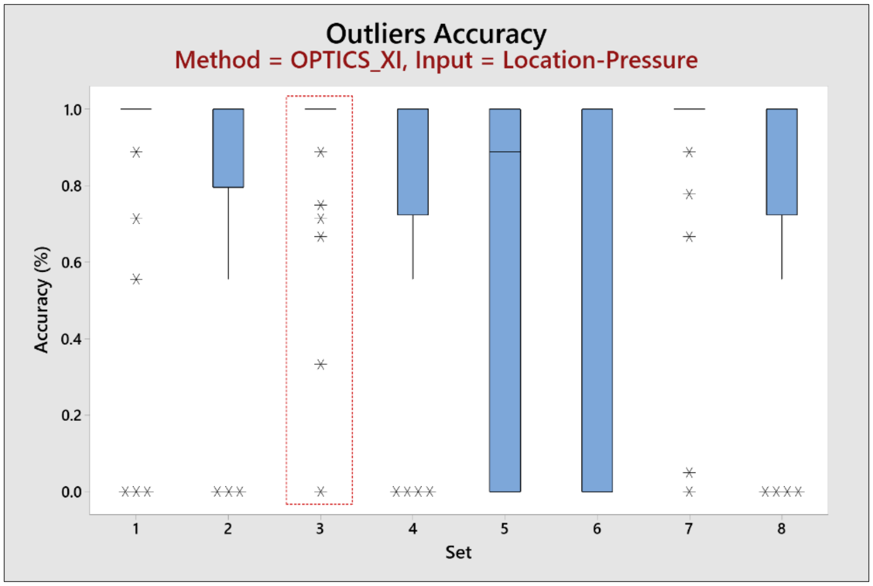

Figure 19. OPTICS_XI – Outliers accuracy boxplots by set (location-pressure input data)

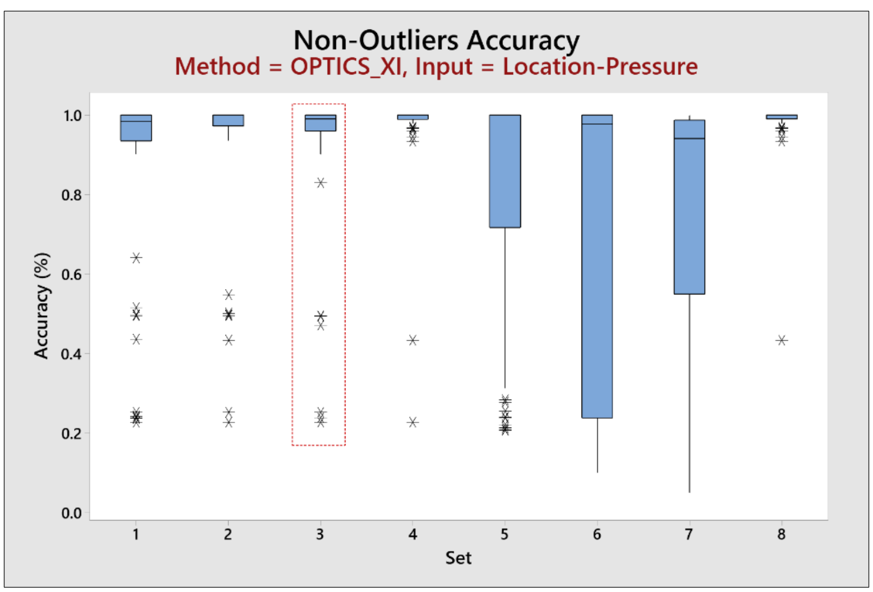

Figure 20. OPTICS_XI – Non-outliers accuracy boxplots by set (location-pressure input data)

Figure 21 shows examples of outlier reference maps where Outlier accuracies below 0.50 were found when using parameter settings in set 3 (location-pressure input data). Similarly, Figure 22 shows examples of seating pressure maps where Non-Outliers accuracies were below 0.50 for the same set (3). OPTICS_XI is shown to be somewhat inconsistent when detecting outliers; in some instances it was conservative in marking pressure readings as outliers (see Fig. 21), while in other cases, the majority of true contact pressure readings were being marked as outliers (see Fig. 22). This inconsistency in the accuracies results makes the use of OPTICS_XI an unreliable technique for detecting outlier and non-outliers seating pressure readings in a 32x32 pressure map.

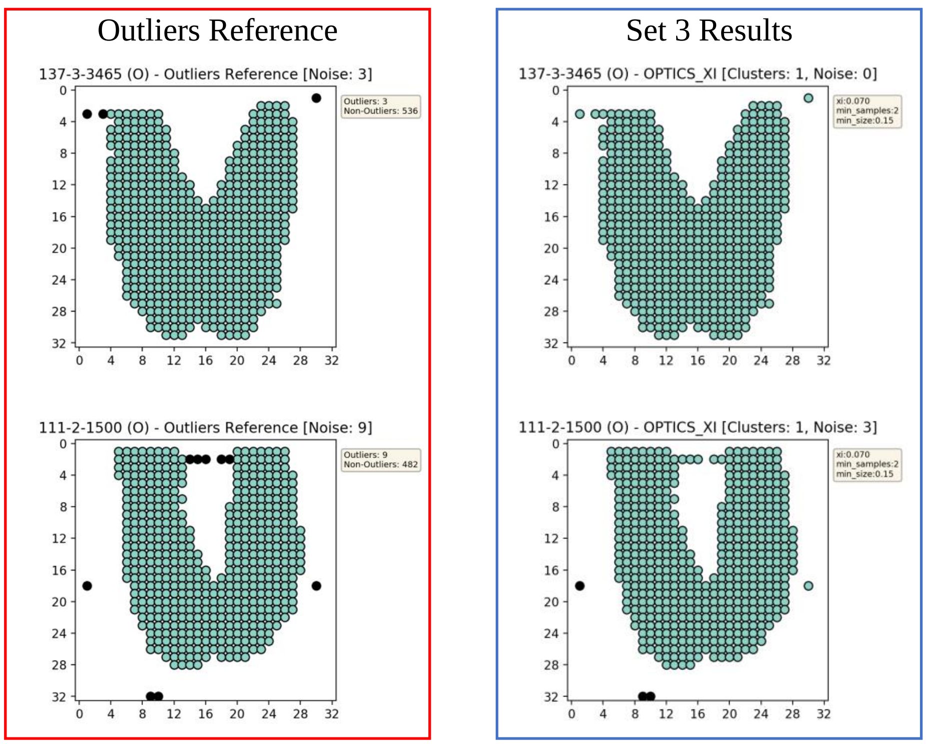

Figure 21. OPTICS_XI – Low outlier accuracy samples in set 3 (location-pressure input data)

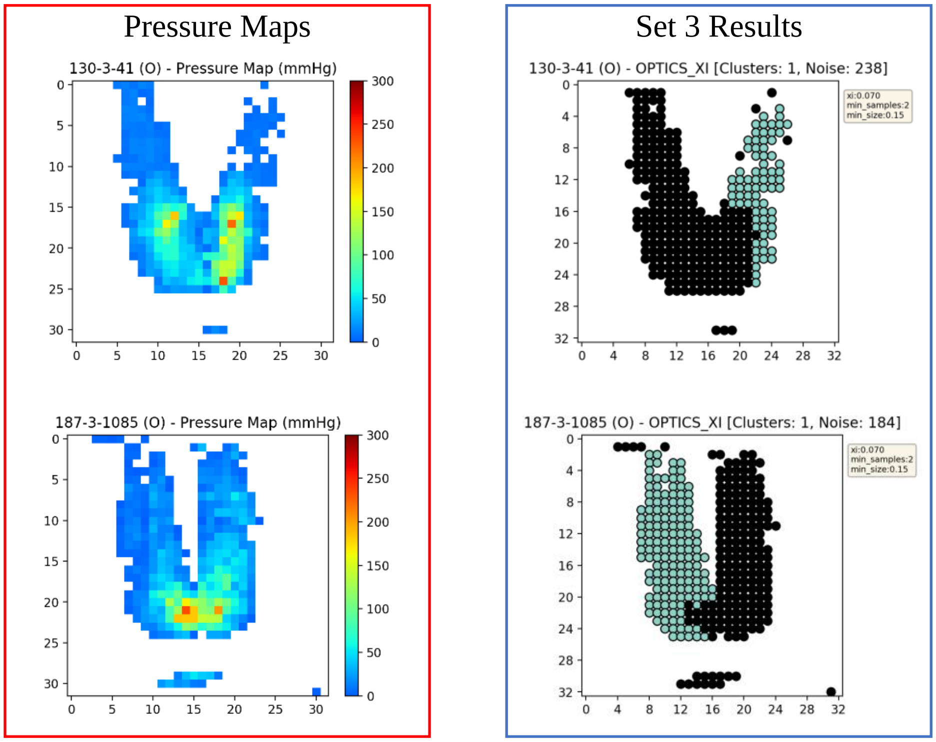

Figure 22. OPTICS_XI – Low non-outliers accuracy samples in set 3 (location-pressure input)

OPTICS_DBSCAN

OPTICS_DBSCAN algorithms were also implemented from the Python module Scikit-learn (v0.20.3) (Pedregosa et al., 2011). A graphical summary of the average accuracies obtained when using OPTICS_DBSCAN, with both location and location-pressure data input, is presented in Figure 23. As with similar figures, the top-left panel show average overall accuracies for each set of parameters and input data. Right panels show average outliers (top-right) and non-outliers (bottom-right) accuracies for each set of parameters when using seating pressure map samples with pre-identified outliers. The bottom-left panel shows average non-outlier when using seating pressure map samples without outliers. Results indicate that OPTICS_DBSCAN algorithms generally show acceptable outlier and non-outlier accuracies either when using only the location information as input data or both pressure readings and location information as input data.

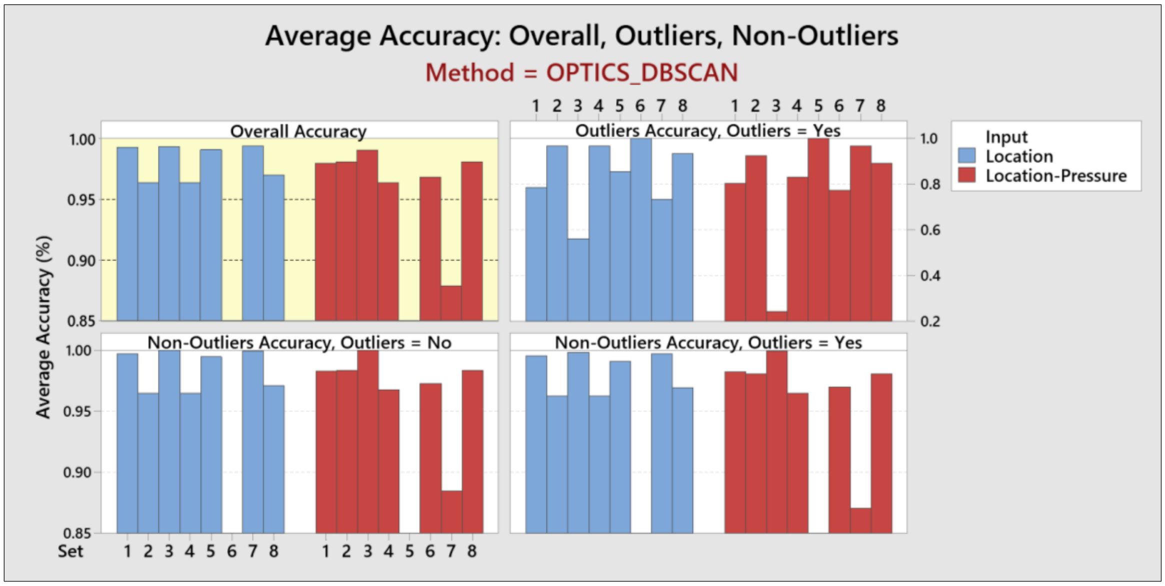

Figure 23. OPTICS_DBSCAN – Overall, Outliers, Non-Outliers average accuracy by set

Table 14 show descriptive statistics of accuracies results for all sets of parameters used in OPTICS_XI algorithms when using the location information as input data. OPTICS_DBSCAN parameters from sets 2 and 4, using location input data, yielded the same accuracy results in each sample (see Table 14). A good combination of high outlier and non-outlier average accuracies were obtained by sets 2, 4 and 8. Other sets either marked all readings as outliers (e.g., set 6) or were more conservative in marking outliers (e.g., sets 1, 3, 5, and 7). Using location input data and OPTICS_DBSCAN with parameters in sets 2/4 and 8, resulted in high average outlier accuracies (0.968 and 0.933 respectively) and high average non-outlier accuracies (0.964 and 0.97 respectively). Figure 24 shows boxplots for OPTICS_DBSCAN outlier accuracies for all parameter sets when using location input data. Results from sets 2 and 8 are highlighted to show points of individual pressure maps where Outliers accuracies were not 1 (100%). Some of these individual pressure maps are presented in Figure 25.

Table 14. OPTICS_DBSCAN – Accuracy results by set (location input data)

Variable	Set	Mean	StDev	Minimum	Maximum
Overall Accuracy	7	0.994	0.012	0.941	1.000
	1	0.993	0.011	0.941	1.000
	3	0.993	0.012	0.941	1.000
	5	0.991	0.010	0.943	0.998
	8	**0.970**	**0.012**	**0.941**	**0.992**
	2/4	**0.964**	**0.012**	**0.939**	**0.989**
	~~6~~	~~0.011~~	~~0.014~~	~~0.000~~	~~0.059~~
Outliers Accuracy	~~6~~	~~1.000~~	~~0.000~~	~~1.000~~	~~1.000~~
	2/4	**0.968**	**0.122**	**0.444**	**1.000**
	8	**0.933**	**0.160**	**0.333**	**1.000**
	5	0.853	0.223	0.333	1.000
	1	0.786	0.320	0.000	1.000
	7	0.734	0.349	0.000	1.000
	3	0.560	0.381	0.000	1.000
Non-Outliers Accuracy	3	0.999	0.002	0.985	1.000
	7	0.998	0.003	0.982	1.000
	1	0.996	0.004	0.982	1.000
	5	0.993	0.008	0.965	0.998
	8	**0.970**	**0.011**	**0.943**	**0.991**
	2/4	**0.964**	**0.012**	**0.937**	**0.989**
	~~6~~	~~0.000~~	~~0.000~~	~~0.000~~	~~0.000~~

***Note**: Sets in **bold** are chosen for further evaluation (accuracies > 0.90)*

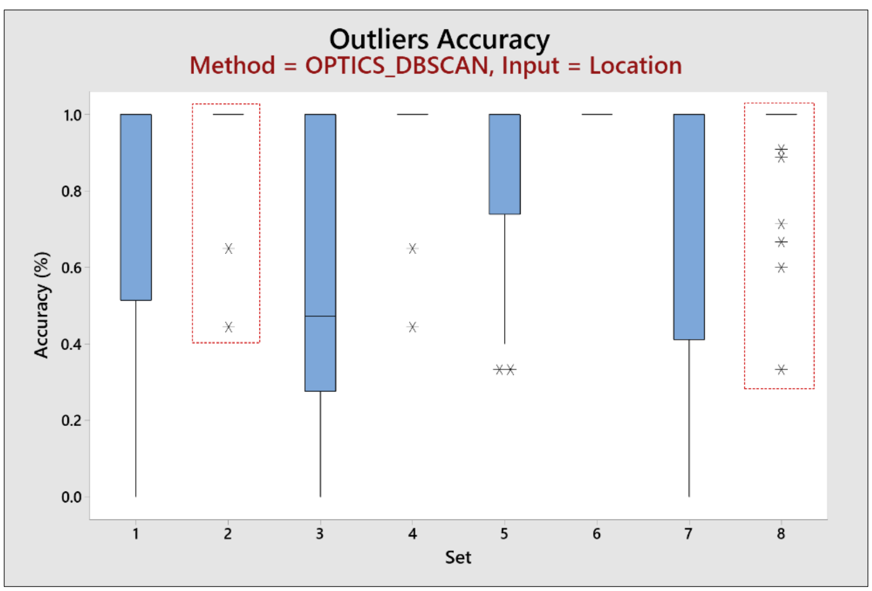

Figure 24. OPTICS_DBSCAN – Outliers accuracy boxplots by set (location input data)

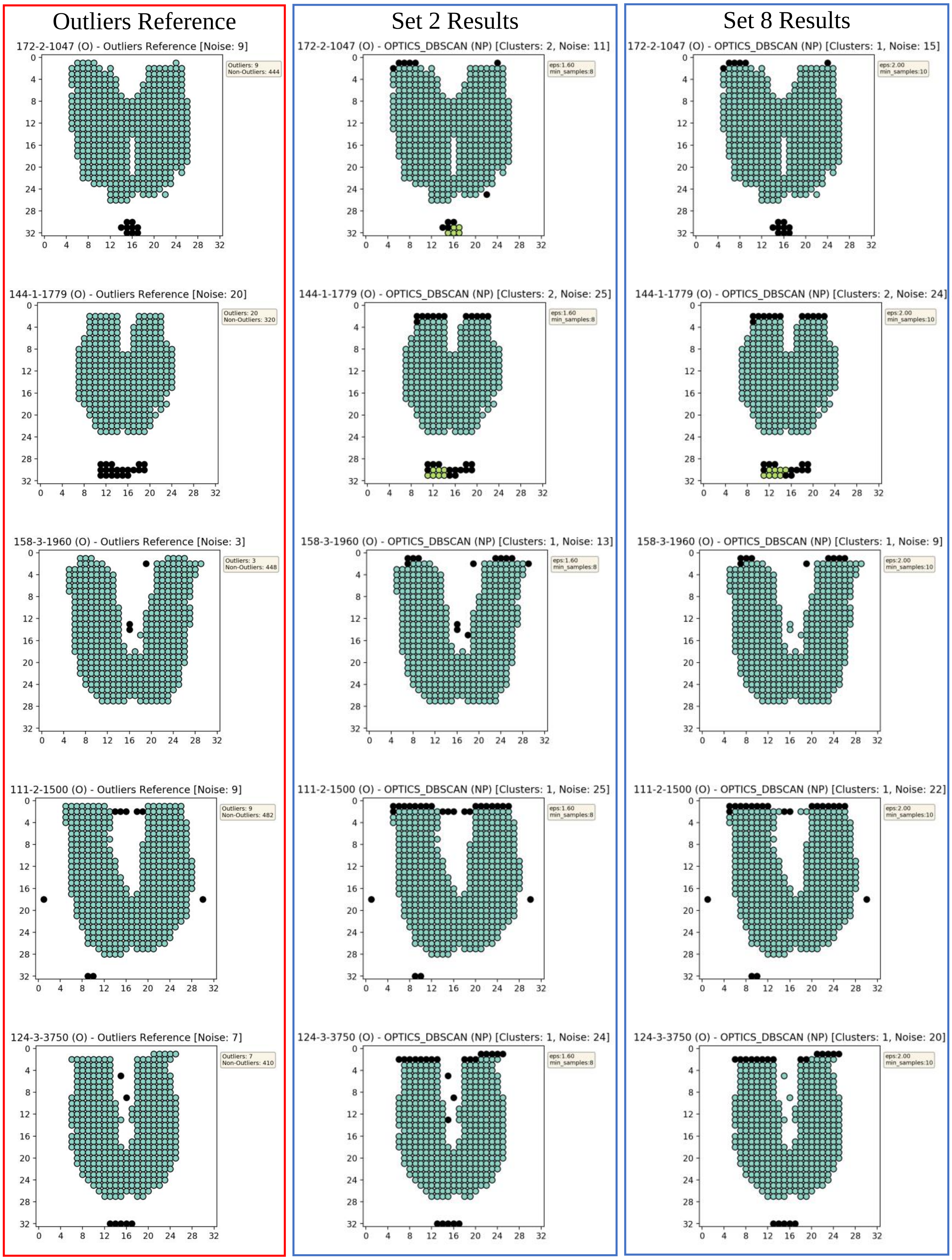

Figure 25. OPTICS_DBSCAN – Low outlier accuracy samples in sets 2 and 8 (location input)

Using the location information as input data, Figure 25 shows examples of outlier reference maps where outlier accuracies below 0.80 were found when using OPTICS_DBSCAN with set 2 or set 8 parameters. While results obtained from set 2 generally show higher accuracies in detecting outliers, set 8 correctly detected the group of outliers present in sample 172-2-1047 (Fig. 25, 1st row), whereas set 2 did not. In both sets (2 and 8), many true contact pressure readings (non-outliers) are being marked as outliers, particularly in the first rows of pressure readings under the legs. Figure 26 confirms that using OPTICS_DBSCAN with parameters from either set (2 or 8) always resulted in a number of non-outlier pressure readings being marked as outliers, as none of the individual map results showed a 100% Non-Outliers accuracy within these sets (see Table 14).

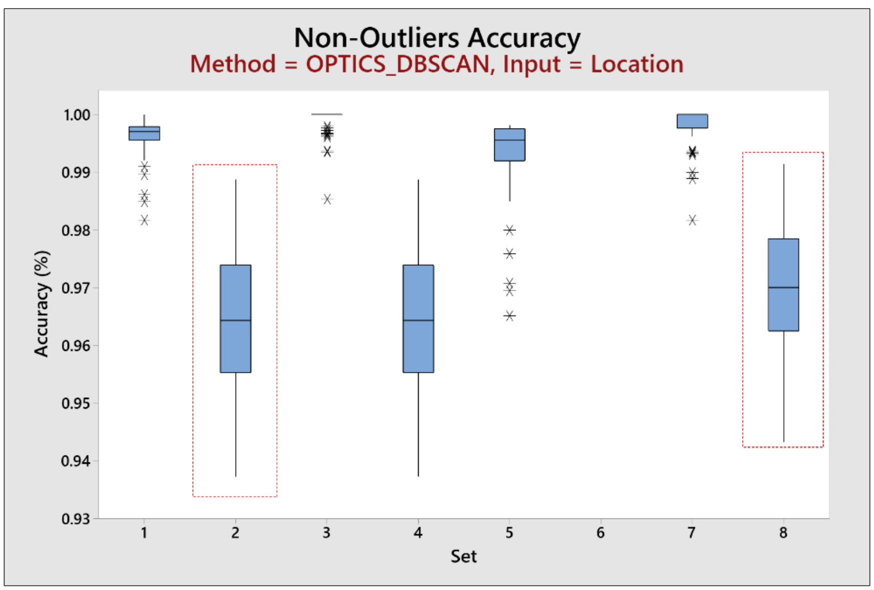

Figure 26. OPTICS_DBSCAN – Non-outliers accuracy boxplots by set (location input data)

Table 15 show descriptive statistics of accuracies results for all sets of parameters used in OPTICS_DBSCAN algorithms when using the location-pressure data input. In this scenario, OPTICS_DBSCAN parameters used in set 2 resulted in high average outlier accuracy (0.925) and high average non-outlier accuracy (0.982). Figure 27 and Figure 28 show boxplots for OPTICS_DBSCAN outlier and non-outlier accuracies, respectively, for all parameter sets when using location-pressure input data. Set 2 is again highlighted to show results of individual pressure maps where low outlier and non-outlier accuracies were detected.

Table 15. OPTICS_DBSCAN – Accuracy results by set (location-pressure input data)

Variable	Set	Mean	StDev	Minimum	Maximum
Overall Accuracy	3	0.991	0.013	0.941	1.000
	2	**0.981**	**0.014**	**0.940**	**0.998**
	8	0.981	0.013	0.950	0.998
	1	0.980	0.017	0.924	1.000
	6	0.968	0.021	0.903	1.000
	4	0.964	0.023	0.895	1.000
	7	0.879	0.042	0.756	0.952
	~~5~~	~~0.019~~	~~0.018~~	~~0.000~~	~~0.074~~
Outliers Accuracy	~~5~~	~~1.000~~	~~0.000~~	~~1.000~~	~~1.000~~
	7	0.968	0.122	0.444	1.000
	2	**0.925**	**0.178**	**0.333**	**1.000**
	8	0.891	0.195	0.333	1.000
	4	0.830	0.264	0.111	1.000
	1	0.804	0.300	0.000	1.000
	6	0.774	0.312	0.000	1.000
	3	0.245	0.282	0.000	1.000
Non-Outliers Accuracy	3	1.000	0.001	0.994	1.000
	1	0.983	0.013	0.939	1.000
	2	**0.982**	**0.012**	**0.942**	**0.998**
	8	0.982	0.012	0.949	0.998
	6	0.971	0.018	0.918	1.000
	4	0.966	0.021	0.895	1.000
	7	0.878	0.043	0.751	0.951
	~~5~~	~~0.008~~	~~0.013~~	~~0.000~~	~~0.042~~

***Note**: Sets in **bold** are chosen for further evaluation (accuracies > 0.90)*

When introducing pressure information, OPTICS_DBSCAN results from using parameter settings in set 2 showed a higher average Non-Outlier accuracy (0.982) than results from the best location-only sets (0.964 or 0.98, from sets 2 and 8 respectively). Unfortunately, a lower average outlier accuracy (0.925) was seen when using the location-pressure input data with this set (2) when compared to the best location-only sets (0.933 or 0.968, from sets 2 and 8 respectively), indicating a more conservative approach when marking outliers. However, there were only five instances (out of twenty-eight) where outlier accuracies were below 0.80, with all other samples having outlier accuracies at 100% (see Fig. 27).

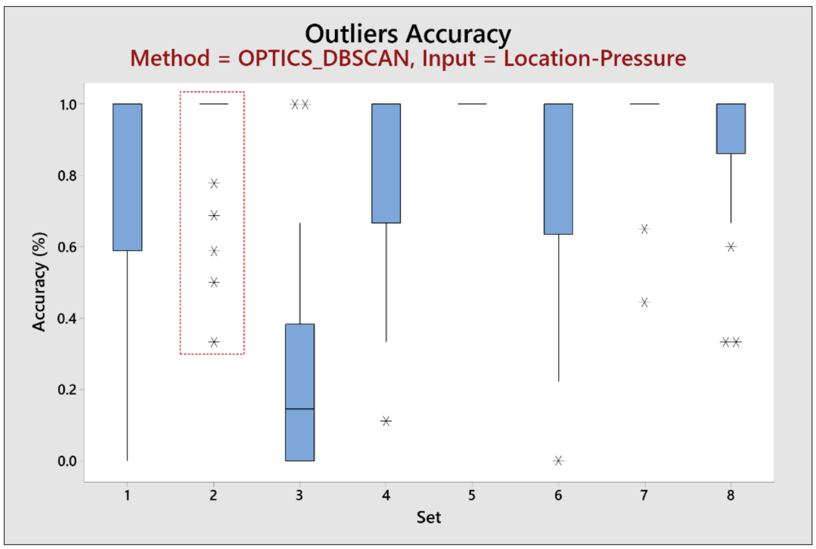

Figure 27. OPTICS_DBSCAN – Outliers accuracy by set (location-pressure input data)

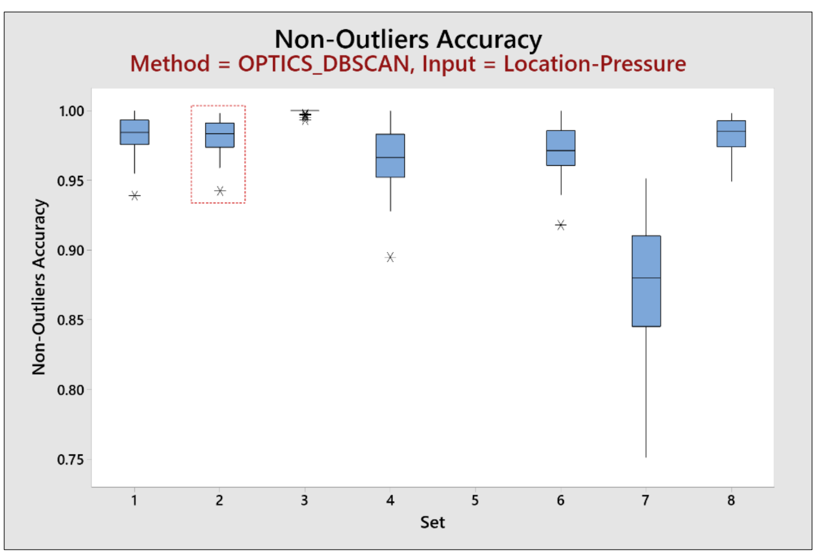

Figure 28. OPTICS_DBSCAN – Non-outliers accuracy by set (location-pressure input data)

Figure 29 shows examples of outlier reference maps where outlier accuracies below 0.80 were found when using OPTICS_DBSCAN with location-pressure input data and set 2 parameters. The results shown in this figure indicate that OPTICS_DBSCAN (set 2) was unable to properly mark outliers when a cluster of outliers separate from the main group of true contact pressure readings is present in the pressure map. Additionally, a number of true pressure readings are also being marked as outliers in these samples. Results indicate that the use of OPTICS_DBSCAN as outlier dectection method comes at the expense of marking true pressure readings as outliers when either using location-only or location-pressure input data (see Figs. 25, 29).

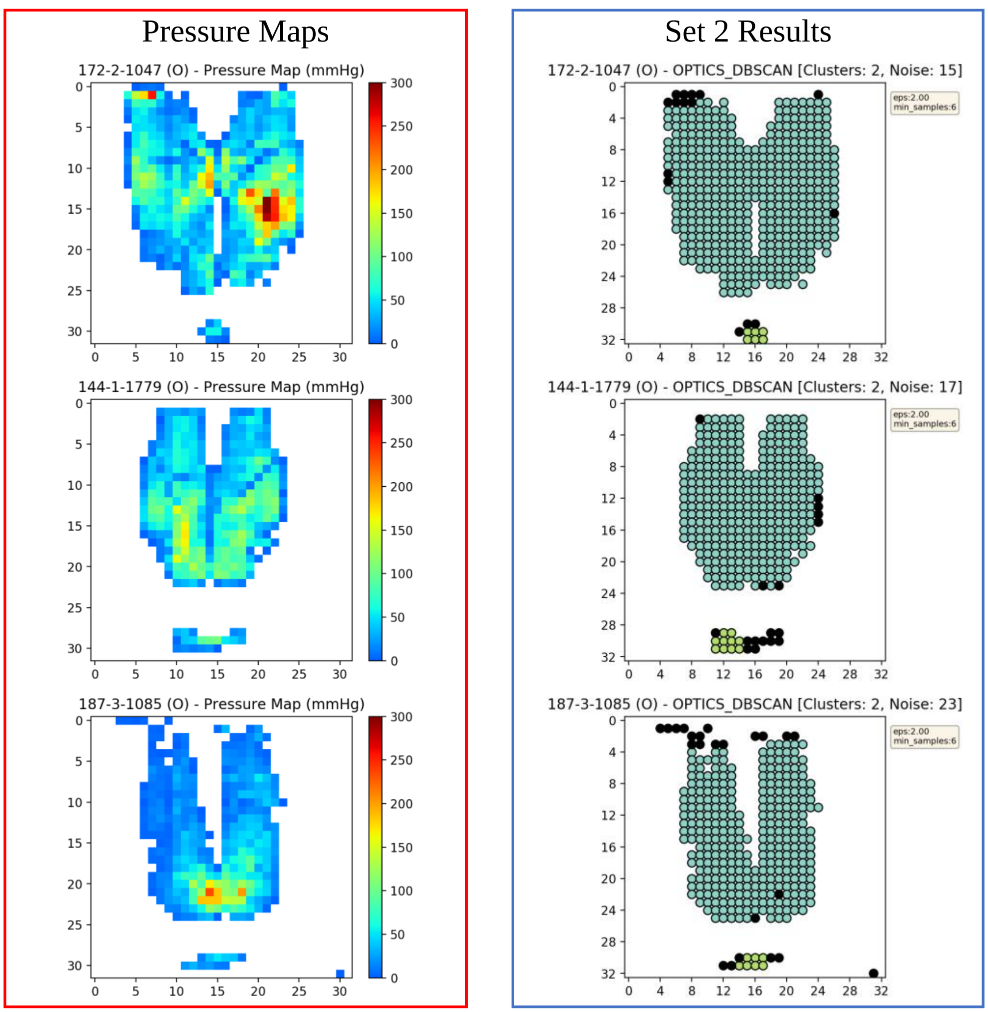

Figure 29. OPTICS_DBSCAN – Low outlier accuracy samples in set 2 (location-pressure input)

HDBSCAN

HDBSCAN algorithms were implemented from the Python module *hdbscan* (v0.8.20) (McInnes et al., 2017). A graphical summary of the average accuracies obtained when using HDDBSCAN, with both location and location-pressure data input, is presented in Figure 30. As with similar figures, the top-left panel show average overall accuracies for each set of parameters and input data. Right panels show average outliers (top-right) and non-outliers (bottom-right) accuracies for each set of parameters when using seating pressure map samples with pre-identified outliers. The bottom-left panel shows average non-outlier when using seating pressure map samples without outliers. Results indicate that HDBSCAN algorithms behave somewhat similar in terms of average outlier and non-outlier accuracies when either using the location information as input data or both pressure and location information as input data.

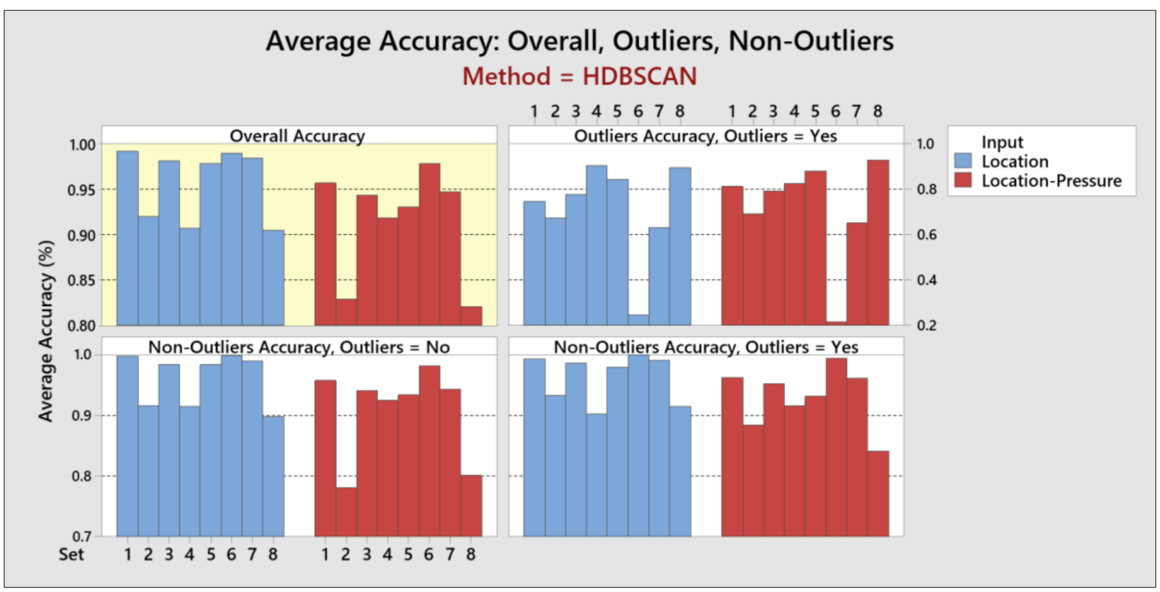

Figure 30. HDBSCAN – Overall, Outliers, Non-Outliers average accuracy by set

Table 16 show descriptive statistics of accuracies results for all sets of parameters used in HDBSCAN algorithms when using the location information as input data. Only results obtained when using set 4 show average Outlier and Non-Outlier accuracies above 0.90. When using the location-pressure input data, none of the sets showed paired accuracies above 0.90 (see Table 17).

Table 16. HDBSCAN – Accuracy results by set (location input data)

Variable	**Set**	**Mean**	**StDev**	**Minimum**	**Maximum**
Overall Accuracy	1	0.992	0.013	0.941	1.000
	6	0.990	0.014	0.941	1.000
	7	0.985	0.014	0.941	1.000
	3	0.981	0.018	0.929	1.000
	5	0.979	0.021	0.929	1.000
	2	0.920	0.034	0.845	0.997
	4	**0.907**	**0.033**	**0.833**	**1.000**
	8	0.905	0.034	0.816	0.996
Outliers Accuracy	**4**	**0.904**	**0.285**	**0.000**	**1.000**
	8	0.895	0.296	0.000	1.000
	5	0.843	0.323	0.000	1.000
	3	0.776	0.379	0.000	1.000
	1	0.746	0.366	0.000	1.000
	2	0.674	0.452	0.000	1.000
	7	0.631	0.468	0.000	1.000
	6	0.247	0.364	0.000	1.000
Non-Outliers Accuracy	6	0.999	0.002	0.988	1.000
	1	0.996	0.009	0.968	1.000
	7	0.990	0.011	0.957	1.000
	3	0.985	0.017	0.929	1.000
	5	0.982	0.021	0.929	1.000
	2	0.925	0.043	0.842	1.000
	4	**0.909**	**0.038**	**0.831**	**1.000**
	8	0.907	0.039	0.816	1.000

Note*: Sets in* ***bold*** *are chosen for further evaluation (accuracies > 0.90)*

Figure 31 show boxplots for HDBSCAN outlier accuracies for all parameter sets when using the location input data. Set 4 is highlighted to show points of individual pressure maps where Outliers accuracies were not 1 (100%). This figure shows only three instances (out of twenty-eight) where outlier accuracies were below 0.4. These instances are shown in Figure 32, where it can be seen that HDBSCAN, when using set 4 parameters and location input data, had issues detecting outliers when in the presence of large group of outliers. Instead, the clustering algorithm marked them as a secondary pressure cluster group. In all other cases, the clustering algorithm detected the outliers in all other pressure maps successfully (see Fig. 31).

Table 17. HDBSCAN – Accuracy results by set (location-pressure input data)

Variable	Set	Mean	StDev	Minimum	Maximum
Outliers Accuracy	8	0.929	0.254	0.000	1.000
	5	0.879	0.301	0.000	1.000
	4	0.826	0.347	0.000	1.000
	1	0.812	0.363	0.000	1.000
	3	0.792	0.382	0.000	1.000
	2	0.693	0.439	0.000	1.000
	7	0.651	0.444	0.000	1.000
	6	0.217	0.347	0.000	1.000
Non-Outliers Accuracy	6	0.988	0.020	0.896	1.000
	1	0.960	0.040	0.834	1.000
	7	0.952	0.052	0.813	1.000
	3	0.947	0.050	0.822	1.000
	5	0.933	0.059	0.789	1.000
	4	0.921	0.063	0.755	1.000
	2	0.833	0.127	0.549	1.000
	8	0.821	0.116	0.527	1.000

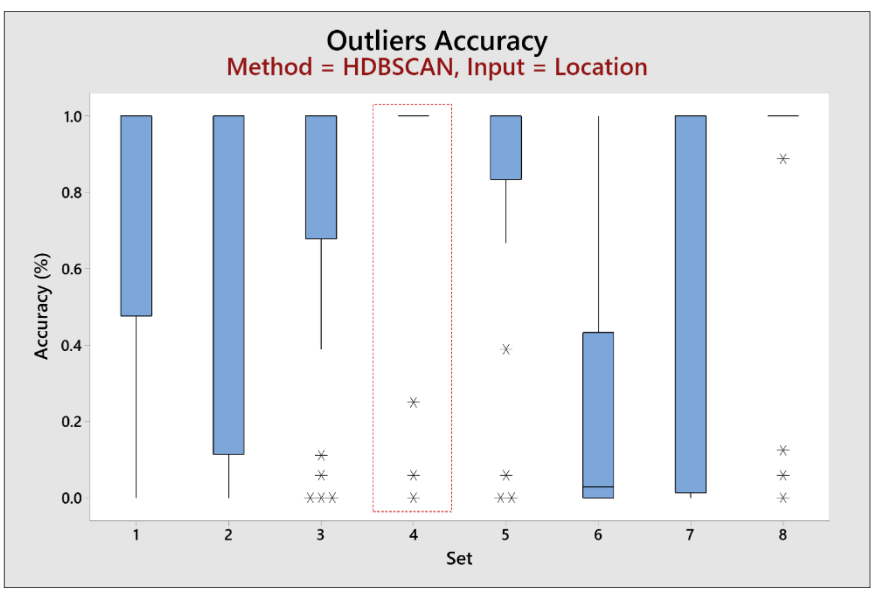

Figure 31. HDBSCAN – Outliers’ accuracy boxplots (location input data)

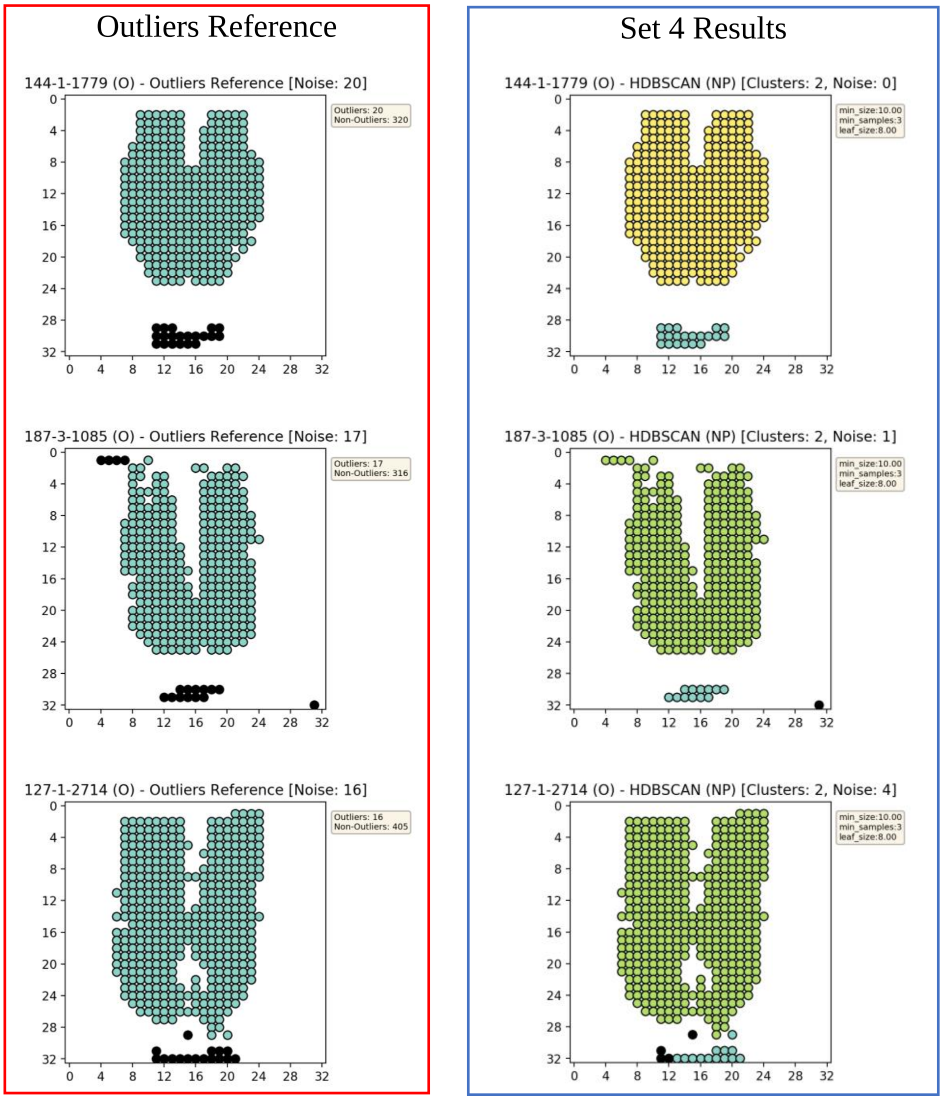

Figure 32. HDBSCAN – Samples with low outlier accuracy in set 4 (location input data)

Figure 33 show non-outlier accuracies boxplots for all HDBSCAN parameter sets when using the location input data. Set 4 (highlighted in figure) show many instances where non-outlier accuracies are low (<0.9). Examples of these instances can be seen in Figure 34, where outlier reference maps and cluster results are shown. When using set 4 parameters with location input data, HDBSCAN appears to be somewhat sensitive to pressure readings outlining the main pressure cluster (marking them as outliers). The algorithm also marks a number of internal non-outlier pressure readings as outliers. Due to these low non-outlier accuracies, HDBSCAN appears to be unreliable for detecting outlier/non-outliers pressure readings in a 32x32 pressure map.

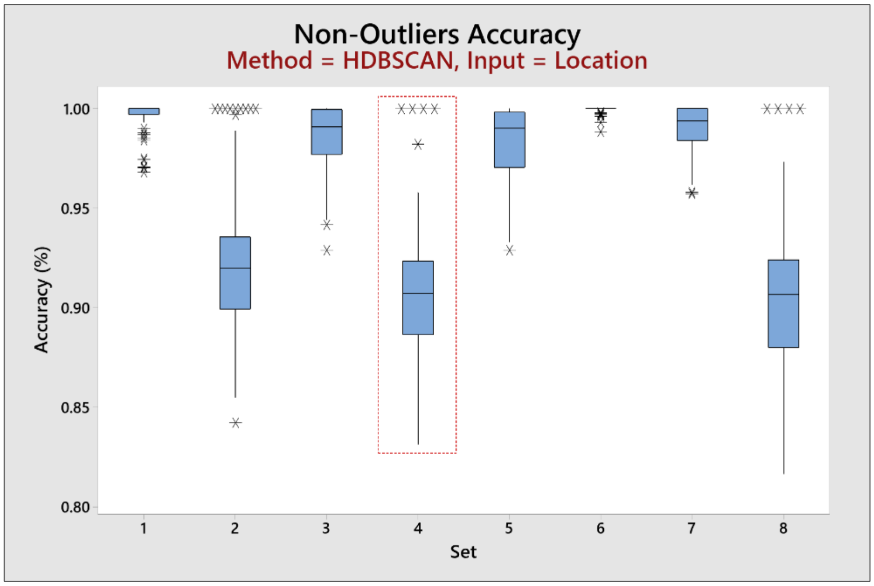

Figure 33. HDBSCAN – Non-outliers' accuracy boxplots (location input data)

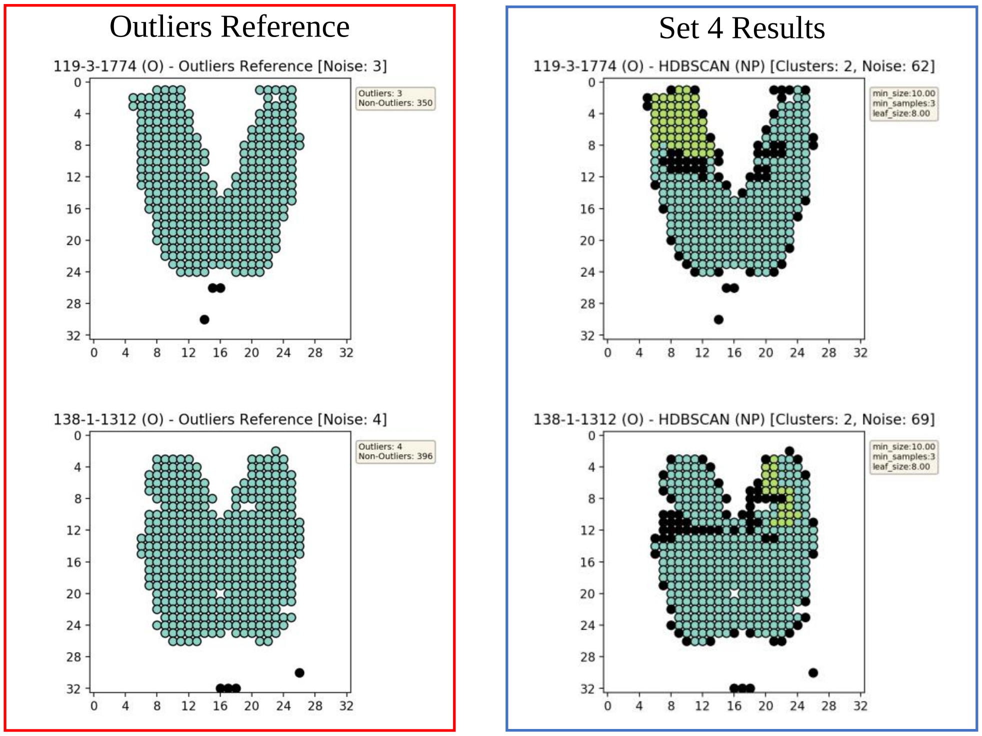

Figure 34. HDBSCAN – Samples with low non-outlier accuracy in set 4 (location input data)

DENCLUE

DENCLUE algorithms were implemented from the Python module *denclue* (v2.0) (Mgarrett, 2017). A graphical summary of the average accuracies obtained when using DENCLUE, with both location and location-pressure data input, is presented in Figure 35. As with similar figures, the top-left panel show average overall accuracies for each set of parameters and input data. Right panels show average outliers (top-right) and non-outliers (bottom-right) accuracies for each set of parameters when using seating pressure map samples with pre-identified outliers. The bottom-left panel shows average non-outlier when using seating pressure map samples without outliers. Unbalanced Outliers and Non-Outliers average accuracies are seen in some sets using the location-pressure input data, indicating that one accuracy increases at the expense of the other. DENCLUE algorithms generally show higher average accuracies for detecting outliers when using only the location information of pressure readings as input data. Table 18 show descriptive statistics of accuracy results for all sets of parameters used in DENCLUE algorithms when using the location information as input data.

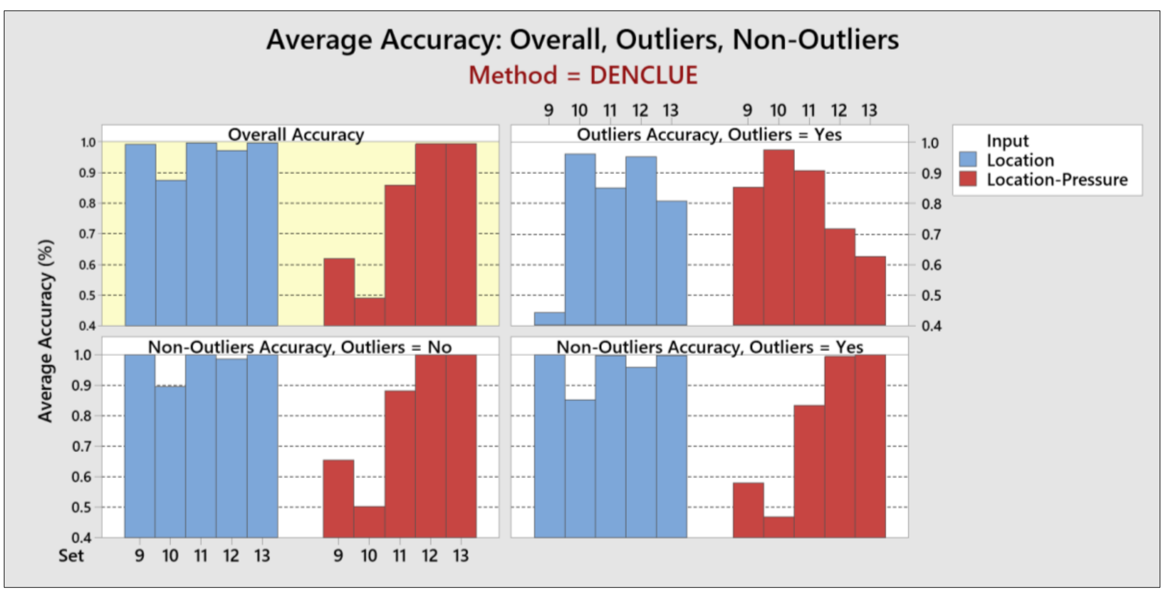

Figure 35. DENCLUE – Overall, Outliers, Non-Outliers average accuracy by set

Table 18. DENCLUE – Accuracy results by set (location input data)

Variable	Set	Mean	StDev	Minimum	Maximum
Overall Accuracy	11	0.996	0.009	0.953	1.000
	13	0.996	0.010	0.941	1.000
	9	0.993	0.012	0.941	1.000
	12	**0.972**	**0.088**	**0.494**	**1.000**
	10	0.874	0.287	0.000	1.000
Outliers Accuracy	10	0.962	0.154	0.200	1.000
	12	**0.952**	**0.155**	**0.200**	**1.000**
	11	0.850	0.282	0.000	1.000
	13	0.806	0.306	0.000	1.000
	9	0.443	0.383	0.000	1.000
Non-Outliers Accuracy	9	1.000	0.000	1.000	1.000
	13	0.999	0.004	0.975	1.000
	11	0.998	0.005	0.975	1.000
	12	**0.973**	**0.090**	**0.476**	**1.000**
	10	0.874	0.291	0.000	1.000

***Note**: Sets in **bold** are chosen for further evaluation (accuracies > 0.90)*

Results in Table 18 show that, when using DENCLUE algorithms with the location information as input data, parameters settings from set 12 resulted in high average outlier accuracies (0.952) and high average non-outlier accuracies (0.973). Figure 36 shows boxplots for DENCLUE outlier accuracies for all parameter sets when using location input data. Set 12 is highlighted to show points of individual pressure maps where Outliers accuracies were not 1 (100%).

Figure 37 shows examples of outlier reference maps where Outlier accuracies were 0.20 (Fig. 37, top) and 0.83 (Fig. 37, bottom) when using location input data with DENCLUE and set 12 parameters. While DENCLUE algorithms generally create multiple clusters from the pressure readings within a pressure map, it is still favorable for detecting outliers (marked as noise); only one sample (out of twenty-eight) had an outlier accuracy less than 0.80 due to the presence of a large group of outliers (see Fig. 37, top).

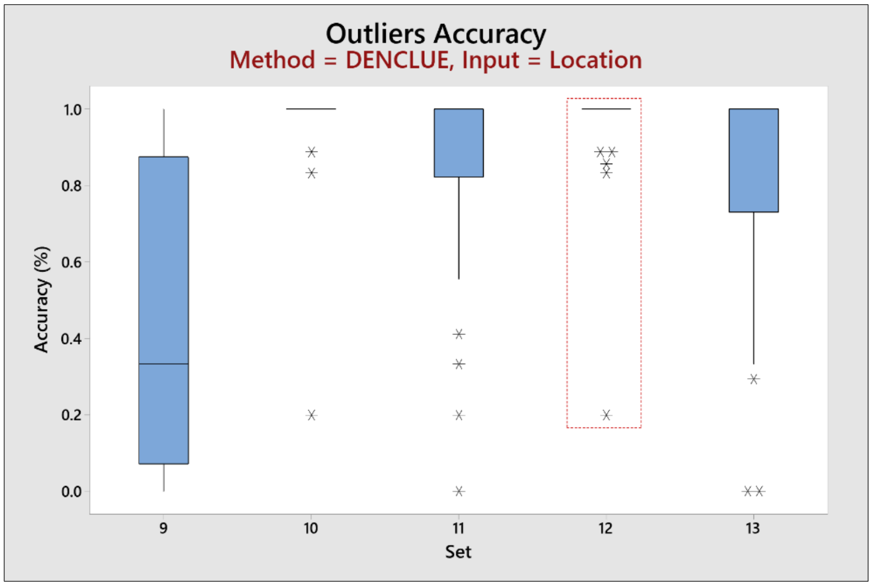

Figure 36. DENCLUE – Outliers accuracy boxplots by set (location input data)

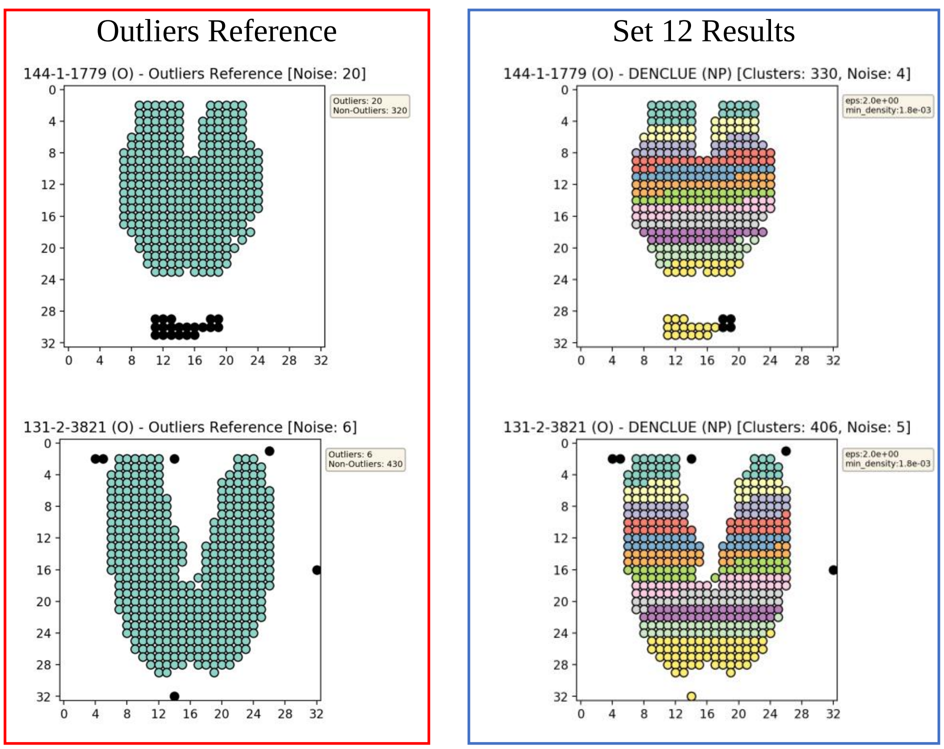

Figure 37. DENCLUE – Samples with low outlier accuracy in set 12 (location input data)

High non-outlier accuracies (average of 0.973) were also obtained when using the parameters settings from set 12 with the location information as data input. Figure 38 shows boxplots for DENCLUE non-outlier accuracies for all parameter sets when using the location input data. Set 12 is highlighted to show points of individual pressure maps where Non-Outliers accuracies were not 1 (100%). Out of the twenty-eight samples with pre-identified outliers, only three showed Non-Outliers accuracies less than 0.90 when using this DENCLUE set (2) and the location data input. Figure 39 shows outlier reference maps of all instances where non-outlier accuracies were less than 0.90 when using DENCLUE with set 12 parameters and location data input. This figure shows how using the DENCLUE algorithm with set 12 parameters and location data input create instances where true contact pressure readings outlining the main pressure cluster are being identified as outliers (noise). While this outlier detection behavior is only seen in three samples, the number of true contact pressure readings being marked as outliers is significant in these samples.

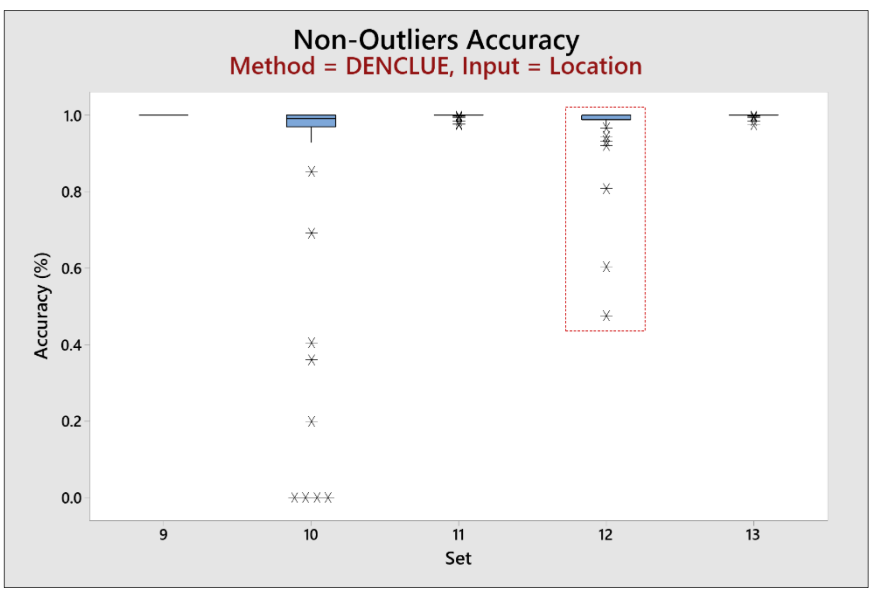

Figure 38. DENCLUE – Non-outliers accuracy boxplots by set (location input data)

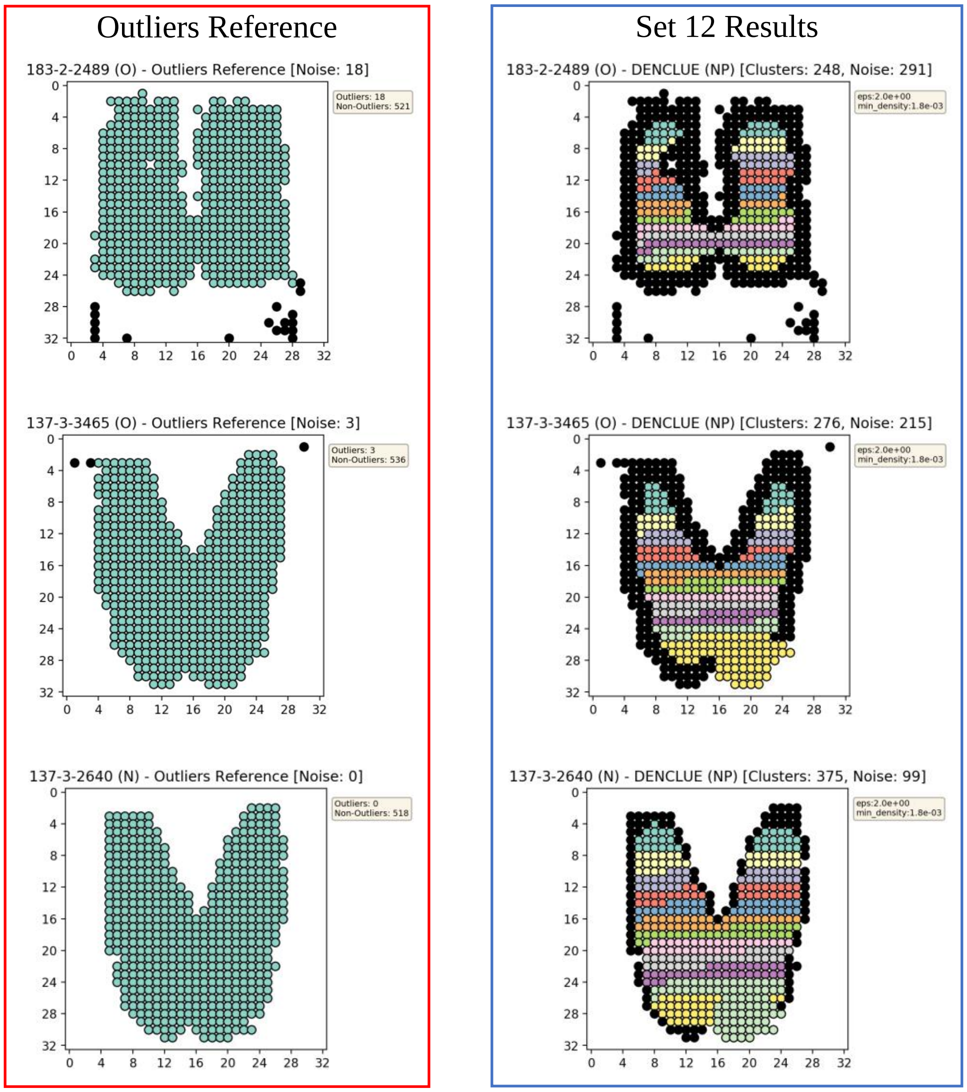

Figure 39. DENCLUE – Samples with low non-outlier accuracy in set 12 (location input data)

To maximize the non-outlier accuracies found in set 12 (Table 18), additional runs were performed using the DENCLUE clustering algorithm with the location information as input data. The DENCLUE parameter for minimum density (*min_density*) was found to be influential in marking pressure readings as outliers, and it was fine-tuned to reduce instances such as the ones depicted in Figure 39. The additional sets of DENCLUE parameters evaluated in this study are shown in Table 19, these are again used with the location input data.

Non-outlier accuracies increased by reducing the minimum density value (from the value of 1.8e-03 used in set 12). Unfortunately, this increasing in non-outlier accuracies were at the expense of lower outlier accuracies. However, acceptable tradeoffs were found where increased non-outlier accuracies were obtained while still maintaining a high average outlier accuracy (>0.90). Table 20 shows accuracies results for the additional DENCLUE sets. Results from sets 14 and 15 show an increase in average non-outliers accuracies when compared to the results obtained from set 12; also, the minimum non-outliers accuracies are also significantly higher.

Table 19. DENCLUE additional parameter sets for location input data

Set	**DENCLUE (NP)**
14	eps:2 min_density:1.7e-03
15	eps:0.01 min_density:1.65e-03

Note: NP = No Pressure → Location input data

Table 20. DENCLUE – Accuracy results for additional sets (location input data)

Variable	**Set**	**Mean**	**StDev**	**Minimum**	**Maximum**
Overall Accuracy	15	0.995	0.010	0.953	1.000
	14	0.992	0.020	0.868	1.000
	12	0.972	0.088	0.494	1.000
Outliers Accuracy	12	0.952	0.155	0.200	1.000
	14	0.926	0.175	0.200	1.000
	15	0.907	0.187	0.200	1.000
Non-Outliers Accuracy	15	0.997	0.008	0.952	1.000
	14	0.993	0.020	0.864	1.000
	12	0.973	0.090	0.476	1.000

Figure 40 shows outlier accuracy boxplots for these additional DENCLUE sets (14 and 15). Even if lower outlier accuracies are seen when compared to set 12, high outlier accuracies (i.e., greater than 0.90) are still obtained in most of the samples, notably for results obtained from set 14. Figure 41 shows non-outlier accuracy boxplots for these additional sets. A signicant increase in non-outlier accuracies were obtained when using parameters from sets 14 and 15, when compared to results from set 12.

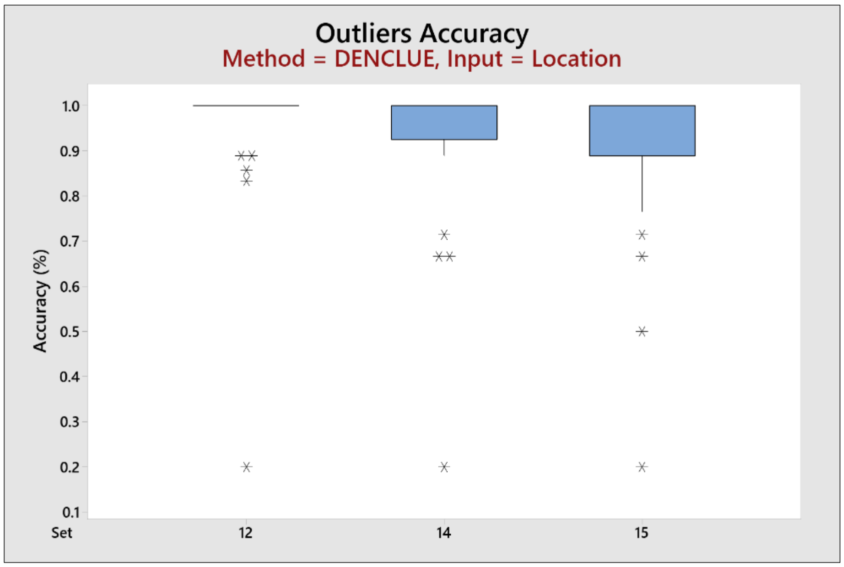

Figure 40. DENCLUE – Additional outliers accuracy boxplots (location input data)

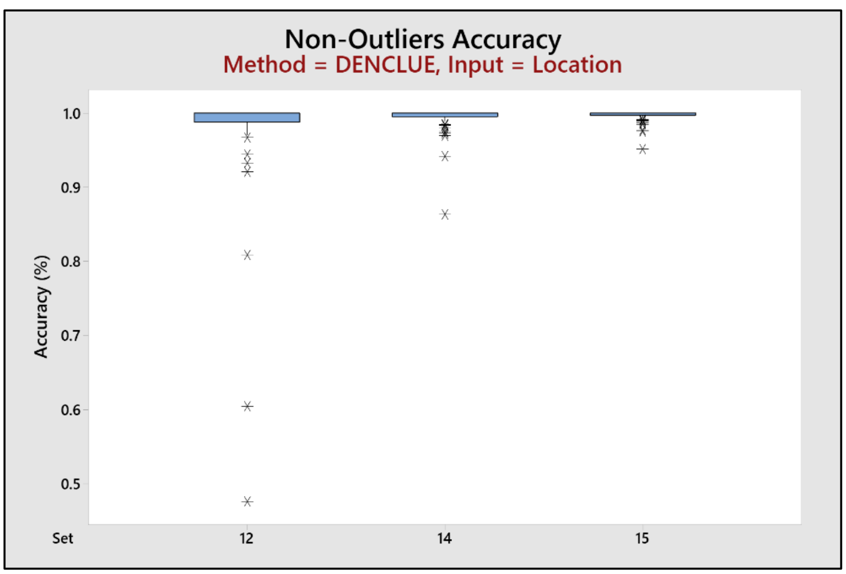

Figure 41. DENCLUE – Additional non-outliers accuracy boxplots (location input data)

Figure 42 shows a comparative visual analysis between the results from sets 12, 14 and 15 in instances where low outlier accuracies (Fig. 37) or low non-outlier accuracies (Fig. 39) were found in set 12. Examples of low outlier accuracies among these sets (12, 14, and 15) are shown in Figure 42 (first and second row in the figure). Generally, using parameter settings from set 12 result in detecting and marking outlier with higher accuracy by correcly detecting more scattered outliers than results when using parameter settings from sets 14 or set 15 (e.g., 2nd row in Figure 42). But in other instances, results obtained from all sets were similar in their inability to detect a distinct cluster group of outliers as extrinsic pressure artifacts (e.g., 1st row in Figure 42).

The benefits of running the additional sets (14 and 15) are seen in their improvement of non-outlier accuriaces when compared to set 12 results. Instances where low non-outlier accuracies were seen when using parameter settings in set 12 are now greatly improved when using parameter settings from either set 14 or set 15 (e.g., see rows 3-5 in Figure 42). While the DENCLUE algorithm is more relaxed when using parameter settings from set 14 or 15 (in terms of detecting and marking outliers), it still offers high outlier accuracies (>0.90) in most of the pressure map samples (see Fig. 40) with greatly improved non-outlier accuracies (see Fig. 41).

In summary, using the location information as input data, parameters of minimum density between 1.65e-03 to 1.7e-03, and epsilon parameters between 0.01 to 2, as used in sets 14 and 15, were shown to be adequate when using DENCLUE algorithms for detecting outlier/non-outliers sitting pressure readings in a 32x32 pressure map.

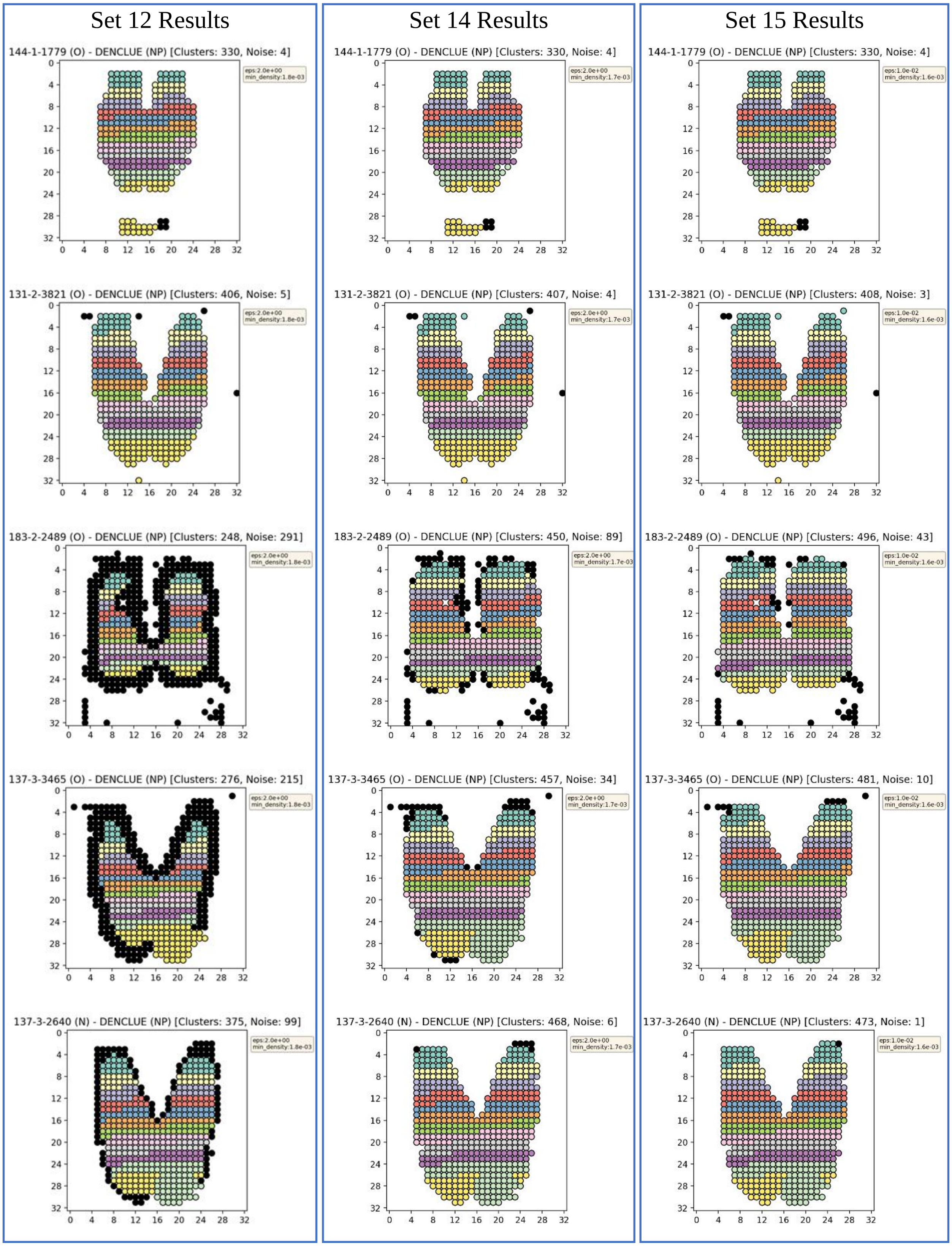

Figure 42. DENCLUE – Samples with low accuracies in sets 12, 14 and 15 (location input data)

DBCLASD

DBCLASD algorithms were implemented from the Python module *py-dbclasd* (Palacio, 2015). A graphical summary of the average accuracies obtained when using DBCLASD, with both location and location-pressure data input, is presented in Figure 43. As with similar figures, the top-left panel show average overall accuracies for each set of parameters and input data. Right panels show average outliers (top-right) and non-outliers (bottom-right) accuracies for each set of parameters when using seating pressure map samples with pre-identified outliers. The bottom-left panel shows average non-outlier when using seating pressure map samples without outliers.

Results indicate that DBCLASD algorithms generally show higher average outlier and non-outlier accuracies when using the pressure readings' location as input data, as compared to using location-pressure as input data.

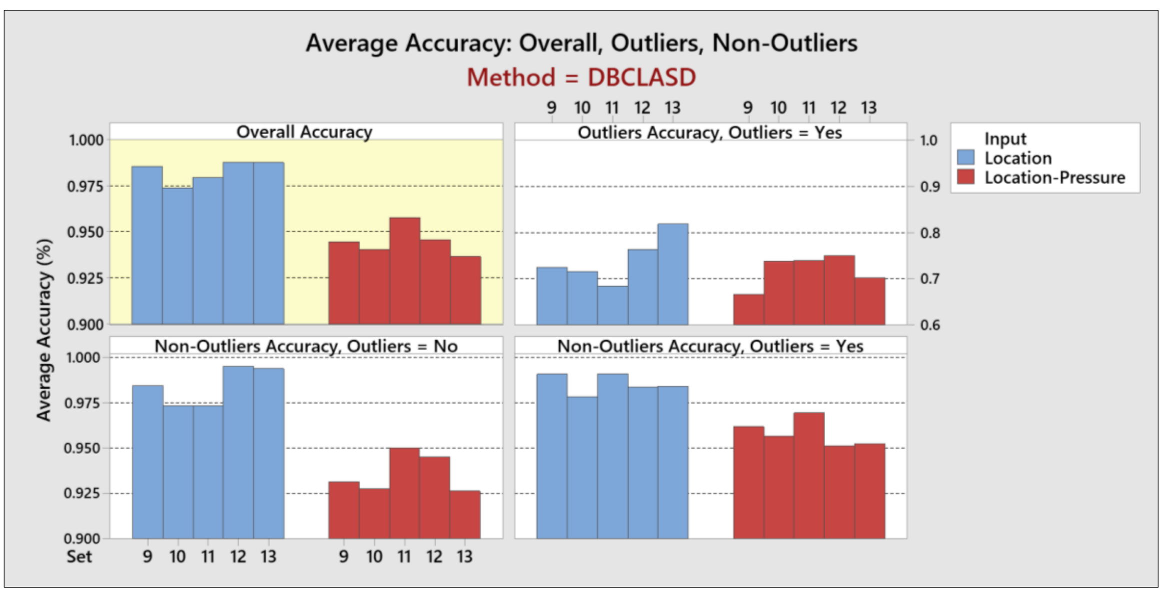

Figure 43. DBCLASD – Overall, Outliers, Non-Outliers average accuracy by set

Table 21 show descriptive statistics of accuracy results for all sets of parameters used in DBCLASD algorithms when using location information as input data. Unfortunately, none of these sets show both average outlier and non-outlier accuracies above 0.90. The highest Outliers accuracy is seen when using the parameter settings in set 13 with a 0.819 accuracy in detecting pre-defined outlier pressure readings (i.e., extrinsic pressure artifacts).

Table 21. DBCLASD – Accuracy results by set (location input data)

Variable	**Set**	**Mean**	**StDev**	**Minimum**	**Maximum**
Overall Accuracy	12	0.987	0.036	0.826	1.000
	13	0.987	0.030	0.838	1.000
	9	0.985	0.051	0.650	1.000
	11	0.979	0.039	0.851	1.000
	10	0.974	0.065	0.755	1.000
Outliers Accuracy	13	0.819	0.236	0.167	1.000
	12	0.764	0.294	0.000	1.000
	9	0.725	0.342	0.000	1.000
	10	0.716	0.353	0.000	1.000
	11	0.685	0.366	0.000	1.000
Non-Outliers Accuracy	12	0.989	0.036	0.826	1.000
	13	0.989	0.030	0.842	1.000
	9	0.988	0.051	0.650	1.000
	11	0.982	0.039	0.851	1.000
	10	0.976	0.066	0.755	1.000

Figure 44 shows boxplots for DBCLASD outlier accuracies for all parameter sets when using the location input data. Set 13 is highlighted to show points of individual pressure maps where Outliers accuracies were not 1 (100%). While results of using parameter setting described in set 13 show many samples with high outlier accuracy (median = 0.944), there are many instances where the detection of outliers was poor. Figure 45 show examples where low outlier accuracies were obtained. In some instances, the DBCLASD algorithm appears to have issues in detecting scattered outliers points within seating pressure maps (see Fig. 45, top).

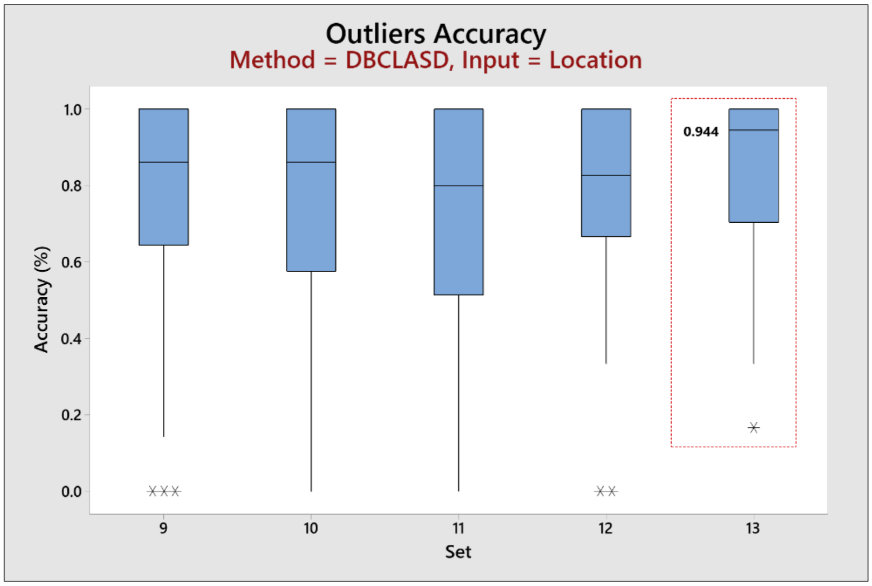

Figure 44. DBCLASD – Outliers accuracy boxplots by set (location input data)

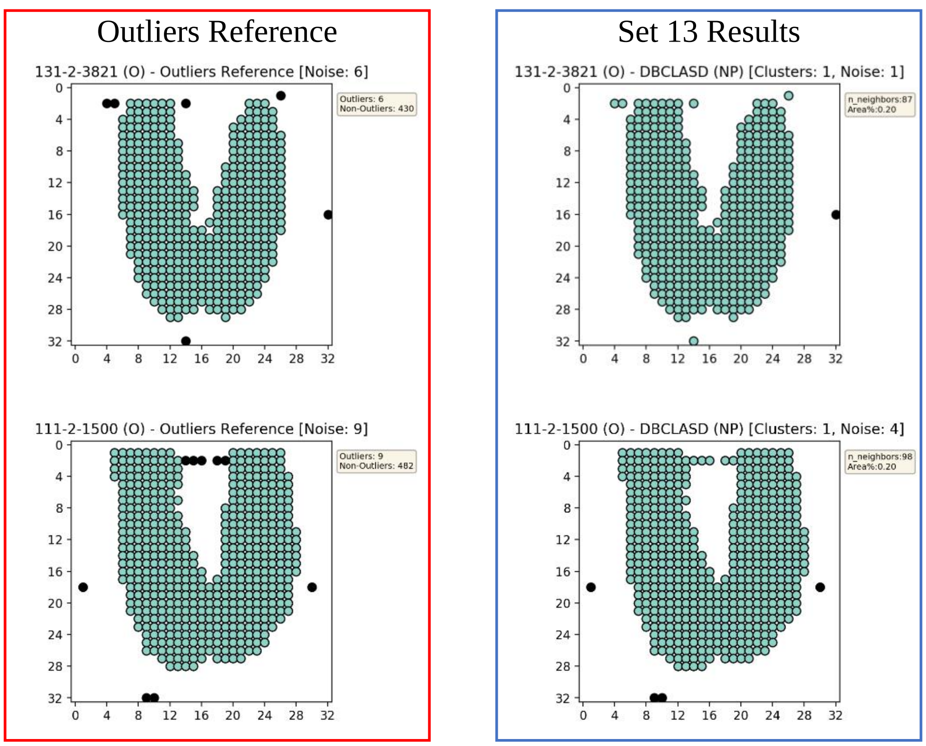

Figure 45. DBCLASD – Samples with low outlier accuracy in set 13 (location input data)

Some of the results obtained while using DBCLASD algorithms with location input data and parameter settings in set 13 were unusual. Figure 46 show some examples were low non-outlier accuracies were obtained. This figure shows a number of true contact pressure readings (i.e., non-outliers) being incorrectly marked as outliers in an unusual manner. Due to algorithms' inability to detect outliers and non-outliers with high accuracies, DBCLASD appears to be an inadequate technique for detecting unwanted pressure readings in a 32x32 pressure map.

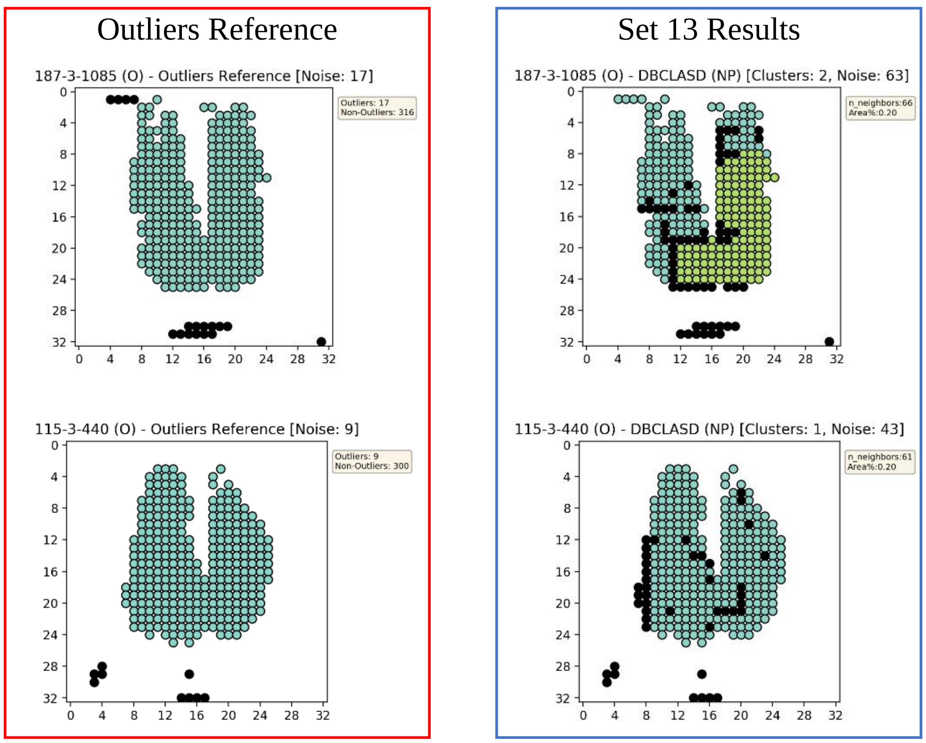

Figure 46. DBCLASD – Samples with low non-outlier accuracy in set 13 (location input data)

Spatial Clustering Summary

Many spatial clustering methods were shown to be adequate for detecting outlier/non-outliers seating pressure readings in a 32x32 pressure map. DBSCAN and DENCLUE algorithms, in particular, showed superior average outlier and non-outlier accuracies among the various clustering methods evaluated. Given the results obtained from these clustering algorithms, recommended parameters for DBSCAN and DENCLUE algorithms are shown in Table 22.

An absolute superiority of a particular combination of clustering method/parameter settings against others cannot be reached. Irrespective of the clustering method used, a tradeoff between outlier and non-outlier accuracies is usually seen when trying to increase one or the other. While a particular method/parameter combination cannot be chosen as the best, results indicate that better outlier/non-outlier accuracies are typically obtained when only using location information of the pressure readings as input data in most of the evaluated clustering algorithms.

Table 22. Summary of analysis results for recommended clustering methods

Method	Parameters	Input	Average Accuracy			Avg. Proc Time
			Outliers	Non-Outliers	Overall	
DBSCAN	eps: 1.60, 1.80 min_samples: 8	Location	0.949	0.989	0.988	5.8ms
DENCLUE	eps: 2 min_density: 1.7e-03	Location	0.926	0.993	0.992	11.1s
DBSCAN	eps: 2.00, 2.20 min_samples: 10	Location	0.925	0.995	0.994	5.8ms
DENCLUE	eps: 0.01 min_density: 1.65e-03	Location	0.907	0.997	0.995	11.5s
DBSCAN	eps: 2.5 min_samples: 10	Location	0.817	0.999	0.997	5.7ms

Among the recommended methods (Table 22), the highest average outlier accuracy was achieved by DBSCAN when using parameters of epsilon between 1.6-1.8 and setting minimum samples at 8. This combination produced a 94.9% average outlier accuracy rating while maintaining an average non-outlier accuracy close to 99% (0.989). The highest average non-outlier accuracy, while maintaining an average outlier accuracy greater than 90%, is achieved by DENCLUE when using a minimum density of 1.65e-03, with a 99.7% average non-outlier accuracy rating. A good balance between average outlier and non-outlier accuracies were achieved by DENCLUE when using a minimum density of 1.7e-03, with 92.6% and 99.3% respectively.

If preservation of all true contact pressure readings is of utmost importance, a DBSCAN algorithm with parameters epsilon parameter minimum samples set at 2.5 and 10, respectively, showed very high non-outlier accuracies when using the location input data (see Table 22). This particular combination produced 52 out of 56 samples with 100% non-outlier accuracy scores, and the remaining samples with non-outlier accuracy scores greater than 97.51%. Considering its high non-outlier accuracies, an acceptable average outlier accuracy score of 81.7% was also achieved by these DBSCAN settings. Another alternative for preserving most of the true contact pressure readings is to use a DENCLUE algorithm with minimum density set at 1.65e-0.3 and use the location information as input data. This DENCLUE combination showed very high average non-outlier accuracies (0.997), and an improved average outlier accuracy (0.907) when compared to the previously discussed DBSCAN combination (epsilon at 2.5 and minimum samples at 10).

The processing times for each clustering method were also recorded. Table 22 show DBSCAN algorithms with average processing times of around 5.8ms when detecting outliers/non-outliers in 32x32 pressure maps, while DENCLUE showed average processing times of around 11s. DBSCAN algorithms implemented in this research come from the module scikit-learn (Pedregosa et al., 2011), a well-known fully-optimized machine learning python package. On the other hand, the DENCLUE module available for python and used in this research is non-optimized. This DENCLUE module has also been used in other research studies (L. Liao et al., 2017). The need for a fully optimized DENCLUE python package (introducing multiprocessing optimization during hill climb algorithms) will be beneficial for future pressure mapping analyses using the python programming language.

Spatial Autocorrelation and Image Statistical Features

The following subsections show results of the analysis of spatial autocorrelation measures and image statistical features for the following datasets: (1) static data subset, and (2) paired data subset. Results of correlation and regression analysis are discussed with the aim of finding meaningful differences between highly correlated variables, and eliminating correlated variables via dimension reduction techniques (e.g., high correlation filters). Computation demands for calculating various measures are also discussed.

Static Data Subset

An average coefficient of variation was calculated for each subject using seating pressure maps collected during their sitting session trials. Stratified sampling of subjects' pressure maps was used following the distribution of the average coefficient of variation by subject (see Fig. 47). Twenty (20) samples of seating pressure maps were selected to create the static data subset (see Appendix H).

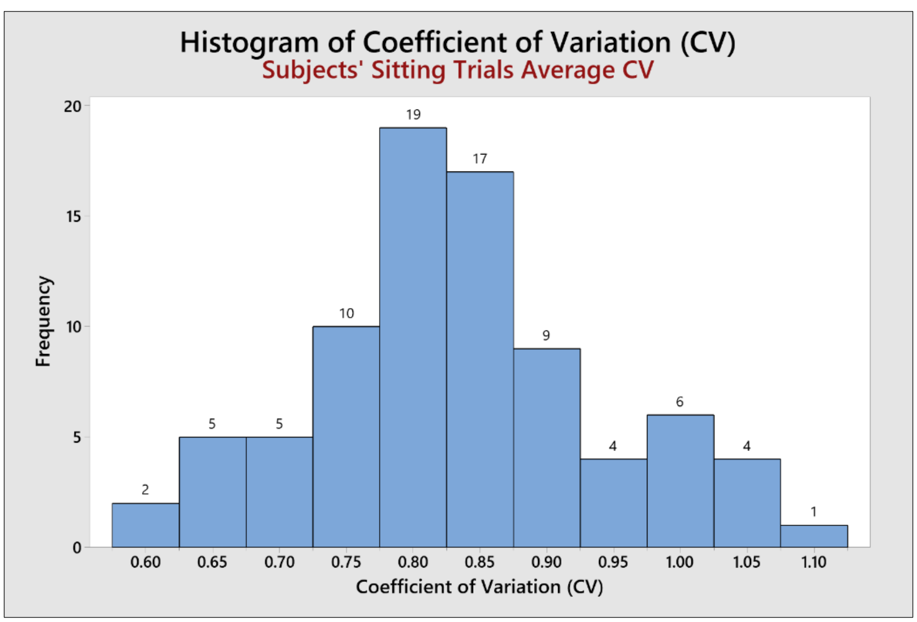

Figure 47. Histogram of subjects' average coefficient of variation

Spatial Autocorrelation. Measures of Moran's I and Geary's C were calculated using modules from the Python Spatial Analysis Library (PySAL v1.14.4) (Rey & Anselin, 2007). The results showed that the measures are inversely identical to each other within the context of seating pressure mapping (using the static data subset). Regardless of the weight matrix used, both measures showed a very strong correlation between each other with correlation values of $r = -1$, $r = -0.998$, and $r = -0.999$ for the queen, constant-distance, and inverse-distance weight matrices respectively. By having very similar behavior to Gearys' C and easier interpretability (with a defined autocorrelation range from -1 to 1), Moran's I spatial correlation measure appears to be a better candidate as a new pressure measure.

On the other hand, computational demands using the PySAL python package were very different between these measures, even if formulas have a similar degree of complexity (see Eq. 1 and Eq. 2). Figure 48 shows the average processing times when calculating the spatial autocorrelation measures in the static data subset samples.

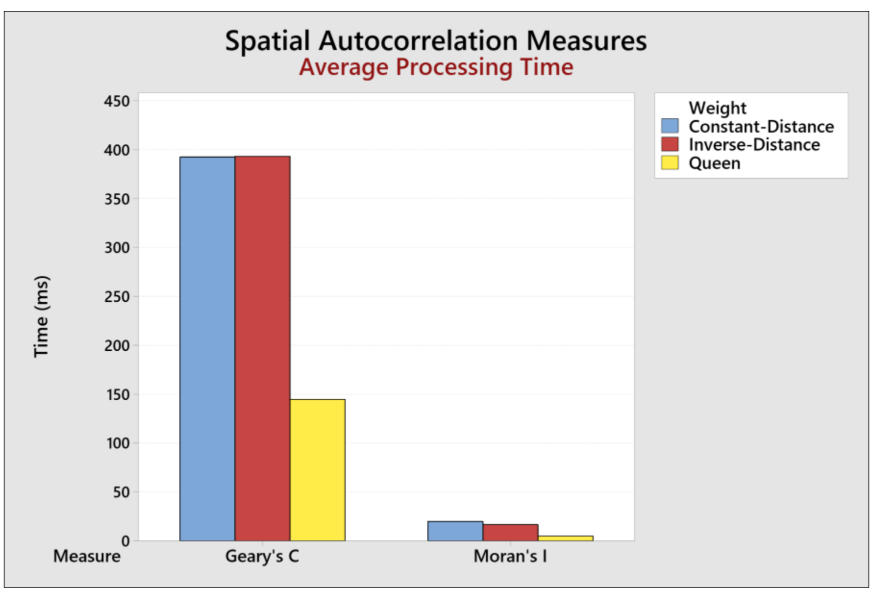

Figure 48. Spatial autocorrelation measures average processing time (static data subset)

Average processing time for calculating Moran's I was under 25ms in all weight matrices; Geary's C, on the other hand, showed an average processing time of around 150ms when using the queen matrix (3x3), and around 400ms when using other larger weight matrices (5x5) (see Fig. 48). The effect of choosing different weight matrices not only affected the computing time, but also the magnitude of the spatial autocorrelation measure. Figure 49 shows Moran's I spatial autocorrelation measures using different weight matrices for all samples in the static data subset. Moran's I results show moderate to very strong positive spatial autocorrelation within all pressure map samples, with consistently higher measures when using the queen weight matrix (Q). Using weight matrices with a larger area (5x5 instead of 3x3) affected the Moran's I values. When using the Inverse-Distance weight matrix (ID) and Constant-Distance weight matrix (CD), both using a 5x5 matrix, Moran's I values are reduced by approximately 10.6% and 15.1% respectively, compared to results obtained when using the Queen weight matrix (Q) (3x3) (see Fig. 49).

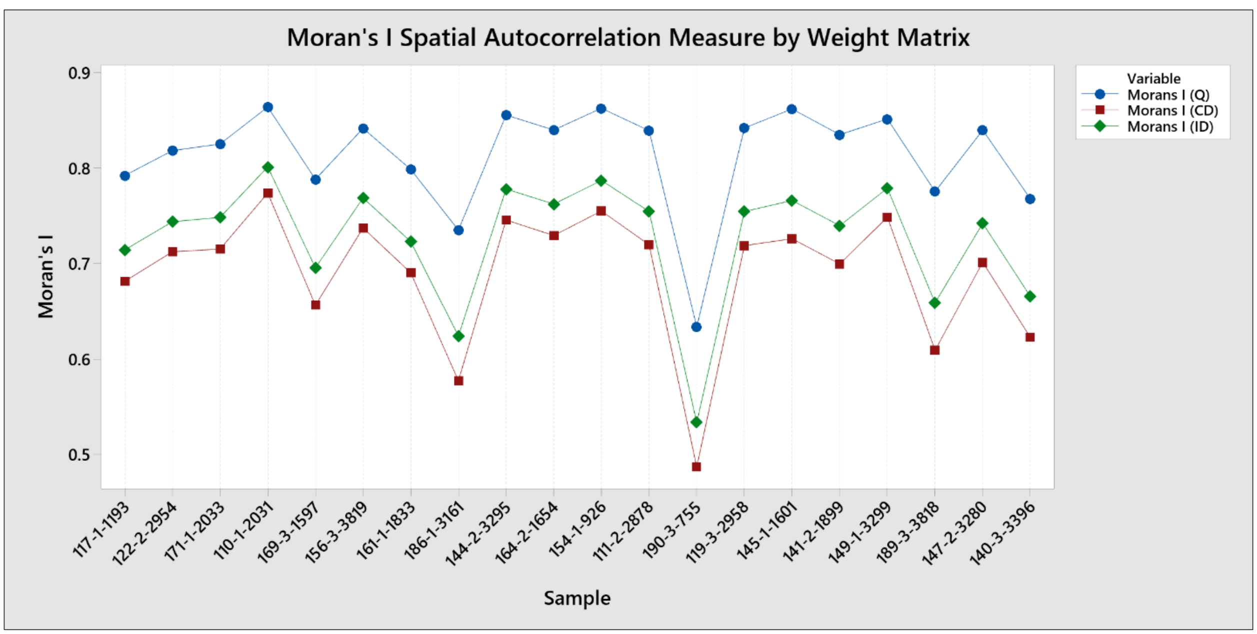

Figure 49. Moran's I spatial autocorrelation by weight matrix (static data subset)

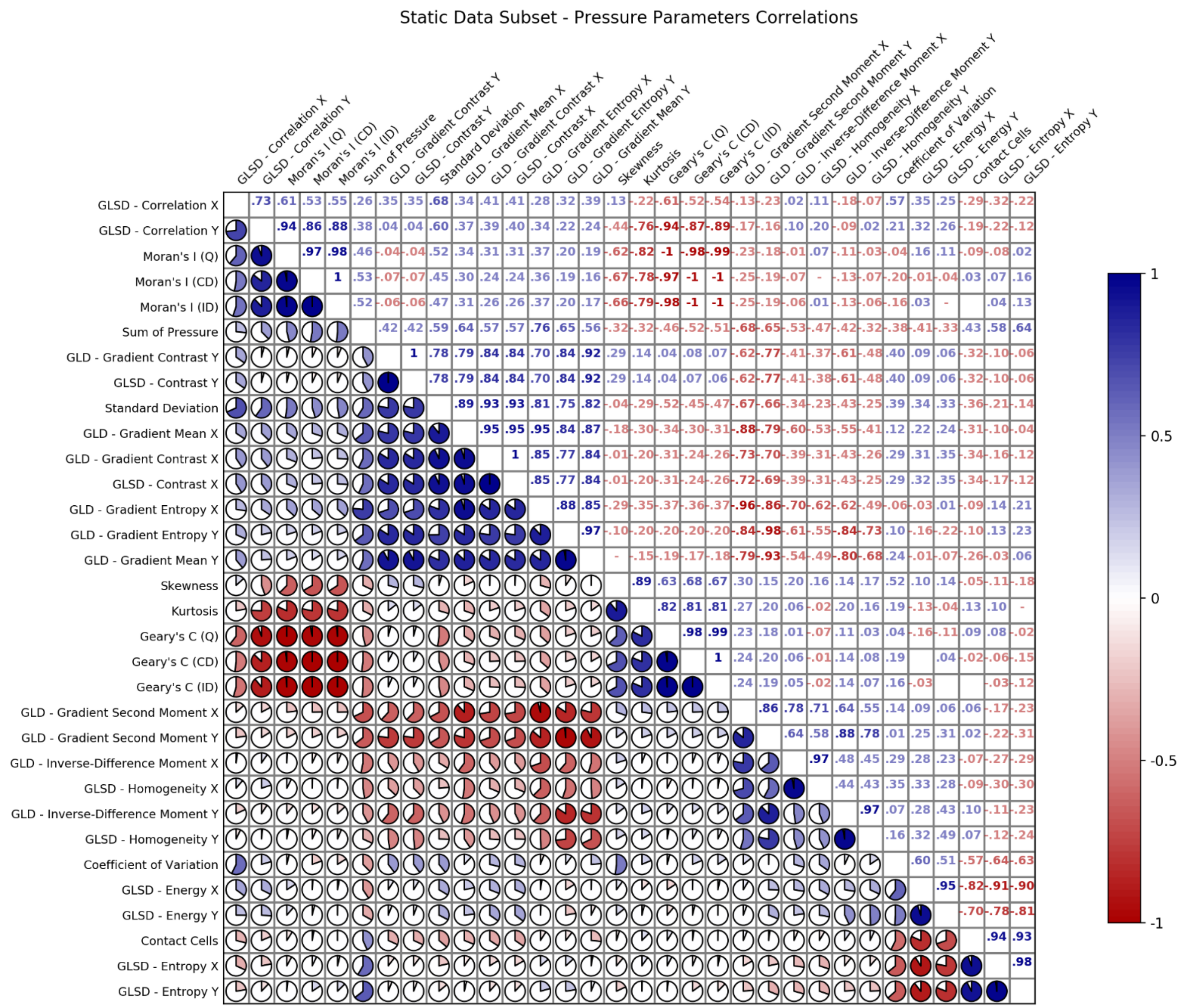

Figure 50. Correlation matrix between pressure measures (static data subset)

A correlation analysis using Pearson product-moment was used to assess the relationship between all known and proposed pressure map measures using the samples in the static data subset. Figure 50 shows the results of the correlation matrix presented as a hierarchical clustered correlogram.

Focusing on the correlated clusters where spatial autocorrelation measures are included (Fig. 50, top left), other meaningful correlations besides the ones between themselves (Moran's I and Geary's C) are also seen. The correlation measures obtained from Gray-Level Spatial-Dependence (GLSD) statistical features in the Y direction (GLSD – Correlation Y) and Moran's I (Q) (queen matrix) show a strong positive correlation ($R^2 = 0.891$). Figures 51 and 52 show the regression model, fitted line plot, and standardized residual plots between these measures. An unusual observation ($std.residual > |2|$) detected while fitting the regression model can also be seen in these figures. Figure 53 shows the pressure map of this unusual observation (Fig. 53a), along with calculated Moran's I and GLSD Correlation Y measures.

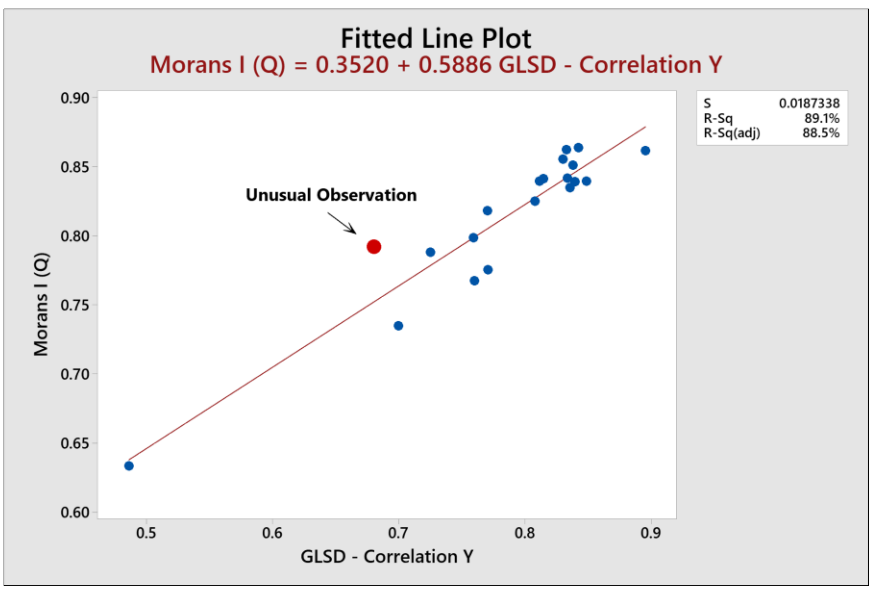

Figure 51. Moran's I vs GLSD Correlation Y regression (static data subset)

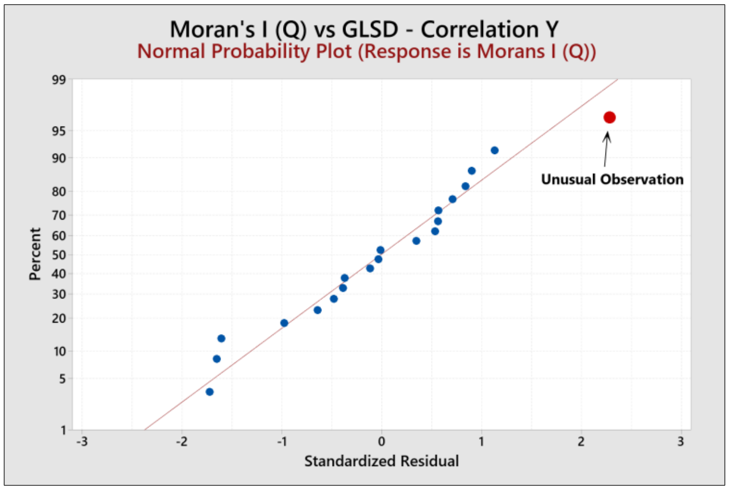

Figure 52. Moran’s I vs GLSD Correlation Y residuals (static data subset)

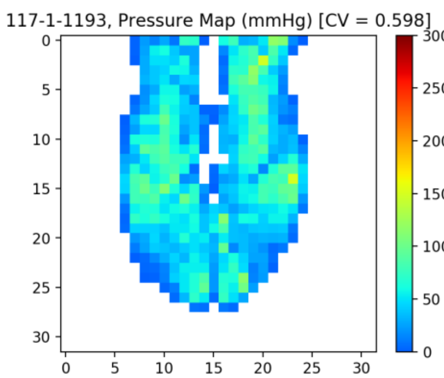

(a) 117-1-1193 Pressure Map

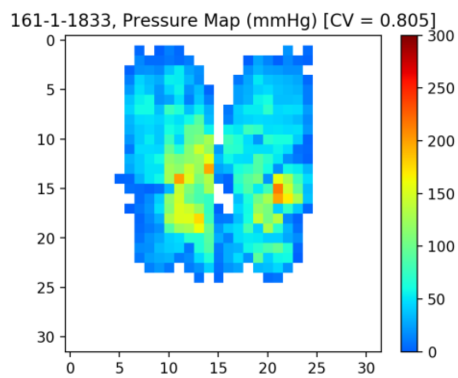

(b) 161-1-1833 Pressure Map

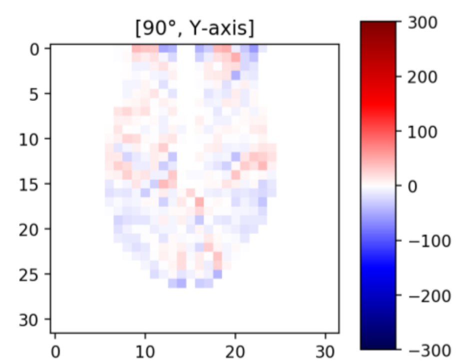

(c) 117-1-1193 Second Gradient Map

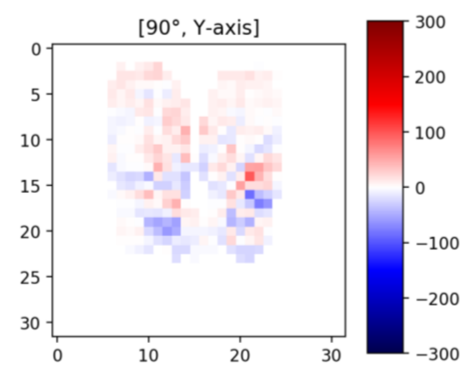

(d) 161-1-1833 Second Gradient Map

Sample	117-1-1193*	161-1-1833
Moran’s I (Q)	0.79220	0.798580
GLSD – Correlation Y	0.67993	0.759185

*Unusual Observation

Figure 53. Moran’s I vs GLSD Correlation Y unusual observation (static data subset)

For comparative purposes, Figure 53 also shows a secondary pressure map (Fig. 53b) with a similar Moran's I measure, but with a GLSD Correlation Y result close to the expected value $(std.residual = -0.01)$. Second gradient maps along the Y-axis (90°) are also presented in this figure for each one of the pressure maps; these are calculated by using second order accurate central differences in the interior points of the images, and first order accurate one-sides (forward or backwards) differences at the image boundaries at a given direction. By comparing the second gradient maps between these samples, more scaterring of positive/negative gradients are seen in Figure 53c, while Figure 53d has more defined gradient clusters. GLSD Correlation measures appear to be sensitive to these pressure gradient variations at a given direction (e.g., $90°$), while measures of Moran's I appear to give more emphasis in measuring presence of correlated pressure cluster with more robustness to these pressure gradient variations.

It is also important to highlight that measures of correlation using GLSD do not require any weight matrix. The magnitude of Moran's I spatial autocorrelation measure was significantly affected by defining weight matrices with different areas of interest (i.e., moving window) (see Fig. 49). For the seating pressure maps evaluated in this study, the use of a queen weight matrix appears to be a more conservative approach when calculating Moran's I spatial autocorrelation measures. As the max-min size of autocorrelated high pressure clusters (e.g., ischial tuberosities) are usually within a 3 x 3 region of pressure cells (see Appendix H), higher Moran's I spatial autocorrelations values are obtained due to matching the size of these high-pressure clusters to the size of the queen weight matrix. Therefore, there appears to be a relationship between the expected max-min size of pressure correlated regions and selecting the size of the regions of interest in a weight matrix. A weight matrix with a region of interest greater than the max-min size of autocorrelated high-pressure clusters could potentially weaken the spatial autocorrelation values.

While Moran's I and GLSD Correlation measures showed similar behaviors ($R^2 = 0.891$), they were found to be unique pressure map descriptors, and are adequate measures of spatial autocorrelation of pressure maps. In the context of seating pressure maps, high spatial autocorrelation values indicate presence of distinct pressure clusters of various levels formed by contiguous pressure readings, while low values indicate scattered low/high pressure readings or distinct low-area high-pressure points (e.g., acute pressure points). Appendix I include results of measures of spatial autocorrelation (Moran's I and GLSD Correlation) for all samples in the static data subset (Appendix H).

Researchers have the option to measure spatial autocorrelation within pressure maps using Moran's I, which allows them to choose the size/weight of the area of interest (i.e., moving window) and is more robust to gradient variations, or use GLSD Correlation, which does not require a described weight matrix and is more sensitive to localized pressure gradient variations.

Image Statistical Features. Results from the correlation matrix and clustered correlogram also show instances where many image statistical features and known pressure measures are grouped into highly positive or negative correlated clusters (see Fig. 50). Measures of Gradient Contrast (GLD) and Contrast (GLSD) behave almost identically ($R^2 \approx 100\%$) regardless of the measure's direction [$0°$ (X) or $90°(Y)$]. Other measures, such as Gradient Contrast (GLD) and Gradient Mean (GLD), also behave similarly at either direction with $R^2 \approx 84.5\%$ at $90°$, and $R^2 \approx 90.3\%$ at $0°$. Despite this, there were some instances where unusual observations were observed during regression analyses in both directions [$0°$ (X) and $90°(Y)$], these are shown in Figures 54 to 57.

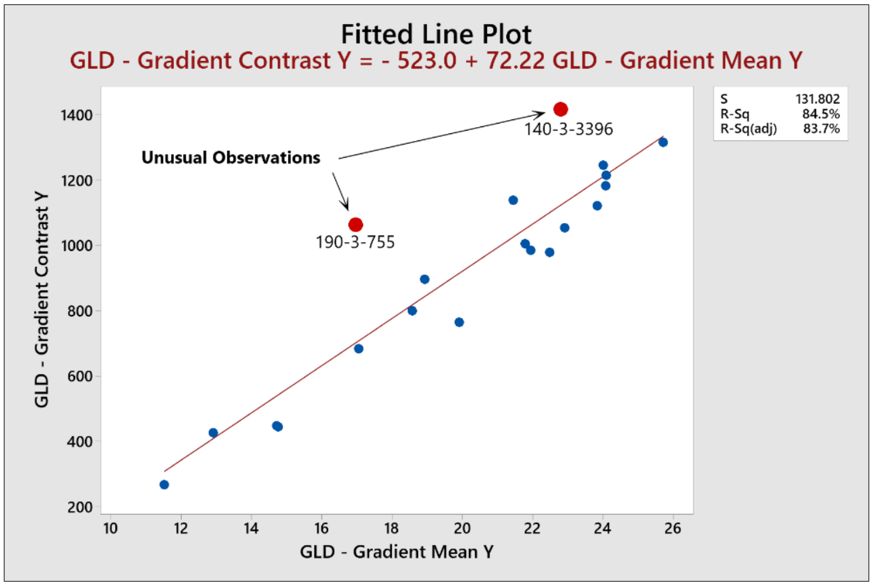

Figure 54. GLD Gradient Contrast Y vs GLD Gradient Meant Y regression (static data subset)

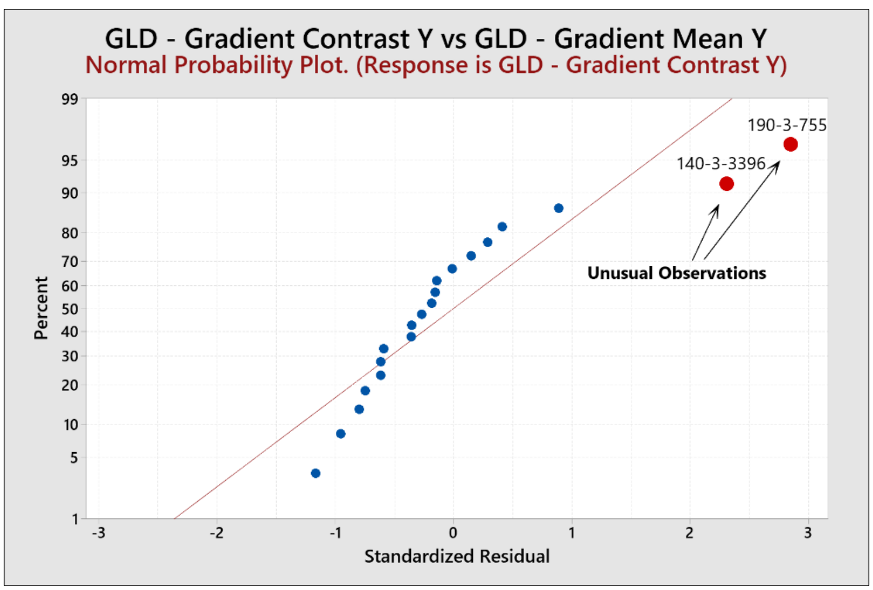

Figure 55. GLD Gradient Contrast Y vs GLD Gradient Meant Y residuals (static data subset)

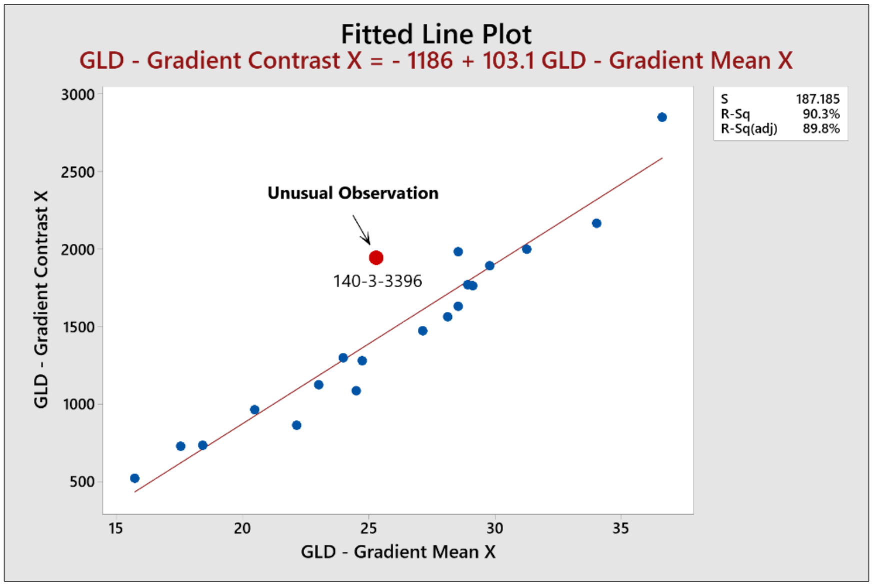

Figure 56. GLD Gradient Contrast X vs GLD Gradient Meant X regression (static data subset)

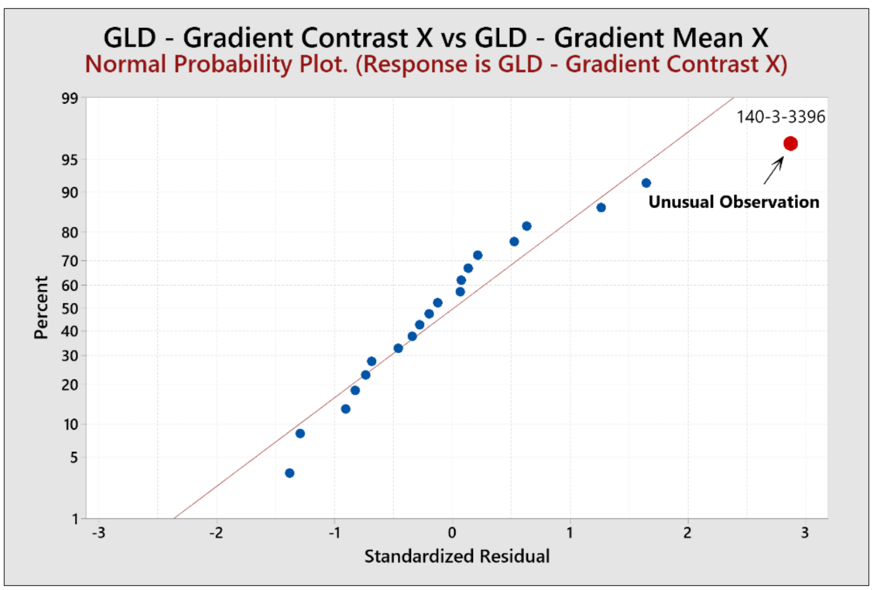

Figure 57. GLD Gradient Contrast X vs GLD Gradient Meant X residuals (static data subset)

Figure 58 shows pressure maps of the samples where measures of GLD Gradient Contrast [in 0° (X) or 90°(Y)] were unusual and higher than predicted. The figure shows that Gradient

Contrast values are significantly higher, considering values of Gradient Mean, when pressure maps have either a single or small group(s) of acute high-pressure cells. These instances are captured better by measures of GLD Gradient Contrast due their sensitivities for high gradients (see Eq. 6 and Eq. 9). These two measures (GLS Gradient Contrast and GLD Gradient Mean) are considered adequate as global measures of pressure gradients within a pressure map due to their uniqueness as pressure map descriptors.

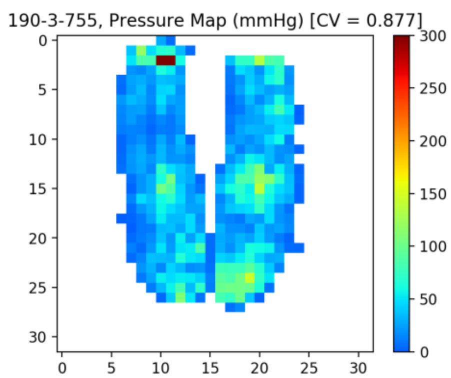

(a) 190-3-755 Pressure Map

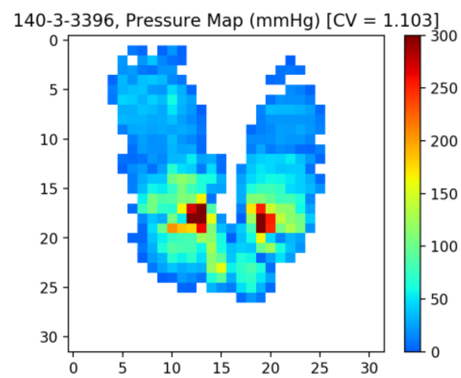

(b) 140-3-3396 Pressure Map

Sample	190-3-755	140-3-3396
GLD - Gradient Contrast X	962.358	*1943.149
GLD - Gradient Mean X	20.475	25.279
GLD - Gradient Contrast Y	*1062.769	*1417.125
GLD - Gradient Mean Y	16.962	22.803

*Unusual Observation

Figure 58. GLD Gradient Contrast vs Gradient Mean unusual observations (static data subset)

Results from the correlation matrix and clustered correlogram presented in Figure 50 also show other sets of statistical features that are grouped in strongly positive or negative correlated clusters. Measures of Homogeneity (GLSD), Inverse-Difference Moment (GLD), and Gradient Second Moment (GLD) are shown as positively correlated, and are measures commonly used to quantify an image texture. An image texture measures the variations of the surface intensity and quantifies properties of smoothness, coarseness and regularity (Kurani et al., 2004, p. 1). Measures of Homogeneity (GLSD) and Inverse-Difference Moment (GLD) behave similarly when measured at $90°$ ($R^2 \approx 94.5\%$) or $0°$ ($R^2 \approx 94.2\%$) with no unusual observations in the regression models.

A strong negative correlation was found between Gradient Second Moment (GLD) and Gradient Entropy (GLD) in both $90°\,(R^2 \approx 96.5\%)$ and $0°\,(R^2 \approx 92.2\%)$ directions. GLD measures of Gradient Mean and Gradient Entropy also behave similarly when measured either at 90^o ($R^2 \approx 95\%$) or 0^o ($R^2 \approx 90\%$). The Gradient Second Moment (GLD) measure looks for lack of noise (or disorder) in pixel intensities, whereas Gradient Entropy (GLD) increases with noise/disorder; both of these measures are being affected, in opposite directions, by an overall increase in pressure gradients (i.e., an increase in pressure gradients [Gradient Mean (GLD)] is usually associated with an increase in image noise [Gradient Entropy (GLD)] and, thus, a decrease in surface smoothness [Gradient Second Moment (GLD)] within a pressure map image).

Statistical features of Gradient Second Moment (GLD) and Homogeneity (GLSD) do not show a very strong correlation between themselves ($R^2 \approx 61\%$ at $90°$, and $R^2 \approx 50\%$ at $0°$), even when both are measures of a pressure map texture and/or smoothness. Figure 59 shows line plots for values of both of these measure at $90°$ (Y) for all samples in the static data subset. Two samples are highlighted to indicate where significant differences or unusual observations were seen during regression analyses ($std.residuals > |2.29|$). Figure 60 shows pressure maps, gradient maps, and values of Gradient Second Moment (GLD) and Homogeneity (GLSD) for these unusual observations. First-order gradient maps are calculated as absolute differences in pressure in a given direction.

First-order gradient map from sample 122-2-2954 (Fig. 60c) shows low variations in the magnitudes of absolute gradients (low texture), reflected as a high Gradient Second Moment (GLD) value due to this. On the other hand, a higher texture is seen in gradient map from sample 145-1-1601 (Fig. 60d), resulting in a lower Gradient Second Moment (GLD) value. In contrast, the measure of Homogeneity (GLSD) in sample 122-2-2954 is higher than expected due to the presence of pressure clusters with identical high-pressure readings (300 mmHg), a consequence of the pressure interface mat limits (max. pressure response). Results indicate that Homogeneity (GLSD) measures are sensitive when a number of contiguous equal-value pressure readings are present in the pressure maps (i.e., homogeneity within various pressure cluster levels), while measures of Gradient Second Moment (GLD) are more sensitive to gradient transitions.

Both Gradient Second Moment (GLD) and Homogeneity (GLSD) measures are adequate, and complementary, measures of pressure map texture and homogeneity. Higher values on these measures will generally indicate a pressure map with smoother transitions between pressure levels, with less coarseness within the pressure map, and more homogeneous pressure cluster levels.

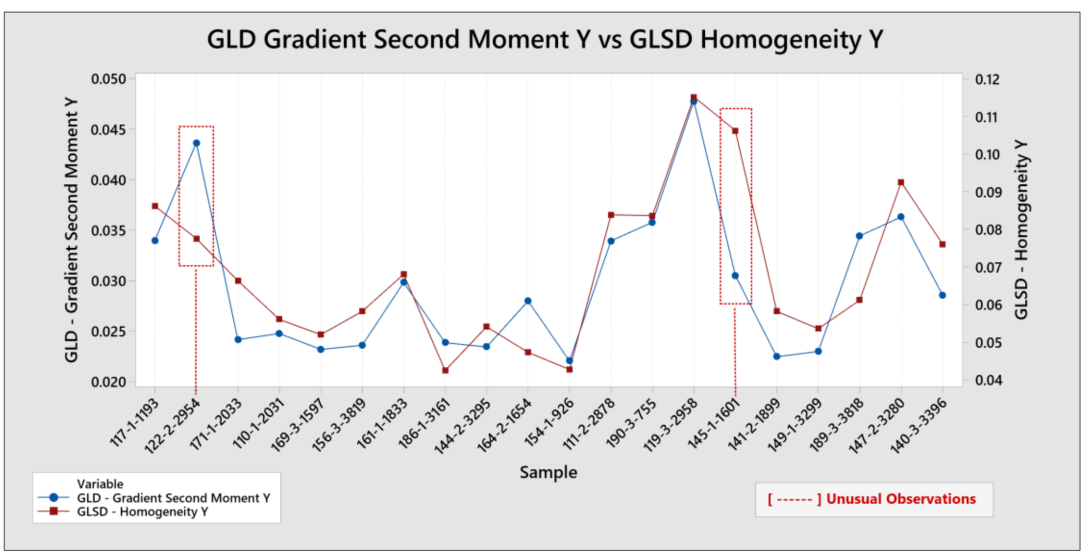

Figure 59. GLD Gradient Second Moment Y vs GLSD Homogeneity Y (static data subset)

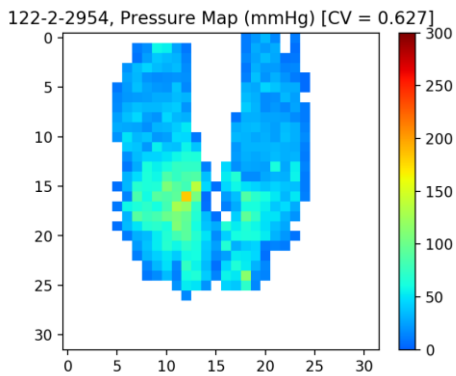

(a) 122-2-2954 Pressure Map

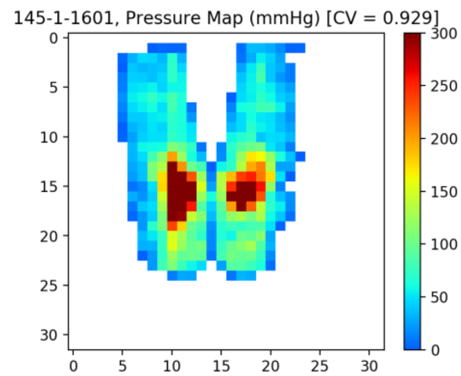

(b) 145-1-1601 Pressure Map

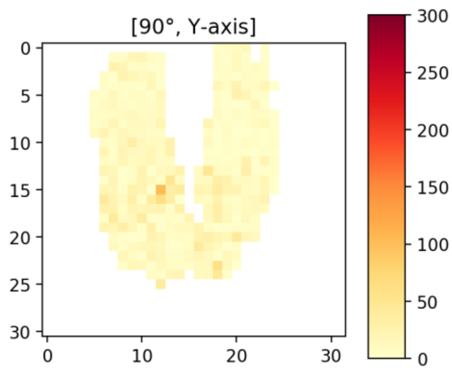

(c) 122-2-2954 Gradient Map

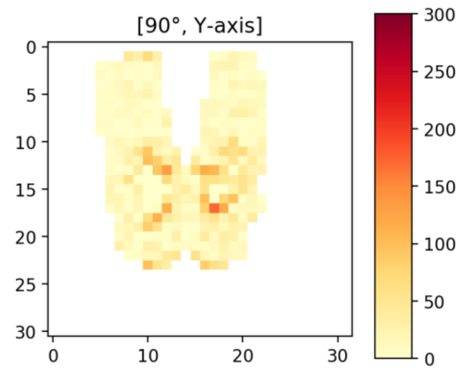

(d) 145-1-1601 Gradient Map

Sample	122-2-2954	145-1-1601
GLD - Gradient Second Moment X	0.0336	0.0174
GLSD - Homogeneity X	0.0786	0.0593
GLD - Gradient Second Moment Y	*0.0436	0.0305
GLSD - Homogeneity Y	0.0775	*0.1062

*Unusual Observation

Figure 60. GLD Gradient Second Moment vs GLSD Homogeneity unusual observations (static data subset)

Other sets of statistical features that also show strong correlations are Energy (GLSD), Entropy (GLSD), and Contact Cells (see Fig. 50). An initial assessment found that the direction of measurement does not significantly affect the behavior of Entropy (GLSD) [$R^2 \approx 96.1\%$ between $90°(Y)$ and $0°(X)$]. Similarly, measures of Energy (GLSD) are also generally not affected by the direction of measurement $(R^2 \approx 92\%$ between $90°(Y)$ and $0°(X))$. Measures of Energy (GLSD) and Entropy (GLSD) are almost inversely identical to each other with $R^2 > 97.7\%$ in either $90°(Y)$ or $0°(X)$. Regression results for measures of Energy (GLSD) and Entropy (GLSD) were obtained by excluding sample 145-1-1601 (see Fig. 60b). Figure 61 shows the relationship between these image statistical features while highlighting measures' discrepancies found in sample 145-1-1601. Note that the measure scale for Energy (GLSD) is in inverse proportion. Energy (GLSD) and Entropy (GLSD) are significantly affected when a pressure map shows pressure clusters at max pressure response readings (300 mmHg) (see Fig. 60b). A higher entropy (e.g. ~9.25), and much lower energy (e.g. ~1/582.67), is to be expected for this sample if the max pressure response of the pressure mat interface was higher than subject's true maximum exerted pressure in a given cell. For this reason, sample 145-1-1601 was excluded during regression analysis. With the use of a proper pressure mapping interface with no capped-pressure readings and clusters, single measure such as Entropy (GLSD) at $0°(X)$ is representative of the second-order map texture.

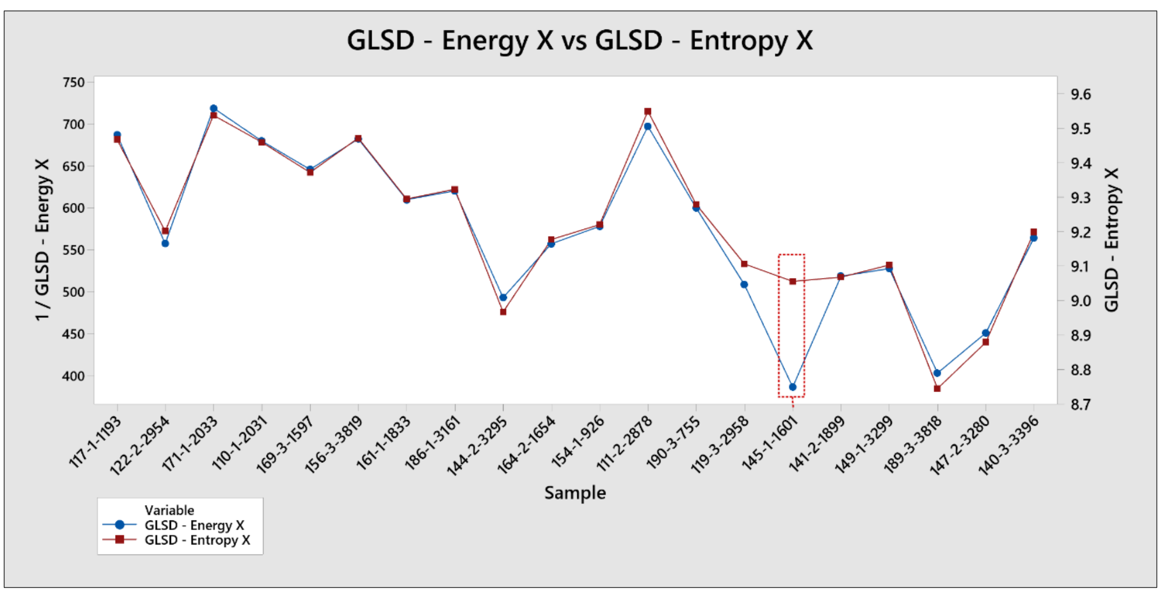

Figure 61. GLSD Energy X vs GLSD Entropy X (static data subset)

Measures of Entropy (GLSD) [at $0°(X)$] and Contact Cells also show a strong positive correlation ($R^2 \approx 89.3\%$) when considering all samples included in the static data subset. Two unusual observations were found during regression analyses where the observed entropy values were lower than expected (see Figs. 62, 63).

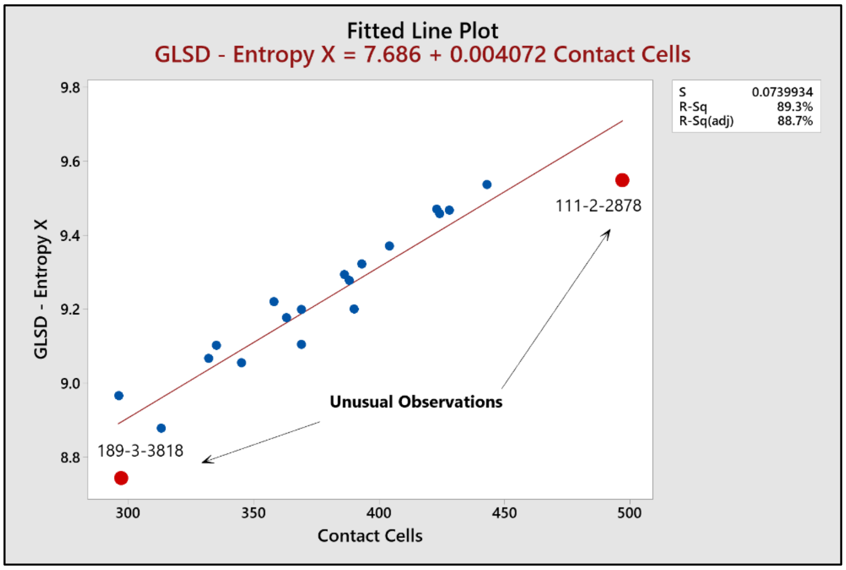

Figure 62. GLDS Entropy X vs Contact Cells regression (static data subset)

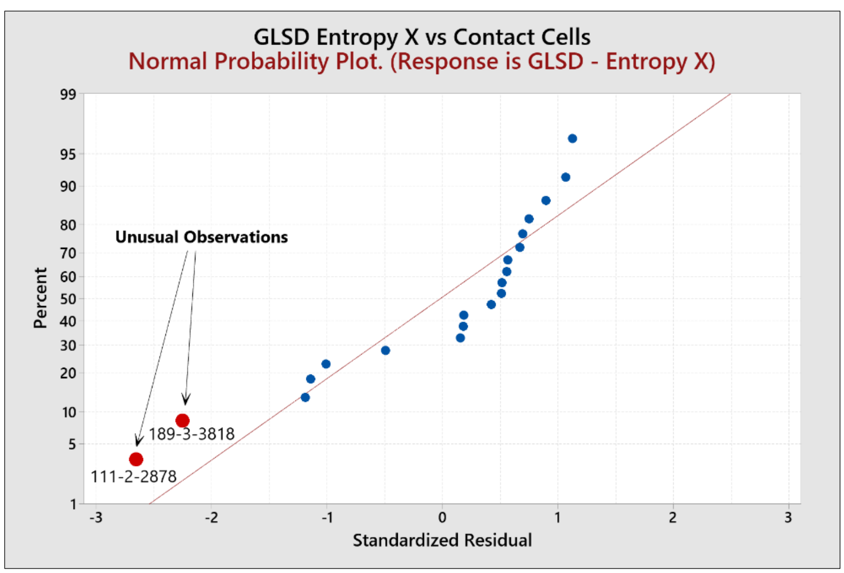

Figure 63. GLDS Entropy X vs Contact Cells residuals (static data subset)

By considering localized pressure changes to identify randomness (noise) in the pairwise pressure distribution at a given direction, GLSD Entropy values are expected to increase when the number of contact cells increase as a higher diversity of pressure readings is expected. But presence of homogeneous regions within a pressure map, relative to the contact pressure area, are also affecting the entropy value. Figure 64 shows pressure maps where measures of Entropy (GLSD) were unusual and lower than expected considering the size of the pressure maps.

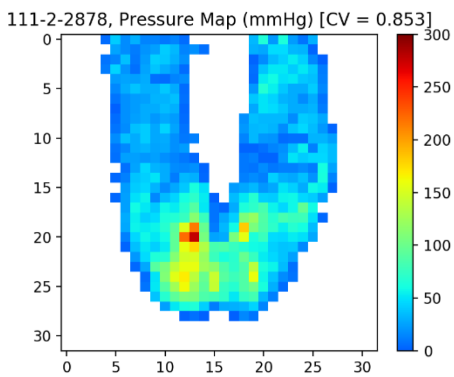

(a) 111-2-2878 Pressure Map

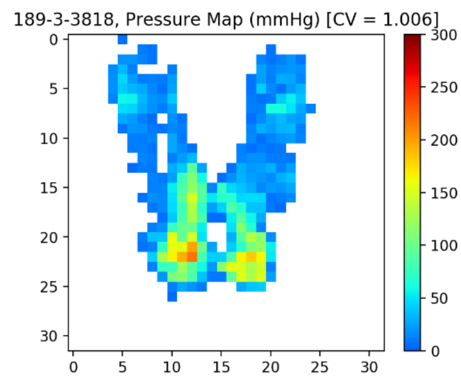

(c) 189-3-3818 Pressure Map

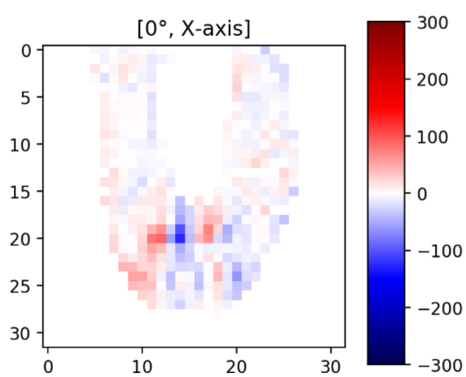

(b) 111-2-2878 Second Gradient Map

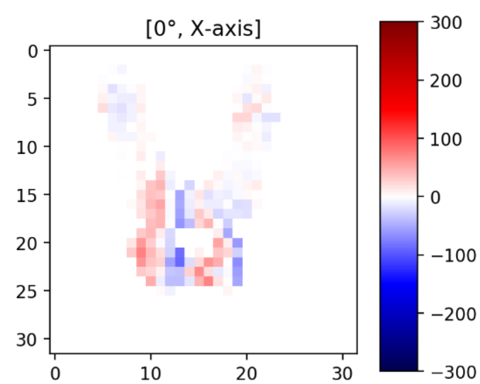

(d) 189-3-3818 Second Gradient Map

Sample	111-2-2878	189-3-3818
Contact Cells	497	297
GLSD – Entropy X	9.5496*	8.7443*
GLSD – Energy X	0.001434	0.002479

*Unusual Observation

Figure 64. Contact Cells vs GLSD Entropy unusual observations (static data subset)

Common pressure measures, such as Sum of Pressure or Coefficient of Variation, do not show high correlations with proposed pressure measures; with measures of Skewness and Kurtosis only relating to each other ($R^2 \approx 79.7\%$). On the other hand, Standard Deviation shows high correlations with various contrast measures, being the highest with the measure of Gradient Contrast X (GLD) ($R^2 \approx 86.5\%$). But while the relationship between these measures is high, their approach for measuring contrast and variability is fundamentally different. Measures of Gradient Contrast are dependent on the spatial relationship of pressure readings, whereas Standard Deviation do not take this spatial relationship into consideration. Illustrative examples can be seen in Figure 65. The measure of Gradient Contrast in sample 186-1-3161 is high due to the presence of a spatially-related high-pressure region located among low pressure readings (see Fig. 65b), while measures of Standard Deviation are very similar for both of the pressure maps shown in this figure (i.e., no spatial relationships are considered).

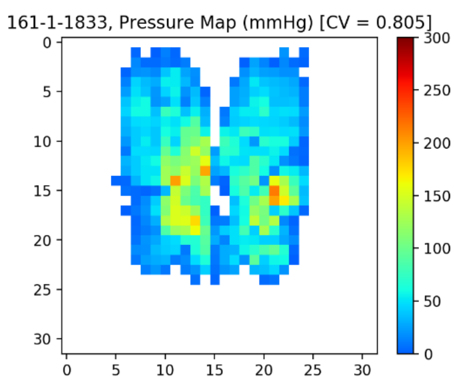

(a) 161-1-1833 Pressure Map

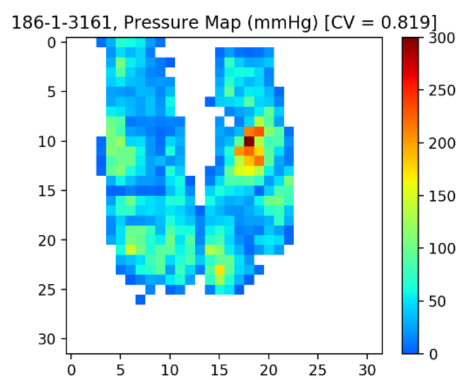

(b) 186-1-3161 Pressure Map

Sample	161-1-1833	186-1-3161
Sum of Pressure	19,865.39	19,567.5
Contact Cells	386	393
Standard Deviation	41.44064	40.77126
GLD - Gradient Contrast X	1278.728863	1562.537572

Figure 65. Standard Deviation vs GLD Gradient Contrast X example (static data subset)

Static Data Subset Summary. In terms of spatial correlation measures, Morans' I appears to be more convenient to use than Geary's C. While they both behave similarly, Moran's I is easier to interpret. Analysis of the selection of the weight matrix for spatial autocorrelation measures indicate that higher spatial autocorrelations are obtained if area of interest (matrix moving window) is similar to the max-min size of expected autocorrelated high-pressure clusters. GLSD Correlation is also an acceptable measure of spatial autocorrelation; it does not require a described weight matrix and is more sensitive to localized pressure gradient variations. Higher GLSD Correlation values are usually obtained when measured in the anterior-posterior sitting direction $[90°(Y)]$.

Many of the introduced image statistical features were also strongly correlated. In terms of measures of variability and gradients, Gradient Contrast (GLD) and Contrast (GLSD) are relatively the same measure, but the former is easier to compute and interpret. The same can be stated for Gradient Mean (GLD) and Gradient Entropy (GLD), being the former easier to compute and interpret. Measures of Gradient Contrast (GLD) and Gradient Mean (GLD) are both acceptable global measures of pressure map gradients. While they share many similarities, the Gradient Contrast (GLD) is more sensitive to pressure maps exhibiting a single or small group(s) of acute pressure points, while the Gradient Mean (GLD) is more robust to these high-pressure points. For these contrast measures, higher contrast values are usually obtained when measured in the lateral sitting direction $[0°(X)]$. Compared to common measures of pressure variability such as Standard Deviation or Coefficient of Variation, Gradient Contrast (GLD) and Gradient Mean (GLD) also consider the spatial relationship of the pressure readings when assessing pressure map's variability.

Measures of Gradient Second Moment (GLD) and Homogeneity (GLSD) are unique and complementary measures for evaluating pressure maps' texture, smoothness and pressure regularity. Their differences lie in that Gradient Second Moment (GLD) is more sensible to changes in pressure gradients, while Homogeneity (GLSD) emphasizes more in measuring the transition and similarities within various pressure levels. Higher values in both measures are usually obtained when measured in the anterior-posterior sitting direction $[90°(Y)]$.

Measures of Entropy (GLSD) and Energy (GLS) were found to be relatively the same. These measures are also correlated with Contact Cells (i.e., number of non-zero pressure readings), but they react differently if pressure maps exhibit high or low homogeneity given the size of the contact area. Using measures of Entropy (GLSD) or Energy (GLS) as global pressure descriptors is somewhat redundant if information on the number of contact cells and measures of homogeneity, such as Gradient Second Moment (GLD), are available. The information provided by contact cells and homogeneity can predict entropy/energy values with high accuracy $(R^2 \approx 95\%)$.

A dimensional reduction process focused on feature selection was followed by using high correlation filters $(R^2 \geq 0.8)$ in combination with analyses of regression models an evaluation of unusual observations. The goal was to select a set of measures where each selected feature is able to explain a unique user-chair interaction phenomenon. The selected pressure measures resulting from this analysis can be seen in Table 23. Important common pressure measures are also included in this set. Each proposed measure has been categorized according to its potential use in pressure mapping analysis, along with important notes and recommendations for their applications.

In the following section, this reduced set of meaningful pressure measures are evaluated using paired-samples of static pressure maps from different subjects. As a result of information loss, these paired samples show no significant differences among common pressure measures (e.g. Contact Cells, Sum of Pressure, and Coefficient of Variation). These new measures are analyzed in their ability to discriminate and find differences (if any) among these paired samples, with the goal of effectively recovering the information loss.

Table 23. Set of meaningful pressure measures

Type	Measure	Notes
General	Contact Cells	Indicates size of pressure area. A small high-pass pressure filter (e.g. 5 mmHg) is recommended to remove low pressure artifacts
	Sum of Pressure	Measures the total amount of exerted pressure in contact area
	Skewness	Measures high-low distribution of pressure readings
Spatial Relation	Moran's I	Recommended area of weight matrix similar to max-min size of expected correlated high-pressure clusters
	Correlation (GLSD)	Sensitive to localized pressure gradient variations. Higher values obtained along sitting direction axis (Y).
Pressure Variability and Contrast	Coefficient of Variation	Non-spatial global measure of pressure variability
	Gradient Contrast (GLD)	Sensitive when pressure maps have either a single or small group(s) of acute pressure points
	Gradient Mean (GLD)	Robust to high-pressure points.
Smoothness and Texture	Gradient Second Moment (GLD)	Sensitive to changes in pressure gradients
	Homogeneity (GLSD)	Emphasizes in measuring the similarities within various pressure levels

Paired Data Subset

Similar to the sampling strategy used for creating the static data subset, stratified sampling of subjects' pressure maps was used following the distribution of the average coefficient of variation by subject (see Fig. 47). For each level of coefficient of variation, random paired samples were chosen if no significant differences ($\Delta < 5\%$) were found across the following common pressure measures: Contact Cells, Sum of Pressure, and Coefficient of Variation. Ten (10) paired-samples of pressure maps with various degrees of coefficient of variations were selected to create the paired data subset (see Appendix J).

Paired-Samples Analysis. To evaluate the discriminant power of newly proposed pressure measures, a meaningful difference between paired-samples is considered when a relative difference of at least ten percent is found between values of the proposed pressure measures ($\Delta \geq 10\%$). For calculating Moran's I, an appropriate weight matrix (i.e., Queen, Constant-Distance, or Inverse-Distance) is selected for each paired-sample according to max-min size of the correlated high-pressure clusters in the samples. GLD and GLSD measures are also considered at both direction [$90°(Y)$ and $0°(X)$]. Results of common pressure measures are presented along with any significant finding from the new pressure measures in each paired-sample.

As global descriptors of pressure distributions, the set of meaningful pressure measures in Table 23 are unable to find differences in terms of shape, orientation, or position between pressure maps; their emphasis is in describing pressure distribution patterns and spatial relationships within pressure maps. Their results are useful in identifying differences and similarities of the within-map intra-relationships of the pressure readings. Figures 66 and 67 are good examples of these restrictions; where differences in terms of shape, location, and spatial position of pressure clusters can be seen between paired samples. But focusing on the pressure distribution patterns and the overall relationship of the pressure readings and clusters, some similarities can be seen between these paired maps.

Figure 66 shows a number of small high-pressure clusters in both maps, along with similarities in the spatial relationship between pressure levels. The main difference between these maps is seen in the pressure transitions between the legs and buttocks, where Figure 66b shows a more homogeneous transition than Figure 66a. These small differences are being successfully detected by differences in the measures of pressure texture in the $90°(Y)$ direction.

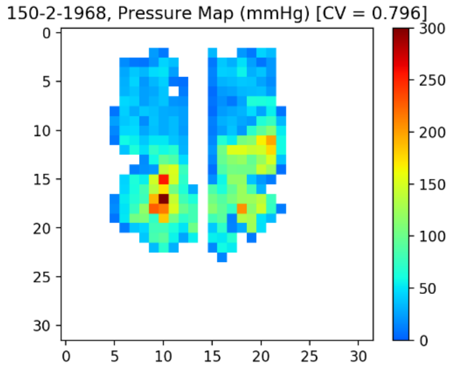

(a) 150-2-1968 Pressure Map

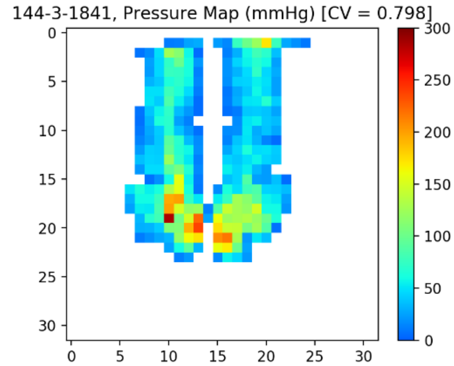

(b) 144-3-1841 Pressure Map

Type	Pressure Measure	Sample		Relative %	Δ Plot
		150-2-1968	144-3-1841		
General	Contact Cells	288	293	1.74%	
	Sum of Pressure	17411.35	17503.15	0.53%	
Variability	Coefficient of Variation	0.7959	0.7978	0.25%	
Texture	GLD - Gradient Second Moment Y	0.0276	0.0320	16.00%	
	GLSD - Homogeneity Y	0.0615	0.0709	15.19%	

*Red highlight: No meaningful differences are found (Δ ≤ 10%)

Figure 66. Pressure measures for samples 150-2-1968 vs 144-3-1841 (paired data subset)

With respect to Figure 67, many similarities are also seen between the paired maps. These maps show similar pressure distribution patterns and similar high-pressure clusters in terms of size and magnitude (albeit in different locations). Minor differences can be seen in terms of pressure scattering as Figure 67b shows more texture and roughness in the right leg regions and Figure 67a shows more delineated acute pressure points close to the right ischial tuberosity. These minor differences are being successfully detected by differences in the values of gradient contrast (detecting acute points) and homogeneity (detecting texture differences).

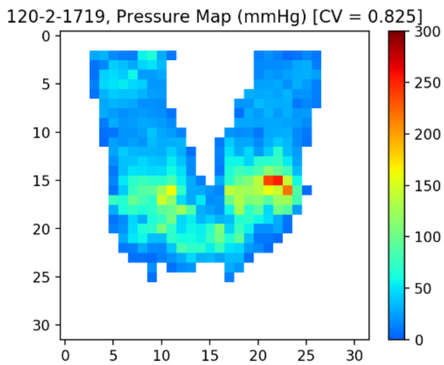

(a) 120-2-1719 Pressure Map

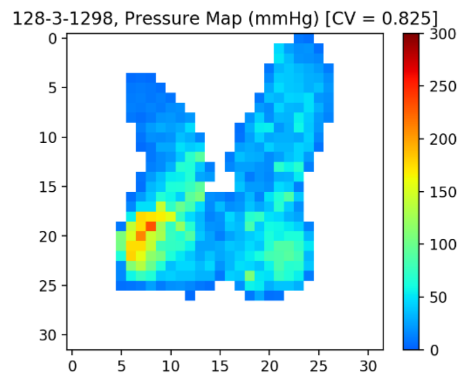

(b) 128-3-1298 Pressure Map

Type	Pressure Measure	Sample		Relative %	Δ Plot
		120-2-1719	128-3-1298		
General	Contact Cells	388	386	-0.52%	
	Sum of Pressure	16877.71	16871.47	-0.04%	
Variability	Coefficient of Variation	0.8247	0.8249	0.03%	
	GLD - Gradient Contrast Y	664.2320	592.9861	-10.73%	
Texture	GLSD - Homogeneity X	0.1026	0.0891	-13.10%	

*Red highlight: No meaningful differences are found (Δ ≤ 10%)

Figure 67. Pressure measures for samples 120-2-1719 vs 128-3-1298 (paired data subset)

In general, paired-samples from Figures 66 and 67 are somewhat similar, with only minor differences seen in their pressure distributions. Only few of the reduced set of meaningful measures (Table 23) were able to effectively capture these slight differences. The following selected examples show paired-samples where more significant differences were detected by the newly proposed pressure measures. A recurrent theme in these analyses is to also highlight the limitations of common pressure measures. All figures presented in this section show differences in measures of Contact Cells, Sum of Pressure, and Coefficient of Variation to be less than 5% ($\Delta < 5\%$), highlighting the information loss due to their inability to detect certain pressure distribution patterns. The full set of results for all paired-samples are shown in Appendix K.

Figure 68 shows paired-samples were significant differences are seen between maps' pressure distributions. The pressure map in Figure 68a shows better spatial relationship among pressure readings, with distinct presences of clusters of low- and high-pressure levels, smoother transitions between pressure levels, and greater homogeneity within the pressure levels. On the other hand, Figure 68b shows high-pressure readings being scattered throughout the map (e.g., upper legs and tuberosities), and higher variability among contiguous readings.

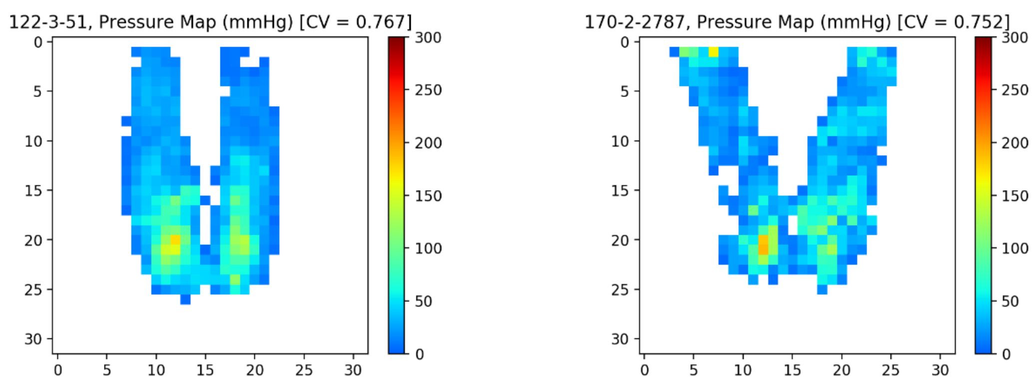

(a) 122-3-51 Pressure Map (b) 170-2-2787 Pressure Map

Type	Pressure Measure	Sample		Relative %	Δ Plot
		122-3-51	170-2-2787		
General	Contact Cells	305	307	0.66%	
	Sum of Pressure	11340.58	11345.89	0.05%	
	Skewness	1.7478	2.2060	26.22%	
Spatial	GLSD - Correlation X	0.6824	0.4327	-36.60%	
	GLSD - Correlation Y	0.8530	0.6351	-25.54%	
Variability	Coefficient of Variation	0.7669	0.7525	-1.89%	
	GLD - Gradient Contrast X	535.50	927.20	73.15%	
	GLD - Gradient Mean X	15.94	20.03	25.65%	
	GLD - Gradient Contrast Y	234.37	541.71	131.14%	
	GLD - Gradient Mean Y	10.04	15.53	54.65%	
Texture	GLD - Gradient Second Moment X	0.0345	0.0283	-17.77%	
	GLSD - Homogeneity X	0.0782	0.0617	-21.07%	
	GLD - Gradient Second Moment Y	0.0553	0.0378	-31.62%	
	GLSD - Homogeneity Y	0.1026	0.0753	-26.61%	

*Red highlight: No meaningful differences are found (Δ ≤ 10%)

Figure 68. Pressure measures for samples 122-3-51 vs 170-2-2787 (paired data subset)

The information loss while relying in common pressure measures is evident. Proposed pressure measures were able to effectively detect differences between the pressure maps shown in Figure 68. The scatteredness of high-pressure readings and the high-variability among contiguous readings in Figure 68b translate to lower spatial measures, higher gradient measures, and lower smoothness measures (i.e., increased texture) when compared to Figure 68a. Figure 69 shows another set of samples to further illustrate the discriminability of the new pressure measures.

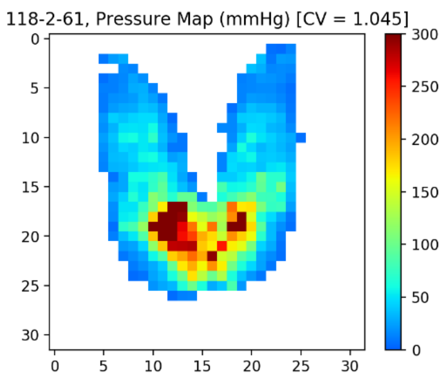

(a) 118-2-61 Pressure Map

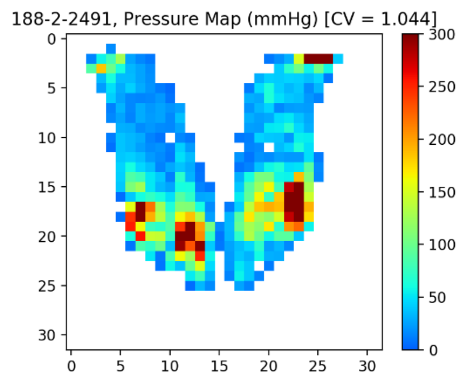

(b) 188-2-2491 Pressure Map

Type	Pressure Measure	Sample		Relative %	Δ Plot
		118-2-61	188-2-2491		
General	Contact Cells	368	364	-1.09%	
	Sum of Pressure	25704.47	25628.04	-0.30%	
Spatial	Moran's I (CD)	0.7905	0.5501	-30.41%	
	GLSD - Correlation X	0.8539	0.6808	-20.28%	
	GLSD - Correlation Y	0.8646	0.7400	-14.41%	
Variability	Coefficient of Variation	1.0451	1.0441	-0.10%	
	GLD - Gradient Contrast X	1622.49	3663.97	125.82%	
	GLD - Gradient Mean X	25.11	38.17	52.01%	
	GLD - Gradient Contrast Y	1471.59	2819.38	91.59%	
	GLD - Gradient Mean Y	22.29	31.86	42.93%	
Texture	GLD - Gradient Second Moment X	0.0255	0.0180	-29.41%	
	GLSD - Homogeneity X	0.0797	0.0559	-29.94%	
	GLD - Gradient Second Moment Y	0.0317	0.0231	-27.17%	

*Red highlight: No meaningful differences are found (Δ ≤ 10%)

Figure 69. Pressure measures for samples 118-2-61 vs 188-2-2491 (paired data subset)

By comparing the pressure maps shown in Figure 69, the scattered high-pressure clusters seen in Figure 69b significantly influence the measures of spatial relationship, pressure gradients, and map's texture when compared to Figure 69a. Sample 188-2-2491 (Fig. 69b) also shows higher variability among contiguous readings and presence of acute pressure points in the upper legs. On the other hand, Figure 69a shows smoother transitions between pressure levels and more homogenous readings within clusters of various pressure levels. The coefficient of variation, commonly used to measure how evenly is the pressure distributed across the surface map, was unable to detect these differences in terms of the number of high-pressure clusters in Figure 69b.

Figure 70 shows another example with similar results to the ones shown in Figures 68 and 69. In this figure, the pressure map in Figure 70b shows higher texture and variability, and an increased number of disconnected high-pressure points/clusters. This leads to significant differences in measures of spatial relationship, gradients, and pressure homogeneity.

With the common pressure measures still showing similar values for the pressure maps in Figure 70, the measure of skewness is also indicating differences between the maps. Figure 70b is more positively skewed, that is, higher frequencies in the lower side of the pressure spectrum (0-300 mmHg) is seen in the distribution of pressure readings. Seating pressure maps are expected to show positive skewness, as the number of relative low-pressure readings is usually significantly higher than the number of relative high-pressure readings. The skewness measure is able to quantify the degree of this relationship.

A visual representation of the distribution of the pressure readings for the pressure maps in Figure 70 is shown in Figure 71. The presence of a higher frequency of low-mid pressure readings (50-110 mmHg) in sample 158-3-3717 (Fig. 70b) is traduced as a higher skewness value when compared to sample 137-2-922 (Fig. 70a). Sample 137-2-922 shows a higher frequency of mid-pressure readings (110-180 mmHg), and lower frequency of low-mid pressure readings (50-110 mmHg) when compared to sample 158-3-3717, making the pressure distributions more negatively skewed. Note that measures of sum of pressure (i.e., the total exerted pressure in the pressure sensing area) and number of contact cells are relatively almost the same.

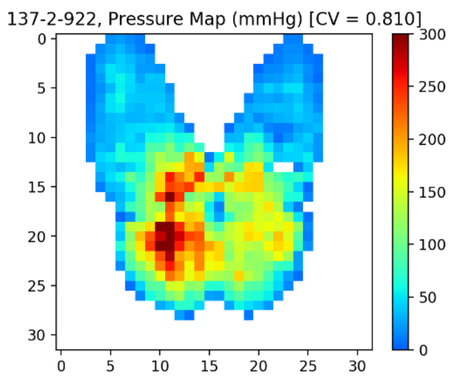

(a) 137-2-922 Pressure Map

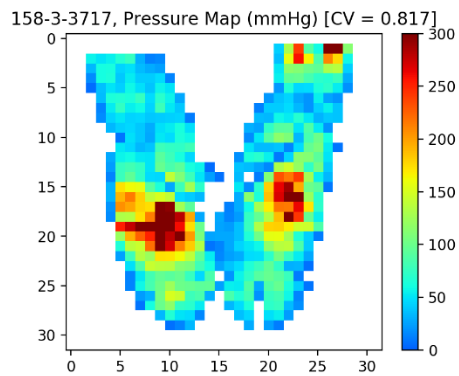

(b) 158-3-3717 Pressure Map

Type	Pressure Measure	Sample		Relative %	Δ Plot
		137-2-922	158-3-3717		
General	Contact Cells	501	503	0.40%	
	Sum of Pressure	43027.83	42878.06	-0.35%	
	Skewness	0.9667	1.5394	59.25%	
Spatial	Moran's I (CD)	0.8281	0.6828	-17.54%	
	GLSD - Correlation X	0.8557	0.7699	-10.02%	
Variability	Coefficient of Variation	0.8102	0.8168	0.82%	
	GLD - Gradient Contrast X	1381.04	2290.37	65.84%	
	GLD - Gradient Mean X	26.02	32.50	24.91%	
	GLD - Gradient Contrast Y	1065.68	1762.09	65.35%	
	GLD - Gradient Mean Y	22.69	29.31	29.16%	
Texture	GLD - Gradient Second Moment X	0.0212	0.0179	-15.52%	
	GLD - Gradient Second Moment Y	0.0241	0.0197	-18.20%	
	GLSD - Homogeneity Y	0.0672	0.0503	-25.22%	

*Red highlight: No meaningful differences are found (Δ ≤ 10%)

Figure 70. Pressure measures for samples 137-2-922 vs 158-3-3717 (paired data subset)

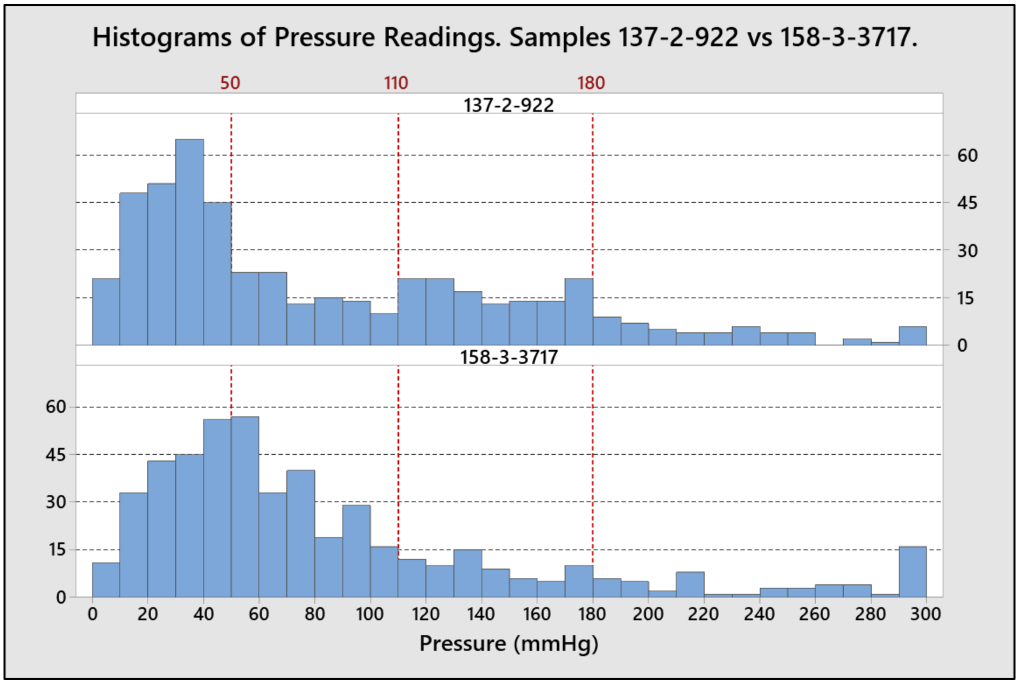

Figure 71. Pressure histograms for samples 137-2-922 vs 158-3-3717 (paired data subset)

Paired Data Subset Summary. Comparative results of the samples included in the paired data subset emphasize the importance of introducing new pressure measures to recover the information loss by current common pressure measures. The proposed measures of spatial relationship, variability, gradients, and smoothness and texture are useful complements to commonly used pressure measures; these new pressure measures are able to detect specific and unique pressure distribution patterns that commonly used pressure measures are unable to. The results in this section confirm that the set of meaningful pressure measures (Table 23**)** are valid and feasible to be used as global descriptors of pressure distribution within pressure maps. If used for comparative purposes, note that these measures are unable to identify differences in terms of shape, location and/or spatial position of pressure clusters. To overcome these limitations, image registration techniques are implemented and evaluated in the following section.

Image Registration and Similarity/Dissimilarity Coefficients

The following subsections show the results of applying image registration techniques to compare pressure maps where significant changes are seen in terms of the shape, orientation, position and/or location of the pressure readings. Results from the following datasets are presented accordingly: (1) transformed data subset, used for evaluating performance and accuracy of registration techniques, and (2) registration data subset, used to analyze feasibility and practicality of proposed comparative techniques (image registration and similarity/dissimilarity coefficients) when significant movements occur (e.g., pressure map shifts, sitting reorientation or relocations).

While analyzing the transformed data subset, the similarity and dissimilarity coefficients are initially used as a supplementary benchmark to evaluate the accuracies and performances of the image registration techniques. Because the transformed pressure maps included in transformed data subset are in fact the same pressure maps as the reference maps (with very small differences due to the random transformation being applied), the resulting values of the similarity and dissimilarity coefficients at registration optimality can be used to benchmark the registrations procedure. A good registration procedure should result in approximately 1 in measures of similarity and 0 in measures of dissimilarity.

It is important to note that for pressure maps that are inherently different, such as the ones included in the registration data subset, the roles of the similarity and dissimilarity coefficients are changed to post-hoc comparative measures instead of benchmarking measures. In these instances, similarity and dissimilarity coefficients are only used to evaluate differences between registered maps at optimality. Higher (lower) values in measures of similarity (dissimilarity) do not necessarily indicate that a better registration was achieved by a particular registration method; but in cases where pressure map images share a number of commonalities and features, a proper correspondence between registered pressure map images generally results in an increase (decrease) of the similarities (dissimilarities) measures.

Transformed Data Subset

To evaluate the translational and rotational capabilities of the image registration techniques, a subset of the dataset consisting of ten (10) samples of pressure maps was used. Stratified sampling based on different levels of contact area was used to select the pressure map samples and create the transformed data subset (see Fig. 12). Two random transformations, each with a random translational and rotational shift, were applied to each pressure map sampled; these were also included in the transformed data subset. Selected samples with applied random transformations are shown in Appendix L.

Before running the optimal linear registration techniques [i.e., maximization of the Mutual Information (MI), or minimization of the Mean Square Errors (MSE)], the pressure map samples were upscaled to a factor of 10 (i.e., from a 32 x 32 map to a 320 x 320 map) to allow fine adjustments of the position and orientation of the pressure maps during image registration procedures.

Image registration algorithms were implemented from the SimpleITK (v1.2.0) python package, which was developed at the US National Institutes of Health (NIH) and also available in multiple programming languages (Yaniv et al., 2018). Before the registration process starts, an initial transformation is applied to center the images, and is defined by the geometric moments of gray level values computed from both images. This approach assumes that the moments of both pressure maps are similar, and hence the best initial guess for registering the images is to superimpose both mass centers (i.e., center of pressures).

After the initial centering, a number of transformations occur during the registration process. The transform used in this study applies a rigid transformation in 2D space with rotations represented by a Euler angle, and are specified as a rotation around an arbitrary center, followed by a translation. Linear interpolations are used to calculate resulting pressure map images during these transformations. Both registration method (MI and MSE) use the same acceleration settings, convergence settings, and optimality parameters during the registration process. Gradient descent is being used as the optimization algorithm during image registration.

Initial centering based on the geometric moments significantly reduced any translation and location differences between pressure maps. Unfortunately, significant rotational differences between pressure maps were found to have meaningful effects during registration procedures. After applying Mutual Information (MI) image registrations to the transformed data subset, results showed instances where large initial rotation differences between the maps significantly affected the registration performance and accuracy. An example is shown in Figure 72 where pre-registered pressure maps for sample 126-2-2177 are shown. The template image shown is the resulting map after applying a random transformation (60° rotation, and horizontal and vertical translations).

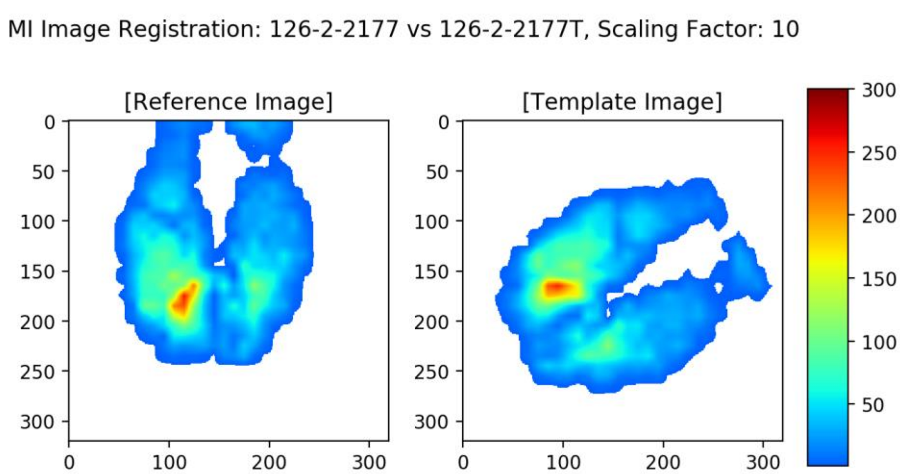

Figure 72. Sample 126-2-2177, original and transformed maps (transformed data subset)

Figure 73 shows the results of registering the pressure maps presented in Figure 72 with both registration methods (MI and MSE). Results of the Mutual Information (MI) registration were not appropriate at optimality (25 iterations), as additional rotation transformations are needed for better images' correspondence (see Fig. 73, top). Similarity and dissimilarity coefficients are also shown in the figure. Note that non-standardized metrics such as L_1 Norm and Squared L_2 Norm are in magnitude of 10^2 due to scaling factors. The registration error obtained at MI registration optimality led to a non-scaled L_1 Norm measure (non-masked) of 10,983.49 mmHg, representing approximately a 90.45% pressure error in pressure maps' correspondence.

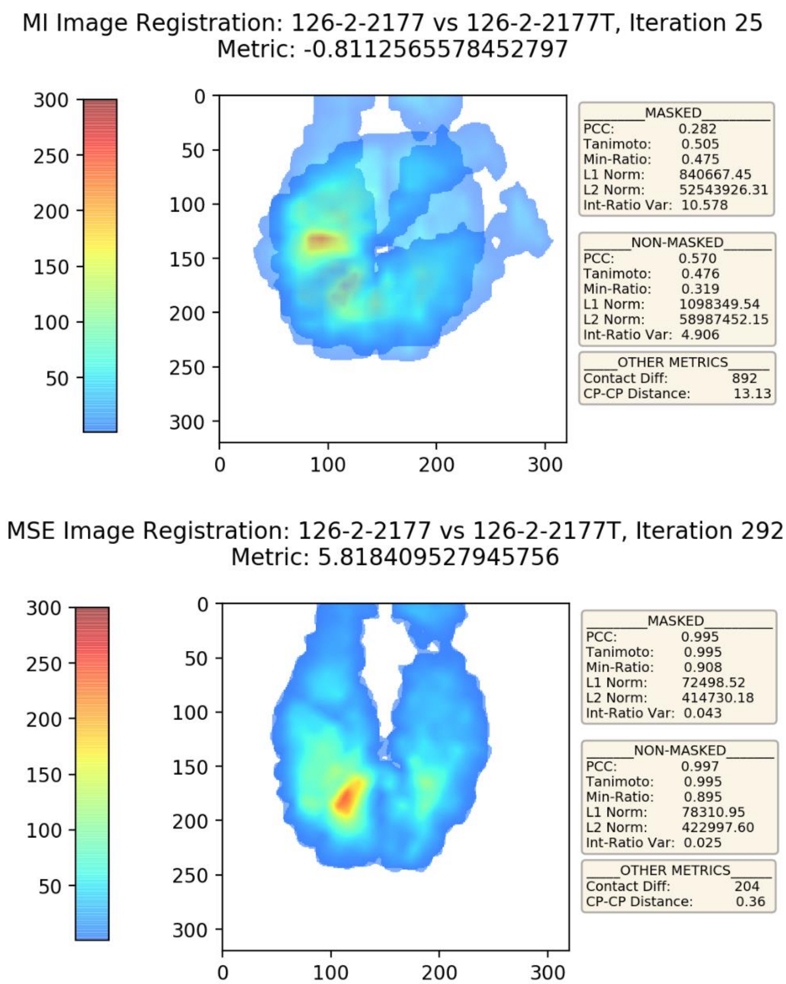

Figure 73. Sample 126-2-2177, optimal MI and MSE registration (transformed data subset)

Figure 73 also shows the results of registering the pressure maps presented in Figure 72 with the Mean Square Error (MSE) registration method (see Fig. 73, bottom). MSE results shows an improvement in the registration procedure by obtaining better images' correspondence when compared to MI results. MSE registration shows a non-scaled L_1 Norm (non-masked) of 783.11 mmHg, representing approximately a 6.45% pressure error between images, with optimality being achieved after 292 iterations (3.2s processing time).

Figure 74 shows pressure map differences at MSE optimality (see Fig. 73, bottom). These pressure map differences are calculated by subtracting the pressure readings of the transformed template pressure map (i.e. moving map) to the pressure readings in the reference pressure map (i.e. fixed map). This figure shows a low-pressure lattice pattern for the pressure differences across the pressure maps with some slight pressure differences around the left ischial tuberosity. This lattice pattern is expected if a proper and successful registration is made on equal pressure maps.

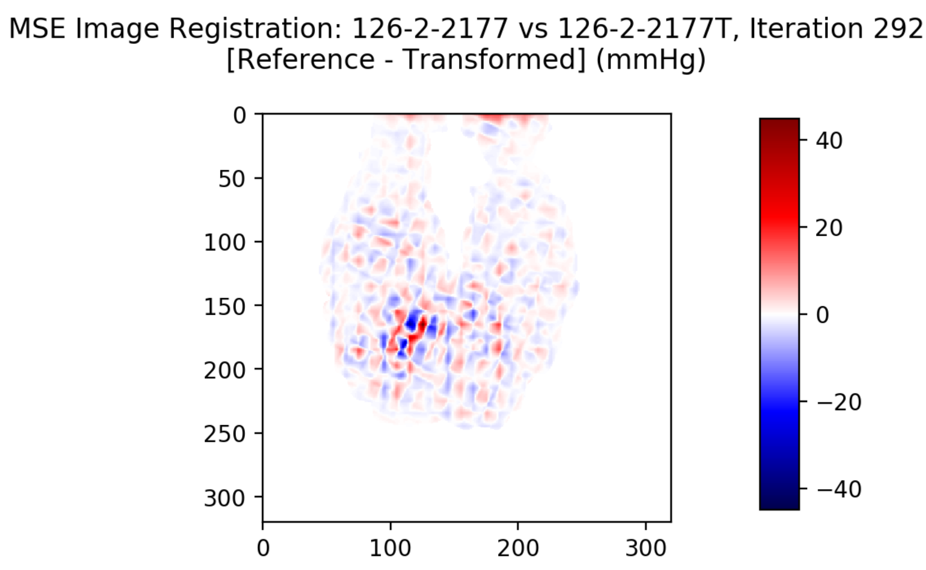

Figure 74. Sample 126-2-2177, optimal MSE registration differences (transformed data subset)

Another example where the registration procedure was affected by the significant rotation difference between pre-registered pressure map is shown in Figure 75. This figure shows the reference pressure map for sample 175-3-1142 along the template image resulting after applying a random transformation ($35°$ rotation, and horizontal and vertical translations).

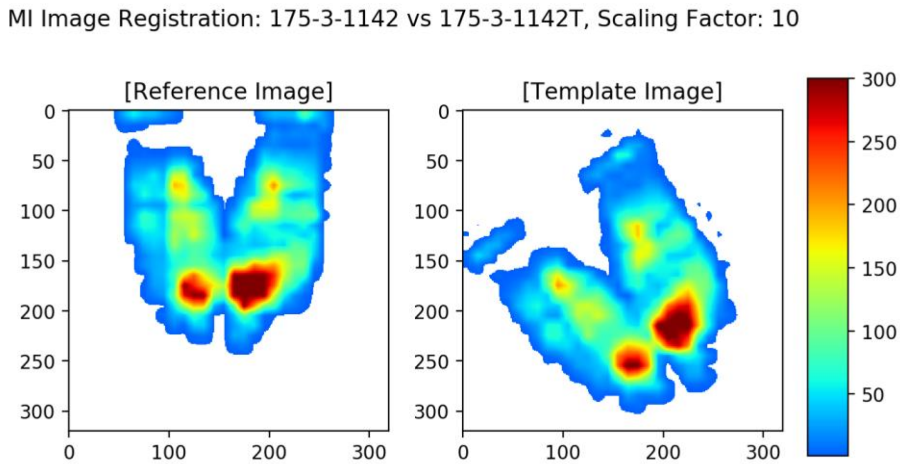

Figure 75. Sample 175-3-1142, original and transformed maps (transformed data subset)

Figure 76 shows the results of registering the pressure maps presented in Figure 75 with both registration methods (MI and MSE). Results of using MI registration were again unsuccessful between these pressure maps, with additional rotation transformations still needed for better images' correspondence (see Fig. 76, top). An 83.27% pressure error in images' correspondence is detected by the L_1 Norm measure (non-masked) at MI optimality. On the other hand, a successful and proper registration was achieved when using MSE registration, with a 6.37% pressure error as per the L_1 Norm measure (non-masked). Figure 77 shows pressure map differences at MSE optimality. This figure shows the expected low-pressure lattice pattern of the pressure differences between the pressure maps, with slight pressure differences around the mid-ischial tuberosities region.

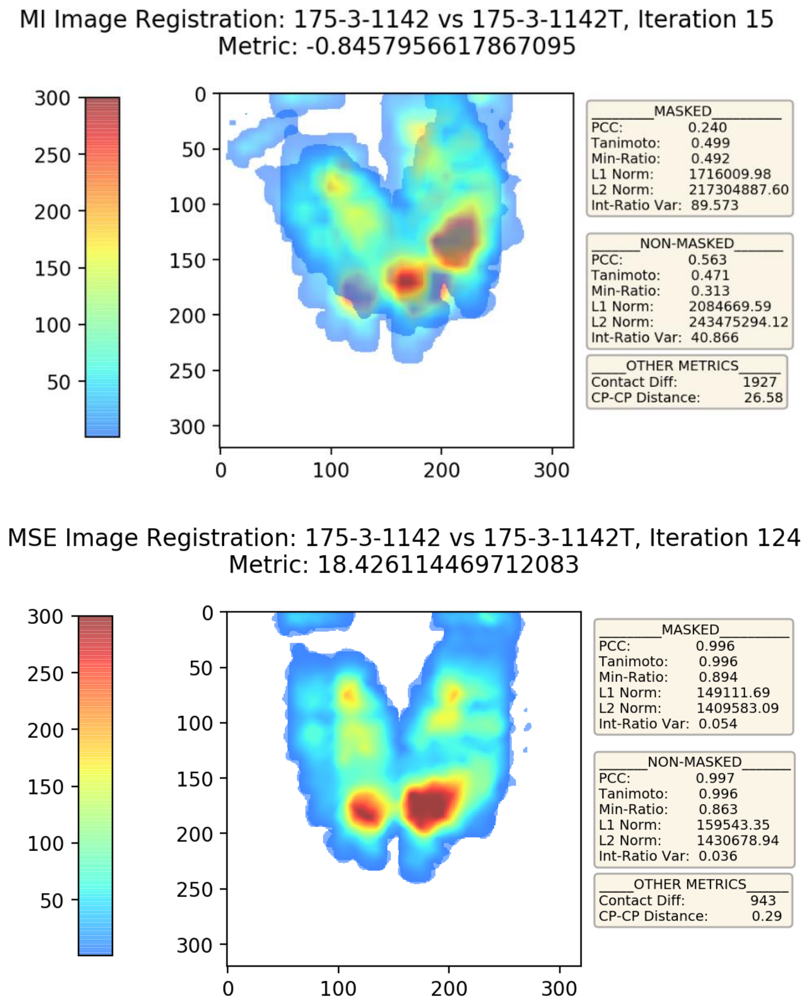

Figure 76. Sample 175-3-1142, optimal MI and MSE registration (transformed data subset)

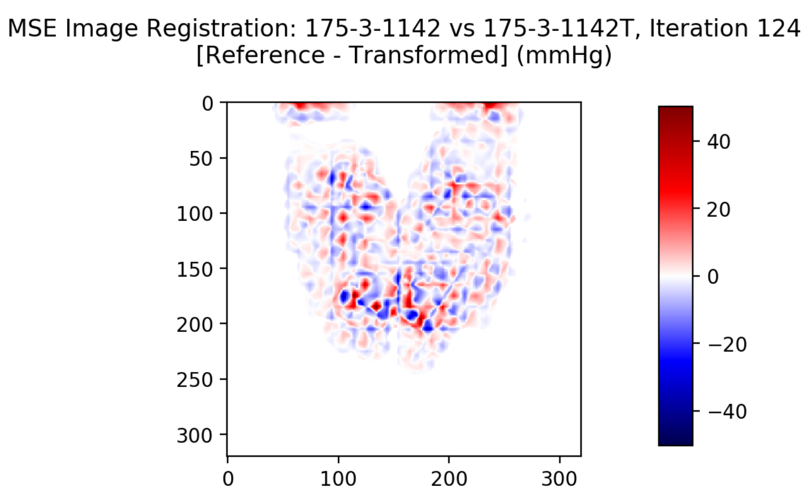

Figure 77. Sample 175-3-1142, optimal MSE registration differences (transformed data subset)

Previous examples demonstrate how significant differences in rotation between pressure map images can have adverse effects when performing MI registration procedures; however, this is not always the case. Figure 78 shows pre-registered pressure maps for sample 109-2-265 along with the template image resulting from applying a random transformation ($36°$ rotation, and vertical and horizontal translation). While this transformation is similar to the one applied in Figure 75, the registration results were successful when using both registration methods. Figure 79 shows proper registrations when using MI or MSE, with better results being obtained when using the latter (10.55% and 5.59% L_1 Norm (non-masked) pressure error for MI and MSE respectively).

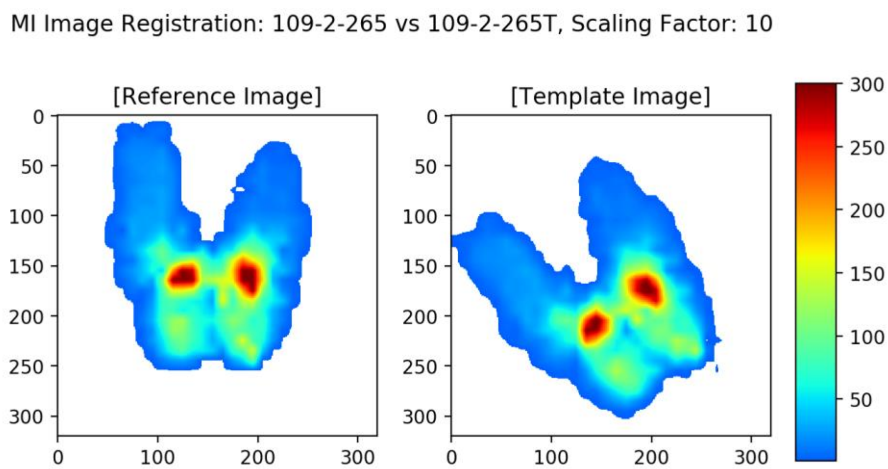

Figure 78. Sample 109-2-265, original and transformed pressure maps (transformed data subset)

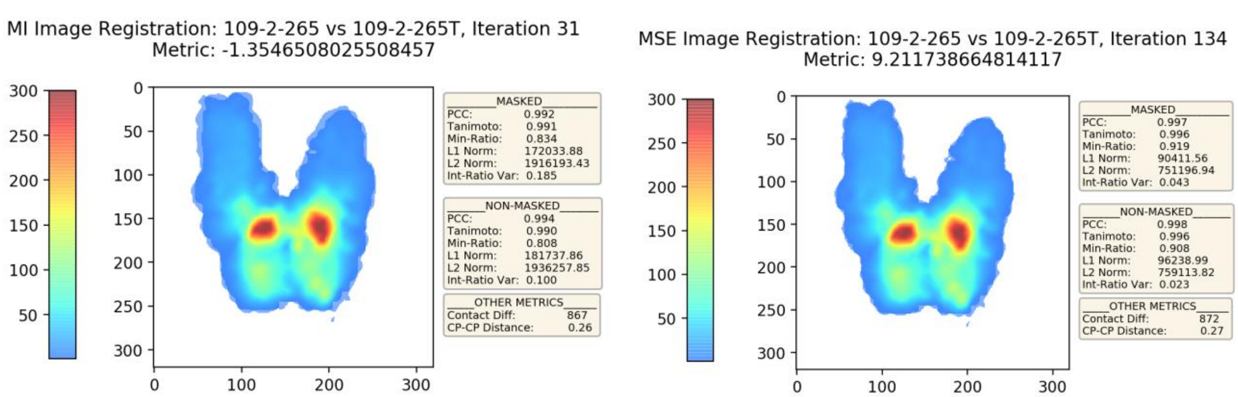

Figure 79. Sample 109-2-265, optimal MI and MSE registration (transformed data subset)

Excluding unsuccessful registrations for samples 126-2-2177 (Fig. 73) and 175-3-1142 (Fig. 76), proper registrations where generally achieved by MI for all other samples, with an average L_1 Norm (non-masked) pressure error of 8.92% and non-masked Pearson Correlation Coefficients of at least 0.9 ($r \geq 0.9$). However, using optimal linear registration based on Mean Square Errors (MSE) minimization generally results in more accurate registration procedures.

Excluding unsuccessful registrations, Figure 80 shows the non-masked similarity and non-masked dissimilarity scores at registration method's optimality for all other samples in the transformed data subset. A total of twenty registrations (ten pressure map samples, each with two applied random transformations) were completed by each registration method. Individual points in the figure represents the similarity/dissimilarity score achieved by the registration method in each registered sample. Tanimoto similarity scores are not shown in the figure as their behavior was almost the same as the Pearson similarity scores ($R^2 = 99.85\%$). As seen in the figure, higher similarities scores and lower dissimilarities scores are generally obtained with MSE registration.

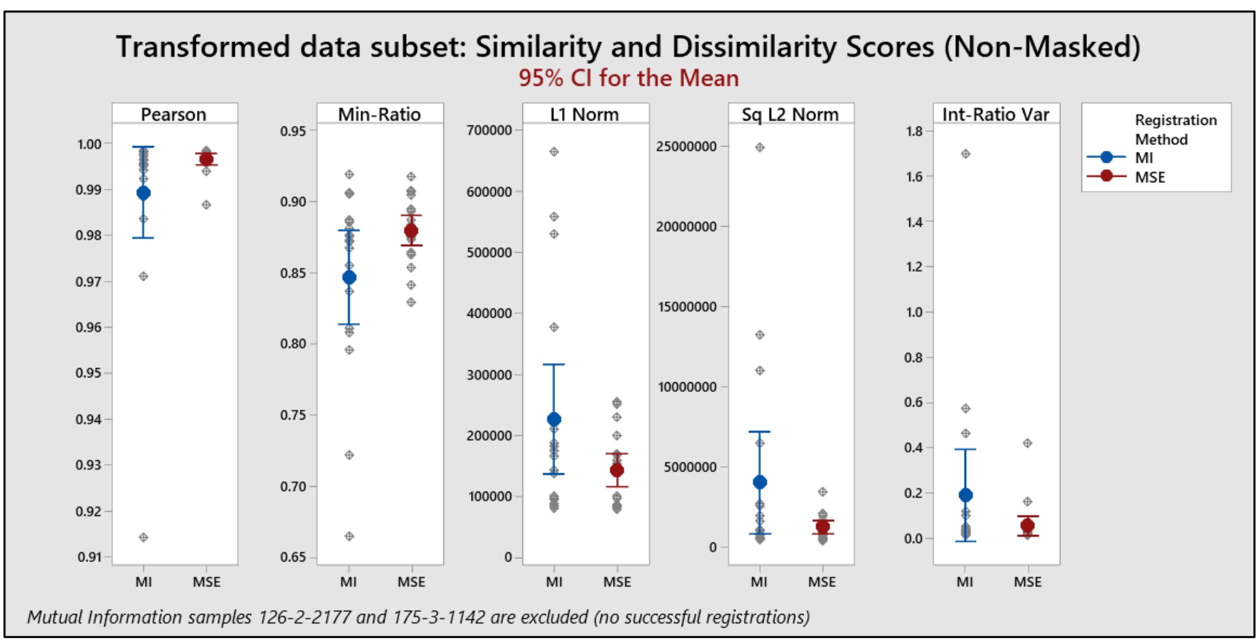

Figure 80. Non-masked similarity and dissimilarity scores plots (transformed data subset)

As explained earlier in this section, the similarity and dissimilarity coefficients are being used as a supplementary benchmark to evaluate the accuracies and performances of the image registration techniques while evaluating the transformed data subset. Due to the fact that registered pressure maps are almost identical to the reference maps, with differences being due to random applied transformations, a registration method achieving a high similarity and low dissimilarity is desired. The similarity and dissimilarity coefficient results obtained at MSE optimality generally outperform the ones obtained at MI optimality. Visual feedback of the registration process also confirms that MSE generally achieves optimal registrations with higher accuracies and better images' correspondences. Table 24 shows the results of one-sided Wilcoxon signed-rank tests, including results from all samples, of the similarity and dissimilarity metric scores between MI and MSE optimalities. These paired difference tests show that MSE registration achieves significantly better results than MI registration at $\alpha = 0.05$. The results of samples' similarity and dissimilarity coefficients obtained at MI and MSE optimalities are shown in Appendix M.

Table 24. MI vs MSE: Wilcoxon signed-rank tests for similarity and dissimilarity results (transformed data subset)

Hypothesis	$H_o: \mu_{MI} \geq \mu_{MSE}$		$H_o: \mu_{MI} \leq \mu_{MSE}$		
Metric	Pearson	Min-Ratio	L_1 Norm	Sq L_2 Norm	Int-Ratio Var
P-Value	0.001	0.003	0.002	0.001	0.004

Transformed Data Subset Summary. Image registration methods based on optimal linear models of Mutual Information (MI maximization) or Mean Square Errors (MSE minimization) were, for most samples, suitable for aligning the pressure map images in the transformed data subset (i.e., mostly identical pressure maps). The pressure map resolutions obtained with these samples (32x32) required upscaling (e.g., factor of 10) to allow fine rotation and translation adjustments during the registration process. Initial centering using image moments (i.e., center of pressures) and subsequent 2D rigid transformation were generally adequate to achieve good registration for both MI and MSE registration methods.

In some instances, Mutual Information exhibited registration issues when significant rotation differences are present among pressure map images. On the other hand, results using MSE provided proper and accurate registration for all samples included in the transformed data subset. While Mutual Information generally reached optimality at a faster rate (53 less iterations on average when compared to MSE registration), MSE provided significantly higher accuracy and better images' correspondence at optimality (see Fig. 80 and Table 24).

Similarity and dissimilarity coefficients, which quantify the relationship between pressure images, generally confirmed good registrations at optimality, particularly for MSE. Use of MSE registration resulted in an average Pearson Correlation Coefficient of $r = 0.9966$ and a 6.11% average pressure error from L_1 Norm among all registered samples.

Registration Data Subset

This section shows the results and evaluations of using image registration techniques and similarity and dissimilarity measures for analyzing and comparing pressure maps during dynamic sitting. For this purpose, the registration data subset was created using twenty (20) samples of pairs of pressure maps selected by stratified sampling based on the different levels of contact area (Fig. 12). Each sample pair was selected from indexes in a continuous sitting interval (within-subject) where a potential significant positional shift or movement is detected. A potential significant movement is considered as a translation of the center of pressure greater than one inch ($\Delta\, CP > 1\ in$) within a twenty seconds time window. Sample pairs selection was done while screening the dynamic movement to confirm that pressure maps selected are not within-movement, but rather to select pre-movement pressure maps (with relative pre-movement stability) and a post-movement pressure maps (with relative post-movement stability). Appendix N shows the selected pressure map indexes from various sitting intervals (within-subjects) with the translation distances of the Center of Pressure (CP) and the time window in frames (1 index ~ 1 second). Sampled pressure maps were again upscaled by a factor of 10 for registration purposes. Upscaled pressure maps of selected sample pairs are shown in Appendix O.

Given that MI and MSE registrations have different optimality metrics, and that the use of similarity and dissimilarity coefficients as a registration benchmark is not appropriate for pressure maps that are inherently different, visual feedback was used to assess images' registrations and correspondences results for MI and MSE registration optimality in all pairs of pressure map samples. Subjective assessments of the seating pressure map alignments completed by each registration method was done using expert knowledge. Iterative pressure map overlays and maps with highlights of pressure differences during registrations were used for visual feedback assessments. The results of MI and MSE registration optimalities for all pairs of pressure map samples, along with notes from the subjective visual feedback assessments, can be seen in Appendix Q.

Assessments via visual feedback found that in twelve out of the twenty registered samples, there were no visually noticeable differences between the optimality results of MI registration and MSE registration, with both registration methods producing proper and accurate alignments between the seating pressure maps. Visual assessments also showed that optimal results from MI and MSE were found to be visually distinguishable in six others of the registered samples (see notes in Appendix Q), with MSE producing better image correspondences in all of these samples.

Figures 81 and 82 show some of the examples where visually distinct registrations are found between image registrations (MI and MSE). In both of these examples, MSE registration was able to identify and correctly align the locations of the ischial tuberosities and legs regions during the registration, greatly improving the images' correspondence. The improvement in the images' correspondence achieved by MSE registration results in some measures showing higher (lower) similarities (dissimilarities) when compared to results from the MI registration (e.g., Figure 81 shows MSE results of 0.904 and 7,778.48 mmHg for non-masked variations of Pearson and non-scaled L_1 Norm respectively, while MI shows results of 0.851 and 7,802.28 mmHg for these same measures). Note that not every similarity or dissimilarity coefficient improves when using MSE registration over MI registration (e.g., Figure 82 shows higher non-masked Pearson values when using MSE over MI [0.819 vs 0.786], but lower non-masked non-scaled L_1 Norm values are obtained when using MI [6,631.85 mmHg vs 7,778.48 mmHg]).

Visual feedback assessments also found two pairs of samples where misalignments of the pressure map images are present at optimality when using either registration (MI or MSE). Figures 83 and 84 show the pressure maps for these pairs of samples along with optimal registration results from MI and MSE, where evidence of incorrect alignments at registration optimalities are seen.

For the pressure map samples obtained from subject 169 (Fig. 83), both MI and MSE registrations attempted to align the pressure clusters in the ischial tuberosities from the template image (moving image) with the pressure clusters in the mid-tights regions of the reference image (fixed image). In this instance, the lack of distinct high-pressure clusters around the ischial tuberosities in the reference image and the significant difference in the size between pressure maps greatly affected the images' correspondence during both MI and MSE registration procedures.

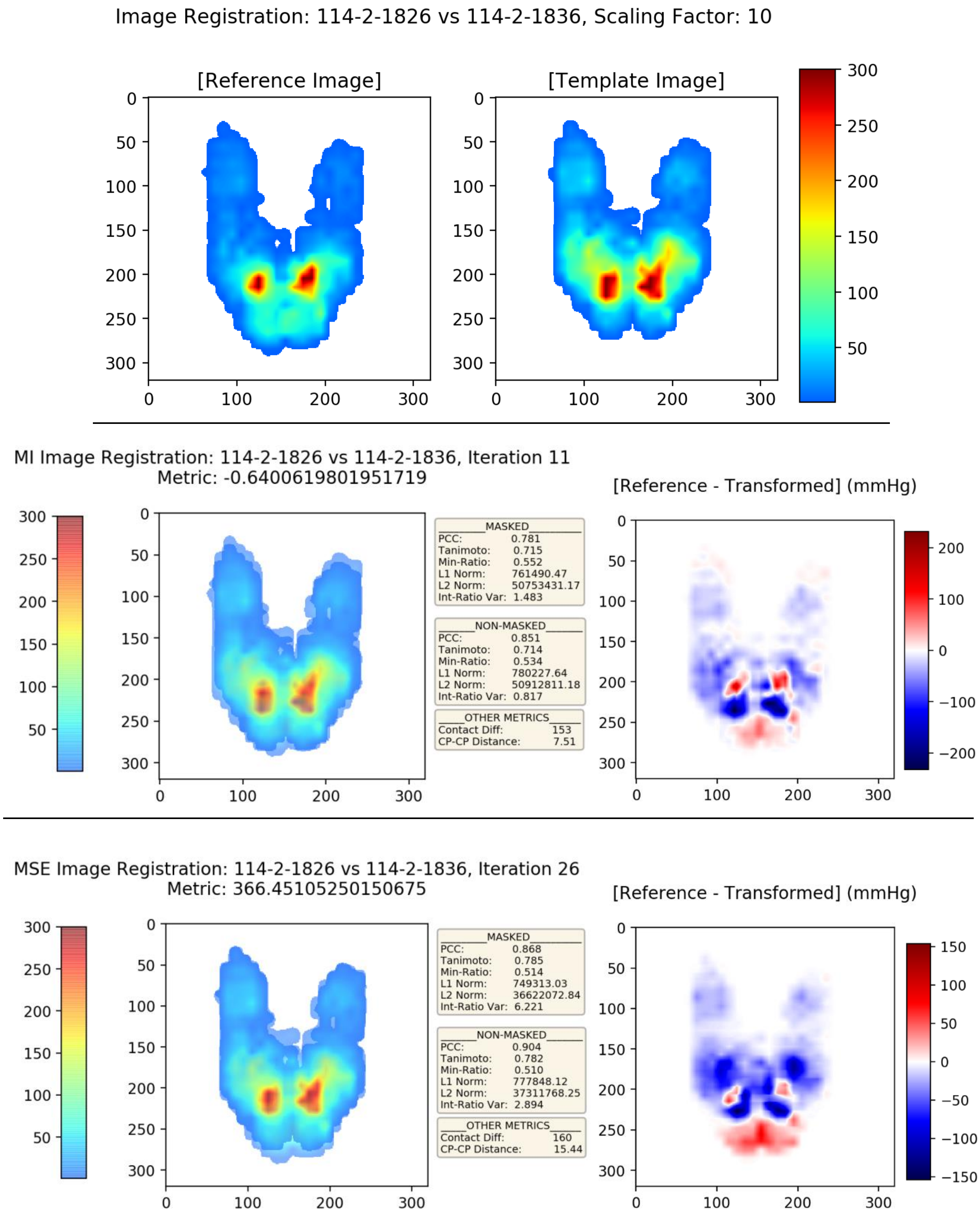

Figure 81. Subject 114, optimal image registration: MI vs MSE (registration data subset)

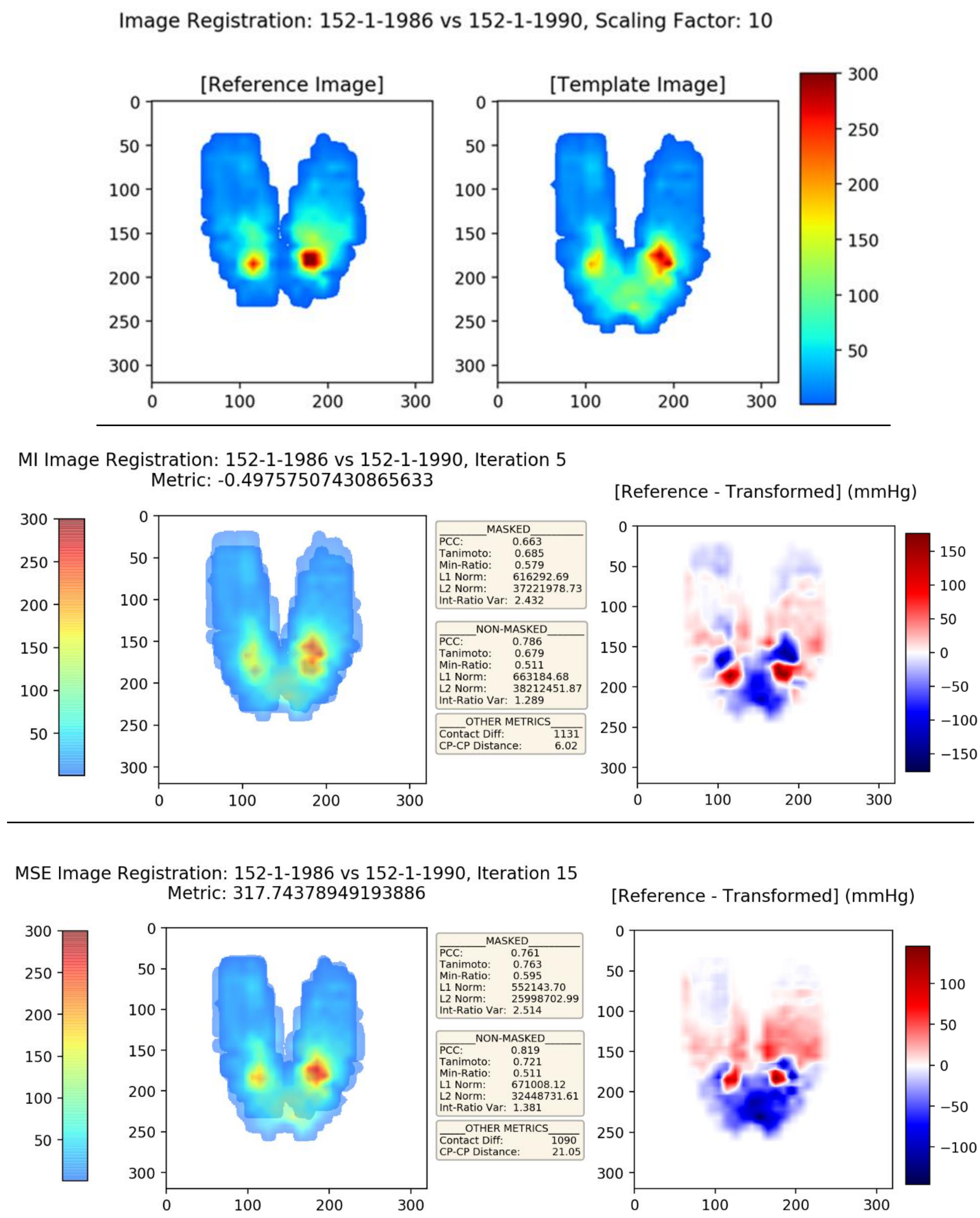

Figure 82. Subject 152, optimal image registration: MI vs MSE (registration data subset)

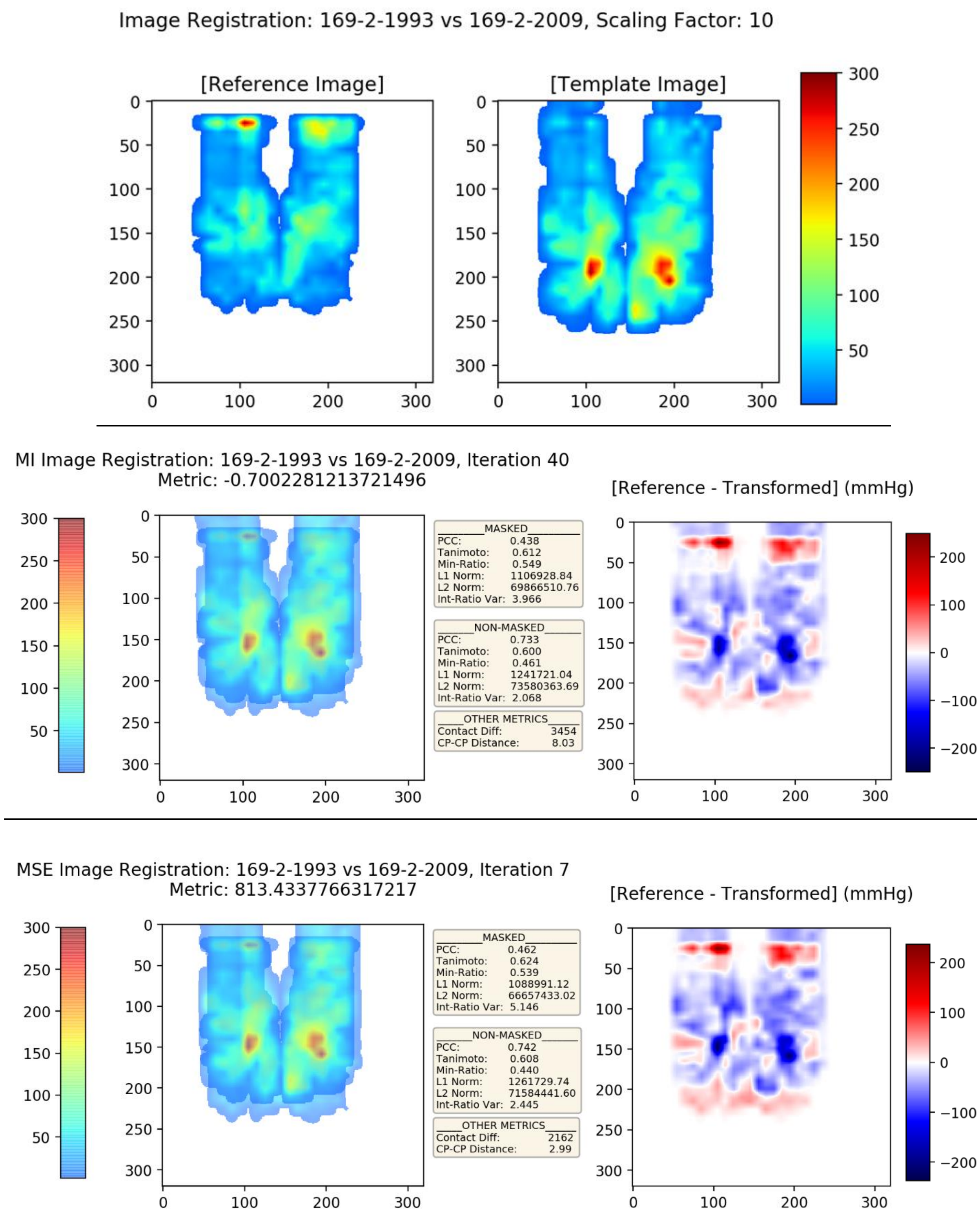

Figure 83. Subject 169, optimal image registration: MI vs MSE (registration data subset)

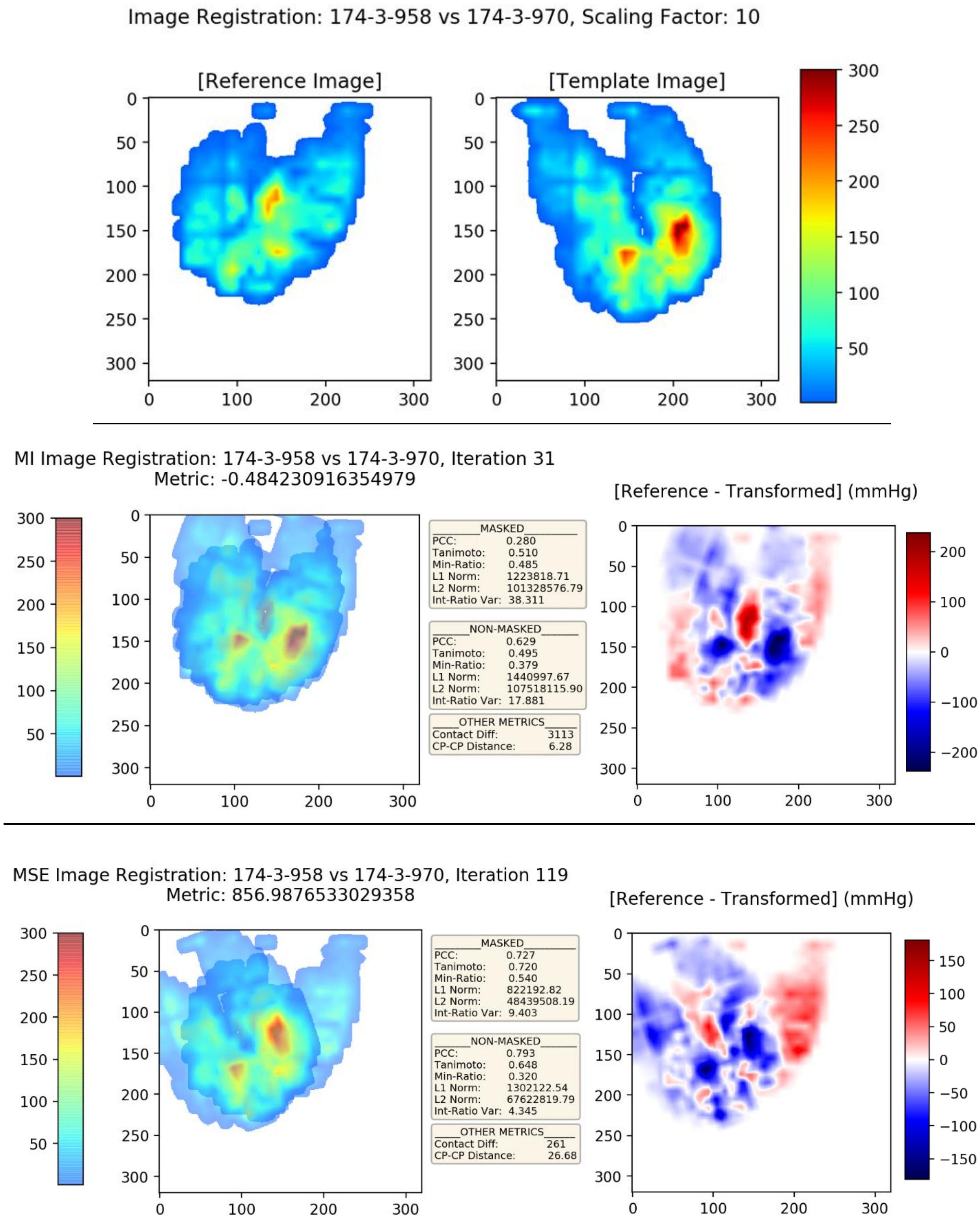

Figure 84. Subject 174, optimal image registration: MI vs MSE (registration data subset)

In samples obtained from subject 174 (Fig. 84), the differences in the seating pressure maps from index 958 to 970 (approximately twelve seconds) shows a complete re-orientation of the legs. Image registration methods have to account for a rotational difference of around 70^0 to be able to provide an adequate registration with proper images' correspondence. Compared to MSE registration results, MI registration was able to detect the need for significant rotational transformations by showing registered pressure maps with better alignments, particularly in the legs regions, but more rotation transformations are still needed for a proper registration. On the other hand, MSE registration focused on aligning the mid- and high-level pressure clusters around the mid-regions of the pressure maps, where most of the pressure is located. The pressure readings under the leg regions were possibly not significantly considered by the MSE registration procedures due to having relatively low-pressure values, with the rotational transformations applied by the MSE registration actually being made in the opposite direction (not in alignment with the legs orientation).

Findings from the visual feedback assessments indicate that using image registration methods based on the minimization of the Mean Square Errors (MSE) results in alignments of seating pressure map images that are equal to or better than the ones obtained when using MI image registration. In twelve out of the twenty registered samples (60%), no visually noticeable differences were seen between the registration methods, but significantly improved alignments and images' correspondences where seen in six of out of the twenty registered samples (30%) when using MSE registration.

As explained earlier in this section, higher (lower) values in measures of similarity (dissimilarity) do not necessarily indicate that a better registration is achieved by a particular registration method. Nonetheless, an increase (decrease) in similarity (dissimilarity) measures is generally seen if proper correspondences are obtained at registration optimality between images that truly share a number of commonalities and features. In the pairs of samples where the MSE registration resulted in better pressure map alignments and images' correspondence, significant improvements in the measures of similarity such as Pearson and Tanimoto and dissimilarity measures such as L_1 Norm and Squared L_2 Norm were seen, possibly due to the better image correspondences achieved by MSE (see Appendix P). Measures of similarity and dissimilarity were not significantly different in instances where the registration results from MI and MSE were not visually distinguishable; but values of these coefficients where marginally better, in most cases, when using MSE registration due to slightly better images' correspondences (see Appendix P).

Different approaches for measuring similarities and dissimilarities (masked vs non-masked) were used in this study. Differences of their use and application are now more evident when using the registration data subset; this is due to the pressure maps images included in this dataset being inherently different (as opposed to the ones used in the transformed dataset). When calculating similarities and dissimilarities coefficients using the masked approach, only non-zero pressure readings sharing the same locations in both pressure map images are considered, while the non-masked approach considers these unbalanced pressure readings (i.e., for a particular pressure map location, one pressure map has a non-zero pressure reading while the other pressure map does not).

When using the non-masked approach, a penalty while calculating the similarity and dissimilarity coefficients was expected due to unbalanced pressure readings being considered. Most of the similarity and dissimilarity measures concur with this logic, as measures such as Tanimoto, Minimum Ratio, L_1 Norm, and Squared L_2 Norm show lower (higher) similarities (dissimilarities) when using the non-masked approach. But a contrasting behavior is seen for the

Pearson Correlation Coefficient and Intensity-Ratio Variance measures, as these improve when considering unbalanced paired readings (see Appendix P).

The improvements obtained by the Pearson Correlation Coefficient and Intensity-Ratio Variance measures when considering a non-masked approach are possibly due to the fact that most pressure readings' location mismatches (i.e., non-overlapping pressure readings) occur around the outlines of the pressure maps, where readings with low-pressure values are mainly present. These mismatches in the outlines of the pressure maps (e.g., a low-pressure reading in a pressure map matched with a zero pressure readings in the other pressure map) can result to a higher Pearson Correlation Coefficient or lower Intensity-Ratio Variance due to their approach in calculating Sum of Squares Error (SSE) (see Equations 17 and 22).

The non-masked and masked approaches for measuring the similarities and dissimilarities between pressure map images have their unique purpose and use. A research study where the goal is measuring the similarity/dissimilarity of only shared features (i.e. overlaps) between pressure map images might be inclined on evaluating the masked variation of these coefficients. While a research study where the goal is measuring all true differences between pressure map images might be inclined to evaluate the non-masked variation of the similarity/dissimilarity coefficients.

Throughout this study, the non-masked variation was the favored approach as it considers all pressure readings differences between pressure map images. The following analysis evaluates the differences in the similarity and dissimilarity coefficient values obtained for each registration method when using the non-masked approach.

Figure 85 shows the paired differences in the similarity and dissimilarity values between image registration optimalities. These paired differences are calculated by subtracting the results obtained when using MSE registration to the ones obtained when using MI registration. In this figure, similarity measures from Pearson and Tanimoto and dissimilarity measures from L_1 Norm and Square L_2 Norm indicate that higher (lower) similarities (dissimilarities) are seen between registered pressure map samples when using MSE registration, again, possibly due to better images correspondences' of pressure map samples. Ratio based measures (i.e., Minimum-Ratio and Intensity-Ratio Variance) indicate that similarities/dissimilarities seen between registered pressure map samples are very similar when using MI registration or MSE registration (see Fig. 85).

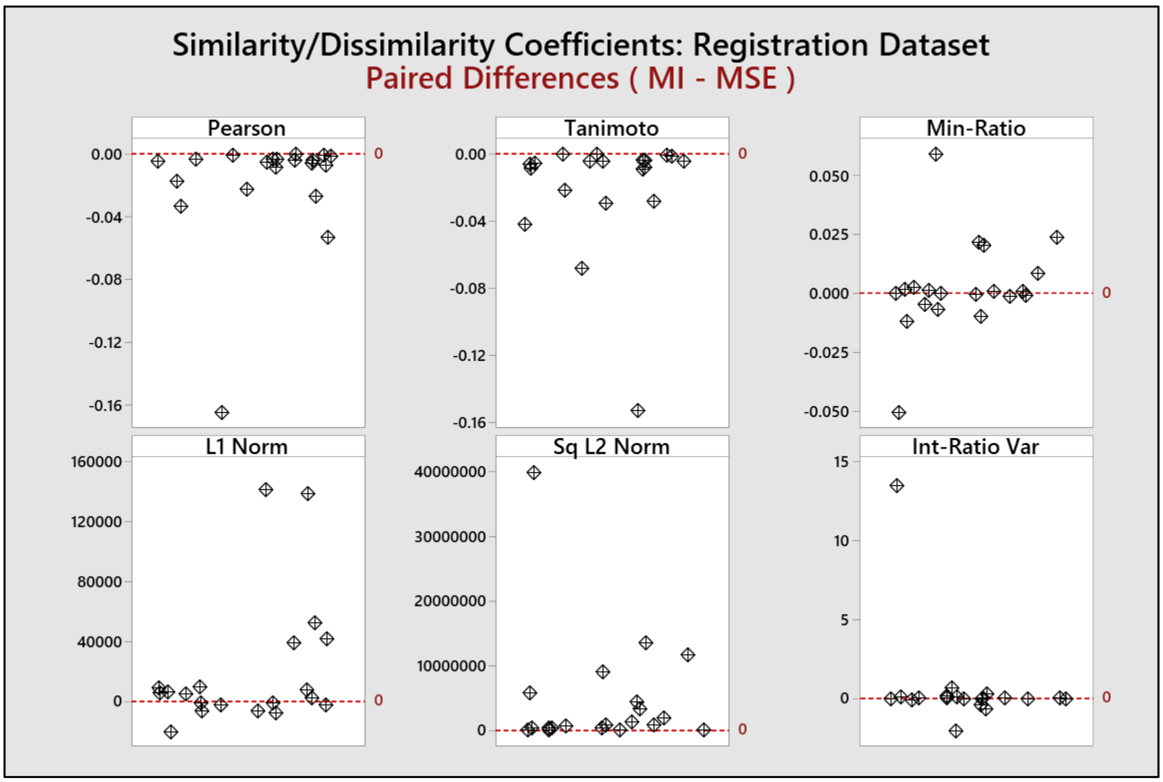

Figure 85. MI vs MSE non-masked similarity/dissimilarity differences (registration data subset)

Table 25 shows descriptive statistics for all similarity and dissimilarity coefficients along with one-way Wilcoxon signed-rank tests to compare results from the image registration methods (MI vs MSE). At $\alpha = 0.05$, significant differences are generally seen between the similarity and dissimilarity values obtained by each registration method. These results indicate that significantly higher (lower) similarities (dissimilarities) are generally seen between registered pressure map when using MSE registration as compared to MI registration. Again, it is important to emphasize that higher similarities or lower dissimilarities do not necessarily indicate that a better registration or alignment between pressure maps was found by a particular registration method. These differences in values of similarity and dissimilarity coefficients between the registration methods are possibly due to the fact that pressure map alignments attained by MSE generally resulted in better registrations and correspondences of the pressure readings (as confirmed via visual feedback assessments). On the other hand, values for ratio-based measures indicate that the similarities (dissimilarities) seen between the registered pressure map samples are not significantly different when using MI or MSE registration. The ratio-based measures are somewhat unique compared to other coefficients, with them being particularly sensitive to pressure map shapes and/or scale differences; more details on their sensitivities are presented in the case study (Chapter 6).

Table 25. Non-masked similarity/dissimilarity coefficients: descriptive statistics, one-sided Wilcoxon signed-rank tests (registration data subset)

	Coefficient	Method	Mean	StDev	Min	Median	Max	p-value	
Similarity	Pearson	MI	0.8543	0.0764	0.6286	0.8522	0.9616	0.001	$H_o: \mu_{MI} \geq \mu_{MSE}$
		MSE	0.8726	0.055	0.7416	0.8688	0.9675		
	Tanimoto	MI	0.7564	0.1183	0.495	0.773	0.9366	0.001	
		MSE	0.7764	0.1022	0.5342	0.7815	0.9457		
	Min-Ratio	MI	0.5832	0.093	0.3793	0.5867	0.7472	0.743	
		MSE	0.5805	0.1018	0.3201	0.5791	0.7463		
Dissimilarity	L_1 Norm	MI	854,234	298,948	547,894	730,774	1,498,689	0.032	$H_o: \mu_{MI} \leq \mu_{MSE}$
		MSE	833,580	271,001	538,889	713,017	1,357,217		
	Sq L_2 Norm	MI	4.2E+07	2.9E+07	1.1E+07	3.6E+07	1.2E+08	0.001	
		MSE	3.8E+07	2.3E+07	1.1E+07	3.3E+07	1.0E+08		
	Int-Ratio Var	MI	2.063	4.034	0.164	0.766	17.881	0.294	
		MSE	1.48	1.848	0.165	0.536	6.525		

Information about the number of iterations and processing time for each pairs of registered samples are shown in Appendix P. When using the SimpleITK (v1.2.0) python package, it is important to emphasize that the stopping criteria for the registration procedures do not necessarily trigger during the optimal iteration. Multiple points of interest are generally found during registration procedures, and a single optimal point is chosen by the algorithm among the points of interest. As an example, Figure 86 shows a time series plot of the Mutual Information (MI) values during the registration process for paired-samples 110-2-1065 and 110-2-1073.

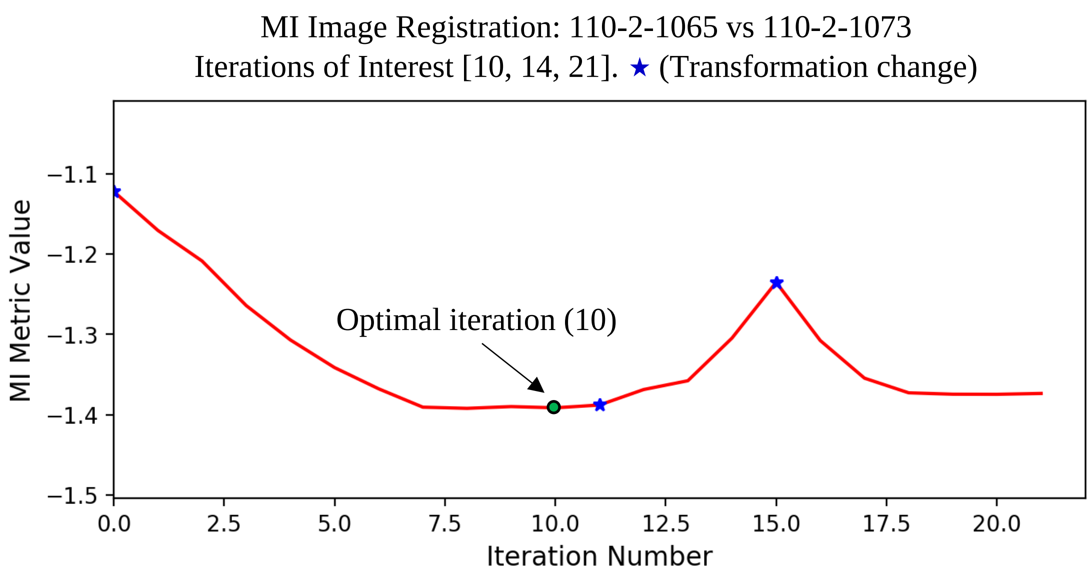

Figure 86. MI iteration values, samples 110-2-1065 vs 110-2-1073 (registration data subset)

In addition to the initial transformation (iteration 0), two other preliminary transformations where used by the MI registration process of these paired-samples. These transformations occurred in iterations 11 and 15, and are represented as blue stars in the figure (see Fig. 86). Transformations following each preliminary transformation attempted to increase the mutual information values between registered pressure map images, by using the minimization of the negative mutual information as the objective function during gradient descent optimization. This same principle is used for MSE transformations using the minimization of the mean squared errors as the objective function during gradient descent optimization. For the example shown in Figure 86, three points of interest were found in this registration process [10, 14, 21], with the tenth iteration (10) being chosen as the optimal iteration due its lower negative mutual information value.

Figure 87 shows boxplots of the processing times when using MI and MSE registrations for the pressure map samples in the registration data subset. On average, MSE registration requires approximately 28 more iterations than MI registration, which translates to an additional time of 1.93 seconds. The highest processing time observed was 2.58 seconds (52 iterations) using MI registration and 15.59 seconds (171 iterations) using MSE registration. For the sample with the highest processing time using MSE registration (171 iterations), the registration process actually reached local optimality at iteration 17, with subsequent iterations trying different transformations to improve registration results (generally the case for MSE registrations). On average, MI required 1.14 seconds to complete the registration process while MSE required 3.07 seconds.

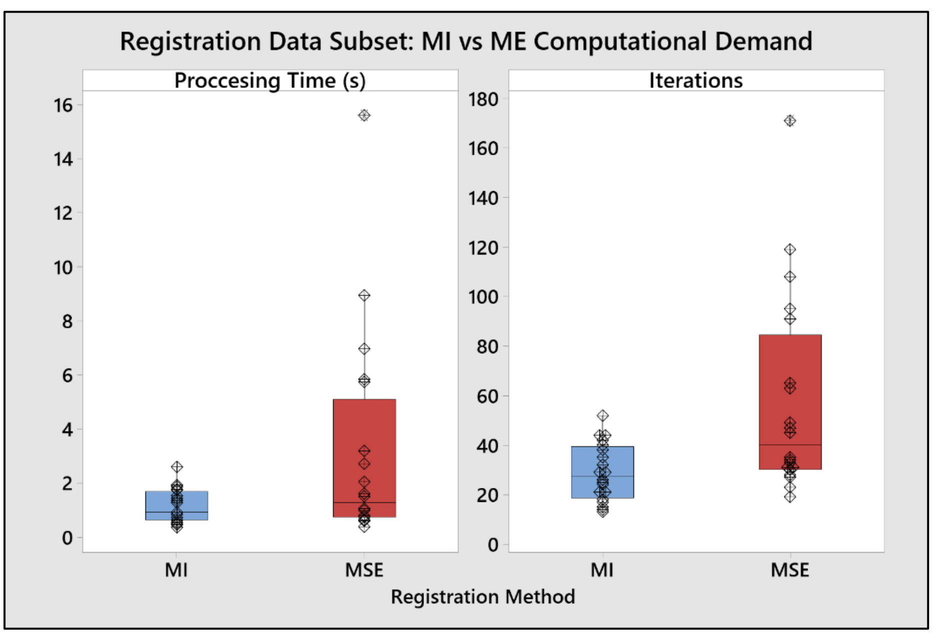

Figure 87. MI vs MSE computing time (registration data subset)

Registration Data Subset Summary. Results of the implementation of image registration techniques and similarity and dissimilarity measures for analyzing and comparing pressure maps during dynamic sitting (e.g., Δ CP>1 in) were generally successful. MI image registration methods were found to provide adequate alignments of pressure map images in most cases, but MSE image registration results were found to be equal to or better than the ones obtained by MI registrations. In twelve out of the twenty registered samples (60%), no visually noticeable differences were seen between the registration methods, but significantly improvements in alignments and images' correspondences where seen in six of out of the twenty registered samples (30%) when using MSE registration. Pearson and Tanimoto similarity measures, and L_1 Norm and Square L_2 Norm dissimilarity measures indicate that significantly higher (lower) similarities (dissimilarities) are observed between registered pressure map samples when using MSE image registration compared to MI image registration, possibly due to the better images correspondences' of pressure map samples achieved by the MSE registrations.

Evidence of incorrect alignments of the pressure map images at registration optimalities were found in two pairs of samples (10%) when using either MI or MSE image registration methods. Pressure maps commonalities, such as shared delineated shapes and similar locations of high- and low-pressure cluster, significantly improves the registration procedures; a significant lack of any of these could possibly result in inadequate optimal registrations (see Figs. 83, 84). The lack of distinct high-pressure clusters (e.g., those normally found around the ischial tuberosities), significant differences in pressure map sizes, and/or significant re-orientations of relatively low-pressure readings (e.g., changes in facing of the legs) were possible factors that attributed to inaccurate registration for these misaligned samples.

Measures of similarity and dissimilarity using proposed coefficients were found to be adequate for measuring and comparing differences between pressure map images. Variations when calculating the similarity and dissimilarity coefficients (i.e., masked or non-masked approach) provided different comparison basis. The masked approach is aimed at research studies where the goal is to compare pressure map images while only considering common pressure regions (i.e. overlaps), while the non-masked approach is aimed at research studies where the goal is to measure all true differences between pressure map images.

In the context of seating pressure map images, similarity measures of Tanimoto and Minimum Ratio were found to be generally lower when using the non-masked approach, while dissimilarity measures of L_1 Norm and Squared L_2 Norm were generally higher. This is due to the non-masked approach taking into consideration all true differences between the pressure map images. But a contrasting behavior is seen for the Pearson Correlation Coefficient and Intensity-Ratio Variance measures, as these improve when using the non-masked approach. This is possibly due to the fact that most pressure readings' location mismatches (i.e., non-overlapping pressure readings) occur around the outlines of the pressure maps, where readings with low-pressure values are mainly present.

In regard to computational times, MSE image registrations, on average, required approximately 28 more iterations than MI image registrations, which translates in requiring and average time of 3.07 seconds to complete the registration process while MI image registrations only required 1.14 seconds on average. Both were implemented using the SimpleITK (v1.2.0) python package.

CHAPTER VI

CASE STUDY

Results from Chapter 5 show that a number of spatial data analytics and image processing techniques are useful and effective for cleansing, evaluating, aligning, and comparing pressure map images. In this case study, the applications of selected techniques are evaluated in terms of continuous sitting, where subjects' pressure maps are constantly captured within a given time interval. A 5-minute sitting interval sample (referred as to dynamic data subset) with a number of sequential spatio-temporal pressure images from one of the subjects in the dataset is used for this case study. As seating subject's frequently change their seating postures during prolonged sitting, changes in pressure distributions and location and orientation of the pressure readings are made constantly. The main goal in this case study is to evaluate the real-life applications of these methods and techniques under dynamic sitting.

The effectiveness of selected spatial clustering methods as pre-processing techniques for continuous pressure mapping are initially examined. Selected spatial clustering methods are evaluated by their performances in continuous data cleansing (i.e., removing unwanted pressure artifacts from continuous pressure maps). The density-based spatial clustering technique providing the highest overall accuracies in detecting extrinsic pressure artifacts (outliers) and true contact pressure readings (non-outliers) is selected as the pre-processing techniques applied to the dynamic data subset for subsequent analyses.

After the extraneous pressure maps artifacts are removed, the set of meaningful pressure measures featured in Table 23 were calculated and evaluated in terms of their practicality and feasibility as measures of dynamic pressure. The application of sequential image registration (using minimization of the Mean Squared Errors [MSE]) as a tool to align dynamic pressure map images is also evaluated. Similarity and dissimilarity coefficients are also evaluated as comparative dynamic measures for post-registered continuous pressure maps. Comparisons to the initial reference index (Index 1) are used as a way of measuring continuous pressure map changes over time. Computation demands for continuous pre-processing (data cleansing) and sequential image registrations (pressure map alignments) are also discussed in this chapter.

Data Sample

To evaluate the applications of selected spatial data analytics and image processing techniques under continuous dynamic sitting, a single 5-minute sitting interval sample of continuous pressure maps was used (dynamic data subset). The sampled interval includes a number of within-subject sequential spatio-temporal pressure maps, and was selected from the first sitting interval during the second data collection session (Trial 2) of Subject 109. This 5-minute interval contains 281 individual frames with extrinsic pressure artifacts continuously present within the recorded pressure maps. Significant pressure redistributions and potential evidence of dynamic sitting are also present in the sampled interval.

Pre-Processing: Spatial Clustering

The results compiled in Table 22 (Chapter 5) show that algorithms based on DBSCAN and DENCLUE, when using only the pressure readings' location information as input data, were suitable for pre-processing seating pressure maps. With proper parameter settings, these algorithms exhibited high accuracies when discriminating extrinsic pressure artifacts (outliers) and true contact pressure readings (non-outliers) in seating pressure maps. These density-based spatial clustering algorithms are evaluated in this case study for their abilities in detecting extrinsic pressure readings artifacts in continuous pressure map.

Unwanted pressure readings and extrinsic artifacts were defined and selected via expert knowledge for all 281 pressure maps withing the dynamic data subset. Selected density-based spatial clustering algorithms (see Table 26) were then executed while calculating measures of outliers and non-outlier accuracies for all continuous pressure maps. The aim is to select the best-performing combination (i.e., clustering methods and parameter settings) from Table 26 by using the overall accuracy (i.e., calculated weighted average of both outliers and non-outliers accuracies) as the measuring criteria. The best-performing combination was used as the pre-processing techniques applied to the dynamic data subset for subsequent analyses.

Table 26. Parameter settings and clustering methods evaluated (dynamic data subset)

Method	Parameters	Input Data
DBSCAN-1	eps: 1.60, 1.80 min_samples: 8	Location
DENCLUE-1	eps: 2 min_density: 1.7e-03	Location
DBSCAN-2	eps: 2.00, 2.20 min_samples: 10	Location
DENCLUE-2	eps: 0.01 min_density: 1.65e-03	Location
DBSCAN-3	eps: 2.5 min_samples: 10	Location

The pressure map samples included in the dynamic data subset show high consistency in the locations of extrinsic pressure artifacts cluster and locations of scattered unwanted pressure readings. Figure 88 shows original pressure maps (non-cleansed) of some of the samples where various extrinsic pressure artifacts (outliers) are present. This figure also shows the expert-created outliers references maps where these outliers are being pre-identified as noise (black dots); these served as basis for calculating clustering algorithms' accuracies.

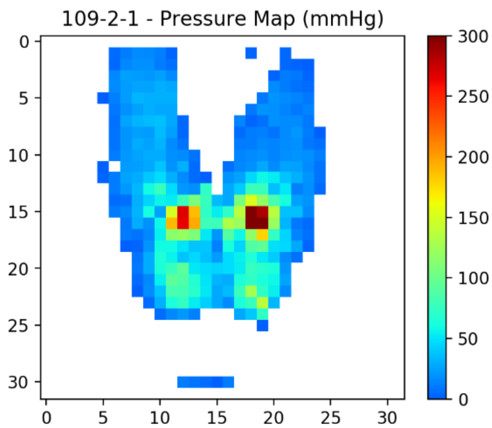

(a) Original 109-2-1 Pressure Map

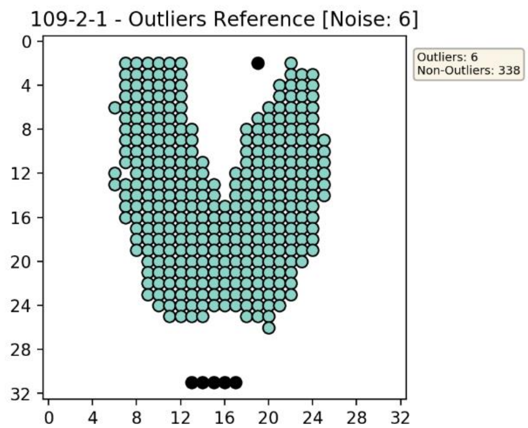

(b) 109-2-1 pre-identified outliers (black)

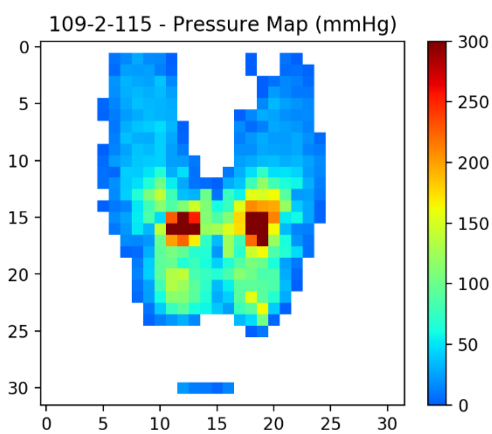

(c) Original 109-2-115 Pressure Map

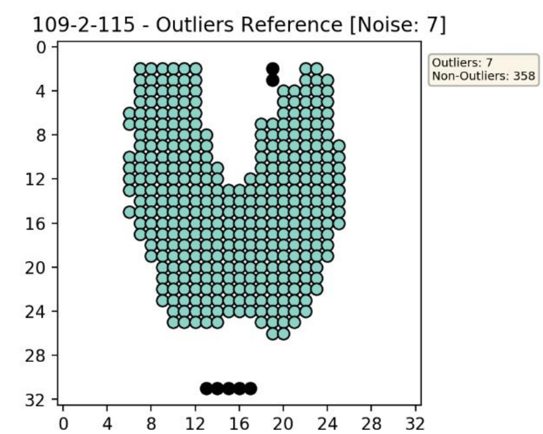

(d) 109-2-115 pre-identified outliers (black)

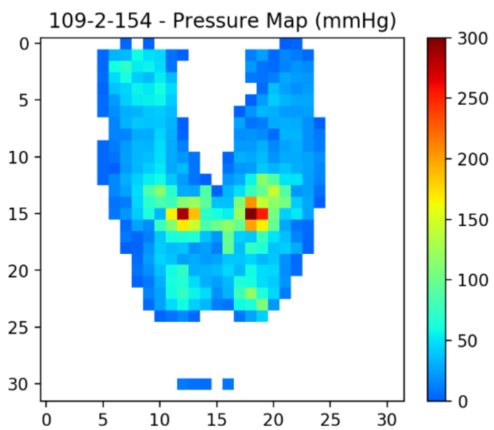

(e) Original 109-2-154 Pressure Map

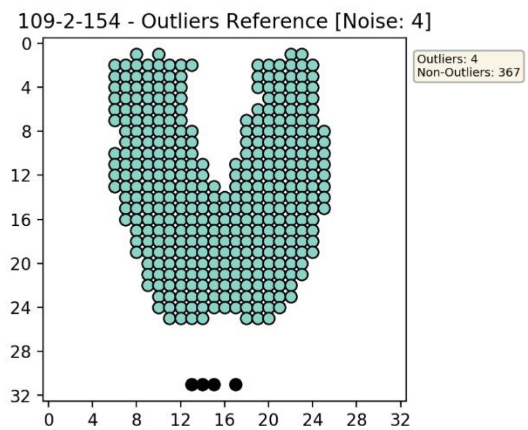

(f) 109-2-154 pre-identified outliers (black)

Figure 88. Examples of original pressure maps from interval sample 109-2 with marked outliers

The original pressure maps presented in Figure 88 show clearly demarked regions of pressure outliers caused by extrinsic artifacts at the bottom of the pressure map images, with other pressure reading outliers being scattered throughout these pressure maps. Pre-processing techniques for continuous data cleansing are needed for eliminating these unwanted pressure readings and artifacts.

For most of the pressure maps in the dynamic data subset, the selected density-based spatial clustering algorithms (Table 26) were able to correctly identify and classify pressure artifacts (outliers) and true contact pressure readings (non-outliers). However, the algorithms were not able to correctly discriminate these extrinsic artifacts from the true pressure readings in some of the pressure maps. Figure 89 shows the pressure map sample (109-2-203) where the lowest overall accuracies were observed for the DBSCAN-1 and DBSCAN-2 clustering methods, both marking a number of non-outlier pressure readings as outliers. Clustering algorithms results from DBSCAN-3, DENCLUE-1, and DENCLUE-2 showed a 100% overall accuracy while classifying outlier and non-outliers for this specific sample.

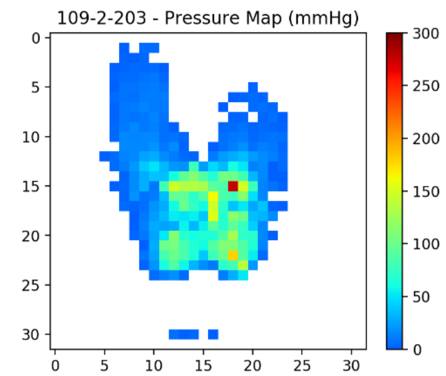

(a) Original 109-2-203 Pressure Map

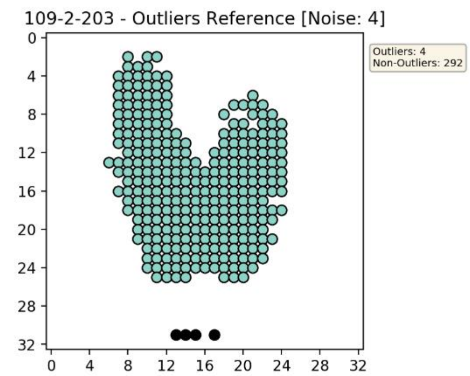

(b) 109-2-203 Outlier Reference

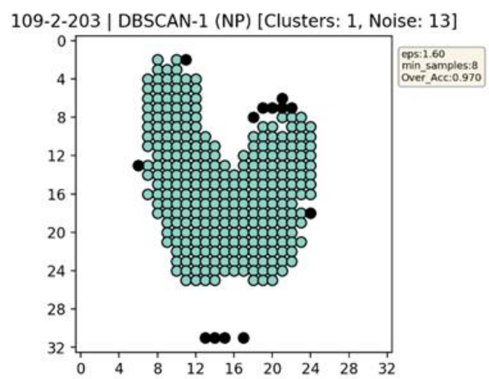

(c) 109-2-203 Results (DBSCAN-1)

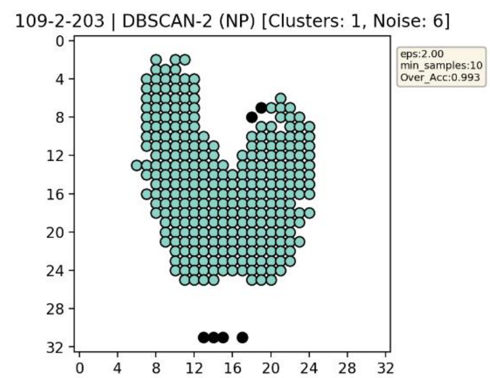

(d) 109-2-203 Results (DBSCAN-2)

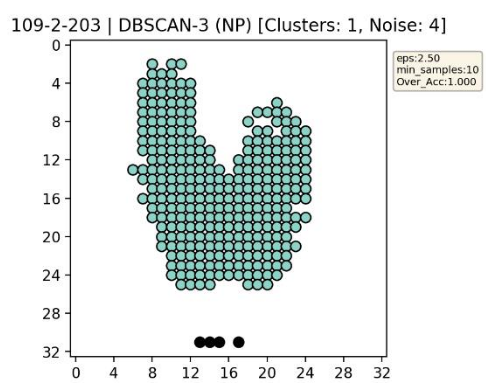

(e) 109-2-203 Results (DBSCAN-3)

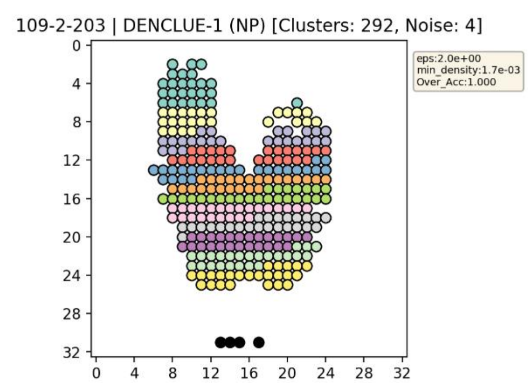

(f) 109-2-203 Results (DENCLUE-1/2)

Figure 89. Clustering results for sample 109-2-203 (location-only data)

The lowest overall accuracies observed for the DBSCAN-3, DENCLUE-1, and DENCLUE-2 clustering algorithms were seen in sample 102-2-208 (see Fig. 90). While these clustering algorithms were able to identify the cluster of outliers at the bottom of the pressure map, Figure 90 shows their inefficacy in correctly identifying some of the pre-identified outliers in the leg regions, thus significantly affecting their outlier accuracy scores. DBSCAN-1 and DBSCAN-2 clustering algorithms were able to classify all the pre-identified outliers included in this pressure map sample. Unfortunately, their more aggressive approach in marking pressure readings as outliers resulted in a number of true contact pressure readings (non-outliers) being incorrectly classified as extrinsic pressure artifacts (outliers).

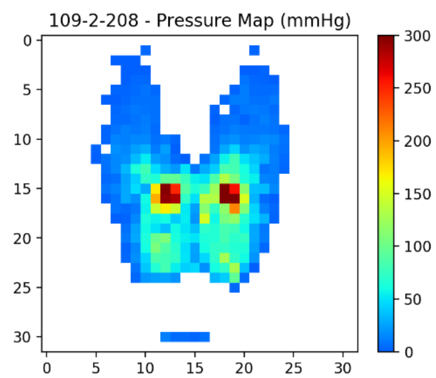

(a) Original 109-2-208 Pressure Map

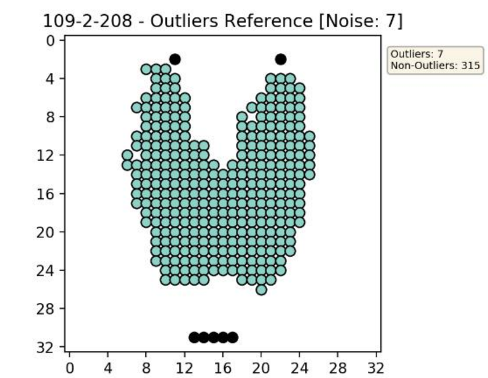

(b) 109-2-208 Outlier Reference

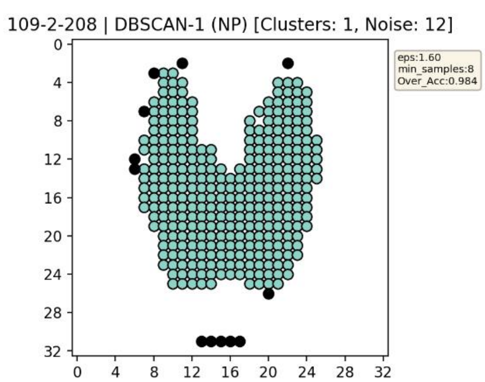

(c) 109-2-208 Results (DBSCAN-1)

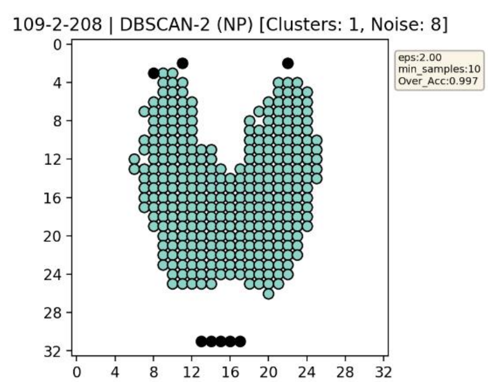

(d) 109-2-208 Results (DBSCAN-2)

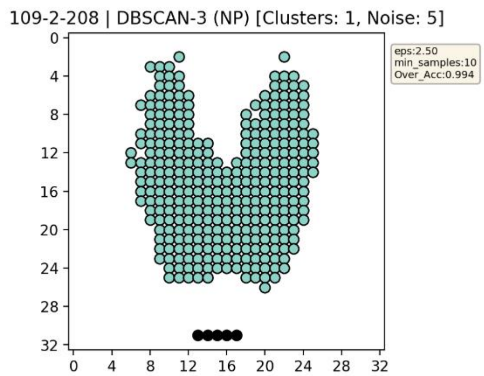

(e) 109-2-208 Results (DBSCAN-3)

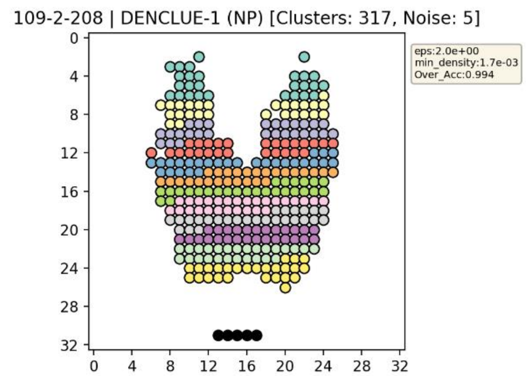

(f) 109-2-208 Results (DENCLUE-1/2)

Figure 90. Clustering results for sample 109-2-208 (location-only data)

A summary of the results obtained by using the selected clustering methods to pre-process the dynamic data subset can be seen in Table 27. Results of the performances and accuracies of these clustering method are generally high, with average Outliers and average Non-Outliers accuracies greater than 90% for any of methods. Results also show tradeoffs between these accuracies, with some methods being more aggressive in classifying pressure readings as outliers, while others exhibiting a more conservative approach when marking outliers.

Table 27. Dynamic data subset clustering methods results of accuracies and processing times

Method	Parameters	Input	Average (Min) Accuracy			Avg. (Max) Proc Time
			Outliers	Non-Outliers	Overall	
DBSCAN-1	eps: 1.60 min_samples: 8	Location	100% (100%)	99.431% (96.918%)	99.440% (96.959%)	3.285ms (15.991ms)
DENCLUE-1	eps: 2 min_density: 1.7e-03	Location	95.035% (71.429%)	100% (100%)	**99.914%** **(99.379%)**	8.597s (11.764s)
DBSCAN-2	eps: 2.00 min_samples: 10	Location	100% (100%)	99.909% (99.315%)	99.910% (99.324%)	2.895ms (7.995ms)
DENCLUE-2	eps: 0.01 min_density: 1.65e-03	Location	92.900% (71.429%)	100% (100%)	99.879% (99.379%)	8.493s (10.370s)
DBSCAN-3	eps: 2.5 min_samples: 10	Location	92.298% (71.429%)	99.999% (99.685%)	99.866% (99.379%)	2.870ms (4.997ms)

Results from Table 27 show that only DBSCAN-1 and DBSCAN-2 were able to correctly classify all extrinsic pressure artifacts as outliers, however, they also show the lowest Non-Outlier average accuracies among the clustering methods' results. This indicate that these variations of DBSCAN favor a more aggressive approach when detecting outliers, by incorrectly classifying true contact pressure readings as outliers. It is important to note that, in spite of having the lowest non-outlier accuracies among the clustering methods, average non-outlier accuracies are above 99% for any of the selected methods. Results from the table also show that both clustering methods using DENCLUE algorithms were able classify all true contact pressure readings as non-outliers, indicating a more conservative approach when marking pressure readings as outliers.

A good balance between average Outliers and Non-Outliers accuracies were obtained by most of the clustering methods being evaluated, with two clustering methods excelling over the others. Clustering results (Table 27) show DENCLUE-1 having an average Overall accuracy of 99.914% which resulted from a very high average Outliers accuracy score (95.04%) and a perfect Non-Outliers accuracy score (100%) in all pressure maps, and DBSCAN-2 having an average Overall accuracy of 99.910% which resulted from with a very high average Non-Outliers accuracy score (99.91%) and a perfect Outliers accuracy score (100%) in all pressure maps.

While all clustering methods were found to be adequate for pre-processing the pressure maps included in the dynamic data subset, this case study selected DENCLUE-1 due to having a slight edge in the Overall accuracy score and also for being able to keep all true contact pressure readings for subsequent analyses. Unfortunately, the non-optimized python package use in this study (Mgarrett, 2017, n. DENCLUE 2.0) resulted in very high computational demands while processing all samples in the dynamic data subset (see Table 27).

The average processing time when using DENCLUE-1 was around 8.6 seconds per frame on average, and the total processing time required to pre-process all 281 individual pressure maps was around 40 minutes. In contrast, the processing times obtained from any of the DBSCAN algorithms, implemented from a fully-optimized python package, were around 3 milliseconds per frame on average, with the total time required to pre-process all 281 individual pressure maps being less than 1 second. These drastic differences in the processing times between these clustering methods can be attributed to many factors (e.g., programming optimizations, multiprocessing capabilities, and/or clustering algorithm complexities), and need to be considered for real-life applications. Fully optimized DBSCAN algorithms are available in many commercially available packages and programming languages, and they generally achieve very good results when using seating pressure maps (see Table 27). As an example, DBSCAN-3 clustering was still able to achieve very high Non-Ouliers accuracies (average of 99.999%) and reasonable Outliers accuracies (average of 92.298%) while still required less than a second; this could be an alternative method to DENCLUE algorithms if preservation of the true contact pressure readings is of utmost importance.

For the purpose of this study, the algorithm’s performance in classifying outliers and non-outliers outweighs their required computation time, therefore, the density-based clustering algorithm DENCLUE-1 is used as the pre-processing technique applied to the dynamic data subset due to the high overall accuracies obtained while cleaning the pressure map images included in the dataset. The (pre-processed) dynamic data subset is now ready for subsequent analyses using measures of spatial autocorrelation, image statistical features, and comparative techniques using image registration and similarity/dissimilarity coefficients.

Dynamic Measures: Spatial Autocorrelation and Image Statistical Features

Meaningful pressure measures featured in Table 23 (Chapter 5) were calculated and evaluated in terms of their practicality and feasibility as measures of dynamic pressure using the pre-processed dynamic data subset. Validation of their use as dynamic measures was done via visual feedback of time series plots. Emphasis is given in selecting and evaluating a sequence of indexes where significant changes in these measures occur in a short period of time. Comparative visual feedback between pressure maps within a sequence of indexes is used to confirm in-chair-movements (i.e., dynamic sitting), while evaluating measures' sensitivities and changes over time.

Figure 91 shows the time series plots for the general pressure measures of Contact Cells, Sum of Pressure, and Skewness for the full 5-minute interval length of this sample (281 indexes).

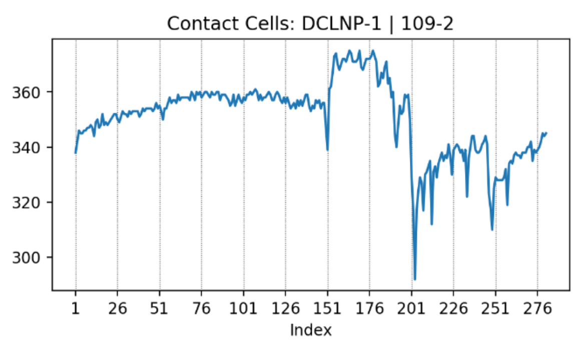

(a) Contact Cells

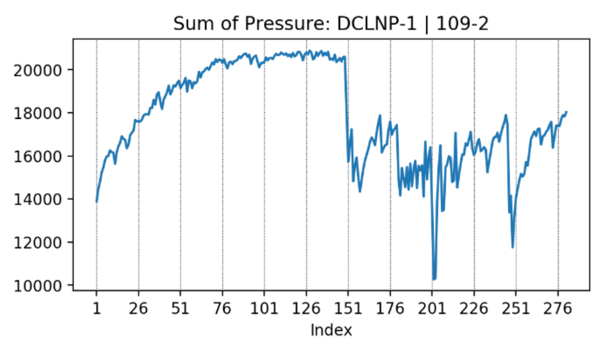

(b) Sum of Pressure

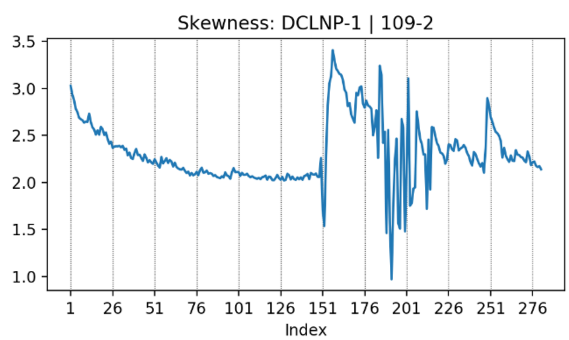

(c) Skewness

Figure 91. Pressure measures: general overview, dynamic data subset (sample 109-2)

Results in Figure 91 show a consistent increase in Sum of Pressure during the first minutes of the sitting interval (approximately 2.5 min), indicating a possible pressure creep effect. It also shows that the number of contact cells increased slightly in the same period of time. The pressure creep effect was confirmed via visual feedback, where pressure readings in the ischial tuberosities were consistently increasing over time. This increase in pressure and somewhat stability in contact cells is also being detected by the skewness measure. The skewness is decreasing over time within the same time frame due the increase in the relative frequency of cells with high-pressure and mid-pressure values.

At around index 150, considerable changes in the values across all measures are also seen in the time series plots in Figure 91, possibly indicating an In-Chair-Movement (ICM). These measures are also identifying possible ICMs (i.e., dynamic sitting) occurring around indexes 200 and 250; with measures of skewness also identifying continuous changes in the pressure between indexes 180 and 200 that other measures are less sensitive to it.

Figure 92 shows a sequence of pressure maps between indexes 148 and 156 (elapsed time of approximately 8 seconds) where the first considerable changes in the values of the general pressure measures are seen. The sequences of indexes presented in this case study generally show a pre-movement pressure map (with relative pre-movement stability) and a post-movement pressure map (with relative post-movement stability). The figure also show values and trendlines for all meaningful pressure measures featured in Table 23 (Chapter 5) along a comparison between the pre-movement index (148) and post-movement index (156) as relative changes in percentage (%) across these measures.

A significant reduction of the overall pressure can be seen in the sequence of indexes shown in Figure 92. The magnitudes and cluster sizes of the high-pressure regions exerted by the ischial

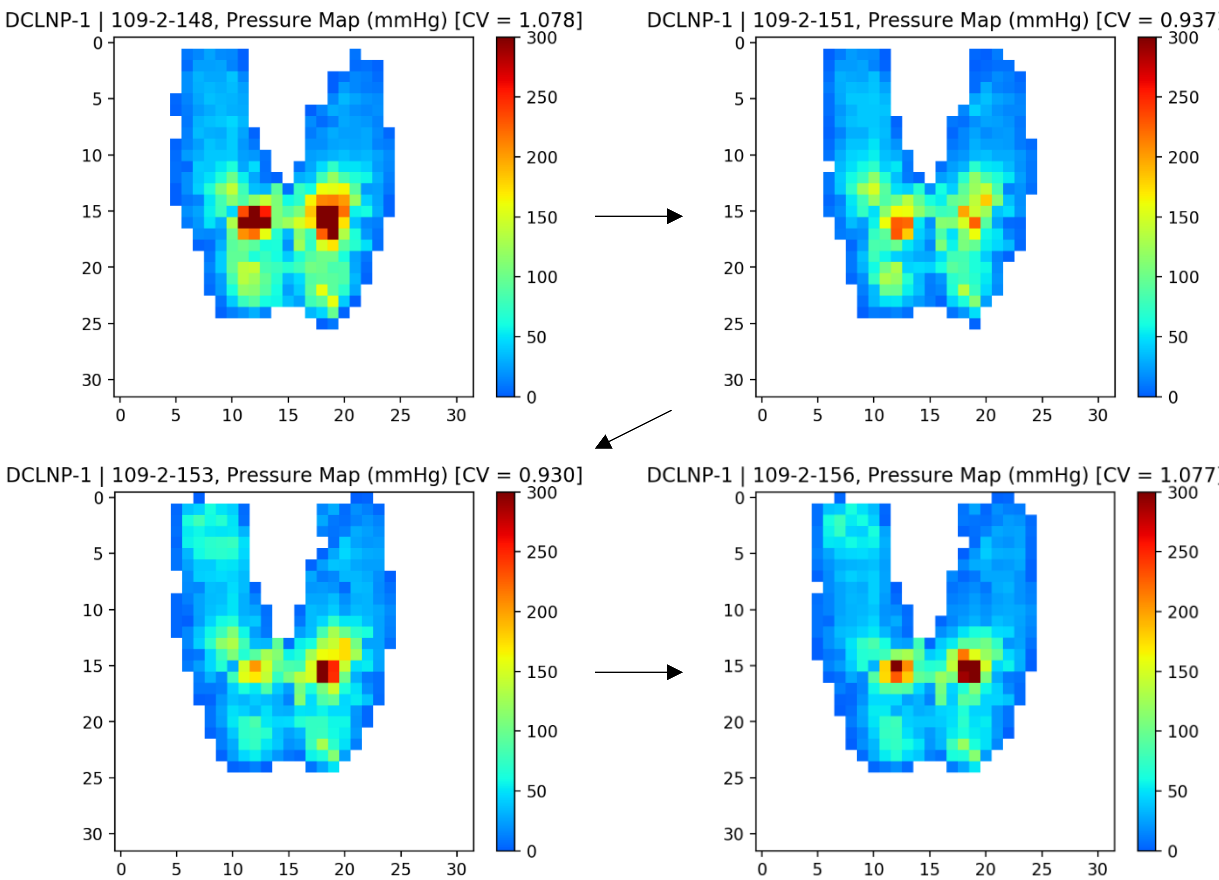

Type	Pressure Measure	Index 148	Index 151	Index 153	Index 156	Trends	Relative % (148 vs 156)	Δ Plot (148 vs 156)
General	Contact Cells	356	339	362	374		5.06%	
	Sum of Pressure	20,587.41	15,729.90	17,239.33	15,924.67		-22.65%	
	Skewness	2.0592	1.7074	2.2829	3.1282		51.91%	
Spatial	Moran's I (Q)	0.8420	0.8227	0.8203	0.7857		-6.69%	
	GLSD - Correlation X	0.7668	0.6806	0.7310	0.7283		-5.02%	
	GLSD - Correlation Y	0.8415	0.7983	0.7819	0.7582		-9.89%	
Variability	Coefficient of Variation	1.0781	0.9366	0.9301	1.0773		-0.07%	
	GLD - Gradient Contrast X	1,856.50	1,218.77	1,069.60	1,176.53		-36.63%	
	GLD - Gradient Contrast Y	1,240.52	759.06	850.71	1,025.44		-17.34%	
	GLD - Gradient Mean X	27.16	23.80	22.30	20.81		-23.38%	
	GLD - Gradient Mean Y	21.08	17.70	17.75	16.80		-20.33%	
Texture	GLD - Gradient Second Moment X	0.0241	0.0244	0.0245	0.0289		20.11%	
	GLD - Gradient Second Moment Y	0.0350	0.0349	0.0344	0.0427		21.87%	
	GLSD - Homogeneity X	0.0698	0.0623	0.0585	0.0642		-7.95%	
	GLSD - Homogeneity Y	0.0991	0.0855	0.1157	0.1254		26.49%	

Figure 92. Changes in pressure measures between indexes 148 and 156 (sample interval 109-2)

tuberosities, along with the pressure in the buttock regions, have decreased in the latter frames. A slight increase in the pressure map size is also seen post-movement, with the number of contact cells increasing by around 5%. This decrease in the overall pressure and increase in contact cells also affect the skewness measure considerably. A larger relative presence of low and low-mid pressure reading values are seen within the post-movement pressure map (109-2-156), this being indicated as a relative increase of the skewness value of around 50%.

Figure 92 also shows a considerable higher contrast is pre-movement frames, mainly due to the presence of larger high-pressure clusters under the ischial tuberosities and increased pressure in buttocks region, with both Gradient Contrast and Gradient Means measures indicating so. Note that the Coefficient of Variation (CV) measure, while changing its values in the within-movement frames, does not show any significant difference between the pre-movement pressure map (Index 148) and post-movement pressure map (Index 156) with a 0.07% relative difference.

An increase in pressure homogeneity is also obtained after the ICM in Figure 92. Measures of Gradient Second Moment and Homogeneity (Y) show considerable increases in their values, generally indicating a seating pressure map with more congruent pressure readings and with smoother pressure transitions (e.g., less pronounced gradients) between pressure levels.

Time series plots shown in Figure 93 are of measures of spatial relationship for the 5-minute interval length included in the dynamic data subset. The effect of pressure creep around the ischial tuberosities can also be seen for measures of spatial relationship, as they increase consistently over time until the first considerable ICM (Index 148) occurs. Spatial relationship measures, just like general pressure measures (Fig. 91), are also able to capture dynamic sitting with considerable changes in their values occurring specially around indexes 150 and 200.

For the ICM around Index 150 (see Fig. 92), decreases between five to ten percent are seen across the spatial relationship measures. While the pressure map obtained after the in-chair-movement is more homogeneous and with less pressure variability/contrast, the pre-movement pressure map actually exhibits pressure readings with higher spatial relationship. This pre-movement map (Fig. 92, top left) shows a higher number of distinct cluster of various pressure levels, with similar-value pressure readings usually found in contiguity among themselves; indicating a higher spatial relationship compared to latter frames.

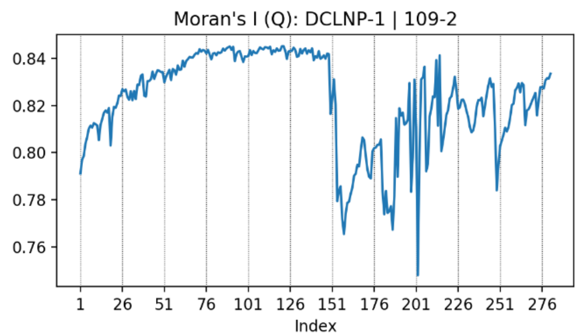

(a) Moran’s I: Queen Weight Matrix

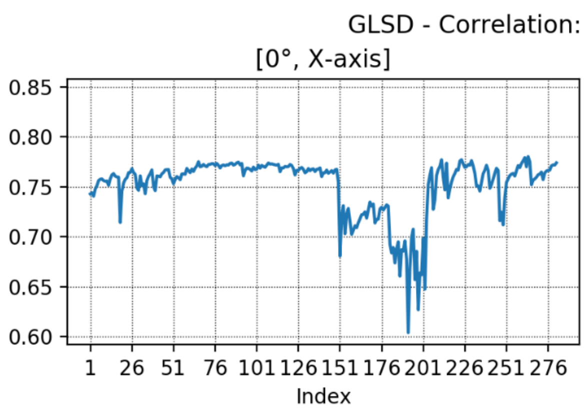

(b) GLSD – Correlation X ($\theta = 0°$)

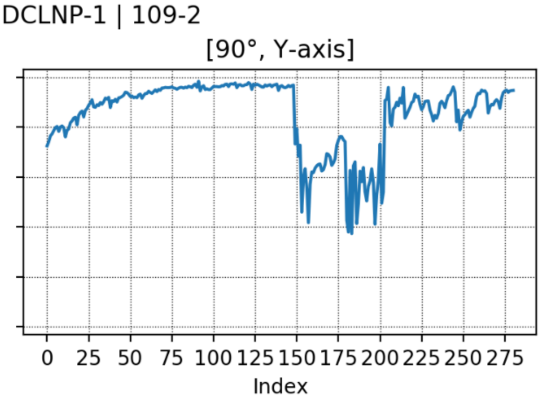

(c) GLSD – Correlation Y ($\theta = 90°$)

Figure 93. Pressure measures: spatial relationship, dynamic data subset (sample 109-2)

Figure 94 shows the time series plots for measures of pressure variability and contrast for all indexes included in the dynamic data subset. In the indexes previous to the first considerable ICM (Index 148), measures of Gradient Contrast and Gradient Mean are also constantly increasing due to the pressure creep factor around the ischial tuberosities. It has already been established, as in the case with other meaningful pressure measures, that significant changes in pressure map contrast and variability also occurred between indexes 148 and 156 mainly due to the decrease in size of the large high-pressure clusters and decrease pressure in buttocks region in the latter frames (see Fig. 92). Additionally, measures of variability and contrast, just as many other meaningful measures, are also reacting to potential in-chair-movement around Index 200.

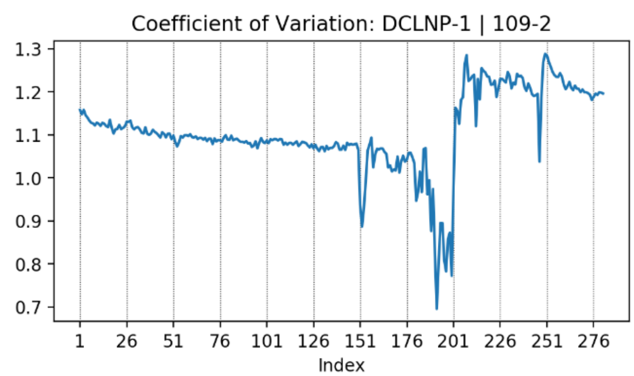

(a) Coefficient of Variation

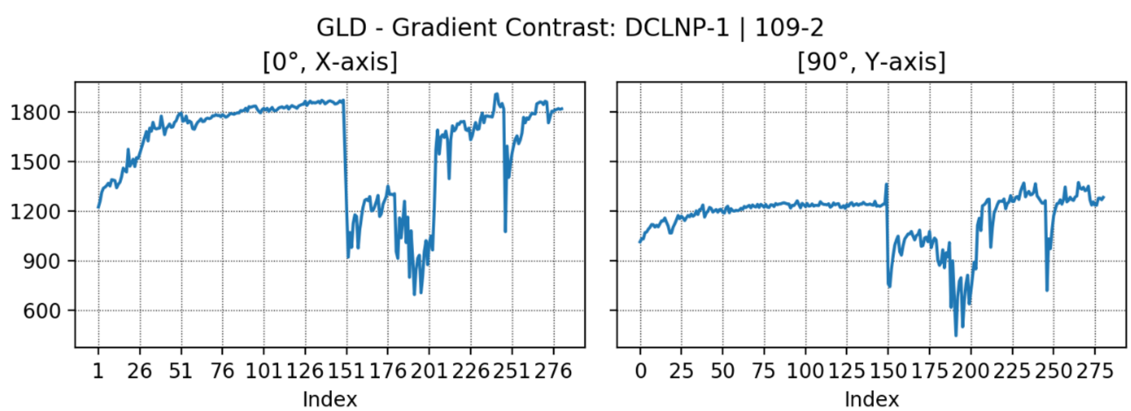

(b) GLD – Gradient Contrast X ($\theta = 0°$) (c) GLD – Gradient Contrast Y ($\theta = 90°$)

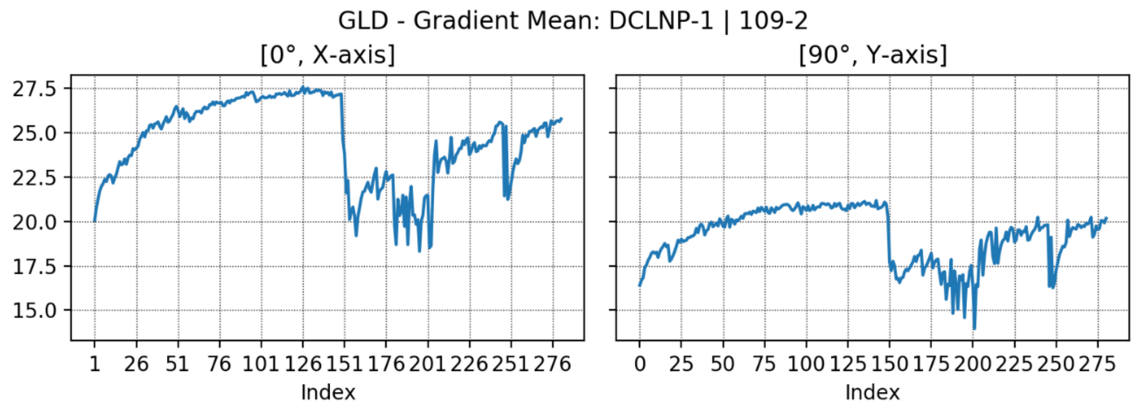

(d) GLD – Gradient Mean X ($\theta = 0°$) (e) GLD – Gradient Mean Y ($\theta = 90°$)

Figure 94. Pressure measures: variability and contrast, dynamic data subset (sample 109-2)

Figure 95 shows a sequence of pressure maps between indexes 186 and 209 (elapsed time of approximately 23 seconds) where the second considerable shifts in the values of meaningful pressure measures are seen. As with similar figures, the figure also show values and trendlines for all meaningful pressure measures featured in Table 23 (Chapter 5) along with a comparison between the pre-movement index (186) and post-movement index (209) as relative changes in percentage (%) across these measures.

The sequence of seating pressure maps presented in Figure 95 indicate an occurrence of In-Chair-Movement (ICM). While the total pressure (Sum of Pressure) exerted into the pressure interface stayed relatively the same before and after the ICM, significant differences on how pressure is distributed are seen. Areas under the legs show overall reductions in exerted pressure after movement (Index 209), but gains are otherwise seen in areas around the ischial tuberosities and buttock regions. These differences in relative pressure distribution are being detected by the measures of skewness, being significantly lower in the latter frames. This increase in the exerted

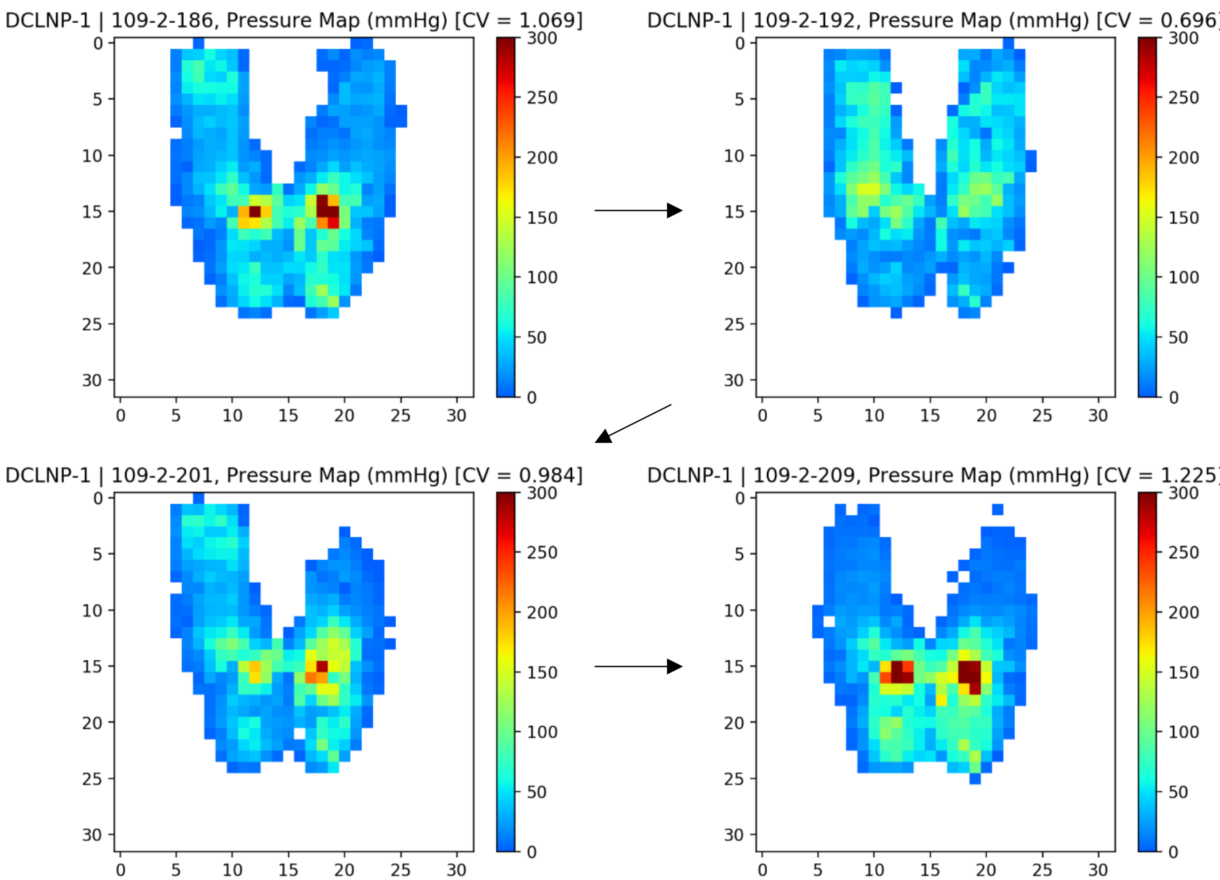

Type	Pressure Measure	Index				Trends	Relative % (186 vs 209)	Δ Plot (186 vs 209)
		186	192	201	209			
General	Contact Cells	371	340	329	330		-11.05%	
	Sum of Pressure	15,484.79	14,513.51	13,591.37	15,460.33		-0.16%	
	Skewness	3.1429	0.9690	2.0989	2.4634		-21.62%	
Spatial	Moran's I (Q)	0.7772	0.8157	0.8105	0.8152		4.89%	
	GLSD - Correlation X	0.6949	0.6040	0.6984	0.7613		9.55%	
	GLSD - Correlation Y	0.7652	0.7353	0.7830	0.8181		6.91%	
Variability	Coefficient of Variation	1.0694	0.6956	0.9835	1.2253		14.58%	
	GLD - Gradient Contrast X	1,258.43	693.75	1,009.55	1,660.92		31.98%	
	GLD - Gradient Contrast Y	946.23	444.73	712.54	1,237.05		30.73%	
	GLD - Gradient Mean X	21.47	20.34	21.47	23.50		9.44%	
	GLD - Gradient Mean Y	16.45	15.04	16.42	18.79		14.20%	
Texture	GLD - Gradient Second Moment X	0.0282	0.0258	0.0266	0.0313		11.23%	
	GLD - Gradient Second Moment Y	0.0429	0.0345	0.0371	0.0441		3.02%	
	GLSD - Homogeneity X	0.0673	0.0432	0.0452	0.0972		44.47%	
	GLSD - Homogeneity Y	0.1238	0.0782	0.0867	0.1166		-5.78%	

Figure 95. Changes in pressure measures between indexes 186 and 209 (sample interval 109-2)

pressure around the ischial tuberosities and buttock regions are also affecting the values of measures of contrast and variability during and after the in-chair-movement, with measures of Gradient Contrast, Gradient Mean, and Coefficient of Variation being considerably higher in the latter frames.

The changes in the pressure distributions between the pre-movement pressure map (Index 186) and post-movement pressure map (Index 209) in Figure 95 have also significantly affected measures of texture and smoothness. There is a considerable increase in the uniformity of the pressure readings at the post-movement seating pressure map (Fig. 95, bottom right), which is translated as an increase in measures of Gradient Second Moment and Homogeneity (X). This increase in post-movement homogeneity is also strengthened by the higher spatial relationship seen among the pressure readings within various levels of pressure, with the late frame (Index 209) showing less variability within these clusters of pressure levels and increase contiguity between similar-value pressure readings. Moran’s I and the GLSD Correlation measures are detecting this increase in the spatial relationships among similar-value pressure readings.

Figure 96 shows the time series plots for the measures of texture, smoothness, and homogeneity for all indexes included in the dynamic data subset. The changes in smoothness (e.g., less texture) and homogeneity occurring during the in-chair-movement around Index 200 (Fig. 95) were the highest relative changes among sequential indexes in the dynamic data subset.

In the indexes previous to the first considerable ICM (Index 148), measures of Gradient Second Moment (GLD) are decreasing over time due to the pressure creep factor in the ischial tuberosities and buttock regions. Gradient Second Moment measures are known to be sensitive to changes in pressure levels and gradients when measuring smoothness and texture, while measures of Homogeneity are somewhat more robust to these pressure variations and have more emphasis in measuring the similarities of the pressure readings within various pressure levels. Measures of Homogeneity show more stability in their values for the indexes prior to the first considerable ICM (Index 148). This indicate that, while the total pressure exerted to the pressure interface is increasing over this period of time, the homogeneity within the pressure cluster levels is relatively stable, that is, the contiguity and grouping aspect of similar-value pressure readings are relatively similar across these indexes.

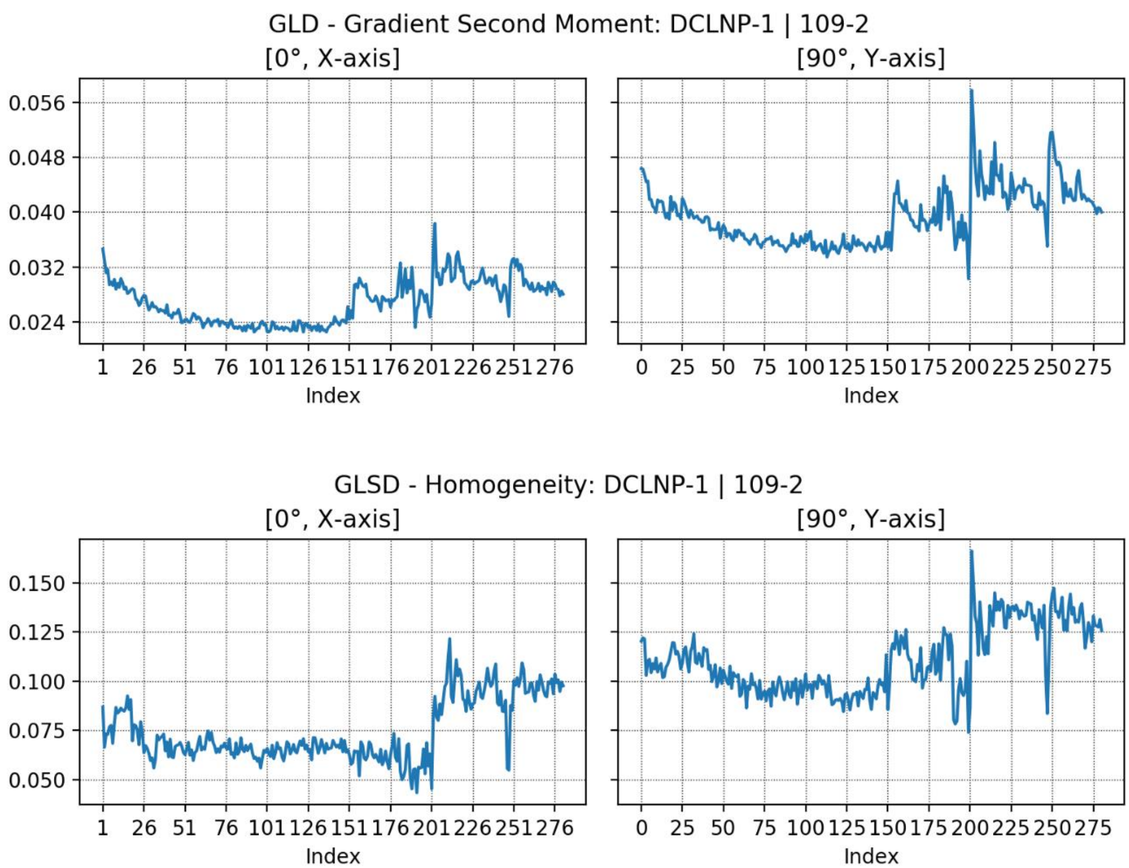

Figure 96. Smoothness and texture pressure measures (sample interval 109-2)

Most meaningful measures are also detecting a possible in-chair-movement around Index 250 (see Figs. 91, 93, 94, 96). In most of these time series plots, a defined spike in their values (upward or downward) is generally seen, with most of the measures' values returning close to they were before the movement (spike) occurred.

Figure 97 shows the sequence of pressure maps between indexes 246 and 252 (elapsed time of approximately 6 seconds) where the last considerable changes in the values of the meaningful pressure measures are seen. These measures are mostly reacting to a side-to-side in-chair-movement as detected from the seating pressure maps presented in Figure 97. Pressure is seen tilting, particularly around the ischial tuberosities and buttock regions, from one side to the other within this time interval. Some changes in meaningful pressure measures' values are seen in the resulting post-movement seating pressure map (Index 252). While all meaningful pressure measures are changing and reacting to the in-chair-movement between these indexes accordingly, the post-movement seating pressure map (Index 252), contrary to previously detected in-chair-movements, does not show large differences to the pre-movement (Index 246) seating pressure map; this is in agreement to the spikes seen in the time series plots where values of the meaningful pressure measures are somewhat returning back to pre-movement values (see Figs. 91, 93, 94, 96).

The post-movement seating pressure map in Figure 97 (bottom, right) does show some slight differences when compared to the pre-movement seating pressure map (top, left). The total pressure exerted to the pressure interface is reduced, particularly around the buttocks area. This modifies the values of skewness (more positive due to higher frequency of relatively low- and mid-low pressure readings) and variability/contrast measures (less pressure in the buttock regions and tuberosities). The spatial relationships are not significantly different between these maps (Index 246 vs Index 252), but a slightly higher homogeneity is obtained in the late frames due to a reduction of the gradients between pressure levels.

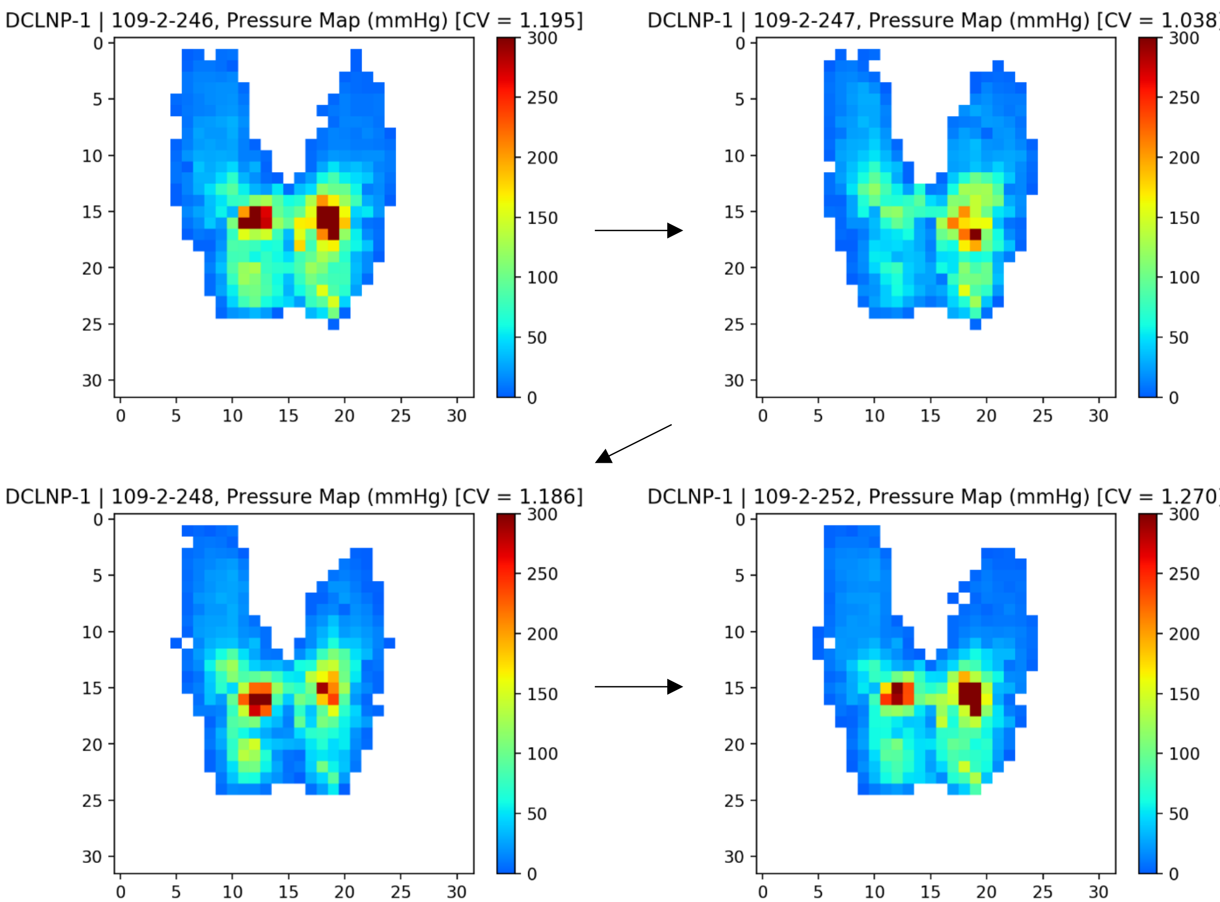

Type	Pressure Measure	Index				Trends	Relative % (246 vs 252)	Δ Plot (246 vs 252)
		246	247	248	252			
General	Contact Cells	341	323	318	328		-3.81%	
	Sum of Pressure	17,445.56	13,387.17	14,153.42	14,469.36		-17.06%	
	Skewness	2.2049	2.1037	2.3669	2.6441		19.92%	
Spatial	Moran's I (Q)	0.8278	0.8292	0.8099	0.8051		-2.75%	
	GLSD - Correlation X	0.7664	0.7161	0.7246	0.7578		-1.11%	
	GLSD - Correlation Y	0.8351	0.8053	0.8171	0.8124		-2.72%	
Variability	Coefficient of Variation	1.1955	1.0379	1.1863	1.2696		6.20%	
	GLD - Gradient Contrast X	1,817.41	1,073.85	1,591.88	1,597.69		-12.09%	
	GLD - Gradient Contrast Y	1,262.39	718.35	1,030.86	1,209.40		-4.20%	
	GLD - Gradient Mean X	25.47	21.44	25.35	22.78		-10.55%	
	GLD - Gradient Mean Y	19.81	16.34	19.11	17.71		-10.62%	
Texture	GLD - Gradient Second Moment X	0.0291	0.0269	0.0248	0.0321		10.34%	
	GLD - Gradient Second Moment Y	0.0412	0.0384	0.0350	0.0498		20.68%	
	GLSD - Homogeneity X	0.0902	0.0556	0.0547	0.0979		8.52%	
	GLSD - Homogeneity Y	0.1386	0.1035	0.0835	0.1473		6.28%	

Figure 97. Changes in pressure measures between indexes 246 and 252 (sample interval 109-2)

When calculating measures of Gray-Level Differences (GLD) and Gray-Level Spatial-Dependence (GLSD), a significance effect in measures' values when considering a different axis direction is seen for the time series plots in Figures 93, 94, and 96. GLD measures of Gradient Contrast and Gradient Mean are identifying higher variabilities when measured in the horizontal or lateral direction ($\theta = 0°$, X) (see Fig. 94), while GLSD measures of Correlation, Gradient Second Moment, and Homogeneity show higher values when measured in the vertical or anterior-posterior direction ($\theta = 90°$, Y) (see Figs. 93, 96).

While the direction when calculating pressure map gradients have significant effects in GLD and GLSD measures, there is a strong dynamic relationship between both directions ($\theta = 0°$ and $\theta = 90°$) among the indexes included in the dynamic data subset. The dynamic behavior of GLD and GLSD measures are very similar in both directions with the most notable difference being in significant offsets in the measures' values between both directions ($\theta = 0°$ and $\theta = 90°$). Figure 98 shows the pressure map for the first index of the 5-minute sitting interval (Sample 109-2-1), along with the first-order and second-order gradient maps for the same sample. Seating pressure maps usually have an elongated shape towards the anterior-posterior direction ($\theta = 90°$) due to the fact that buttock-popliteal lengths are generally greater than hip breadths (see Table 3).

First-order and second-order gradient maps in Figure 98 also show how seating pressure maps generally exhibit higher pressure gradients in the lateral direction ($\theta = 0°$) due to closeness of high-pressure clusters (e.g., ischial tuberosities) to lateral edges. When measured in the anterior-posterior direction ($\theta = 90°$), pressure transitions are smoother and with less gradients as pressure in the leg regions increase gradually when approximating to high-pressure clusters in the tuberosities. This is translated as an increase in homogeneity, smoothness, and spatial relationship when measured in the anterior-posterior direction ($\theta = 90°$) (see Fig. 98, bottom right).

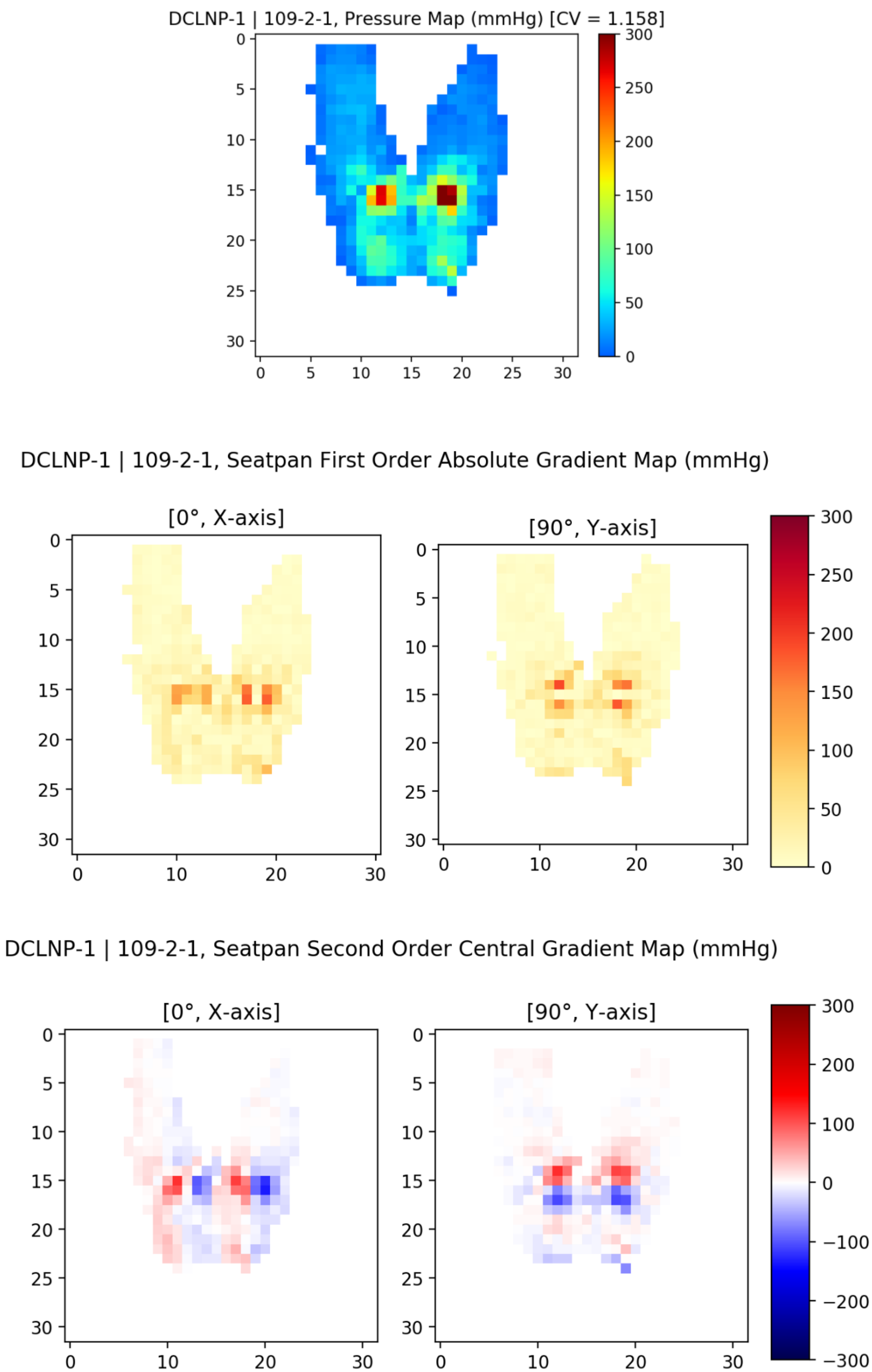

Figure 98. First-order and second-order gradient maps, directions $\theta = 0°, 90°$ (sample 109-2-1)

In this section, many examples of the potential use of spatial relationship measures and image statistical features as dynamic pressure measures are shown. It has been shown that these meaningful pressure measures can be used as global pressure map descriptors in a static environment (within a single pressure map) and dynamic environments (continuous pressure maps) to measure distinct and unique phenomena within seating pressure maps.

While spatial relationship measures and image statistical features can help in identifying in-chair-movements, these measures are not able to track changes in terms of shape, location and/or spatial position of pressure readings. To evaluate these changes, continuous comparative techniques using image registration and dynamic similarity/dissimilarity coefficients are implemented and studied in the following section.

Sequential Image Registration and Similarity/Dissimilarity Coefficients

In this case study, a sequential image registration technique (using minimization of the Mean Squared Errors [MSE]) is evaluated as a tool to align the dynamic pressure map images included in the dynamic data subset. Given the results of the image registration methods in the previous chapter (Chapter 5), MSE registration was chosen due to the higher accuracy and improved image correspondence achieved when aligning various seating pressure map images. Similarity and dissimilarity coefficients are also evaluated as comparative dynamic measures for post-registered continuous pressure maps. Comparisons to the initial reference index (Index 1) are used as a way of measuring continuous pressure map changes over time.

Figure 99 shows the reference pressure map that will be used as a comparison basis (sample 109-2-1). A visual feedback assessment of the pressure maps following this first frame confirmed the use of sample 109-2-1 to be an appropriate basis for comparison. The pressure map images following sample 109-2-1 showed relative stability in the pressure distributions and locations of pressure readings when compared to the first sampled index.

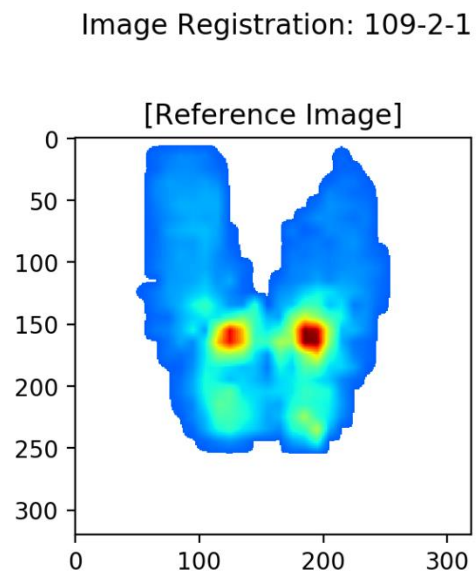

Figure 99. Image registration reference map (Sample 109-2-1)

MSE registrations were completed to align all indexes in the dynamic dataset to the reference index (Fig. 99). Similarity and dissimilarity coefficients were calculated using a non-masked approach (unbalanced pairwise pressure cells are allowed) with an epsilon parameter equal to one ($\varepsilon = 1$) for ratio-based measures. The non-masked approach was used in this case study as the goal is to measure all true differences between the initial sitting pressure map and consecutive pressure map images. Results of the similarities and dissimilarities coefficients of the post-registration comparisons are shown in Appendix R

As the indexes included in the dynamic data subset were sampled from an interval where the subject used a fixed sitting surface (i.e., same seat pan contour), similarities and dissimilarities coefficients were expected to indicate a high correspondence between the successive pressure map images and the initial pressure map image (Index 1). It was expected that the overall shapes and sizes of the continuous pressure maps to not be significantly different from one another unless significant In-Chair-Movements (ICM) occurred. Results in general show high correspondence between the pressure map images following the reference frame (Index 1). Figure 100 shows time series plots of the similarity measures (compared to the reference pressure map) for all indexes in the dynamic data subset.

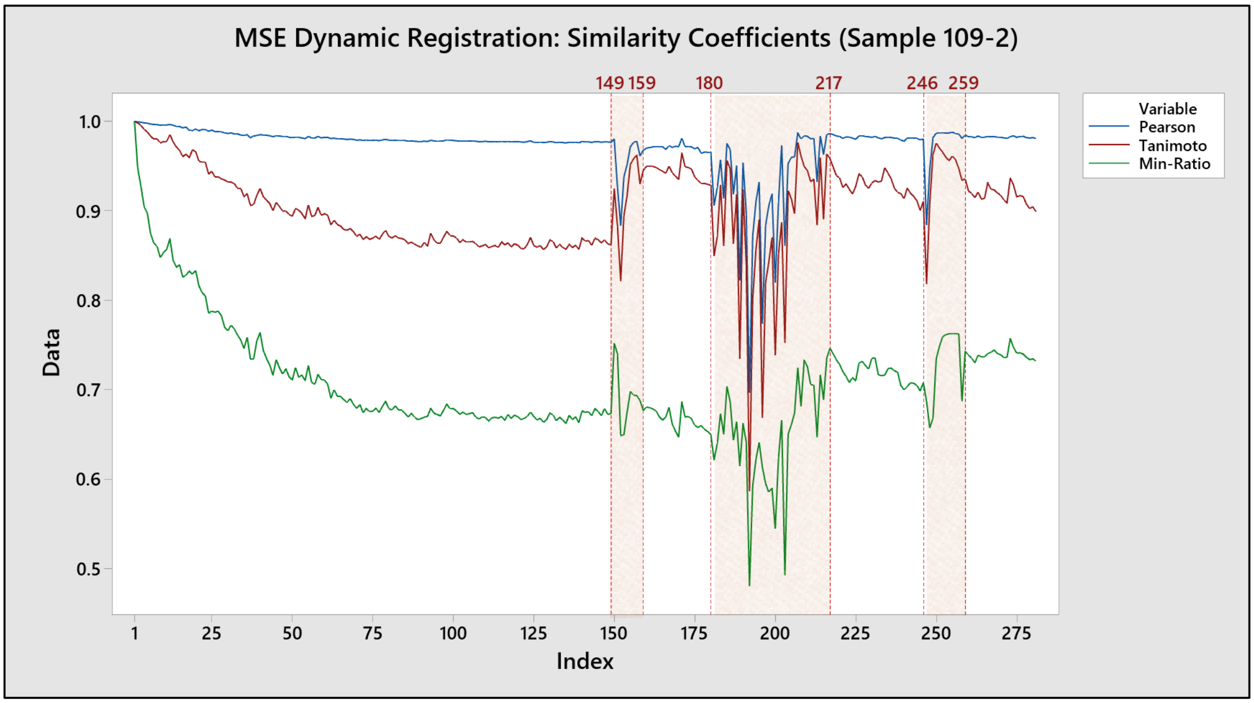

Figure 100. Similarity coefficients (non-masked): MSE registration (sample interval 109-2)

Values of Pearson Correlation Coefficient (PCC) show relative stability in the similarities of images between Index 1 and Index 149 (see Fig. 100), a behavior somewhat similar to measures of GSLD Homogeneity during this same interval (see Fig. 96). Other similarity measures are indicating a decrease in the similarities of successive pressure maps when compared to the initial seating pressure map. Measures of Tanimoto and Minimum Ratio are more sensitive to the pressure differences in pair-wise pressure readings when comparing seating pressure map images. This decrease in similarities throughout Index 1 and Index 149 is due to the pressure creep phenomenon found when evaluating measures of Sum of Pressure (see Fig. 91) and contrast measures (see Fig. 94). The Minimum Ratio measure is more sensible to the increase in pressure seen in some of the pairwise readings (the ratio is lower when greater differences are found). Meanwhile, the Tanimoto measures consider these pressure differences as well, but also considers their relationships (similar to Pearson), making the values of Tanimoto similarities somewhere in between the PCC and Minimum Ratio values.

Measures of dissimilarity are also reacting to the pressure creep phenomenon occurring between indexes 1 and 149. Figure 101 shows time series plots of the dissimilarity measures (compared to the reference pressure map) for all indexes in the dynamic data subset.

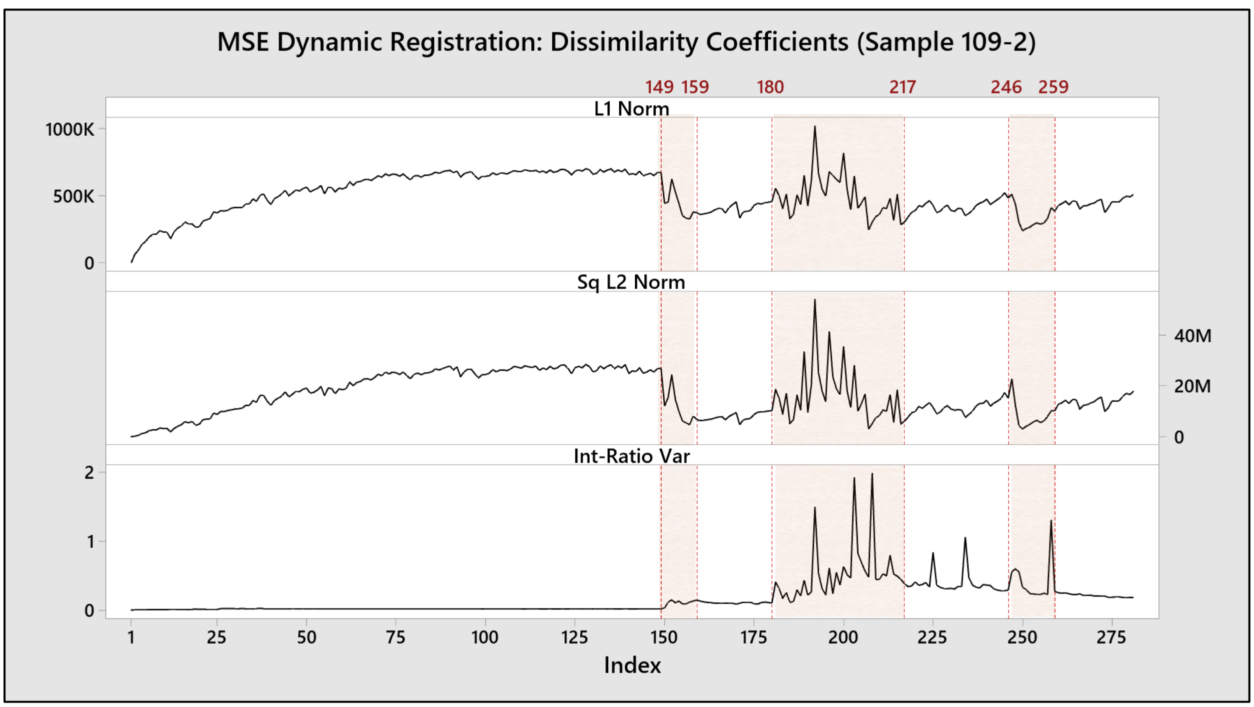

Figure 101. Dissimilarity coefficients (non-masked): MSE registration (sample interval 109-2)

The results in Figure 101 show measures of L_1 Norm and Squared L_2 Norm increasing in their dissimilarity values due to differences in pressure between the initial reference index (Index 1) and successive indexes before index 150. Similar to Tanimoto and Minimum Ratio measures, this behavior is due to the pressure creep phenomenon during this time frame. To evaluate the pressure creep effect, the registration results between the initial frame (Index 1) and Index 149 (before the first considerable in-chair-movement) are presented in Figure 102, along with measures of similarity/dissimilarity and a visual highlights of pressure differences between these images.

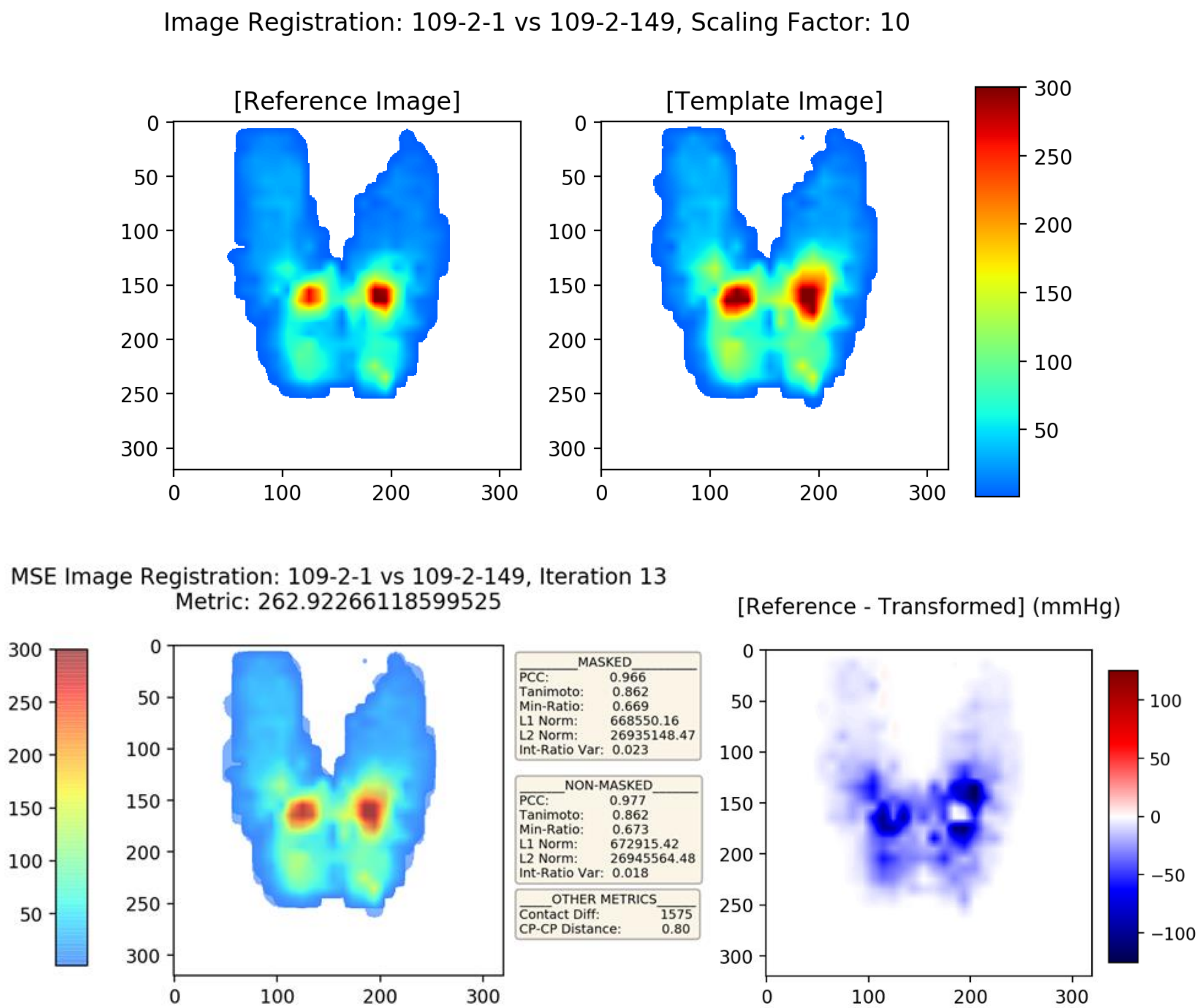

Figure 102. Optimal MSE image registration: Index 1 vs Index 149 (sample interval 109-2)

MSE registration achieved appropriate alignments and image correspondence between the seating pressure maps presented in Figure 102. The pressure distributions in terms of location and spatial relationship of pressure readings are similar, but the magnitudes of the pressure readings at Index 149 are considerable increased (see Fig. 102 bottom right). Larger high-pressure clusters are seen under the ischial tuberosities in the latter frame, with higher pressures also being exerted in the top buttock regions. Given these pressure differences, a decrease (increase) in pressure map similarities (dissimilarities) are seen by the Tanimoto, Minimum Ratio, L_1 Norm and Squared L_2 Norm measures; all being sensitive to those pairwise differences in pressure. Measures such as Pearson, not being sensitive to differences in pressure scale, finds the relationship among pressure maps somewhat similar (non-masked $r = 0.977$) The Intensity Ratio Variance also show low dissimilarities between these maps due to the robustness of this measure to pressure scaling differences (non-masked $R_V = 0.018$). Intensity Ratio Variance is more sensitive to overlapping differences in terms of shapes (when using the non-masked approach). The overall shapes of these pressure maps from Index 1 to Index 149 were very consistent and similar (see Fig. 102, top row).

Another important measure obtained when using sequential image registration procedures (i.e., alignment of continuous images) is the distance traveled by the center of mass [Center of Pressure (CP)] of the template image (i.e. moving image) to reach registration optimality. The template pressure maps (i.e. moving maps) were all registered according to the initial reference pressure map (i.e. fixed map). The translation required to align these pressure map images to the reference map can be calculated as the distance traveled by the center of pressure during registration. A CP to CP distance is calculated as the Euclidean distance between the CP locations of the of the pre-registered map and post-registered map. Note that this distance between CP locations are not calculating differences in the CP locations between the template map and reference maps, but the translation of CP within the template map after registration. Figure 103 shows the CP translation results of the registration process for aligning each subsequent pressure map to the reference map (Index 1).

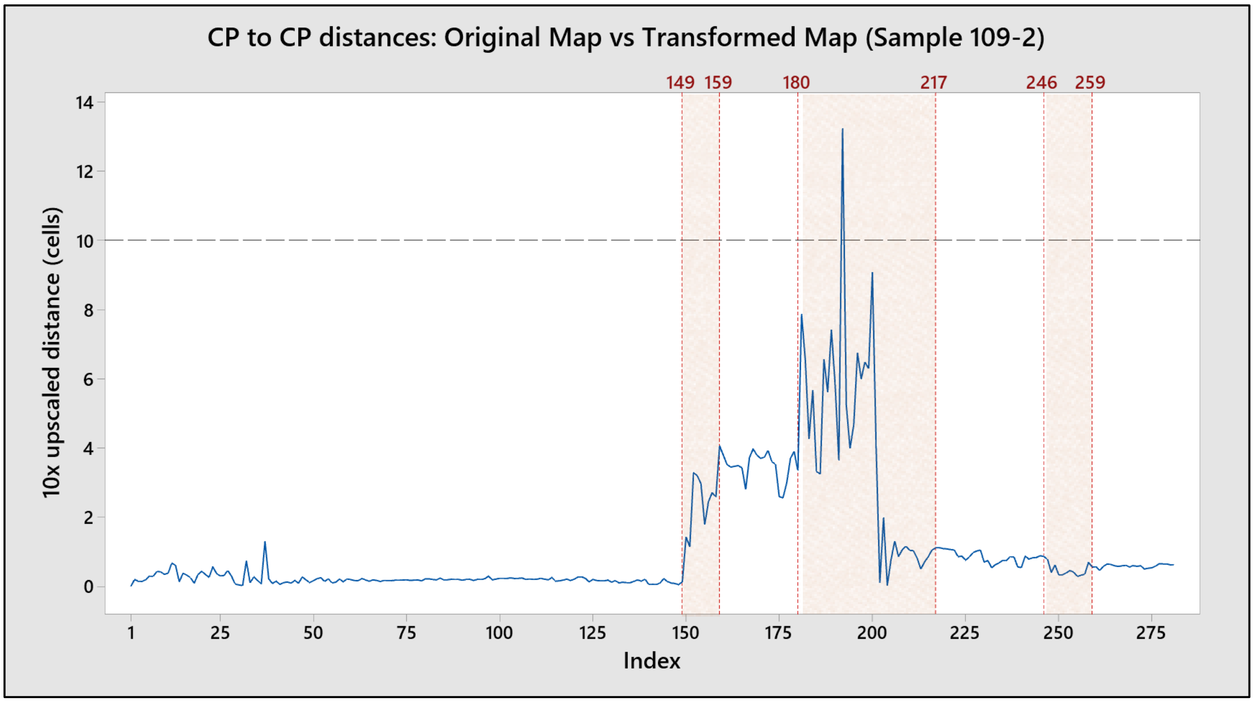

Figure 103. Original vs Transformed CP locations: Cells distances (sample interval 109-2)

The required translations to align the pressure maps from index 1 through 149 were minimum, with most registrations doing CP translations of less than 1 cell (see Fig. 103). It is important to emphasize that pressure maps were scaled by a factor of ten to allow fine-tuning transformations during registrations. Therefore, the resulting CP to CP distances (in units of cells) presented in Figure 103 are also in factor of ten. To obtain real distances (in units of cells) between the original and transformed CP locations, the cell distances need to be divided by 10. It is also important to highlight that meaningful differences in CP movement were considered when translations of CP were greater than one inch ($CP > 1\ in$); one inch being the approximate distance required to travel one unit of cell. Hence, a distance of 10 cells in the current scale of CP to CP distances roughly equates to a 1-inch movement in CP location. Figure 103 only show one instance (Index 192) where a translation greater than 1 inch (10 upscaled cells) was needed to align the template pressure map to the reference pressure map, indicating that the subject was sitting in a relative stable location throughout the entire 5-minute sitting interval.

Time series plots in Figures 100, 101 and 103 also show highlights of index ranges where possible in-chair-movement is detected. The first region shows a considerable shift in values of similarities and dissimilarities between indexes 149 and 159. Figure 104 shows a close examination of the similarity measures for this range of indexes. This figure shows that similarity measures had a considerable decrease in Index 152 during an in-chair-movement. This same in-chair-movement was also detected using values of meaningful pressure measures as dynamic pressure measures (see Fig. 92).

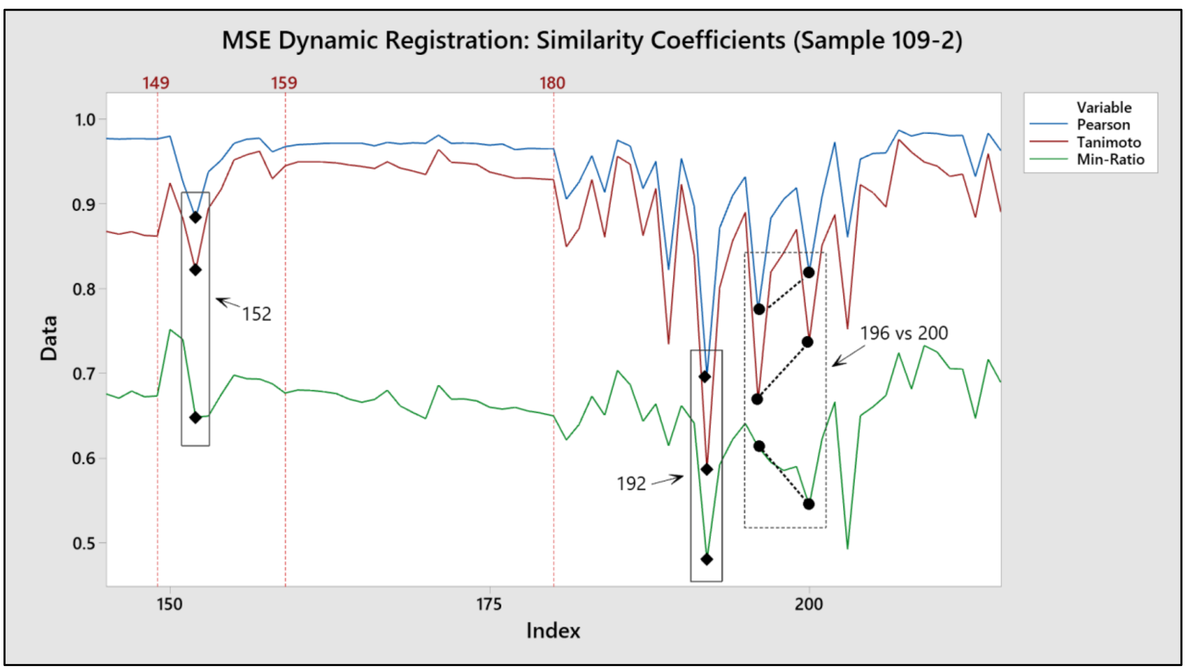

Figure 104. Similarity coefficients highlights: MSE registration (sample interval 109-2)

To evaluate the pressure map differences during the first considerable in-chair-movement, the registration results between the initial frame (Index 1) and Index 152 are presented in Figure 105, with measures of similarity/dissimilarity and a visual highlights of pressure differences between these images also being presented.

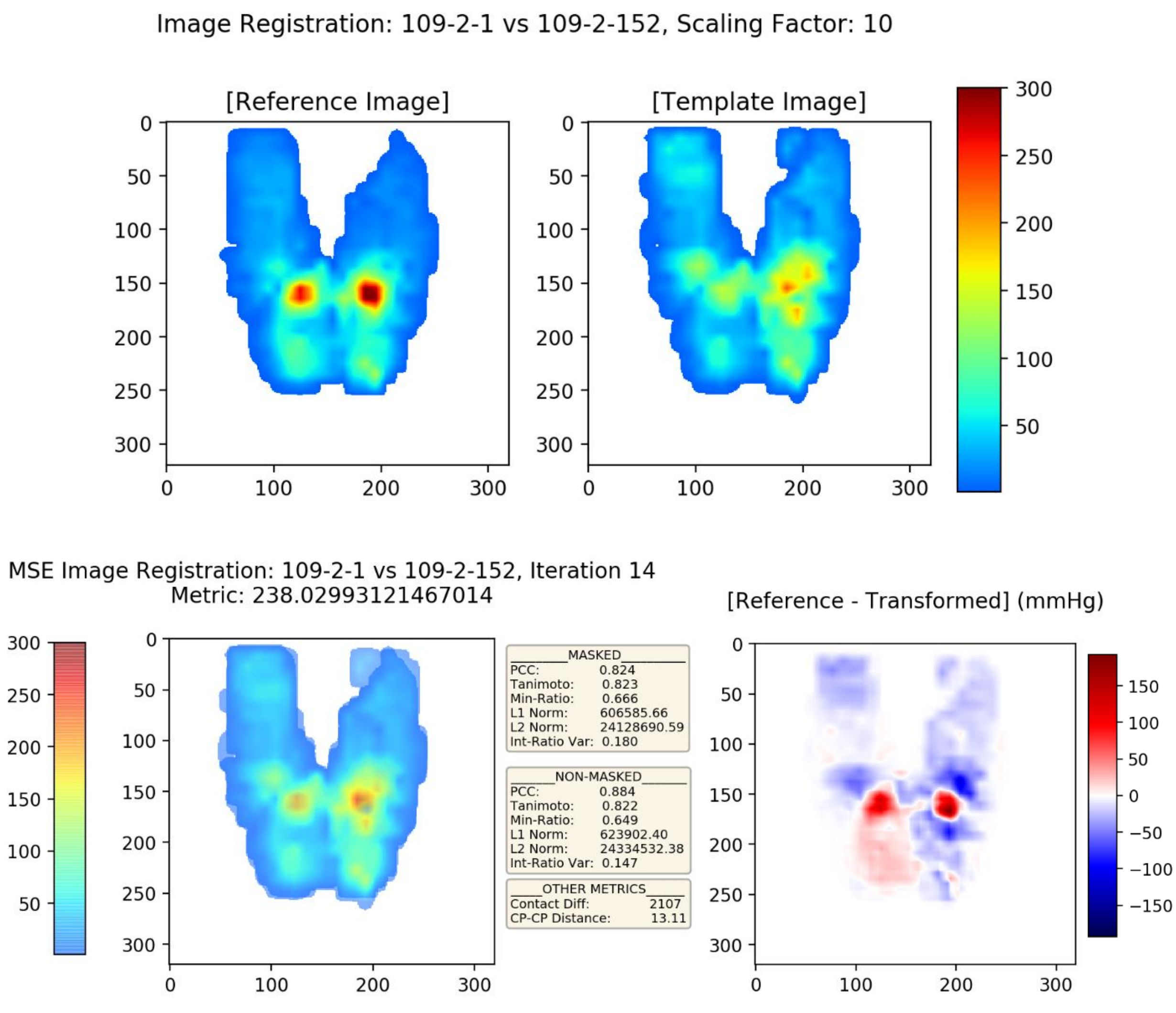

Figure 105. Optimal MSE image registration: Index 1 vs Index 152 (sample interval 109-2)

Figure 105 shows considerable changes in pressure distributions at index 152 when compared to the initial seating pressure map. The reference index (109-2-1) shows a distinct presence of high-pressure clusters under the ischial tuberosities while the pressure map in index 152 shows higher pressure being exerted under the leg regions (see Fig. 105, bottom right). These pressure differences are still being accounted by the Tanimoto, Minimum Ratio, L_1 Norm and Squared L_2 Norm similarity and dissimilarity measures, but now measures of Pearson Correlation Coefficient (PCC) and Intensity Ratio Variance are also indicating considerable changes. A decrease in non-masked PCC similarity is now seen from 0.977 in the pre-movement index 149 to 0.884 during the in-chair-movement at index 152 (see Figs. 102, 105). Likewise, the non-masked Intensity Ratio Variance dissimilarity measures increased from 0.018 in pre-movement index 149 to 0.147 during the in-chair-movement at index 152 (see Figs. 102, 105). These changes in these two similarity/dissimilarity measures are due to significant differences in pressure distributions (e.g., pressure under ischial tuberosities) and differences in shape (e.g., no overlaps or intersections between pressure readings in the top left leg region).

Other possible in-chair-movements are detected within the highlighted regions of interest shown in Figures 100, 101 and 103. The second region of interest show a number of possible in-chair-movement between indexes 180 and 217. A close examination of the similarity measures for this range of indexes is also shown in Figure 104. The first index to be evaluated for this region is Index 192, where considerable decreases in similarities are seen during the in-chair-movements. This same in-chair-movement was also detected using values of meaningful pressure measures as dynamic pressure measures (see Fig. 95).

Figure 106 shows the registration results between the initial frame (Index 1) and Index 192, along with measures of similarity/dissimilarity and visual highlights of pressure differences between these images. Pronounced pressure differences are now seen between the reference map and Index 192 when compared to differences between the reference map and Index 152 (Fig. 105).

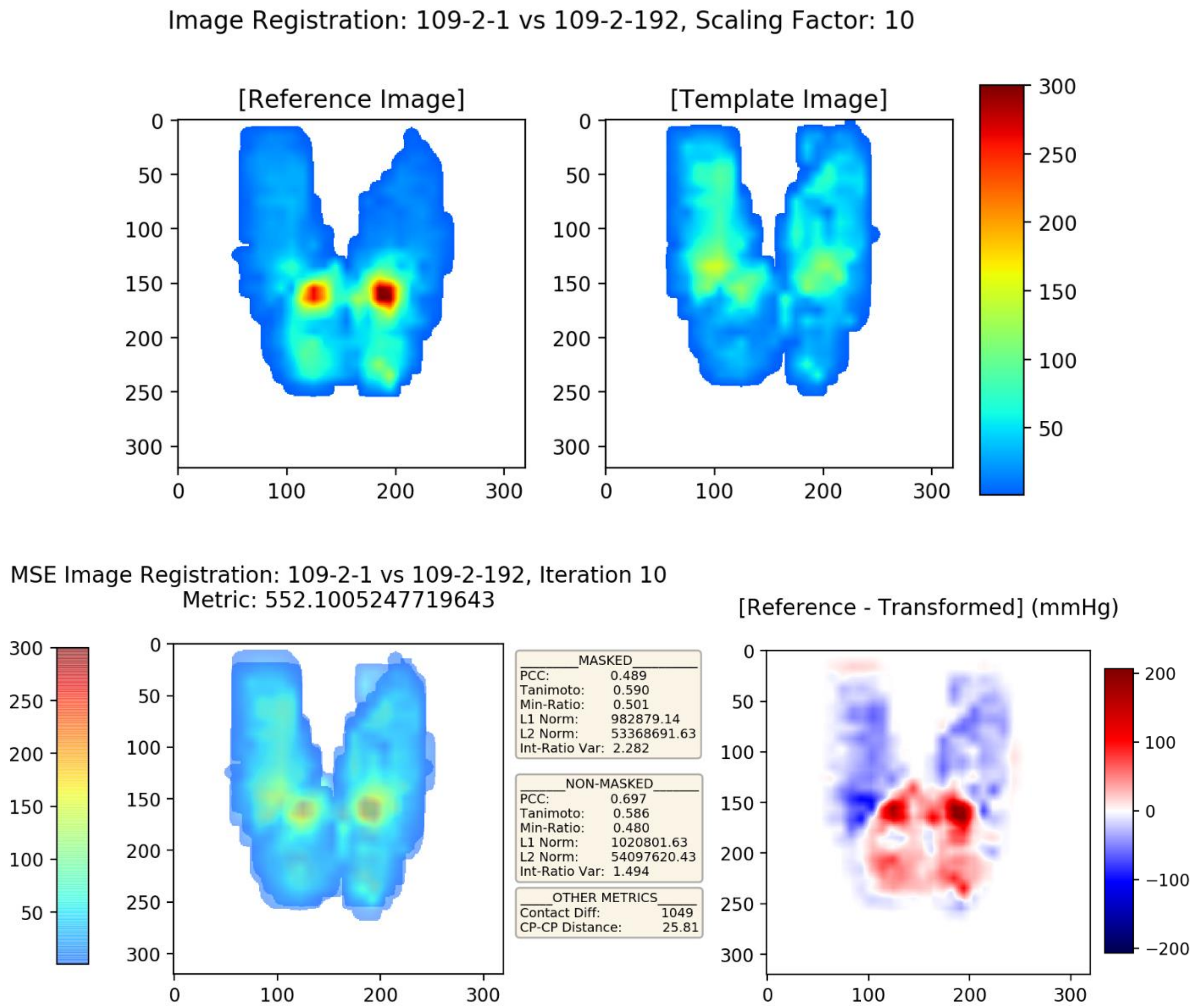

Figure 106. Optimal MSE image registration: Index 1 vs Index 192 (sample interval 109-2)

Differences in the pressure distributions between Index 192 and the reference map (Index 1) are seen in the high-pressure cluster under the ischial tuberosities and higher-pressure values around the buttocks area in the reference map, while the pressure map in Index 192 shows more pressure in both leg regions (see Fig. 106, bottom right). According to similarity values, these pronounced differences are the highest seen among compared indexes (see Fig. 104). A close examination of the dissimilarity measures for this range of indexes, seen in Figure 107, also shows that Index 192 is where the highest dissimilarities are obtained according to most of the measures.

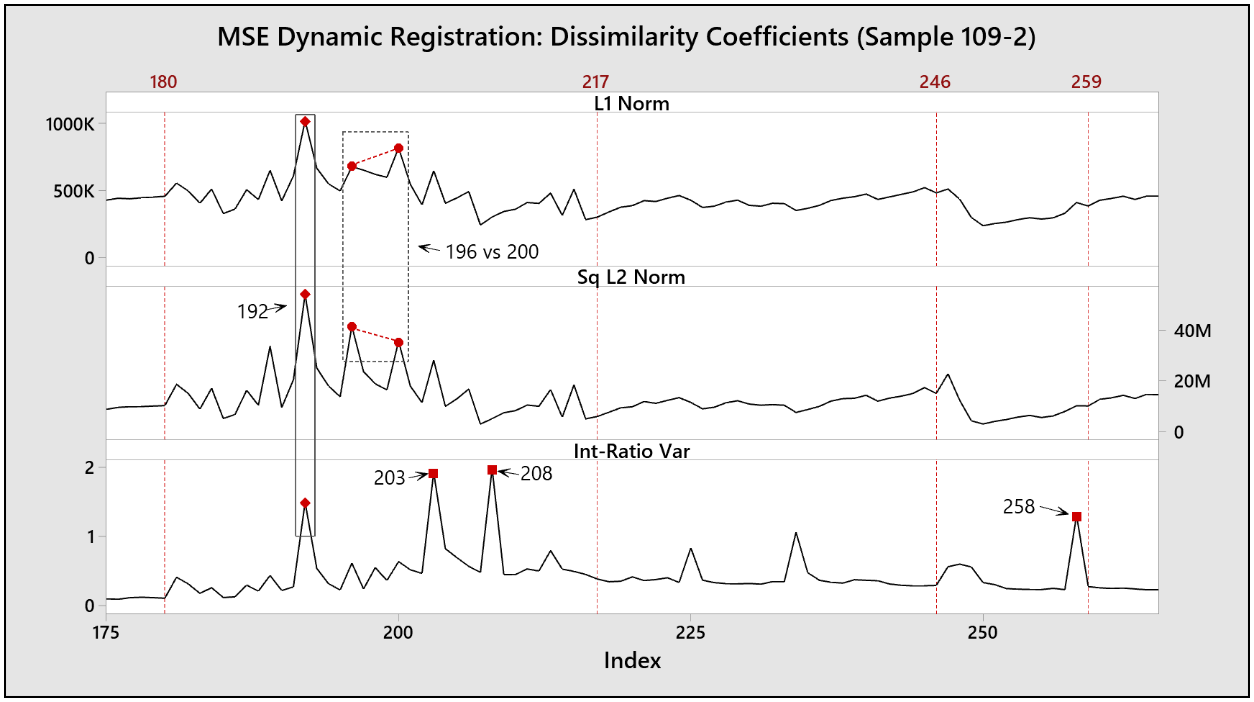

Figure 107. Dissimilarity coefficients highlights: MSE registration (sample interval 109-2)

Index 192 is also where the distance traveled by the Center of Pressure (CP) is the largest (13.24 cells) among the translations needed to reach registration optimality across all indexes (see Fig. 103). The registered pressure map overlays in Figure 106 (bottom left) shows how the template image (Index 192) had to be slightly moved down in the Y-axis (anterior-posterior direction) to have a better match of the pressure map shape and correspondence of the locations of high-pressure within each map.

In addition, a significant number of potentials in-chair-movements are also seen within the second region of interest (indexes 180 and 217). Figures 104 and 107 show close examination of the similarity and dissimilarity measures for this range of indexes respectively, where differences in the behavior or sensitivities between similarity/dissimilarity measures are seen between indexes 196 and 200. Measures such as Pearson, Tanimoto, and Squared L_2 Norm show higher (lower) similarity (disimilarity) between Index 200 and the reference index, than the ones obtained when comparing Index 196 to the reference index. Other measures such as L_1 Norm and Minimum Ratio show opposite results, by detecting higher (lower) similarity (disimilarity) between Index 196 and the reference index than the ones obtained when comparing Index 200 to the reference index. To evaluate these discrepancies between similarity and dissimilarity measures, the registration results between the initial frame (Index 1) and Index 196, and between the initial frame (Index 1) and Index 200 are presented in Figures 108 and 109 respectively. Measures of similarity/dissimilarity and visual highlights of pressure differences between images are also presented in these figures.

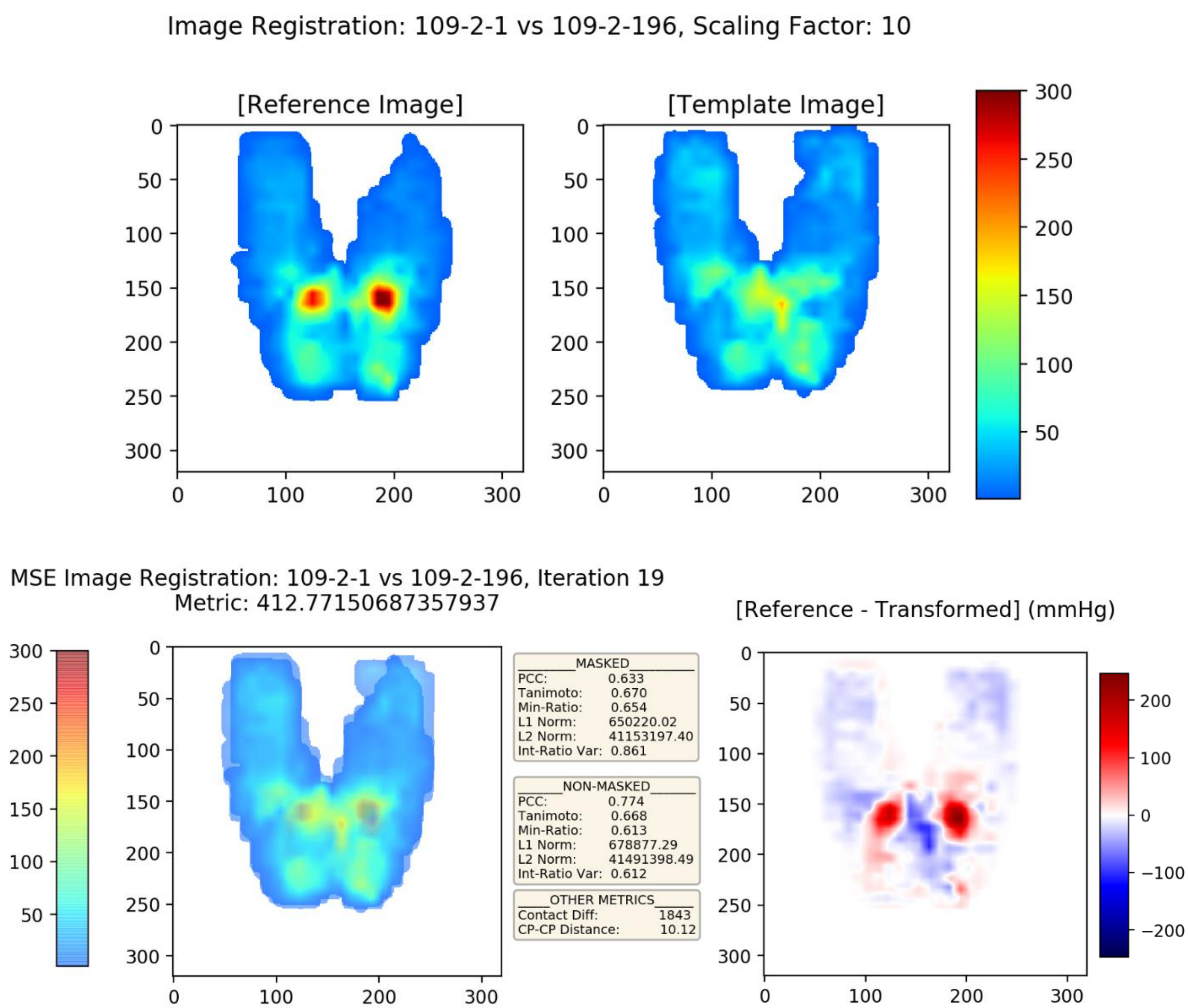

Figure 108. Optimal MSE image registration: Index 1 vs Index 196 (sample interval 109-2)

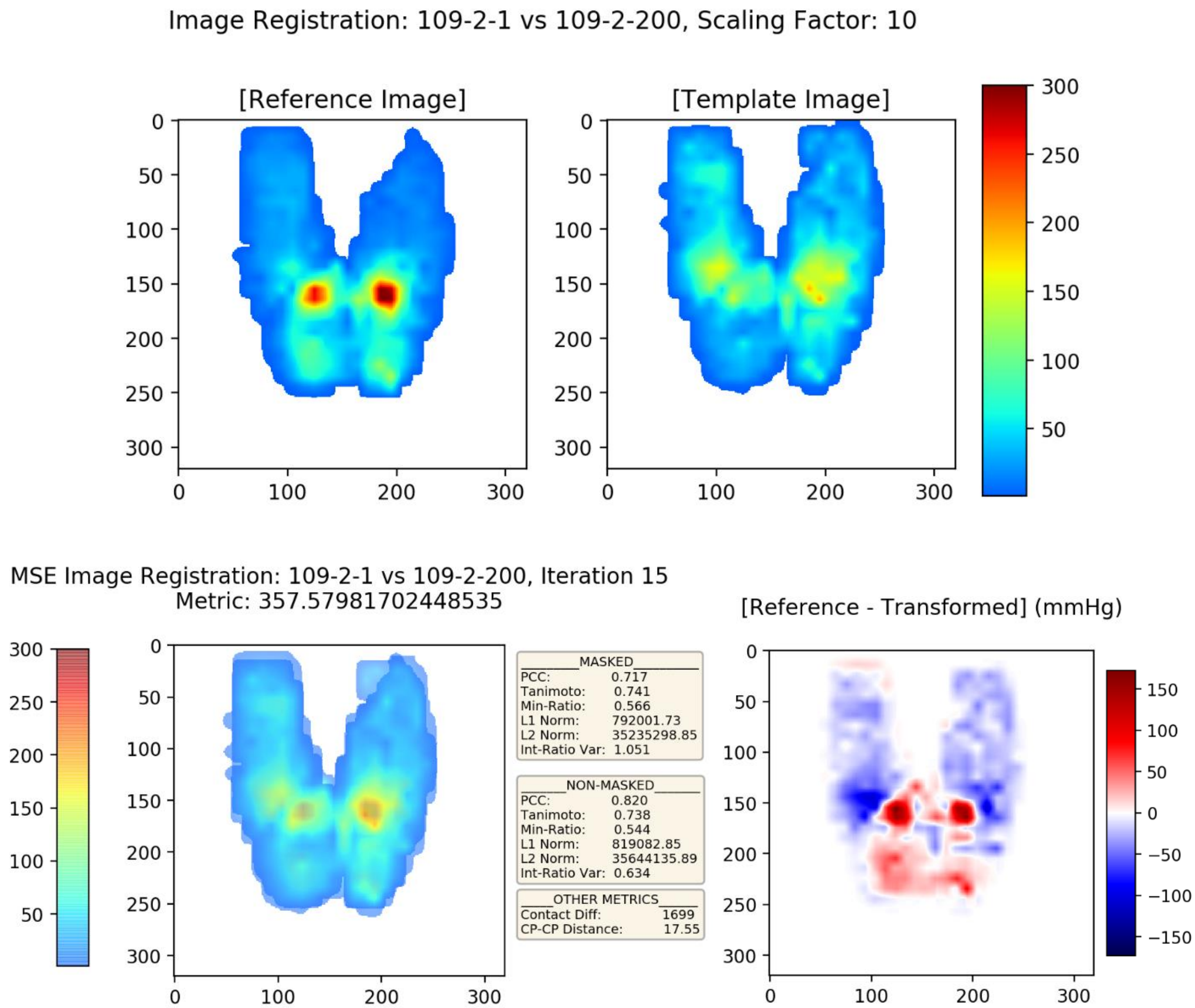

Figure 109. Optimal MSE image registration: Index 1 vs Index 200 (sample interval 109-2)

Differences between the reference index (Index 1) and Index 196 show lower differences in pairwise pressure readings than the ones between the reference index (Index 1) and Index 200 (see Figs. 108, 109, bottom right). The lower overall differences in pressure among the pairwise pressure readings seen when registering Index 196 (Fig. 108), compared to the ones obtained when registering Index 200 (Fig. 109), are being detected by measures of L_1 Norm and Minimum Ratio. Values of non-masked L_1 Norm and Minimum Ratio are at 6,788.77 mmHg and 0.613 respectively when registering Index 196, compared to values of 8,190.81 mmHg and 0.544 respectively when registering Index 200.

While lower overall pressure differences (L_1 Norm values) are obtained when registering Index 196, compared to the ones obtained when registering Index 200, the differences in pressure in specific regions are greater when registering Index 196. The map of pressure differences seen in Figure 108 (bottom right) shows higher pressure differences around the ischial tuberosities (differences between 200-250 mmHg between pairwise cells), compared to map of pressure differences seen in Figure 109 (bottom right) where the pressure differences around the ischial tuberosities are lower (differences between 150-175 mmHg between pairwise cells). These large pairwise pressure differences seen when registering Index 196 (Fig. 108) affects the measures of Pearson, Tanimoto, and Squared L_2 Norm, with these measures agreeing that higher (lower) similarities (dissimilarities) are seen when registering Index 200, instead of 196. This is a good example of the differences and sensitivities of various similarity and dissimilarity coefficients.

Compared to other similarity and dissimilarity measures, the Intensity Ratio Variance has a unique behavior and sensitivity when comparing pressure map images. The Intensity Ratio Variances do not show major significant shifts when comparing all indexes to the reference map, but spikes in their values are seen in the time series plot in Figure 101, indicating a reaction to specific differences between pressure maps.

Figure 107 shows particular instances where changes in Intensity Ratio Variance values are considerable higher when compared to other similarity and dissimilarity coefficients. Indexes 203, 208, and 258 are instances where unique spikes are seen in the values of Intensity Ratio Variance. Other similarity and dissimilarity coefficients do not react in a similar way when these indexes are compared, suggesting that Intensity Ratio Variance measures are sensitive to specific differences between pressure maps. To evaluate the uniqueness of the Intensity Ratio Variance measure, the registration results and similarity and dissimilarity coefficients obtained when comparing these indexes [203, 208, and 258] to the reference maps are presented in Figure 110.

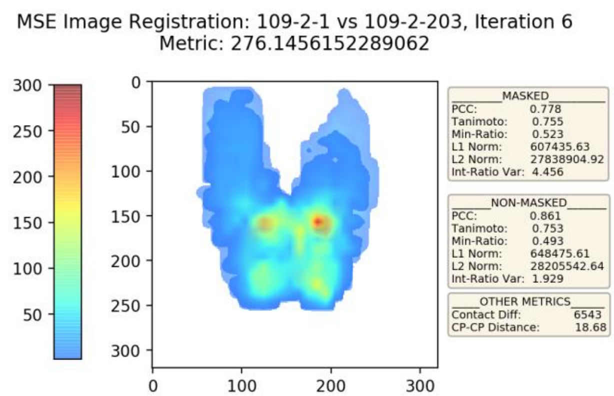

(a) 109-2-1 vs 109-2-203

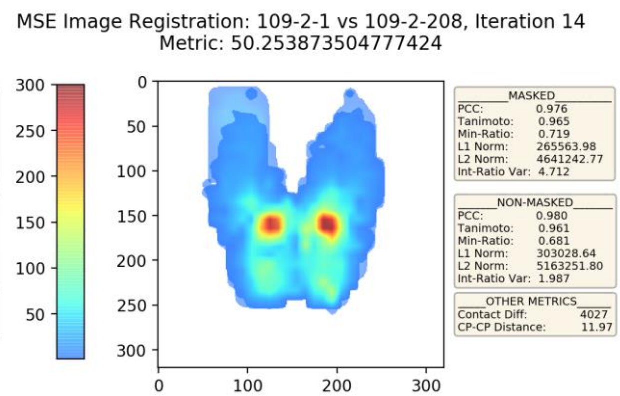

(b) 109-2-1 vs 109-2-208

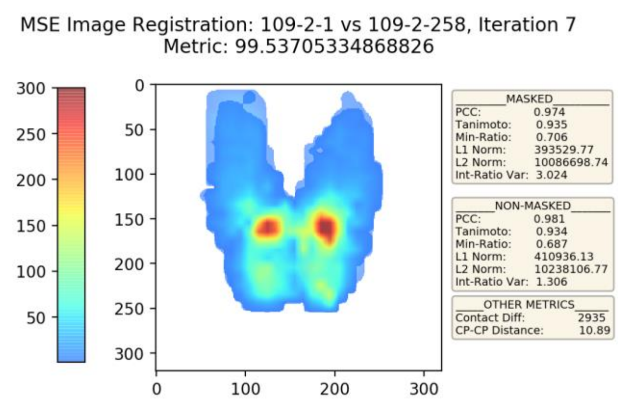

(c) 109-2-1 vs 109-2-258

Figure 110. Optimal MSE image registration: Indexes 203, 208, and 258 (sample interval 109-2)

Figure 110a shows the results when comparing Index 203 to the reference map. For this particular index, all similarity and dissimilarity coefficients detect considerable differences between the maps (e.g., non-masked Pearson Correlation Coefficient = 0.861), but measures of Intensity Ratio Variance show a considerable change when compared to results from other indexes. As an indicator, 92.88% of compared indexes show values of non-masked Intensity Ratio Variance less than 0.5, with the average value being 0.16; due to this, a non-masked Intensity Ratio Variance value greater than one is considered significant for this dynamic data subset sample.

In all three indexes, measures of Intensity Ratio Variance indicated considerable pressure map differences (see Fig. 107). Index 203 (Fig. 110a) shows a significant non-masked Intensity Ratio Variance value of 1.929, while indexes 208 (Fig. 110b) and 258 (Fig. 110c) show non-masked Intensity Ratio Variance values of 1.987 and 1.306 respectively. The high values of Intensity Ratio Variance are due to differences in the shapes between the pressure maps; considerable regions with non-overlapping pressure readings are found, particularly in the leg regions. Also note that similarity and dissimilarity coefficients other than Intensity Ratio Variance are indicating relatively high (low) similarities (dissimilarities), particularly when comparing indexes 208 and 258 (e.g., non-masked Pearson Correlation Coefficient are set at 0.980 and 0.981 respectively). The examples shown in Figure 110 indicate that measures of Intensity Ratio Variance are particularly sensitive to these differences in shapes (i.e., non-overlapping pressure readings) when compared to sensitivities from other similarity and dissimilarity coefficients.

The last section in this case study is devoted to evaluating the computational demands for continuous dynamic image registration. To register all 281 indexes in the dynamic data subset, the total MSE registration process was executed in 676.33 seconds (approximately 11 minutes). Figure 111 shows a histogram of the processing time for all indexes. Results show that alignment of pressure maps was done in one second or less for 66.5% of the indexes included in the dynamic data subset, with MSE registration taking longer than 5 seconds in just 10% of the indexes when aligning them to the reference map. The maximum recorded processing time for a particular index was 45 seconds (Index 256, with total of 235 iterations and optimality at iteration 13).

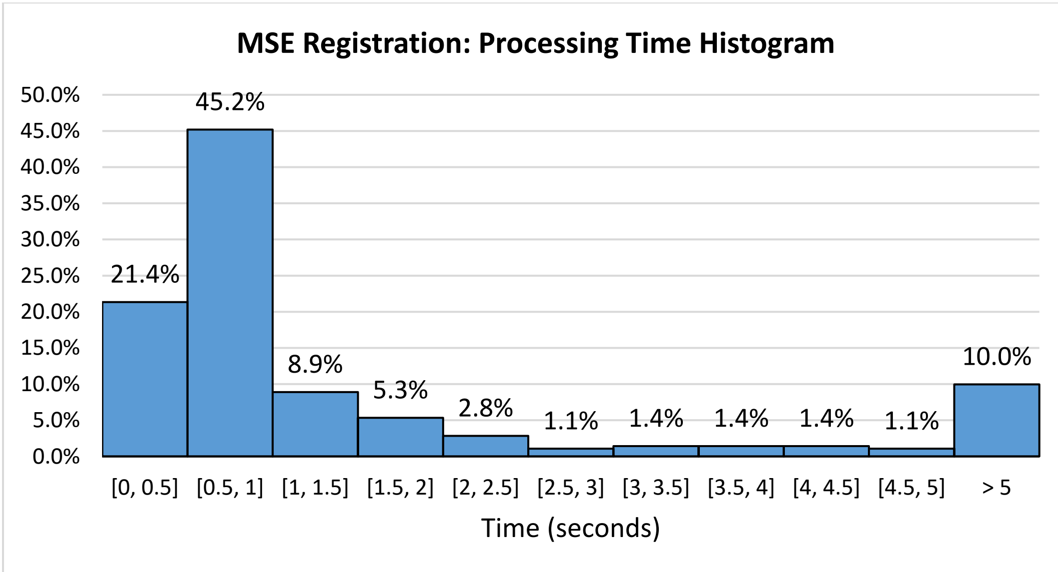

Figure 111. MSE image registration processing times (Sample 109-2)

The results in this section show the potential of using similarity and dissimilarity coefficients as complementary dynamic pressure measures for identifying and evaluating in-chair-movements (ICM). Sequential image registration using MSE attained the intended results for the 5-minute sitting interval sample evaluated in this case study; proper alignments, centering, and correspondences in pressure maps' image features were achieved. While the method chosen for this case study is based on comparisons of all pressure maps to the initial reference map (Index 1), other comparison basis could have been chosen (e.g., other pressure maps index or an aggregate map) with different interpretable results.

Similarities and dissimilarities coefficients were suitable comparative techniques between post-registered pressure maps with potential uses for dynamic sitting applications. These coefficients can evaluate differences in the pressure distributions between pressure maps and be used as global comparative measures, each with a unique take, while the use of new proposed pressure measures in Table 23 (Chapter 5) can highlight the features that makes each map different.

CHAPTER VII

CONCLUSIONS

This work evaluated the applications of machine learning, spatial data analytics, digital image processing, and optimal image registration as new techniques for analyzing pressure maps. The applications, feasibilities, and practicalities of introduced techniques were made within the context of seating research. Results obtained in this study indicate that many of these techniques are suitable for analyzing pressure maps, with applications for pre-processing, analysis and evaluation, and comparisons of seating pressure map images. These techniques were found to also be cross-functional for applications in static (i.e., single map) and dynamic (i.e., sequential temporal maps) environments.

The research objectives were successfully fulfilled by achieving the following:

(1) The study introduced appropriate methods for detecting and removing extrinsic pressure artifacts (i.e., pressure reading outliers), with overall accuracies over ninety-nine percent (99%), by using density-based spatial clustering techniques. The feasibility and practicality of applying these techniques for cleansing continuous pressure maps (e.g., dynamic sitting) was also demonstrated.

(2) Various pressure measures based on spatial autocorrelation and image statistical features were introduced and validated as new pressure measures. These new measures were found to be appropriate and suitable for measuring certain aspects of the pressure maps, such as specific pressure distribution patterns (e.g., homogeneity, acute points,

and low-high distributions), overall spatial relationships, and pressure contrasts that commonly used pressure measures were not able to describe due to information loss. Their values and usefulness as dynamic pressure measures were also demonstrated.

(3) A toolset for aligning and comparing pressure maps is introduced by using optimal image registration methods and similarity and dissimilarity coefficients. Accurate and appropriate alignments were obtained via image registration, particularly by using the MSE metric. The uniqueness of each similarity/dissimilarity coefficient was explained when comparing pressure patterns between pressure maps, along with demonstrating the feasibility and practicality of applying these techniques for aligning and comparing continuous pressure maps (e.g., dynamic sitting).

A summary of the results obtained in the study is presented in Table 28. This table presents concise findings for each introduced methodology along with their applications and interpretations in the context of seating pressure mapping analysis. One major benefit in introducing these techniques is the increase in objectivity through quantitative evaluation, with no dependence of visual feedback assessments for understanding seating pressure map characteristics, features, and, particularly, dynamic behavior. The human information-processing system is overloaded by sensorial information, with constraints placed in cognitive processes such as attention, perception, recognition, judging, reasoning, and problem solving (Payne, 2003; Smith & Kelly, 2015). Such constraints make the human information-processing system prone to errors and misjudgments.

By assessing values of meaningful pressure measures and similarity/dissimilarity coefficients, particularly during dynamic evaluation of time series plots, a general idea of the seating activity and behavior of the seating pressure distributions is generally obtained without recurring to constant visual feedback – a more-demanding cognitive activity.

Table 28. Summary of study findings, comments and conclusions

	Method(s)/Measure(s)	Findings	Applications	General Comments	Conclusions
Spatial Clustering	DBSCAN	Highest outlier accuracy at 94.9% (non-outlier at 98.9%). Highest non-outlier accuracy at 99.9% (outlier at 81.7%).	Unwanted extrinsic pressure readings detection (outliers)	Parameters of epsilon and minimum samples are important. For a 32 x 32 seating pressure map, parameters of epsilon between 1.6-2.5 and minimum samples between 8-10 were appropriate.	Use of location information as data input provided betters results for both DBSCAN and DENCLUE clustering methods when detecting pressure reading outliers. An absolute superiority of a particular combination of clustering method/parameter settings couldn't be reached. Parameters selection comes with accuracy tradeoffs, as methods can be set to be more aggressive or conservative when classifying pressure readings as outliers. For pre-processing continuous pressure maps (data cleansing), a good balance between average outlier and non-outlier accuracies were obtained by these clustering methods. DENCLUE was used as the pre-processing method for the 5-minute interval sample due to achieving the highest overall accuracy (99.914%) in the dynamic data subset.
	DENCLUE	Highest outlier accuracy at 92.6% (non-outlier at 99.3%). Highest non-outlier accuracy at 99.7% (outlier at 90.7%).	Unwanted extrinsic pressure readings detection (outliers)	Selection of minimum density parameter is crucial. For a 32 x 32 seating pressure map, parameter of minimum density between 1.65e-3 and 1.7e-3 were appropriate.	
Spatial Autocorrelation	Moran's I	Measure sparseness of high/low pressure readings. Emphasis in measuring presence of correlated pressure clusters and spatial relationships among similar-value pressure readings	Static and dynamic pressure measures	Moderate to strong positive spatial autocorrelation are generally found in seating pressure maps. Measure's magnitude is significantly affected by selected weight matrix. Higher spatial autocorrelations are obtained if matrix area of interest is similar to the max-min size of expected autocorrelated high-pressure clusters.	Use of Moran's I spatial autocorrelation measures is valuable in pressure mapping analysis (static and dynamic) due to its ability to detect spatial relationships within pressure maps. Moran's I is useful for detecting spatial-relationship changes during dynamic sitting pressure redistributions via use of time series plots.
Statistical Features	Skewness	Measure frequency distribution of relatively low/high pressure cells	Static and dynamic pressure measures	Measure is sensitive to presence of mid- and high-pressure readings, and distinct high/low pressure regions. Measure is sensitive to pressure creep phenomenon during dynamic sitting.	Useful as a global pressure map descriptor (static and dynamic) due to its ability in measuring pressure reading's distributions within pressure map images. Skewness time series plots are useful for evaluating dynamic sitting.

Table 28—Continued

	Method(s)/Measure(s)	Findings	Applications	General Comments	Conclusions
Statistical Features	GLSD: Correlation	Measures spatial relationships among similar-value pressure readings. More sensitive to localized pressure gradient variations.	Static and dynamic pressure measures	Unlike Moran's I, does not require a described weight matrix. Higher values when measured at the anterior-posterior direction [90°(Y)].	Measures based on image statistical features are feasible as global pressure map descriptors, both for static and dynamic applications, due to their abilities in measuring distinct and unique pressure distribution patterns and/or pressure features within pressure maps. Measures recover some of the information loss by current common pressure measures. Measures are useful for detecting certain pressure distribution changes during dynamic sitting via use of time series plots. Measures can help in identifying in-chair-movements, but are not able to track changes in terms of shape, location and/or spatial position of pressure readings across continuous pressure maps. Subject placement and orientation on the pressure map interface must be considered for some of these measures.
	GLD: Gradient Contrast GLD: Gradient Mean	Measures pressure map variability and contrast. Complementary to the Coefficient of Variation (CV) measure.	Static and dynamic pressure measures	GLD Gradient Contrast: Sensitive when pressure maps have either a single or small group(s) of acute pressure points. GLD Gradient Mean: Robust to acute high-pressure points. Measures consider the spatial relationship of the pressure readings. Measures react to changes in the magnitude and size of high-pressure regions (i.e., ischial tuberosities). Higher measures when measured at the lateral direction [0°(X)].	
	GLD: Gradient Second Moment GLSD: Homogeneity	Measure pressure map texture, uniformity, smoothness, and homogeneity	Static and dynamic pressure measures	Measures the variations in contiguous pressure cell readings with emphasis in detecting properties of smoothness, coarseness, and regularity. GLD Gradient Second Moment: Sensitive to changes in pressure gradients. GLSD Homogeneity: Emphasizes in measuring the similarities within various pressure levels. Higher values when measured at the anterior-posterior direction [90°(Y)].	

Table 28—Continued

	Method(s)/Measure(s)	Findings	Applications	General Comments	Conclusions
Image Registration and Similarity/Dissimilarity Coefficients	MSE Registration	An average Pearson correlation of 0.9966 and average pressure error (L_1 Norm) of 6.11% were obtained for the transformed dataset (same map). 90% of samples registered from the registration data subset (Δ CP>1 in) were correctly aligned. 100% of samples registered from the 5-minute interval (within-subject) were correctly aligned.	Pressure map images alignment	Upscaling (e.g., factor of 10) was necessary for fine-adjustments in a 32x32 map. Somewhat robust to high rotational differences. Initial centering using image moments [i.e., center of pressures (CP)] and subsequent 2D rigid transformation were generally adequate to achieve good registrations. CP translation to reach registration optimality can be used as a dynamic pressure measure. CP translation distance can measure positional shifts within the seat pan during dynamic sitting.	Use of MSE registration is suitable for aligning pressure map images. Registration generally results in proper images correspondences and features' matching. MSE registration can be used to compared pressure maps for within-subject analysis or between-subject analysis. Significant scaling differences, shapes mismatch, and/or lack of common features need to be considered for a proper registration. Use of MSE registration as a sequential image registration technique was successful in aligning dynamic sitting pressure maps. A particular reference map (or aggregate) can be chosen as the comparison basis during dynamic sitting, or particular reference maps can be chosen for each pressure map comparison (e.g., incremental comparison).
	Similarity and Dissimilarity Coefficients	Calculation approach (non-masked vs masked) provide different comparison basis	Pressure maps images comparison	Non-masked: Measures all true differences between pressure maps. Lower Tanimoto and Minimum Ratio, and higher L_1 Norm and Squared L_2 Norm. Masked: Compare pressure maps by only considering overlaps. Pearson Correlation Coefficient and Intensity-Ratio Variance measures are generally lower if non-overlaps occur in low pressure regions.	Similarity and dissimilarity coefficients are suitable as global comparison metrics between pressure maps. Image registration is required if translation and rotational differences are significant. Values of similarity and dissimilarity coefficients generally increase after image registration due to a higher correspondences between images. Similarity and dissimilarity measures are complementary to pressure measures when evaluating pressure maps differences as these consider location (x-y regions of space) and/or shape differences between pressure map images.
	Tanimoto, Minimum Ratio	Sensitive to pressure differences in pair-wise pressure readings	Pressure maps images comparison	Minimum Ratio: sensitive to pressure scaling differences between maps. Tanimoto: considers relationships of pair-wise pressure readings (similar to Pearson).	

Table 28—Continued

	Method(s)/Measure(s)	Findings	Applications	General Comments	Conclusions
Similarity/Dissimilarity Coefficients	Pearson Correlation Coefficient	Considers the within-relationships of pressure readings when comparing pressure maps	Pressure maps images comparison	Robust to pressure scaling differences between pressure maps. Dynamic behavior somewhat similar to measures of GSLD Homogeneity.	Similarity and dissimilarity coefficients can be used as complementary dynamic pressure measures for identifying and evaluating in-chair-movements (ICM). Similarity and dissimilarity coefficients can evaluate pressure distributions, locations, and/or shape differences between pressure maps (static or dynamic). As global comparative measures, similarity and dissimilarity coefficients have unique takes when evaluating differences between pressure maps (i.e., how different are they?), while introduced pressure measures could potentially explain and highlight those differences between pressure maps (i.e., why are they different?).
	L_1 Norm, Squared L_2 Norm	Measures raw pair-wise pressure differences between pressure maps	Pressure maps images comparison	Squared L_2 Norm: more sensitive to large pairwise pressure differences. Measures as-is do not provide normalized dissimilarity values. Measures require expert knowledge to identify meaningful differences, in terms of raw pressure differences, between pressure maps. They can also be calculated as relative differences (%) between maps.	
	Intensity Ratio Variance	Sensitive to ratio changes or shape overlapping differences between pressure maps	Pressure maps images comparison	Robust to pressure scaling differences between pressure maps, but sensitive to scale changes among pairwise pressure readings. Dynamic behavior is very sensitive to overlapping shape differences between pressure maps when using non-masked approach.	

While the introduced techniques for pressure mapping analysis were evaluated in a task seating environment (i.e. mousing and typing), the applications of these methodologies, along with their use and interpretation, should be transferable to other seating research environments. For example, research in automobile seating could be enhanced by the analytical capabilities of the introduced methodologies. The automobile seating environment provides certain restrictions in terms of seating postures and movements, thus making seating pressure behavior to be generally stable. Therefore, pressure redistributions during driving activities are important indicators of sitting discomfort, and enhancements in monitoring, tracking, and analysis of seating pressure maps can help in a better understanding of these movement-discomfort relationships (Sammonds et al., 2017).

Other implementations of the introduced methodologies can be in the ergonomic evaluation of aircraft pilot seats, where factors such as inappropriate seat dimensions and improper sitting postures are possible contributors to discomfort. Pilot discomfort due to sitting conditions can lead to distractions and reduction in pilot performance during an air flight, causing concerns in flight safety (Andrade, 2013). By use of pressure mapping interfaces, the introduced techniques could help in evaluating pilot seat designs and seating postures, while helping in further understanding their relation to seating comfort-discomfort.

Another example where introduced methodologies can help expand the analytical capabilities is in paraplegic seating research, where the monitoring of pressures between the soft tissues of the body and the support surface is important in assessing tissue viability (Aissaoui et al., 2001). While body tissues can generally tolerate high pressures for short periods of time, the lack of sitting movement or pressure redistribution is of concern. Blood supply and lymphatic drainage are impaired if high seating pressures are maintained (Aissaoui et al., 2001). The additional information provided by the introduced methodologies can help in identifying unfavorable pressure distribution patterns or stagnant sitting behavior.

In all aforementioned examples, the analysis of the relationships between user-chair interactions and seating comfort-discomfort could be expanded by the introduced pressure mapping techniques; these can help in objectively identifying the seating conditions that can lead to discomfort. While many of the findings in this study are in the context of seating pressure mapping evaluation, the applications of these techniques can also be tailored and employed in non-seating research using pressure map images (e.g., gait analysis, industrial applications, and sports fields), or for research studies using spatially related three-dimensional datasets (e.g., surface topography, contour data, and heat maps).

Limitations

Some of the limitations in this study are in terms of the pressure mapping interface used to collect the pressure maps included in the studied dataset. There were instances where many pressure sensor cells in the pressure mat were maxed out (i.e., 300 mmHg), usually around high-pressure regions such as the ischial tuberosities. Some of the introduced pressure measures, such as homogeneity and spatial relationships measures, were sensitive to clusters of maxed out readings. To obtained more accurate results with introduced measures, the use of pressure mapping interfaces with pressure limits higher than the expected max pressure reading is required.

Introduced methodologies were validated for a grid-base pressure mat interface with 1024 (32 x 32) contiguous pressure elements (sensors). While the applications of many of the introduced measures, techniques, and methodologies should scale well with grid-base pressure mat interfaces with different configurations (e.g., 16 x 16, or 32 x 80 [used in mattress research]), proposed techniques for data cleansing (using density-based spatial clustering) might not be adequate for other pressure mapping applications. This study implemented density-based spatial clustering on the assumption that seating pressure maps generally exhibit a single-body (or a number of large bodies) of contiguous pressure readings. This assumption could be violated in other human-subject pressure mapping applications (e.g., gait analysis, mattress mapping, or dental mapping). In controlled pressure mapping environments, particularly in industrial applications (e.g., sealing packaging, robotic assembly, and ultrasonic welding), extrinsic pressure artifacts might not even be present; making the pre-processing (data cleansing) of collected pressure maps not a requirement.

For the dynamic evaluation of continuous pressure maps, the 5-minute interval sample used in this study provided sufficient dynamic pressure redistributions to evaluate the feasibility of introduced dynamic pressure measures. Unfortunately, significant seat pan repositions did not occur during this sitting time interval. More seating repositions could potentially be observed in longer sitting sessions, where the potential use of measures of registered CP translation distances could be better evaluated. The dynamic evaluation conclusions presented in this study assume that all introduced methodologies and measures are scalable (different pressure map resolutions) and extendable (longer collection of continuous pressure maps).

Evaluations of introduced comparative techniques were limited to comparisons of pressure maps with no significant orientation differences (e.g., rotational differences of more than 90^{o}), or significant scaling differences (e.g., differences in number of contact cells more than 20%). Significant scaling differences can occur when comparing pressure maps between subjects due to differences in subjects' anthropometry, or when comparing within-subject pressure maps where different seating surfaces are examined (e.g., different seating area and/or contour). These scaling differences can have meaningful effects during image registration procedures. While scaling algorithms can be also implemented for comparing pressure maps, it is generally not appropriate for research involving human subjects (e.g., seating research). Scaling algorithms will distort subject's anthropometry and cover dissimilarities due to true differences in size between subjects, and therefore not considered in this study. But other potential pressure mapping research applications where objects are naturally scalable (e.g., tire footprint analysis) might benefit from scaling algorithms during image registrations.

Another major limitation is that seating pressure maps were used as the testing and validation platform for introducing new methods and techniques for pressure mapping analysis. While other pressure mapping applications could benefit from many of the proposed methodologies, their applications and interpretations could possibly change according to what is being researched (human or object) and which contact interaction (surface) is being studied.

Future Research

Possible avenues for future research are in terms of pre-processing (data cleansing) techniques. Additional input data can be provided to density-based clustering algorithms with the purpose of enhancing detection and classification accuracies of extrinsic pressure artifacts (outliers). One possibility could be incorporating pressure distances between individual pressure reading and the map's center of pressure (with appropriate weights) as a way to identify closeness to the main pressure body. Other techniques could include forward or backwards propagation analysis in continuous pressure maps to detect common areas and locations where outliers are detected across sequential pressure maps, or use of multi-phase algorithms (e.g., using combinations of clustering methods, pressure magnitudes, locations, and distances information) to provide outlier scores to pressure readings within a pressure map.

With the introduction of new pressure measures and comparative techniques, future studies in seating research can implement these to further study human-chair interactions. Research can be aimed at determining appropriate ranges of values for the proposed pressure measures in relation to sitting comfort-discomfort. These measures can also be used to understand subjects' anthropometry influences during extended sitting bouts, and further help in understanding the relationships to comfort-discomfort during dynamic sitting.

As one of the limitations in this study is the use of seating pressure maps as the testing and validation platform for introduced methodologies, is also of importance that applications, evaluations, feasibilities, and practicalities of proposed methodologies are studied in other pressure mapping application fields.

REFERENCES

Afanuh, S., & Johnson, A. I. (2017). Using Total Worker Health Concepts to Reduce the Health Risks from Sedentary Work. *DHHS (NIOSH)*, *2017*(131), 1–6. https://www.cdc.gov/niosh/docs/wp-solutions/2017-131/pdfs/2017-131.pdf

Aissaoui, R., Kauffmann, C., Dansereau, J., & De Guise, J. A. (2001). Analysis of pressure distribution at the body-seat interface in able-bodied and paraplegic subjects using a deformable active contour algorithm. *Medical Engineering and Physics*. https://doi.org/10.1016/S1350-4533(01)00052-2

Alpert, N. M., Bradshaw, J. F., Kennedy, D., & Correia, J. A. (1990). The Principal Axes Transformation A Method for Image Registration. *Journal of Nuclear Medicine*, *31*(10), 1717–1723.

Amini, A., Wah, T. Y., & Saboohi, H. (2014). On Density-Based Data Streams Clustering Algorithms: A Survey. *Journal of Computer Science and Technology*, *29*(1), 116–141. https://doi.org/10.1007/s11390-013-1416-3

Andrade, Y. N. (2013). An Ergonomic Evaluation of Aircraft Pilot Seats. *ProQuest Dissertations and Theses*.

Ankerst, M., Breunig, M., Kriegel, H., & Sander, J. (1999). OPTICS: Ordering points to identify the clustering structure. In A. Delis, C. Faloutsos, & S. Ghandeharizadeh (Eds.), *Proceedings of ACM SIGMOD International Conference on Management of Data* (pp. 49–60). https://doi.org/10.1145/304182.304187

Anselin, L. (1992). Spatial data analysis with gis: an introduction to application in the social sciences. *UC Santa Barbara: National Center for Geographic Information and Analysis.*, *August*, 1–54.

Ashruf, C. M. A. (2005). Thin flexible pressure sensors Feature Thin flexible pressure sensors. *Sensor Review*, *22*(2002), 322–327. https://doi.org/10.1108/02602280210444636

Banerjee, S. (2016). Spatial Data Analysis. *Annual Review of Public Health*, *37*, 47–60. https://doi.org/10.1146/annurev-publhealth-032315-021711

Bhatnager, V., Drury, C. G., & Schiro, S. G. (1985). Posture, postural discomfort, and performance. *Human Factors*, *27*(2), 189–199. https://doi.org/10.1177/001872088502700206

Bloss, R. (2011). Real-time pressure mapping system. *Sensor Review*, *31*(2), 101–105. https://doi.org/10.1108/02602281111109943

Bogie, K., Wang, X., Fei, B., & Sun, J. (2008). New technique for real-time interface pressure analysis: Getting more out of large image data sets. *Journal of Rehabilitation Research and Development*, *45*(4), 523–536. https://doi.org/10.1682/JRRD.2007.03.0046

Butt, S. E., Fredericks, T. K., Nelson, J. K., Kumar, A. R., & Bellingar, T. (2005). Aggregating Pressure Maps: A Case Study. *Proceedings of the XIX Annual International Occupational Ergonomics and Safety Conference*, *June*, 165–171.

Campello, R. J. G. B., Moulavi, D., Zimek, A., & Sander, J. (2015). Hierarchical Density Estimates for Data Clustering, Visualization, and Outlier Detection. *ACM Transactions on Knowledge Discovery from Data*, *10*(1), 1–51. https://doi.org/10.1145/2733381

Cascioli, V., Liu, Z., Heusch, A. I., & McArthy, P. W. (2011). Settling down time following initial sitting and its relationship with comfort and discomfort. *Journal of Tissue Viability*, *20*(4), 121–129. https://doi.org/10.1016/j.jtv.2011.05.001

Cascioli, V., Liu, Z., Heusch, A., & McCarthy, P. W. (2016). A methodology using in-chair movements as an objective measure of discomfort for the purpose of statistically distinguishing between similar seat surfaces. *Applied Ergonomics*, *54*, 100–109. https://doi.org/10.1016/j.apergo.2015.11.019

Chester, M. R., Rys, M. J., & Konz, S. A. (2002). Leg swelling, comfort and fatigue when sitting, standing, and sit/standing. *International Journal of Industrial Ergonomics*, *29*(5), 289–296. https://doi.org/10.1016/S0169-8141(01)00069-5

Crawford, S. A., Stinson, M. D., Walsh, D. M., & Porter-Armstrong, A. P. (2005). Impact of sitting time on seat-interface pressure and on pressure mapping with multiple sclerosis patients. *Archives of Physical Medicine and Rehabilitation*, *86*(6), 1221–1225. https://doi.org/10.1016/j.apmr.2004.08.010

De Looze, M. P., Kuijt-Evers, L. F. M., & Van Dieën, J. (2003). Sitting comfort and discomfort and the relationships with objective measures. *Ergonomics*, *46*(10), 985–997. https://doi.org/10.1080/0014013031000121977

Dilmen, N. (2005). *Images from a patient with normal pressure hydrocephalus (NPH)*. Wikimedia Commons, CC BY-SA 3.0. https://commons.wikimedia.org/w/index.php?curid=9404462

Ester, M., Kriegel, H.-P., Sander, J., & Xu, X. (1996). A Density-Based Algorithm for Discovering Clusters in Large Spatial Databases with Noise. *Proceedings of the Second International Conference on Knowledge Discovery and Data Mining*, 226–231. https://doi.org/10.1.1.71.1980

Fenety, P. (1995). Factors Influencing Sitting Comfort and In-Chair Movement in the Office Environment. In *Dalhousie University*. https://doi.org/10.1017/CBO9781107415324.004

Fenety, P., Putnam, C., & Walker, J. M. (2000). In-chair movement: Validity, reliability and implications for measuring sitting discomfort. *Applied Ergonomics*, *31*(4), 383–393. https://doi.org/10.1016/S0003-6870(00)00003-X

Fleischer, A. G., Rademacher, U., & Windberg, H. J. (1987). Individual characteristics of sitting behaviour. *Ergonomics*, *30*(4), 703–709. https://doi.org/10.1080/00140138708969762

Fredericks, T. K., Butt, S. E., Kumar, A. R., & Bellingar, T. (2016). Do users desire symmetrical lumbar supports in task seating? *Ergonomics*, *59*(7), 901–912. https://doi.org/10.1080/00140139.2015.1103904

Fujimaki, G., & Mitsuya, R. (2002). Study of the seated posture for VDT work. *Displays*, *23*(1–2), 17–24. https://doi.org/10.1016/S0141-9382(02)00005-7

Geary, R. C. (1954). The Contiguity Ratio and Statistical Mapping. *The Incorporated Statistician*, *5*(3), 115-127+129-146. https://doi.org/10.2307/2986645

Goodchild, M. F., & Haining, R. P. (2003). GIS and spatial data analysis: Converging perspectives. *Papers in Regional Science*, *83*(1), 363–385. https://doi.org/10.1007/s10110-003-0190-y

Goshtasby, A. A. (2012). Image Registration Principles, Tools and methods. In *Advances in Computer Vision and Pattern Recognition*. Springer. https://doi.org/10.1007/978-1-4471-2458-0_1

Gunaratna, N., Liu, Y., & Park, J. (2005). *Spatial Autocorrelation*. http://www.stat.purdue.edu/~bacraig/SCS/Spatial Correlation new.doc

Hadgraft, N. T., Healy, G. N., Owen, N., Winkler, E. A. H., Lynch, B. M., Sethi, P., Eakin, E. G., Moodie, M., LaMontagne, A. D., Wiesner, G., Willenberg, L., & Dunstan, D. W. (2016). Office workers' objectively assessed total and prolonged sitting time: Individual-level correlates and worksite variations. *Preventive Medicine Reports*, *4*, 184–191. https://doi.org/10.1016/j.pmedr.2016.06.011

Hammond, M. A., Martinez, J. Y., Butt, S. E., Fredericks, T. K., & Bellingar, T. A. (2018). Anthropometric influence on seat pan pressure in task seating. In K. Barke, D. Berry, & C. Rainwater (Eds.), *Proceedings of the 2018 IISE Annual Conference*. Institute for Industrial and Systems Engineering Annual Conference and Expo, May 19-22, Orlando, FL.

Higer, S., & James, T. (2016). Interface pressure mapping pilot study to select surfaces that effectively redistribute pediatric occipital pressure. *Journal of Tissue Viability*, *25*(1). https://doi.org/10.1016/j.jtv.2015.09.001

Hinneburg, A., & Keim, D. A. (1998). An Efficient Approach to Clustering in Large Multimedia Databases with Noise. In R. Agrawal, P. E. Stolorz, & G. Piatetsky-Shapiro (Eds.), *Proceedings of Fourth International Conference on Knowledge Discovery and Data Mining* (pp. 58–65). AAAI. https://ocs.aaai.org/Papers/KDD/1998/KDD98-009.pdf

Januschka, H. (2006). *MRI Head Side*. Wikimedia Commons, CC BY-SA 3.0. https://commons.wikimedia.org/w/index.php?curid=1243492

Kalogirou, S. (2019). *Spatial Autocorrelation*. https://cran.r-project.org/web/packages/lctools/vignettes/SpatialAutocorrelation.pdf

Kumar, A. R. (2007). *A Study to Investigate the Relationship Between a User's Thermal Comfort and Seat Pan Materials* [Western Michigan University]. http://scholarworks.wmich.edu/dissertations/886/

Kumar, N., & Sivasathya, S. (2014). Density-Based Spatial Clustering – A Survey. *International Journal of Computer Science and Mobile Computing*, *3*(3), 1004–1012.

Kurani, A., Xu, D., Furst, J., & Raicu, D. (2004). Co-occurrence matrices for volumetric data. *7th IASTED International Conference on Computer Graphics and Imaging*, 447–452. https://doi.org/10.1.1.69.5262

Liao, L., Li, K., Li, K., Tian, Q., & Yang, C. (2017). Automatic density clustering with multiple kernels for high-dimension bioinformatics data. *Proceedings - 2017 IEEE International Conference on Bioinformatics and Biomedicine, BIBM 2017*, *2017-Janua*, 2105–2112. https://doi.org/10.1109/BIBM.2017.8217984

Liao, M. H., & Drury, C. G. (2000). Posture, discomfort and performance in a vdt task. *Ergonomics*, *43*(3), 345–359. https://doi.org/10.1080/001401300184459

Lis, A. M., Black, K. M., Korn, H., & Nordin, M. (2007). Association between sitting and occupational LBP. *European Spine Journal*, *16*(2), 283–298. https://doi.org/10.1007/s00586-006-0143-7

Makhsous, M., Lin, F., Hanawalt, D., Kruger, S. L., & Lamantia, A. (2012). The effect of chair designs on sitting pressure distribution and tissue perfusion. *Human Factors*, *54*(6), 1066–1074. https://doi.org/10.1177/0018720812457681

Martinez, J. Y., Hammond, M. A., Fredericks, T. K., Butt, S. E., & Bellingar, T. A. (2018). Effect of an Adjustable Seat Pan on Contact Pressure Measures and Subjective Discomfort. In K. Barke, D. Berry, & C. Rainwater (Eds.), *Proceedings of the 2018 IISE Annual Conference*. Institute for Industrial and Systems Engineering Annual Conference and Expo, May 19-22, Orlando, FL.

McInnes, L., Healy, J., & Astels, S. (2017). hdbscan: Hierarchical density based clustering. *The Journal of Open Source Software*. https://doi.org/10.21105/joss.00205

Menafoglio, A., & Secchi, P. (2017). Statistical analysis of complex and spatially dependent data: A review of Object Oriented Spatial Statistics. *European Journal of Operational Research*, *258*(2), 401–410. https://doi.org/10.1016/j.ejor.2016.09.061

Mgarrett. (2017). *DENCLUE*. GitHub. https://github.com/mgarrett57/DENCLUE

Miles, A. K. (2001). The ergonomics and organizational stress relationship. *Dissertation Abstracts International Section A: Humanities and Social Sciences*, *61*(11-A), 4458.

Misiewicz, P. A., Blackburn, K., Richards, T. E., Brighton, J. L., & Godwin, R. J. (2015). The evaluation and calibration of pressure mapping system for the measurement of the pressure distribution of agricultural tyres. *Biosystems Engineering*, *130*, 81–91. https://doi.org/10.1016/j.biosystemseng.2014.12.006

Modersitzki, J. (2004). *Numerical Methods for Image Registration (Numerical Mathematics and Scientific Computation)*. Oxford University Press. http://www.amazon.com/Numerical-Registration-Mathematics-Scientific-Computation/dp/0198528418

Moran, P. A. P. (1950). Notes on Continuous Stochastic. *Biometrika*, *37*(1), 17–23. http://www.jstor.org/stable/2332142

Nagel, A., Fernholz, F., Kibele, C., & Rosenbaum, D. (2008). Long distance running increases plantar pressures beneath the metatarsal heads. A barefoot walking investigation of 200 marathon runners. *Gait and Posture*, *27*(1), 152–155. https://doi.org/10.1016/j.gaitpost.2006.12.012

Oliveira, F. P. M., & Tavares, J. M. R. S. (2014). Medical image registration: A review. In *Computer Methods in Biomechanics and Biomedical Engineering* (Vol. 17, Issue 2, pp. 73–93). Taylor & Francis. https://doi.org/10.1080/10255842.2012.670855

Openshaw, S. D. (2011). *Predicting and quantifying seated comfort and discomfort using objective and subjective measures* [University of Iowa]. http://ir.uiowa.edu/etd/1049/

Palacio, S. (2015). *Python implementation of the DBCLASD algorithm: a non-parametric clustering algorithm*. https://github.com/spalaciob/py-dbclasd

Pataky, T. C., Keijsers, N. L. W., Goulermas, J. Y., & Crompton, R. H. (2009). Nonlinear spatial warping for between-subjects pedobarographic image registration. *Gait and Posture*, *29*(3), 477–482. https://doi.org/10.1016/j.gaitpost.2008.11.006

Payne, S. J. (2003). Users' Mental Models: The Very Ideas. In *HCI Models, Theories, and Frameworks: Toward a Multidisciplinary Science*. https://doi.org/10.1016/B978-155860808-5/50006-X

Peck, J. C. (1992). A Benefits Study of Ergonomically Designed Chairs with Direct Labour Employees. *International Journal of Clothing Science and Technology*, *4*(2/3), 39–44. https://doi.org/10.1108/eb002992

Pedregosa, F., Varoquaux, G., Gramfort, A., Michel, V., & Cournapeau, D. (2011). *Scikit-learn: Machine Learning in Python*. JMLR 12. https://scikit-learn.org

Pentland, Moghaddam, & Starner. (1994). View-based and modular eigenspaces for face recognition. *Proceedings of IEEE Conference on Computer Vision and Pattern Recognition CVPR-94*. https://doi.org/10.1109/CVPR.1994.323814

Pitman, M. S., & Ntuen, C. A. (1996). The effect of prolonged sitting on mental task performance. *Computers and Industrial Engineering*, *31*(1), 499–502. https://doi.org/10.1016/0360-8352(96)00184-2

Reibel, M. (2007). Geographic Information Systems and Spatial Data Processing in Demography: a Review. *Population Research and Policy Review*, *26*(5), 601–618. https://doi.org/10.1007/sl 11 13-007-9046-5

Rey, S. J., & Anselin, L. (2007). PySAL: A Python Library of Spatial Analytical Methods. *The Review of Regional Studies*, *37*(1), 5–27. http://journal.srsa.org/ojs/index.php/RRS/article/view/134/85

Sammonds, G. M., Fray, M., & Mansfield, N. J. (2017). Effect of long term driving on driver discomfort and its relationship with seat fidgets and movements (SFMs). *Applied Ergonomics*. https://doi.org/10.1016/j.apergo.2016.05.009

Smith, A. D., & Kelly, A. (2015). Cognitive Processes. In *The Encyclopedia of Adulthood and Aging*. American Cancer Society. https://doi.org/10.1002/9781118521373.wbeaa213

Stinson, M., Porter, A., & Eakin, P. (2002). Measuring interface pressure: A laboratory-based investigation into the effects of repositioning and sitting. *American Journal of Occupational Therapy*, *56*(2), 185–190. https://doi.org/10.5014/ajot.56.2.185

Stinson, M., Porter, A., & Eakin, P. (2003). Pressure mapping systems: Reliability of pressure map interpretation. *Clinical Rehabilitation*, *17*(5), 504–511. https://doi.org/10.1191/0269215503cr643oa

Studebaker, C. D., & Murphy, B. P. (2014). Current Concepts on the Physiological Effects of Seated Postures at Work. *Profesional Safety, September*, 42–49.

Tan, H. Z., Slivovsky, L. A., & Pentland, A. (2001). A sensing chair using pressure distribution sensors. *IEEE/ASME Transactions on Mechatronics*, *6*(3), 261–268. https://doi.org/10.1109/3516.951364

Tang, M., & Chen, F. (2012). A qualitative meta analysis review on medical image registration evaluation. *Procedia Engineering*, *29*, 499–503. https://doi.org/10.1016/j.proeng.2011.12.750

Thorp, A. A., Healy, G. N., Winkler, E., Clark, B. K., Gardiner, P. A., Owen, N., & Dunstan, D. W. (2012). Prolonged sedentary time and physical activity in workplace and non-work contexts. *International Journal of Behavioral Nutrition and Physical Activity*, *9*(1), 128.

Titus, L., & Polgar, J. M. (2009). Interface Pressure Mapping (Ipm): Clinical Use of the Literature. *Canadian Seating & Mobility Conference*, 1–41. www.hsc.mb.ca/files/IPM_Literature_09.pdf

Turk, M., & Pentland, A. (1991). Eigenfaces for recognition. *Journal of Cognitive Neuroscience*, *3*(1), 71–86. https://doi.org/10.1162/jocn.1991.3.1.71

UCLA: Statistical Consulting Group. (2020). *Detect/address spatial autocorrelation.* https://stats.idre.ucla.edu/other/mult-pkg/faq/general/faq-how-can-i-detectaddress-spatial-autocorrelation-in-my-data/

Waongenngarm, P., Rajaratnam, B. S., & Janwantanakul, P. (2015). Perceived body discomfort and trunk muscle activity in three prolonged sitting postures. *Journal of Physical Therapy Science*, *27*(7), 2183–2187. https://doi.org/10.1589/jpts.27.2183

Winkel, J. (1986). On the significance of physical activity in sedentary work. In B. Knave & G. Wideback (Eds.), *Work with Display Units* (pp. 229–236). Elsevier.

Xiaowei Xu, Ester, M., Kriegel, H.-P., & Sander, J. (1998). A distribution-based clustering algorithm for mining in large spatial databases. *Proceedings 14th International Conference on Data Engineering*, 324–331. https://doi.org/10.1109/ICDE.1998.655795

Xu, X., Ester, M., Kriegel, H. P., & Sander, J. (1997). Clustering and knowledge discovery in spatial databases. *Vistas in Astronomy*, *41*(3), 397–403. https://doi.org/10.1016/S0083-6656(97)00044-5

Yaniv, Z., Lowekamp, B. C., Johnson, H. J., & Beare, R. (2018). SimpleITK Image-Analysis Notebooks: a Collaborative Environment for Education and Reproducible Research. *Journal of Digital Imaging*. https://doi.org/10.1007/s10278-017-0037-8

Zemp, R., Taylor, W. R., & Lorenzetti, S. (2015). Are pressure measurements effective in the assessment of office chair comfort/discomfort? A review. *Applied Ergonomics*, *48*, 273–282. https://doi.org/10.1016/j.apergo.2014.12.010

Zemp, R., Taylor, W. R., & Lorenzetti, S. (2016). Seat pan and backrest pressure distribution while sitting in office chairs. *Applied Ergonomics*, *53*, 1–9. https://doi.org/10.1016/j.apergo.2015.08.004

Appendix A

Institutional Review Board Approval Letters

WESTERN MICHIGAN UNIVERSITY

Human Subjects Institutional Review Board

Date: May 14, 2013

To: Tycho Fredericks, Principal Investigator
Steven Butt, Co-Principal Investigator
James Burns, Student Investigator

From: Amy Naugle, Ph.D., Chair Amy Naugle

Re: HSIRB Project Number 13-05-21

This letter will serve as confirmation that your research project titled "Determining Seat Pan Requirements and Interface Pressures for Self-selected Seating Comfort" has been **approved** under the **expedited** category of review by the Human Subjects Institutional Review Board. The conditions and duration of this approval are specified in the Policies of Western Michigan University. You may now begin to implement the research as described in the application.

Please note: This research may **only** be conducted exactly in the form it was approved. You must seek specific board approval for any changes in this project (e.g., ***you must request a post approval change to enroll subjects beyond the number stated in your application under "Number of subjects you want to complete the study***)." Failure to obtain approval for changes will result in a protocol deviation. In addition, if there are any unanticipated adverse reactions or unanticipated events associated with the conduct of this research, you should immediately suspend the project and contact the Chair of the HSIRB for consultation.

Reapproval of the project is required if it extends beyond the termination date stated below.

The Board wishes you success in the pursuit of your research goals.

Approval Termination: May 14, 2014

Walwood Hall, Kalamazoo, MI 49008-5456
PHONE: (269) 387-8293 FAX: (269) 387-8276

WESTERN MICHIGAN UNIVERSITY

Institutional Review Board
FWA00007042
IRB00000254

Date: July 16, 2019

To: Tycho Fredericks, Principal Investigator
Steven Butt, Co-Principal Investigator
Joan Martinez, Student Investigator for dissertation
Student Investigators: James Burns, Megan Hammond, David Haruza, Anna Konstant, Persefoni Lauhon, Katelyn McComb, Michelle Valente

From: Amy Naugle, Ph.D., Chair Amy Naugle

Re: HSIRB Project Number 13-05-21

This letter will serve as confirmation that the change to your research project titled "Determining Seat Pan Requirements and Interface Pressures for Self-selected Seating Comfort" requested in your memo received July 15, 2019 (to expand dissemination to allow data to be used for Joan Martinez's dissertation) has been approved by the Human Subjects Institutional Review Board.

The conditions and the duration of this approval are specified in the Policies of Western Michigan University.

Please note that you may **only** conduct this research exactly in the form it was approved. You must seek specific board approval for any changes in this project. You must also seek reapproval if the project extends beyond the termination date noted below. In addition, if there are any unanticipated adverse reactions or unanticipated events associated with the conduct of this research, you should immediately suspend the project and contact the Chair of the HSIRB for consultation.

The Board wishes you success in the pursuit of your research goals.

Approval Termination: **May 13, 2020**

Office of the Vice President for Research
Research Compliance Office
1903 W. Michigan Ave., Kalamazoo, MI 49008-5456
PHONE: (269) 387-8293 FAX: (269) 387-8276
WEBSITE: wmich.edu/research/compliance/hsirb

CAMPUS SITE: Room 251 W. Walwood Hall

Appendix B

Copyright Permissions

PLS Clear

PARTIES:

1. **Oxford Publishing Limited** (Company number – 01748118) (Licensor); and
2. **Joan Martinez** (Licensee).

Thank you for your recent permission request. Some permission requests for use of material published by the Licensor, such as this one, are now being facilitated by PLSclear.

Set out in this licence cover sheet (the **Licence Cover Sheet**) are the principal commercial terms under which Licensor has agreed to license certain Licensed Material (as defined below) to Licensee. The terms in this Licence Cover Sheet are subject to the attached General Terms and Conditions, which together with this Licence Cover Sheet constitute the licence agreement (the **Licence**) between Licensor and Licensee as regards the Licensed Material. The terms set out in this Licence Cover Sheet take precedence over any conflicting provision in the General Terms and Conditions.

Licence Terms

Licence Date:	29/07/2019
PLSclear Ref No:	16713

The Licensor

Company name:	Oxford Publishing Limited
Address:	Rights Department Great Clarendon Street Oxford OX2 6DP GB

The Licensee

Licensee Contact Name:	Joan Martinez
Licensee Address:	701 Regency Sq Apt 205 Kalamazoo 49008 United States

Licensed Material

title:	Numerical Methods for Image Registration
ISBN/ISSN:	9780198528418
publisher:	Oxford Publishing Limited

figure number & title / caption	Fig. 4.1. Landmark-based image registration
page number	31
position on page	TOP LEFT
additional information	Image will be used to show applications of image registration methodologies for a dissertation.
reproduction colour	Black and White
reproduction size	Thumbnail
positioning	inside or later pages
Are you requesting permission to reuse your own work?	No. I am NOT the author
Are you using the content as a prop?	content will NOT be used as a prop

figure number & title / caption	Fig. 4.1. Landmark-based image registration
page number	31
position on page	TOP RIGHT
additional information	Image will be used to show applications of image registration methodologies for a dissertation.
reproduction colour	Black and White
reproduction size	Thumbnail
positioning	inside or later pages
Are you requesting permission to reuse your own work?	No. I am NOT the author
Are you using the content as a prop?	content will NOT be used as a prop

figure number & title / caption	Fig. 5.3 PAT registration images from hands using the robust approach
page number	53
position on page	BOTTOM LEFT
additional information	Image will be used to show applications of image registration methodologies for a dissertation.
reproduction colour	Black and White
reproduction size	Thumbnail
positioning	inside or later pages
Are you requesting permission to reuse your own work?	No. I am NOT the author
Are you using the content as a prop?	content will NOT be used as a prop

figure number & title / caption	Fig. 5.3 PAT registration images from hands using the robust approach
page number	53
position on page	BOTTOM MIDDLE
additional information	Image will be used to show applications of image registration methodologies for a dissertation.
reproduction colour	Black and White
reproduction size	Thumbnail

positioning	inside or later pages
Are you requesting permission to reuse your own work?	No. I am NOT the author
Are you using the content as a prop?	content will NOT be used as a prop
figure number & title / caption	Fig. 5.3 PAT registration images from hands using the robust approach
page number	53
position on page	BOTTOM RIGHT
additional information	Image will be used to show applications of image registration methodologies for a dissertation.
reproduction colour	Black and White
reproduction size	Thumbnail
positioning	inside or later pages
Are you requesting permission to reuse your own work?	No. I am NOT the author
Are you using the content as a prop?	content will NOT be used as a prop
figure number & title / caption	Fig 6.5 Four different linear registrations
page number	71
position on page	TOP LEFT
additional information	Image will be used to show applications of image registration methodologies for a dissertation.
reproduction colour	Black and White
reproduction size	Thumbnail
positioning	inside or later pages
Are you requesting permission to reuse your own work?	No. I am NOT the author
Are you using the content as a prop?	content will NOT be used as a prop
figure number & title / caption	Fig 6.5 Four different linear registrations
page number	71
position on page	BOTTOM LEFT
additional information	Image will be used to show applications of image registration methodologies for a dissertation.
reproduction colour	Black and White
reproduction size	Thumbnail
positioning	inside or later pages
Are you requesting permission to reuse your own work?	No. I am NOT the author
Are you using the content as a prop?	content will NOT be used as a prop
figure number & title / caption	Fig 6.5 Four different linear registrations
page number	71
position on page	BOTTOM RIGHT

additional information	Image will be used to show applications of image registration methodologies for a dissertation.
reproduction colour	Black and White
reproduction size	Thumbnail
positioning	inside or later pages
Are you requesting permission to reuse your own work?	No. I am NOT the author
Are you using the content as a prop?	content will NOT be used as a prop

For Use In Licensee's Publication(s)

usage type	Book, Journal, Magazine or Academic Paper...-Thesis
estimated publication date	12/14/2019
language	English
number of pages	300
other relevant Information	A dissertation submitted as a requirement for the degree of Doctor of Philosophy in Industrial Engineering at Western Michigan University.
publication title	A FRAMEWORK FOR PRESSURE MAPPING ANALYSIS USING IMAGE PROCESSING TECHNIQUES AND SPATIAL DATA ANALYTICS
type of document	Dissertation

Rights Granted

Exclusivity:	Non-Exclusive
Format:	THESIS/WHITEPAPER/CONULTATION DOCUMENT
Language:	English
Territory:	USA
Duration:	Lifetime of Licensee's edition
Maximum Circulation:	Total: 1 copies
Additional Terms:	If at some future date your thesis is published it will be necessary to re-clear this permission. Please also note that if the material to be used is acknowledged to any other source, you will need to clear permission with the rights holder and for any electronic version the © line must appear on the same page as the OUP material and the OUP material should not be included under a Creative Commons license, or any other open-access license allowing onward reuse.

Payment Details

Fee Payable:	£0.00 [+ VAT if applicable]
Payment Terms:	Strictly 30 days from date of Licence

GENERAL TERMS AND CONDITIONS

1. <u>Definitions and Interpretation</u>

1.1 Capitalised words and expressions in these General Terms and Conditions have the meanings given to them in the Licence Cover Sheet.

1.2 In this Licence any references (express or implied) to statutes or provisions are references to those statutes or provisions as amended or re-enacted from time to time. The term **including** will be construed as illustrative, without limiting the sense or scope of the words preceding it. A reference to in **writing** or **written** includes faxes and email. The singular includes the plural and vice versa.

2. <u>Grant of Rights</u>

2.1 Subject to payment by Licensee of the Licence Fee in accordance with paragraph 3 below, Licensor grants to Licensee the non-exclusive right to use the Licensed Material as specified in the Licence Cover Sheet.

2.2 The rights licensed to Licensee under this Licence do not include the right to use any third party copyright material incorporated in the Licensed Material. Licensee should check the Licensed Material carefully and seek permission for the use of any such third party copyright material from the relevant copyright owner(s).

2.3 Unless otherwise stated in the Licence Cover Sheet, the Licensed Material may be:

2.3.1 subjected to minor editing, including for the purposes of creating alternative formats to provide access for a beneficiary person (provided that any such editing does not amount to derogatory treatment); and/or

2.3.2 used for incidental promotional use (such as online retail providers' search facilities).

2.4 Save as expressly permitted in this Licence or as otherwise permitted by law, no use or modification of the Licensed Material may be made by Licensee without Licensor's prior written permission.

3. <u>Payment</u>

3.1 Licensee must pay to Licensor the Licence Fee by means of either credit card or on receipt of an invoice, as selected by Licensee during the licence application process via the PLSclear service.

3.2 If payment is by invoice, Licensee agrees to pay the Licence Fee in full by no later than the payment date specified in the relevant invoice.

4. <u>Copyright Notice and Acknowledgement</u>

4.1 Licensee must ensure that the following notices and acknowledgements are reproduced prominently alongside each reproduction by Licensee of the Licensed Material:

4.1.1 the title and author of the Licensed Material;

4.1.2 the copyright notice included in the Licensed Material; and

4.1.3 the statement "Reproduced with permission of the Licensor through PLSclear."

5. <u>Reversion of Rights</u>

5.1 The rights licensed to Licensee under this Licence will terminate immediately and automatically upon the earliest of the following events to occur:

5.1.1 the Licence Fee not being received by Licensor in full by the payment date specified in the relevant invoice;

5.1.2 the Licensed Material not being used by Licensee within 18 months of the Licence Date;

5.1.3 expiry of the Licence Duration; or

5.1.4 the Maximum Circulation being reached.

6. <u>Miscellaneous</u>

6.1 By using the Licensed Material, Licensee will be deemed to have accepted all the terms and conditions contained in this Licence.

6.2 This Licence contains the entire understanding and agreement of the parties relating to its subject matter and supersedes in all respects any previous or other existing arrangements, agreements or understandings between the parties whether oral or written in relation to its subject matter.

6.3 Licensee may not assign this Licence or any of its rights or obligations hereunder to any third party without Licensor's prior written consent.

6.4 This Licence is governed by and shall be construed in accordance with the laws of England and Wales and the parties hereby irrevocably submit to the non-exclusive jurisdiction of the Courts of England and Wales as regards any claim, dispute or matter arising under or in relation to this Licence.

Appendix C

Python Code: Spatial Clustering Algorithms

```
# -*- coding: utf-8 -*-

"""
Created on Thu Mar  7 09:13:08 2019

@author: Joan Martinez
"""

import numpy as np
import pandas as pd
from sklearn.cluster import DBSCAN, OPTICS
from hdbscan import HDBSCAN
from sklearn import metrics
from sklearn.preprocessing import StandardScaler
import matplotlib.pyplot as plt
import sys, time, glob, os
import matplotlib as mpl
from skimage.external import tifffile

sys.path.append(os.getcwd()+'\\DENCLUE-master')
from denclue import DENCLUE # mgarrett, 2017 (github.com/mgarrett57/DENCLUE)

sys.path.append(os.getcwd()+'\\py-dbclasd-master')
from dbclasd2 import dbclasd # Sebastian Palacio, 2015 (github.com/spalaciob/py-dbclasd)

# create colormap
upper = mpl.cm.jet(np.arange(int(256/4.5),256))
cmap = mpl.colors.ListedColormap(upper, name='myColorMap', N=upper.shape[0])

########################### LOAD DATA ##############################################

sheet = 'Seatpan'

# Pressure Mat Info
res1 = 32
res2 = 32
pmax = 300

Y1 = pd.read_excel('Data\\Cluster data subset.xlsx', sheet_name=sheet)
Ylab = pd.read_excel('Data\\Cluster data subset.xlsx', sheet_name=sheet + ' Outliers')

nindex = np.size(Y1.iloc[1,:])

Y = np.float32(Y1.values.reshape(res1,res2,nindex))
Ym = np.ma.masked_where(Y == 0, Y) ## Inactive cells = 0 mmHg

indexlist = list(range(56))

#Setting up column/rows/pressure array
X1 = np.array(np.meshgrid(np.arange(1,res1+1),np.arange(1,res2+1))).T.reshape(-1,2)
X1 = pd.DataFrame(np.hstack((X1,np.zeros(res1*res2).reshape(1,1))),columns=['Row','Column'
,'Pressure'])

#Setting up cluster label variables
cluvarlist = ['db', 'dbnp', 'op', 'opnp', 'opdb', 'opdbnp', 'hdb', 'hdbnp'
              ,'dcl', 'dclnp', 'dbcl', 'dbclnp']
```

```
labvarlist = ['DBSCAN', 'DBSCAN (NP)', 'OPTICS_XI','OPTICS_XI (NP)', 'OPTICS_DBSCAN', 'OPTICS_DBSCAN (NP)', 'HDBSCAN', 'HDBSCAN (NP)', 'DENCLUE', 'DENCLUE (NP)', 'DBCLASD', 'DBCLASD (NP)']
props = dict(boxstyle='round', facecolor='wheat', alpha=0.3)

Results = pd.DataFrame(columns=['File','Sheet','Method','Parameters','Clusters', 'Noise Pts','Cluster Accuracy','Overall Accuracy','Outliers Accuracy', 'Non-Outliers Accuracy', 'Homogeneity','Completeness','V-measure','Adj RI', 'Adj MI', 'Silhouette Coefficient', 'Proc Time'])


start = time.time()
################################ START INDEXING #################################
for i in indexlist:

    filename = Y1.columns[i]
    os.makedirs('Data\\Cluster data subset\\' + filename, exist_ok=True)

    #Plot pressure map
    plt.figure(figsize=(5, 4), dpi=200)
    plt.imshow(Ym[:,:,i], cmap=cmap);
    plt.clim(0,pmax)
    plt.colorbar()
    plt.title(f'{filename} - Pressure Map (mmHg)')
    plt.savefig(f'Data\Cluster data subset\{filename}\Pressure Map - {filename}.tif',
    bbox_inches='tight')
    plt.clf()


    X=X1
    X['Pressure'] = np.array(Y1.iloc[:,i]).reshape(-1,1)
    labels_true = np.array(Ylab.iloc[:,i])

    #Eliminating non-pressure elements
    X = X.drop(X[X.Pressure == 0].index)
    labels_true = np.array([labels_true[j] for j in X.index])
    X = X.reset_index(drop=True)

    # Standardization (Z)
    X['Pressure'] = StandardScaler().fit_transform(X['Pressure'].values.reshape(-1,1))

    ###### NO PRESSURE DATA #######
    Xnp = X.drop('Pressure', axis=1)
    Xnpreord=X[['Column','Row']]

    #Marking all as non-outliers
    core_samples_mask = np.zeros(len(X.iloc[:,0]), dtype=bool)
    core_samples_mask[:] = True

    #Plotting Reference Outlier Map
    real_n_noise = list(labels_true).count(-1)
    real_non_outliers = list(labels_true).count(0)

    unique_labels = set(labels_true)
    colors = [plt.cm.Set3(each)
              for each in np.linspace(0, 1, len(unique_labels))]

    fig, ax = plt.subplots()
    pstr = ('Outliers: %i' %real_n_noise + '\nNon-Outliers: %i' %real_non_outliers)
```

```
        ax.text(res1 + 1.5, 1, pstr, fontsize=7,verticalalignment='top', bbox=props)

        # Black removed and is used for noise instead.
        for k, col in zip(unique_labels, colors):
            if k == -1:
                # Black used for noise.
                col = [0, 0, 0, 1]

            class_member_mask = (labels_true == k)

            xy = X[class_member_mask & core_samples_mask]
            ax.plot(xy['Column'], xy['Row'], 'o', markerfacecolor=tuple(col),
                     markeredgecolor='k', markersize=7)

            xy = X[class_member_mask & ~core_samples_mask]
            ax.plot(xy['Column'], xy['Row'], 'o', markerfacecolor=tuple(col),
                     markeredgecolor='k', markersize=5)

        plt.xticks(np.arange(0, res1+1, res1/8))
        plt.yticks(np.arange(0, res1+1, res1/8))
        plt.title(f'{filename} - Outliers Reference [Noise: {real_n_noise}]')
        ax.axis([-0.5, res1+0.5, -0.5, res2+0.5])
        ax.set_aspect(1)
        ax.invert_yaxis()

        plt.savefig(f'Data\Cluster data subset\{filename}\Reference - {filename}.tif', dpi=200, bbox_inches='tight')
        plt.clf()

        # Compute DBSCAN
        proctime = time.time()
        db = DBSCAN(eps=2.5, min_samples=8, metric='euclidean', algorithm='brute').fit(X)
        dbtime = time.time() - proctime

        proctime = time.time()
        dbnp = DBSCAN(eps=2.2, min_samples=10, metric='euclidean', algorithm='brute').fit(Xnp)
        dbnptime = time.time() - proctime

        # Compute OPTICS XI
        proctime = time.time()
        op = OPTICS(min_samples= 3 , metric='euclidean', cluster_method='xi', xi= 0.1, min_cluster_size = 0.4, algorithm='brute').fit(X)
        optime = time.time() - proctime

        proctime = time.time()
        opnp = OPTICS(min_samples= 3 , metric='euclidean', cluster_method='xi', xi= 0.03, min_cluster_size = 0.4, algorithm='brute').fit(Xnp)
        opnptime = time.time() - proctime

        # Compute OPTICS DBSCAN
        proctime = time.time()
        opdb = OPTICS(min_samples= 8, max_eps= 2.2, metric='euclidean', cluster_method='dbscan', algorithm='brute').fit(X)
        opdbtime = time.time() - proctime

        proctime = time.time()
        opdbnp = OPTICS(min_samples= 10, max_eps= 2, metric='euclidean', cluster_method='dbscan', algorithm='brute').fit(Xnp)
```

```
        opdbnptime = time.time() - proctime

        # Compute HDBSCAN
        proctime = time.time()
        hdb = HDBSCAN(min_cluster_size=12, min_samples=3, metric='euclidean', alpha=1.0, algorithm='best', leaf_size=5,
                      gen_min_span_tree=True, cluster_selection_method='eom', allow_single_cluster=False).fit(X)
        hdbtime = time.time() - proctime

        proctime = time.time()
        hdbnp = HDBSCAN(min_cluster_size=12, min_samples=3, metric='euclidean', alpha=1.0, algorithm='best', leaf_size=5, gen_min_span_tree=True, cluster_selection_method='eom', allow_single_cluster=False).fit(Xnp)
        hdbnptime = time.time() - proctime

        # Compute DENCLUE
        proctime = time.time()
        dcl = DENCLUE(h=None, eps=1, min_density=2e-04, metric='euclidean').fit(X.values)
        dcltime = time.time() - proctime

        proctime = time.time()
        dclnp = DENCLUE(h=None, eps=1, min_density=1.3e-03,
         metric='euclidean').fit(Xnp.values)
        dclnptime = time.time() - proctime

        # Compute DBCLASD
        proctime = time.time()
        dbcldiv = 8
        dbcl = dbclasd(n_neighbors =  int(len(X)/dbcldiv)).fit(X.values)
        dbcltime = time.time() - proctime

        proctime = time.time()
        dbclnpdiv = 5
        dbclnp = dbclasd(n_neighbors =  int(len(X)/dbclnpdiv)).fit(Xnp.values)
        dbclnptime = time.time() - proctime

        for var, lab in zip(cluvarlist,labvarlist):

            # Number of clusters in labels, ignoring noise if present.
            labels = eval(var).labels_
            n_clusters_ = len(set(labels)) - (1 if -1 in labels else 0)
            n_noise_ = list(labels).count(-1)
            cmatrix = metrics.confusion_matrix(labels_true, labels)

            if real_n_noise + n_noise_ == 0:
                outacc = 1
                noutacc = 1
                ovacc = 1
            else:
                correct_n_noise = cmatrix[0][0]
                incorrect_non_outliers = cmatrix[1][0]
                outacc = (correct_n_noise/real_n_noise)
                noutacc = ((real_non_outliers-incorrect_non_outliers)/real_non_outliers)
                ovacc = (correct_n_noise+(real_non_outliers-incorrect_non_outliers))/(real_n_noise + real_non_outliers)

            if n_clusters_+ n_noise_ == 1:
                silhouette=1
```

```
        elif n_clusters_+ n_noise_ == len(labels):
            silhouette=-1
        else:
            silhouette=metrics.silhouette_score(X, labels)

        proctime = eval(var+'time')

        print(f'{filename} , Index: {i}\n____________ {lab} RESULTS _______________')
        print('No of clusters:\t\t\t %d' % n_clusters_)
        print('No of noise points:\t\t %d' % n_noise_)
        print("Cluster Accuracy:\t\t %0.4f" % metrics.accuracy_score(labels_true, labels)) #fraction of correctly classified samples (ALL)

        print("Overall Accuracy:\t\t %0.4f" %ovacc) #fraction of correctly classified samples (ALL)
        print("Outliers Accuracy:\t\t %0.4f" %outacc) #fraction of correctly classified outliers (-1)
        print("Non-Outliers Accuracy:\t\t %0.4f" %noutacc) #fraction of correctly classified non-outliers (non -1)

        print("Homogeneity:\t\t\t %0.4f" % metrics.homogeneity_score(labels_true, labels)) #fraction of correctly classified members of a single class.
        print("Completeness:\t\t\t %0.4f" % metrics.completeness_score(labels_true, labels)) #data points that are members of a given class are elements of the same cluster.
        print("V-measure:\t\t\t %0.4f" % metrics.v_measure_score(labels_true, labels)) #harmonic mean between homogeneity and completeness
        print("Adjusted Rand Index:\t\t %0.4f" #counting pairs that are assigned in the same or different clusters in the predicted and true clusterings.
              % metrics.adjusted_rand_score(labels_true, labels))
        print("Adjusted Mutual Information:\t %0.4f" #measure of the similarity between two labels of the same data
              % metrics.adjusted_mutual_info_score(labels_true, labels, average_method='arithmetic'))
        print("Silhouette Coefficient:\t\t %0.4f" #mean relationship between mean intra-cluster and mean nearest-cluster distances for each sample.
              % silhouette)
        print('Confusion Matrix\n', cmatrix)

        pstr = "Params = None"

        if (var == 'db' or var == 'dbnp'):
            pstr = ('eps:%.2f' %eval(var).eps + '\nmin_samples:%.0f' %eval(var).min_samples)

        if (var == 'op' or var == 'opnp'):
            pstr = ('xi:%.3f' %eval(var).xi + '\nmin_samples:%.0f' %eval(var).min_samples
                    + '\nmin_size:%.2f' %eval(var).min_cluster_size)

        if (var == 'opdb' or var == 'opdbnp'):
            pstr = ('eps:%.2f' %eval(var).max_eps + '\nmin_samples:%.0f' %eval(var).min_samples)

        if (var == 'hdb' or var == 'hdbnp'):
            pstr = ('min_size:%.2f' %eval(var).min_cluster_size + '\nmin_samples:%.0f' %eval(var).min_samples
                    + '\nleaf_size:%.2f' %eval(var).leaf_size)

```

```
        if (var == 'dcl' or var == 'dclnp'):
            pstr = ('eps:%.1e' %eval(var).eps + '\nmin_density:%.1e'
              %eval(var).min_density)

        if (var == 'dbcl'):
            pstr = ('n_neighbors:%i' %eval(var).n_neighbors + '\nArea%%:%.2f'
              %(1/dbcldiv))

        if (var == 'dbclnp'):
            pstr = ('n_neighbors:%i' %eval(var).n_neighbors + '\nArea%%:%.2f'
              %(1/dbclnpdiv))


        Results.loc[len(Results)] = np.array([filename, sheet, lab, pstr, n_clusters_,
         n_noise_,metrics.accuracy_score(labels_true, labels),ovacc, outacc,noutacc,
         metrics.homogeneity_score(labels_true, labels),
         metrics.completeness_score(labels_true, labels),
         metrics.v_measure_score(labels_true, labels),
         metrics.adjusted_rand_score(labels_true, labels),
         metrics.adjusted_mutual_info_score(labels_true, labels,
         average_method='arithmetic'), silhouette, proctime])

        unique_labels = set(labels)
        colors = [plt.cm.Set3(each)
                  for each in np.linspace(0, 1, len(unique_labels))]

        fig, ax = plt.subplots()
        ax.text(res1 + 1.5, 1, pstr, fontsize=7,verticalalignment='top', bbox=props)


        # ############### RESULTS PLOT ########################################
        # Black removed and is used for noise instead.
        for k, col in zip(unique_labels, colors):
            if k == -1:
                # Black used for noise.
                col = [0, 0, 0, 1]

            class_member_mask = (labels == k)

            xy = X[class_member_mask & core_samples_mask]
            ax.plot(xy['Column'], xy['Row'], 'o', markerfacecolor=tuple(col),
                     markeredgecolor='k', markersize=7)

            xy = X[class_member_mask & ~core_samples_mask]
            ax.plot(xy['Column'], xy['Row'], 'o', markerfacecolor=tuple(col),
                     markeredgecolor='k', markersize=5)

        plt.xticks(np.arange(0, res1+1, res1/8))
        plt.yticks(np.arange(0, res1+1, res1/8))
        plt.title(f'{filename} - {lab} [Clusters: {n_clusters_}, Noise: {n_noise_}]')
        ax.axis([-0.5, res1+0.5, -0.5, res2+0.5])
        ax.set_aspect(1)
        ax.invert_yaxis()

        plt.savefig(f'Data\Cluster data subset\{filename}\{lab} - {filename}.tif',
              dpi=200, bbox_inches='tight')
        plt.clf()

    #### Create TIF files
```

```
        with tifffile.TiffWriter(f'Data\Cluster data subset\{filename} {sheet} - Cluster Plots.tif') as stack:
            for fname in sorted(glob.glob(f'Data\Cluster data subset\{filename}\*.tif'), key=os.path.getmtime):
                stack.save(tifffile.imread(fname), compress=6)

# Write Results in Excel
from excelappend import append_df_to_excel
append_df_to_excel(f'Data\Cluster data subset\Cluster Results.xlsx',Results, sheet_name="Results")

print('Processing Time: ', (time.time() - start))

# ############################# END ################################################
```

Appendix D

Python Code: Spatial Autocorrelation and Statistical Features

```
# -*- coding: utf-8 -*-
"""
Created on Thu Apr  4 13:22:31 2019

@author: Joan Martinez
"""

import numpy as np
import pandas as pd
import scipy as sp
import pysal
import matplotlib.pyplot as plt
import matplotlib as mpl
import skimage.feature as sf
import sys
import time
import glob
import os
from skimage.external import tifffile

sys.path.append(os.getcwd()+'\\biokit\\viz')
import corrplot

# create colormap
upper = mpl.cm.jet(np.arange(int(256/4.5),256))
cmap = mpl.colors.ListedColormap(upper, name='myColorMap', N=upper.shape[0])


# ##############################################################################
# Load data

sheet = 'Seatpan'
Dataset = 'Static'
#Dataset = 'Paired'

Y1 = pd.read_excel('Data\\{Dataset} data subset.xlsx', sheet_name=sheet)

os.makedirs('Data\\{Dataset} data subset\\' + sheet + '\\Results' , exist_ok=True)
os.makedirs('Data\\{Dataset} data subset\\' + sheet + '\\Plots', exist_ok=True)

nindex = np.size(Y1.iloc[1,:])

res1 = 32
res2 = 32
pmax = 300

Y = np.float32(Y1.values.reshape(res1,res2,nindex))
Ym = np.ma.masked_where(Y == 0, Y) ## unactive cells = 0 mmHg
Y1m = np.ma.masked_where(Y1 == 0, Y1) ## unactive cells = 0 mmHg

##############################################################################
##############################################################################

#Spatial Autocorrelation Variales
miarrq, gcarrq, miarrc, gcarrc, miarrid, gcarrid = (np.zeros(nindex) for _ in range(6))

# Weight Matrix for Autocorrelation
wq = pysal.lat2W(res1,res2, rook = False)
X = np.array(np.meshgrid(np.arange(1,res1+1),np.arange(1,res2+1))).T.reshape(-1,2)
```

```
wid = pysal.threshold_continuousW_from_array(X,2*2**0.5)
wc = pysal.threshold_continuousW_from_array(X,2*2**0.5, alpha = 0)

#First Order Statistics Variables
ctarr, sumarr, meanarr,sdarr,cvarr, skewarr,kurtarr = (np.zeros(nindex) for _ in range(7))
histarr = np.zeros(shape=(pmax+1, nindex))

#Gradient Variables
diffx = np.ma.array(np.zeros(shape = (res1,res2-1,nindex)))
diffy = np.ma.array(np.zeros(shape = (res1-1,res2,nindex)))
gradx,grady = (np.ma.array(np.zeros(shape = (res1,res2,nindex))) for _ in range(2))
histdiffxarr, histdiffyarr = (np.zeros(shape=(pmax+1, nindex)) for _ in range(2))

#GLD Variables
gradprobdistrx,gradprobdistry = (np.zeros(shape=(pmax+1, nindex)) for _ in range(2))
[gradcontrastx,gradcontrasty,gradsecmomentx,gradsecmomenty,
 gradentropyx,gradentropyy,gradmeanx,gradmeany,
 invdiffmomx,invdiffmomy] = (np.zeros(nindex) for _ in range(10))

#GLSD Variables
[glsd_energyx,glsd_energyy,glsd_contrastx,glsd_contrasty,
 glsd_correlationx,glsd_correlationy,glsd_homogeneityx,glsd_homogeneityy,
 glsd_entropyx,glsd_entropyy] = (np.zeros(nindex) for _ in range(10))


start = time.time()
#INDEX LOOP
i = 0
for i in range(nindex):

    miarrq[i] = "%.5f" %pysal.Moran(Y[:,:,i], wq, permutations=2).I
    gcarrq[i] = "%.5f" %pysal.Geary(Y[:,:,i], wq, permutations=2).C

    miarrc[i] = "%.5f" %pysal.Moran(Y[:,:,i], wc, permutations=2).I
    gcarrc[i] = "%.5f" %pysal.Geary(Y[:,:,i], wc, permutations=2).C

    miarrid[i] = "%.5f" %pysal.Moran(Y[:,:,i], wid, permutations=2).I
    gcarrid[i] = "%.5f" %pysal.Geary(Y[:,:,i], wid, permutations=2).C

    histarr[:,[i]] = np.histogram([Ym[:,:,i]],pmax+1)[0].reshape(pmax+1,1)

    ## Only active cells
    ctarr[i] = np.ma.MaskedArray.count(Y1m[:,i])
    sumarr[i] = np.ma.MaskedArray.sum(Y1m[:,i])
    meanarr[i] = "%.5f"%sp.stats.mstats.describe(Y1m[:,i]).mean
    sdarr[i] = "%.5f"%np.sqrt(sp.stats.mstats.describe(Y1m[:,i]).variance
    cvarr[i] = "%.5f"%sp.stats.mstats.variation(Y1m[:,i])
    skewarr[i] = "%.5f"%sp.stats.mstats.skew(Y1m[:,i])
    kurtarr[i] = "%.5f"%sp.stats.mstats.kurtosis(Y1m[:,i])

    ## FIRST ORDER GRADIENT
    diffy[:,:,i] = abs(np.diff(Ym[:,:,i], axis=0))
    diffx[:,:,i] = abs(np.diff(Ym[:,:,i], axis=1))

    histdiffxarr[:,[i]] = np.histogram(diffx[:,:,i].compressed(),pmax+1, [0,pmax])[0].reshape(pmax+1,1)
    histdiffyarr[:,[i]] = np.histogram(diffy[:,:,i].compressed(),pmax+1, [0,pmax])[0].reshape(pmax+1,1)
```

```

    gradprobdistrx[:,[i]] = histdiffxarr[:,[i]]/np.sum(histdiffxarr[:,[i]])
    gradprobdistry[:,[i]] = histdiffyarr[:,[i]]/np.sum(histdiffyarr[:,[i]])

    gradcontrastx[i] = np.sum(gradprobdistrx[:,[i]]*(np.arange(pmax+1).reshape(pmax+1,1))**2)
    gradcontrasty[i] = np.sum(gradprobdistry[:,[i]]*(np.arange(pmax+1).reshape(pmax+1,1))**2)

    gradsecmomentx[i] = np.sum(gradprobdistrx[:,[i]]**2)
    gradsecmomenty[i] = np.sum(gradprobdistry[:,[i]]**2)

    gradentropyx[i] = sp.stats.entropy(gradprobdistrx[:,[i]], base=2)[0]
    gradentropyy[i] = sp.stats.entropy(gradprobdistry[:,[i]], base=2)[0]

    gradmeanx[i] = np.sum(gradprobdistrx[:,[i]]*(np.arange(pmax+1).reshape(pmax+1,1)))
    gradmeany[i] = np.sum(gradprobdistry[:,[i]]*(np.arange(pmax+1).reshape(pmax+1,1)))

    invdiffmomx[i] = np.sum(gradprobdistrx[:,[i]]/((np.arange(pmax+1).reshape(pmax+1,1))**2+1))
    invdiffmomy[i] = np.sum(gradprobdistry[:,[i]]/((np.arange(pmax+1).reshape(pmax+1,1))**2+1))

    ## SECOND ORDER CENTRAL GRADIENT
    grady[:,:,i] = np.gradient(Ym[:,:,i], edge_order=1, axis=0)
    gradx[:,:,i] = np.gradient(Ym[:,:,i], edge_order=1, axis=1)

    ########################### SECOND ORDER STAT FEATURES ##########

    #Removing first 0 pressure column
    gcm2 = np.float64(sf.greycomatrix(np.uint16(np.round(Ym[:,:,i])),[1],[0, np.pi/2], levels=pmax+1, symmetric=True)[1:,1:,:,:])
    gcm2[:,:,0,0] = gcm2[:,:,0,0]/np.sum(gcm2[:,:,0,0])
    gcm2[:,:,0,1] = gcm2[:,:,0,1]/np.sum(gcm2[:,:,0,1])

    glsd_energyx[i] = (sf.greycoprops(gcm2, "energy")**2)[0,0]
    glsd_energyy[i] = (sf.greycoprops(gcm2, "energy")**2)[0,1]

    glsd_contrastx[i] = sf.greycoprops(gcm2, "contrast")[0,0]
    glsd_contrasty[i] = sf.greycoprops(gcm2, "contrast")[0,1]

    glsd_correlationx[i] = sf.greycoprops(gcm2, "correlation")[0,0]
    glsd_correlationy[i] = sf.greycoprops(gcm2, "correlation")[0,1]

    glsd_entropyx[i] = sp.stats.entropy(np.reshape(gcm2,(-1,2)), base=2)[np.newaxis][0,0]
    glsd_entropyy[i] = sp.stats.entropy(np.reshape(gcm2,(-1,2)), base=2)[np.newaxis][0,1]

    glsd_homogeneityx[i] = sf.greycoprops(gcm2, "homogeneity")[0,0]
    glsd_homogeneityy[i] = sf.greycoprops(gcm2, "homogeneity")[0,1]

print('Processing Indexes Time: ', (time.time() - start))

#### WRITE RESULTS IN EXCEL ####################################

filenames = Y1.columns

```

```
resvarlist = ['filenames', 'miarrq', 'gcarrq', 'miarrc', 'gcarrc', 'miarrid', 'gcarrid', 'ctarr', 'sumarr','meanarr', 'sdarr', 'cvarr', 'skewarr', 'kurtarr']

labvarlist = ['Sample', "Moran's I (Q)", "Geary's C (Q)", "Moran's I (CD)", "Geary's C (CD)", "Moran's I (ID)", "Geary's C (ID)", 'Contact Cells', 'Sum of Pressure', 'Mean Pressure', 'Standard Deviation', 'Coefficient of Variation', 'Skewness', 'Kurtosis']

resvarlistx = ['gradcontrastx', 'gradsecmomentx', 'gradentropyx', 'gradmeanx', 'invdiffmomx', 'glsd_energyx', 'glsd_contrastx', 'glsd_correlationx', 'glsd_entropyx', 'glsd_homogeneityx']

labvarlistx = ['GLD - Gradient Contrast X', 'GLD - Gradient Second Moment X', 'GLD - Gradient Entropy X', 'GLD - Gradient Mean X', 'GLD - Inverse-Difference Moment X', 'GLSD - Energy X', 'GLSD - Contrast X', 'GLSD - Correlation X', 'GLSD - Entropy X', 'GLSD - Homogeneity X']

resvarlisty = ['gradcontrasty', 'gradsecmomenty', 'gradentropyy', 'gradmeany', 'invdiffmomy', 'glsd_energyy', 'glsd_contrasty', 'glsd_correlationy', 'glsd_entropyy', 'glsd_homogeneityy']

labvarlisty = ['GLD - Gradient Contrast Y', 'GLD - Gradient Second Moment Y', 'GLD - Gradient Entropy Y', 'GLD - Gradient Mean Y', 'GLD - Inverse-Difference Moment Y', 'GLSD - Energy Y', 'GLSD - Contrast Y', 'GLSD - Correlation Y', 'GLSD - Entropy Y', 'GLSD - Homogeneity Y']

Results = pd.DataFrame(columns=labvarlist + labvarlistx + labvarlisty)

for var, lab in zip(resvarlist + resvarlistx + resvarlisty,labvarlist + labvarlistx + labvarlisty):
    Results[lab] = eval(var)

from excelappend import append_df_to_excel
append_df_to_excel(f'Data\\{Dataset} data subset\\{sheet}\Results\{Dataset} Pressure Parameteres Results.xlsx',Results,sheet_name=sheet)

corr = Results.corr(method='pearson')
c = corrplot.Corrplot(corr)
c.plot(method='ellipse', shrink=0.8, rotation=45, upper='text', lower='pie')
fig = plt.gcf()
fig.set_size_inches(20, 16);
plt.title(f'{Dataset} Data Subset - Pressure Parameters Correlations')
plt.savefig(f'Data\\{Dataset} data subset\\{sheet}\\{Dataset} Pressure Parameters Correlations.tif', dpi=200, bbox_inches='tight')

append_df_to_excel(f'Data\\{Dataset} data subset\\{sheet}\Results\{Dataset} Pressure Parameteres Correlations.xlsx',corr,sheet_name=sheet)


######## INDEXES MAPS & PLOTS ##############################
start = time.time()
dpishow = 100
dpisave = 200

i = 0
for i in range(nindex):
    plt.clf()
    plt.figure(figsize=(5, 4), dpi=200)
    plt.imshow(Ym[:,:,i], cmap=cmap);
```

```
    plt.clim(0,pmax)
    plt.colorbar()
    plt.title(f'%s, Pressure Map (mmHg) [CV = %.3f]' %(filenames[i],cvarr[i]))
    #plt.show()
    plt.savefig(f'Data\\{Dataset} data subset\\{sheet}\Plots\Pressure Map - Sample %s.tif' %filenames[i], dpi=dpisave, bbox_inches='tight')

    plt.clf()
    plt.figure(figsize=(5, 2), dpi=dpishow)
    plt.hist(Y1m[:,i].compressed(),pmax+1,[0,pmax])
    plt.xlabel('Pressure (mmHg)', fontsize=12)
    plt.title(f'%s, {sheet} Pressure Histogram' %filenames[i])
    #plt.show()
    plt.savefig(f'Data\\{Dataset} data subset\\{sheet}\Plots\Histogram - Sample %s.tif' %filenames[i], dpi=dpisave, bbox_inches='tight')

    plt.clf()
    fig, (ax1, ax2) = plt.subplots(1, 2, dpi=dpishow)
    im1=ax1.imshow(gradx[:,:,i], cmap='seismic', vmin=-pmax, vmax=pmax);
    ax1.set_title('[0°, X-axis]')
    im2=ax2.imshow(grady[:,:,i], cmap='seismic', vmin=-pmax, vmax=pmax);
    ax2.set_title('[90°, Y-axis]')
    fig.subplots_adjust(right=1.2)
    cbar_ax = fig.add_axes([1, 0.15, 0.05, 0.7])
    fig.colorbar(im2, cax=cbar_ax)
    plt.suptitle(f'%s, {sheet} Second Order Central Gradient Map (mmHg)' %filenames[i], horizontalalignment='center')
    fig.tight_layout(rect=[0, 0.03, 1, 0.95])
    #plt.show()
    plt.savefig(f'Data\\{Dataset} data subset\\{sheet}\Plots\Central Gradient Map - Sample %s.tif' %filenames[i], dpi=dpisave, bbox_inches='tight')

    plt.clf()
    fig, (ax1, ax2) = plt.subplots(1,2, dpi=dpishow)
    gim1=ax1.imshow(diffx[:,:,i], cmap='YlOrRd', vmin=0, vmax=pmax);
    ax1.set_title('[0°, X-axis]')
    im2=ax2.imshow(diffy[:,:,i], cmap='YlOrRd', vmin=0, vmax=pmax);
    ax2.set_title('[90°, Y-axis]')
    fig.subplots_adjust(right=1.2)
    cbar_ax = fig.add_axes([1, 0.15, 0.05, 0.7])
    fig.colorbar(im2, cax=cbar_ax)
    plt.suptitle(f'%s, {sheet} First Order Absolute Gradient Map (mmHg)' %filenames[i], horizontalalignment='center')
    fig.tight_layout(rect=[0, 0.03, 1, 0.95])
    #plt.show()
    plt.savefig(f'Data\\{Dataset} data subset\\{sheet}\Plots\Absolute Gradient Map - Sample %s.tif' %filenames[i], dpi=dpisave, bbox_inches='tight')

    plt.clf()
    fig, (ax1, ax2) = plt.subplots(1,2, figsize=(8,3), dpi=dpishow, sharey=True)
    im1=ax1.hist(diffx[:,:,i].compressed(),pmax+1,[0,pmax]);
    ax1.set_title('[0°, X-axis]')
    ax1.set_xticks(np.arange(0, pmax+1, 50))
    ax1.set_xlabel('Pressure (mmHg)', fontsize=10)
    im2=ax2.hist(diffy[:,:,i].compressed(),pmax+1,[0,pmax]);
    ax2.set_title('[90°, Y-axis]')
    ax2.set_xticks(np.arange(0, pmax+1, 50))
    ax2.set_xlabel('Pressure (mmHg)', fontsize=10)
```

```python
    plt.suptitle(f'%s, {sheet} First Order Absolute Gradient Histogram (mmHg)' %filenames[i], horizontalalignment='center')
    fig.tight_layout(rect=[0, 0.03, 1, 0.95])
    #plt.show()
    plt.savefig(f'Data\\{Dataset} data subset\\{sheet}\Plots\Absolute Gradient Histogram - Sample %s.tif' %filenames[i], dpi=dpisave, bbox_inches='tight')
    plt.clf()

#### Create TIF files
with tifffile.TiffWriter(f'Data\\{Dataset} data subset\\{sheet}\{Dataset} Data Subset Pressure Maps.tif') as stack:
    for fname in sorted(glob.glob(f'Data\\{Dataset} data subset\\{sheet}\Plots\Pressure Map - Sample*.tif'), key=os.path.getmtime):
        stack.save(tifffile.imread(fname), compress=6)

with tifffile.TiffWriter(f'Data\\{Dataset} data subset\\{sheet}\{Dataset} Data Subset Pressure Histograms.tif') as stack:
    for fname in sorted(glob.glob(f'Data\\{Dataset} data subset\\{sheet}\Plots\Histogram - Sample*.tif'), key=os.path.getmtime):
        stack.save(tifffile.imread(fname), compress=6)

with tifffile.TiffWriter(f'Data\\{Dataset} data subset\\{sheet}\{Dataset} Data Subset, Central Gradient Map.tif') as stack:
    for fname in sorted(glob.glob(f'Data\\{Dataset} data subset\\{sheet}\Plots\Central Gradient Map - Sample*.tif'), key=os.path.getmtime):
        stack.save(tifffile.imread(fname), compress=6)

with tifffile.TiffWriter(f'Data\\{Dataset} data subset\\{sheet}\{Dataset} Data Subset Absolute Gradient Map.tif') as stack:
    for fname in sorted(glob.glob(f'Data\\{Dataset} data subset\\{sheet}\Plots\Absolute Gradient Map - Sample*.tif'), key=os.path.getmtime):
        stack.save(tifffile.imread(fname), compress=6)

with tifffile.TiffWriter(f'Data\\{Dataset} data subset\\{sheet}\{Dataset} Data Subset Absolute Gradient Histogram.tif') as stack:
    for fname in sorted(glob.glob(f'Data\\{Dataset} data subset\\{sheet}\Plots\Absolute Gradient Histogram - Sample*.tif'), key=os.path.getmtime):
        stack.save(tifffile.imread(fname), compress=6)

print('Processing Plots Time: ', (time.time() - start))
```

Appendix E

Python Code: Image Registration and Similarity/Dissimilarity Coefficients

```
# -*- coding: utf-8 -*-
"""
Created on Mon Aug 5 10:22:04 2019

@author: Joan Martinez
"""

import numpy as np
import pandas as pd
import scipy as sp
import matplotlib.pyplot as plt
import matplotlib as mpl
import time
import glob
import os
from skimage.external import tifffile
from scipy.ndimage import rotate, shift
import SimpleITK as sitk

# create colormap
upper = mpl.cm.jet(np.arange(int(256/4.5),256))
cmap = mpl.colors.ListedColormap(upper, name='myColorMap', N=upper.shape[0])

# ##############################################################################
# Load data

Dataset = "Synthetic"
sheet = 'Seatpan'
sheet2 = 'Template'

Y1 = pd.read_excel(f'Data\\{Dataset} data subset.xlsx', sheet_name=sheet)
Y2 = pd.read_excel(f'Data\\{Dataset} data subset.xlsx', sheet_name=sheet2)

Y1m = np.ma.masked_where(Y1 == 0, Y1) ## unactive cells = 0 mmHg
Y2m = np.ma.masked_where(Y2 == 0, Y2) ## unactive cells = 0 mmHg

nindex1 = np.size(Y1.iloc[1,:])
nindex2 = np.size(Y2.iloc[1,:])

res1 = 32
res2 = 32
pmax = 300

X1 = np.float32(Y1.values.reshape(res1,res2,nindex1))
X1m = np.ma.masked_where(X1 == 0, X1) ## unactive cells = 0 mmHg

X2 = np.float32(Y2.values.reshape(res1,res2,nindex2))
X2m = np.ma.masked_where(X2 == 0, X2) ## unactive cells = 0 mmHg


##############################################################################
##############################################################################

i = 0
j = 0
eps = 1

filename1 = Y1.columns[i]
filename2 = Y2.columns[j]
```

```
if Dataset == "Synthetic":
    # Apply transformation
    hloc = 1
    vloc = -1
    rot = -15

    template = shift(X2[:,:,j], [-vloc,hloc],order=0,prefilter=False)
    template = rotate(template, rot, reshape=False)
else:
    [hloc,vloc,rot] = (0 for _ in range(3))
    template = X2[:,:,j]

plt.imshow(X1[:,:,i])
plt.show()
plt.imshow(template)
print("\n",filename1," vs ", filename2)

os.makedirs(f'Data\{Dataset} data subset\\' + filename1 + ' vs ' + filename2 ,
             exist_ok=True)

dpishow = 100
dpisave = 200

for method in ["MI","MSE"]:

    # Callback invoked when the StartEvent happens, sets up our new data.
    def start_plot():
        global metric_values, multires_iterations

        metric_values = []
        multires_iterations = []

    # Callback invoked when the EndEvent happens, do cleanup of data and figure.
    def end_plot():
        global metric_values, multires_iterations

        del metric_values
        del multires_iterations
        # Close figure, we don't want to get a duplicate of the plot latter on.
        plt.close()

        # Callback invoked when the IterationEvent happens, update our data and
        # save an image that includes a visualization of the registered images and
        # the metric value plot.
        def save_plot(registration_method, fixed, moving, transform, file_name_prefix):

            #
            # Plotting the similarity metric values, resolution changes are marked with
            # a blue star.
            #
            global metric_values, multires_iterations, ref, trans, regmetric, iterreg

            metric_values.append(registration_method.GetMetricValue())


            moving_transformed = sitk.Resample(moving, fixed, transform,
                                               sitk.sitkLinear, 0.0,
                                               moving_image.GetPixelIDValue())

```

```python
        ref = np.dstack((ref, sitk.GetArrayFromImage(fixed)))
        trans = np.dstack((trans,sitk.GetArrayFromImage(moving_transformed)))
        regmetric = np.append(regmetric,registration_method.GetMetricValue())
        iterreg = [index for index in multires_iterations]

    # Callback invoked when the sitkMultiResolutionIterationEvent happens, update the Index into the metric_values list.
    def update_multires_iterations():
        global metric_values, multires_iterations
        multires_iterations.append(len(metric_values))

    if __name__ == '__main__':

        # Read the images
        factor = 10
        ref = np.zeros(shape = (res1*factor,res2*factor,0))
        trans = np.zeros(shape = (res1*factor,res2*factor,0))
        regmetric = np.zeros(0)
        iterreg = np.zeros(0)

        fixed_image =  sitk.Expand(sitk.GetImageFromArray(X1[:,:,i]),[factor]*2, sitk.sitkLinear)
        moving_image = sitk.Expand(sitk.GetImageFromArray(template),[factor]*2, sitk.sitkLinear)

        fig, (ax1, ax2) = plt.subplots(1, 2, dpi=dpishow)
        im1 = ax1.imshow(np.ma.masked_where(sitk.GetArrayFromImage(fixed_image) < 1, sitk.GetArrayFromImage(fixed_image)), cmap=cmap, vmax = pmax)
        ax1.set_title(f'[Reference Image]')
        ax2.imshow(np.ma.masked_where(sitk.GetArrayFromImage(moving_image) < 1, sitk.GetArrayFromImage(moving_image)), cmap=cmap, vmax = pmax)
        ax2.set_title(f'[Template Image]')
        fig.subplots_adjust(right=1.2)
        cbar_ax = fig.add_axes([1, 0.15, 0.05, 0.7])
        fig.colorbar(im1, cax=cbar_ax)
        plt.suptitle(f'{method} Image Registration: {filename1} vs {filename2}, Scaling Factor: {factor}', horizontalalignment='center')
        fig.tight_layout(rect=[0, 0.03, 1, 0.95])
        plt.savefig(f'Data\{Dataset} data subset\{filename1} vs {filename2}\{method} Image Registration, {filename1} vs {filename2} Template.tif', dpi=200, bbox_inches='tight')

        # Multi-resolution rigid registration
        registration_method = sitk.ImageRegistrationMethod()

        # Initial alignment of the two volumes
        transform = sitk.CenteredTransformInitializer(fixed_image,
                                                      moving_image,
                                                      sitk.Euler2DTransform(),
                                                      sitk.CenteredTransformInitializerFilter.MOMENTS)


        if method == "MI":
            registration_method.SetMetricAsJointHistogramMutualInformation(numberOfHistogramBins=50, varianceForJointPDFSmoothing = 1.5)
        elif method == "MSE":
            registration_method.SetMetricAsMeanSquares()

```

```
            registration_method.SetInterpolator(sitk.sitkLinear)
            registration_method.SetOptimizerAsGradientDescent(learningRate=1.0,
                                                                  numberOfIterations=300,
                                                                  convergenceMinimumValue=1e-5, convergenceWindowSize=5)

            registration_method.SetOptimizerScalesFromPhysicalShift()
            registration_method.SetShrinkFactorsPerLevel(shrinkFactors = [4,2,1]) #1,1,1
            registration_method.SetSmoothingSigmasPerLevel(smoothingSigmas=[0,0,0])
            registration_method.SmoothingSigmasAreSpecifiedInPhysicalUnitsOn()
            registration_method.SetInitialTransform(transform)

            # Add all the callbacks responsible for ploting
            registration_method.AddCommand(sitk.sitkStartEvent, start_plot)
            registration_method.AddCommand(sitk.sitkEndEvent, end_plot)
            registration_method.AddCommand(sitk.sitkMultiResolutionIterationEvent, update_multires_iterations)
            registration_method.AddCommand(sitk.sitkIterationEvent, lambda: save_plot(registration_method, fixed_image, moving_image, transform, f'Data/{Dataset} data subset/{filename1} vs {filename2}/{method} iteration_plot'))

        start = time.time()
        registration_method.Execute(fixed_image, moving_image)
        #sitk.WriteTransform(transform, 'Data/Similarities/ct2mrT1.tfm')
        print(time.time()-start)

        refm2d = np.ma.masked_where(ref < 1, ref)
        transm2d = np.ma.masked_where(trans < 1, trans)
        refm1d = refm2d.reshape(res1*factor*res2*factor,len(ref[0,0,:]))
        transm1d = transm2d.reshape(res1*factor*res2*factor,len(trans[0,0,:]))
        diffm2d = np.ma.array(refm2d.data-transm2d.data,
                  mask=np.logical_and(refm2d.mask,transm2d.mask))

        [pcc2imgreg, pcc3imgreg, tm1imgreg, tm2imgreg, minr1imgreg, minr2imgreg,
         l1n1imgreg, l1n2imgreg, l2n1imgreg, l2n2imgreg, irvar1imgreg, irvar2imgreg,
         ct_ireg, ct_jreg, sum_ireg, sum_jreg, mean_ireg, mean_jreg, cv_ireg, cv_jreg,
         cpx_ireg, cpx_jreg, cpy_ireg, cpy_jreg, ct_regdiff, cp_regdiff] = (np.zeros(len(ref[0,0,:])) for _ in range(26))


        # Plot the similarity metric values
        plt.clf()
        plt.plot(regmetric, 'r')
        plt.plot(iterreg, [regmetric[index] for index in iterreg], 'b*')
        plt.xlabel('Iteration Number',fontsize=12)
        plt.ylabel(f'{method} Metric Value',fontsize=12)
        if max(regmetric)>1000:
            plt.axis([0, len(regmetric), min(regmetric)-0.1*1000, 1000])
        else:
            plt.axis([0, len(regmetric), min(regmetric)-abs(0.1*max(regmetric)), abs(0.1*max(regmetric))+max(regmetric)])
        plt.suptitle(f'{method} Image Registration: {filename1} vs {filename2}, Iterations of Interest {np.array(iterreg[1:])-1})', horizontalalignment='center')
        plt.savefig(f'Data\{Dataset} data subset\{filename1} vs {filename2}\{method} Image Registration, {filename1} vs {filename2} Iteration Metric Plot.tif', dpi=200, bbox_inches='tight')
```

```
        props = dict(boxstyle='round', facecolor='wheat', alpha=0.3)
        for x in range(len(ref[0,0,:])):

            ## PRESSURE PARAMETERS
            ct_ireg[x] = np.ma.MaskedArray.count(refm1d[:,x])
            sum_ireg[x] = np.ma.MaskedArray.sum(refm1d[:,x])
            mean_ireg[x] = sp.stats.mstats.describe(refm1d[:,x]).mean  ## Only active cells
            cv_ireg[x] = sp.stats.mstats.variation(refm1d[:,x])
            cpx_ireg[x] = sp.ndimage.measurements.center_of_mass(refm2d[:,:,x])[0]
            cpy_ireg[x] = sp.ndimage.measurements.center_of_mass(refm2d[:,:,x])[1]

            ct_jreg[x] = np.ma.MaskedArray.count(transm1d[:,x])
            sum_jreg[x] = np.ma.MaskedArray.sum(transm1d[:,x])
            mean_jreg[x] = sp.stats.mstats.describe(transm1d[:,x]).mean # Only active cells
            cv_jreg[x] = sp.stats.mstats.variation(transm1d[:,x])

            if ct_jreg[x]>0:
                cpx_jreg[x] = sp.ndimage.measurements.center_of_mass(transm2d[:,:,x])[0]
                cpy_jreg[x] = sp.ndimage.measurements.center_of_mass(transm2d[:,:,x])[1]

            ct_regdiff[x]=abs(ct_ireg[x]-ct_jreg[x])
            cp_regdiff[x]=((cpx_ireg[x]-cpx_jreg[x])**2+(cpy_ireg[x]-cpy_jreg[x])**2)**0.5


            # SIMILARITY MEASURES #######################################################
            #Person Correlation Coefficient
            pcc2imgreg[x] = np.ma.corrcoef(refm1d[:,x],transm1d[:,x])[0,1] #Masked
            pcc3imgreg[x] = np.corrcoef(refm1d[:,x].data,transm1d[:,x].data)[0,1] #Non-Masked

            #Tanimoto Measure
            tm1imgreg[x] = np.ma.sum(refm1d[:,x]*transm1d[:,x])/(np.ma.sum((refm1d[:,x]-transm1d[:,x])**2)+np.ma.sum(refm1d[:,x]*transm1d[:,x])) #Masked
            tm2imgreg[x] = np.sum(refm1d[:,x].data*transm1d[:,x].data)/(np.sum((refm1d[:,x].data-transm1d[:,x].data)**2)+np.sum(refm1d[:,x].data*transm1d[:,x].data)) #Non-Masked

            #Min-Ratio
            minr1reg = np.ma.minimum([refm1d[:,x]/transm1d[:,x]],[transm1d[:,x]/refm1d[:,x]]).reshape(-1,1)
            minr1reg = np.ma.array(minr1reg,mask=np.logical_or(refm1d[:,x].mask,transm1d[:,x].mask))
            minr1imgreg[x] = np.ma.mean(minr1reg) #Masked

            Y1epsreg = refm1d[:,x]+eps
            Y2epsreg = transm1d[:,x]+eps
            minr2reg = np.minimum([Y1epsreg/Y2epsreg],[Y2epsreg/Y1epsreg]).reshape(-1,1)
            minr2reg = np.ma.array(minr2reg, mask = np.logical_and(Y1epsreg.mask, Y2epsreg.mask))
            minr2imgreg[x] = np.mean(minr2reg) #Non-Masked ()

            # DISSIMILARITY MEASURES ########################################################

            #L1 Norm
            l1n1imgreg[x] = np.ma.sum(abs(refm1d[:,x]-transm1d[:,x])) #Masked
            l1n2imgreg[x] = np.sum(abs(refm1d[:,x].data-transm1d[:,x].data)) #Non-Masked

```

```
        #L2 Norm
        l2n1imgreg[x] = np.ma.sum((refm1d[:,x]-transm1d[:,x])**2) #Masked
        l2n2imgreg[x] = np.sum((refm1d[:,x].data-transm1d[:,x].data)**2) #Non-Masked

        #Intensity-Ratio Variance
        irvar1imgreg[x] = np.ma.var(refm1d[:,x]/transm1d[:,x]) #Masked

        irvar2reg = np.ma.array(Y1epsreg/Y2epsreg, mask = np.logical_and(Y1epsreg.mask, Y2epsreg.mask))
        irvar2imgreg[x] = np.var(irvar2reg) #Non-Masked

        plt.clf()
        fig = plt.figure()
        ax1 = fig.add_subplot(111)
        #fig, (ax1, ax2) = plt.subplots(1, 2, dpi=dpishow)
        im1=ax1.imshow(refm2d[:,:,x], cmap=cmap,alpha=.5,vmax=pmax);
        #ax1.set_title(f'{filename1}, Index %i, [Reference Image]' %i)
        im2=ax1.imshow(transm2d[:,:,x], cmap=cmap, alpha=.5, vmax=pmax);
        pstrm = (f'_________MASKED__________\nPCC:\t\t   {pcc2imgreg[x]:.3f}\nTanimoto:\t{tm1imgreg[x]:.3f}'
                 f'\nMin-Ratio:\t {minr1imgreg[x]:.3f}\nL1 Norm:\t{l1n1imgreg[x]:.2f}\nL2 Norm:\t{l2n1imgreg[x]:.2f}'
                 f'\nInt-Ratio Var:\t{irvar1imgreg[x]:.3f}').expandtabs()
        pstrnm = (f'_______NON-MASKED_______\nPCC:\t\t   {pcc3imgreg[x]:.3f}\nTanimoto:\t{tm2imgreg[x]:.3f}'
             f'\nMin-Ratio:\t {minr2imgreg[x]:.3f}\nL1 Norm:\t{l1n2imgreg[x]:.2f}\nL2 Norm:\t{l2n2imgreg[x]:.2f}'
             f'\nInt-Ratio Var:\t{irvar2imgreg[x]:.3f}').expandtabs()
        pstrmet = (f'____OTHER METRICS_____\nContact Diff:\t\t    {ct_regdiff[x]:.0f}'
             f'\nCP-CP Distance:\t\t {cp_regdiff[x]:.2f}').expandtabs()
        plt.text((res1 + 1.5)*factor, 1*factor, pstrm, fontsize=7,verticalalignment='top', bbox=props)
        plt.text((res1 + 1.5)*factor, 13*factor, pstrnm, fontsize=7,verticalalignment='top', bbox=props)
        plt.text((res1 + 1.5)*factor, 24*factor, pstrmet, fontsize=7,verticalalignment='top', bbox=props)
        plt.title(f'{method} Image Registration: {filename1} vs {filename2}, Iteration {x}\nMetric: {regmetric[x]}\n', horizontalalignment='center')
        cbar_ax = fig.add_axes([0, 0.145, 0.04, 0.6])
        cbar = plt.colorbar(im1, cax=cbar_ax)
        cbar.ax.yaxis.set_ticks_position('left')
        fig.tight_layout(rect=[-0.2, 0.03, 1, 0.95])
        plt.savefig(f'Data\{Dataset} data subset\{filename1} vs {filename2}\{method} Image Registration, {filename1} vs {filename2}, Iteration {x}.tif', dpi=200, bbox_inches='tight')

    for x in range(len(ref[0,0,:])):
        plt.clf()
        fig = plt.figure()
        ax1 = fig.add_subplot(111)
        clim = max(np.abs(np.min(diffm2d[:,:,x])),np.max(diffm2d[:,:,x]))
        im1=ax1.imshow(diffm2d[:,:,x], cmap='seismic', vmin=-clim, vmax=clim)
        plt.title(f'{method} Image Registration: {filename1} vs {filename2}, Iteration {x}\n[Reference - Transformed] (mmHg)\n', horizontalalignment='center')
        cbar_ax = fig.add_axes([0.70, 0.145, 0.04, 0.6])
        fig.colorbar(im1, cax=cbar_ax)
        fig.tight_layout(rect=[-0.2, 0.03, 1, 0.95])


```

```
    plt.savefig(f'Data\{Dataset} data subset\{filename1} vs {filename2}\{method} Im
            age Registration, {filename1} vs {filename2} Differences, Iteration {x}.tif',
            dpi=200, bbox_inches='tight')


        #### Create TIF files
        with tifffile.TiffWriter(f'Data\{Dataset} data subset\{filename1} vs {filename2}\
          {method} Image Registration Results, {filename1} vs {filename2}.tif') as stack:
            for fname in sorted(glob.glob(f'Data\{Dataset} data subset\{filename1} vs {file
              name2}\{method} Image Registration, {filename1} vs {filename2}*.tif'),
              key=os.path.getmtime):
                stack.save(tifffile.imread(fname), compress=6)

        ResultsReg = pd.DataFrame(data = np.transpose([np.repeat(sheet,x+1),np.repeat
           (filename1,x+1),np.repeat(i,x+1), np.repeat(filename2,x+1),np.repeat(j,x+1),
           np.repeat(method,x+1),np.repeat(f'{hloc},{vloc},{rot}',x+1),list(range(x+1)),
       regmetric, ct_ireg, ct_jreg, ct_regdiff, sum_ireg, sum_jreg, mean_ireg, mean_jreg,
            cv_ireg, cv_jreg, cpx_ireg, cpy_ireg, cpx_jreg, cpy_jreg, cp_regdiff,
            pcc3imgreg, pcc2imgreg, tm2imgreg, tm1imgreg, minr2imgreg, minr1imgreg,
            l1n2imgreg, l1n1imgreg, l2n2imgreg, l2n1imgreg, irvar2imgreg, irvar1imgreg]),
            columns=['Sheet','File1','Index1','File2','Index2','Reg Method', 'H,V,ROT',
             'Iteration', 'Metric Score', ‘Contact Cells 1', 'Contact Cells 2',
             'Contact Cells Diff', 'Pressure Sum 1', 'Pressure Sum 2',
             'Mean Pressure 1', 'Mean Pressure 2', 'CV 1', 'CV 2', 'CPX 1', 'CPY 1',
             'CPX 2', 'CPY 2', 'CP Diff', 'Pearson','Pearson (M)', 'Tanimoto',
             'Tanimoto (M)','Min-Ratio','Min-Ratio (M)',
             'L1 Norm', 'L1 Norm (M)', 'Sq L2 Norm', 'Sq L2 Norm (M)','Int-Ratio Var',
             'Int-Ratio Var (M)'])

        # Write Results in Excel
        from excelappend import append_df_to_excel
        append_df_to_excel(f'Data\{Dataset} data subset\\' + filename1 + ' vs ' +
             filename2 + '\Image Registration Results.xlsx',ResultsReg,sheet_name=method)
```

Appendix F

Cluster Data Subset: Samples with Outliers

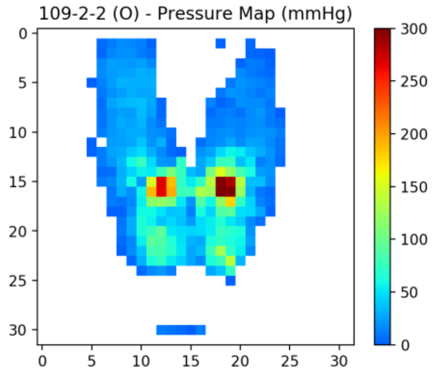
109-2-2 (O) - Pressure Map (mmHg)

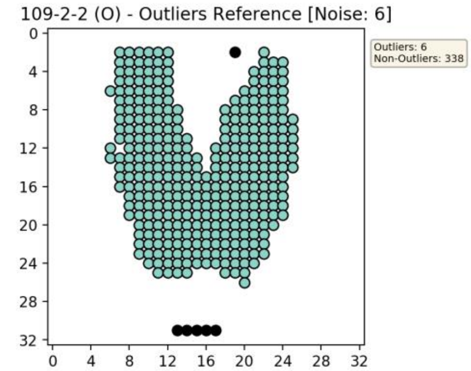
109-2-2 (O) - Outliers Reference [Noise: 6]
Outliers: 6
Non-Outliers: 338

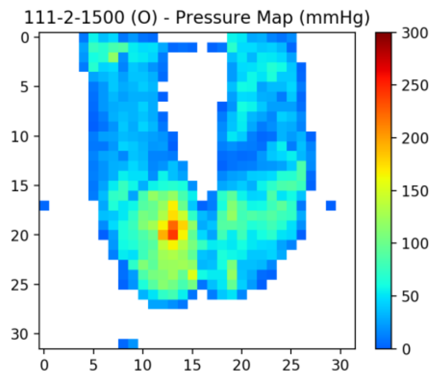
111-2-1500 (O) - Pressure Map (mmHg)

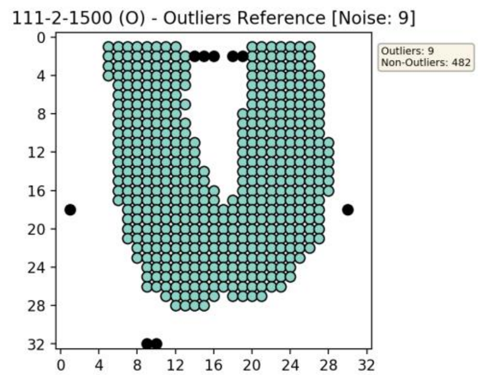
111-2-1500 (O) - Outliers Reference [Noise: 9]
Outliers: 9
Non-Outliers: 482

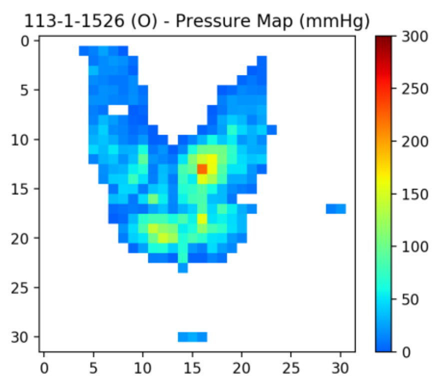
113-1-1526 (O) - Pressure Map (mmHg)

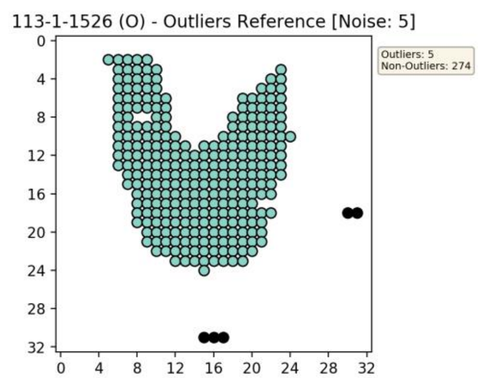
113-1-1526 (O) - Outliers Reference [Noise: 5]
Outliers: 5
Non-Outliers: 274

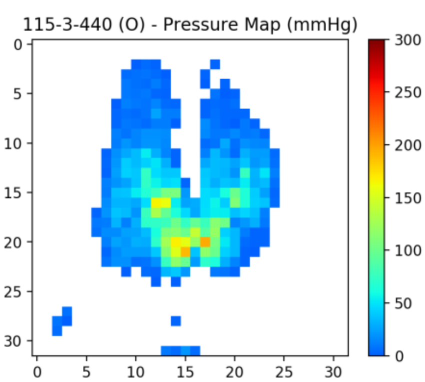
115-3-440 (O) - Pressure Map (mmHg)

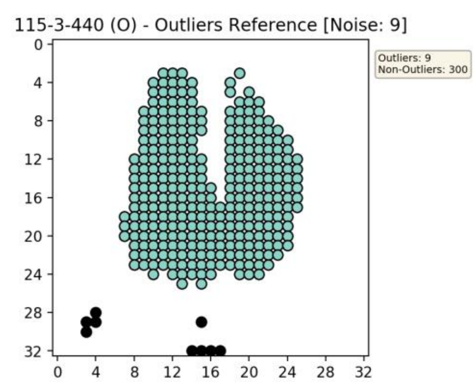
115-3-440 (O) - Outliers Reference [Noise: 9]
Outliers: 9
Non-Outliers: 300

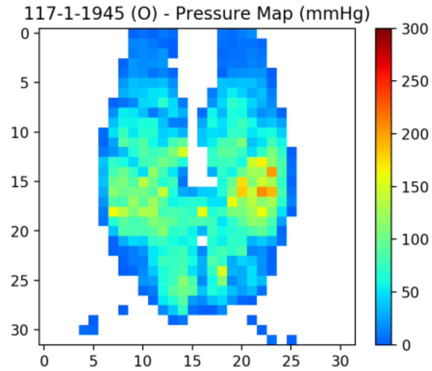
117-1-1945 (O) - Pressure Map (mmHg)

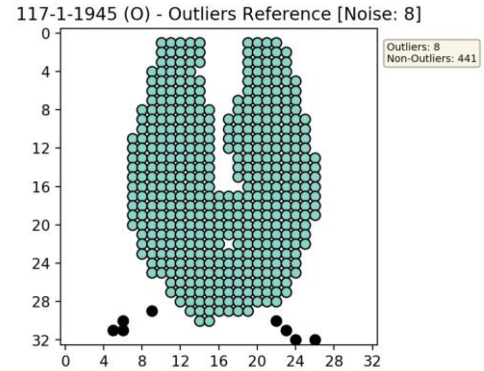
117-1-1945 (O) - Outliers Reference [Noise: 8]
Outliers: 8
Non-Outliers: 441

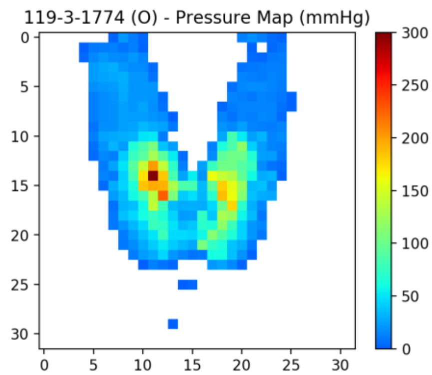
119-3-1774 (O) - Pressure Map (mmHg)

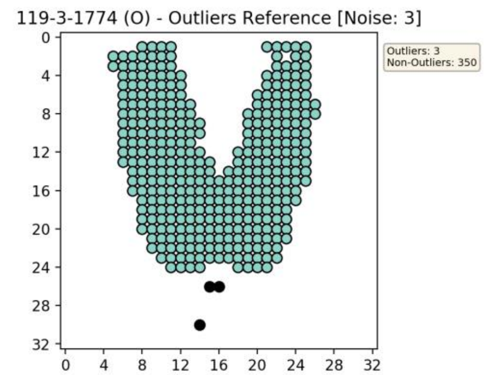
119-3-1774 (O) - Outliers Reference [Noise: 3]
Outliers: 3
Non-Outliers: 350

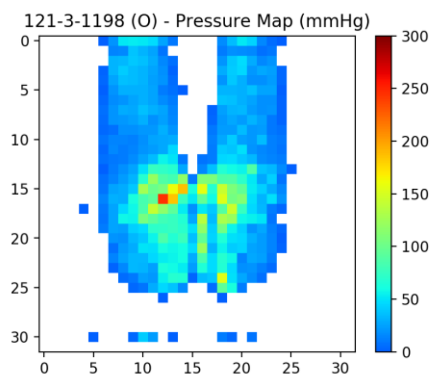
121-3-1198 (O) - Pressure Map (mmHg)

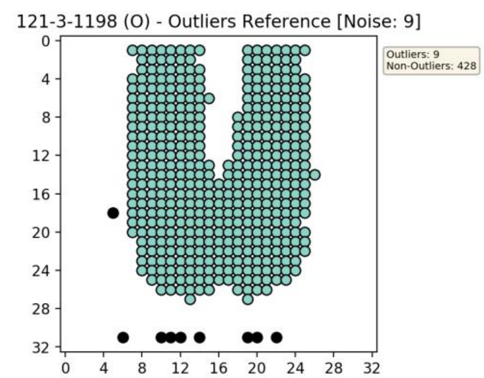
121-3-1198 (O) - Outliers Reference [Noise: 9]
Outliers: 9
Non-Outliers: 428

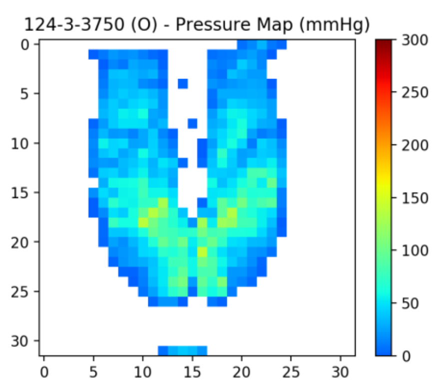
124-3-3750 (O) - Pressure Map (mmHg)

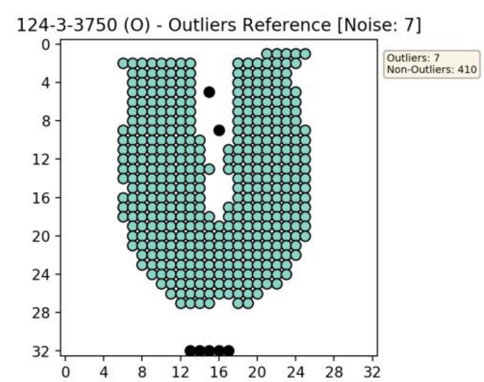
124-3-3750 (O) - Outliers Reference [Noise: 7]
Outliers: 7
Non-Outliers: 410

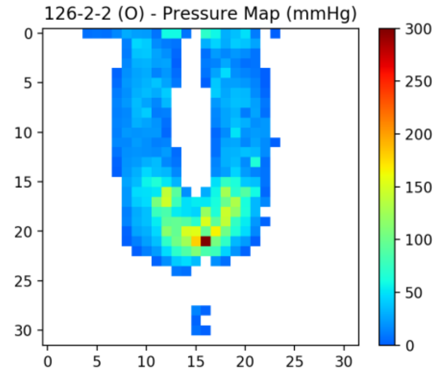
126-2-2 (O) - Pressure Map (mmHg)

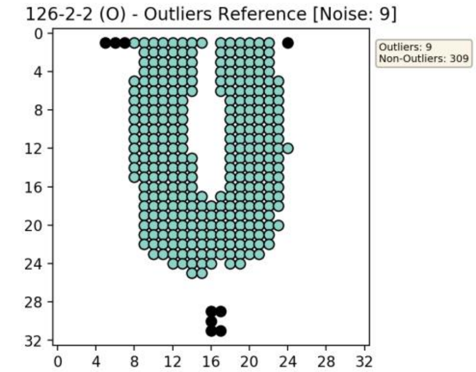
126-2-2 (O) - Outliers Reference [Noise: 9]
Outliers: 9
Non-Outliers: 309

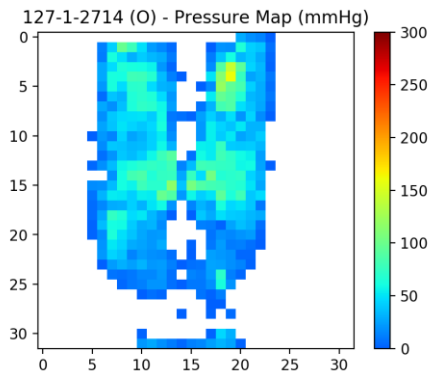
127-1-2714 (O) - Pressure Map (mmHg)

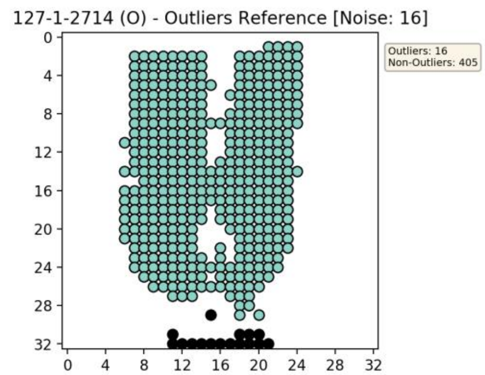
127-1-2714 (O) - Outliers Reference [Noise: 16]
Outliers: 16
Non-Outliers: 405

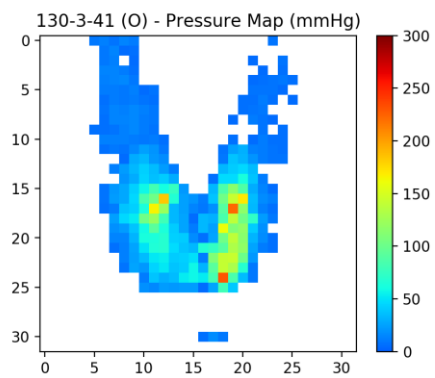
130-3-41 (O) - Pressure Map (mmHg)

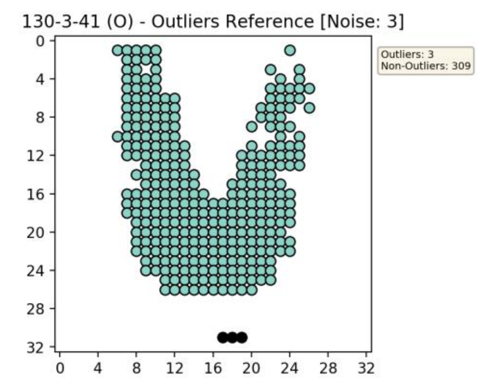
130-3-41 (O) - Outliers Reference [Noise: 3]
Outliers: 3
Non-Outliers: 309

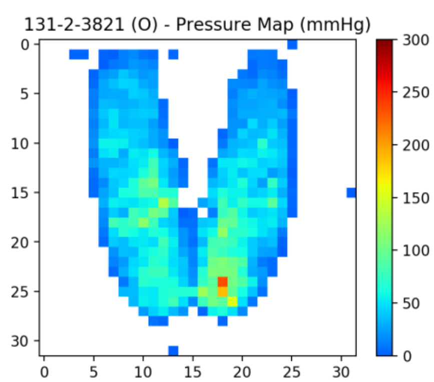
131-2-3821 (O) - Pressure Map (mmHg)

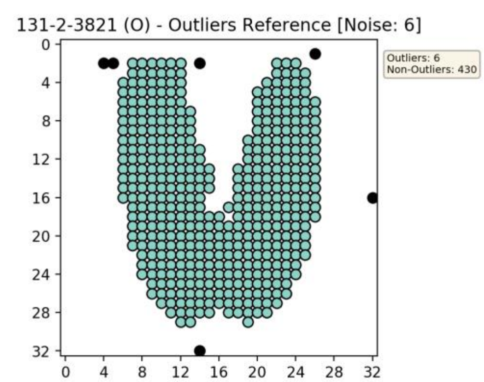
131-2-3821 (O) - Outliers Reference [Noise: 6]
Outliers: 6
Non-Outliers: 430

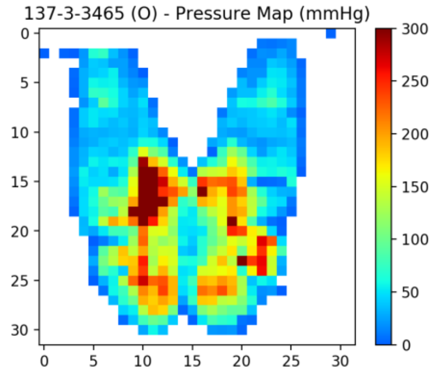
137-3-3465 (O) - Pressure Map (mmHg)

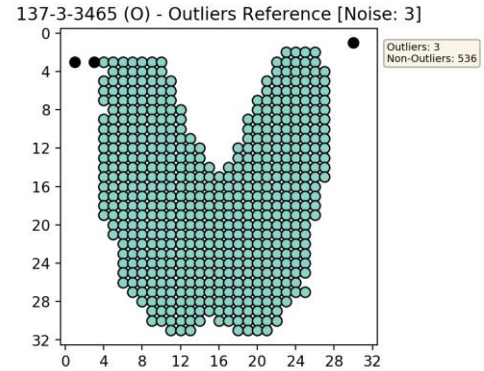
137-3-3465 (O) - Outliers Reference [Noise: 3]
Outliers: 3
Non-Outliers: 536

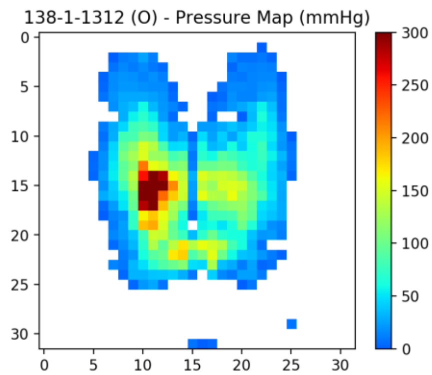
138-1-1312 (O) - Pressure Map (mmHg)

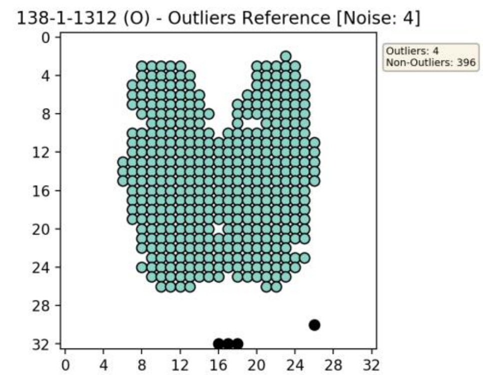
138-1-1312 (O) - Outliers Reference [Noise: 4]
Outliers: 4
Non-Outliers: 396

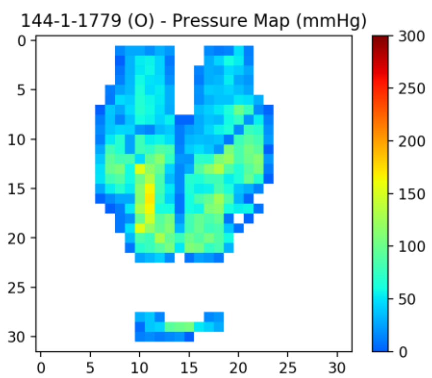
144-1-1779 (O) - Pressure Map (mmHg)

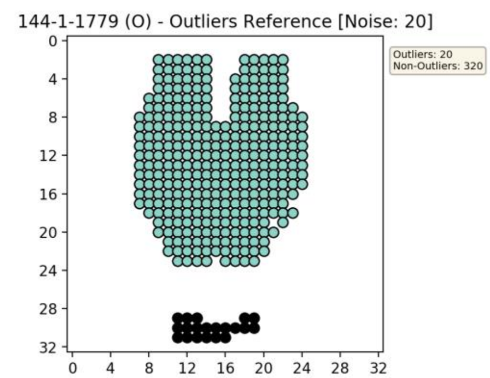
144-1-1779 (O) - Outliers Reference [Noise: 20]
Outliers: 20
Non-Outliers: 320

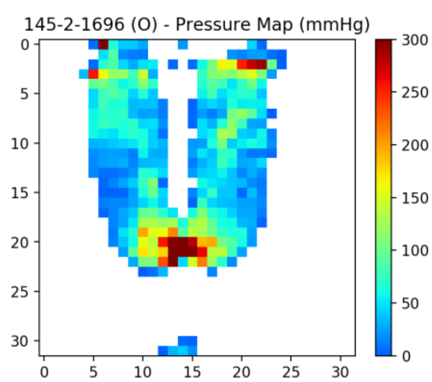
145-2-1696 (O) - Pressure Map (mmHg)

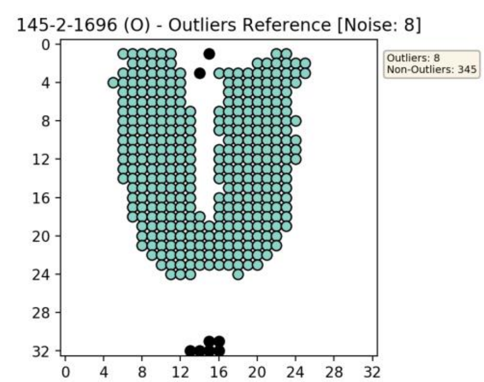
145-2-1696 (O) - Outliers Reference [Noise: 8]
Outliers: 8
Non-Outliers: 345

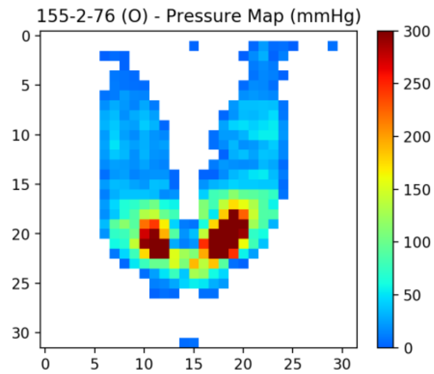
155-2-76 (O) - Pressure Map (mmHg)

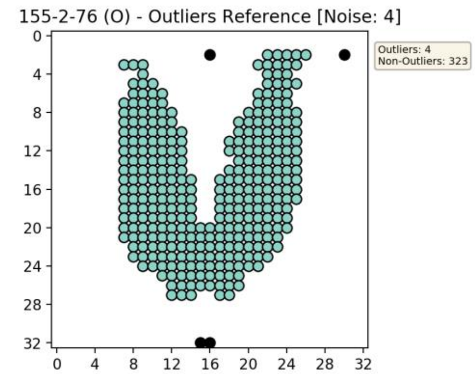
155-2-76 (O) - Outliers Reference [Noise: 4]
Outliers: 4
Non-Outliers: 323

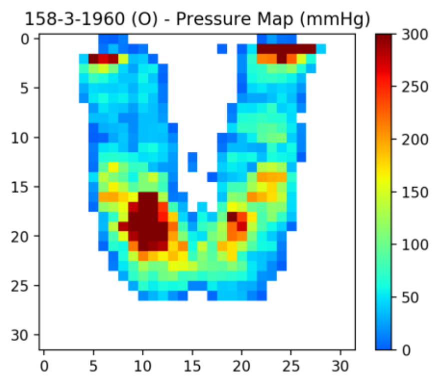
158-3-1960 (O) - Pressure Map (mmHg)

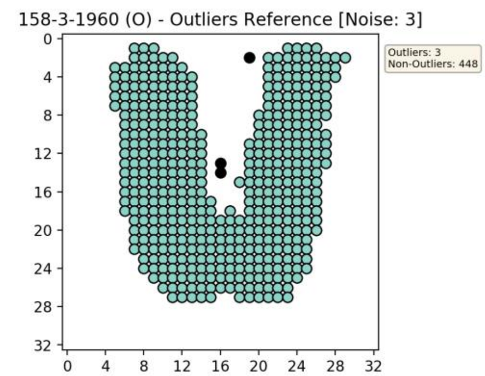
158-3-1960 (O) - Outliers Reference [Noise: 3]
Outliers: 3
Non-Outliers: 448

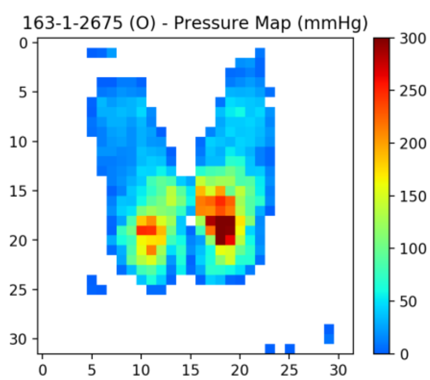
163-1-2675 (O) - Pressure Map (mmHg)

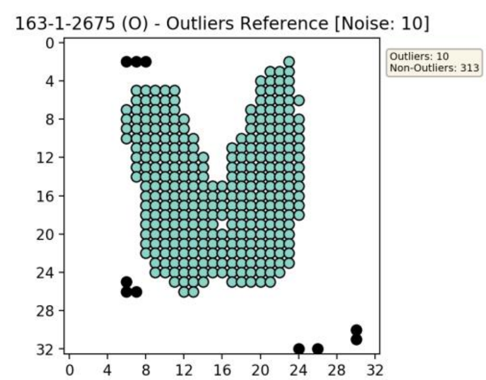
163-1-2675 (O) - Outliers Reference [Noise: 10]
Outliers: 10
Non-Outliers: 313

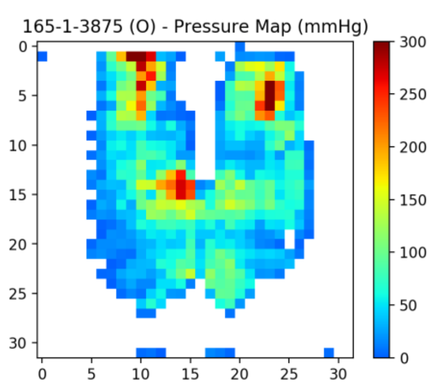
165-1-3875 (O) - Pressure Map (mmHg)

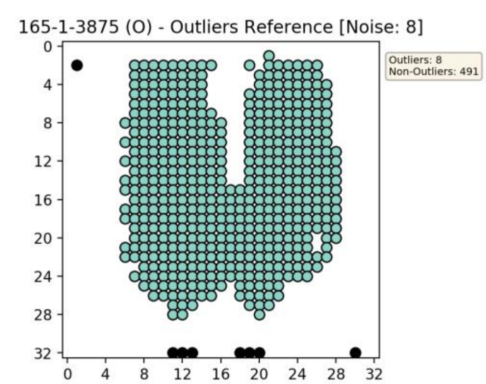
165-1-3875 (O) - Outliers Reference [Noise: 8]
Outliers: 8
Non-Outliers: 491

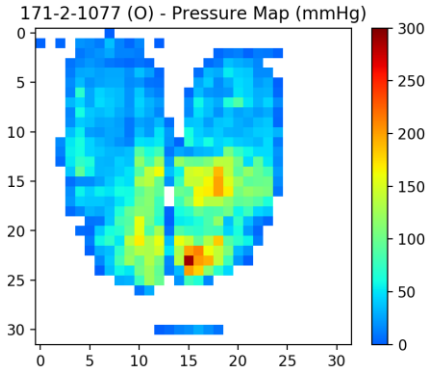
171-2-1077 (O) - Pressure Map (mmHg)

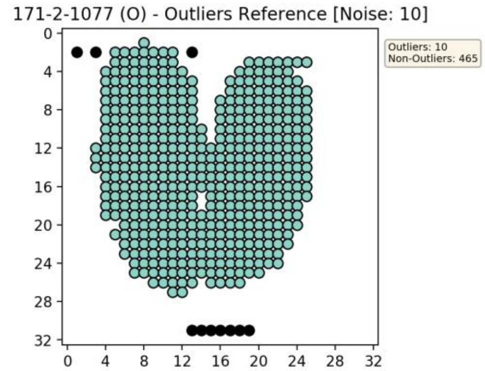
171-2-1077 (O) - Outliers Reference [Noise: 10]
Outliers: 10
Non-Outliers: 465

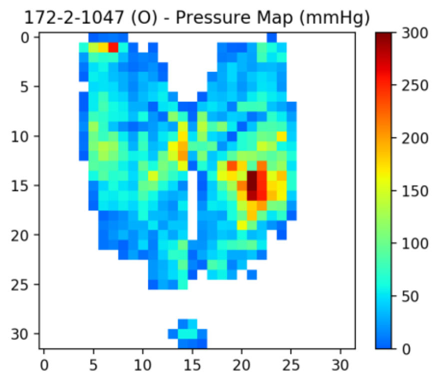
172-2-1047 (O) - Pressure Map (mmHg)

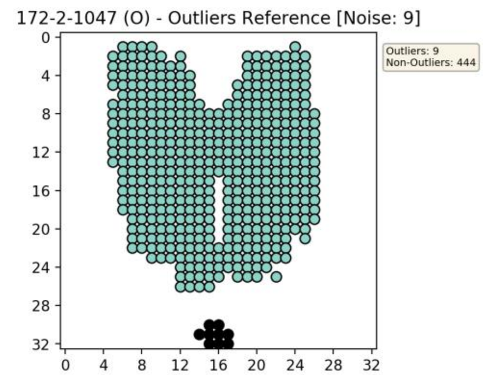
172-2-1047 (O) - Outliers Reference [Noise: 9]
Outliers: 9
Non-Outliers: 444

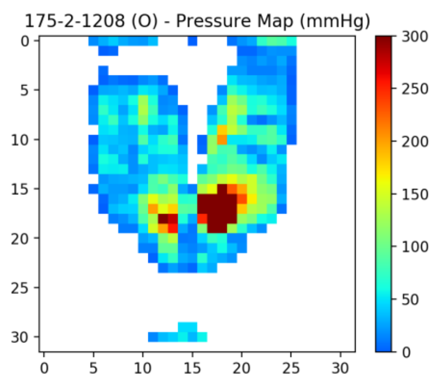
175-2-1208 (O) - Pressure Map (mmHg)

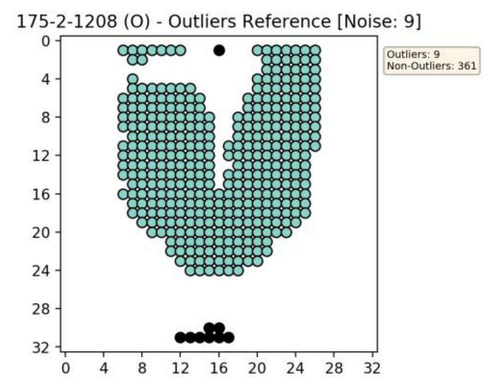
175-2-1208 (O) - Outliers Reference [Noise: 9]
Outliers: 9
Non-Outliers: 361

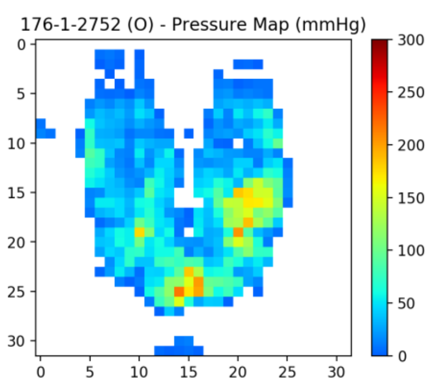
176-1-2752 (O) - Pressure Map (mmHg)

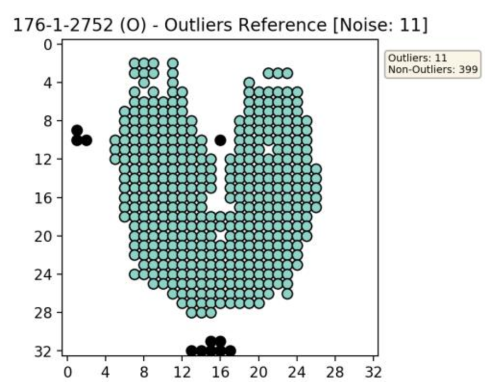
176-1-2752 (O) - Outliers Reference [Noise: 11]
Outliers: 11
Non-Outliers: 399

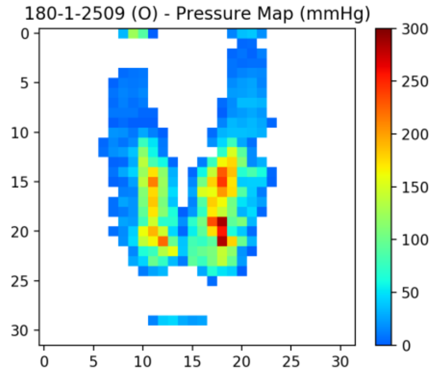
180-1-2509 (O) - Pressure Map (mmHg)

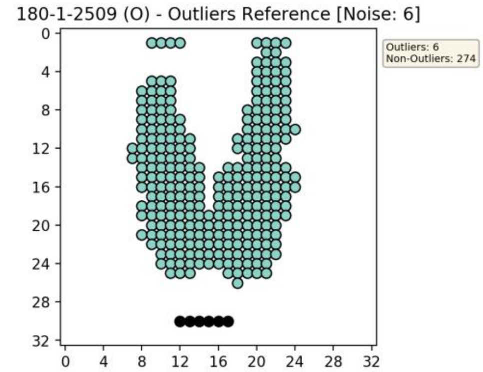
180-1-2509 (O) - Outliers Reference [Noise: 6]
Outliers: 6
Non-Outliers: 274

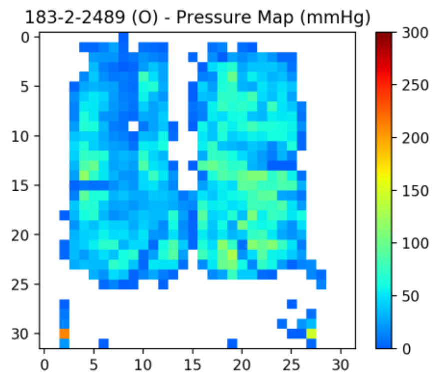
183-2-2489 (O) - Pressure Map (mmHg)

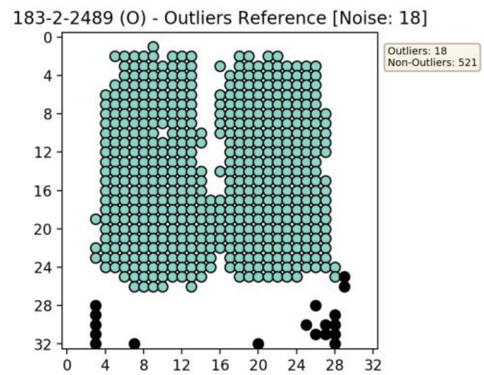
183-2-2489 (O) - Outliers Reference [Noise: 18]
Outliers: 18
Non-Outliers: 521

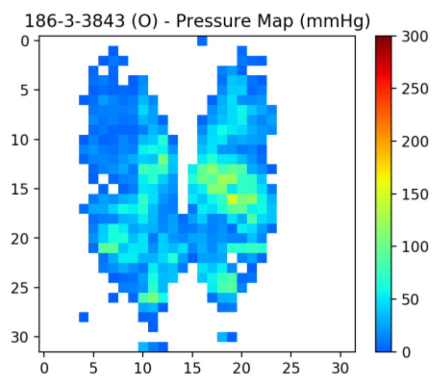
186-3-3843 (O) - Pressure Map (mmHg)

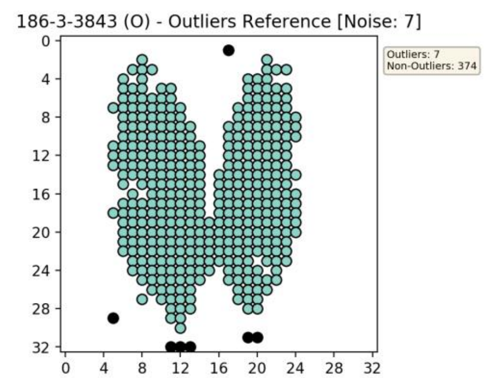
186-3-3843 (O) - Outliers Reference [Noise: 7]
Outliers: 7
Non-Outliers: 374

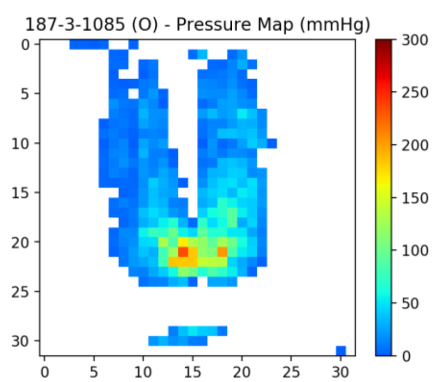
187-3-1085 (O) - Pressure Map (mmHg)

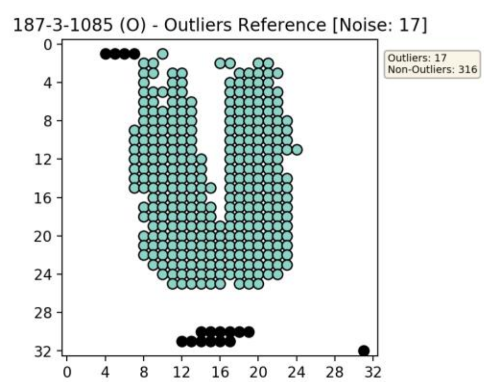
187-3-1085 (O) - Outliers Reference [Noise: 17]
Outliers: 17
Non-Outliers: 316

Appendix G

Cluster Data Subset: Samples without Outliers

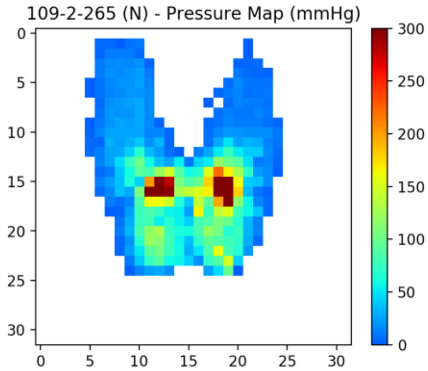
109-2-265 (N) - Pressure Map (mmHg)

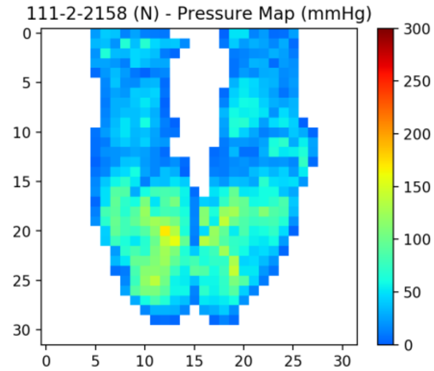
111-2-2158 (N) - Pressure Map (mmHg)

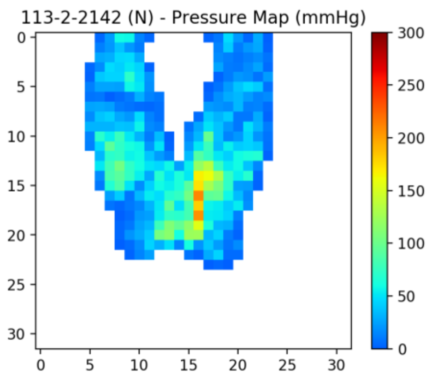
113-2-2142 (N) - Pressure Map (mmHg)

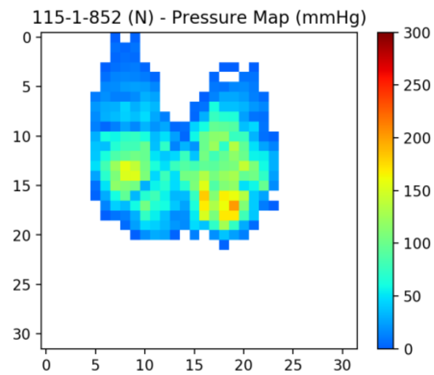
115-1-852 (N) - Pressure Map (mmHg)

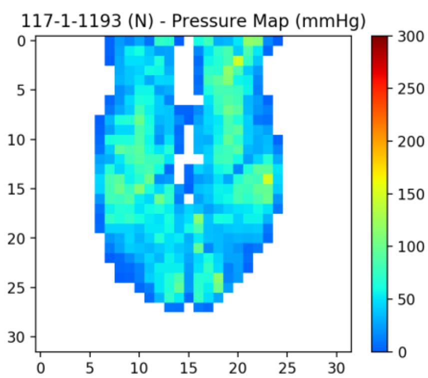
117-1-1193 (N) - Pressure Map (mmHg)

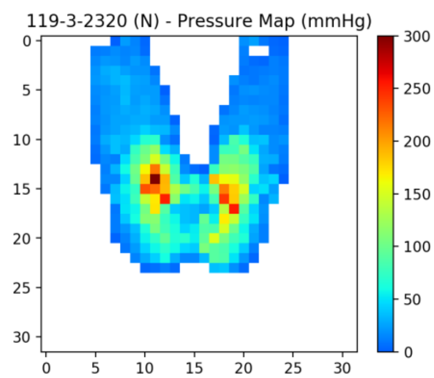
119-3-2320 (N) - Pressure Map (mmHg)

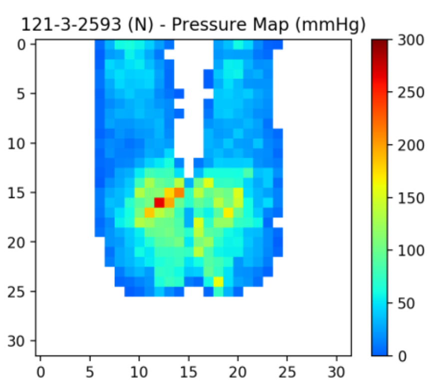
121-3-2593 (N) - Pressure Map (mmHg)

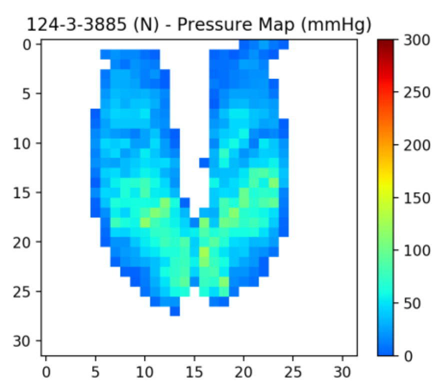
124-3-3885 (N) - Pressure Map (mmHg)

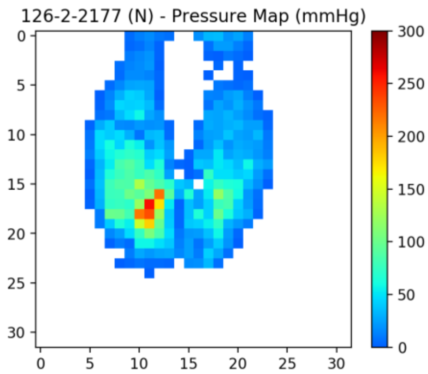
126-2-2177 (N) - Pressure Map (mmHg)

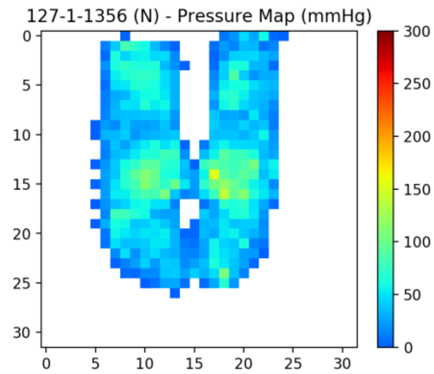
127-1-1356 (N) - Pressure Map (mmHg)

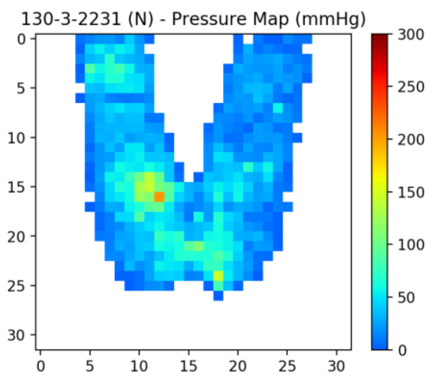
130-3-2231 (N) - Pressure Map (mmHg)

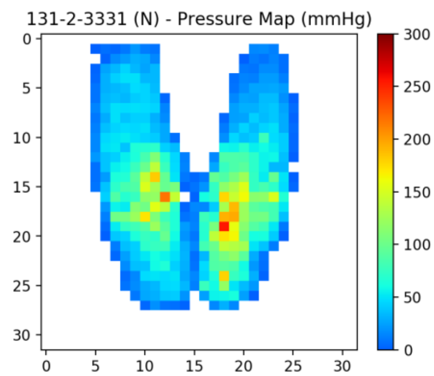
131-2-3331 (N) - Pressure Map (mmHg)

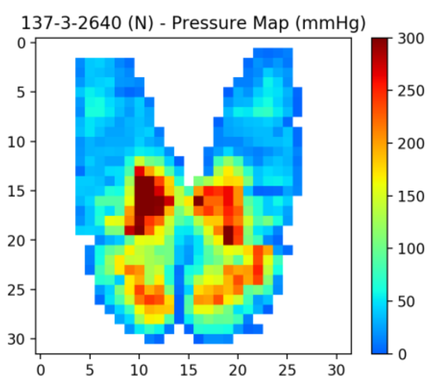
137-3-2640 (N) - Pressure Map (mmHg)

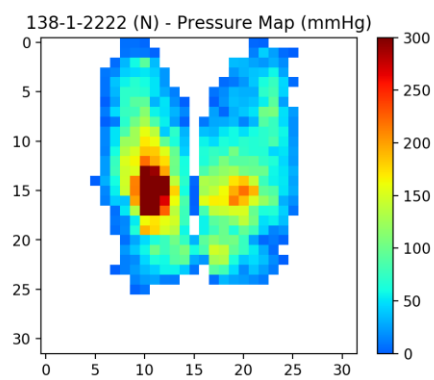
138-1-2222 (N) - Pressure Map (mmHg)

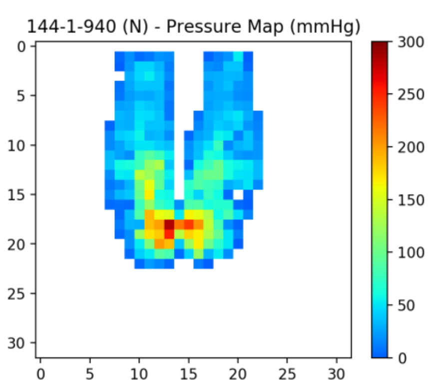
144-1-940 (N) - Pressure Map (mmHg)

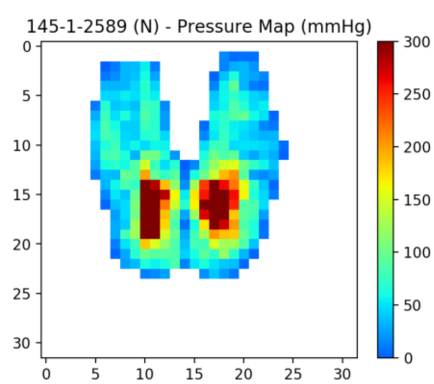
145-1-2589 (N) - Pressure Map (mmHg)

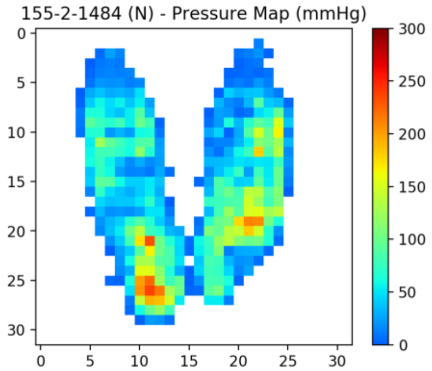
155-2-1484 (N) - Pressure Map (mmHg)
0 5 10 15 20 25 30
0 50 100 150 200 250 300

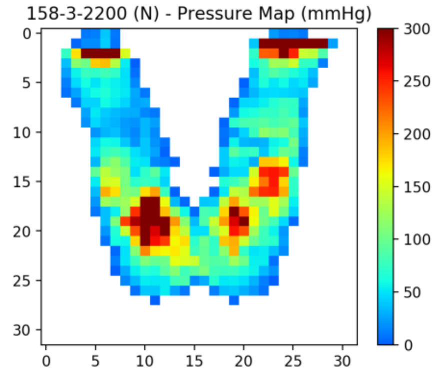
158-3-2200 (N) - Pressure Map (mmHg)
0 5 10 15 20 25 30
0 50 100 150 200 250 300

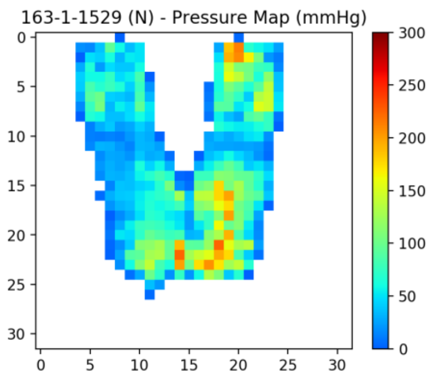
163-1-1529 (N) - Pressure Map (mmHg)
0 5 10 15 20 25 30
0 50 100 150 200 250 300

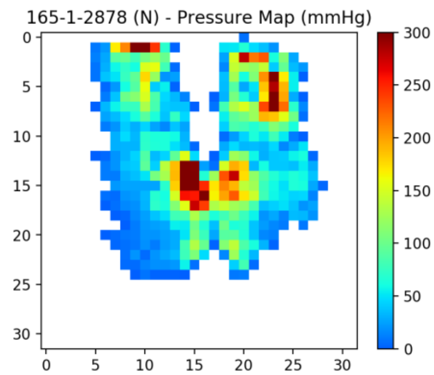
165-1-2878 (N) - Pressure Map (mmHg)
0 5 10 15 20 25 30
0 50 100 150 200 250 300

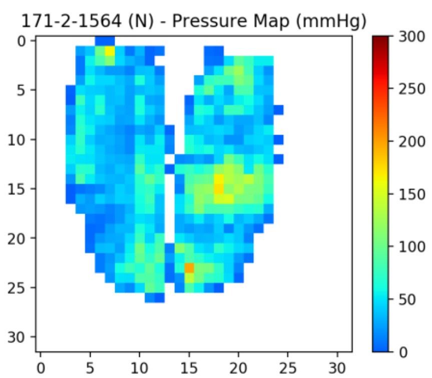
171-2-1564 (N) - Pressure Map (mmHg)
0 5 10 15 20 25 30
0 50 100 150 200 250 300

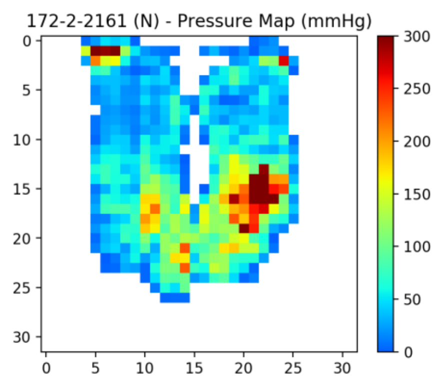
172-2-2161 (N) - Pressure Map (mmHg)
0 5 10 15 20 25 30
0 50 100 150 200 250 300

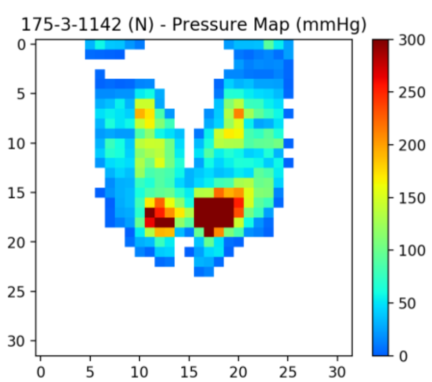
175-3-1142 (N) - Pressure Map (mmHg)
0 5 10 15 20 25 30
0 50 100 150 200 250 300

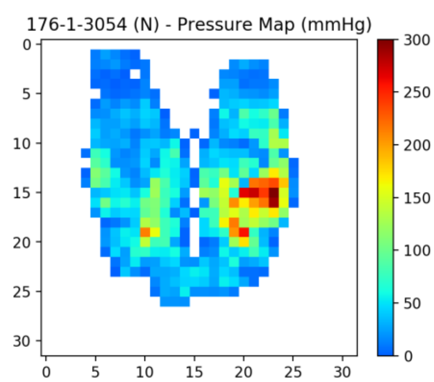
176-1-3054 (N) - Pressure Map (mmHg)
0 5 10 15 20 25 30
0 50 100 150 200 250 300

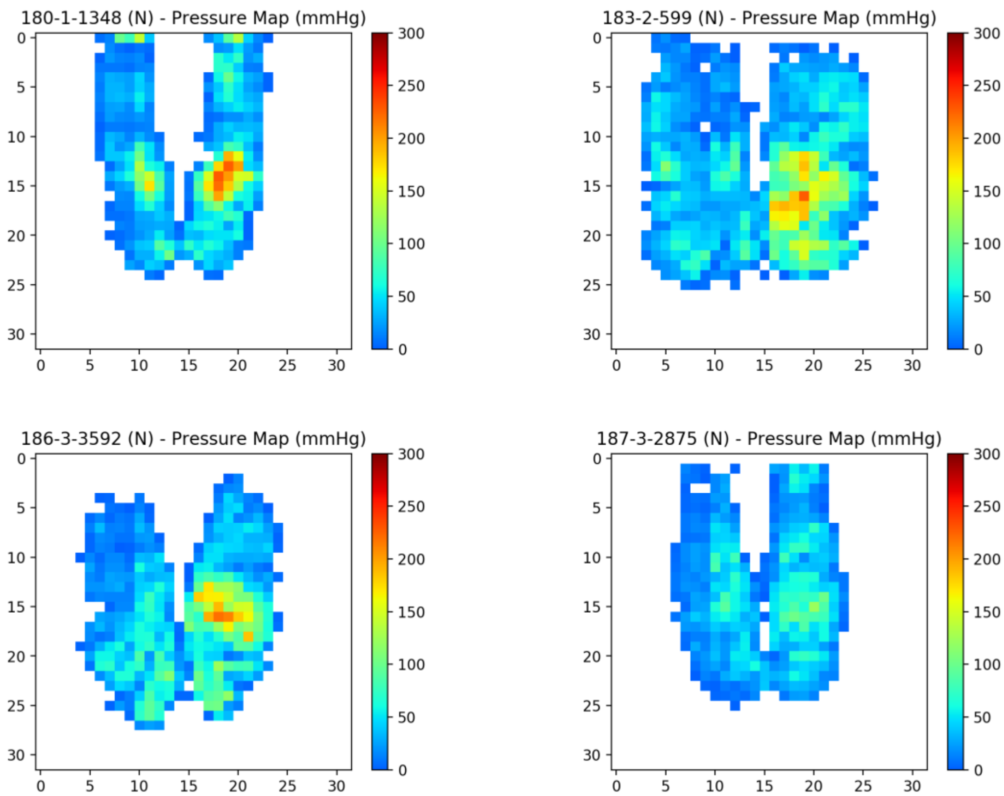
180-1-1348 (N) - Pressure Map (mmHg)
183-2-599 (N) - Pressure Map (mmHg)
186-3-3592 (N) - Pressure Map (mmHg)
187-3-2875 (N) - Pressure Map (mmHg)

Appendix H

Static Data Subset: Samples based on CV levels

117-1-1193, Pressure Map (mmHg) [CV = 0.598]

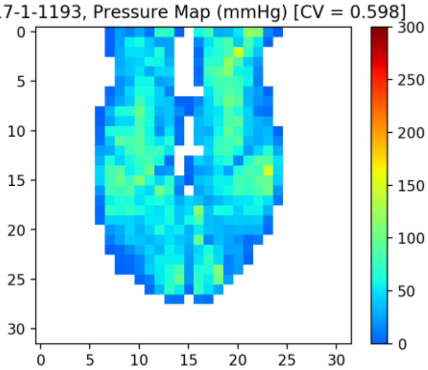

122-2-2954, Pressure Map (mmHg) [CV = 0.627]

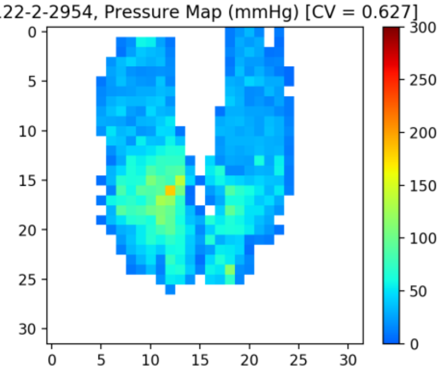

171-1-2033, Pressure Map (mmHg) [CV = 0.702]

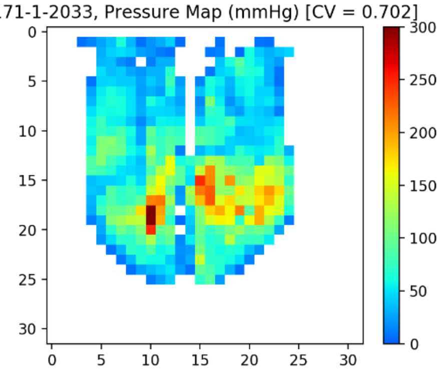

110-1-2031, Pressure Map (mmHg) [CV = 0.757]

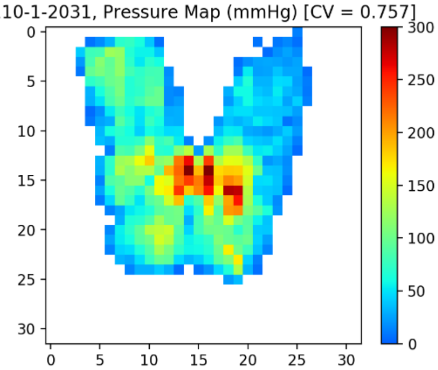

169-3-1597, Pressure Map (mmHg) [CV = 0.772]

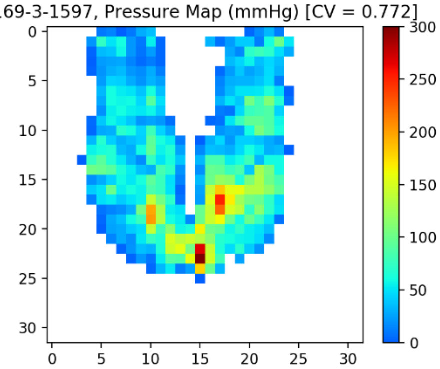

156-3-3819, Pressure Map (mmHg) [CV = 0.794]

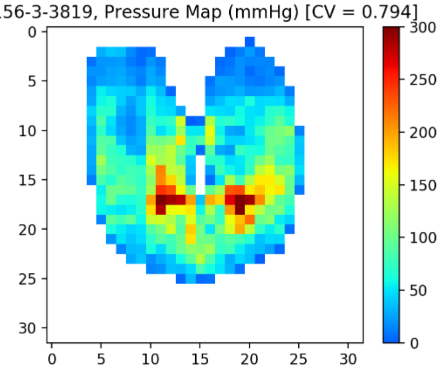

161-1-1833, Pressure Map (mmHg) [CV = 0.805]

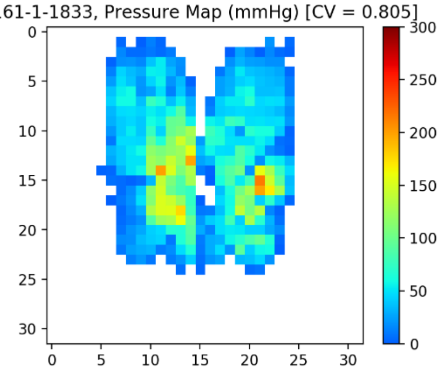

186-1-3161, Pressure Map (mmHg) [CV = 0.819]

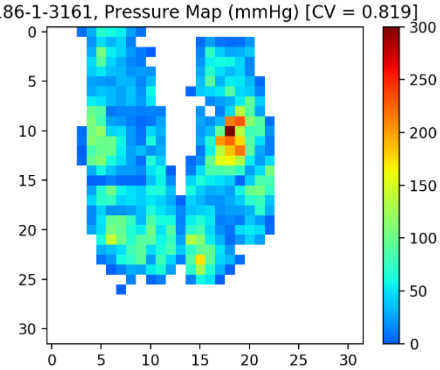

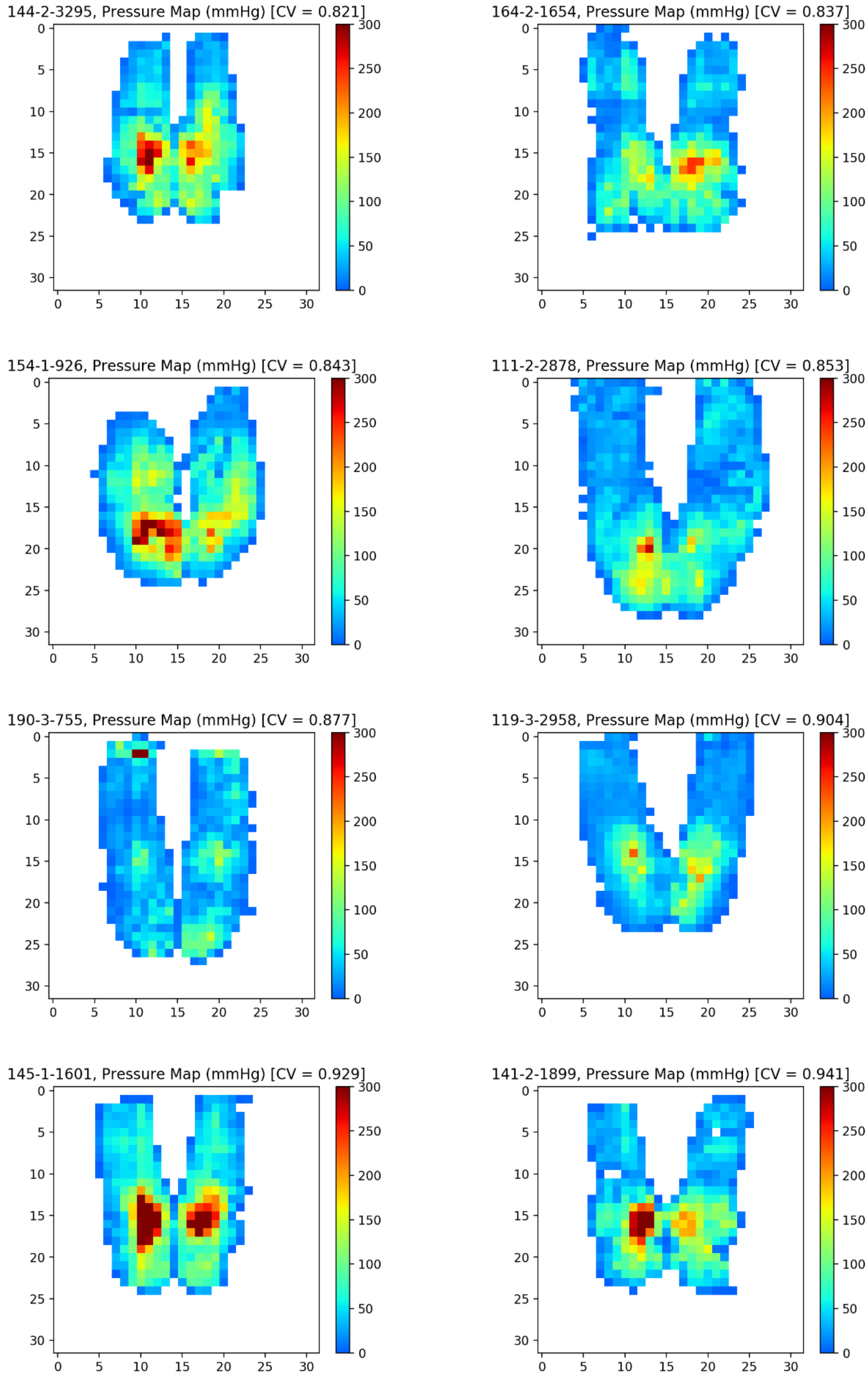
144-2-3295, Pressure Map (mmHg) [CV = 0.821]
164-2-1654, Pressure Map (mmHg) [CV = 0.837]
154-1-926, Pressure Map (mmHg) [CV = 0.843]
111-2-2878, Pressure Map (mmHg) [CV = 0.853]
190-3-755, Pressure Map (mmHg) [CV = 0.877]
119-3-2958, Pressure Map (mmHg) [CV = 0.904]
145-1-1601, Pressure Map (mmHg) [CV = 0.929]
141-2-1899, Pressure Map (mmHg) [CV = 0.941]

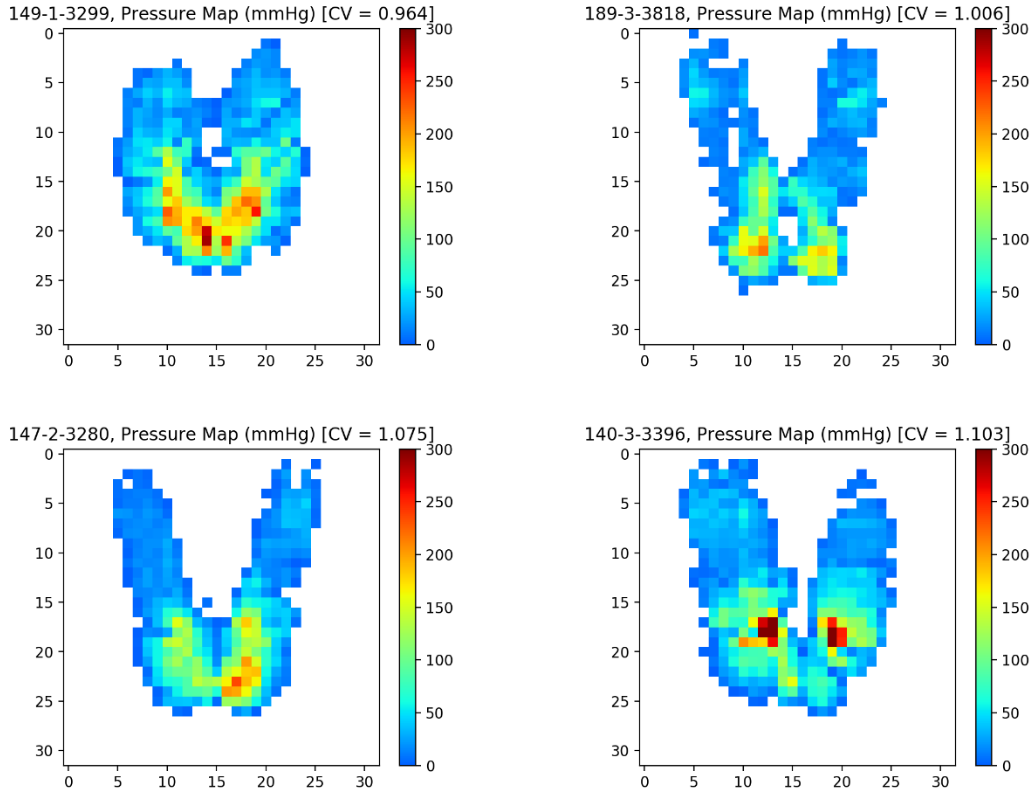
149-1-3299, Pressure Map (mmHg) [CV = 0.964]
189-3-3818, Pressure Map (mmHg) [CV = 1.006]
147-2-3280, Pressure Map (mmHg) [CV = 1.075]
140-3-3396, Pressure Map (mmHg) [CV = 1.103]

Appendix I

Static Data Subset: Spatial Autocorrelation

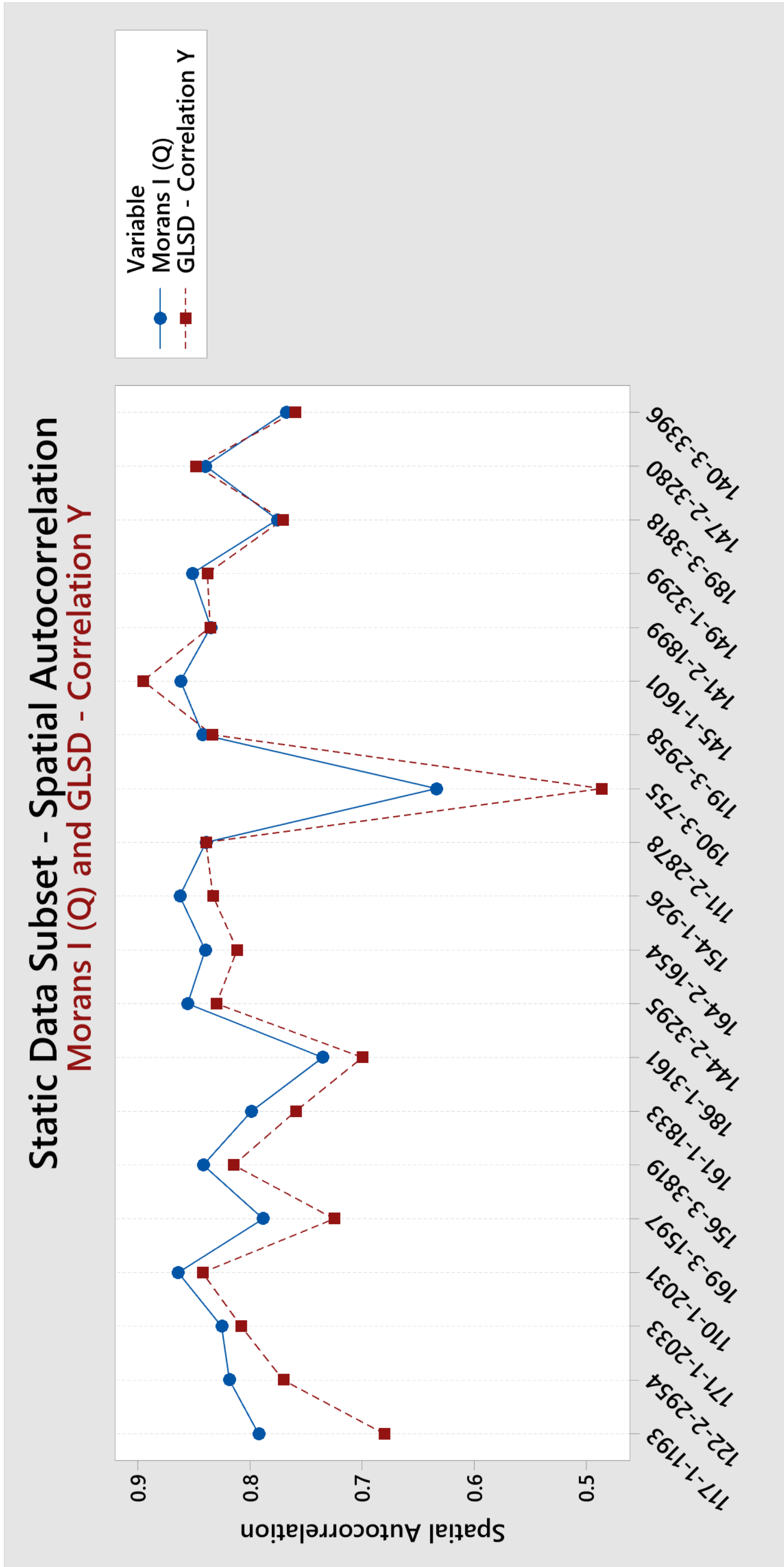
Static Data Subset - Spatial Autocorrelation
Morans I (Q) and GLSD - Correlation Y
Spatial Autocorrelation
0.9
0.8
0.7
0.6
0.5
117-1-1193
122-2-2954
171-1-2033
110-1-2031
169-3-1597
156-3-3819
161-1-1833
186-1-3161
144-2-3295
164-2-1654
154-1-926
111-2-2878
190-3-755
119-3-2958
145-1-1601
141-2-1899
149-1-3299
189-3-3818
147-2-3280
140-3-3396
Variable
Morans I (Q)
GLSD - Correlation Y

Appendix J

Paired Data Subset: Samples based on Contact, Pressure and CV levels

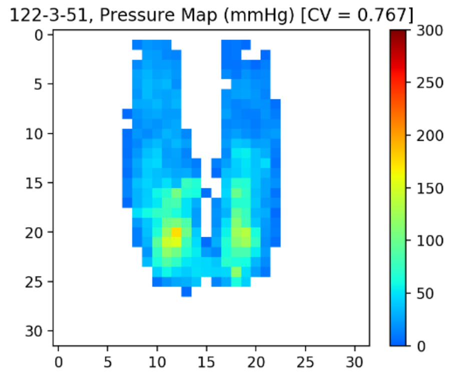
122-3-51, Pressure Map (mmHg) [CV = 0.767]

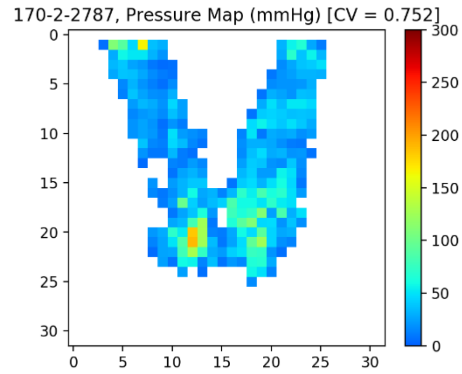
170-2-2787, Pressure Map (mmHg) [CV = 0.752]

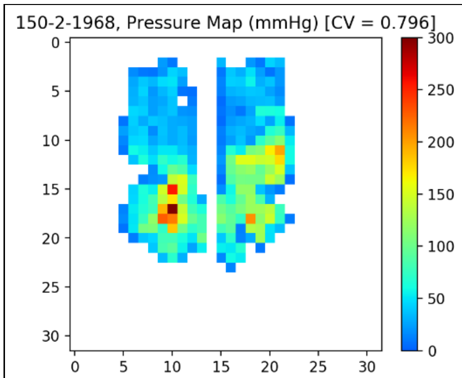
150-2-1968, Pressure Map (mmHg) [CV = 0.796]

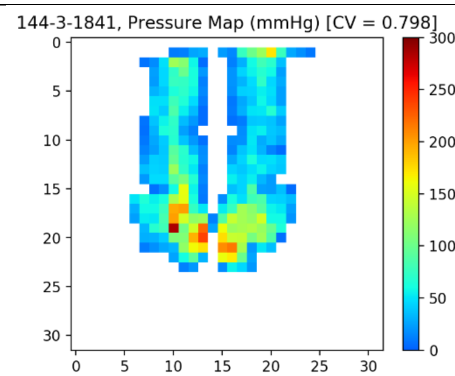
144-3-1841, Pressure Map (mmHg) [CV = 0.798]

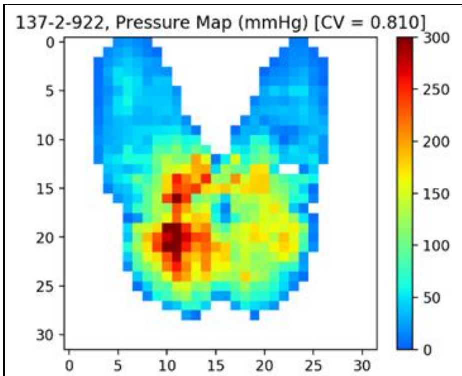
137-2-922, Pressure Map (mmHg) [CV = 0.810]

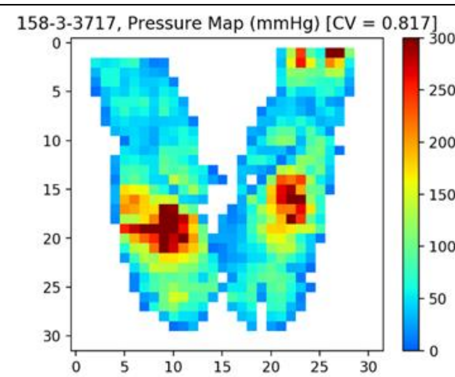
158-3-3717, Pressure Map (mmHg) [CV = 0.817]

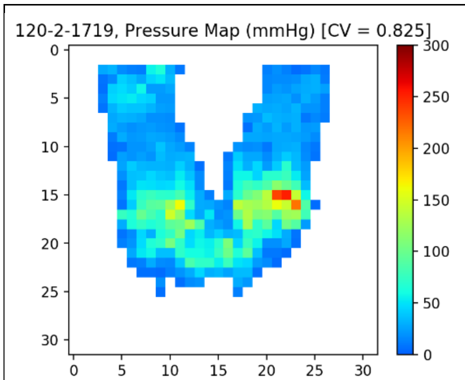
120-2-1719, Pressure Map (mmHg) [CV = 0.825]

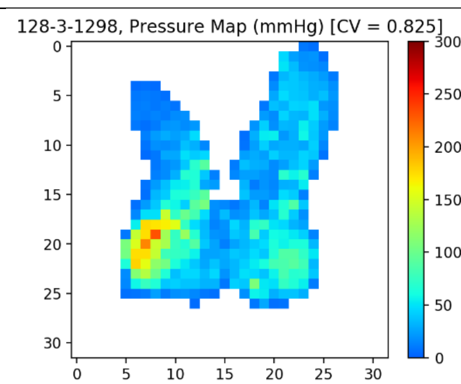
128-3-1298, Pressure Map (mmHg) [CV = 0.825]

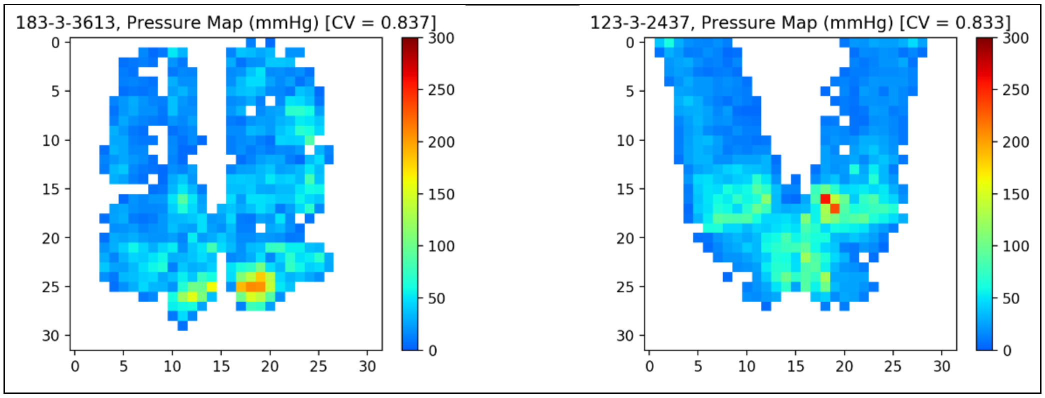
183-3-3613, Pressure Map (mmHg) [CV = 0.837]
123-3-2437, Pressure Map (mmHg) [CV = 0.833]

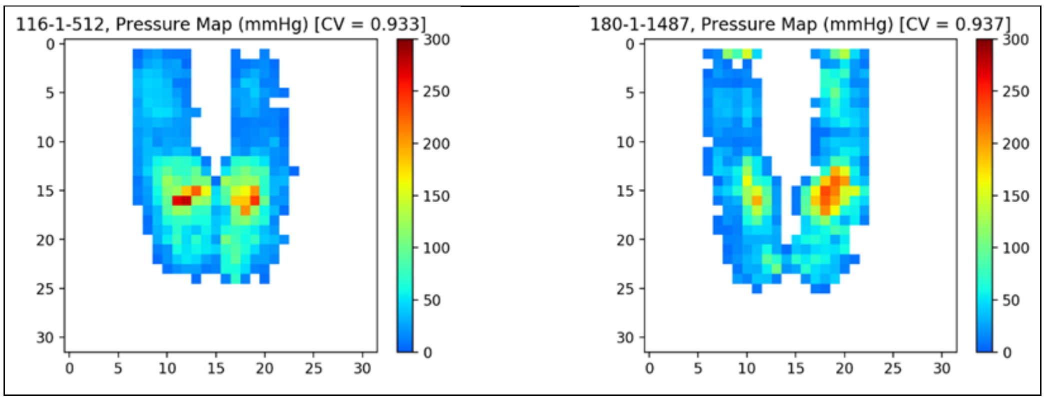
116-1-512, Pressure Map (mmHg) [CV = 0.933]
180-1-1487, Pressure Map (mmHg) [CV = 0.937]

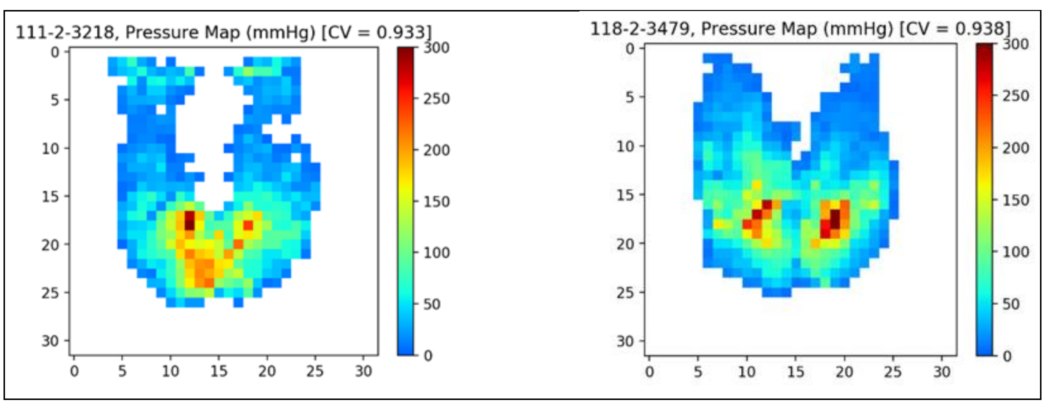
111-2-3218, Pressure Map (mmHg) [CV = 0.933]
118-2-3479, Pressure Map (mmHg) [CV = 0.938]

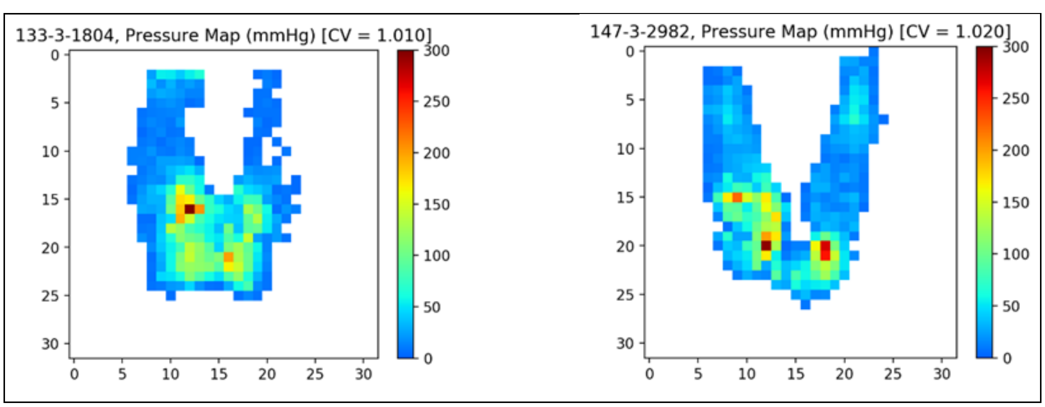
133-3-1804, Pressure Map (mmHg) [CV = 1.010]
147-3-2982, Pressure Map (mmHg) [CV = 1.020]

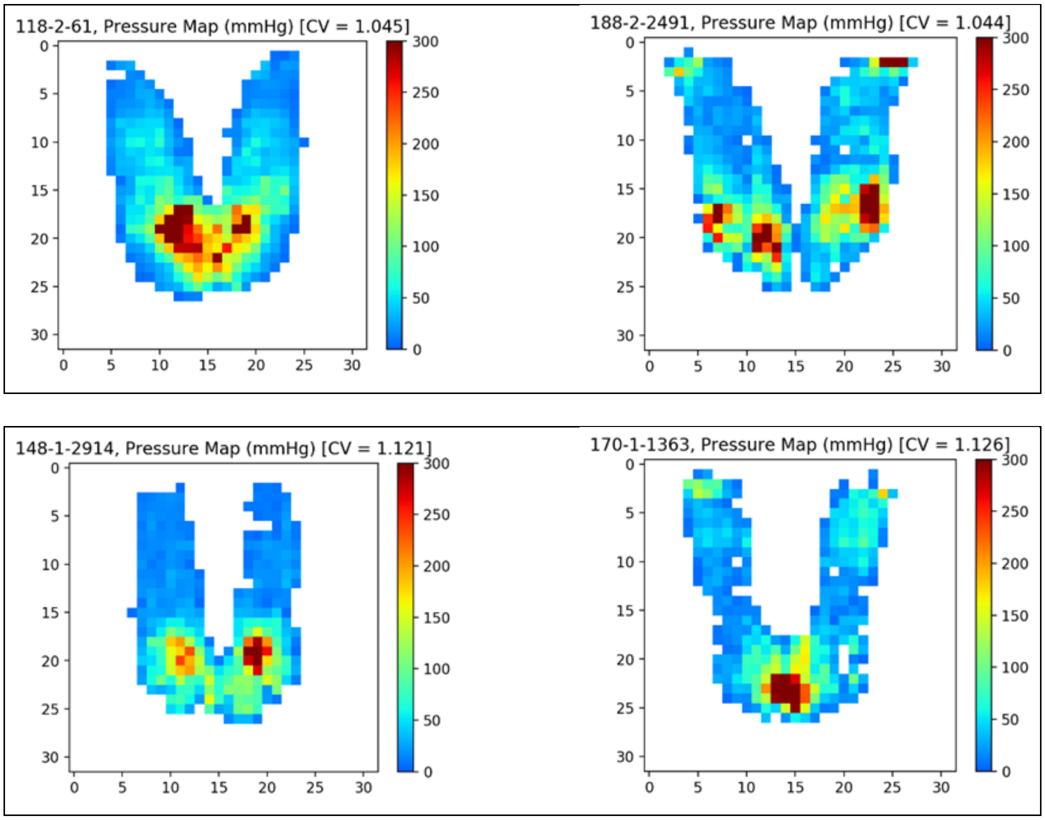
118-2-61, Pressure Map (mmHg) [CV = 1.045]
188-2-2491, Pressure Map (mmHg) [CV = 1.044]
148-1-2914, Pressure Map (mmHg) [CV = 1.121]
170-1-1363, Pressure Map (mmHg) [CV = 1.126]
0 5 10 15 20 25 30
0 50 100 150 200 250 300

Appendix K

Paired Data Subset: Pressure Measures Results

Type	Pressure Measure	Sample		Relative %	Δ Plot
		122-3-51	170-2-2787		
General	Contact Cells	305	307	0.66%	
	Sum of Pressure	11340.58	11345.89	0.05%	
	Skewness	1.7478	2.2060	26.22%	
Spatial	GLSD - Correlation X	0.6824	0.4327	-36.60%	
	GLSD - Correlation Y	0.8530	0.6351	-25.54%	
Variability	Coefficient of Variation	0.7669	0.7525	-1.89%	
	GLD - Gradient Contrast X	535.50	927.20	73.15%	
	GLD - Gradient Mean X	15.94	20.03	25.65%	
	GLD - Gradient Contrast Y	234.37	541.71	131.14%	
	GLD - Gradient Mean Y	10.04	15.53	54.65%	
Texture	GLD - Gradient Second Moment X	0.0345	0.0283	-17.77%	
	GLSD - Homogeneity X	0.0782	0.0617	-21.07%	
	GLD - Gradient Second Moment Y	0.0553	0.0378	-31.62%	
	GLSD - Homogeneity Y	0.1026	0.0753	-26.61%	

Type	Pressure Measure	Sample		Relative %	Δ Plot
		150-2-1968	144-3-1841		
General	Contact Cells	288	293	1.74%	
	Sum of Pressure	17411.35	17503.15	0.53%	
Variability	Coefficient of Variation	0.7959	0.7978	0.25%	
Texture	GLD - Gradient Second Moment Y	0.0276	0.0320	16.00%	
	GLSD - Homogeneity Y	0.0615	0.0709	15.19%	

Type	Pressure Measure	Sample		Relative %	Δ Plot
		137-2-922	158-3-3717		
General	Contact Cells	501	503	0.40%	
	Sum of Pressure	43027.83	42878.06	-0.35%	
	Skewness	0.9667	1.5394	59.25%	
Spatial	Moran's I (CD)	0.8281	0.6828	-17.54%	
	GLSD - Correlation X	0.8557	0.7699	-10.02%	
Variability	Coefficient of Variation	0.8102	0.8168	0.82%	
	GLD - Gradient Contrast X	1381.04	2290.37	65.84%	
	GLD - Gradient Mean X	26.02	32.50	24.91%	
	GLD - Gradient Contrast Y	1065.68	1762.09	65.35%	
	GLD - Gradient Mean Y	22.69	29.31	29.16%	
Texture	GLD - Gradient Second Moment X	0.0212	0.0179	-15.52%	
	GLD - Gradient Second Moment Y	0.0241	0.0197	-18.20%	
	GLSD - Homogeneity Y	0.0672	0.0503	-25.22%	

Type	Pressure Measure	Sample		Relative %	Δ Plot
		120-2-1719	128-3-1298		
General	Contact Cells	388	386	-0.52%	
	Sum of Pressure	16877.71	16871.47	-0.04%	
Variability	Coefficient of Variation	0.8247	0.8249	0.03%	
	GLD - Gradient Contrast Y	664.2320	592.9861	-10.73%	
Texture	GLSD - Homogeneity X	0.1026	0.0891	-13.10%	

Type	Pressure Measure	Sample		Relative %	Δ Plot
		183-3-3613	123-3-2437		
General	Contact Cells	488	482	-1.23%	
	Sum of Pressure	16311.05	16440.84	0.80%	
	Skewness	2.9147	2.5989	-10.84%	
Spatial	Moran's I (CD)	0.5220	0.6802	30.30%	
	GLSD - Correlation Y	0.6588	0.7377	11.98%	
Variability	Coefficient of Variation	0.8367	0.8327	-0.48%	
	GLD - Gradient Contrast Y	548.94	428.37	-21.96%	
	GLD - Gradient Mean Y	15.27	12.01	-21.35%	
Texture	GLD - Gradient Second Moment X	0.0397	0.0455	14.55%	
	GLSD - Homogeneity X	0.0911	0.1035	13.70%	
	GLD - Gradient Second Moment Y	0.0359	0.0479	33.40%	
	GLSD - Homogeneity Y	0.0642	0.1255	95.57%	

Type	Pressure Measure	Sample		Relative %	Δ Plot
		116-1-512	180-1-1487		
General	Contact Cells	303	294	-2.97%	
	Sum of Pressure	14273.5	14200.87	-0.51%	
	Skewness	2.2856	2.0434	-10.60%	
Spatial	Moran's I (CD)	0.7010	0.6037	-13.88%	
Variability	Coefficient of Variation	0.9328	0.9369	0.44%	
	GLD - Gradient Contrast X	1123.4829	1465.3984	30.43%	
	GLD - Gradient Mean X	20.90	26.78	28.15%	
	GLD - Gradient Mean Y	16.96	20.10	18.54%	
Texture	GLD - Gradient Second Moment X	0.0294	0.0222	-24.40%	
	GLSD - Homogeneity X	0.0673	0.0520	-22.74%	
	GLD - Gradient Second Moment Y	0.0398	0.0294	-26.00%	
	GLSD - Homogeneity Y	0.1003	0.0684	-31.75%	

Type	Pressure Measure	Sample		Relative %	Δ Plot
		111-2-3218	118-2-3479		
General	Contact Cells	388	392	1.03%	
	Sum of Pressure	22778.76	22877.61	0.43%	
	Skewness	1.56029	1.89197	21.26%	
Variability	Coefficient of Variation	0.9330	0.9384	0.58%	
	GLD - Gradient Contrast X	1123.53	1407.48	25.27%	
Texture	GLD - Gradient Second Moment Y	0.0260	0.0310	19.08%	
	GLSD - Homogeneity Y	0.0669	0.0773	15.50%	

Type	Pressure Measure	Sample		Relative %	Δ Plot
		133-3-1804	147-3-2982		
General	Contact Cells	279	281	0.72%	
	Sum of Pressure	12629.66	12567.88	-0.49%	
	Skewness	1.7632	2.4782	40.55%	
Spatial	Moran's I (Q)	0.8238	0.7364	-10.61%	
	GLSD - Correlation X	0.7340	0.5978	-18.55%	
Variability	Coefficient of Variation	1.0103	1.0199	0.95%	
	GLD - Gradient Contrast X	1169.28	1837.02	57.11%	
	GLD - Gradient Mean X	22.50	26.54	17.98%	
	GLD - Gradient Contrast Y	919.11	1135.76	23.57%	
Texture	GLD - Gradient Second Moment X	0.0299	0.0255	-14.71%	
	GLSD - Homogeneity X	0.0733	0.0593	-19.08%	
	GLD - Gradient Second Moment Y	0.0380	0.0334	-11.89%	
	GLSD - Homogeneity Y	0.1053	0.0868	-17.65%	

Type	Pressure Measure	Sample		Relative %	Δ Plot
		118-2-61	188-2-2491		
General	Contact Cells	368	364	-1.09%	
	Sum of Pressure	25704.47	25628.04	-0.30%	
Spatial	Moran's I (CD)	0.7905	0.5501	-30.41%	
	GLSD - Correlation X	0.8539	0.6808	-20.28%	
	GLSD - Correlation Y	0.8646	0.7400	-14.41%	
Variability	Coefficient of Variation	1.0451	1.0441	-0.10%	
	GLD - Gradient Contrast X	1622.49	3663.97	125.82%	
	GLD - Gradient Mean X	25.11	38.17	52.01%	
	GLD - Gradient Contrast Y	1471.59	2819.38	91.59%	
	GLD - Gradient Mean Y	22.29	31.86	42.93%	
Texture	GLD - Gradient Second Moment X	0.0255	0.0180	-29.41%	
	GLSD - Homogeneity X	0.0797	0.0559	-29.94%	
	GLD - Gradient Second Moment Y	0.0317	0.0231	-27.17%	

Type	Pressure Measure	Sample		Relative %	Δ Plot
		148-1-2914	170-1-1363		
General	Contact Cells	302	301	-0.33%	
	Sum of Pressure	15917.33	15918.89	0.01%	
	Skewness	2.1262	2.6473	24.51%	
Variability	Coefficient of Variation	1.1210	1.1259	0.44%	
	GLD - Gradient Contrast Y	1150.61	1622.08	40.98%	
	GLD - Gradient Mean Y	19.32	21.99	13.80%	
Texture	GLD - Gradient Second Moment X	0.0330	0.0240	-27.40%	
	GLSD - Homogeneity X	0.0929	0.0590	-36.53%	
	GLD - Gradient Second Moment Y	0.0414	0.0317	-23.51%	
	GLSD - Homogeneity Y	0.0990	0.0672	-32.12%	

Appendix L

Transformed Data Subset: Upscaled Samples and Transformations

Original Non-Scaled Pressure Map

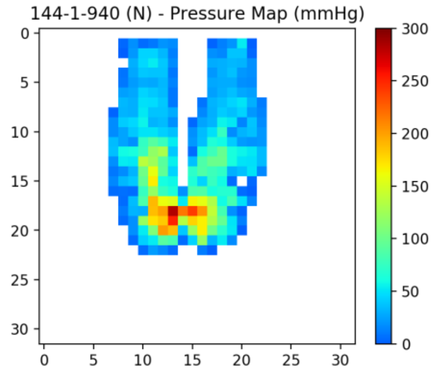

Transformation 1 [Horizontal: $+3$, Vertical: -3, Rotation: $+15°$]

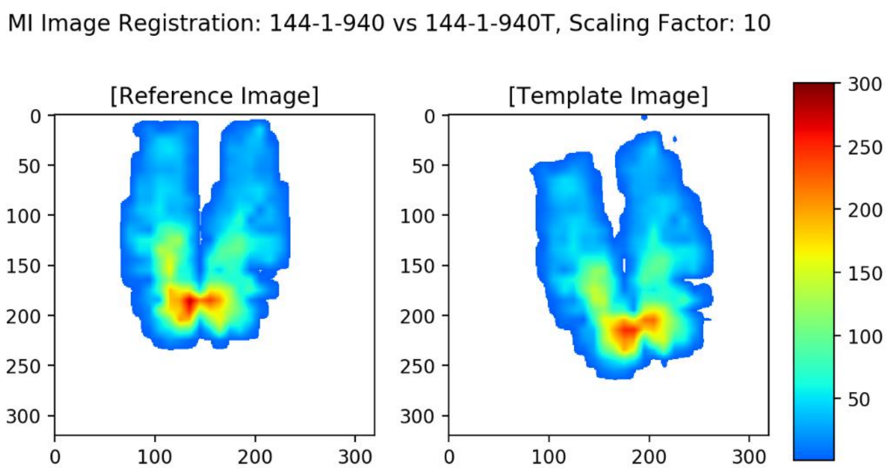

Transformation 2 [Horizontal: -2, Vertical: -1, Rotation: $-6°$]

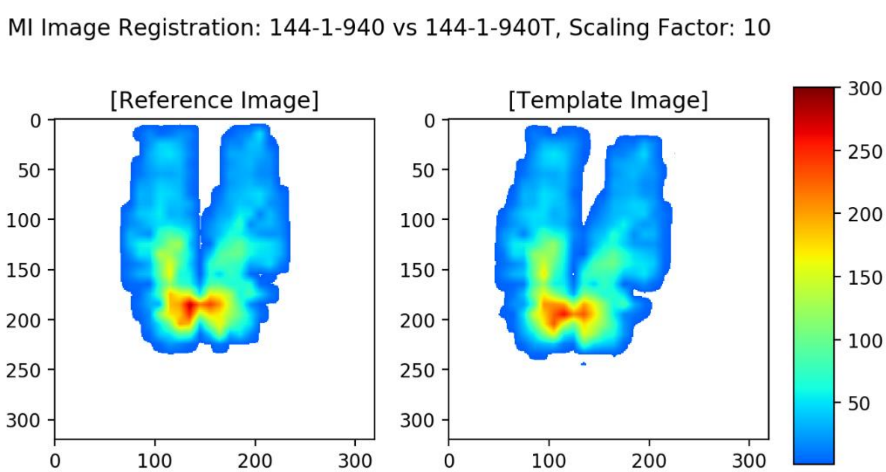

Original Non-Scaled Pressure Map

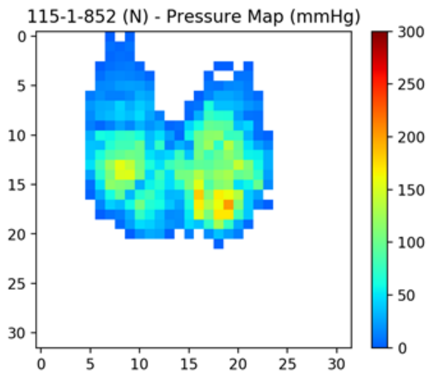

Transformation 1 [Horizontal: +4, Vertical: −7, Rotation: −20°]

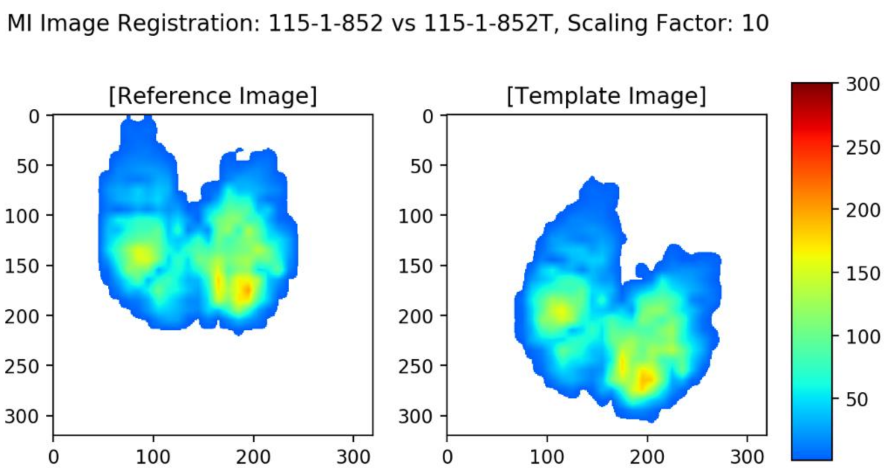

Transformation 2 [Horizontal: +3, Vertical: −2, Rotation: +8°]

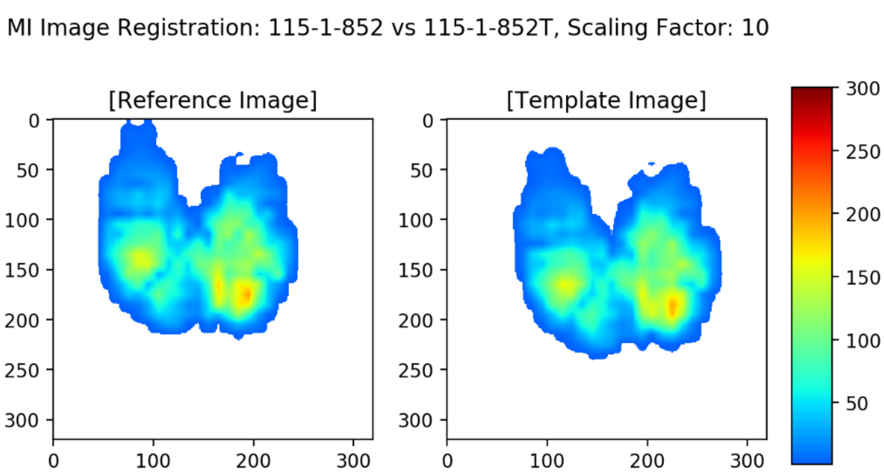

Original Non-Scaled Pressure Map

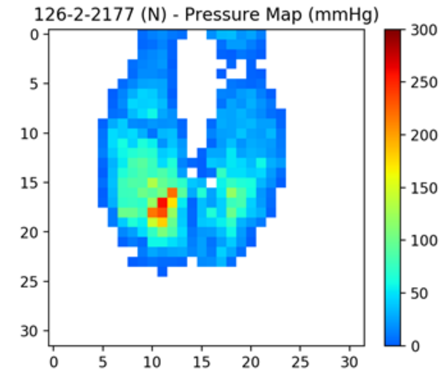

Transformation 1 [Horizontal: $+2$, Vertical: -4, Rotation: $-60°$]

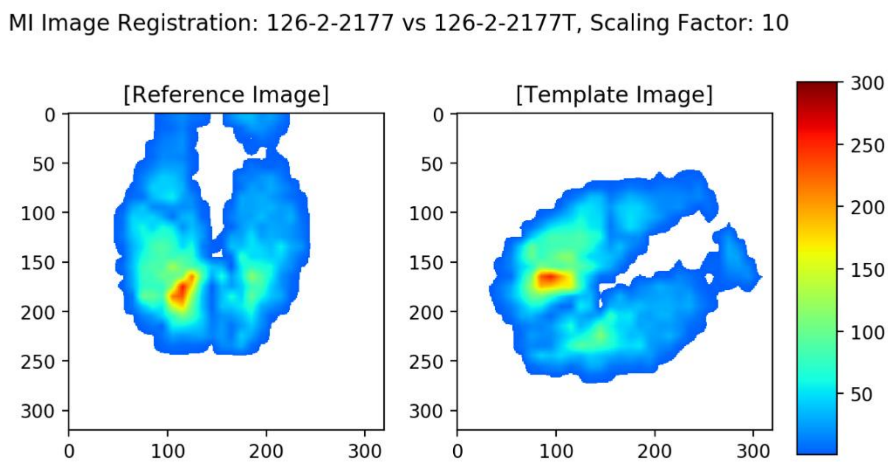

Transformation 2 [Horizontal: -2, Vertical: -3, Rotation: $+10°$]

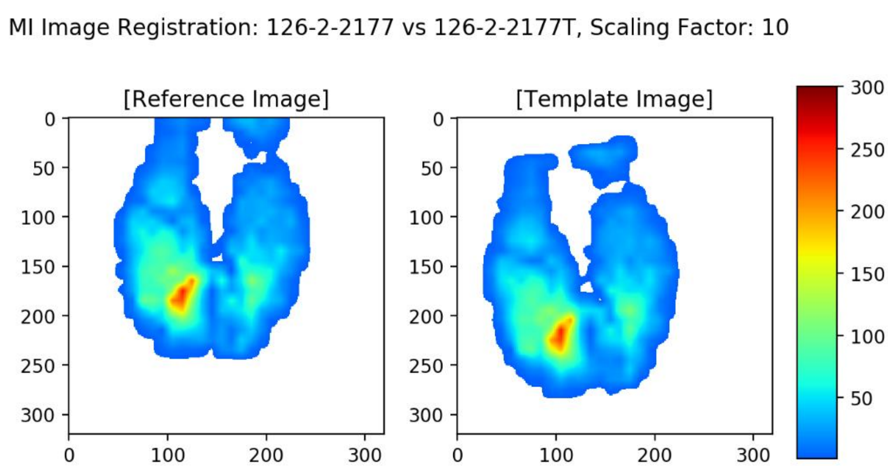

Original Non-Scaled Pressure Map

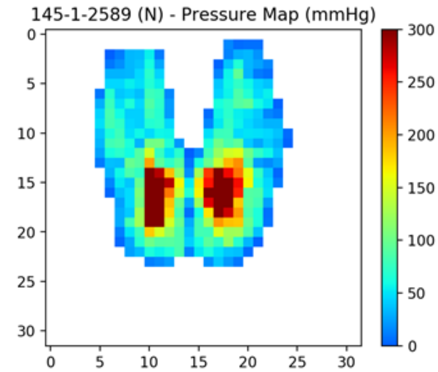

Transformation 1 [Horizontal: −1, Vertical: −3, Rotation: +17°]

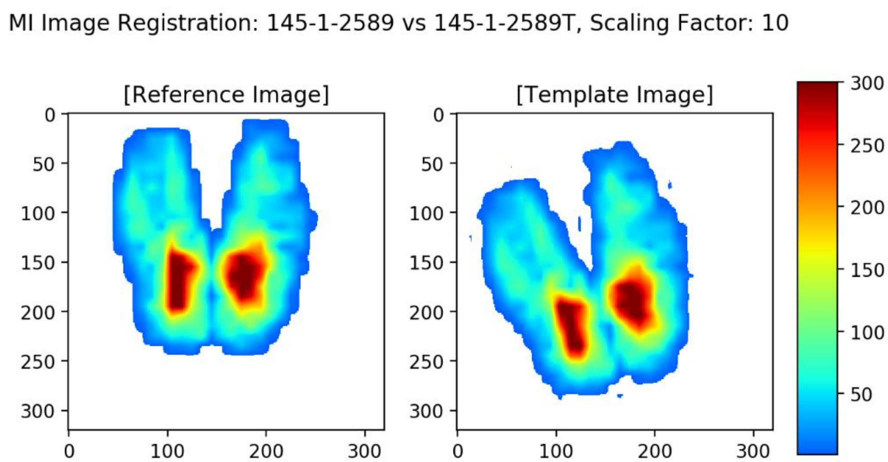

Transformation 2 [Horizontal: +4, Vertical:+1, Rotation: −7°]

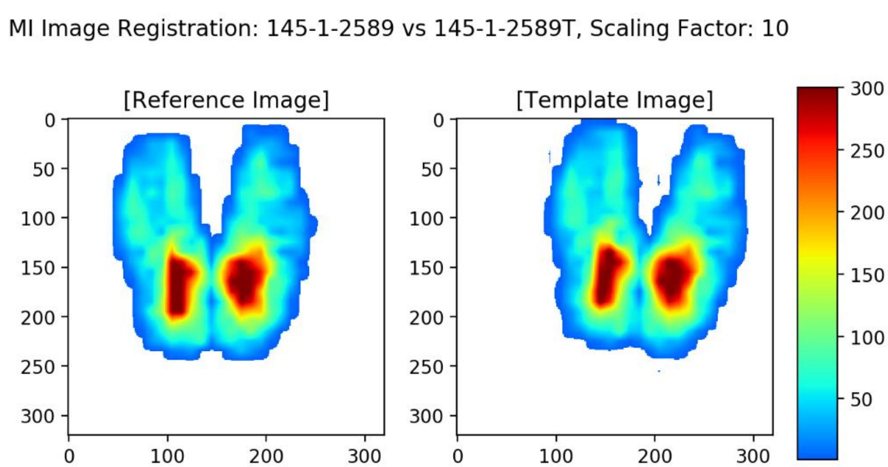

Original Non-Scaled Pressure Map

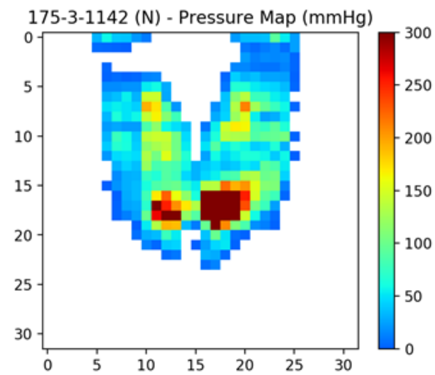

Transformation 1 [Horizontal: -1, Vertical: -6, Rotation: $+35°$]

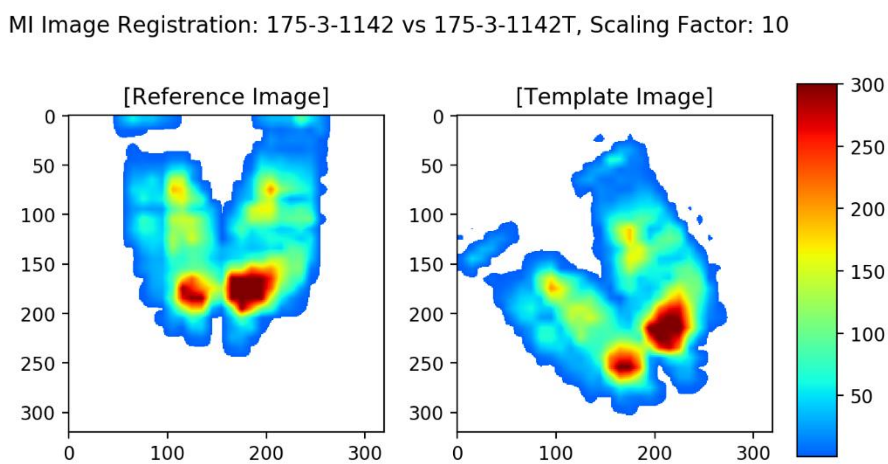

Transformation 2 [Horizontal: $+3$, Vertical: -2, Rotation: $-5°$]

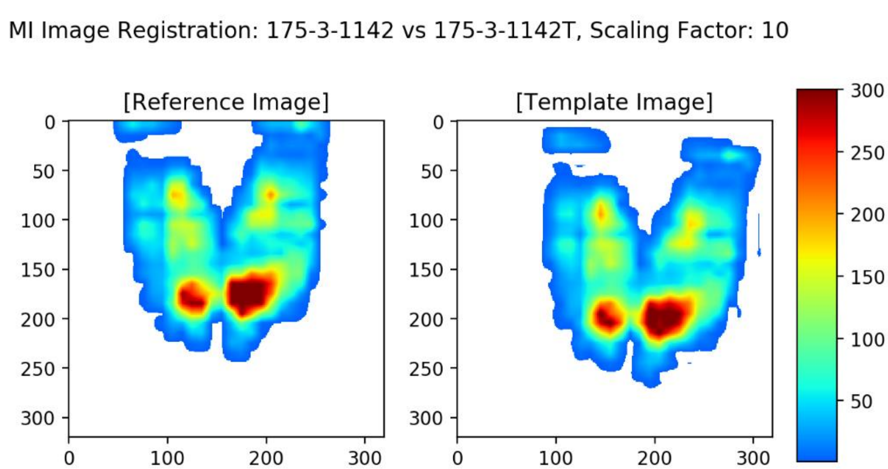

Original Non-Scaled Pressure Map

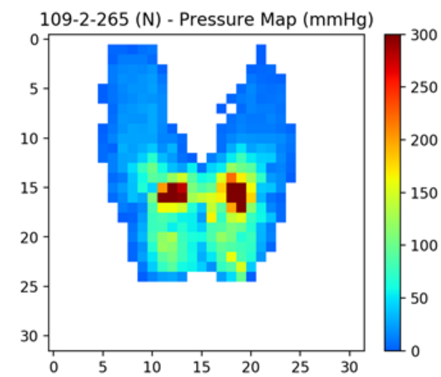

Transformation 1 [Horizontal: -1, Vertical: -3, Rotation: $+36°$]

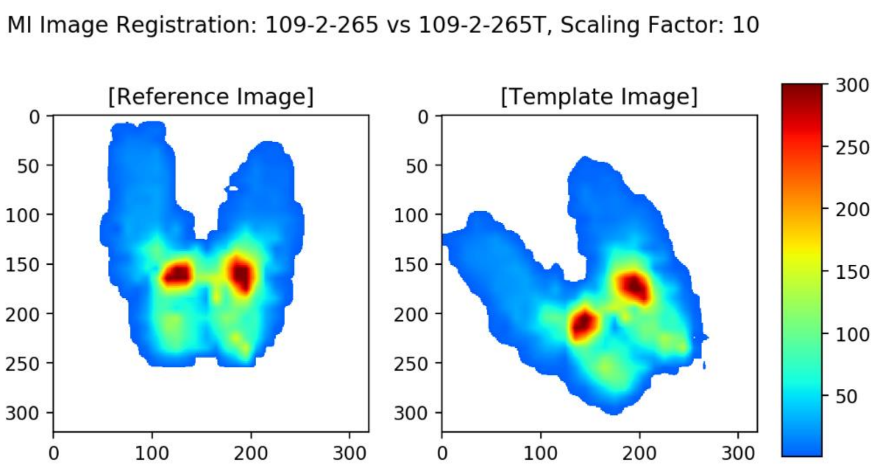

Transformation 2 [Horizontal: $+4$, Vertical: -1, Rotation: $-5°$]

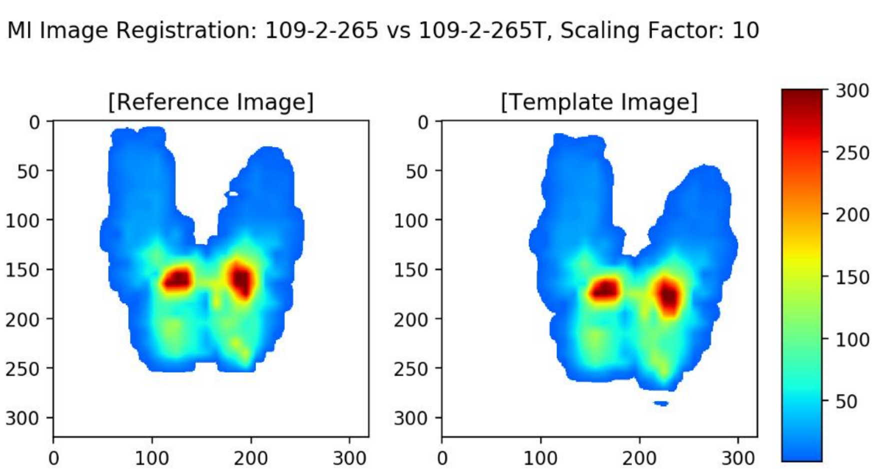

Original Non-Scaled Pressure Map

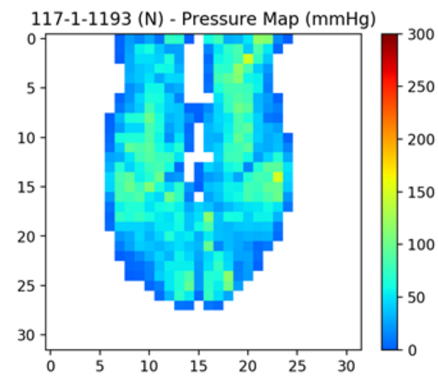

Transformation 1 [Horizontal: −2, Vertical: −3, Rotation: +22°]

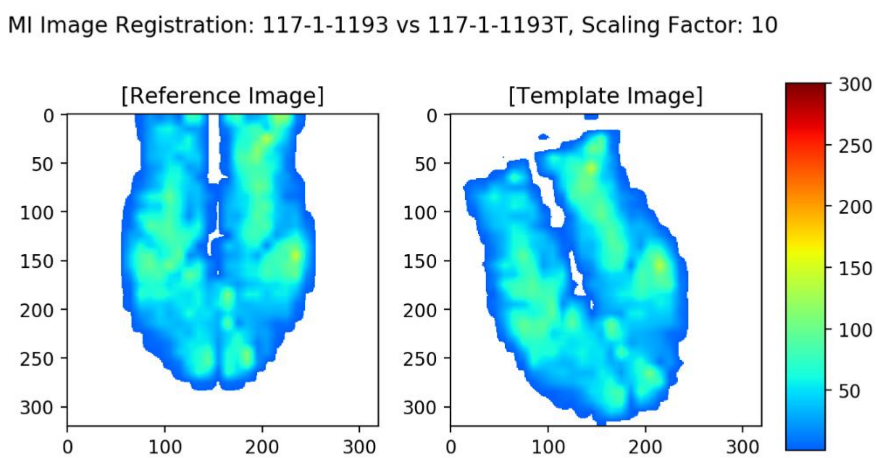

Transformation 2 [Horizontal: +3, Vertical:0, Rotation: −9°]

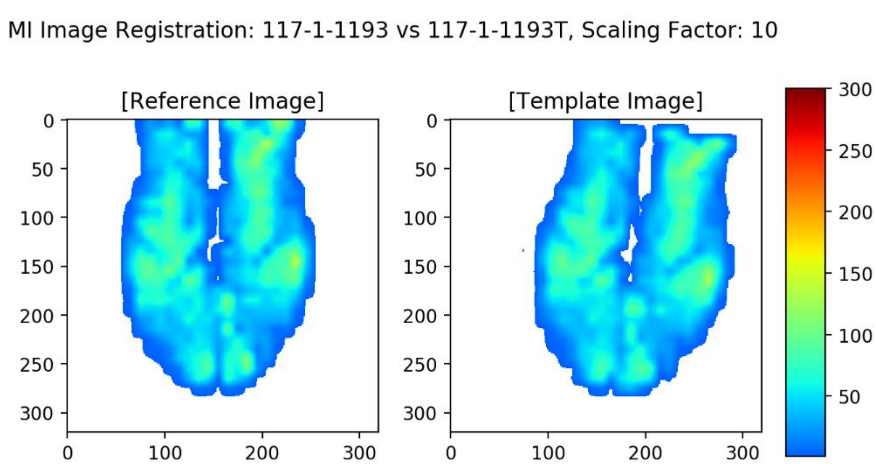

Original Non-Scaled Pressure Map

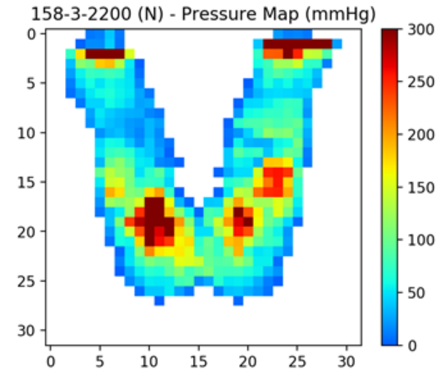

Transformation 1 [Horizontal: +2, Vertical: −5, Rotation: +25°]

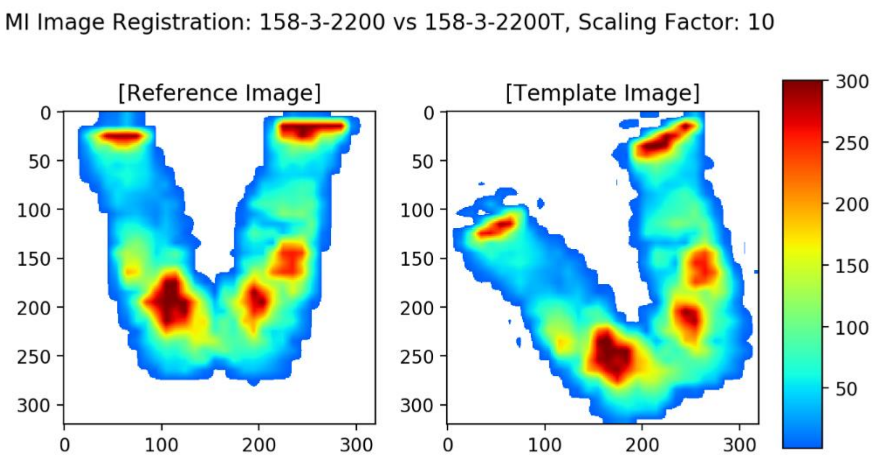

Transformation 2 [Horizontal: 0, Vertical:−3, Rotation: −10°]

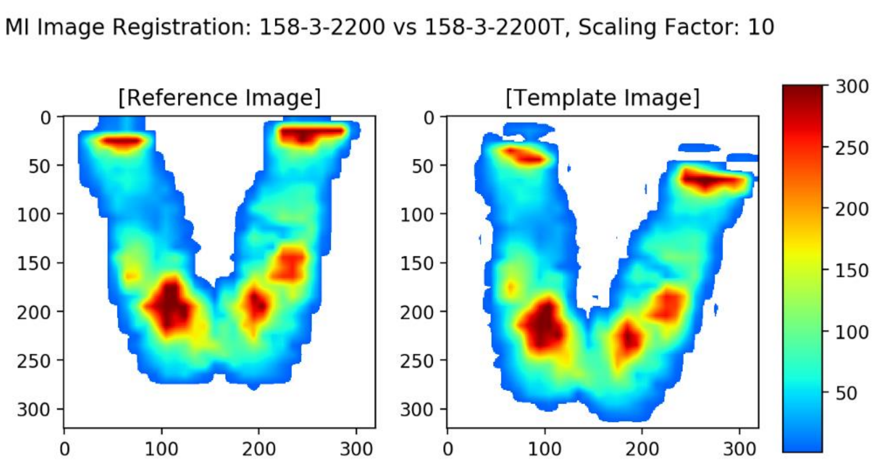

Original Non-Scaled Pressure Map

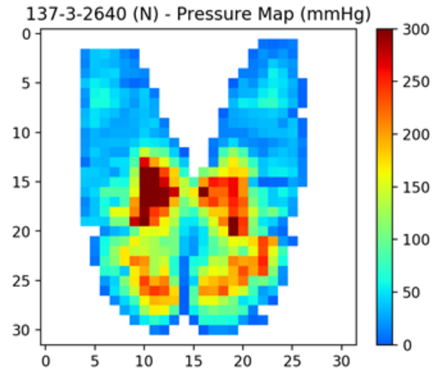

Transformation 1 [Horizontal: +2, Vertical: −1, Rotation: +30°]

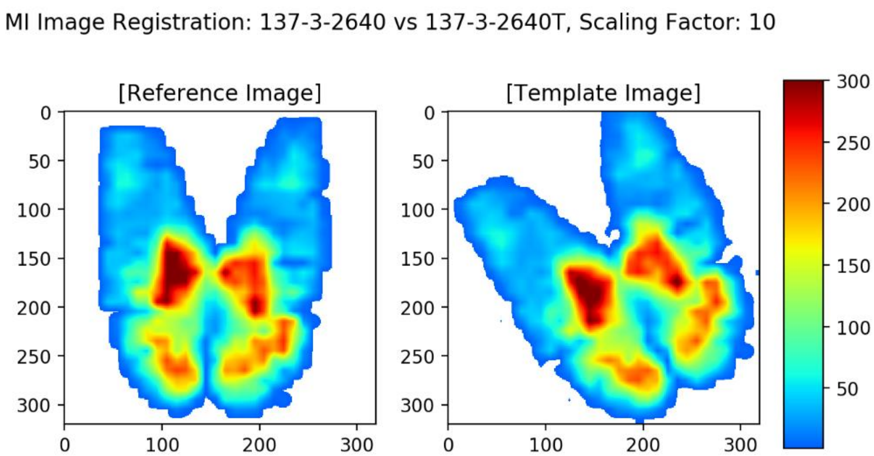

Transformation 2 [Horizontal: −3, Vertical:+1, Rotation: −6°]

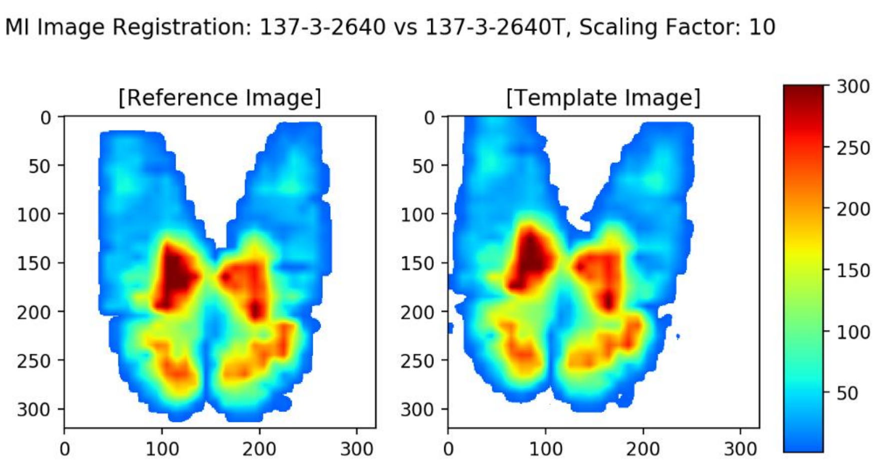

Original Non-Scaled Pressure Map

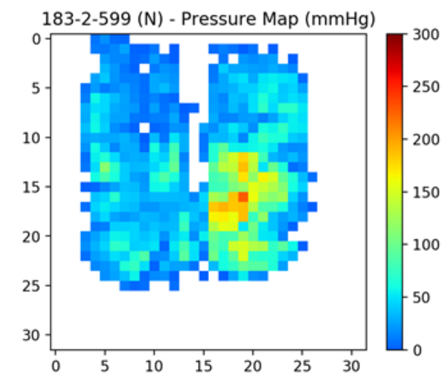

Transformation 1 [Horizontal: −1, Vertical: −4, Rotation: −12°]

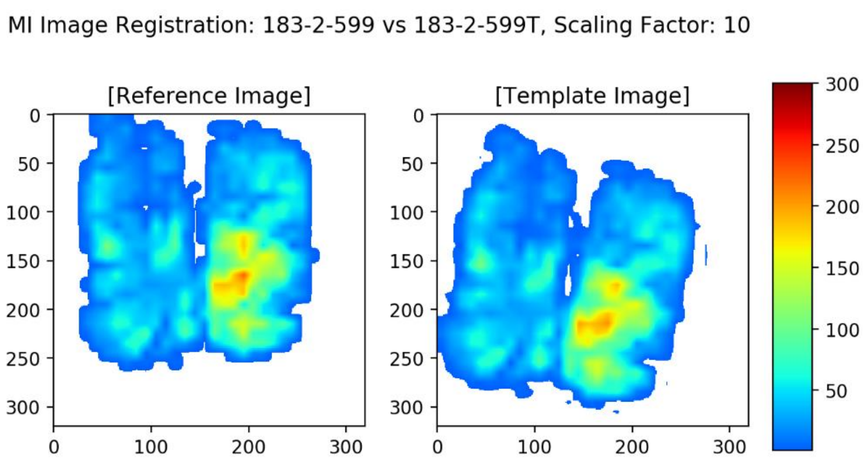

Transformation 2 [Horizontal: +4, Vertical:0, Rotation: +9°]

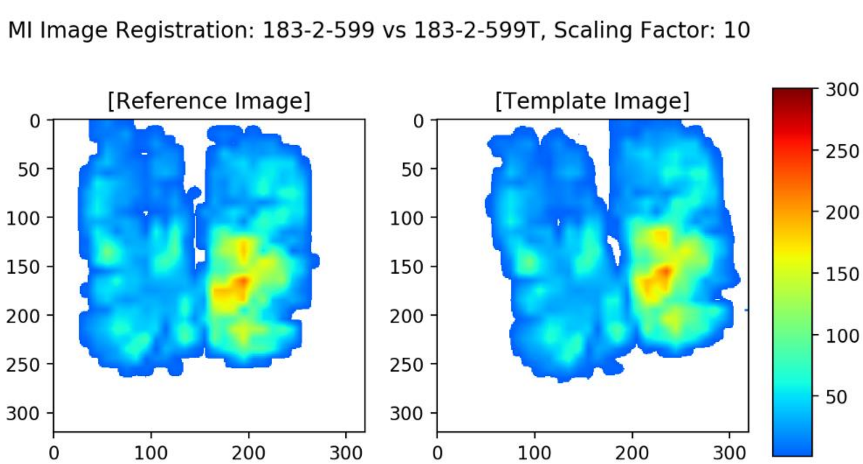

Appendix M

Transformed Data Subset: Registration Results

Sample	Trans	Method	Iter	Pearson	Pearson (M)	Tanimoto	Tanimoto (M)	Min-Ratio	Min-Ratio (M)	L1 Norm	L1 Norm (M)	Sq L2 Norm	Sq L2 Norm (M)	Int-Ratio Var	Int-Ratio Var (M)
144-1-940	T1	MI	60	0.9967	0.9944	0.9945	0.9946	0.8815	0.9094	96,113	87,743	759,270	744,431	0.0257	0.0451
144-1-940	T1	MSE	72	0.9967	0.9945	0.9945	0.9946	0.8802	0.9087	96,170	87,732	752,434	737,319	0.0257	0.0441
144-1-940	T2	MI	36	0.9964	0.9939	0.9939	0.9940	0.8768	0.9075	100,087	91,714	837,138	821,193	0.0257	0.0403
144-1-940	T2	MSE	132	0.9964	0.9938	0.9939	0.9940	0.8754	0.9063	101,109	92,681	840,975	824,783	0.0260	0.0406
115-1-852	T1	MI	129	0.9979	0.9960	0.9966	0.9967	0.9065	0.9214	81,119	75,797	436,196	430,165	0.0154	0.0244
115-1-852	T1	MSE	76	0.9979	0.9959	0.9966	0.9966	0.9050	0.9194	82,070	76,753	442,399	436,381	0.0160	0.0253
115-1-852	T2	MI	59	0.9974	0.9950	0.9958	0.9958	0.9054	0.9181	88,163	82,992	543,399	537,552	0.0180	0.0294
115-1-852	T2	MSE	59	0.9975	0.9951	0.9959	0.9960	0.9075	0.9200	86,312	81,211	527,503	521,845	0.0173	0.0288
126-2-2177	T1	MI	25	0.5702	0.2821	0.4759	0.5048	0.3188	0.4746	1,098,349	840,667	58,987,452	52,543,926	4.9064	10.5775
126-2-2177	T1	MSE	292	0.9969	0.9950	0.9949	0.9950	0.8949	0.9076	78,311	72,499	422,998	414,730	0.0247	0.0433
126-2-2177	T2	MI	56	0.9964	0.9941	0.9940	0.9941	0.8720	0.8813	94,343	88,965	498,356	491,014	0.0360	0.0618
126-2-2177	T2	MSE	100	0.9972	0.9954	0.9954	0.9954	0.8933	0.9017	79,751	74,921	385,734	380,175	0.0257	0.0435
145-1-2589	T1	MI	59	0.9985	0.9975	0.9975	0.9976	0.8872	0.9194	136,942	125,906	1,030,536	1,006,991	0.0198	0.0324
145-1-2589	T1	MSE	100	0.9983	0.9972	0.9973	0.9973	0.8795	0.9113	147,821	136,532	1,121,878	1,096,205	0.0236	0.0367
145-1-2589	T2	MI	41	0.9984	0.9974	0.9974	0.9975	0.8732	0.9133	143,142	131,403	1,067,124	1,040,910	0.0247	0.0419
145-1-2589	T2	MSE	80	0.9985	0.9975	0.9975	0.9976	0.8733	0.9134	139,641	127,904	1,014,023	987,662	0.0249	0.0421
175-3-1142	T1	MI	15	0.5628	0.2402	0.4706	0.4991	0.3130	0.4922	2,084,670	1,716,010	243,475,294	217,304,888	40.8657	89.5725
175-3-1142	T1	MSE	124	0.9974	0.9958	0.9958	0.9958	0.8629	0.8940	159,543	149,112	1,430,679	1,409,583	0.0360	0.0536
175-3-1142	T2	MI	36	0.9952	0.9921	0.9921	0.9922	0.8372	0.8779	211,152	199,319	2,682,313	2,650,593	0.0428	0.0616
175-3-1142	T2	MSE	78	0.9970	0.9951	0.9951	0.9952	0.8542	0.8920	167,006	155,372	1,658,699	1,629,499	0.0374	0.0526
109-2-265	T1	MI	31	0.9944	0.9918	0.9904	0.9905	0.8080	0.8344	181,738	172,034	1,936,258	1,916,193	0.1002	0.1848
109-2-265	T1	MSE	134	0.9978	0.9968	0.9962	0.9963	0.9082	0.9195	96,239	90,412	759,114	751,197	0.0228	0.0435
109-2-265	T2	MI	28	0.9983	0.9975	0.9970	0.9971	0.9194	0.9300	84,504	78,700	604,594	594,820	0.0118	0.0183
109-2-265	T2	MSE	104	0.9983	0.9976	0.9971	0.9971	0.9180	0.9287	84,755	78,921	587,589	577,317	0.0122	0.0188
117-1-1193	T1	MI	31	0.9142	0.7830	0.8913	0.8997	0.6649	0.7346	558,642	507,791	13,262,068	12,116,813	1.7029	3.5742
117-1-1193	T1	MSE	47	0.9941	0.9846	0.9920	0.9922	0.8762	0.9060	140,826	132,204	924,616	905,953	0.0301	0.0492
117-1-1193	T2	MI	17	0.9836	0.9608	0.9781	0.9801	0.8552	0.8852	187,076	172,973	2,547,984	2,300,789	0.5750	1.3146
117-1-1193	T2	MSE	38	0.9867	0.9684	0.9820	0.9839	0.8646	0.8936	170,443	157,096	2,082,477	1,859,181	0.4203	0.9230
158-3-2200	T1	MI	26	0.9710	0.9512	0.9586	0.9597	0.7221	0.8104	666,206	628,492	24,969,182	24,312,965	0.4657	0.8566
158-3-2200	T1	MSE	57	0.9960	0.9935	0.9942	0.9945	0.8292	0.9041	255,853	232,598	3,465,272	3,277,621	0.1634	0.3547
158-3-2200	T2	MI	17	0.9925	0.9876	0.9891	0.9894	0.7956	0.8701	378,286	354,629	6,502,339	6,296,600	0.1170	0.2405
158-3-2200	T2	MSE	24	0.9960	0.9937	0.9942	0.9945	0.8414	0.9114	250,933	229,661	3,429,156	3,254,815	0.0677	0.1373
137-3-2640	T1	MI	26	0.9884	0.9823	0.9838	0.9839	0.8111	0.8490	530,496	511,041	11,031,337	10,928,516	0.1162	0.1946
137-3-2640	T1	MSE	121	0.9979	0.9970	0.9971	0.9972	0.8777	0.9126	230,998	213,633	1,978,557	1,891,590	0.0342	0.0585
137-3-2640	T2	MI	17	0.9983	0.9975	0.9976	0.9977	0.8859	0.9161	210,245	197,158	1,642,402	1,568,910	0.0334	0.0586
137-3-2640	T2	MSE	76	0.9984	0.9977	0.9978	0.9979	0.8877	0.9187	200,189	186,591	1,501,870	1,416,182	0.0321	0.0569
183-2-599	T1	MI	29	0.9958	0.9936	0.9941	0.9943	0.8761	0.8964	166,967	155,432	1,026,962	997,315	0.0308	0.0480
183-2-599	T1	MSE	56	0.9964	0.9944	0.9949	0.9951	0.8839	0.9041	152,788	141,443	888,407	861,321	0.0278	0.0449
183-2-599	T2	MI	18	0.9956	0.9931	0.9937	0.9940	0.8673	0.8901	174,709	162,398	1,098,093	1,055,197	0.0525	0.1039
183-2-599	T2	MSE	45	0.9964	0.9945	0.9949	0.9951	0.8830	0.9055	150,690	139,002	889,825	851,835	0.0433	0.0867

(M) → Masked, Red Highlight → Unsuccessful registration

Appendix N

Registration Data Subset: Center of Pressure Distances

Sample 1	Contact Cells 1	Pressure Sum 1	Sample 2	Contact Cells 1	Pressure Sum 1	Index Diff	CP Diff (in)
152-1-1986	264	5,939.71	152-1-1990	253	5,112.39	4	1.560
114-2-1826	283	8,127.56	114-2-1836	286	5,522.38	10	1.145
180-2-2584	286	6,217.83	180-2-2592	259	3,487.49	8	1.602
141-1-2658	294	8,688.91	141-1-2668	330	8,717.82	10	1.491
148-1-3551	323	9,764.61	148-1-3557	322	8,341.11	6	1.503
145-1-1445	329	13,140.82	145-1-1449	291	12,020.36	4	1.352
185-1-1610	355	5,322.23	185-1-1620	374	8,044.00	10	1.568
130-1-232	367	5,117.66	130-1-242	398	5,262.02	10	2.134
164-3-3886	370	15,848.20	164-3-3896	330	10,256.29	10	1.686
182-1-2048	373	12,764.16	182-1-2058	351	10,731.04	10	1.703
174-3-958	377	10,643.80	174-3-970	317	7,331.81	12	2.385
129-2-1842	397	9,355.04	129-2-1852	350	7,215.39	10	1.526
124-1-705	408	7,458.99	124-1-719	400	6,216.85	14	1.519
112-2-1696	412	9,862.96	112-2-1708	396	9,474.47	12	1.891
169-2-1993	418	11,450.02	169-2-2009	331	7,544.58	16	2.506
181-1-3436	422	16,117.60	181-1-3446	407	13,246.74	10	1.134
110-2-1065	453	14,112.06	110-2-1073	421	11,342.65	8	2.002
123-1-2504	486	6,883.90	123-1-2524	497	7,869.10	20	1.793
132-1-1990	504	10,616.64	132-1-2002	498	10,480.87	12	1.228
183-3-2335	558	10,027.45	183-3-2342	545	8,890.86	7	1.302

Appendix O

Registration Data Subset: Upscaled Sample Pairs

Image Registration: 152-1-1986 vs 152-1-1990, Scaling Factor: 10

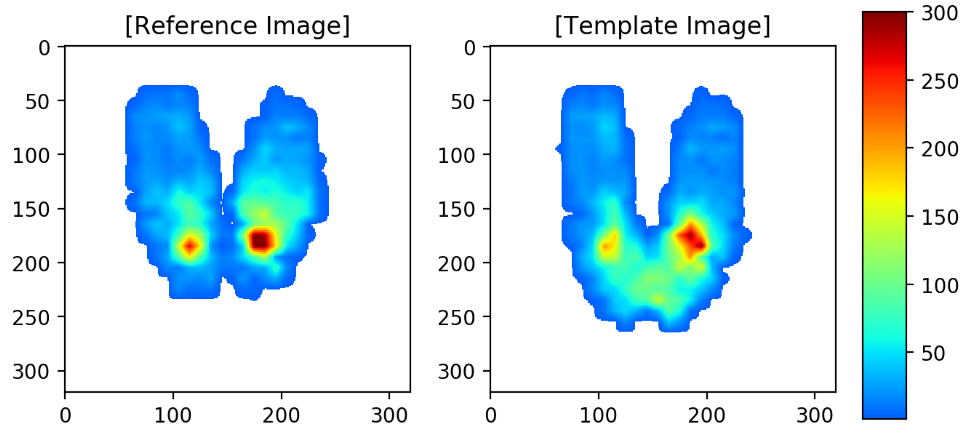

Image Registration: 114-2-1826 vs 114-2-1836, Scaling Factor: 10

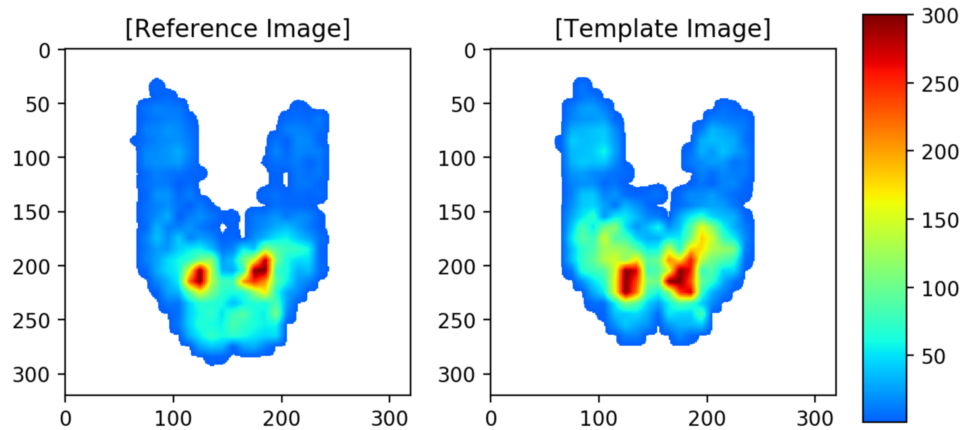

Image Registration: 180-2-2584 vs 180-2-2592, Scaling Factor: 10

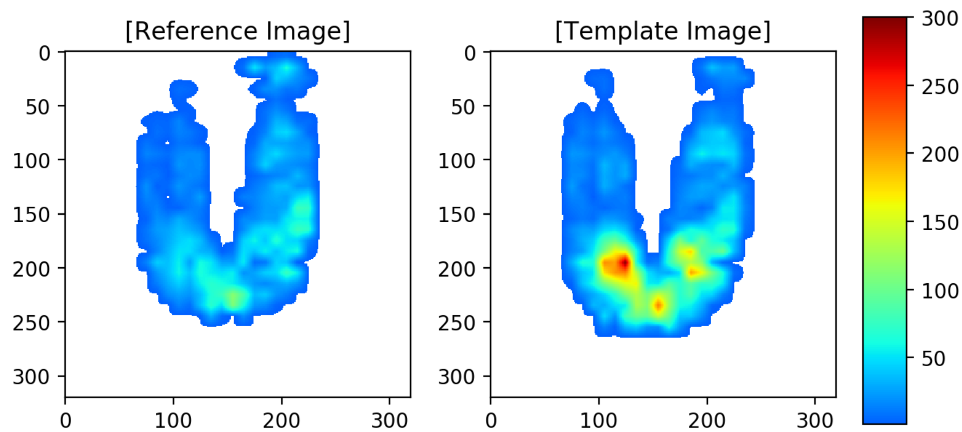

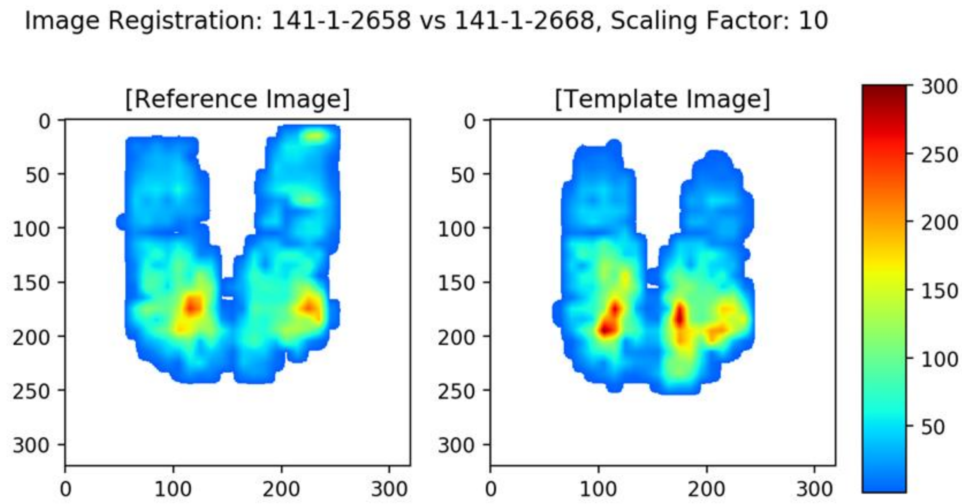
Image Registration: 141-1-2658 vs 141-1-2668, Scaling Factor: 10
[Reference Image]
[Template Image]
0
50
100
150
200
250
300
0
100
200
300
50
100
150
200
250
300

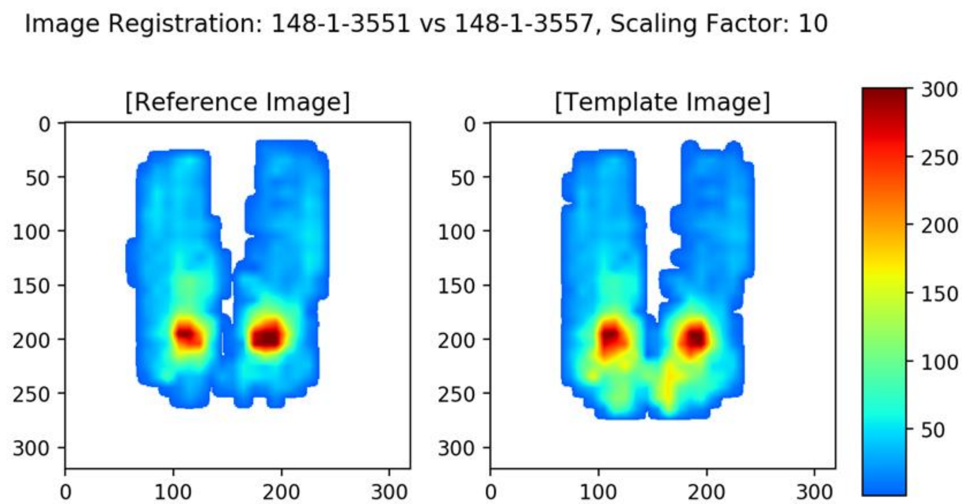
Image Registration: 148-1-3551 vs 148-1-3557, Scaling Factor: 10
[Reference Image]
[Template Image]
0
50
100
150
200
250
300
0
100
200
300
50
100
150
200
250
300

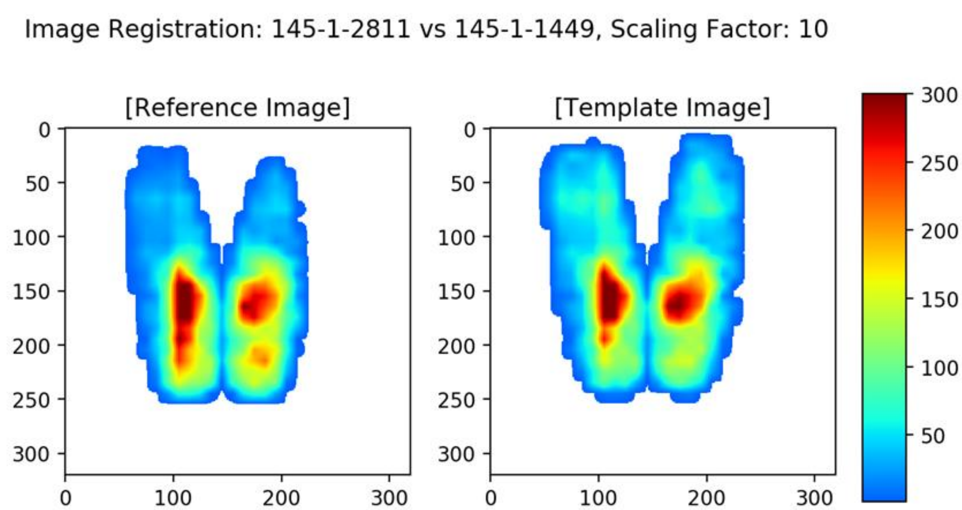
Image Registration: 145-1-2811 vs 145-1-1449, Scaling Factor: 10
[Reference Image]
[Template Image]
0
50
100
150
200
250
300
0
100
200
300
50
100
150
200
250
300

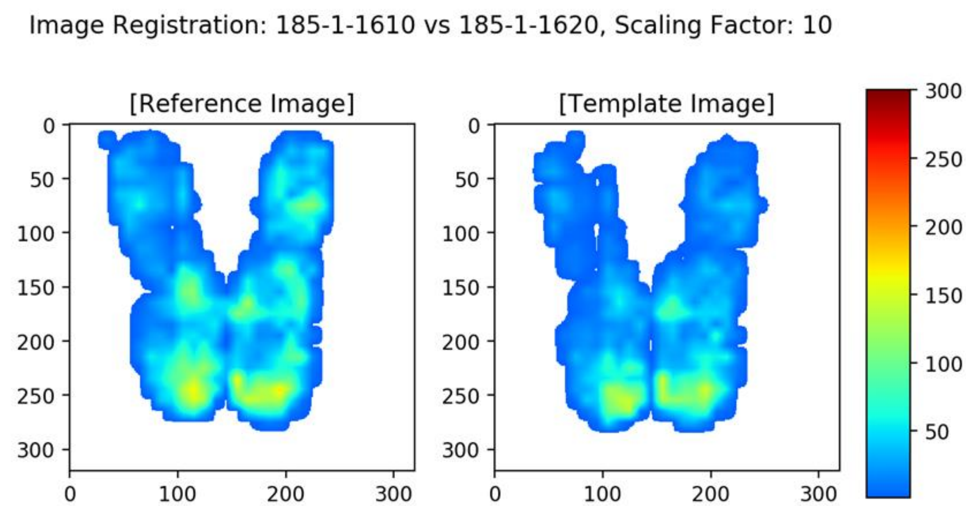
Image Registration: 185-1-1610 vs 185-1-1620, Scaling Factor: 10
[Reference Image]
[Template Image]
0
50
100
150
200
250
300

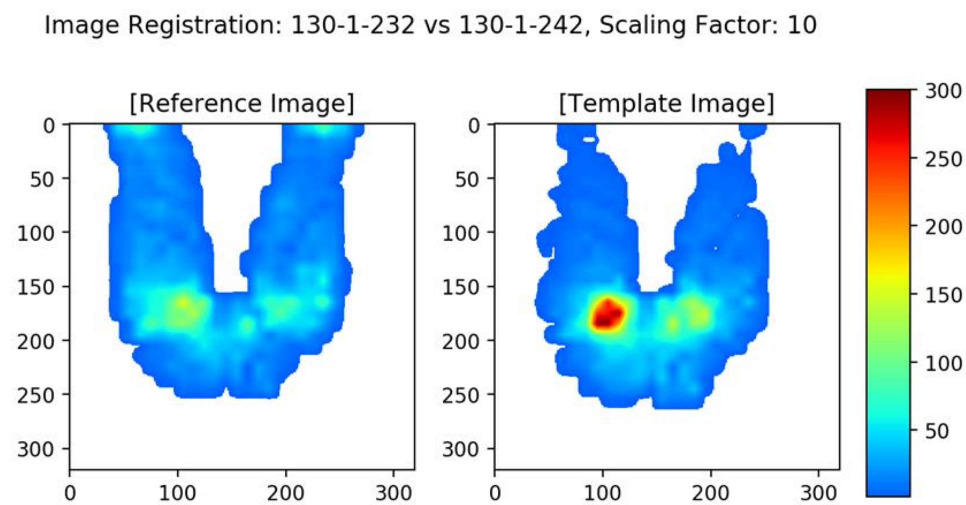
Image Registration: 130-1-232 vs 130-1-242, Scaling Factor: 10
[Reference Image]
[Template Image]
0
50
100
150
200
250
300

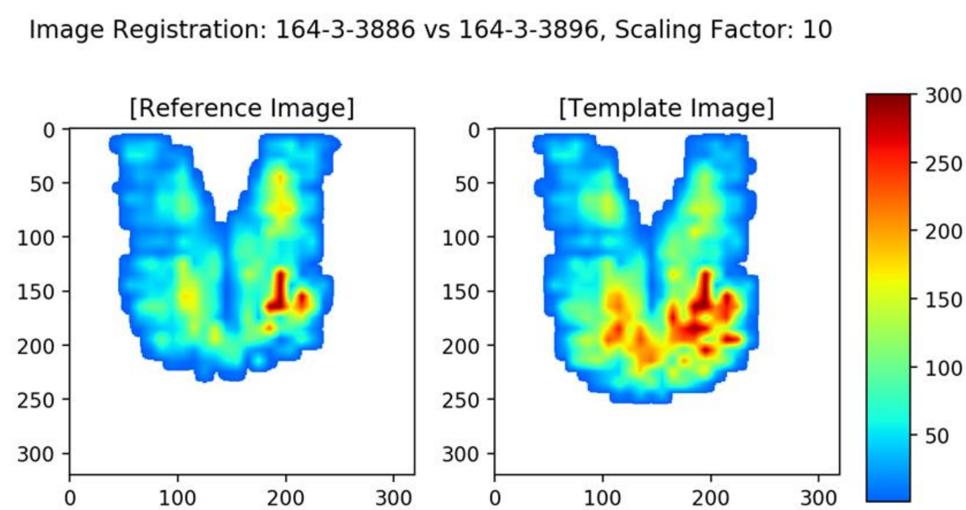
Image Registration: 164-3-3886 vs 164-3-3896, Scaling Factor: 10
[Reference Image]
[Template Image]
0
50
100
150
200
250
300

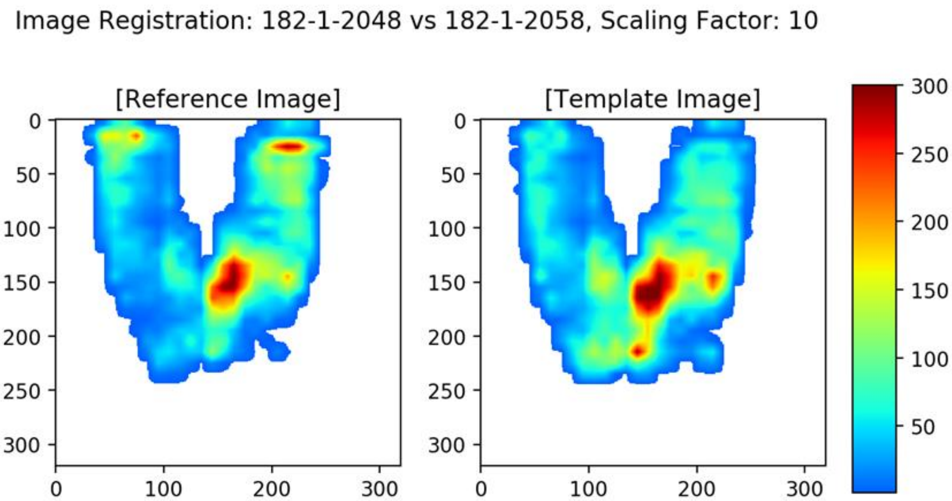
Image Registration: 182-1-2048 vs 182-1-2058, Scaling Factor: 10
[Reference Image]
[Template Image]

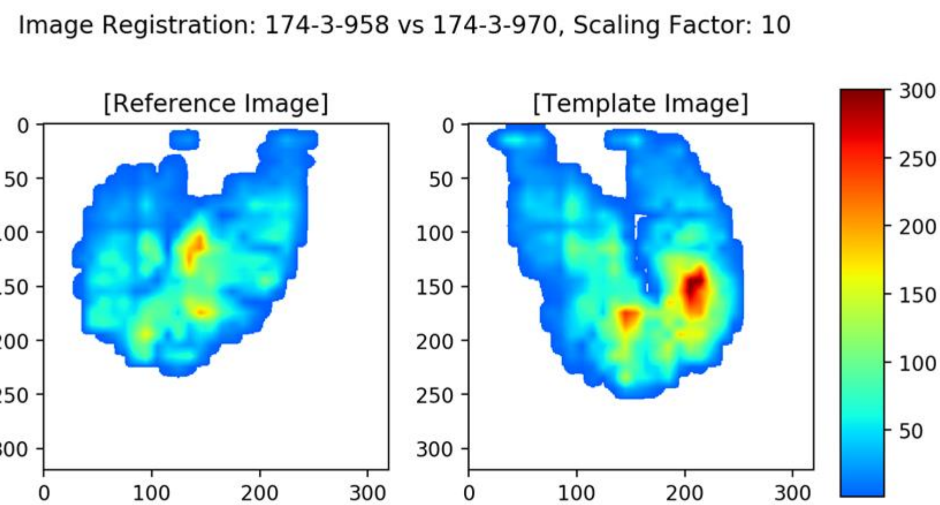
Image Registration: 174-3-958 vs 174-3-970, Scaling Factor: 10
[Reference Image]
[Template Image]

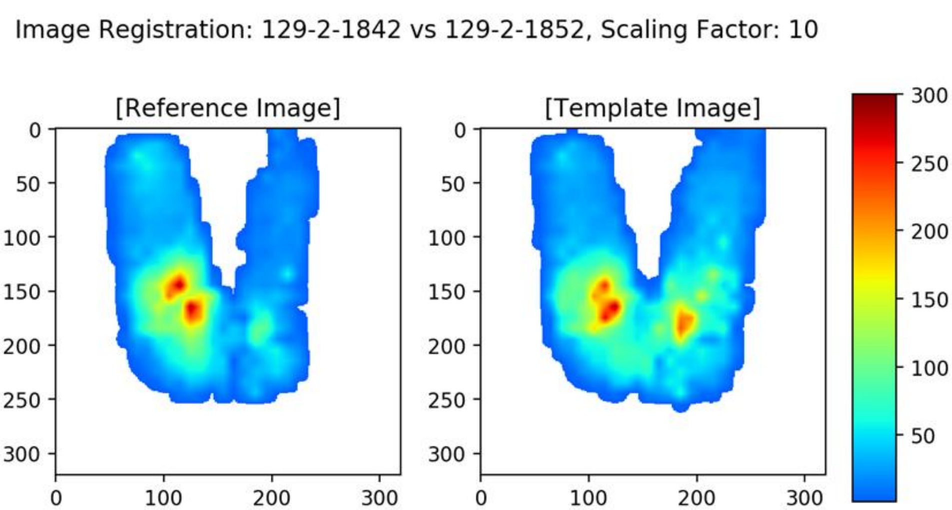
Image Registration: 129-2-1842 vs 129-2-1852, Scaling Factor: 10
[Reference Image]
[Template Image]

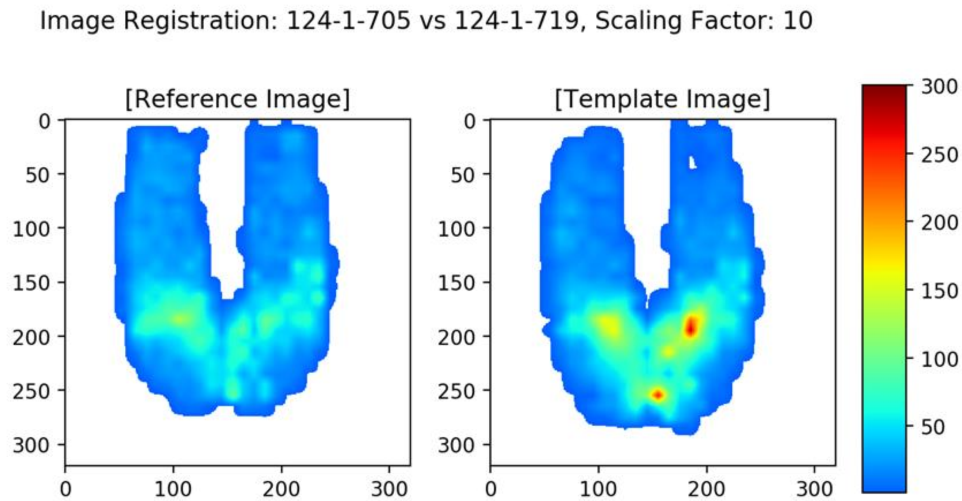
Image Registration: 124-1-705 vs 124-1-719, Scaling Factor: 10
[Reference Image]
[Template Image]
0
50
100
150
200
250
300

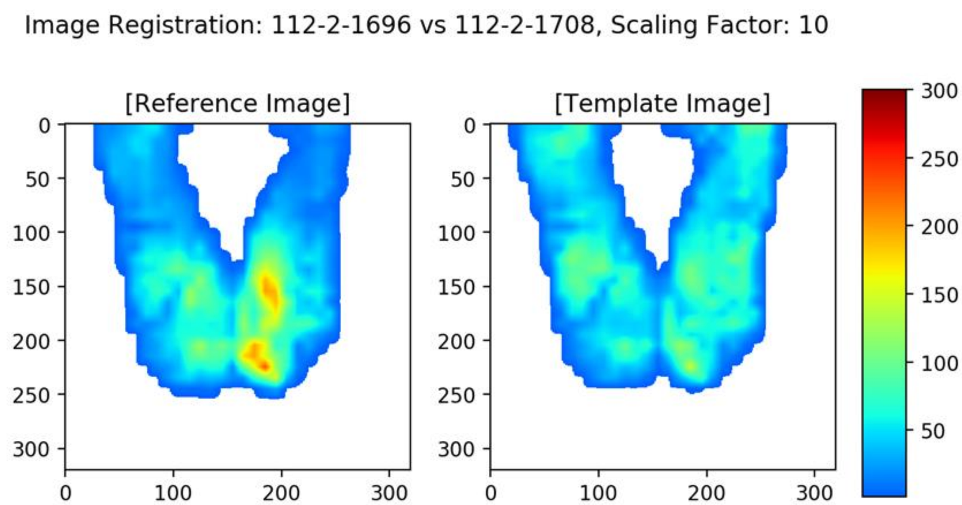
Image Registration: 112-2-1696 vs 112-2-1708, Scaling Factor: 10
[Reference Image]
[Template Image]
0
50
100
150
200
250
300

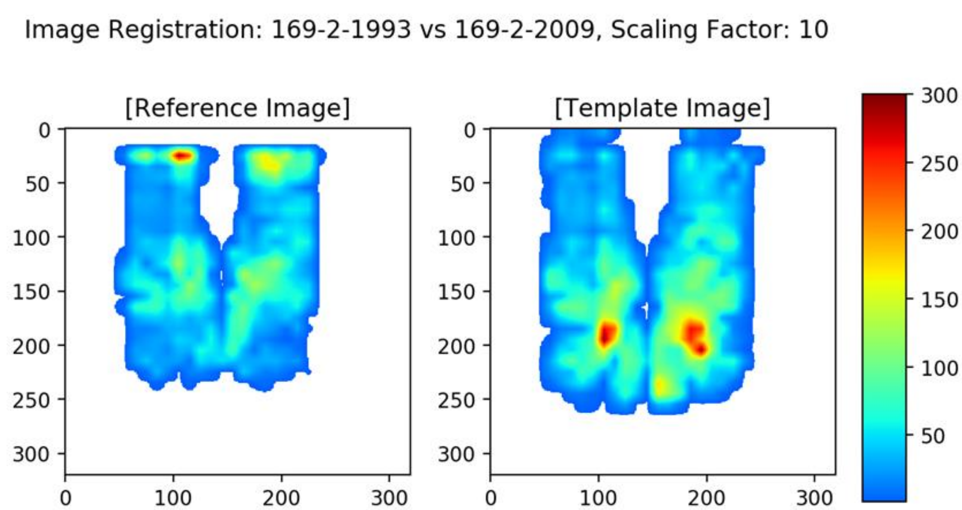
Image Registration: 169-2-1993 vs 169-2-2009, Scaling Factor: 10
[Reference Image]
[Template Image]
0
50
100
150
200
250
300

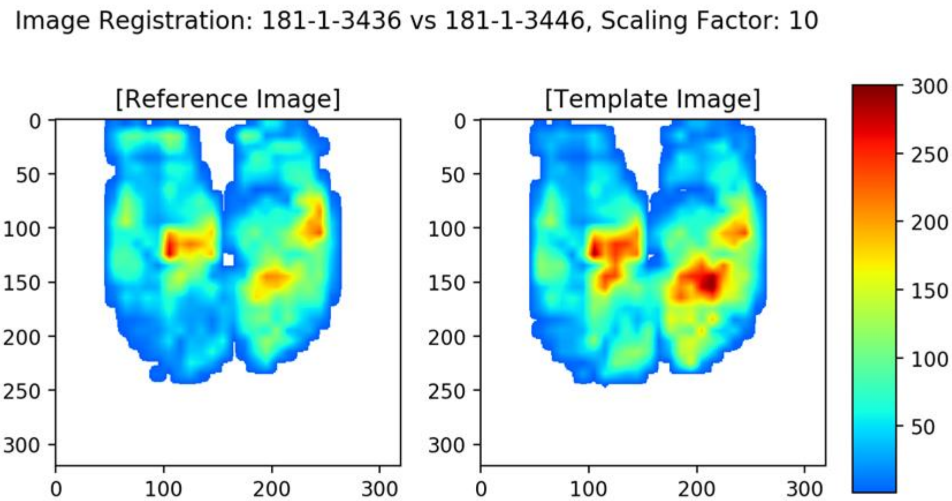
Image Registration: 181-1-3436 vs 181-1-3446, Scaling Factor: 10
[Reference Image]
[Template Image]
0
50
100
150
200
250
300

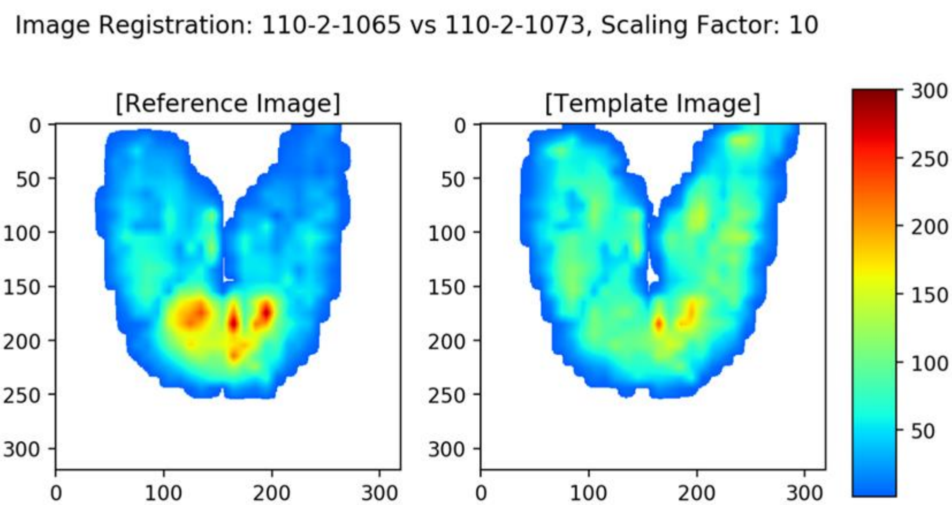
Image Registration: 110-2-1065 vs 110-2-1073, Scaling Factor: 10
[Reference Image]
[Template Image]
0
50
100
150
200
250
300

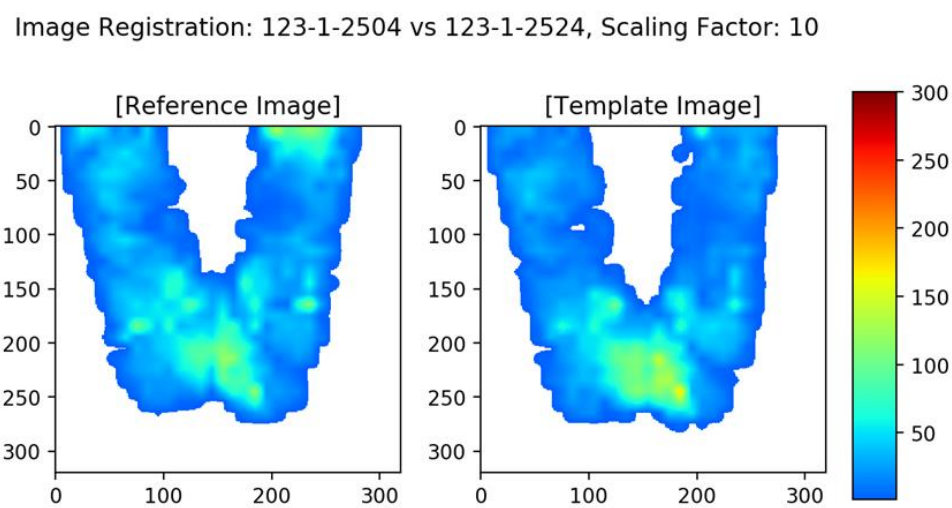
Image Registration: 123-1-2504 vs 123-1-2524, Scaling Factor: 10
[Reference Image]
[Template Image]
0
50
100
150
200
250
300

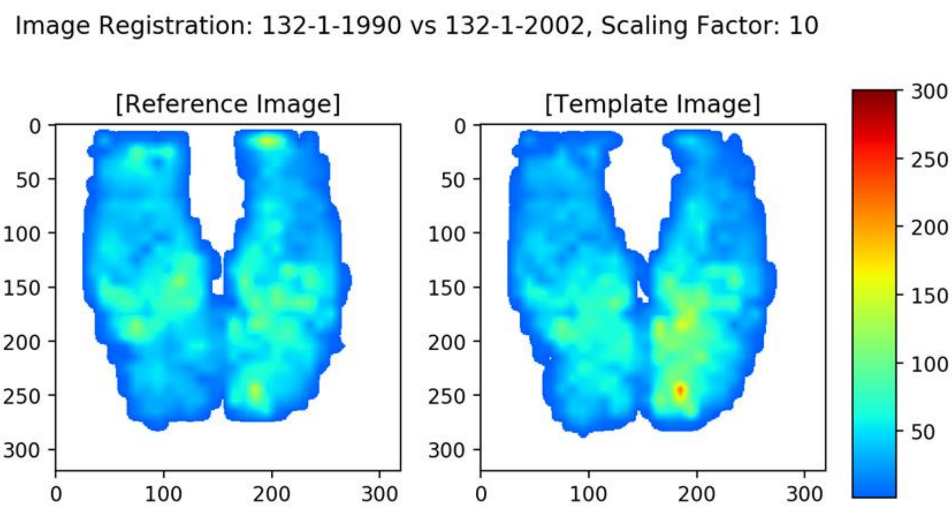
Image Registration: 132-1-1990 vs 132-1-2002, Scaling Factor: 10
[Reference Image]
[Template Image]
0
50
100
150
200
250
300

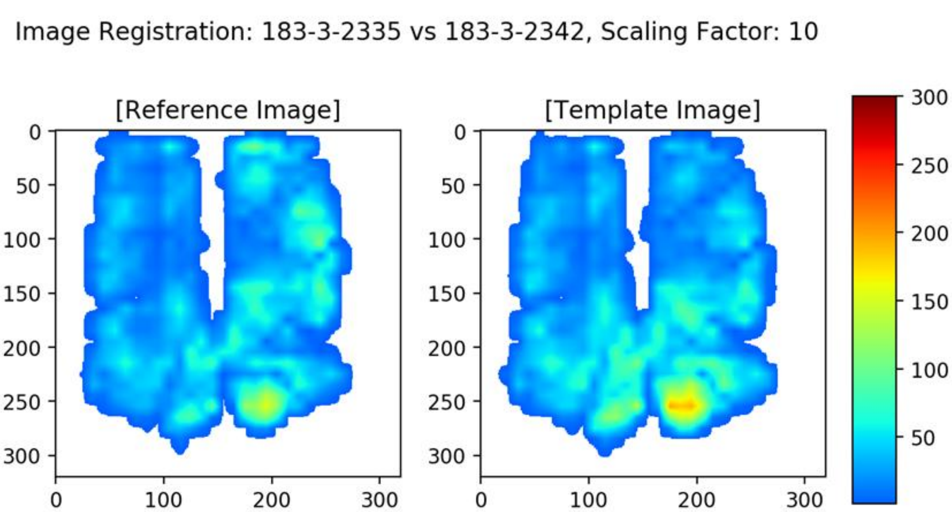
Image Registration: 183-3-2335 vs 183-3-2342, Scaling Factor: 10
[Reference Image]
[Template Image]
0
50
100
150
200
250
300

Appendix P

Registration Data Subset: Registration Results

Sample 1	Sample 2	Method	Iteration Optimal	Pearson	Pearson (M)	Tanimoto	Tanimoto (M)	Min-Ratio	Min-Ratio (M)	L1 Norm	L1 Norm (M)	Sq L2 Norm	Sq L2 Norm (M)	Int-Ratio Var	Int-Ratio Var (M)	Proc Time	Total Iterations
152-1-1986	152-1-1990	MI	5	0.7856	0.6626	0.6789	0.6846	0.5106	0.5785	663,185	616,293	38,212,452	37,221,979	1.2888	2.4323	0.3602	13
152-1-1986	**152-1-1990**	**MSE**	**15**	**0.8186**	**0.7606**	**0.7206**	**0.7629**	**0.5110**	**0.5952**	**671,008**	**552,144**	**32,448,732**	**25,998,703**	**1.3809**	**2.5136**	**0.5978**	**28**
114-2-1826	114-2-1836	MI	11	0.8510	0.7814	0.7140	0.7147	0.5344	0.5522	780,228	761,490	50,912,811	50,753,431	0.8172	1.4830	0.4584	14
114-2-1826	**114-2-1836**	**MSE**	**26**	**0.9040**	**0.8676**	**0.7822**	**0.7853**	**0.5105**	**0.5140**	**777,848**	**749,313**	**37,311,768**	**36,622,073**	**2.8938**	**6.2213**	**0.7845**	**34**
180-2-2584	180-2-2592	MI	44	0.8436	0.7328	0.5302	0.5328	0.5184	0.5597	672,903	639,928	41,944,347	41,501,738	1.0254	2.2007	1.8631	44
180-2-2584	180-2-2592	MSE	35	0.8486	0.7425	0.5342	0.5371	0.5253	0.5723	667,046	630,718	41,491,072	41,001,770	0.9118	1.9431	1.0470	35
141-1-2658	141-1-2668	MI	42	0.8305	0.7183	0.7466	0.7691	0.4890	0.5644	963,637	837,841	46,517,267	41,138,079	5.8926	13.3292	1.7357	42
141-1-2658	**141-1-2668**	**MSE**	**65**	**0.8477**	**0.7527**	**0.7680**	**0.7923**	**0.4987**	**0.5816**	**911,343**	**776,803**	**42,063,924**	**36,496,904**	**6.5255**	**15.1659**	**2.6996**	**65**
148-1-3551	148-1-3557	MI	38	0.9163	0.8720	0.8564	0.8592	0.6622	0.7005	649,330	618,236	29,966,846	29,286,159	0.4260	0.7485	1.5274	38
148-1-3551	148-1-3557	MSE	12	0.9163	0.8717	0.8565	0.8590	0.6631	0.6997	651,471	621,105	29,940,001	29,325,576	0.4323	0.7758	6.9631	108
145-1-2811	145-1-1449	MI	8	0.9616	0.9401	0.9366	0.9399	0.6020	0.6749	715,891	655,135	23,085,658	21,811,528	0.1806	0.2352	0.4657	15
145-1-2811	**145-1-1449**	**MSE**	**23**	**0.9675**	**0.9513**	**0.9457**	**0.9496**	**0.6067**	**0.6821**	**673,908**	**606,596**	**19,678,000**	**18,178,586**	**0.2125**	**0.2885**	**0.7927**	**31**
185-1-1610	185-1-1620	MI	17	0.9228	0.8769	0.8174	0.8183	0.5628	0.5732	639,784	624,277	16,201,295	16,104,100	1.0001	1.8740	0.7032	21
185-1-1610	185-1-1620	MSE	29	0.9260	0.8829	0.8214	0.8224	0.5609	0.5732	634,821	618,136	15,811,222	15,701,607	1.0241	1.9343	1.4964	45
130-1-232	130-1-242	MI	15	0.8428	0.8336	0.6866	0.7004	0.5396	0.5670	610,829	540,682	25,305,492	23,709,449	5.1953	12.5285	0.7133	24
130-1-232	130-1-242	MSE	33	0.8460	0.8372	0.6903	0.7035	0.5309	0.5584	616,958	547,655	24,943,524	23,427,988	5.1524	12.1656	0.9790	33
164-3-3886	164-3-3896	MI	11	0.8351	0.6676	0.6843	0.6867	0.5249	0.5621	1,498,689	1,448,558	115,170,070	113,879,602	0.9040	1.5686	0.6117	18
164-3-3886	**164-3-3896**	**MSE**	**22**	**0.8622**	**0.7438**	**0.7122**	**0.7245**	**0.5752**	**0.6313**	**1,357,217**	**1,251,734**	**103,508,823**	**97,424,074**	**0.2559**	**0.3506**	**5.7342**	**91**
182-1-2048	182-1-2058	MI	50	0.8747	0.7824	0.8082	0.8096	0.6265	0.6413	995,364	972,051	54,997,173	54,496,579	0.6087	0.8275	2.5876	52
182-1-2048	**182-1-2058**	**MSE**	**15**	**0.8971**	**0.8222**	**0.8374**	**0.8381**	**0.6265**	**0.6404**	**956,221**	**937,866**	**45,972,960**	**45,734,508**	**0.4910**	**0.7421**	**0.7339**	**30**
174-3-958	174-3-970	MI	31	0.6286	0.2803	0.4950	0.5098	0.3793	0.4849	1,440,998	1,223,819	107,518,116	101,328,577	17.8812	38.3111	1.3512	35
174-3-958	174-3-970	MSE	119	0.7931	0.7266	0.6476	0.7195	0.3201	0.5398	1,302,123	822,193	67,622,820	48,439,508	4.3454	9.4027	8.9406	119
129-2-1842	129-2-1852	MI	22	0.8712	0.7997	0.7961	0.8044	0.5905	0.6497	745,657	674,163	31,432,958	29,834,999	0.2699	0.4142	1.7599	40
129-2-1842	129-2-1852	MSE	11	0.8754	0.8077	0.8014	0.8122	0.5702	0.6413	752,126	665,915	30,530,796	28,473,329	0.3240	0.5394	0.3786	19
124-1-705	124-1-719	MI	21	0.8940	0.8313	0.7727	0.7732	0.6834	0.6941	547,894	536,592	20,609,301	20,551,565	0.3290	0.4823	0.9180	29
124-1-705	124-1-719	MSE	20	0.9011	0.8451	0.7809	0.7817	0.6832	0.7005	538,889	524,726	19,775,124	19,675,750	0.3134	0.4833	2.0441	49
112-2-1696	112-2-1708	MI	7	0.8318	0.6735	0.7679	0.7712	0.5896	0.6167	945,164	911,327	34,590,097	33,963,859	0.4552	0.6780	0.5257	17
112-2-1696	112-2-1708	MSE	13	0.8359	0.6820	0.7724	0.7758	0.5871	0.6198	937,709	901,574	33,833,062	33,191,036	0.4051	0.5933	5.8250	95
169-2-1993	169-2-2009	MI	40	0.7335	0.4381	0.6001	0.6124	0.4614	0.5486	1,241,721	1,106,929	73,580,364	69,866,511	2.0679	3.9656	1.9084	44
169-2-1993	169-2-2009	MSE	7	0.7416	0.4618	0.6076	0.6244	0.4397	0.5391	1,261,730	1,088,991	71,584,442	66,657,433	2.4445	5.1459	0.6226	23
181-1-3436	181-1-3446	MI	20	0.9412	0.8884	0.8787	0.8791	0.6707	0.6879	992,547	977,668	41,153,593	40,985,873	0.7141	1.2256	0.9050	25
181-1-3436	181-1-3446	MSE	21	0.9442	0.8943	0.8825	0.8828	0.6719	0.6876	982,943	969,077	39,796,882	39,652,043	0.5718	0.9052	0.7863	31
110-2-1065	110-2-1073	MI	10	0.8303	0.7123	0.7733	0.7760	0.5838	0.6028	1,245,901	1,211,682	57,130,125	56,257,199	0.2595	0.3305	0.8216	21
110-2-1065	110-2-1073	MSE	17	0.8307	0.7133	0.7737	0.7766	0.5831	0.6021	1,246,731	1,210,580	57,024,495	56,068,771	0.2534	0.3271	15.5981	171
123-1-2504	123-1-2524	MI	22	0.8534	0.7542	0.8060	0.8076	0.6507	0.6674	578,362	558,394	15,166,842	15,012,600	1.2602	2.3136	0.9140	26
123-1-2504	123-1-2524	MSE	39	0.8574	0.7612	0.8119	0.8133	0.6628	0.6773	571,748	553,905	14,697,618	14,559,631	0.9979	1.7970	1.6104	47
132-1-1990	132-1-2002	MI	29	0.9134	0.8174	0.8912	0.8917	0.7374	0.7502	591,360	579,653	13,691,705	13,617,244	0.5122	1.0281	1.2570	29
132-1-1990	132-1-2002	MSE	63	0.9137	0.8177	0.8915	0.8920	0.7359	0.7494	592,107	580,298	13,652,348	13,578,906	0.5005	0.9730	3.1804	63
183-3-2335	183-3-2342	MI	24	0.9240	0.8673	0.8884	0.8886	0.7472	0.7508	565,240	558,923	11,253,868	11,234,030	0.1639	0.2114	1.4280	32
183-3-2335	183-3-2342	MSE	19	0.9252	0.8698	0.8897	0.8899	0.7463	0.7494	567,650	561,457	11,121,913	11,100,960	0.1654	0.2170	0.6352	27

MSE → Better visual registration || Red → Unsuccessful visual registration || (M) → Masked variation of similarity/dissimilarity coefficient

Appendix Q

Registration Data Subset: Optimality Registration Results Maps

Reference (fixed) and Template (moving) pressure maps

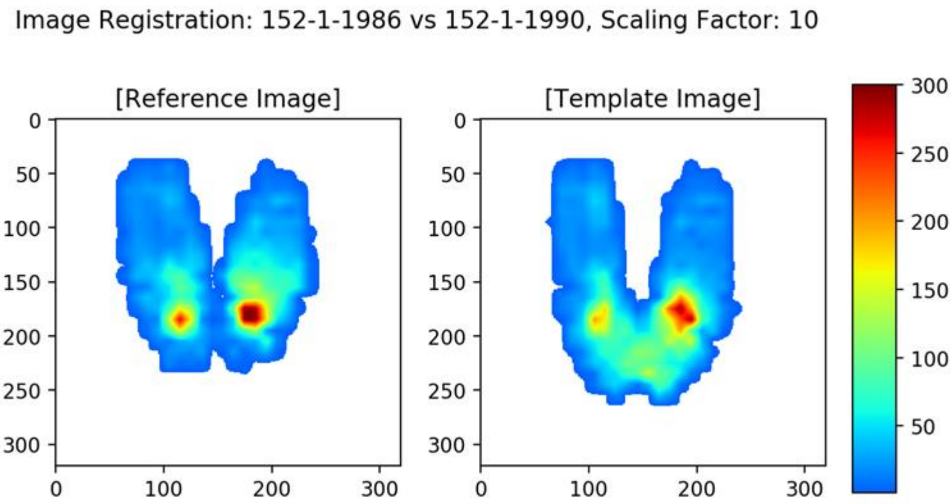

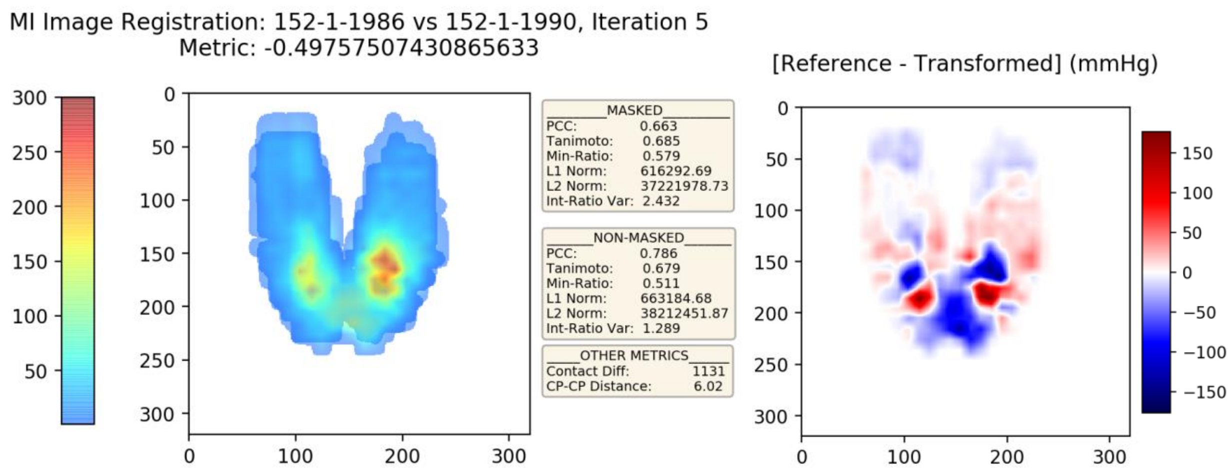

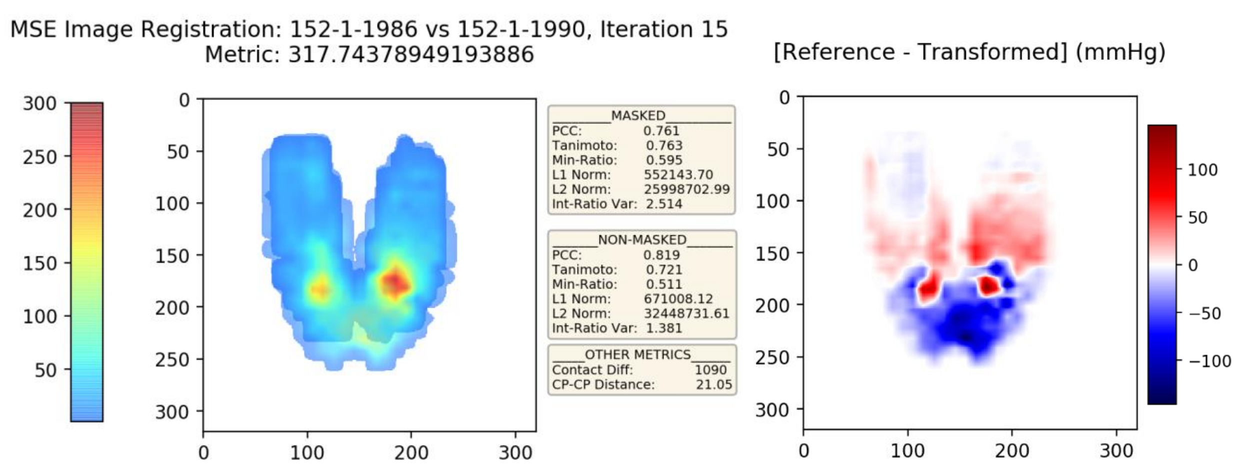

Visual feedback: **MSE** registration produced better correspondence in tuberosities and legs.

Reference (fixed) and Template (moving) pressure maps

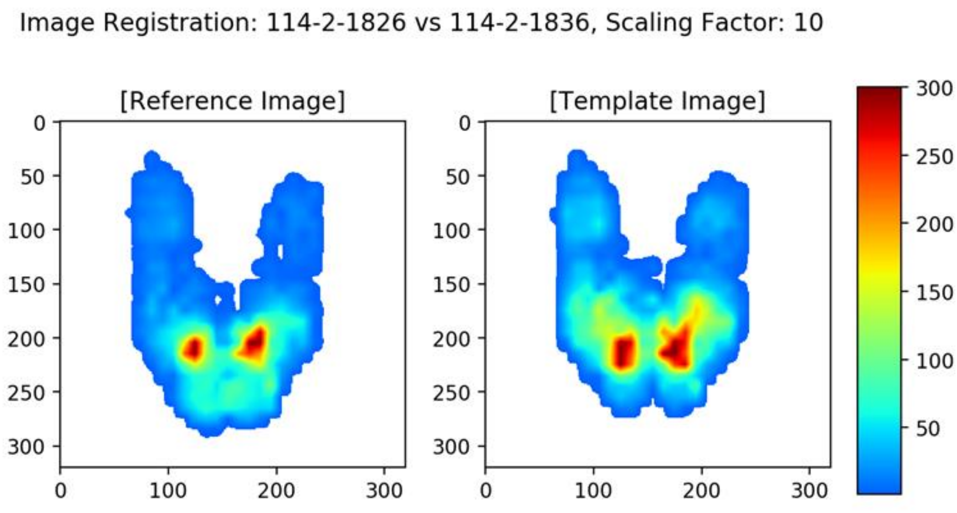

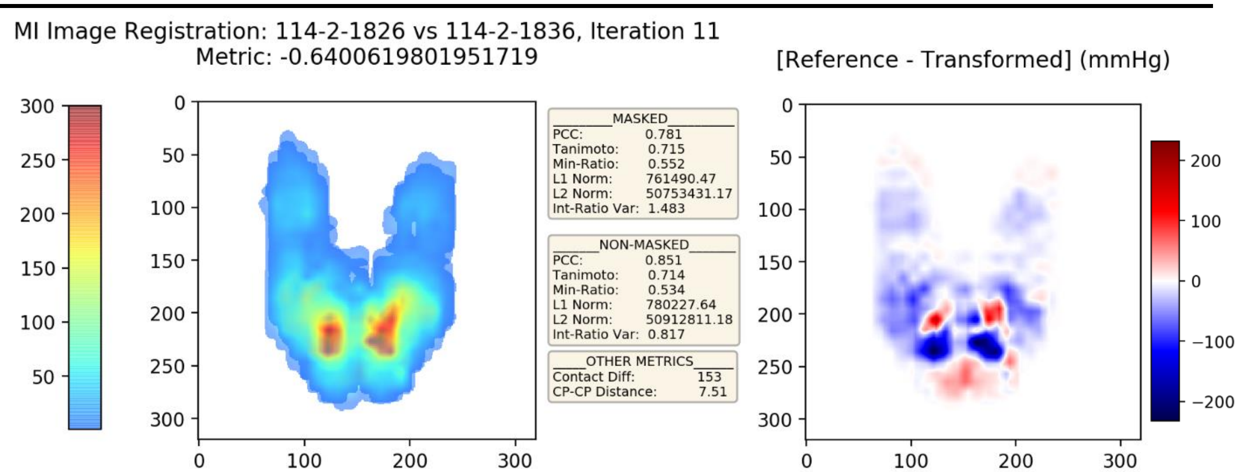

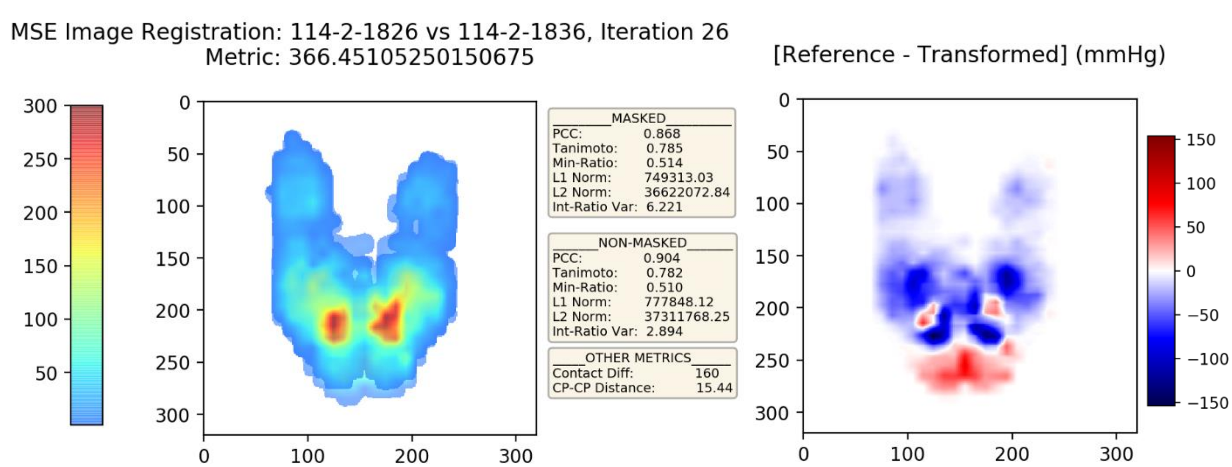

Visual feedback: **MSE** registration produced better correspondence in tuberosities and legs.

<u>Reference (fixed) and Template (moving) pressure maps</u>

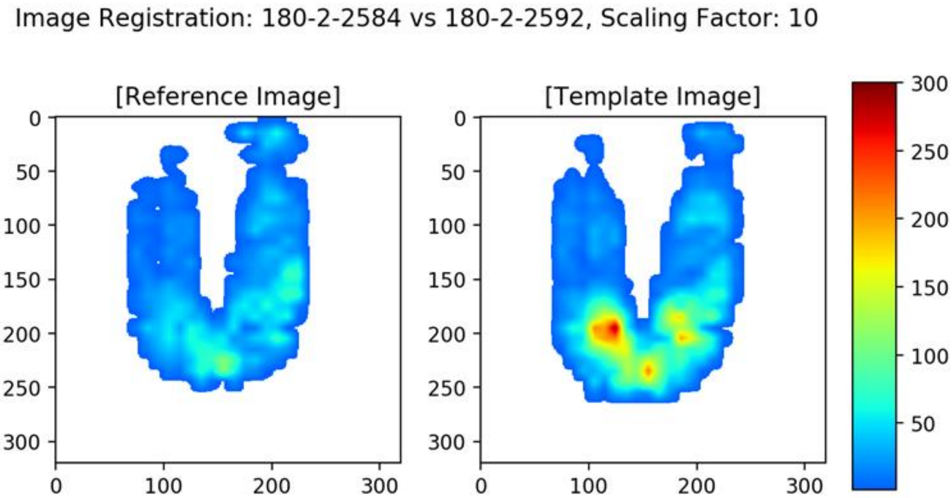

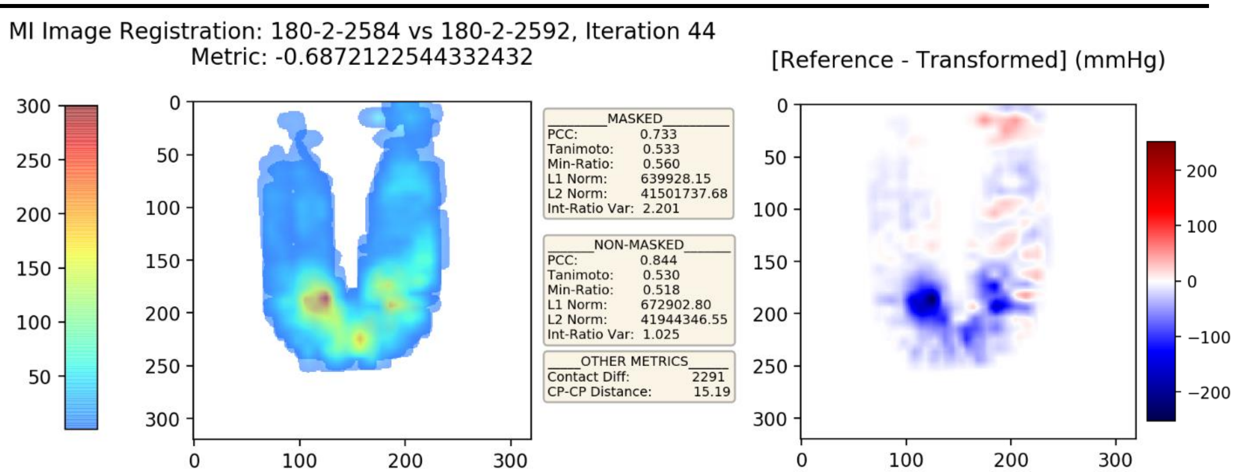

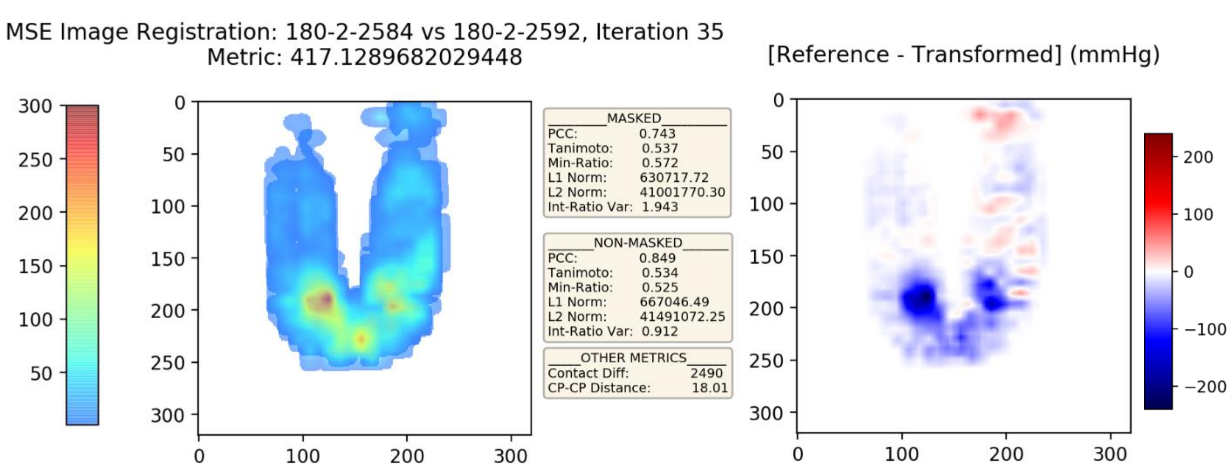

Visual feedback: Both MI and MSE did similar and appropriate registrations.

Reference (fixed) and Template (moving) pressure maps

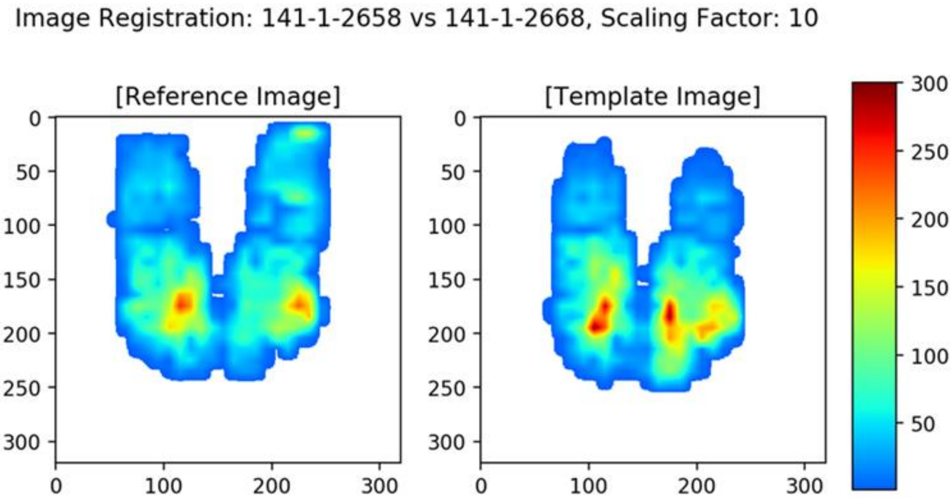

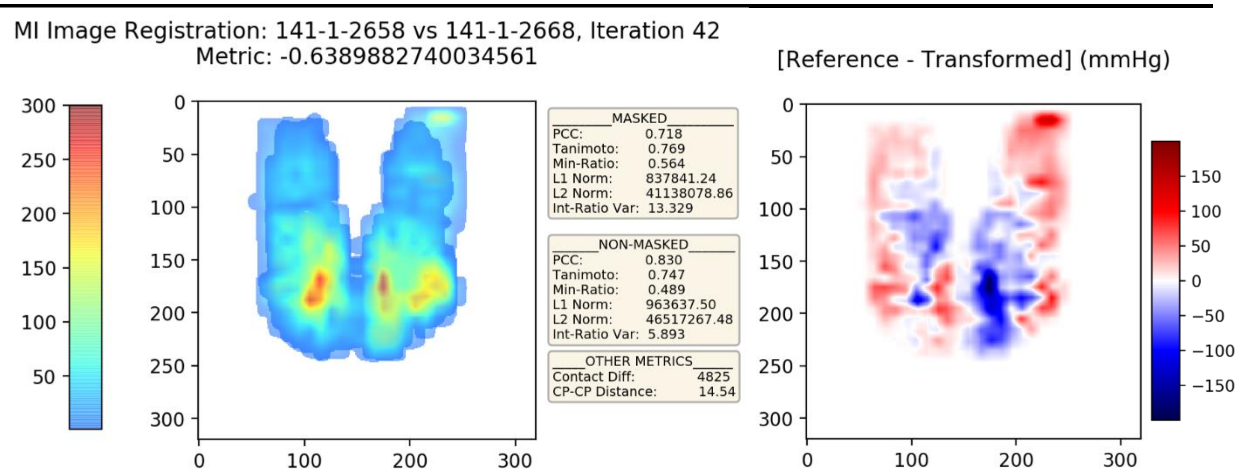

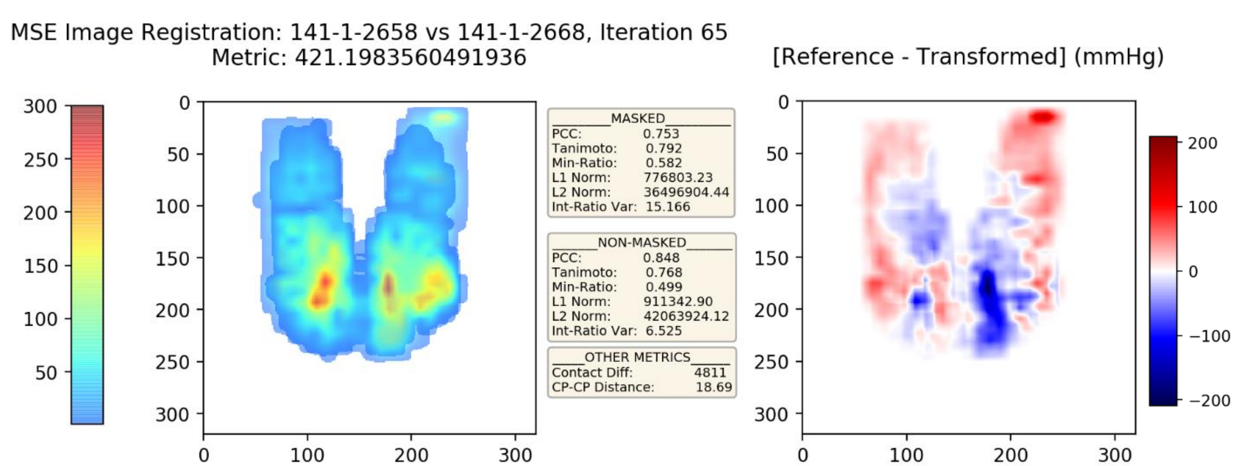

Visual feedback: **MSE** registration produced slightly better correspondence in the left tuberosity.

Reference (fixed) and Template (moving) pressure maps

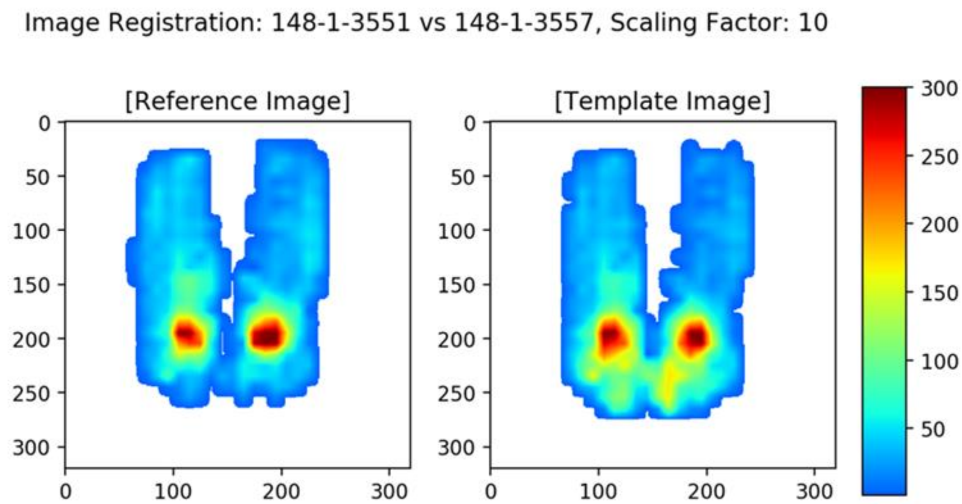

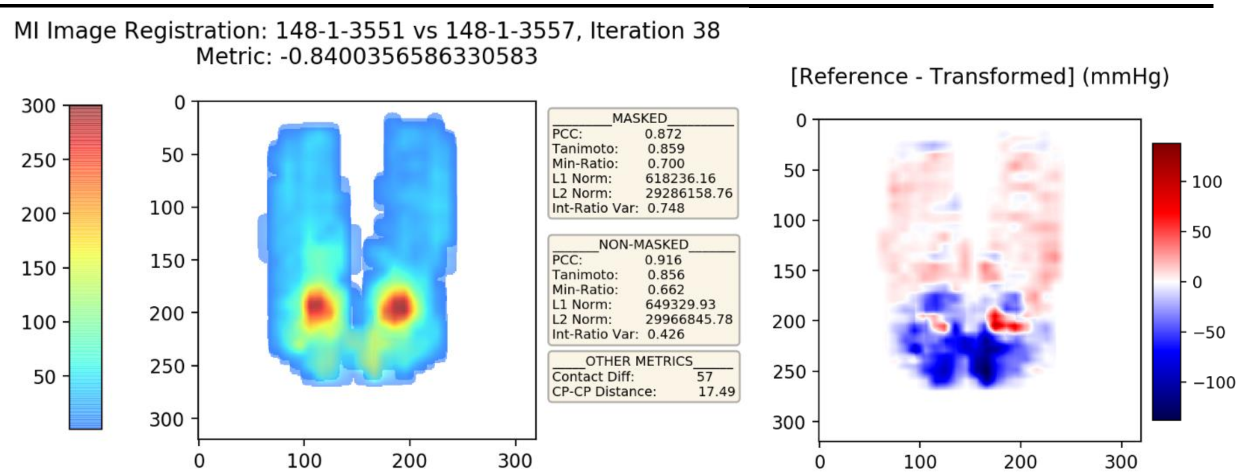

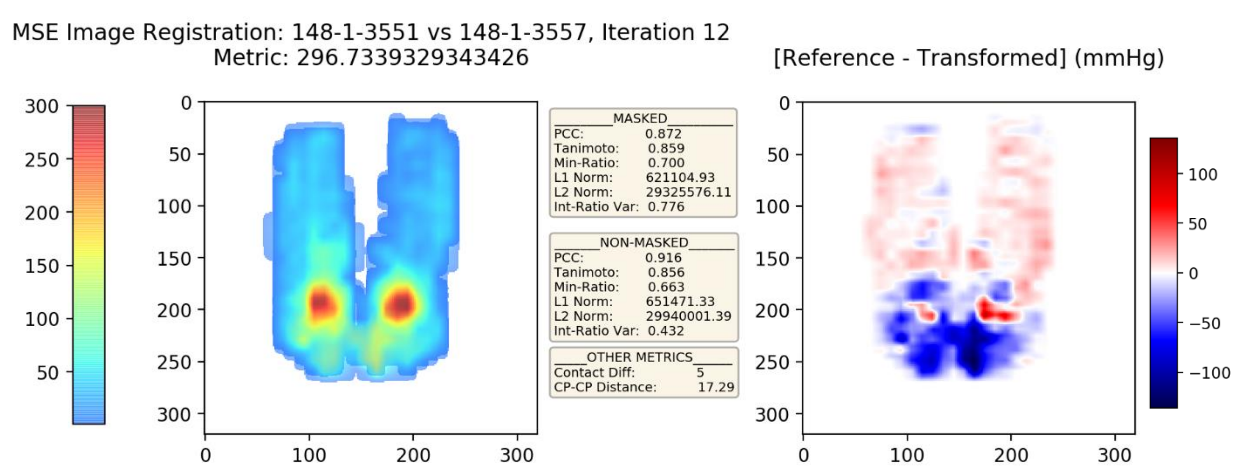

Visual feedback: Both MI and MSE did similar and appropriate registrations.

Reference (fixed) and Template (moving) pressure maps

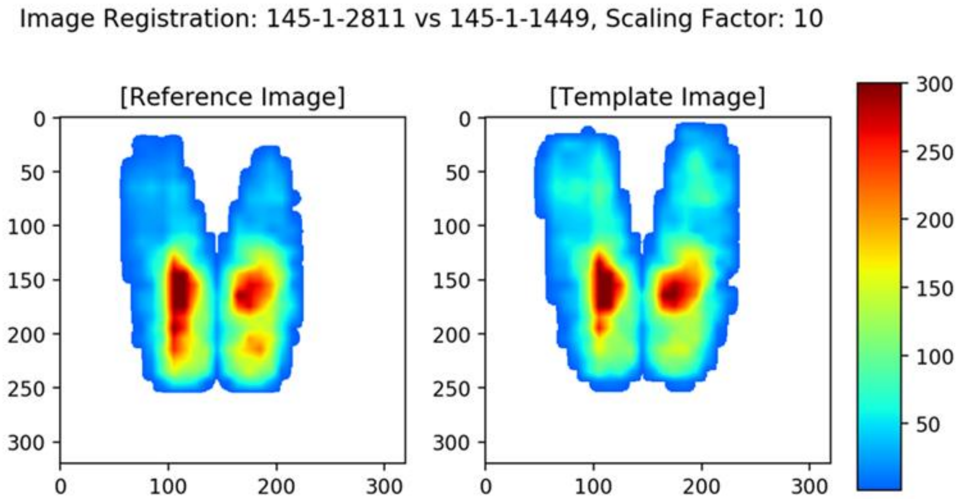

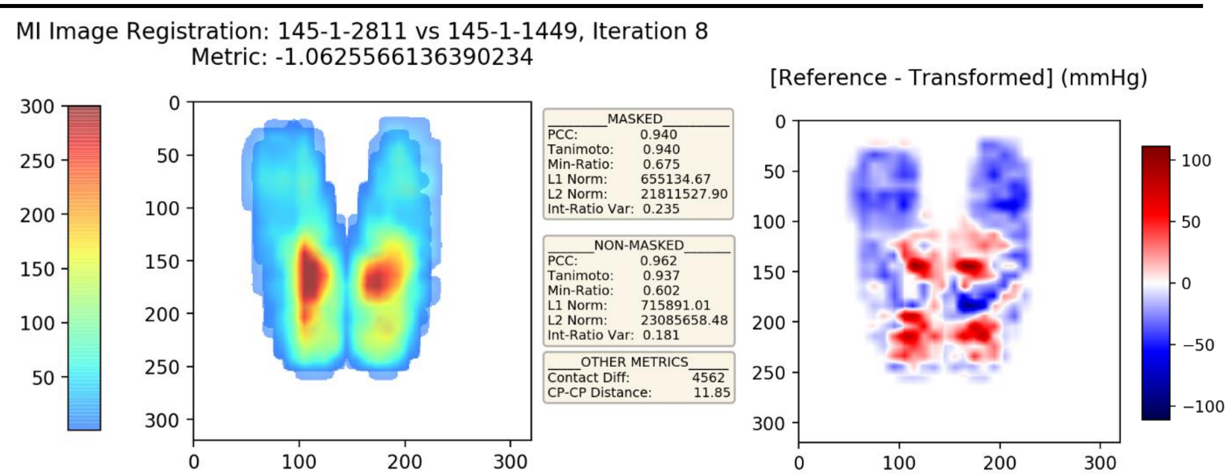

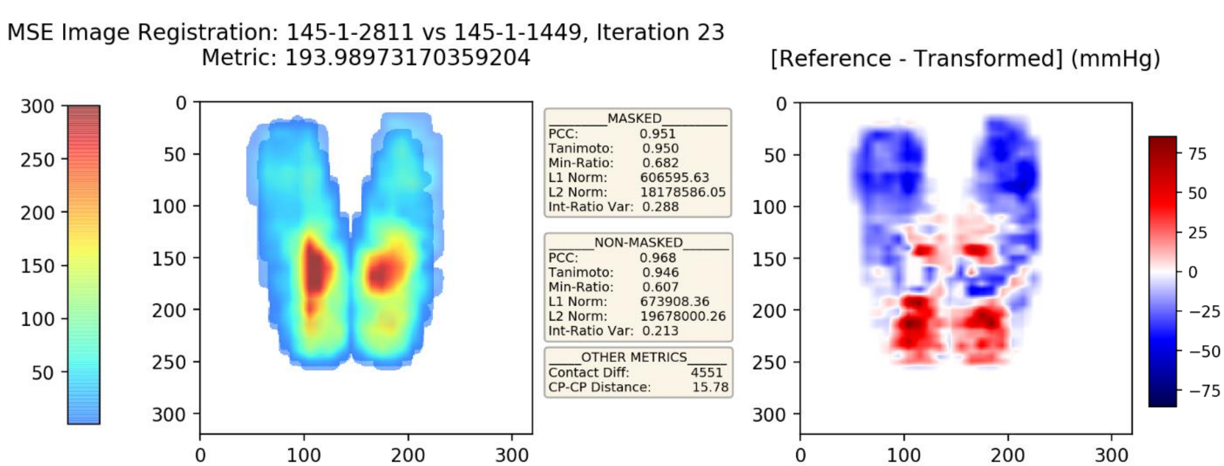

Visual feedback: **MSE** produced slightly better correspondence in tuberosities and top buttocks.

Reference (fixed) and Template (moving) pressure maps

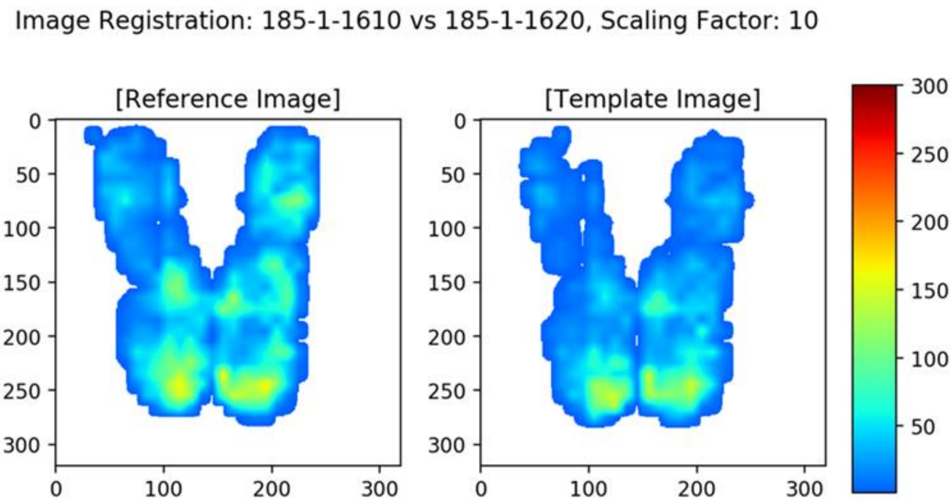

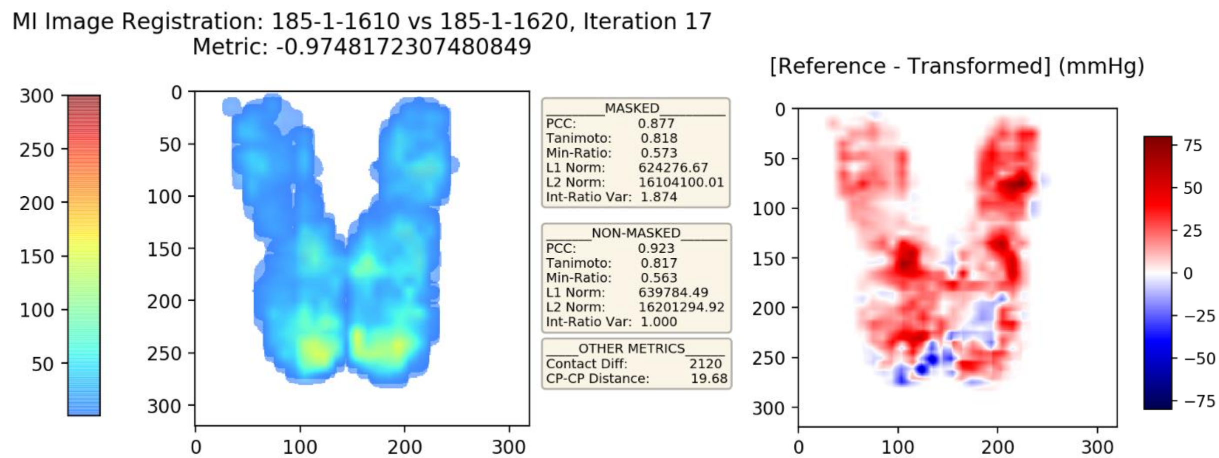

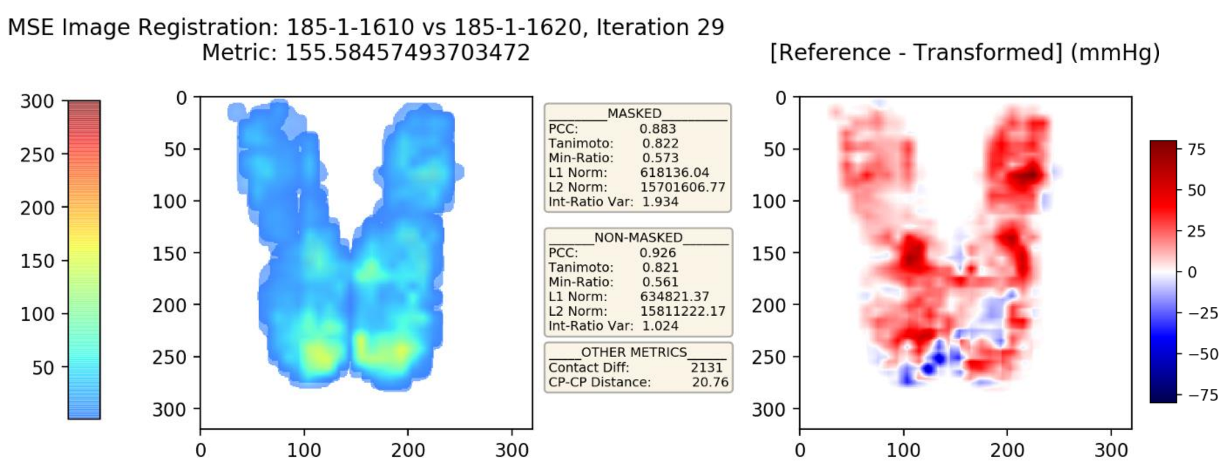

Visual feedback: Both MI and MSE did similar and appropriate registrations.

Reference (fixed) and Template (moving) pressure maps

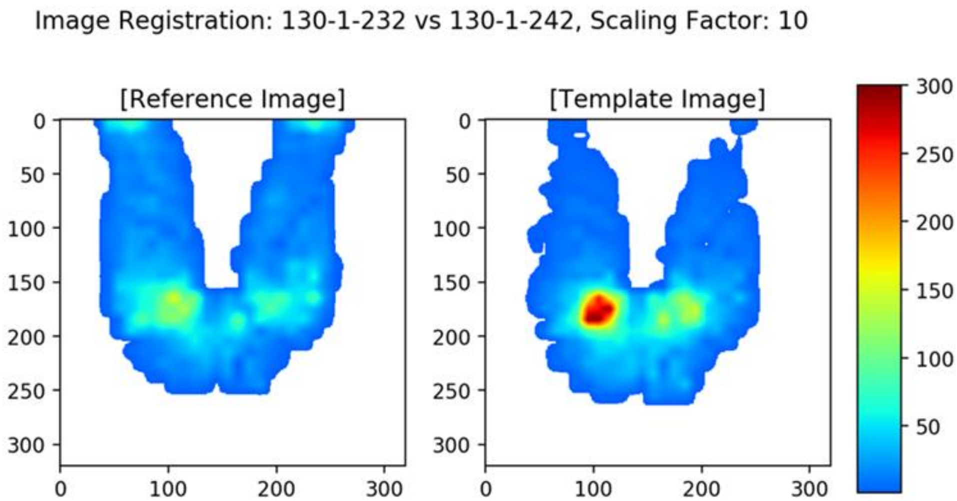

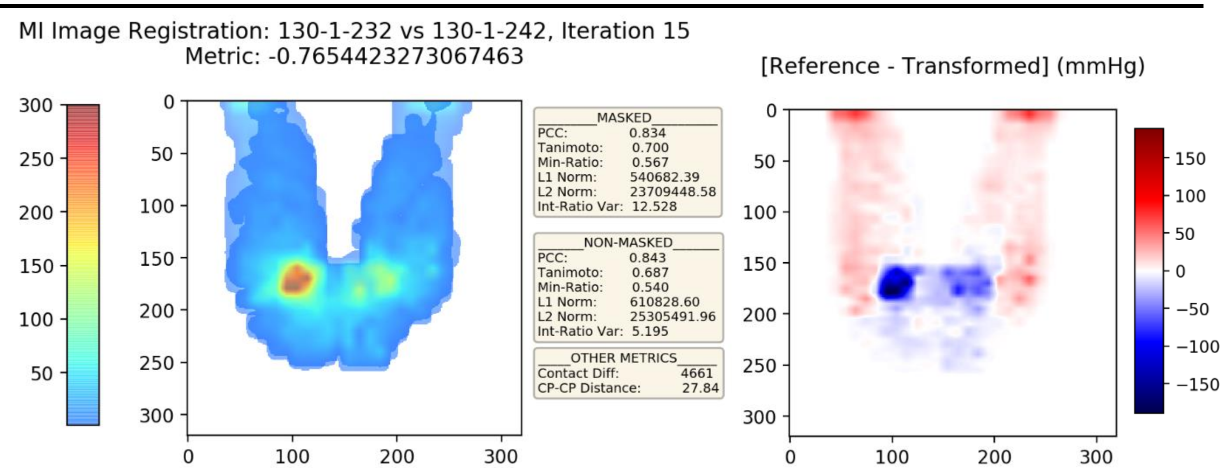

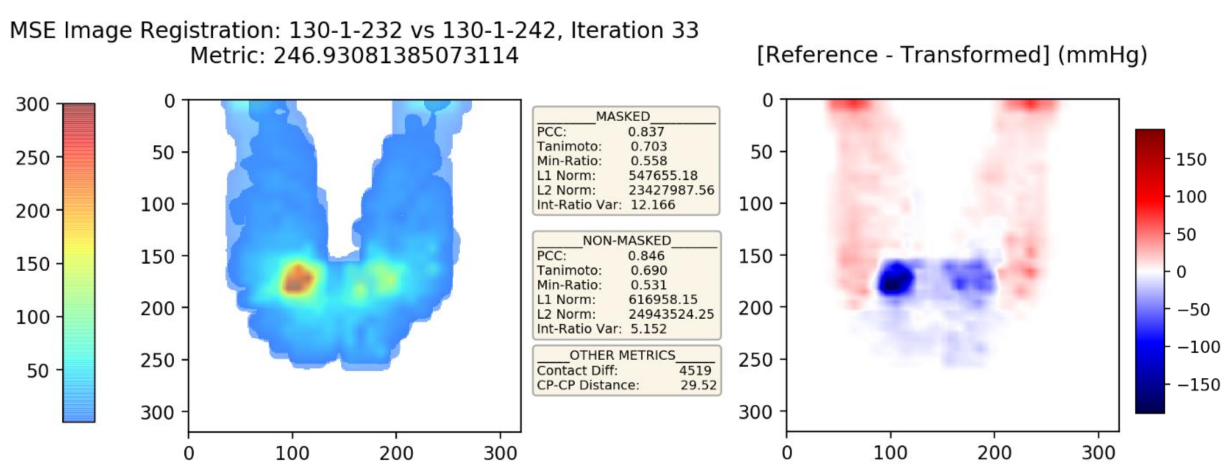

Visual feedback: Both MI and MSE did similar and appropriate registrations.

Reference (fixed) and Template (moving) pressure maps

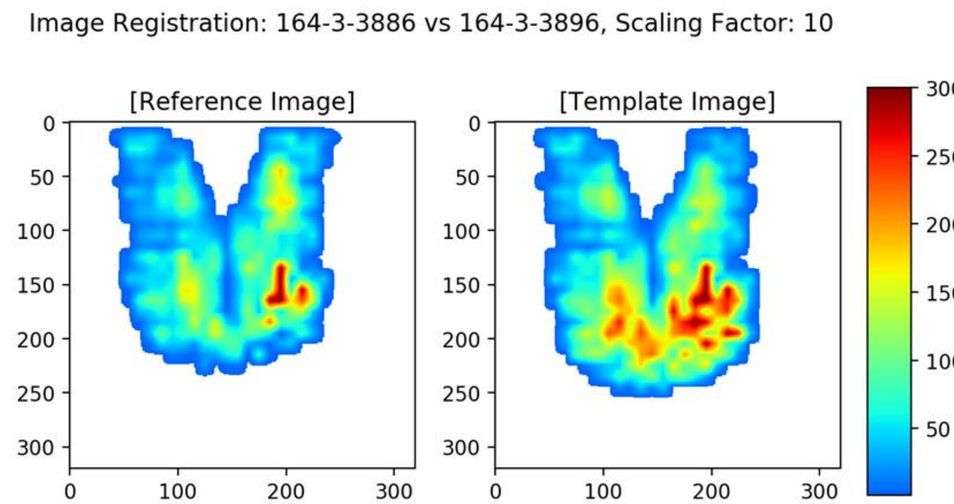

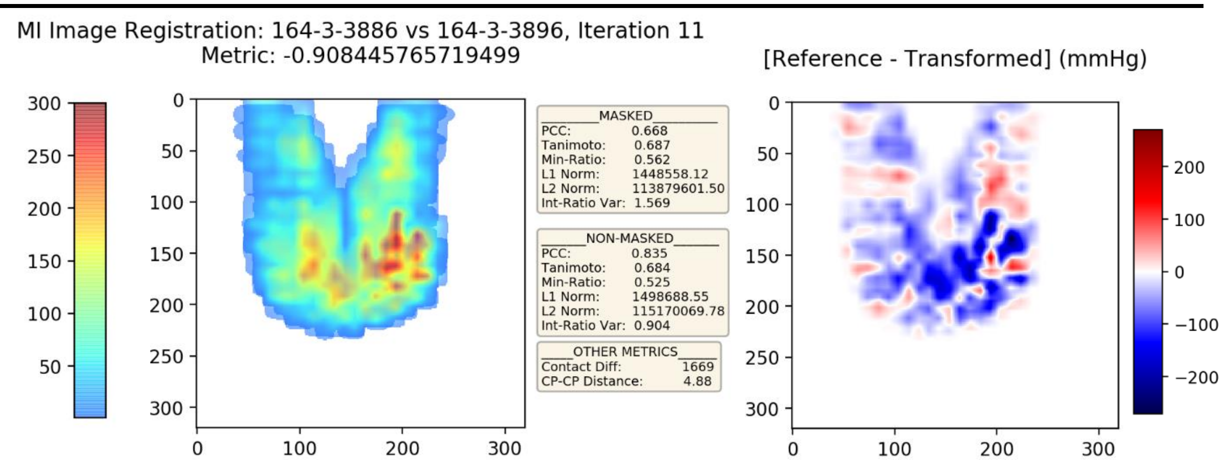

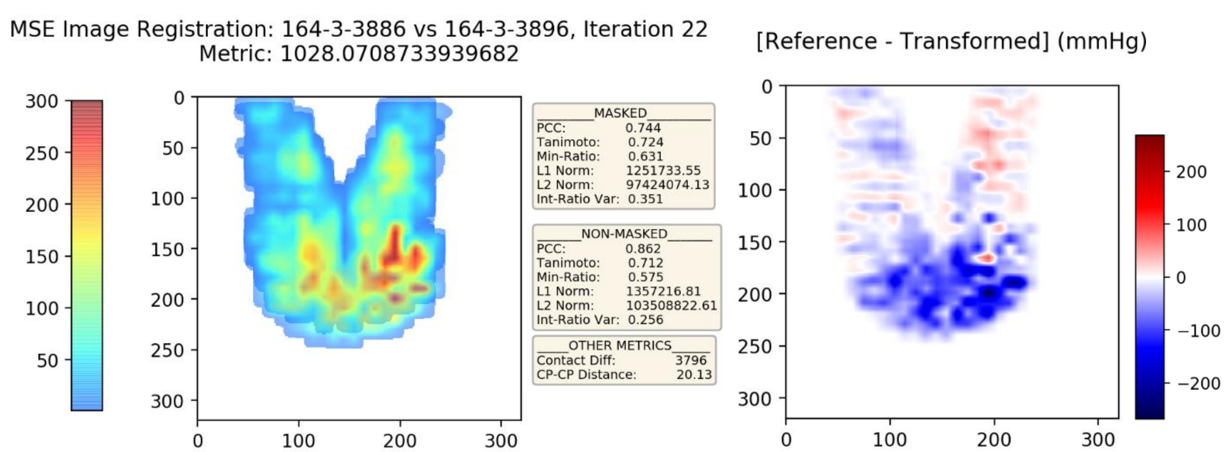

Visual feedback: **MSE** registration produced better correspondence in tuberosities and legs.

Reference (fixed) and Template (moving) pressure maps

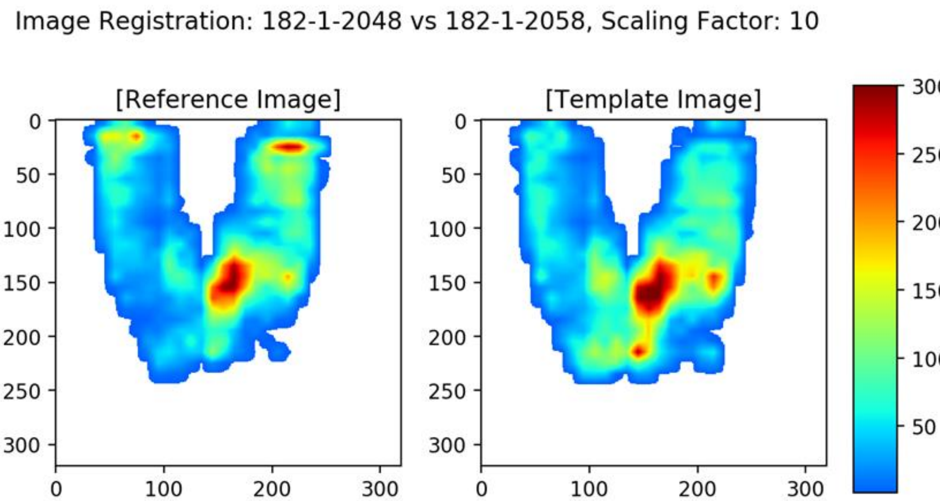

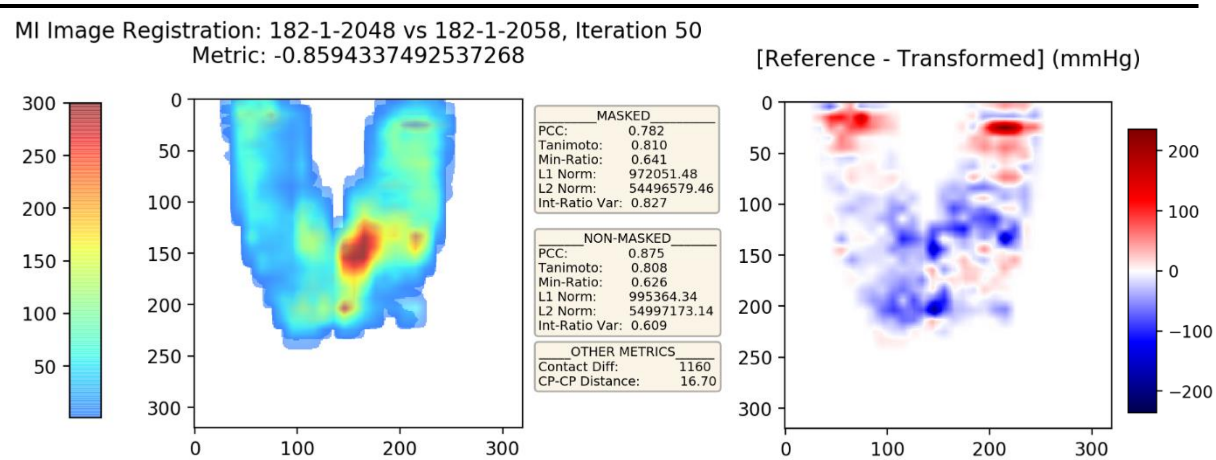

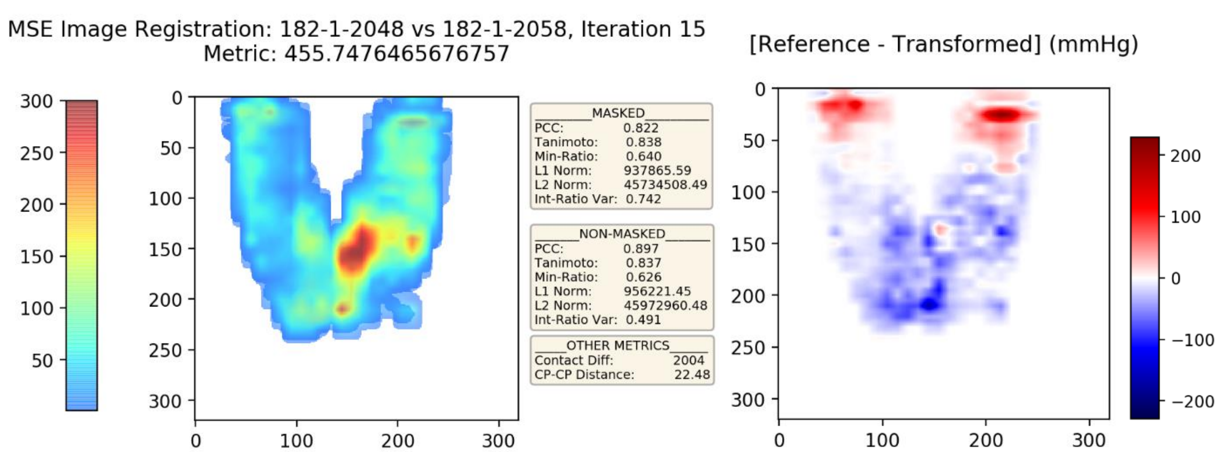

Visual feedback: **MSE** produced better correspondence in tuberosities, legs, and top buttocks.

Reference (fixed) and Template (moving) pressure maps

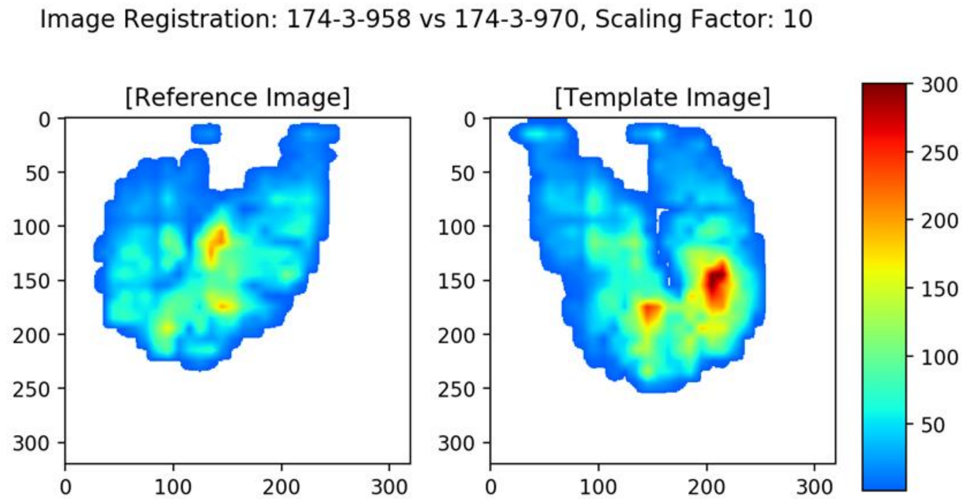

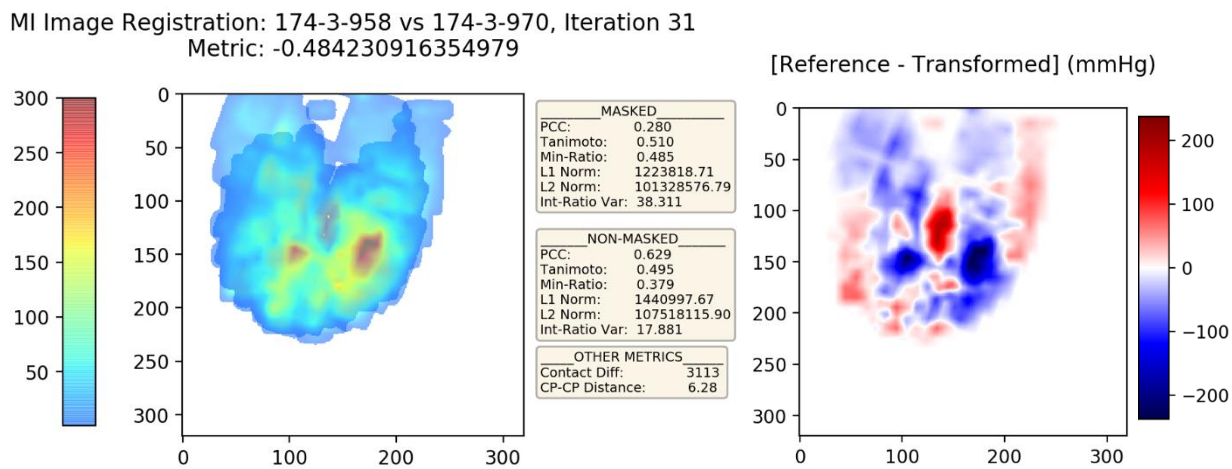

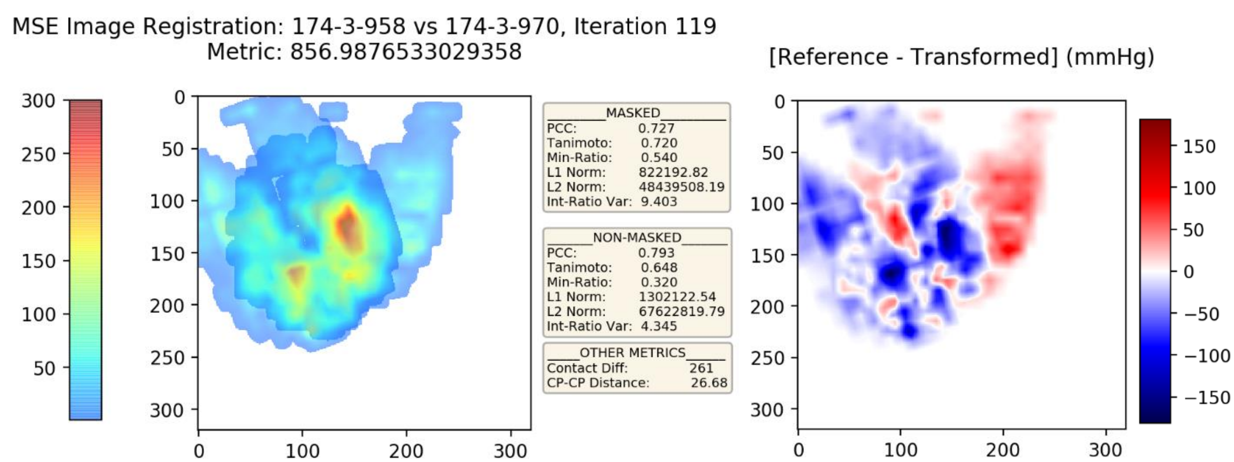

Visual feedback: While neither MI nor MSE produced a successful registration, MI is better.

<u>Reference (fixed) and Template (moving) pressure maps</u>

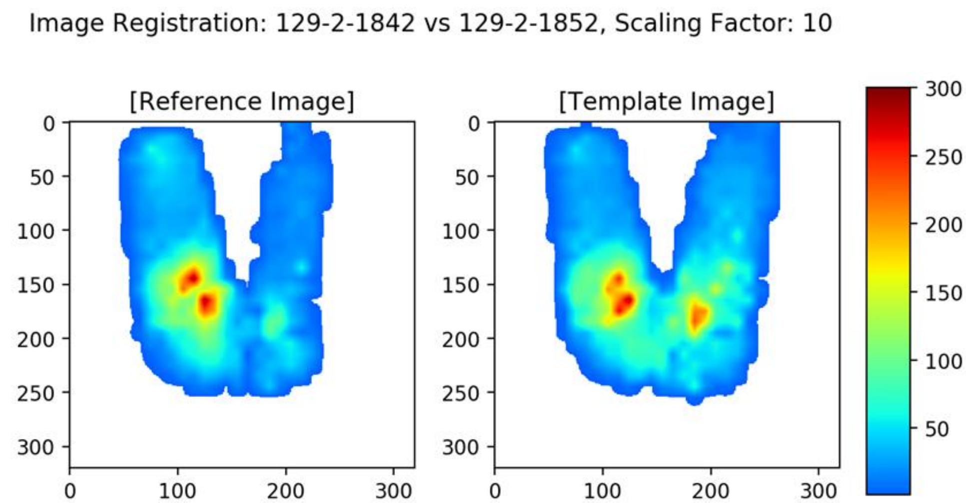

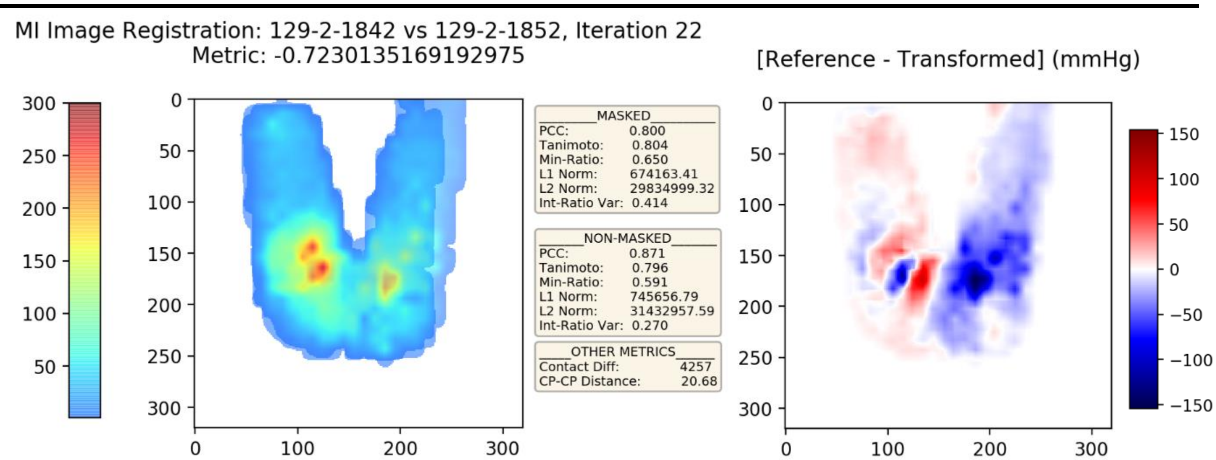

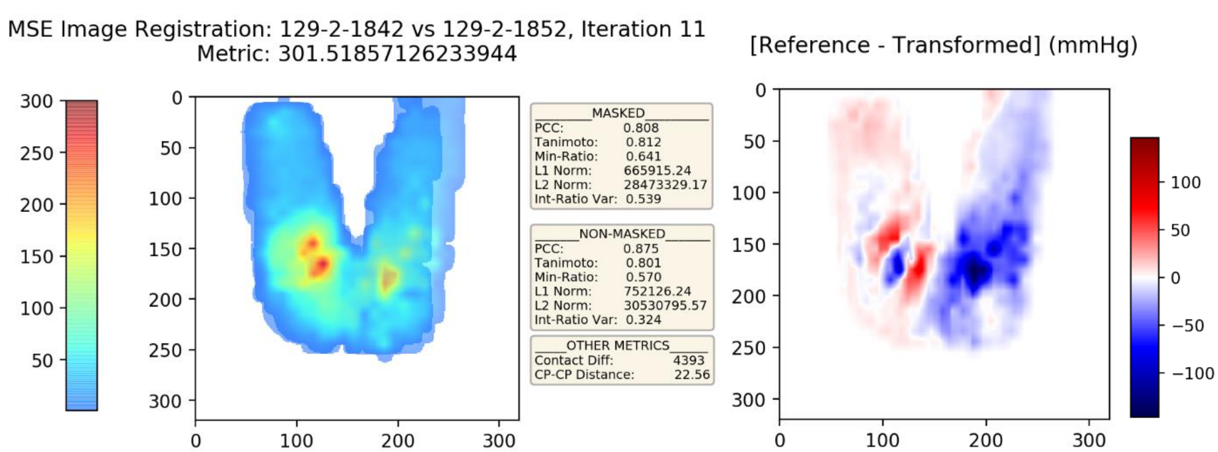

Visual feedback: Both MI and MSE did similar and appropriate registrations.

Reference (fixed) and Template (moving) pressure maps

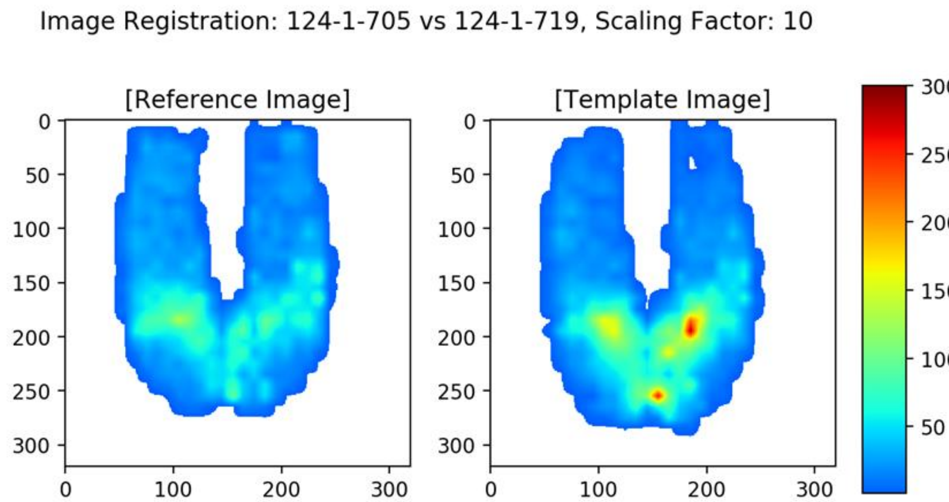

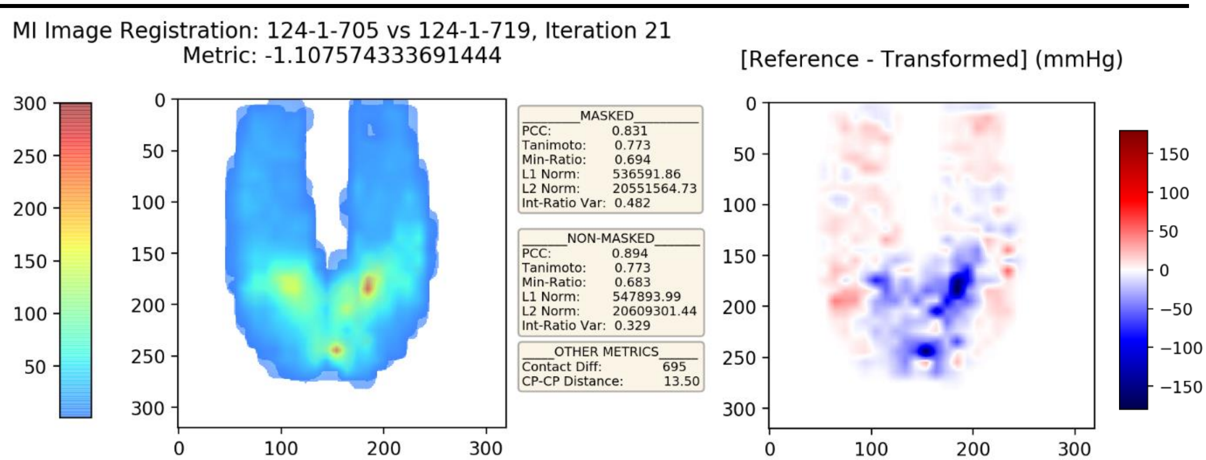

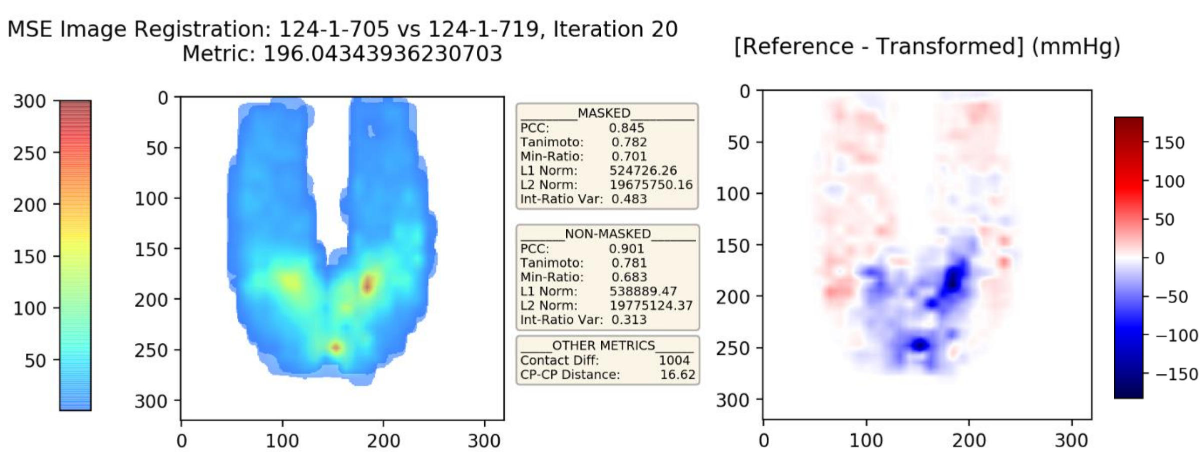

Visual feedback: Both MI and MSE did similar and appropriate registrations.

Reference (fixed) and Template (moving) pressure maps

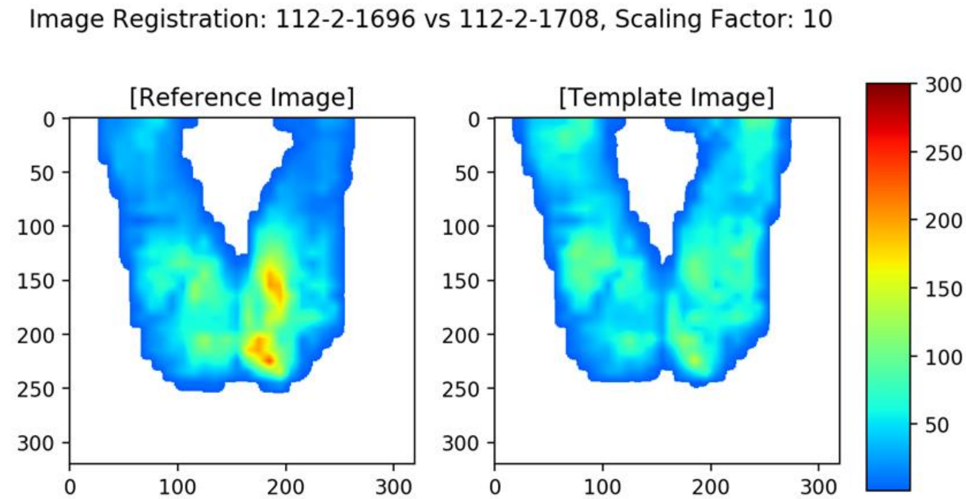

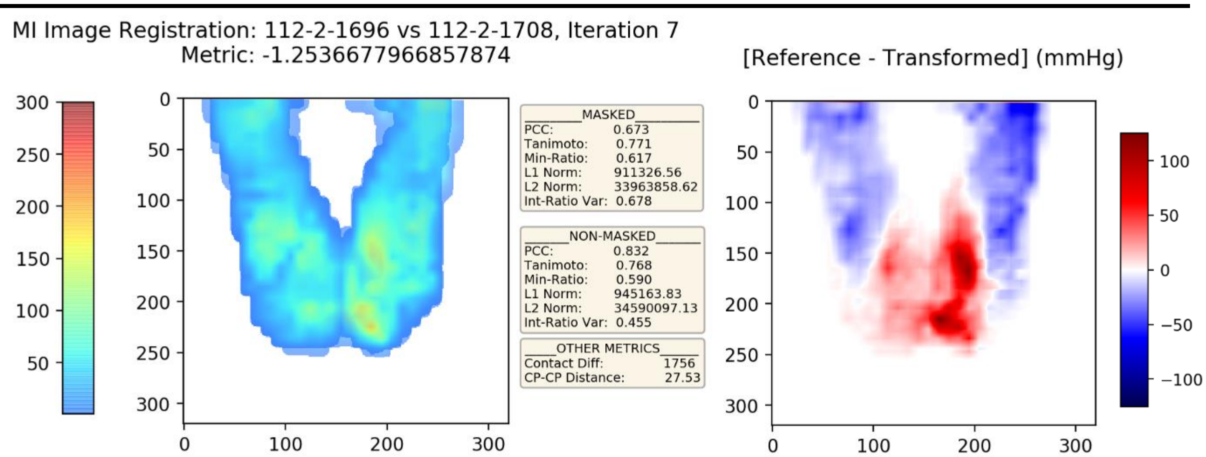

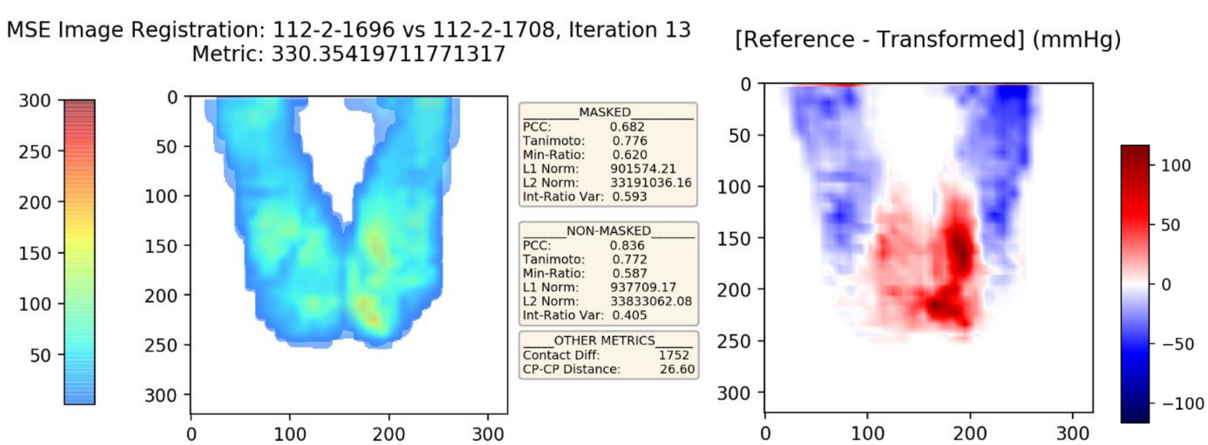

Visual feedback: Both MI and MSE did similar and appropriate registrations.

Reference (fixed) and Template (moving) pressure maps

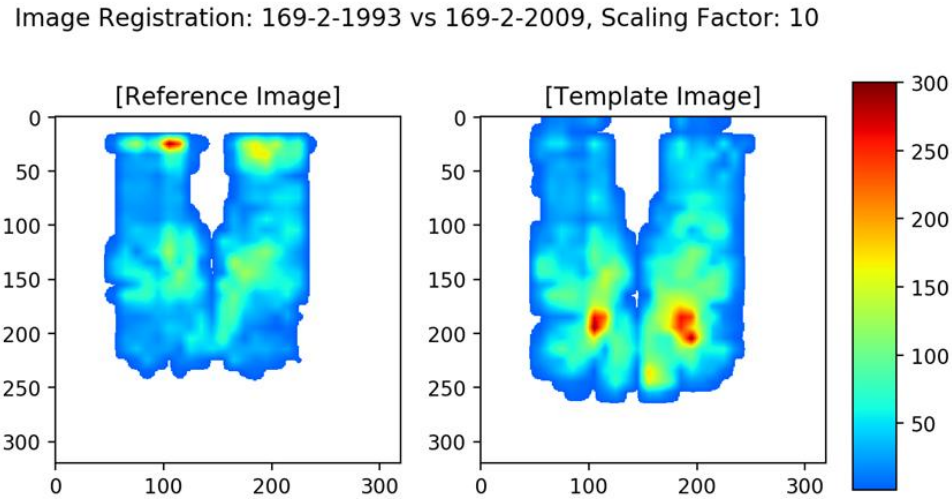

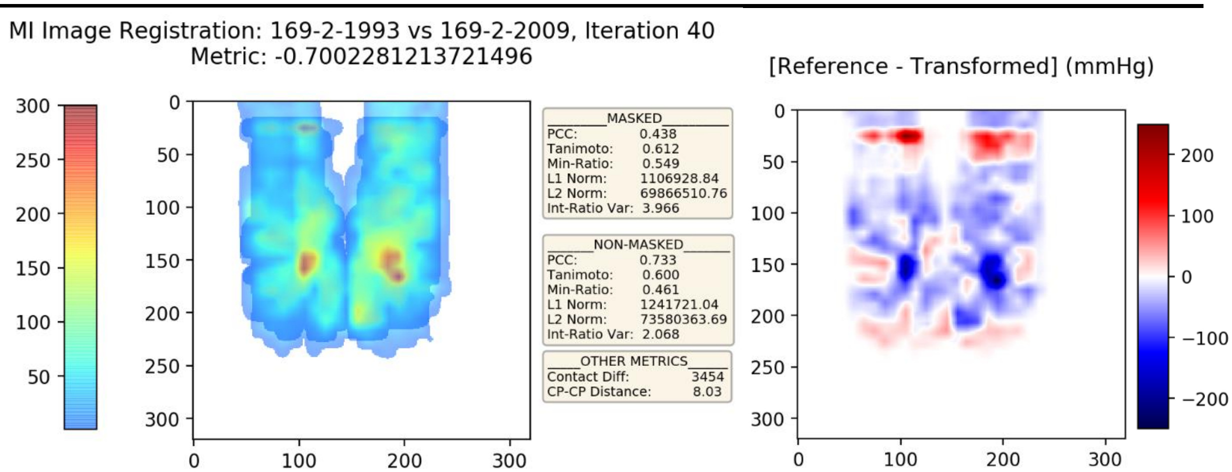

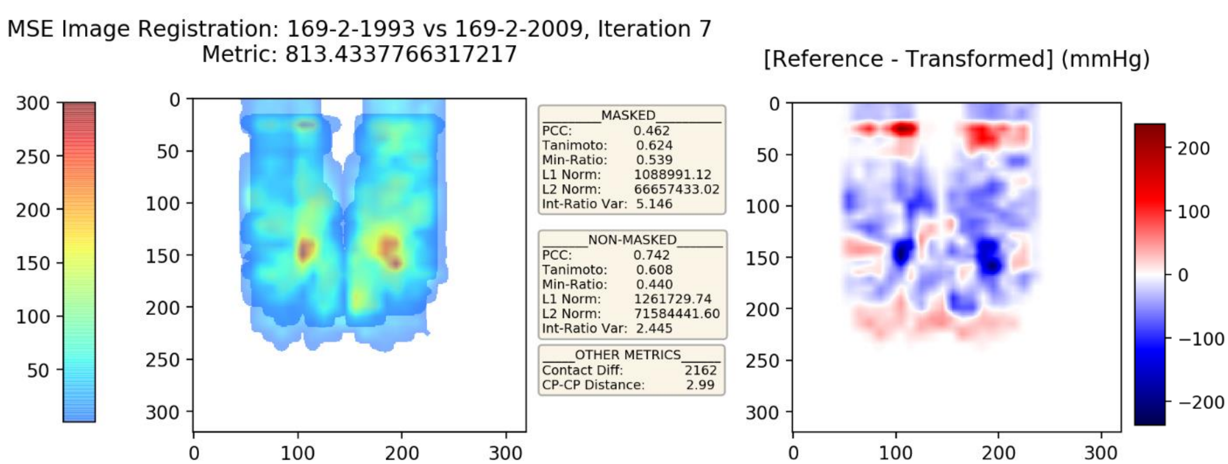

Visual feedback: Neither MI nor MSE produced a successful registration.

<u>Reference (fixed) and Template (moving) pressure maps</u>

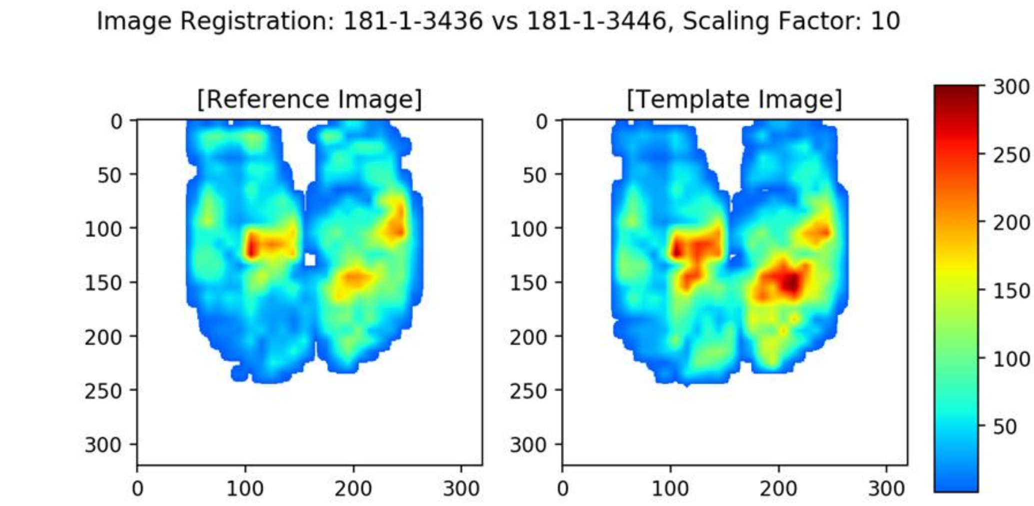

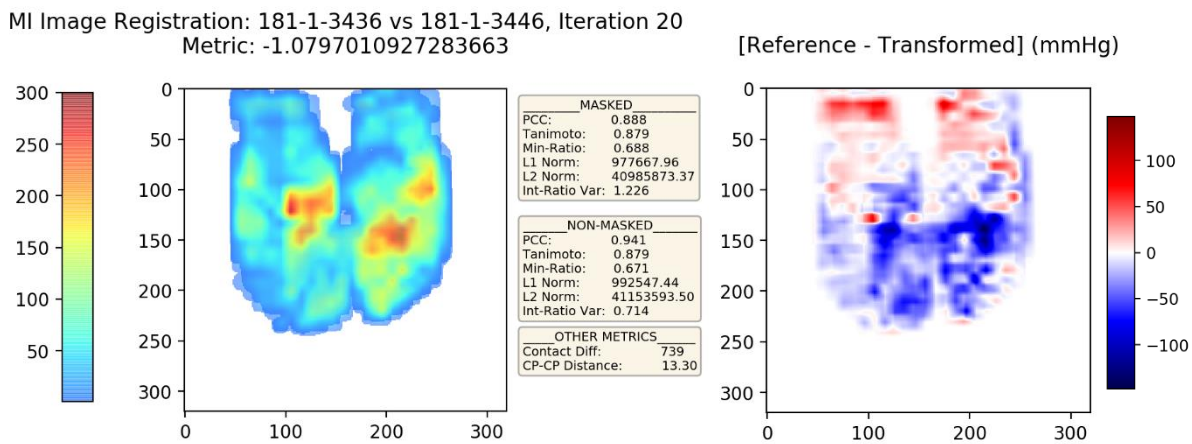

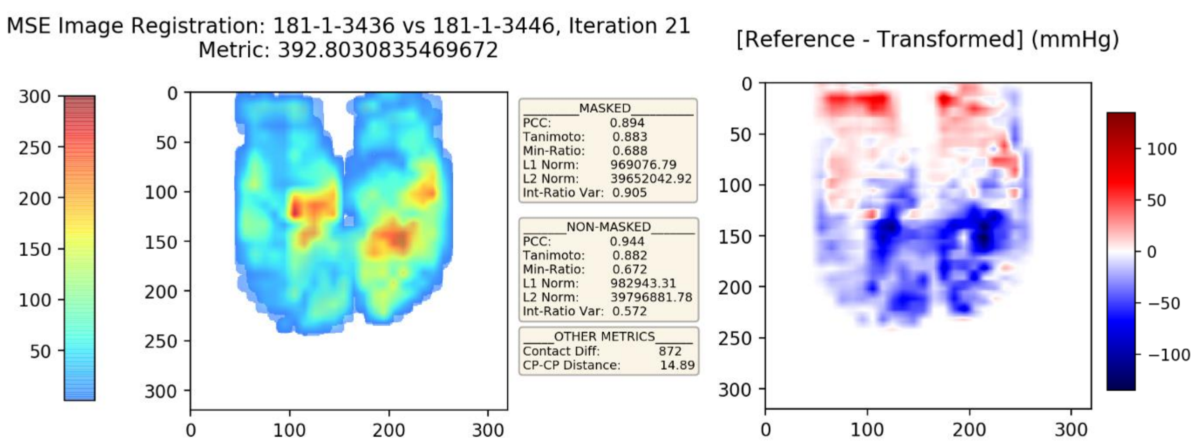

Visual feedback: Both MI and MSE did similar and appropriate registrations.

Reference (fixed) and Template (moving) pressure maps

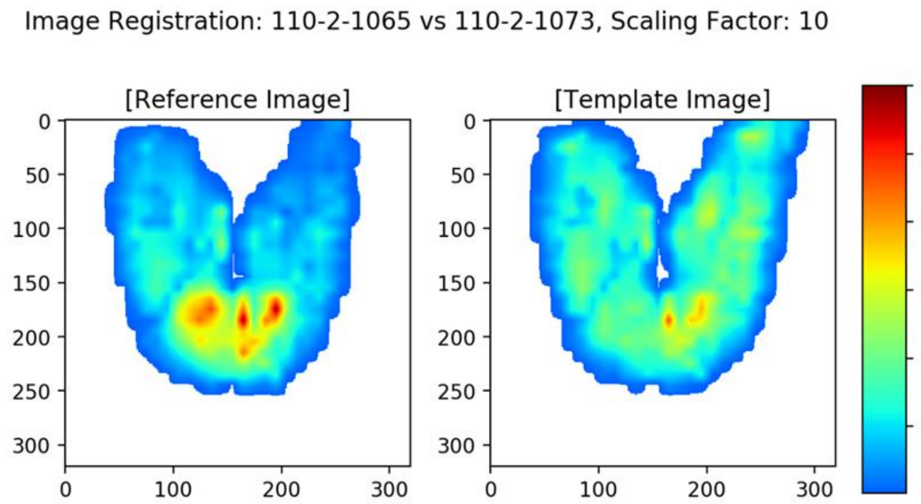

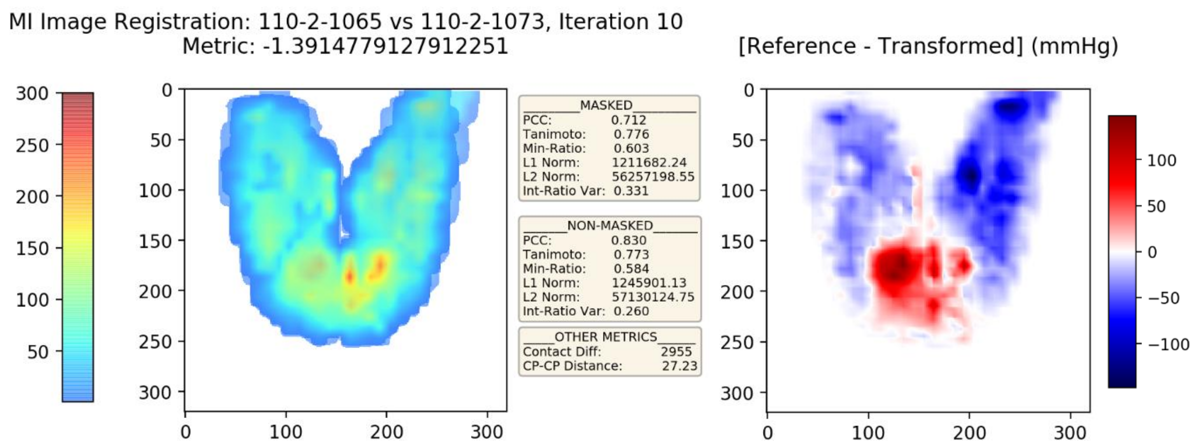

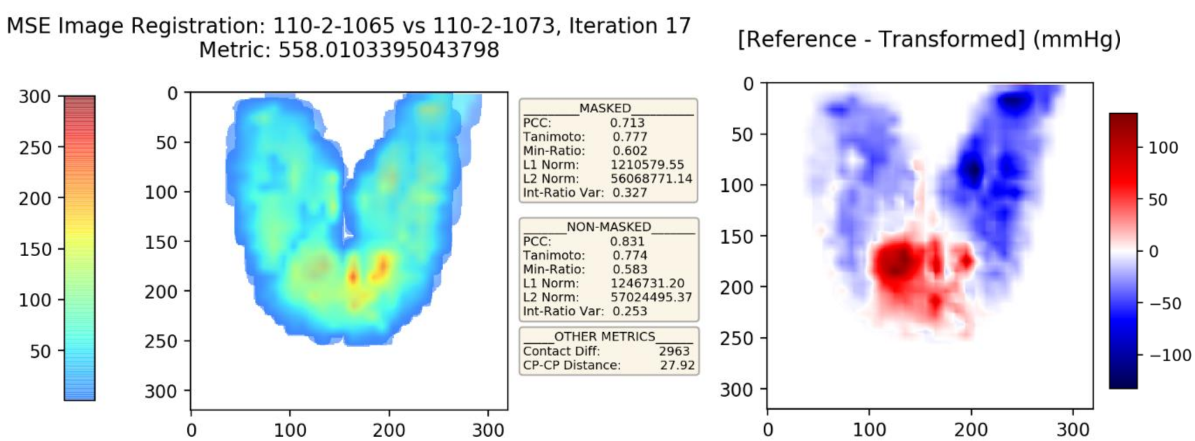

Visual feedback: Both MI and MSE did similar and appropriate registrations.

Reference (fixed) and Template (moving) pressure maps

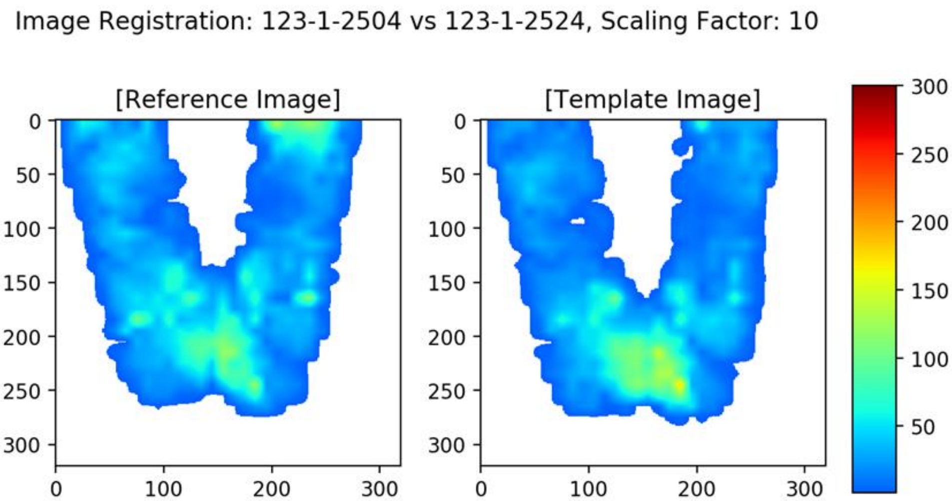

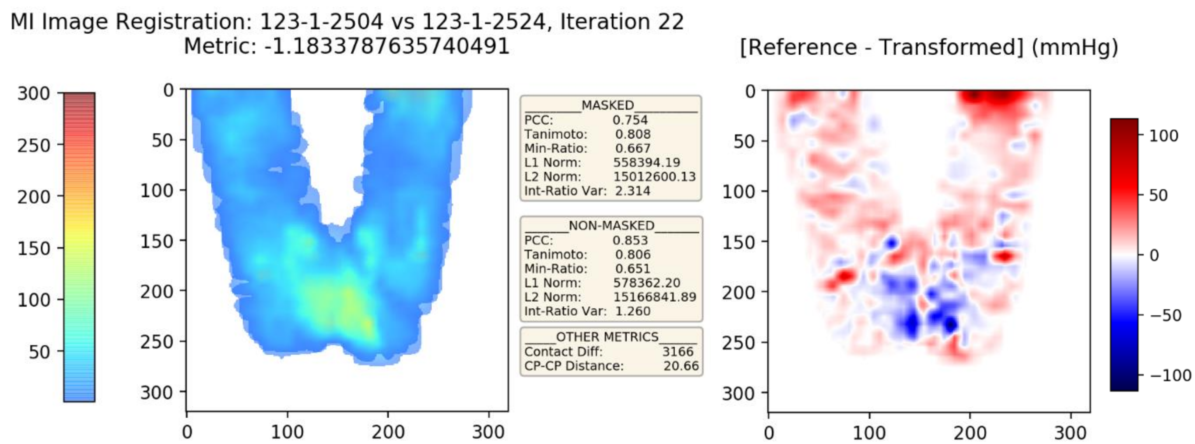

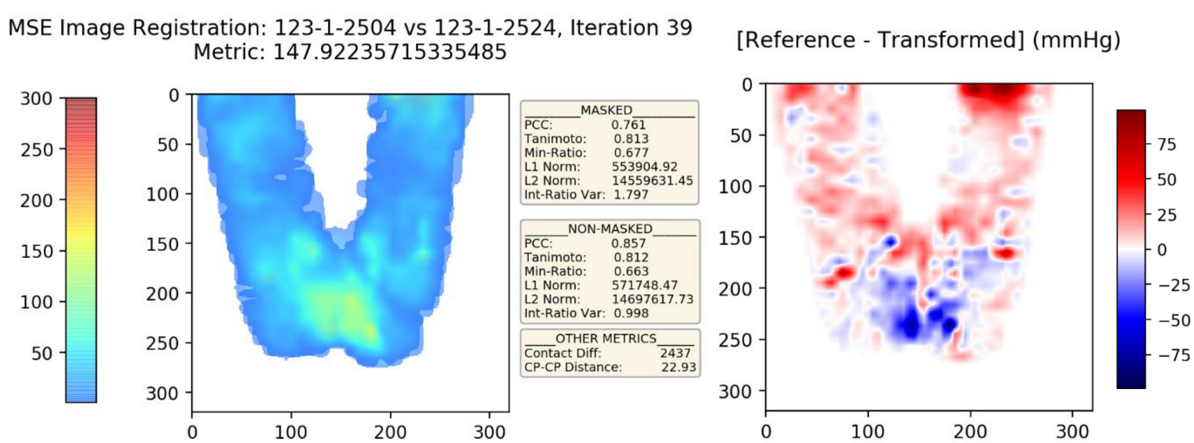

Visual feedback: Both MI and MSE did similar and appropriate registrations.

Reference (fixed) and Template (moving) pressure maps

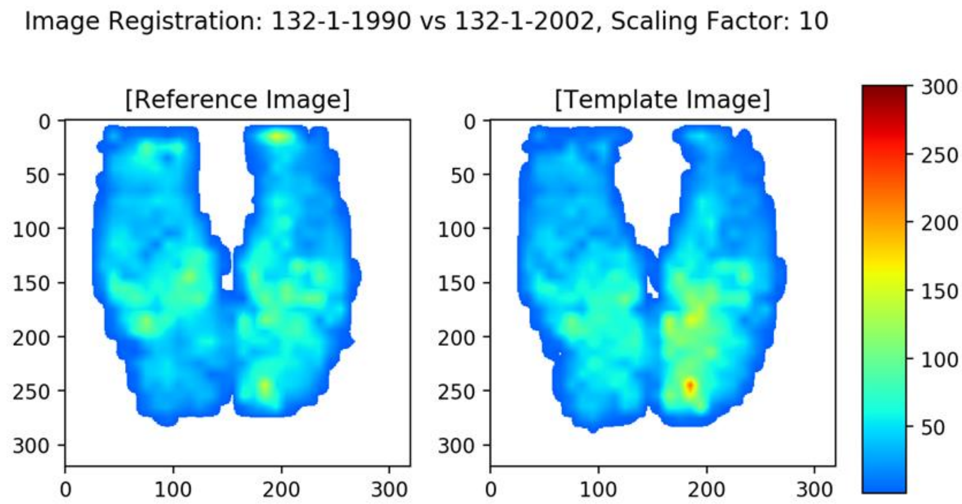

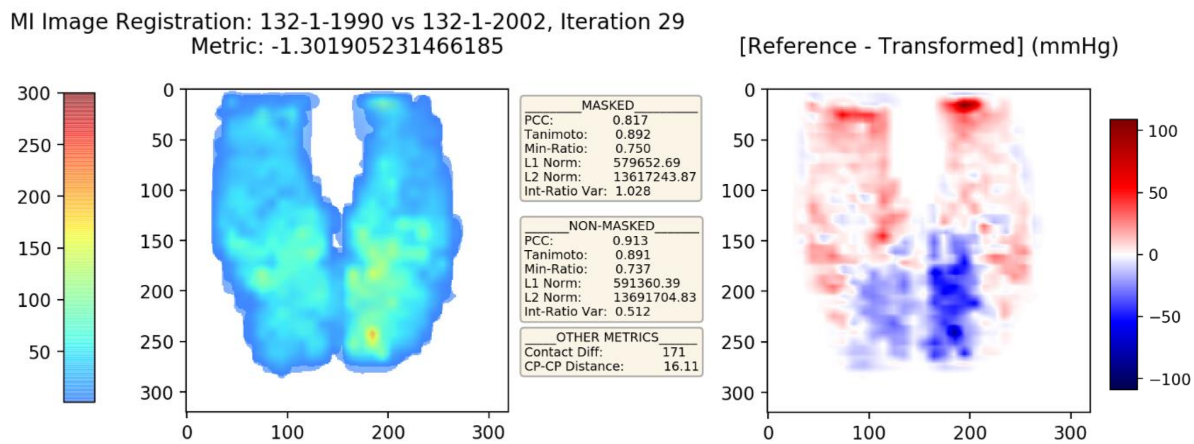

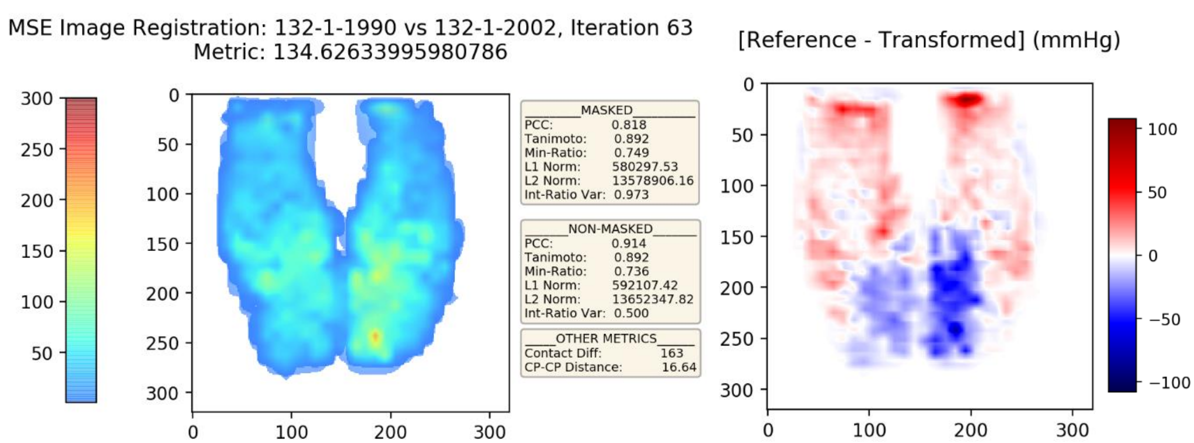

Visual feedback: Both MI and MSE did similar and appropriate registrations.

Reference (fixed) and Template (moving) pressure maps

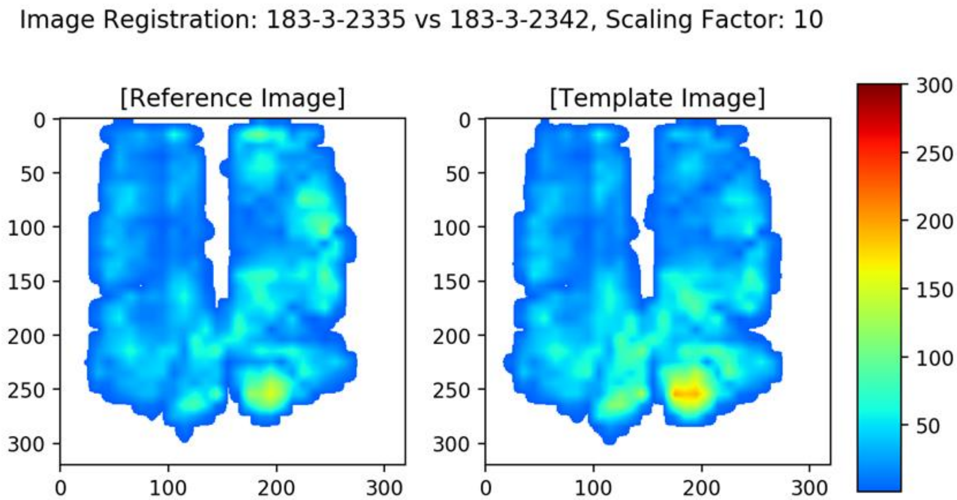

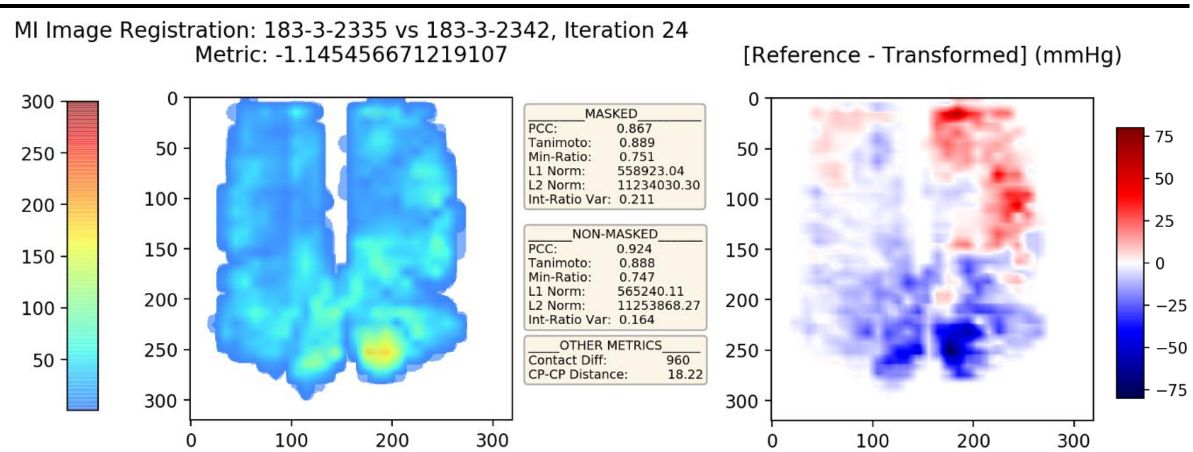

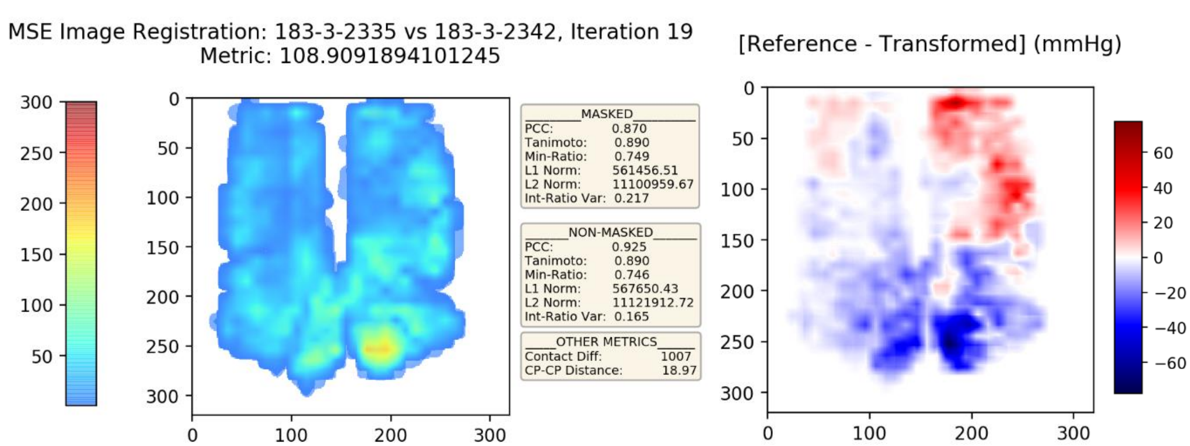

Visual feedback: Both MI and MSE did similar and appropriate registrations.

Appendix R

Case Study: Sequential Registration and Comparative Results

Template	CP-CP Diff	Pearson	Tanimoto	Min-Ratio	L1 Norm	Sq L2 Norm	Int-Ratio Var	Proc Time
109-2-1	0	1	1	1	0.00	0.00	0	0
109-2-2	0.1965	0.9995	0.9982	0.9479	62,000.53	227,841.49	0.0022	0.5887
109-2-3	0.1486	0.9991	0.9957	0.9274	93,892.10	561,214.08	0.0037	0.9744
109-2-4	0.1420	0.9983	0.9910	0.9044	137,321.15	1,200,237.43	0.0050	1.2533
109-2-5	0.1912	0.9980	0.9883	0.8973	157,662.23	1,580,425.12	0.0040	0.4887
109-2-6	0.2962	0.9971	0.9833	0.8741	192,627.88	2,308,566.96	0.0060	1.2893
109-2-7	0.2889	0.9966	0.9805	0.8639	210,233.39	2,731,405.03	0.0062	0.8835
109-2-8	0.4328	0.9964	0.9805	0.8604	212,712.12	2,723,526.09	0.0074	0.5587
109-2-9	0.4175	0.9958	0.9760	0.8477	238,079.86	3,415,251.42	0.0065	1.4772
109-2-10	0.3456	0.9960	0.9773	0.8533	229,342.14	3,213,429.02	0.0062	1.0304
109-2-11	0.3810	0.9961	0.9777	0.8571	226,961.76	3,155,578.15	0.0060	0.6316
109-2-12	0.6728	0.9966	0.9853	0.8688	179,536.13	1,992,752.48	0.0104	0.6057
109-2-13	0.6026	0.9957	0.9771	0.8447	231,895.62	3,238,896.46	0.0105	0.6137
109-2-14	0.1305	0.9946	0.9715	0.8369	258,227.00	4,108,337.76	0.0096	1.3772
109-2-15	0.3775	0.9942	0.9675	0.8395	273,149.78	4,754,045.33	0.0078	0.5867
109-2-16	0.3225	0.9929	0.9607	0.8258	302,995.07	5,874,813.41	0.0084	0.4467
109-2-17	0.2519	0.9935	0.9633	0.8281	290,116.12	5,449,490.24	0.0071	0.5767
109-2-18	0.0911	0.9901	0.9594	0.8327	289,272.22	6,007,286.25	0.0103	0.7446
109-2-19	0.3397	0.9898	0.9682	0.8292	264,672.59	4,494,050.03	0.0140	0.5877
109-2-20	0.4329	0.9914	0.9662	0.8332	266,727.21	4,892,842.84	0.0108	0.4797
109-2-21	0.3447	0.9896	0.9556	0.8163	309,365.97	6,655,635.01	0.0116	0.5077
109-2-22	0.2591	0.9909	0.9544	0.8084	320,083.84	6,921,572.37	0.0098	0.3238
109-2-23	0.5650	0.9908	0.9544	0.8049	329,519.96	6,916,756.31	0.0110	0.3128
109-2-24	0.3713	0.9890	0.9413	0.7856	379,187.06	9,290,573.64	0.0110	0.4557
109-2-25	0.2999	0.9903	0.9441	0.7877	371,628.49	8,803,556.80	0.0096	0.4218
109-2-26	0.3126	0.9886	0.9378	0.7866	387,521.47	9,937,806.99	0.0210	1.1613
109-2-27	0.4614	0.9886	0.9380	0.7878	385,342.64	9,901,964.98	0.0226	2.2497
109-2-28	0.2954	0.9882	0.9358	0.7826	392,225.94	10,323,479.52	0.0215	0.2828
109-2-29	0.0670	0.9872	0.9344	0.7697	407,855.18	10,550,953.65	0.0221	6.5533
109-2-30	0.0392	0.9865	0.9325	0.7657	411,181.21	10,889,107.36	0.0208	0.6346
109-2-31	0.0220	0.9871	0.9320	0.7722	412,184.02	11,018,266.91	0.0187	0.4178
109-2-32	0.7373	0.9858	0.9304	0.7678	410,755.86	11,285,542.13	0.0234	3.5740
109-2-33	0.0999	0.9860	0.9253	0.7611	439,117.98	12,343,076.28	0.0180	1.4232
109-2-34	0.2767	0.9848	0.9251	0.7556	438,815.03	12,314,604.31	0.0206	3.5930
109-2-35	0.1717	0.9842	0.9159	0.7457	476,652.96	14,242,191.83	0.0200	0.4827
109-2-36	0.0721	0.9852	0.9192	0.7589	457,211.91	13,572,534.60	0.0216	0.5017
109-2-37	1.3022	0.9817	0.9058	0.7343	504,007.54	16,311,355.74	0.0260	0.3218
109-2-38	0.2166	0.9837	0.9070	0.7341	511,214.62	16,169,554.72	0.0198	0.5307
109-2-39	0.0818	0.9842	0.9173	0.7546	465,801.46	13,931,907.86	0.0187	0.6057
109-2-40	0.1483	0.9852	0.9251	0.7638	433,759.04	12,339,135.93	0.0195	1.3892
109-2-41	0.0585	0.9848	0.9159	0.7439	477,924.01	14,270,228.64	0.0192	0.7006
109-2-42	0.1061	0.9846	0.9119	0.7350	492,972.20	15,128,198.49	0.0196	0.6107
109-2-43	0.1243	0.9840	0.9082	0.7276	511,894.36	15,932,884.54	0.0204	0.5617
109-2-44	0.0940	0.9829	0.9001	0.7159	541,005.65	17,708,500.49	0.0198	1.6691
109-2-45	0.1695	0.9840	0.9094	0.7336	499,534.02	15,663,254.63	0.0179	0.5987
109-2-46	0.0909	0.9837	0.9049	0.7246	520,390.73	16,659,594.57	0.0214	0.6256
109-2-47	0.2707	0.9833	0.8996	0.7174	542,430.23	17,851,270.95	0.0202	0.6596
109-2-48	0.1870	0.9833	0.8999	0.7233	535,972.38	17,798,425.37	0.0184	0.5297
109-2-49	0.1105	0.9824	0.8959	0.7145	553,028.28	18,672,321.57	0.0210	1.4942
109-2-50	0.1663	0.9819	0.8939	0.7106	563,537.26	19,114,063.24	0.0190	0.6117
109-2-51	0.2207	0.9825	0.9025	0.7248	528,533.12	17,121,651.30	0.0195	0.7796
109-2-52	0.2522	0.9824	0.9009	0.7140	542,714.27	17,498,992.32	0.0206	0.5607
109-2-53	0.1398	0.9814	0.8969	0.7162	554,385.11	18,361,993.43	0.0196	0.6626
109-2-54	0.2145	0.9809	0.8911	0.7101	575,629.36	19,716,547.36	0.0190	0.6966
109-2-55	0.0985	0.9832	0.9069	0.7271	513,260.15	16,175,911.60	0.0190	0.5447
109-2-56	0.1184	0.9816	0.8937	0.7080	564,191.58	19,149,147.83	0.0191	0.4997
109-2-57	0.2087	0.9815	0.8948	0.7061	559,727.22	18,886,059.36	0.0191	0.6976
109-2-58	0.1328	0.9832	0.9038	0.7170	528,137.06	16,877,957.51	0.0186	0.6147

Template	CP-CP Diff	Pearson	Tanimoto	Min-Ratio	L1 Norm	Sq L2 Norm	Int-Ratio Var	Proc Time
109-2-59	0.2107	0.9815	0.8949	0.7114	556,675.71	18,844,673.53	0.0193	0.6456
109-2-60	0.1958	0.9822	0.8967	0.7107	550,617.87	18,464,483.74	0.0185	0.6846
109-2-61	0.1669	0.9822	0.8950	0.7060	560,628.81	18,867,385.82	0.0182	0.6656
109-2-62	0.1630	0.9809	0.8842	0.6903	603,617.26	21,425,775.11	0.0185	0.8175
109-2-63	0.2252	0.9812	0.8895	0.7000	577,725.38	20,143,442.64	0.0185	0.7086
109-2-64	0.1841	0.9806	0.8846	0.6925	601,563.62	21,303,732.10	0.0186	0.6586
109-2-65	0.1471	0.9806	0.8829	0.6925	605,806.03	21,749,848.70	0.0191	0.5147
109-2-66	0.1877	0.9803	0.8793	0.6889	617,780.19	22,641,968.59	0.0190	0.4507
109-2-67	0.1699	0.9799	0.8783	0.6857	623,162.66	22,849,906.94	0.0191	0.8485
109-2-68	0.1392	0.9802	0.8803	0.6899	613,348.37	22,380,424.70	0.0190	0.5517
109-2-69	0.1728	0.9799	0.8765	0.6835	630,205.39	23,316,402.68	0.0188	0.4957
109-2-70	0.1668	0.9789	0.8714	0.6790	647,708.35	24,589,363.55	0.0192	0.4198
109-2-71	0.1650	0.9794	0.8739	0.6833	637,932.34	23,973,980.79	0.0189	0.4398
109-2-72	0.1770	0.9787	0.8681	0.6742	662,838.79	25,465,066.25	0.0196	0.4948
109-2-73	0.1745	0.9792	0.8710	0.6790	649,791.41	24,718,158.47	0.0189	0.4687
109-2-74	0.1825	0.9786	0.8681	0.6753	661,446.63	25,436,621.69	0.0191	0.4407
109-2-75	0.1893	0.9789	0.8694	0.6761	658,058.29	25,138,609.91	0.0190	0.4697
109-2-76	0.1725	0.9791	0.8717	0.6792	645,362.27	24,518,916.44	0.0188	0.7086
109-2-77	0.1776	0.9785	0.8680	0.6745	662,394.00	25,470,120.54	0.0190	0.4018
109-2-78	0.1847	0.9793	0.8739	0.6812	637,081.60	23,952,453.75	0.0186	0.6706
109-2-79	0.1580	0.9799	0.8783	0.6869	618,923.76	22,859,867.66	0.0183	0.6606
109-2-80	0.2134	0.9791	0.8714	0.6787	647,708.79	24,592,891.53	0.0186	1.6690
109-2-81	0.2171	0.9787	0.8697	0.6773	650,332.72	25,029,721.03	0.0188	0.6816
109-2-82	0.1988	0.9790	0.8720	0.6820	638,718.31	24,434,411.42	0.0185	0.6756
109-2-83	0.1855	0.9786	0.8696	0.6772	653,189.57	25,033,922.21	0.0188	0.6866
109-2-84	0.2353	0.9786	0.8691	0.6772	653,508.95	25,192,312.04	0.0188	2.3547
109-2-85	0.1885	0.9786	0.8675	0.6735	661,131.99	25,614,237.08	0.0188	0.7046
109-2-86	0.1899	0.9778	0.8634	0.6694	676,017.88	26,668,524.81	0.0192	0.7506
109-2-87	0.2043	0.9781	0.8649	0.6735	667,113.95	26,269,976.01	0.0186	0.5867
109-2-88	0.1956	0.9778	0.8627	0.6691	679,049.68	26,849,971.28	0.0188	0.6566
109-2-89	0.1974	0.9775	0.8608	0.6665	686,108.97	27,363,314.69	0.0188	0.6107
109-2-90	0.1773	0.9774	0.8592	0.6677	688,667.07	27,794,921.00	0.0189	0.4337
109-2-91	0.1976	0.9780	0.8649	0.6693	673,124.04	26,272,467.04	0.0187	0.7925
109-2-92	0.2034	0.9775	0.8604	0.6701	682,850.61	27,480,347.20	0.0188	0.5477
109-2-93	0.1710	0.9790	0.8751	0.6792	639,788.97	23,609,730.48	0.0184	0.8465
109-2-94	0.2031	0.9783	0.8675	0.6736	663,986.52	25,573,558.12	0.0185	0.5407
109-2-95	0.1955	0.9778	0.8638	0.6723	673,940.08	26,557,581.33	0.0186	0.6886
109-2-96	0.2201	0.9778	0.8639	0.6706	678,776.23	26,526,792.42	0.0186	0.5257
109-2-97	0.2931	0.9783	0.8706	0.6771	648,513.83	24,743,544.48	0.0192	0.8465
109-2-98	0.1880	0.9793	0.8770	0.6837	624,345.80	23,142,670.95	0.0184	0.8115
109-2-99	0.2079	0.9791	0.8723	0.6785	644,736.57	24,361,990.27	0.0178	0.9005
109-2-100	0.2335	0.9787	0.8718	0.6788	644,327.93	24,473,077.63	0.0181	0.9744
109-2-101	0.2335	0.9784	0.8698	0.6763	649,207.81	24,961,162.42	0.0183	0.7646
109-2-102	0.2300	0.9779	0.8645	0.6723	670,047.31	26,363,347.29	0.0184	0.7436
109-2-103	0.2425	0.9780	0.8675	0.6748	656,234.36	25,562,249.57	0.0185	0.8215
109-2-104	0.2263	0.9779	0.8651	0.6725	666,810.00	26,205,688.84	0.0183	0.7316
109-2-105	0.2314	0.9781	0.8651	0.6730	667,969.63	26,216,043.85	0.0183	0.8455
109-2-106	0.2405	0.9779	0.8658	0.6743	662,251.38	26,032,612.71	0.0184	0.7776
109-2-107	0.1984	0.9778	0.8633	0.6692	676,343.78	26,687,590.41	0.0182	0.7776
109-2-108	0.2132	0.9773	0.8596	0.6673	686,881.73	27,667,680.90	0.0183	0.9325
109-2-109	0.1997	0.9774	0.8609	0.6694	680,900.92	27,338,830.19	0.0182	0.7086
109-2-110	0.2053	0.9778	0.8622	0.6689	681,874.37	26,996,254.49	0.0180	0.8165
109-2-111	0.2334	0.9772	0.8588	0.6649	692,565.89	27,909,461.64	0.0177	0.6496
109-2-112	0.2061	0.9772	0.8602	0.6685	686,780.68	27,508,219.94	0.0185	0.6107
109-2-113	0.1872	0.9774	0.8612	0.6691	682,913.44	27,233,915.67	0.0194	0.6456
109-2-114	0.2532	0.9771	0.8590	0.6682	689,344.66	27,822,677.58	0.0192	0.6936
109-2-115	0.1496	0.9777	0.8653	0.6699	675,237.56	26,131,635.56	0.0176	0.6236
109-2-116	0.1571	0.9772	0.8620	0.6656	683,558.34	26,993,311.39	0.0179	1.0254

Template	CP-CP Diff	Pearson	Tanimoto	Min-Ratio	L1 Norm	Sq L2 Norm	Int-Ratio Var	Proc Time
109-2-117	0.1797	0.9776	0.8641	0.6723	671,584.88	26,462,576.02	0.0178	0.4447
109-2-118	0.2084	0.9771	0.8597	0.6678	690,816.13	27,630,505.09	0.0181	0.9694
109-2-119	0.1700	0.9774	0.8631	0.6713	674,725.35	26,719,139.64	0.0178	0.8295
109-2-120	0.2071	0.9773	0.8616	0.6699	679,964.42	27,103,813.62	0.0177	0.7566
109-2-121	0.2700	0.9770	0.8581	0.6666	695,855.29	28,070,239.14	0.0180	0.4338
109-2-122	0.2758	0.9767	0.8574	0.6678	695,691.55	28,250,602.68	0.0180	0.4647
109-2-123	0.2261	0.9775	0.8623	0.6701	681,475.06	26,935,633.43	0.0176	0.4877
109-2-124	0.1312	0.9781	0.8704	0.6750	656,811.97	24,795,152.21	0.0187	0.5917
109-2-125	0.2000	0.9768	0.8611	0.6699	683,366.22	27,210,917.73	0.0188	0.8155
109-2-126	0.1687	0.9766	0.8595	0.6661	692,447.82	27,650,017.66	0.0190	0.8115
109-2-127	0.1585	0.9769	0.8611	0.6680	683,703.10	27,203,981.12	0.0179	0.4607
109-2-128	0.1568	0.9764	0.8568	0.6634	701,492.75	28,383,995.10	0.0184	0.6456
109-2-129	0.1807	0.9767	0.8594	0.6664	692,987.61	27,662,110.46	0.0181	1.1753
109-2-130	0.1235	0.9774	0.8675	0.6737	660,264.82	25,511,766.94	0.0179	0.8475
109-2-131	0.1617	0.9771	0.8657	0.6717	667,638.58	25,973,508.78	0.0185	0.8545
109-2-132	0.0998	0.9762	0.8585	0.6652	693,940.79	27,884,952.38	0.0186	0.7296
109-2-133	0.1175	0.9767	0.8626	0.6691	677,610.37	26,768,747.24	0.0182	0.8515
109-2-134	0.1086	0.9765	0.8592	0.6662	691,274.29	27,712,103.94	0.0178	0.8225
109-2-135	0.1030	0.9759	0.8569	0.6622	699,907.61	28,311,388.07	0.0194	0.6506
109-2-136	0.1453	0.9768	0.8625	0.6713	677,623.87	26,823,159.96	0.0178	0.4737
109-2-137	0.1826	0.9766	0.8589	0.6664	691,452.65	27,794,580.47	0.0180	0.5147
109-2-138	0.1530	0.9768	0.8614	0.6695	679,933.23	27,124,626.41	0.0178	0.8575
109-2-139	0.2083	0.9761	0.8570	0.6631	697,195.06	28,306,886.24	0.0211	1.8420
109-2-140	0.0527	0.9776	0.8697	0.6761	658,753.07	24,919,729.75	0.0177	0.5647
109-2-141	0.0568	0.9771	0.8659	0.6746	664,171.96	25,898,960.92	0.0176	0.7356
109-2-142	0.0540	0.9771	0.8669	0.6753	657,545.55	25,647,116.94	0.0177	0.9355
109-2-143	0.0912	0.9765	0.8612	0.6708	682,434.80	27,138,652.28	0.0182	0.7196
109-2-144	0.2236	0.9773	0.8693	0.6788	648,549.80	25,000,333.09	0.0185	0.8685
109-2-145	0.1381	0.9773	0.8677	0.6757	657,195.13	25,450,403.25	0.0185	0.8305
109-2-146	0.0960	0.9768	0.8643	0.6707	667,071.85	26,307,141.50	0.0183	0.8935
109-2-147	0.0815	0.9771	0.8674	0.6791	651,054.06	25,513,247.73	0.0183	0.7946
109-2-148	0.0511	0.9770	0.8629	0.6723	672,018.43	26,728,351.31	0.0188	0.7106
109-2-149	0.1286	0.9769	0.8621	0.6733	672,915.42	26,945,564.48	0.0182	0.4817
109-2-150	1.4304	0.9802	0.9248	0.7518	442,689.54	12,098,316.68	0.0309	0.8055
109-2-151	1.1416	0.9266	0.8831	0.7402	452,095.37	15,477,984.15	0.1176	7.2849
109-2-152	3.2833	0.8836	0.8216	0.6485	623,902.40	24,334,532.38	0.1469	4.5154
109-2-153	3.2028	0.9381	0.8946	0.6496	528,217.95	14,707,069.15	0.1060	27.8482
109-2-154	2.9640	0.9518	0.9174	0.6750	442,223.89	9,928,467.12	0.1297	18.3176
109-2-155	1.7837	0.9717	0.9520	0.6979	349,581.73	6,113,663.32	0.0907	17.7829
109-2-156	2.4463	0.9766	0.9582	0.6937	333,273.59	5,464,037.07	0.0918	0.7916
109-2-157	2.7084	0.9777	0.9623	0.6933	325,956.55	4,685,832.21	0.1153	0.5367
109-2-158	2.5824	0.9616	0.9300	0.6878	380,026.51	8,193,219.54	0.1316	8.6771
109-2-159	4.0594	0.9677	0.9451	0.6768	371,565.43	6,688,413.65	0.1472	6.4723
109-2-160	3.7926	0.9701	0.9498	0.6804	359,970.57	6,349,583.85	0.1294	7.7846
109-2-161	3.5167	0.9707	0.9498	0.6799	364,898.96	6,496,509.04	0.1186	4.7753
109-2-162	3.4491	0.9716	0.9496	0.6784	370,339.61	6,674,497.31	0.1106	0.8845
109-2-163	3.4697	0.9720	0.9486	0.6762	377,341.99	6,908,500.27	0.1076	0.9355
109-2-164	3.4910	0.9719	0.9462	0.6696	394,145.61	7,354,888.00	0.0990	2.5086
109-2-165	3.4264	0.9718	0.9443	0.6659	404,862.54	7,711,529.85	0.0998	2.0678
109-2-166	2.7979	0.9687	0.9420	0.6692	403,592.12	7,889,935.49	0.0959	3.0752
109-2-167	3.7177	0.9728	0.9500	0.6800	370,118.12	6,690,794.79	0.0993	3.1032
109-2-168	3.9747	0.9710	0.9425	0.6616	411,417.51	7,975,347.02	0.0988	2.1987
109-2-169	3.7919	0.9722	0.9390	0.6537	433,868.63	8,744,200.08	0.0975	9.8274
109-2-170	3.7025	0.9717	0.9348	0.6466	453,775.07	9,505,759.65	0.0865	14.7876
109-2-171	3.7307	0.9813	0.9646	0.6863	333,129.69	4,663,447.62	0.0998	5.3819
109-2-172	3.9309	0.9716	0.9493	0.6695	380,371.33	6,685,048.62	0.1139	1.2903
109-2-173	3.6043	0.9721	0.9484	0.6698	382,825.20	6,945,035.50	0.1144	25.4345
109-2-174	3.5332	0.9714	0.9467	0.6675	389,109.59	7,218,678.04	0.1126	1.3312

Template	CP-CP Diff	Pearson	Tanimoto	Min-Ratio	L1 Norm	Sq L2 Norm	Int-Ratio Var	Proc Time
109-2-175	2.5924	0.9695	0.9378	0.6600	428,474.02	8,793,746.65	0.0938	0.6296
109-2-176	2.5578	0.9709	0.9342	0.6579	442,697.80	9,593,890.09	0.0867	1.3123
109-2-177	2.9833	0.9641	0.9303	0.6598	438,696.06	9,855,009.46	0.1094	0.6317
109-2-178	3.6925	0.9657	0.9307	0.6557	446,172.31	9,906,333.97	0.1164	0.6246
109-2-179	3.9010	0.9654	0.9296	0.6532	451,484.01	10,096,955.64	0.1103	1.3123
109-2-180	3.3463	0.9656	0.9287	0.6497	457,275.25	10,294,157.84	0.1020	1.4942
109-2-181	7.8654	0.9057	0.8494	0.6213	556,070.83	18,672,499.48	0.4075	3.6389
109-2-182	6.5447	0.9260	0.8713	0.6398	497,656.21	15,085,892.26	0.3102	5.5059
109-2-183	4.2701	0.9572	0.9291	0.6732	405,519.86	8,912,997.86	0.1728	1.6301
109-2-184	5.6732	0.9139	0.8612	0.6504	511,335.32	17,141,713.52	0.2547	1.8739
109-2-185	3.3176	0.9753	0.9563	0.7035	328,431.81	5,224,131.25	0.1124	14.3858
109-2-186	3.2500	0.9684	0.9470	0.6865	362,019.05	6,756,749.56	0.1221	3.0493
109-2-187	6.5742	0.9184	0.8629	0.6434	506,508.00	16,361,562.91	0.2934	5.0681
109-2-188	5.6131	0.9501	0.9181	0.6640	432,743.80	10,403,257.04	0.2045	1.9639
109-2-189	7.4210	0.8225	0.7345	0.6146	651,084.85	33,611,357.61	0.4330	3.2531
109-2-190	5.8420	0.9540	0.9238	0.6622	422,941.28	9,510,541.43	0.2142	8.5012
109-2-191	3.6464	0.8977	0.8396	0.6412	609,495.22	20,480,627.60	0.2668	6.5743
109-2-192	13.2381	0.6970	0.5865	0.4799	1,020,801.63	54,097,620.43	1.4943	4.5774
109-2-193	5.2403	0.8719	0.8015	0.5923	667,066.93	25,075,145.30	0.5349	2.1238
109-2-194	3.9862	0.9097	0.8560	0.6218	550,352.62	18,013,753.66	0.3130	1.1134
109-2-195	4.6708	0.9324	0.8901	0.6410	496,936.85	13,771,678.91	0.2221	0.8555
109-2-196	6.7538	0.7742	0.6682	0.6135	678,877.29	41,491,398.49	0.6116	1.5751
109-2-197	5.9931	0.8835	0.8197	0.5950	652,185.13	23,642,337.08	0.2357	1.7190
109-2-198	6.4901	0.9057	0.8425	0.5853	620,923.48	18,864,376.04	0.5466	4.2516
109-2-199	6.2919	0.9191	0.8701	0.5899	599,178.69	16,491,721.02	0.3597	12.2710
109-2-200	9.0868	0.8197	0.7383	0.5442	819,082.85	35,644,135.89	0.6335	3.9937
109-2-201	4.0434	0.9089	0.8513	0.6225	547,426.71	17,981,789.70	0.5154	0.7526
109-2-202	0.1108	0.9733	0.8874	0.6661	393,309.59	11,457,981.18	0.4623	8.3042
109-2-203	1.9841	0.8613	0.7526	0.4928	648,475.61	28,205,542.64	1.9291	1.4092
109-2-204	0.0301	0.9531	0.9229	0.6500	405,608.11	9,999,153.37	0.8211	2.4191
109-2-205	0.7681	0.9598	0.9133	0.6607	445,762.04	13,013,642.83	0.6894	0.6007
109-2-206	1.3122	0.9604	0.8965	0.6739	492,883.37	16,789,312.53	0.5656	4.4665
109-2-207	0.8588	0.9873	0.9765	0.7243	243,082.18	3,011,510.48	0.4773	0.5617
109-2-208	1.0505	0.9803	0.9613	0.6814	303,028.64	5,163,251.80	1.9868	1.5831
109-2-209	1.1634	0.9841	0.9496	0.7329	343,947.70	7,476,011.10	0.4455	1.0804
109-2-210	1.0412	0.9832	0.9449	0.7254	360,856.86	8,310,767.55	0.4469	2.7103
109-2-211	1.0301	0.9807	0.9327	0.7057	411,073.89	10,514,166.04	0.5272	2.6126
109-2-212	0.8183	0.9810	0.9354	0.7050	403,991.32	10,011,088.34	0.4971	0.4118
109-2-213	0.5002	0.9325	0.8839	0.6472	481,097.92	16,603,483.46	0.7937	11.4588
109-2-214	0.7043	0.9839	0.9595	0.7166	314,775.33	5,718,354.36	0.5245	1.4012
109-2-215	0.8590	0.9629	0.8904	0.6890	509,799.40	18,428,152.15	0.4916	0.5902
109-2-216	1.0509	0.9854	0.9637	0.7353	283,181.79	5,061,066.36	0.4479	1.3138
109-2-217	1.1104	0.9863	0.9584	0.7463	301,995.99	6,017,154.21	0.3809	0.7985
109-2-218	1.1149	0.9853	0.9488	0.7400	340,616.69	7,690,280.54	0.3416	1.8709
109-2-219	1.0912	0.9837	0.9393	0.7334	376,008.23	9,405,414.10	0.3486	1.3124
109-2-220	1.0822	0.9832	0.9369	0.7282	387,832.45	9,832,182.12	0.4118	1.8955
109-2-221	1.0622	0.9810	0.9260	0.7202	424,733.09	11,901,814.69	0.3588	0.8355
109-2-222	1.0463	0.9826	0.9300	0.7148	418,556.98	11,181,041.48	0.3727	1.7780
109-2-223	0.8551	0.9825	0.9242	0.7081	442,918.52	12,345,753.09	0.3996	0.4178
109-2-224	0.8715	0.9813	0.9188	0.7133	463,139.74	13,421,744.32	0.3307	1.1304
109-2-225	0.7578	0.9801	0.9274	0.7098	427,990.64	11,542,908.18	0.8333	29.1255
109-2-226	0.8425	0.9839	0.9414	0.7297	374,161.11	9,011,502.79	0.3639	1.0035
109-2-227	0.9751	0.9840	0.9381	0.7316	383,529.14	9,641,442.77	0.3290	19.8965
109-2-228	1.0215	0.9832	0.9291	0.7271	414,263.03	11,393,399.16	0.3144	38.7839
109-2-229	1.0499	0.9828	0.9250	0.7228	428,538.78	12,202,600.11	0.3105	13.5126
109-2-230	0.6993	0.9822	0.9313	0.7350	389,761.55	10,890,384.41	0.3158	0.5017
109-2-231	0.7445	0.9833	0.9338	0.7355	383,312.10	10,444,120.87	0.3064	0.5767
109-2-232	0.5358	0.9817	0.9323	0.7167	405,416.92	10,670,076.21	0.3434	0.4787

Template	CP-CP Diff	Pearson	Tanimoto	Min-Ratio	L1 Norm	Sq L2 Norm	Int-Ratio Var	Proc Time
109-2-233	0.6253	0.9806	0.9332	0.7156	402,532.48	10,430,281.80	0.3434	0.3348
109-2-234	0.6769	0.9819	0.9484	0.7163	351,690.11	7,595,047.58	1.0606	0.4038
109-2-235	0.7516	0.9824	0.9424	0.7235	367,532.45	8,740,055.45	0.4735	0.6406
109-2-236	0.7537	0.9821	0.9358	0.7242	389,655.02	9,994,200.16	0.3623	0.5267
109-2-237	0.8588	0.9813	0.9253	0.7211	426,142.91	12,065,557.56	0.3344	0.4417
109-2-238	0.8496	0.9811	0.9206	0.7196	443,229.31	13,026,332.23	0.3213	0.5447
109-2-239	0.5615	0.9793	0.9193	0.7048	454,296.21	13,178,086.90	0.3707	0.3768
109-2-240	0.5436	0.9780	0.9135	0.6997	474,052.22	14,355,969.15	0.3628	0.4118
109-2-241	0.8745	0.9812	0.9254	0.7034	434,009.81	12,030,182.05	0.3559	0.9285
109-2-242	0.7867	0.9816	0.9198	0.7077	452,664.62	13,230,067.54	0.3090	0.8505
109-2-243	0.8245	0.9814	0.9162	0.7071	471,657.56	14,000,203.17	0.2904	0.3798
109-2-244	0.8345	0.9810	0.9112	0.7047	489,928.68	15,056,888.58	0.2821	0.3566
109-2-245	0.8833	0.9794	0.9005	0.6987	521,921.88	17,368,288.32	0.2829	0.4158
109-2-246	0.8624	0.9803	0.9108	0.7078	482,896.33	15,102,029.28	0.2881	0.5457
109-2-247	0.7810	0.8840	0.8188	0.6867	511,713.55	22,817,530.44	0.5596	0.6027
109-2-248	0.4029	0.9471	0.9095	0.6570	436,270.68	12,401,863.42	0.5973	4.2456
109-2-249	0.6181	0.9818	0.9629	0.6684	299,369.94	4,301,015.71	0.5557	2.3272
109-2-250	0.3359	0.9868	0.9759	0.7344	237,770.90	3,062,046.60	0.3293	12.7042
109-2-251	0.3321	0.9873	0.9701	0.7485	254,110.27	4,069,329.04	0.3002	2.3367
109-2-252	0.3873	0.9873	0.9655	0.7593	264,555.75	4,821,947.44	0.2419	1.8020
109-2-253	0.4549	0.9870	0.9598	0.7615	283,747.99	5,782,514.29	0.2330	1.7200
109-2-254	0.4140	0.9870	0.9561	0.7625	297,504.56	6,435,188.16	0.2306	1.2803
109-2-255	0.2866	0.9880	0.9612	0.7628	287,371.68	5,589,643.35	0.2284	5.3342
109-2-256	0.3208	0.9865	0.9572	0.7627	296,680.84	6,228,702.81	0.2454	44.6619
109-2-257	0.3504	0.9859	0.9473	0.7627	331,096.51	7,997,641.40	0.2274	4.3213
109-2-258	0.6898	0.9810	0.9341	0.6874	410,936.13	10,238,106.77	1.3059	0.5170
109-2-259	0.5559	0.9848	0.9357	0.7427	384,539.83	10,149,671.93	0.2710	0.4083
109-2-260	0.5677	0.9829	0.9224	0.7386	428,041.04	12,756,783.76	0.2525	0.3728
109-2-261	0.4551	0.9827	0.9195	0.7352	441,491.91	13,353,105.84	0.2440	0.3728
109-2-262	0.5823	0.9820	0.9147	0.7298	458,139.40	14,341,651.08	0.2495	0.3573
109-2-263	0.6435	0.9835	0.9210	0.7387	433,814.07	13,091,032.14	0.2369	0.3588
109-2-264	0.6310	0.9823	0.9131	0.7368	458,203.45	14,710,205.93	0.2250	0.3768
109-2-265	0.5945	0.9824	0.9139	0.7370	457,633.62	14,556,929.45	0.2248	0.4108
109-2-266	0.5760	0.9832	0.9316	0.7401	400,395.14	10,881,386.56	0.2352	0.4368
109-2-267	0.5906	0.9828	0.9242	0.7419	423,914.77	12,383,351.60	0.2118	0.4078
109-2-268	0.6074	0.9829	0.9234	0.7441	425,094.94	12,542,388.78	0.2119	0.5117
109-2-269	0.5615	0.9825	0.9201	0.7406	437,872.12	13,213,568.53	0.2166	0.3580
109-2-270	0.5989	0.9823	0.9174	0.7389	445,572.87	13,777,164.99	0.2042	0.3588
109-2-271	0.5793	0.9815	0.9121	0.7361	462,622.60	14,880,049.22	0.2041	0.3668
109-2-272	0.5935	0.9811	0.9088	0.7360	473,490.06	15,600,132.91	0.2026	0.3700
109-2-273	0.5012	0.9829	0.9367	0.7574	374,030.06	9,861,505.08	0.2007	0.4395
109-2-274	0.5238	0.9839	0.9289	0.7473	412,133.19	11,471,299.39	0.1870	0.5451
109-2-275	0.5353	0.9822	0.9157	0.7408	456,168.31	14,143,743.76	0.1875	1.8929
109-2-276	0.5854	0.9832	0.9169	0.7412	452,647.96	13,947,883.17	0.1898	0.4200
109-2-277	0.6543	0.9833	0.9161	0.7397	453,953.36	14,133,047.57	0.1908	0.4058
109-2-278	0.6479	0.9819	0.9076	0.7363	480,402.04	15,915,639.20	0.1829	0.4088
109-2-279	0.6466	0.9813	0.9025	0.7335	496,323.81	17,038,751.52	0.1787	0.4602
109-2-280	0.6208	0.9819	0.9045	0.7344	490,892.03	16,623,143.60	0.1847	0.4068
109-2-281	0.6268	0.9809	0.8989	0.7321	508,296.72	17,865,931.90	0.1818	28.3385